Transactions of the ASME®

Transactions of the ASME, Journal of Turbomachinery (ISSN 0889-504X) is published quarterly (Jan., Apr., July, Oct.) by The American Society of Mechanical Engineers, Three Park Avenue, New York, NY 10016. Periodicals postage paid at New York, NY and additional mailing offices. POSTMASTER: Send address changes to Transactions of the ASME, Journal of Turbomachinery, c/o THE AMERICAN SOCIETY OF MECHANICAL ENGINEERS, 22 Law Drive, Box 2300, Fairfield, NJ 07007-2300.
CHANGES OF ADDRESS must be received at Society headquarters seven weeks before they are to be effective. Please send old label and new address.
STATEMENT from By-Laws. The Society shall not be responsible for statements or opinions advanced in papers or ... printed in its publications (B7.1, Par. 3).

INDEXED by Applied Mechanics Reviews and Engineering Information, Inc. Canadian Goods & Services Tax Registration #126148048

Journal of Turbomachinery

Published Quarterly by The American Society of Mechanical Engineers

VOLUME 124 • NUMBER 3 • JULY 2002

TECHNICAL PAPERS

(**Contents continued on inside back cover**)

This journal is printed on acid-free paper, which exceeds the ANSI Z39.48-1992 specification for permanence of paper and library materials. ♾™
♻ 85% recycled content, including 10% post-consumer fibers.

Journal of Turbomachinery **Volume 124, Number 3** **JULY 2002**

Axial Compressor Aerodesign Evolution at General Electric

Leroy H. Smith, Jr.
Fellow ASME,
Consultant,
GE Aircraft Engines,
Cincinnati, OH 45215
e-mail: leroy.smith@ae.ge.com

This paper traces the origins of the GE Design System and how it has evolved from early methods to underlie and supplement present CFD methods, which are not themselves discussed herein. The two main elements of the detailed aero design process are vector diagram establishment and airfoil design. Their evolution is examined, and examples of how they were used to design some early GE compressors of interest are given. By the late 1950s, some transonic airfoil shapes were being custom tailored using internal blade station data from more complete radial equilibrium solutions. In the 1960s, rules for shaping transonic passages were established, and by the 1970s, custom tailoring was done for subsonic blading as well. The preliminary design layout process for a new compressor is described. It involves selecting an annulus shape and blading overall proportions that will allow a successful detailed design to follow. This requires establishment of stage loading limits that permit stall-free operation, and an efficiency potential prediction method for state-of-the-art blading. As design methods evolved, the newer approaches were calibrated with data-match experience, a process that is expected to always be needed. [DOI: 10.1115/1.1486219]

1 Introduction

It was in the 1930s that practical axial flow compressors first were realized. Keller [1] in Switzerland employed airfoil theory as a design basis. The first British compressor, Anne, ran in 1938; Constant [2]. Work in Germany, unknown to the outside world at the time, was well underway. NACA was developing an axial flow compressor in Cleveland in 1940.

General Electric interest started in 1939, and in 1941 an Army contract was awarded to build a turboprop engine with an axial flow compressor. This was the TG100 (T31). This engine ran and was ultimately flown, but the real cornerstone of General Electric compressor technology in the early days was the TG180, started in 1943 at Schenectady. Its 11 stages delivered a pressure ratio of 4.0 with a polytropic efficiency in the high 80s.

This story is told from the point of view of a compressor aerodesigner. Several other very important technologies, e.g., aeromechanics and materials development, are outside the scope of this work. Also excluded are the aero methods used during the compressor optimization process to rematch stages and to derive optimum variable stator schedules, even though it is the same aero design personnel who do this work.

First, the aerodesigner's role is outlined. Then, the methods that have been used to design GE compressors are presented, and some interesting results are pointed out along the way. The narrative ends in the early 1980s when CFD began to be a significant design tool, but some timeless advice is given in Concluding Remarks.

2 Compressor Aerodesigner's Role

During the preliminary design phase for a new engine, several candidate compressor configurations are usually evaluated in an attempt to arrive at the best overall engine architecture. Although the compressor is only one of many components being optimized, it is a particularly important one because failure to provide adequate axial length and speed capability in the engine can lead to later stall problems that turn into engine development disasters. In the interest of cost and weight saving, the preliminary design chief will sometimes try to pressure the aero designer into overoptimistic commitments. The best defense against such pressure is the use of a rational *stall prediction* method that has been calibrated against known past experience. If some parameter goes beyond past experience, then early demonstration tests and a backup plan need to be in place.

The efficiency potentials of the several preliminary design candidates also need to be identified. Efficiency affects engine performance in two ways. In addition to its obvious direct effect on performance, inefficiency also reduces cycle pressure ratio because compressor exit temperature is limited by available materials' capabilities. So a rational *efficiency potential prediction* method is also needed. Later, when the compressor is tested, the efficiency potential calculation serves as a useful criterion for success.

The designer's main role is to successfully execute the design. This means specifying blading and annulus shapes in detail. There are two main phases to this work, although they overlap in time. The first is *vector diagram design*, which means distributing circumferentially-averaged properties radially and axially through the machine at the aerodynamic design point. The annulus shape is largely specified here, and hub and tip loadings are balanced so that neither blade end precipitates stall prematurely. The second phase is *detailed blade design*.

In the following sections we will take up how these four topics have been handled at General Electric, but in an order more suitable to historical explanations.

3 Vector Diagram Determination

Knowledge of the relationship between energy exchange and the change in tangential velocity across a rotor dates back to at least the 19th century. In early compressor designs, it was usually assumed that all streamlines should have the same energy added to them, but the designer could choose how to radially distribute the tangential velocity ahead of each rotor. Having done this, it was then necessary to find the corresponding radial distributions of axial velocity so that the velocity vectors and flow angles needed to shape the blades could be determined. The level of the axial velocity is known at each axial station from the preliminary design, but its radial distribution is governed by a force and momentum balance relationship that is often called the radial equilibrium equation. When meridional streamline slope and curvature effects are ignored, the term ''simple radial equilibrium'' is used. If free-vortex tangential velocity distributions are employed, simple radial equilibrium yields a radially constant axial velocity, which in turn may be compatible with small meridional streamline

Contributed by the International Gas Turbine Institute for publication in the JOURNAL OF TURBOMACHINERY. Manuscript received by the IGTI, November 14, 2001. revised manuscript received April 2, 2002. Associate Editor: C. Koch.

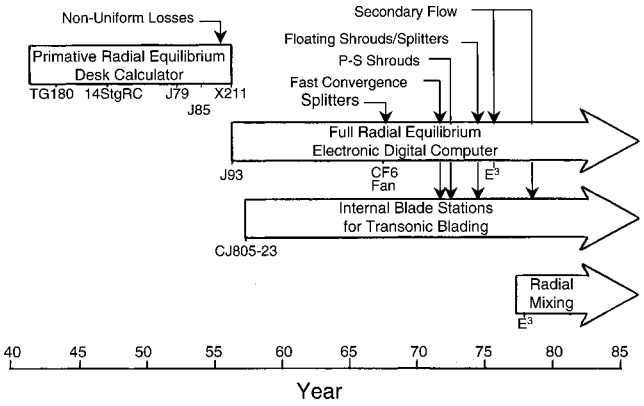

Fig. 1 Compressor vector diagram calculation methods

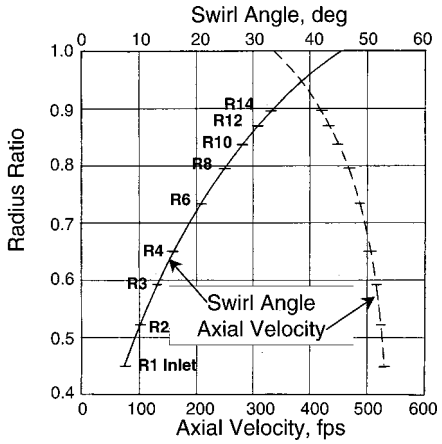

Fig. 2 14 Stage Research Compressor rotor inlet swirl and axial velocity distributions

slopes and curvatures, thus justifying its use. So radially constant axial velocity was often employed for free-vortex designs.

Figure 1 outlines General Electric methods. Only certain noteworthy compressors are identified, usually the first to use a method. The 11-stage *TG180* had an inlet radius ratio of 0.69, and its inlet guide vanes provided 36 deg pre-swirl, radially constant. This was transitioned to a free-vortex design by stage four. The casing was cylindrical, as was the hub aft of stage 8. I can find no record of what the axial velocity distribution in the first 3 stages was assumed to be when the blades were designed in 1943, but later analyses used simple radial equilibrium at rotor inlets. Total pressure and total temperature were assumed to be radially constant.

The high efficiency of the TG180 led to its use for many years in Schenectady products. Four stages were added on the back in an extension of the cylindrical annulus for higher pressure ratio, and then the inlet guide vanes were opened 12 deg to increase the flow and the pressure ratio to 6.6. Later, the inlet guide vanes were opened still further in the *Frame Size 3* series of engines. And in 1999, the writer directed a blading redesign for Nuovo Pignone using modern aircraft engine methods while keeping the same 15-stage annulus to achieve a pressure ratio of 8.1 with a polytropic efficiency of 91% for upgrades of some of the many Frame Size 3 machines in the field.

In 1946 the TG180, which had seen aircraft engine use as the J35, was zero staged and its blades opened and mechnically tweaked to produce the *J47* aircraft engine, which was mass-produced. The zero stage had a 5% larger casing radius at inlet and a radius ratio of 0.63. The inlet guide vanes provided a pre-swirl of 34 deg at the tip and 17 deg at the hub, with uncertain design axial velocity, but full radial equilibrium calculations done in 1957 showed the axial velocity varied from 402 fps at the tip to 500 at the hub. The overall pressure ratio was 5.0.

In 1948 the J53 project was formed to work on engines with higher flows and pressure ratios. As part of that effort, work on a 14-stage research compressor that had been designed in 1947 was started. This was a landmark compressor for General Electric for two reasons: it had a very high efficiency, and it was the vehicle used for demonstrating the great benefit of variable stators. Its vector diagram determination was also noteworthy. In those days the fear of transonic Mach numbers led to the use of high pre-swirl ahead of rotor tips. In the 14 Stage Research Compressor, the inlet guide vanes were designed to give a tangential velocity at the tip of 31% of the rotor tip speed, and tangential velocity was specified to be proportional to radius squared at the lower radii. Simple radial equilibrium was used to calculate the axial velocities. The resulting swirl angle and axial velocity distributions are shown on *Fig. 2*. Then, to complete the rest of the compressor design, these distributions were held fixed at all rotor inlets. The casing was cylindrical, and as the density increased through the compressor, these distributions were simply chopped off at the hub radius as needed to satisfy continuity. Furthermore, this same axial velocity distribution was assumed to exist at rotor exit stations. Although it must have been known that the radial gradient of axial velocity should be more severe at rotor exits, this was ignored, it being reasoned that in a high-aspect-ratio compressor like this, radial mass flow shifts could not be large, and meridional streamline curvature effects that were being ignored would provide a compensating contribution to the radial static pressure gradient. Total pressures and temperatures were again assumed to be radially constant. When testing was start in 1949, the compressor mass flow was found to be 5.5% lower than design because of an error in application of Weinig's deviation angle method (see Section 4.1), but the polytropic efficiency achieved was over 92%. The first 12 stages of this design, but with the rotors staggered open to get back the flow, were used for the *J73* engine compressor, which had a pressure ratio of seven and used variable inlet guide vanes. Also, to minimize vibration, shrouds were added to the stators, with sealing that was probably inadequate. As a result of these changes, the J73 compressor's polytropic efficiency was only 87%.

In 1950, the compressor for the J53 engine was designed using a radial equilibrium variant, created by Messrs. Russ Hall and Bill Cornell, called the ''mean swirl method.'' Here, radially constant total pressure and total temperature were still assumed, but except for the inlet guide vanes, the simple radial equilibrium equation was applied using absolute tangential velocities that were the averages of those entering and leaving a blade row. This yielded a proper mean axial velocity radial gradient because the oscillating meridional streamline curvatures are nearly zero midway through a row. But this same gradient was also applied between blade rows to get the vector diagrams for blading design, it again being argued that aspect ratios were high enough to preclude much axial velocity profile oscillation.

The *J53* design was historically interesting because of its extreme departure from free-vortex flow. *Figure 3* gives rotor inlet absolute swirl angles and axial velocities. In the front stages the distributions are as might be expected, but why the designer chose to use such extreme stator twists in the rear stages is unclear. The rotor inlet Mach numbers were everywhere less than 0.78, but after rotor 2 they were higher at the hub than at the tip, which does not now seem like a good idea. But the fact that the J53 achieved its design airflow and pressure ratio with reasonable efficiency (88.5% polytropic peak) proved that designers could safely depart from free-vortex designs as much as they wished. Several J53 engines were built, but this engine did not go into production.

The compressor for the prototype of the *J79* engine was designed in 1952, also using the mean swirl method, but with much

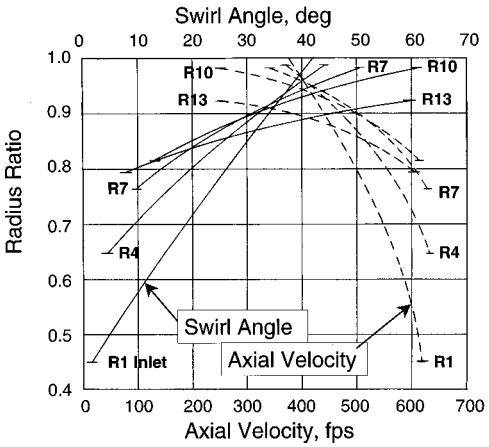

Fig. 3 J53 Compressor rotor inlet swirl and axial velocity distributions

milder radial gradients; the mean swirl angle was radially constant. This compressor was laid out to have a very low frontal area (its inlet radius ratio was 0.35), and a high axial Mach number was used. To keep blading Mach numbers below 0.85, a rather low tip speed (950 fps=290 m/s) was used. This led to very low hub blade speeds in the first few stages. The design pressure ratio was 12, and variable stators were specified to control the flow into the first seven of the compressor's 17 stages. The engine was designed for Mach 2 flight, which meant that the compressor needed to deliver a relatively high mass flow at 85% corrected speed, so it had been intended that the variable stators remain at their design settings down to that speed. Tests quickly showed that, even though the design point was achieved with some margin, the flow and pressure ratio at 85% speed were too low because of hub stall in the front stages. This problem was easily fixed in the second build by twisting open the variable vanes to increase dynamic pressures, thus reducing aerodynamic loadings toward the inner radii. This moved the design toward one with more rotational flow and radially nonuniform total pressure, high toward the hub. The J79 went on to a long production run with only minor further compressor blading aerodynamic tweaks. In its commercial version, the CJ805, it operated with a pressure ratio of 13 and a cruise polytropic efficiency of 89%.

The *J85* was General Electric's first real attempt to employ NACA transonic compressor technology. Being a free-vortex design, it was first laid out assuming radially constant axial velocity. It had a cylindrical casing, and its relatively high aspect ratios and high stage pressure ratios led to rather large hub slopes. Then-current blade design methods did not adequately recognize this (nor quite how to handle the transonic tip Mach numbers), and as a result, the total pressure was high at the tip, which starved the hub and led to an unsatisfactory stall line. After much development trimming and the addition of stages, two satisfactory models were achieved and produced.

The *X211* and *J93* were two different large engines with very similar compressor aerodynamics. The writer had been hired by Mr. Dick Novak in 1954 to formulate an improved vector diagram determination method, and a year later we had a code that recognized radially varying properties and meridional streamline curvatures running on an IBM 701 computer. As Fig. 1 shows, the J93 was designed with this code, but the blading was not much different from that of the X211. Both compressors had stall problems, but for reasons not much related to their vector diagrams. This will be discussed in Section 5.1.

The first design that employed custom tailored transonic blading was the aft fan for the *CJ805-23* commercial engine. This design, done in 1957, used the new radial equilibrium computer code with several stations inside each blade row. As explained by Wright and Novak [3], work input and losses were distributed radially and axially throughout the blade domains, and the blade meanline shapes followed the flow direction with blending to incidence and deviation angles at the edges. For this first through-blade design, radial blade force terms were not yet included in the radial equilibrium equation, but blade thickness blockage was accounted for. All terms were included by 1958; Smith [4].

Flow splitter modeling capability was added in 1967, and used to design the island over the quarter stage in the CF6 fan; Smith [5]. Part-span shrouds were modeled as ring boundaries in 1973. In 1975 an inverse design capability for part-span shrouds was added. With it the designer could input a radial distance between twin streamlines to represent shroud thickness and shroud wake displacement. The resulting ''limp body'' shroud shape has no radial force on it.

The acronym CAFD was given to the radial equilibrium code, standing for Compressor Axisymmetric Flow Determination. Although this acronym is still used, its meaning was changed in 1964 to represent Circumferential Average Flow Determination. There were two reasons for this change: 1) turbine designers were by then also using this code, and 2) the flow in a real turbomachine is anything but axisymmetric; the argument sometimes used that the solution applied to an equivalent machine with an infinite number of infinitely thin blades was not physically appealing, as was pointed out by a revered colleague, Hans Kraft. So the equations were rederived by taking circumferential averages of the three-dimensional equations, and some leftover Reynolds-stress-type terms were identified and shown to have only a small effect on radial equilibrium for a typical transonic compressor rotor; Smith [4].

During the 1960s, when data-match calculations were being done for multistage compressors using CAFD, it was noticed that unreasonable spanwise distributions of loss were needed after stage 3 or 4 to match the measured radial distributions of total temperature. Higher loss coefficients near mid passage than near the endwalls were often implied. This strongly suggested that some of the higher temperature fluid near the endwalls was being convected to midpassage by secondary flows. To model this, simplified secondary flow and empirically calibrated mixing calculations were added to CAFD in 1977; Adkins and Smith [6]. This version, named CAFMIX, was widely used for design and analysis until the mid 1990s. Improved loss and blockage modules were then added to give CAFMIX 2, which is still in use. A perspective on mixing mechanisms was given by Wisler, Bauer, Okiishi and numerous discussors [7].

4 Compressor Blading Design

4.1 Design of Series Airfoils. By ''series'' we mean that a standard thickness distribution is placed around a standard meanline shape. At GE, a modified NACA 65-Series thickness distribution with a circular arc meanline was almost always used. Frequently, to reduce manufacturing cost, two or more successive blade rows were made from the same forging with tips clipped and roots staggered appropriately. For example, for the J79 there were eight forgings for the 17 rotors and 10 forgings for the 20 stators. This ''grouping'' was no longer possible when the blading was designed to recognize higher losses at the endwalls.

Figure 4 gives a chronology of the methods used. For the *TG180*, all hub solidities were close to unity and chords were radially constant. The vector diagrams had been selected to give rotor hub lift coefficients based on the vector mean velocity of 0.84. Rotors from stage 7 aft and all stators had radially constant cambers and thicknesses, but were twisted to give the lift coefficients implied by the vector diagrams. The exact method used is unknown to this writer, but it likely involved an angle-of-attack between the airfoil's zero-lift direction and the vector mean velocity, with lift-curve slope obtained from Weinig's flat-plate cascade theory.

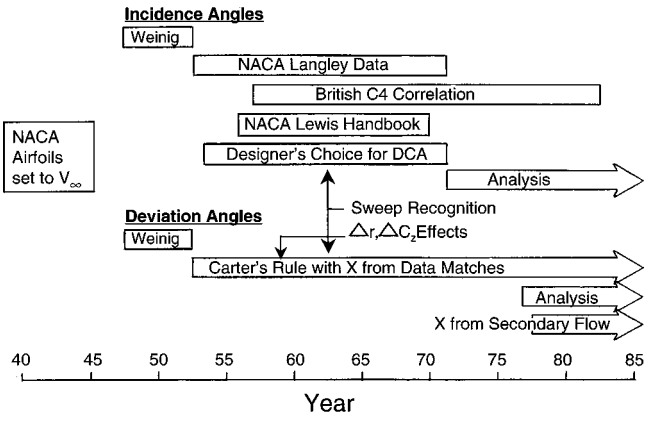

Fig. 4 Methods used for design of series airfoils

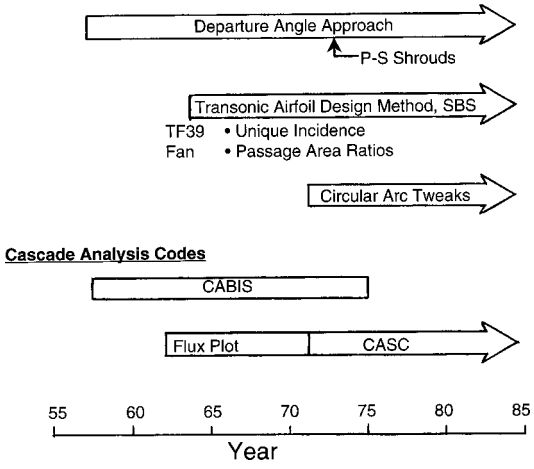

Fig. 5 Airfoil custom tailoring methods

After World War II, Weinig himself came to work for GE Aircraft Engines and instructed designers to use his theory derived for thin circular-arc profiles with small camber; Weinig [8]. This gave a deviation angle and an equal negative incidence angle for incompressible flow. In application, the actual tangential velocity change was increased by 15% before applying this inviscid method, and the Prandtl-Glauert compressibility correction was applied using the inlet and exit Mach numbers.

Starting in 1954, correlations of the NACA Langley low-speed cascade data were used for incidence selection for subsonic stages. This required that the NACA A_{10} meanline, which has infinite curvature at the edges, had to be somehow related to our circular arcs. This was done, but the unfortunate NACA A_{10} choice prevented use of these data for deviation angles. The extensive Langley data set was modeled by GE and others to give curves of loss and deviation angle change versus incidence. Mach number effect adjustments were included, and the resulting module was added to the CAFD procedure for compressor map prediction, but comparison with compressor test data showed it to be generally unsatisfactory and unreliable for predicting stall.

The NACA Lewis Lab work on transonic rotors in the early 1950s led to adoption of double-circular-arc (DCA) airfoils for a whole blade when tip Mach numbers were above about 0.85. GE designers were guided by NACA experience for incidence selection, and 2 deg was often used. Choke checks were made, as had always been done. It wasn't appreciated until much later that these airfoils were poor for rotor hub duty; losses generated there often showed up at higher radii.

In 1954, GE Aircraft Engines began using Carter's Rule as a basis for deviation angle selection. An empirical adjustment, X, was employed; often X was around 2 deg. It was recognized early that X and the blockage used when determining the vector diagrams were not independent parameters. Until quite recently (after the period covered by this paper) blockage in the multistage environment was usually set based on what had been used in previous designs, and X values were obtained from data-match calculations of test data from those designs and others.

By 1959 adjustments for radius change and axial velocity change were being made; Klapproth [9]. Most earlier designs were done on cylinders, with air exit angles being extrapolated into hubs and casings when necessary; and often the coordinates calculated on cylinders were used on planes for blade manufacture. Slightly later, designs were done by cutting the blades along axisymmetric streamsurfaces, but viewing each cut by looking parallel to the blade axis, which was often a radial line, as recommended by Smith and Yeh [10]. Taken together, these considerations largely explained why many rotors had produced less total pressure rise at the hub than their designers had intended.

When a secondary flow calculation module was added to CAFD in 1977, many of the spanwise variations of X that had been found in data matches could be calculated. The concept of designing a blade to a smooth primary flow exit angle distribution, and using calculated secondary flows to yield the angles used in CAFD, was established at that time and has been used at GE ever since.

4.2 Custom Tailored Airfoils. Methods that have been used are shown on *Fig. 5*.

Departure angle is defined on *Fig. 6*. With CAFD solutions now having internal blade stations, how the blade meanline angle departs from the circumferential-average flow angle could be examined. Generic departure angle distributions can be deduced from cascade analyses or tests for different cascade types and loading distributions, and these will then yield the blade meanline shape for a new design. This approach was suggested to the writer by Wislicenus in the early 1950s; Wislicenus [11]. This is not an entirely satisfactory approach because generic distributions are not always known, but departure angle examination is useful because it at least provides a consistency check on blade shapes and input loading distributions that have been arrived at by other means.

One good application of the departure angle approach is in the design of blades that have part-span shrouds. It is desired that the shroud disrupt the blade loading distribution as little as possible, but the meridional flow is strongly affected by the shroud blockage. Contours of circumferential-average meridional Mach number are shown on *Fig. 7* for a blade candidate designed in 1974 for the YJ101 Low Pressure Compressor. With the smooth distribution of tangential velocity employed consistent with smooth loading, the high meridional velocities near the shroud caused large local angle variations. With the same departure angles employed

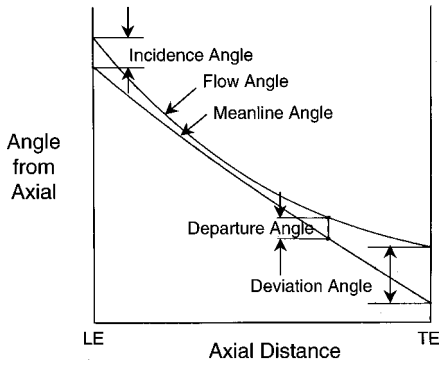

Fig. 6 Departure angle definition

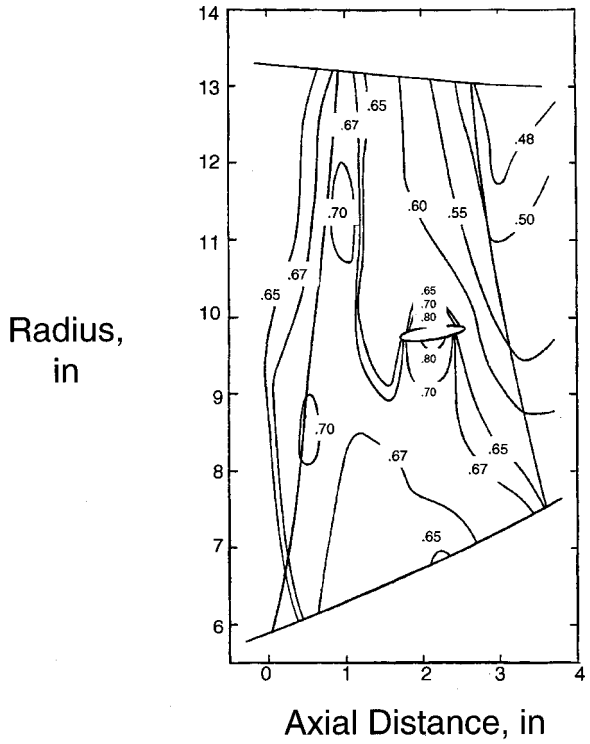

Fig. 7 Circumferential-average meridional mach numbers in transonic rotor. Note overspeed at part-span shroud.

for all streamlines in the shroud vicinity, the blade meanline angle trend follows the flow angle, giving the blade shapes shown on *Fig. 8*. Tests of this blade showed that its shroud loss was lower than that of an uncontoured baseline blade.

The Transonic Airfoil Design Method called out on Fig. 5 was codified in 1964 during development of the TF39 Fan outer panel, although Jack Klapproth and others had used similar concepts earlier. SBS stands for Supersonic Blade Sections. It allows a designer to specify certain important parameters when designing a blade shape. *Figure 9* shows blades cut along a CAFD axisymmetric streamsurface. The free-flow streamline is the path that a particle would take if there were no blades in the annulus but the CAFD lamina thickness distribution existed. This is a useful reference, as it could be used for the suction surface of a thin blade with no boundary layer on it. The $\hat{i}$ defined on Fig. 9 has a small positive value to allow for a finite edge thickness and some blade boundary layer. A negative $\hat{i}$ is not possible because then compression waves would be sent forward that would change the net angular momentum of the oncoming flow. A positive $\hat{i}$ is possible because the angular momentum change from the expansion waves

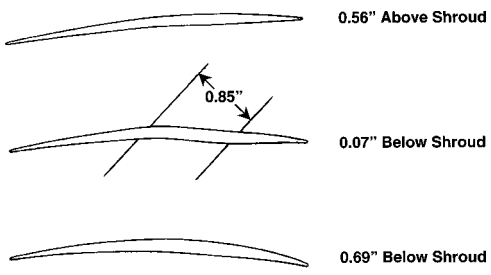

Fig. 8 Blade contoured at shroud to match circumferential-average flow angles

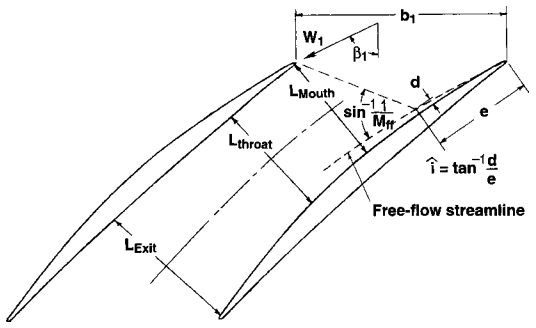

Fig. 9 Projected streamsurface geometry showing free-flow streamline and key area locations

would be counterbalanced by the flow behind a shock standing ahead of the adjacent blade, but this is usually undesirable at the design point.

For transonic flows, one-dimensional area ratios are very important for establishing the design flow and controlling off-design behavior. Relevant areas (see Fig. 9) are the capture area (related to the inlet flow angle and the spacing), and the areas at the passage mouth, throat, and exit. The blade shapes shown on Fig. 9 are generated from user input departure angles at the edges and several internal stations, together with a thickness distribution. The passage widths are multiplied by the CAFD lamina thickness to get the areas. In the case of a rotor with changing streamline radius, the ideal relative total pressure changes along a streamline, and this affects the critical flow area.

Throat area ratios for a typical design are shown on *Fig. 10*. Each of the circles represents a design streamline. The lowest curve is the isentropic relationship for A^*/A versus M for a gas with $\gamma=1.4$. Zero margin is arbitrarily defined assuming a loss caused by a normal shock at M_1. The denominator in the ordinate label accounts for the radius change.

Selection of an appropriate throat area ratio depends on more than just assuring that there is enough margin to avoid choking. On *Fig. 11* we examine what happens to one representative streamline at off-design conditions. As speed is increased, the $\hat{i}$ limit will keep β_1, and hence A_1, approximately constant, and the throat area will be larger than necessary to pass the flow. This will lead to high losses because either 1) the flow in the throat will be supersonic followed by high shock losses, or 2) a separation zone will occur at the throat followed by large mixing losses. But if a smaller design throat area is employed to minimize these losses, then when speed is reduced, the incidence will have to increase and a shock ahead of the passage will form.

Even though the design has enough throat margin to operate at part speed with started flow, as appears to be the case for the design in Fig. 10, this will not be true if the mouth area is larger

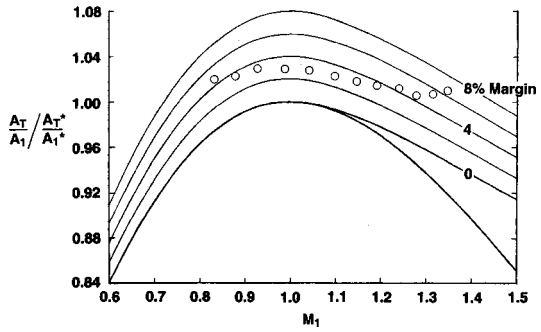

Fig. 10 Throat area/capture area ratios for 12 streamlines at the design point

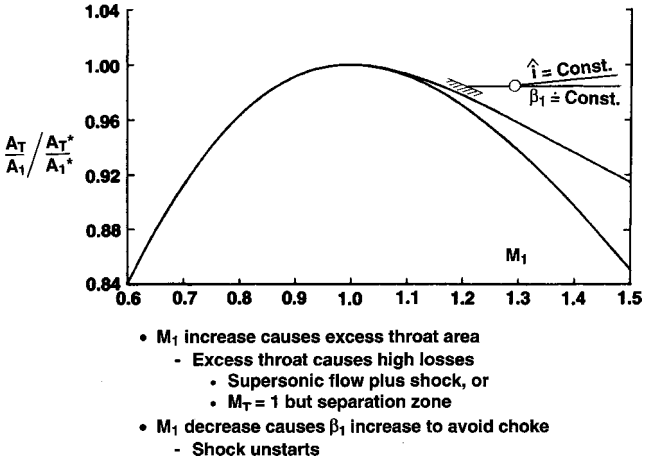

Fig. 11 Consequences of off-design operation for one streamline

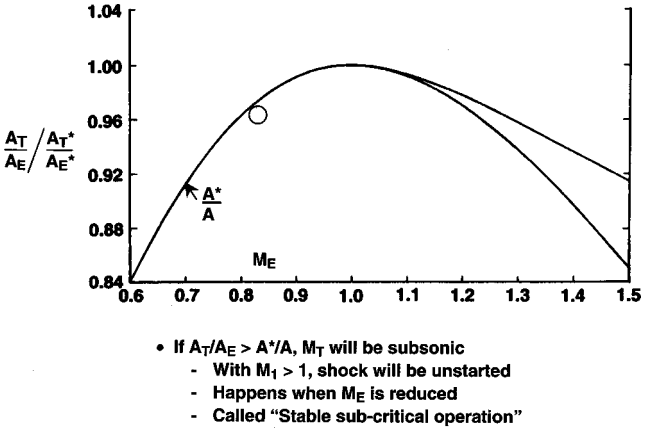

Fig. 13 Passage exit area needs to be large enough to provide subsonic diffusion to exit Mach number

than the throat area (see Fig. 9). Such a passage is said to have internal contraction. To examine this, *Fig. 12* is prepared. Any internal contraction (i.e. ordinate less than unity) will cause a shock ahead of the passage at some reduced speed, with the loss consequences being related to the Mach number at that time.

The passage exit area must be larger than the throat area by the amount needed to provide subsonic diffusion to the exit Mach number. *Figure 13* is prepared to examine this; it is relevant when the throat Mach number is intended to be close to sonic. The distance that a point lies below the line is a measure of how much a blade element can be throttled (M_E reduced) before the shock moves forward of the passage.

Before CFD was available, transonic blade shapes were custom tailored to give the appropriate areas plotted on Figs. 10, 12, and 13. For comparison, these figures were prepared for many existing blade rows of interest using their design CAFDs or data matches. Usually, test experiences could be explained by them. Although 3-D viscous CFD codes are now used for refining blade shape designs, the area ratio plots are still used to start the design process and to compare the final blade to past experience.

The *Circular Arc Tweaks* bar on Fig. 5 refers to a code that starts with a circular arc meanline but allows the user to add or subtract camber locally in the forward and aft regions. Also, some non-NACA thickness distributions can be employed. This code is used in conjunction with a cascade analysis code to custom tailor subsonic cases for which there might not be the internal CAFD stations needed to employ the SBS airfoil generator. Often this method was used to custom tailor blading which was first evaluated in the Low Speed Research Compressor; Wisler [12]. Successful designs were then incorporated into product compressors, e.g., CFM56 and CF6.

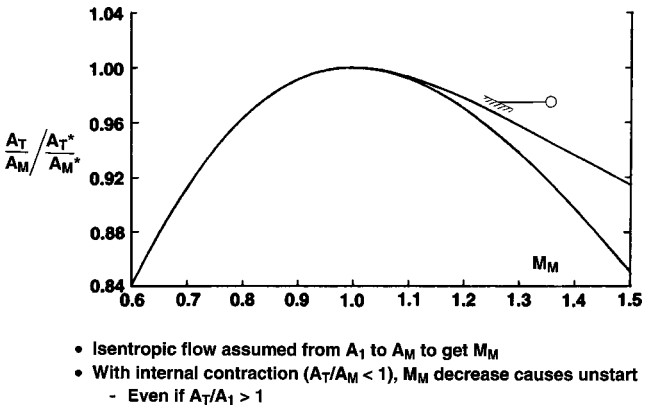

Fig. 12 Internal contraction causes shock unstart at reduced speed

Some of the cascade analysis codes employed are also shown on Fig. 5. *CABIS* is an acronym for Cascade Analysis by Bueckner, Isay and Schnackel. This code was obtained from General Electric's Steam Turbine Department in Schenectady, which had a first-rate fluid mechanics group. Bueckner and Schnackel were GE analysts who adapted the method of Isay [13] to calculate the potential flow around cascaded blades of any shape. The method required inversion of a large matrix, which became practical when the IBM 701 computers arrived. The restriction of CABIS to two-dimensional incompressible flow limited its application as a design method, but it was used to design high-turning outlet guide vanes and for shaping leading edges.

Flux Plot was a compressible finite difference code developed by Dave Prince. It was somewhat unwieldy to use and was superseded by *CASC*, an acronym for cascade analyis by streamline curvature, written by Jim Keith and Dick Caney. CASC accounts properly for radius and lamina thickness changes. It is inviscid, but by a judicial choice of using only seven streamlines between adjacent blades, it predicts deviation angles remarkably well when boundary layers are unseparated. An auxiliary code with a finer grid is used to get better flow definition in the leading edge region. CASC flow property inputs come from CAFD (now CAFMIX), and when custom tailoring, its blade shape information comes from SBS or other profile generation codes. Its main inadequacy is a limitation on surface Mach number to about 1.1.

Today, all blades are custom tailored using 3-D viscous codes, but the older tools are used to start the process and to provide comparisons with past experience.

5 Selection of Basic Design Parameters

Selecting the overall architecture of a new engine is a preliminary design function. During this phase, many compressor candidate configurations are examined that can deliver the required pressure ratio and mass flow with an rpm that is compatible with turbine needs. The basic compressor parameters that are relevant for each candidate are annulus dimensions, number of stages, number of blades in each blade row, chord lengths, and clearances. These allow the weight and cost to be estimated. It is essential that each candidate has the capability to produce its required pressure ratio with adequate stall margin if its detailed design is properly executed. Its efficiency potential also needs to be forecast at this time.

In the following subsections we will take up how these two compressor aero functions have been handled at General Electric.

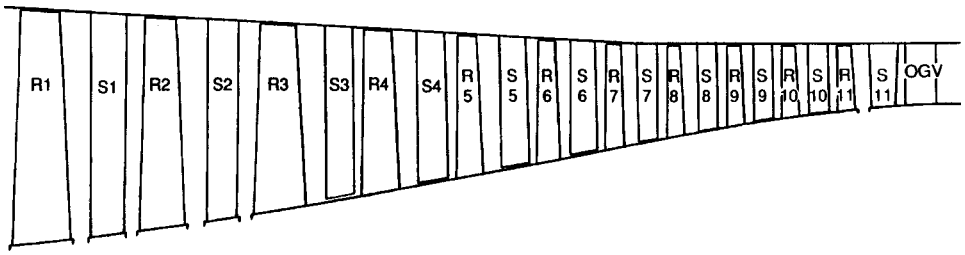

Fig. 14 J93 Compressor flowpath. Note high aspect ratios.

5.1 Stage Loading Criteria. Designers of early GE compressors apparently relied mostly on blading lift coefficients to set stage loadings. As mentioned in Section 4, the TG180 design used 0.84 with a solidity of 1.0 for all rotor hubs. Rotor values elsewhere were lower. Stator lift coefficient values tended to be largest at the outer casing, and these were limited to 0.90. Adequate stall margin above the design point was apparently realized. Up through the J79 design, maximum lift coefficients were limited to 0.9 with maximum solidities around 1.1, and some stall margin was realized above these design points at design speed.

In the early 1950s, NACA came out with its *D*-factor; Lieblein et al. [14], and made the case that it was a more meaningful loading parameter than others that were in use such as lift coefficient or deHaller number (which measures velocity diffusion without accounting for solidity). General Electric started calculating *D*-factor with the J85, and has been doing so ever since. Immediately thereafter, we started having stall problems.

Although the J85's problems were at first blamed on poor design execution with the unfamiliar transonic blading type, the X211 and J93 experiences could not be so explained. In those cases the flow and efficiency at design speed were about as expected, as also were the interstage radial distributions of pressure and temperature; but both machines stalled near their design pressure ratios, with none of the known loading parameters having been reached.

Dick Novak and the writer suspected that the unusually high aspect ratios of these designs were responsible; see *Fig. 14*. My belief was that the radial clearances, while not unusual as a percentage of span, were large as a percentage of chord, and since all blade elements have to produce the same static pressure rise, stall was being initiated at the endwalls without being affected much by two-dimensional loading criteria such as *D*-factor. In 1957, during a technology exchange meeting with Rolls-Royce, General Electric learned that Rolls-Royce had found significant stall line differences when testing compressors that differed mainly in their aspect ratios. With this finding, GE then proceeded along three fronts: 1) designs of longer chord versions of the X211 and J93 were started (ways were found to squeeze the extra compressor lengths into the engines), 2) while blading tweaks were being tried on the original compressors with little success, a twelfth stage was added to the J93, and 3) research programs were started aimed at gaining an understanding of aspect ratio effects. All three approaches were successful, but by 1963 the two engine projects had been cancelled for other reasons.[1]

The main research effort, which was started in late 1957, employed the new Low Speed Research Compressor (LSRC) to test four-stage groups with identical cascade properties at aspect ratios of 5.0, 2.8, and 1.96. Data for the extreme aspect ratios at the same clearance are shown on *Fig. 15*. The lines shown, which do not exactly match the data, are from a unifying theory that explains the essence of aspect ratio effects for blades with moderate to high-aspect ratios; Smith [15].

[1]The long chord J93 compressor went on to have a distinguished career. With three stages added, and some solidity reductions, it was scaled down to yield the GE1 (J97 product); then with two more stages added it was scaled up to be the TF39 compressor (also the CF6-6 and LM2500).

Although it was clearly established by 1960 that aspect ratio significantly affects loading capability, we needed a way to incorporate this into some kind of a loading parameter for general use. While pondering this, we continued LSRC tests using the hardware at hand to investigate solidity variations. The test array, shown on *Fig. 16*, varied solidity from 0.6 to 1.5.

It was known at the time that the maximum pressure rise of a conical diffuser could be correlated with its length normalized by inlet radius. This suggested normalizing blade chord with the square root of the inlet passage area. But this was inconvenient because, for compressor blade rows, the inlet flow area depends on the unknown inlet flow angle at stall. Since the outlet area of a blade row remains nearly constant, the conical diffuser max pressure rise data of Gibson [16] were plotted versus $L/\sqrt{A_2}$, giving the upper curve on *Fig. 17*. LSRC data are shown around the lower curve. The solid symbols are from the tests identified on Fig. 16, which were all we had when the plot was first made in 1962. These could be represented with a single line following the trend of the conical diffuser line. The other data taken later involved variations of stagger, reaction, clearance, and aspect ratio.

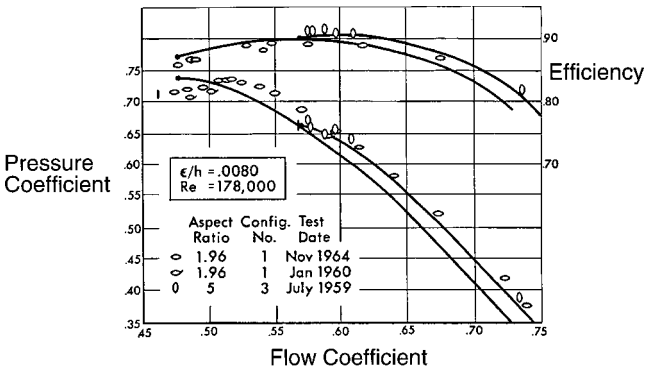

Fig. 15 Low-speed research compressor tests showed significant aspect ratio effects

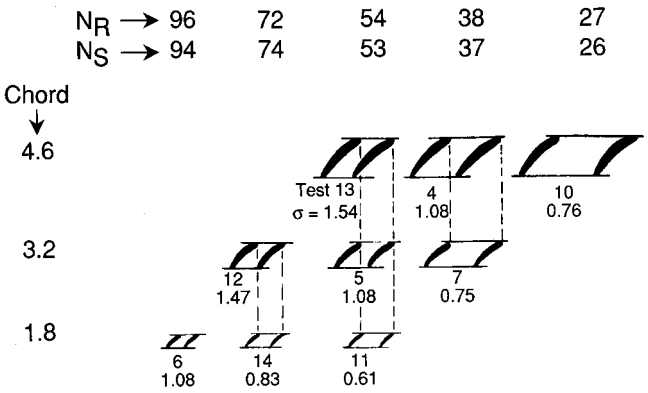

Fig. 16 Aspect ratio and solidity combinations tested

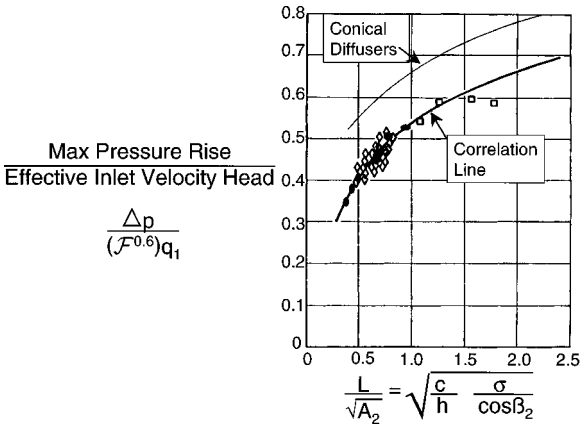

Fig. 17 Stall pressure rise correlation

The scales on Fig. 17 require further explanation. Properties at the arithmetic mean radius are used. The pressure rise is for a stage (rotor and following stator), and it is adjusted downward for the ''diffusion-free'' amount that comes when the radius increases through the rotor. The inlet velocity head is the sum of the rotor and stator inlet values, each modified by a ''dynamic pressure factor'' effect; see *Fig. 18*. The concept here is that, since all flow filaments must sustain essentially the same pressure rise in passing through a blade row, the attainable blade row pressure rise is limited by the dynamic pressure of the wall boundary fluid from the preceding blade row. It is seen in Fig. 18 that, if the boundary layer flow leaving the upstream blade row (in this case a rotor) is presumed to flow at the same relative angle as the free stream fluid, the minimum inlet velocity relative to the downstream blade row will be $C_{\min}$. Furthermore, it is seen that if the included angle between the relative and absolute free stream vectors is less than 90 deg, as shown, $C_{\min}$ will be less than C, but if this included angle is 90 deg or larger, the wall boundary layer fluid from the upstream blade row will have a velocity, and hence a dynamic pressure, equal to or larger than the free stream value. The ratio $C^2_{\min}/C^2$ was named the ''dynamic pressure factor'' because it is the number by which the free stream dynamic pressure is multiplied to get the minimum dynamic pressure entering a blade row. The 90 deg included angle criterion was developed independently at the Langley Lab of NACA under J. R. Erwin at about the same time that the writer developed it at General Electric (1957). It is also relevant to the recovery ratio; Smith [17], as pointed out by Cumpsty [18]. The exponent 0.6 on $\mathcal{F}$ is empirical. It is needed to bring into line compressor stages with $\mathcal{F}$ values substantially less than unity; this is not surprising because the low dynamic pressure filaments must be energized to a certain extent by mixing with free stream fluid as the flow passes through the blade row.

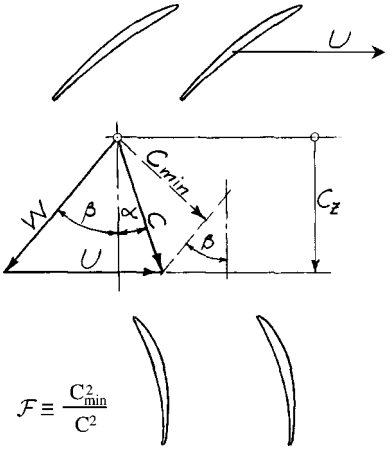

Fig. 18 Dynamic pressure factor definition; stator example shown

The $\mathcal{F}$ concept is quite important in limiting loadings of some multistage blade rows to values below those that might be expected, even after accounting for aspect ratio and clearance effects. An excellent explanation of the essence of these concepts was given by Koch [19].

At GE Aircraft Engines in the late 1950s and early 1960s, compressors were thought of as members of families. There were the J79, J93, T64, and HSL (high-stage loading) families. When a new design was contemplated, it was thought of as being related to one of these families, and stage loading capabilities were obtained by making adjustments for the design departures from that family. Based on the belief that there should be a common set of rules that all the families obey, the writer started a ''compressor unification study'' aimed at demonstrating this. The acronym CUS was adopted, and cross perturbations between the families were examined with some success. In a second attempt, the LSRC correlation line in Fig. 17 was used to predict stage characteristics stall points; this was CUS2. Then for CUS3 we started plotting on Fig. 17 data points for actual compressor stages when the compressor was operating close to stall at design speed. The ratio of the ordinate of each point to that of the LSRC line at the same abscissa value was said to be the ''stall *effectivity*'' of that stage. In this way, effectivity values were found in each stage in every compressor that had ever been tested (casing static pressure taps had always been used at GE). Automatic adjustments for clearances and Reynolds number were included in later models leading to CUS5, which is still in use today.

Of course, any simple model like this has limitations. All blades need to have ''adequate'' camber and ''appropriate'' twist, but camber that is more than adequate can be harmful. Inappropriate twist can lead to premature stalling at the hub or casing before the other blade end is comparably loaded. For these reasons, some low-speed stages do not reach unity effectivity. And in a high-speed compressor, the front stages may be lightly loaded at design-speed stall to improve part-speed performance. But as shown by Koch [19], some block of stages almost always has effectivities near unity when a well-designed compressor stalls.

The pressure rise limit correlated on Fig. 17 basically assumes that a compressor row stalls like a diffuser would, starting at the passage exit. That is why the camber must be adequate; otherwise, leading edge separation could cause early stall. Likewise, a combination of high stagger and large clearance needs to be avoided as this can cause leakage axial backflow that limits pressure rise.

For preliminary design purposes, options in the CUS5 computer code allow the user to input, at the desired design-speed stall point, a stage-wise distribution of effectivity and other design parameters such as casing radii, solidities, aspect ratios, axial velocities, swirl angle levels, and clearances, and a required rotative speed and hub radii will be deduced. Other combinations of these independent or dependent variables may also be specified. Many candidates that should all be capable of obtaining the required high-speed stall margin can be so identified. Concurrently, proprietary correlations give the number of variable stators needed to ensure adequate part-speed stall margin and the shape of the stall line.

The desired high-speed stall point involves specification of a stall margin above the normal engine operating line. For engines in supersonic aircraft, inlet flow distortions contribute significantly to the margin requirement, but there are many other considerations also. A discussion of this important topic is beyond the scope of this paper.

5.2 Compressor Efficiency Potential. An efficiency needs to be assigned to each compressor candidate being considered during the preliminary design process. In the belief that the same one-dimensional parameters that correlate stall capabilities should

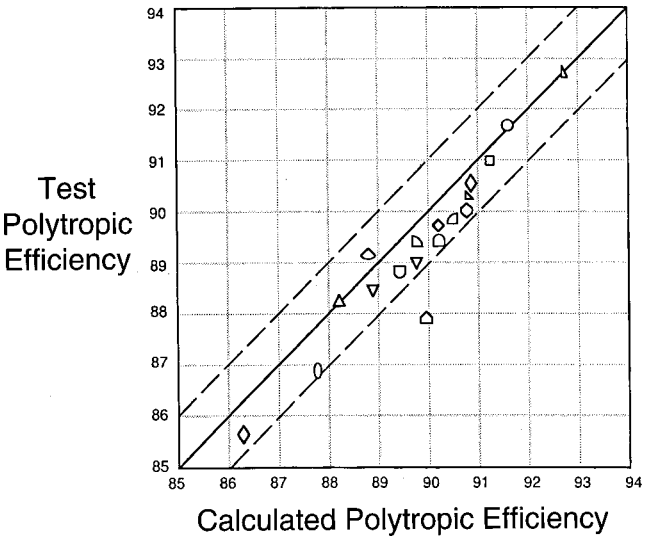

Fig. 19 Test polytropic efficiencies compared with values calculated using CUS5 Code for GE multistage compressors designed before CFD

also largely determine efficiency potential, in the early 1970s we set about formulating an efficiency module to add to CUS5. Work in the LSRC had continued through the 1960s with the main focus on stall line assessment for other vector diagram types, clearances, etc., but efficiencies had always been carefully measured. So we had a solid database for establishing a loss module for subsonic blading, and Mach related losses could then be added. The resulting formulation is given by Koch and Smith [20]. Its application to General Electric compressors tested before 1982 is given on *Fig. 19*. The points clustered in the middle of the figure are mostly product compressors which generally did not quite reach their CUS5 potentials. More recent bladings, custom tailored using 3-D CFD codes, have generally exceeded the CUS5 correlation. At GE we say those designs ''beat CUS5 by _ point(s).''

The compressor on Fig. 19 with the highest efficiency is the 14 Stage Research Compressor designed in 1947. Although its small clearances and other features made it impractical for direct engine application, this early achievement is somewhat of an embarrassment, as it prevents us from plotting efficiency achieved versus calendar year to show how much progress we have made.

In the mid-1970s, the CUS5 code was used to determine the compressor configuration for the NASA/GE E^3 Compressor. Modules were added to estimate weight and erosion life. Preliminary design studies for the whole engine assessed initial cost, maintenance cost, and fuel burn to determine user direct operating cost and return on investment values for various candidates. The compressor finally selected did not have the highest efficiency potential, but it was best for meeting the economic goals. This study for NASA was outlined by Smith [21], and details of the work are given in reports referenced therein. General Electric feels that the resulting E^3 compressor is nearly an optimum for subsonic aircraft engines, and it was scaled for use in the GE90 engine.

6 Concluding Remarks

The evolution of axial flow compressor aero design methods at General Electric has been outlined from the beginning up to the early 1980s, and the evolution has continued since then with ever more use of CFD codes. It is expected that this evolution will continue for some time, if not indefinitely, if we wish to have those codes predict all kinds of stall in multistage compressors. General Electric design practice documents, recognizing this continuing evolution of methods, do not specify that a particular code must be used when producing a new design, but instead, specify that the code being used must have been used to match data from a related compressor previously tested. Inevitably, for multistage compressors, some form of empiricism will have been introduced when conducting the data-match calculations, and this empiricism is used when conducting the new design calculations, although it may be tweaked somewhat if the designer has sufficient reasons. As time goes on and codes are improved the empiricism becomes less, but some will always be needed if only because the actual compressor geometry is not what the analyzer assumes it to be.

The lessons of the past lead to the following recommendations to compressor aero designers on how to get a successful compressor:

1. observe established loading criteria using attainable clearances;
2. ''custom tailor'' the airfoils to match the flow at the design point and at important off-design operating points; and
3. get a good clean mechanical design with small clearances, sealed leakage paths, desired leading edge shapes achieved, no forward facing steps, and appropriate surface finishes.

Acknowledgments

The writer would like to acknowledge all the General Electric compressor aero designers that made significant contributions during this time period but there are too many. A dozen or so names have been mentioned in the text in connection with some item or other, but their contributions were often much greater than that. In addition to those mentioned, the following, as a minimum, should also be acknowledged: Tom Alge, Brent Beacher, Alta Berridge, Bob Brown, Alex Bryans, Link Dumont, Jack Erwin, Bill Foote, Ron Giffin, Paul Griffiths, Bill Harmon, Ginny Haywood, Bob Hendrickson, Jim Isbell, Les King, Ron Klapproth, Karl Kovach, Frank Lenherr, George Liu, Al Medlock, Marlen Miller, Bob Neitzel, John O'Connor, Dave Parker, Jeanne Place, Art Schnacke, Don Seyler, Ray Simonson, Lou Smith, Tom Sullivan, Peter Szucs, Morrie Thorson, and Don Wilcox.

The book by St. Peter [22] giving engine histories was very helpful. So also was the book GE Aircraft Engines [23], which describes the engines that used the compressors and the project leaders and engineers that made them successful.

The author would also like to thank General Electric for the opportunity to spend a lifetime doing very interesting engineering work in an important field, with the satisfaction of knowing that useful products have resulted.

Nomenclature

A = passage area
A^* = critical passage area
b = blade spacing
c = blade chord
C = absolute velocity
d = defined on Fig. 9
e = defined on Fig. 9
$\mathcal{F}$ = defined on Fig. 18
h = passage height
$\hat{i}$ = defined on Fig. 9
L = diffuser length
L = passage width on Fig. 9
M = Mach no.
N_R = no. of rotor blades
N_S = no. of stator vanes
p = static pressure
q = dynamic pressure
r = radius
Re = Reynolds no. based on chord and tip speed
U = blade speed
V_∞ = vector mean velocity
W = relative velocity

X = empirical angle adder
α = absolute flow angle
β = relative flow angle
γ = ratio of specific heats
ε = tip clearance
σ = cascade solidity, c/b

Subscripts

E = passage exit; see Fig. 9
ff = free-flow streamline; see Fig. 9
min = defined on Fig. 18
M = passage mouth; see Fig. 9
T = passage throat; see Fig. 9
z = axial component
1 = blade row inlet
2 = blade row exit

References

[1] Keller, C., 1934, ''Axialgebläse vom Standpunkt der Tragflügeltheorie,'' dissertation, ETH.
[2] Constant, H., 1945, ''Early History of the Axial Type of Gas Turbine Engine,'' Proc. Inst. Mech. Eng., **153**, pp. 411–426.
[3] Wright, L. C., and Novak, R. A., 1960, ''Aerodynamic Design and Development of the General Electric CJ805-23 Aft Fan Component,'' ASME Paper 60-WA-270.
[4] Smith, L. H., Jr., 1966, ''The Radial-Equilibrium Equation of Turbomachinery,'' ASME J. Eng. Power, **88**, pp. 1–12.
[5] Smith, L. H., Jr., 1974, ''Some Aerodynamic Design Considerations for High Bypass Ratio Fans,'' 2nd ISABE Conf., Sheffield, UK.
[6] Adkins, G. G., Jr., and Smith, L. H., Jr., 1982, ''Spanwise Mixing in Axial-Flow Turbomachines,'' ASME J. Eng. Power, **104**, pp. 97–110.
[7] Wisler, D. C., Bauer, R. C., and Okiishi, T. H., 1987, ''Secondary Flow, Turbulent Diffusion, and Mixing in Axial-Flow Compressors,'' ASME J. Turbomach., **109**, pp. 455–482.
[8] Weinig, F., 1934, ''Über die Winkelübertreibung von Turbinenschaufeln,'' *Sonderdruck aus Wasserkraft und Wasserwirtschaft*, Heft 3.
[9] Klapproth, J. F., 1959, Discussion of ''Loss and Stall Analysis of Compressor Cascades,'' ASME J. Basic Eng., **81**, p. 398.
[10] Smith, L. H., Jr., and Yeh, H., 1963, ''Sweep and Dihedral Effects in Axial-Flow Turbomachinery,'' ASME J. Basic Eng., **185**, pp. 401–416.
[11] Wislicenus, G. F., 1986, ''Preliminary Design of Turbopumps and Related Machinery,'' NASA Ref. Pub. 1170, Section 2.5.5, p. 114.
[12] Wisler, D. C., 1985, ''Loss Reduction in Axial-Flow Compressors Through Low-Speed Model Testing,'' ASME J. Eng. Gas Turbines Power, **107**, pp. 354–363.
[13] Isay, W. H., 1953, ''Contribution to Potential Flow in Axial Blade Cascades,'' thesis Z. Angew. Math. Mech., **33**, pp. 397–409.
[14] Lieblein, S., Schwenk, F. C., and Broderick, R. L., 1953, ''Diffusion Factor for Estimating Losses and Limiting Blade Loadings in Axial-Flow-Compressor Blade Elements,'' NACA RM E53D01.
[15] Smith, L. H., Jr., 1970, ''Casing Boundary Layers in Multistage Axial-Flow Compressors,'' *Flow Research on Blading*, Elsevier Publishing Company, Amsterdam, The Netherlands, pp. 275–304.
[16] Gibson, A. H., 1911, ''On the Resistance to Flow of Water through Pipes or Passages having Divergent Boundaries,'' Trans. R. Soc. Edinbrgh, **XLVIII**, Part I, No. 5, p. 97.
[17] Smith, L. H., Jr., 1958, ''Recovery Ratio—A Measure of the Loss Recovery Potential of Compressor Stages,'' Trans. ASME, **80**, pp. 517–524.
[18] Cumpsty, N. A., 1989, *Compressor Aerodynamics*, Longman Scientific and Technical, England, and John Wiley & Sons, New York, NY, Sect. 2.2, p. 62.
[19] Koch, C. C., 1981, ''Stalling Pressure Rise Capability of Axial Flow Compressor Stages,'' ASME J. Eng. Power, **103**, pp. 645–656.
[20] Koch, C. C., and Smith, Jr., L. H., 1976, ''Loss Sources and Magnitudes in Axial-Flow Compressors,'' ASME J. Eng. Power, **98**, pp. 411–424.
[21] Smith, L. H., Jr., 1994, ''NASA/GE Fan and Compressor Research Accomplishments,'' ASME J. Turbomach., **116**, pp. 555–569.
[22] St. Peter, J., 1999, *The History of Aircraft Gas Turbine Engine Development in the United States*, International Gas Turbine Institute, ASME, Atlanta, GA.
[23] GE Aircraft Engines, 1990, *Eight Decades of Progress*, Graphica, Dayton, Ohio, Library of Congress 90-082948.

Aerodynamic Design and Testing of an Axial Flow Compressor With Pressure Ratio of 23.3:1 for the LM2500+ Gas Turbine

A. R. Wadia
e-mail: aspi.wadia@ae.ge.com

D. P. Wolf

F. G. Haaser

GE Aircraft Engines,
Cincinnati, OH 45215

The LM2500+ gas turbine, rated between 39,000–40,200 shaft horsepower (shp), was introduced for field service in 1998. This growth aero-derivative gas turbine is suitable for a variety of power generation applications, such as co-generation and combined cycle, as well as mechanical drive applications. At the heart of the LM2500+ 25% power increase is an up-rated derivative 17-stage axial compressor. This paper describes the aerodynamic design and development of this high-pressure ratio single-spool compressor for the LM2500+ gas turbine. The compressor is derived by zero-staging the highly efficient and reliable LM2500 compressor to increase the flow by 23% at a pressure ratio of 23.3:1. The aerodynamic efficiency of the compressor is further improved by using three-dimensional, custom-tailored airfoil designs similar to those used in the CF6-80C2 high-pressure compressor. The compressor achieved a peak polytropic efficiency above 91%, meeting all its operability objectives. The technical requirements and overall aerodynamic design features of the compressor are presented first. Next, the zero stage match point selection is described and the procedure used to set up the vector diagrams using a through-flow code with secondary flow and mixing is outlined. Detailed design results for the new transonic airfoils in the compressor using three-dimensional viscous analysis are presented. The compressor instrumentation and performance test results are discussed. The performance of the zero stage is separated from that of the baseline compressor with the CF6-80C2 airfoils to show the improvement in efficiency with the new airfoils. [DOI: 10.1115/1.1464562]

Introduction

Application of aero-engine technology to ground-based gas turbines has increased rapidly, especially in the last decade, as documented in the works of Scalzo [1], Kashiwabara [2], Sehra [3]. Smed [4], Janssen [5], and Stringham [6]. The LM2500 gas turbine, derived from the CF6-6/TF39 aircraft engines, has also leveraged off aircraft engine technology development to facilitate the increase in its industrial power rating from the original 24,000 shp to the current 31,200 shp. Market studies initiated in the late eighties and early nineties showed that the LM2500 industrial gas turbine needed additional power (39,000 shp at ISO conditions) to meet customer requirements (Farmer [7]). This up-rated power version of the LM2500 was named the LM2500+ gas turbine. The LM2500+ gas turbine 3-D cutaway presented in Fig. 1 highlights the key modifications made to the engine relative to the LM2500 base engine.

In March 1994, after a series of preliminary design studies on how to achieve the required power increase, it was decided to launch the LM2500+ which was chosen from four candidate configurations based on a cost-and-risk assessment comparison. The preliminary design team evaluated power enhancement techniques such as inter-cooling, inlet supercharging, recuperation and other refinements. The team, however, decided on the basis of design simplicity, program schedule, technology risks and development cost and customer price that increasing the inlet mass flow through the engine was the simplest and most conservative way of increasing the power output. The increased mass flow could be achieved by zero-staging the current production LM2500 compressor. Simultaneously, the increase in the turbine rotor inlet temperatures could be minimized to approximately 35°C (65°F) (Valent [8]) by going to a more efficient compressor design using three-dimensional analytical tools and incorporating custom-tailored compressor airfoils from the CF6-80C2 aircraft engine. It was apparent that this design approach best met the goals of using proven technology at minimal risk. Also, keeping a strong fundamental LM2500 design heritage facilitated product support while meeting the objectives of a base load hot section inspection interval of 25,000 h with engine overhauls at 50,000 h.

Compressor Technical Requirements Summary

The performance requirements for the LM2500+ compressor were less stringent relative to those required by commercial or military aircraft engines. While aircraft engines have multiple operating points such as take-off, cruise, etc., where performance is crucial, the LM2500+ is required to operate at close to its peak efficiency near its high-speed design point. While no specific performance requirements at other speeds were specified, it was desirable for the compressor to preserve good efficiency over a range of speeds.

Additionally, the LM2500+ compressor was also required to operate stall-free with both a single annular combustor (SAC), which results in a smooth compressor operating line, and with a dry low emissions (DLE) combustor, which results in a compressor operating line with steps corresponding to the staging in the combustor. The compressor operating line can vary by as much as 2% below and above the nominal operating line, from the start of the combustor staging to the end of the staging sequence, respectively.

The customer-supplied inlet systems used with industrial gas turbines, such as the LM2500+, are generally quite aerodynamically ''clean'' and use a light wire screen mesh to prevent any

Contributed by the International Gas Turbine Institute and presented at the International Gas Turbine and Aeroengine Congress and Exhibition, Indianapolis, Indiana, June 6–9, 1999. Manuscript received by the IGTI, January 1999; revised manuscript received January 24, 2002. Paper No. 1999-GT-210. Review Chair: D. Wisler.

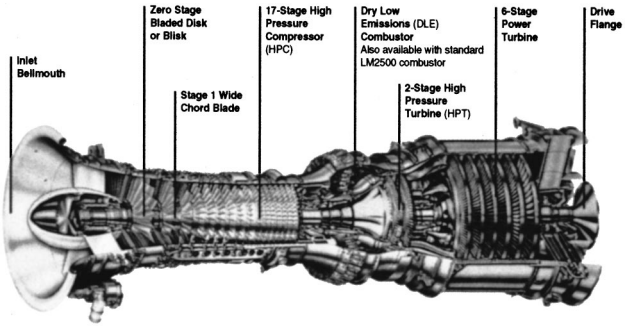

Fig. 1 LM2500+ gas turbine unique features

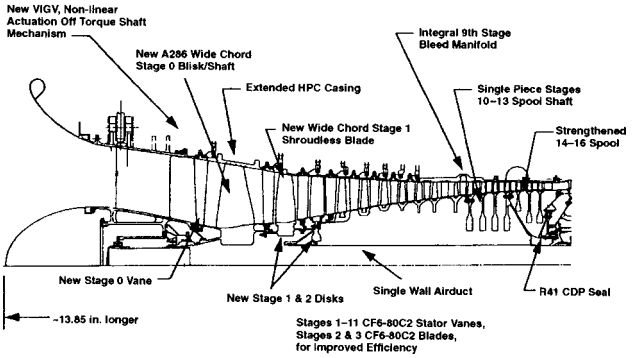

Fig. 2 LM2500+ high pressure compressor improvements relative to the base (LM2500) compressor

large objects being ingested by the compressor. Maneuvers and cross-wind inlet distortion issues are almost nonexistent on these land/marine-based engines, thus easing the operability requirements. Installation design manuals suggest the inlet distortion index to be of the order of 2% or less as most of the operation is with a straight bellmouth or radial volute. To account for any inlet distortion that might be encountered in the field, the compressor was designed with a slight tip radial (i.e., total pressure deficit at the tip) inlet total pressure profile to realistically simulate the tip aerodynamic loading level on the zero stage blade.

Acoustics plays an economic role in land/marine-based systems design, and the goal for the LM2500+ was to maintain the same inlet noise sound pressure level in spite of the 23% higher airflow. This requirement set the vane/blade ratios and the axial spacing between the rotor and the stator using an ''acoustic cutoff'' design criteria.

The compressor operating line was set with a minimum of 12% stall margin to account for any operating line migration that would occur in service during the life of the engine. Start times for the engine are of the order of 2 min, which is less stringent than in aircraft engines. A 4-deg open stator stall margin requirement was conservatively set for the LM2500+ to account for variable stator vanes (VSV) control/rigging variation and deterioration in the field.

Compressor Aerodynamic Design Features

The detailed aerodynamic design of the original CF6-6/LM2500 compressor has been reported by Klapproth et al. [9]. To achieve the increased power output rating, the LM2500+ required a 23% increase in airflow. The 23% increase in flow was achieved by adding an additional compression stage (zero stage) to the LM2500 and flaring the flowpath in front of the existing compressor to form an overall 17-stage axial compressor unit. Figure 2 shows the changes incorporated into the LM2500+ relative to the base compressor. As a result of zero staging of the compressor, the LM2500+ increased in length by 34.3 cm (13.5 in.) and the weight of the engine increased by about 363 kg (800 lb) Table 1 shows the comparison of key aerodynamic design parameters for the LM2500 compressor with those selected for the design of the LM2500+ compressor.

Zero Stage Match Point Selection

Technical information on zero-staging compressors in the open literature is limited. Some of the principles in the development of front stages of axial flow compressors has been reported by Eisenberg [10] and Katoh [11]. A recent compressor zero-staging application to the Taurus 60 axial flow compressor that increases the inlet mass flow by approximately 20% and raises the pressure ratio from 11.2:1 to 16:1 has been reported by Van Leuven [12] and Rocha et al. [13].

The CF6-6/LM2500 compressor performance map has been presented in [9]. The LM2500 compressor achieved a peak polytropic efficiency of 90.7% along the engine operating line at a compressor inlet corrected flow of 60 kg/s (132 lb/s) and pressure ratio of 15:1. The 88.9% polytropic efficiency shown in Table 1 (does not include the compressor exit diffuser losses) represents the compressor performance at the maximum power operating point of the LM2500 engine, which is different from the peak efficiency point on the compressor map.

To achieve maximum compressor performance with the zero stage, the point corresponding to the peak efficiency of the existing LM2500 compressor would be selected as the match point for the LM2500+ compressor design. This sets the zero stage pressure ratio such that the LM2500+ compressor achieves its overall compression ratio goal. In order to achieve this optimum pressure ratio, the zero stage's ''stage effectivity,'' as calculated using the approach formulated by Koch [14], exceeded that demonstrated by the first stage of the compressor in GE Aircraft Engine's energy efficient engine (E^3), which has a similar overall pressure ratio as that for the LM2500+.

The term ''stage effectivity'' is a correlation that is used internally within GE Aircraft Engines to assess a stage's loading relative to the loading at stall. It is synonymous to the peak stage static pressure rise coefficient and has been correlated versus a parameter involving stage average values of solidity and aspect ratio. The correlation serves as an aerodynamic loading limit, and accounts for factors such as blade speed, axial velocity, reaction ratio, clearance and Reynolds number to form a systematic method for analysis or prediction of compressor stall performance.

The selection of the pressure ratio, for the zero stage, was an iterative process to achieve a balance between the design point pressure ratio and its ''stage effectivity'' at stall. This iterative process yielded a zero stage pressure ratio of 1.438, which is slightly less than optimum.

The efficiency potential of the zero stage was determined using the principles outlined by Koch and Smith [15] and the corresponding work input assigned to it. The resultant exit temperature and pressure from Rotor 0 provided the input to calculate the inlet conditions into the following stator. Inlet corrected flow and speed at Stator 0 inlet were then calculated and compared to the measured flow at speed along the base LM2500 compressor operating

Table 1 Compressor aerodynamic design operating point

Parameters	LM2500	LM2500+	Change
Shaft Horsepower	31,200	39,000	25%
Inlet Corrected Flow, kg/s	68 (150 lb/s)	84.5 (186 lb/s)	23%
Inlet Corrected Speed (rpm)	9,418	9,586	1.5%
Pressure Ratio	18.8	23.3	23%
Polytropic Efficiency	88.9%	91%	2.36%

line. The calculations converged quickly to provide a realistic axial match between the new zero stage and the downstream existing compressor.

The aforementioned approach, substantiated by past experience on the E^3 engine and test data from the LM2500 compressor, resulted in matching the LM2500+ zero stage to the original LM2500 compressor at an inlet corrected flow of about 62.7 kg/s (137 lbs/s) (corresponding to an inlet corrected speed of 8,950 rpm) at 90.3% polytropic efficiency.

Compressor Design Vector Diagrams

The vector diagrams used to design the new front stages of the LM2500+ compressor were derived from a data match of a fully instrumented, CF6-80C2 core engine using the circumferentially averaged, through-flow code with secondary flow and mixing (Adkins and Smith [16]). Next, the new zero stage was added to the through-flow analysis. The new set of vector diagrams obtained were such that the velocity triangle quantities—such as the inlet relative flow angle, inlet relative Mach number and inlet meridional Mach number into stage 2 blade—were the same as the data match values.

The axial distribution of solidity, aspect ratio, axial velocity, diffusion factor, Mach number, inlet and exit flow angles and airfoil camber and stagger angles for all the LM2500 blading has been published [9]. Table 2 summarizes some of the key airfoil geometry and vector diagram quantities for the first three stages of the LM2500+ compressor.

A preliminary design analysis resulted in the selection of 16 blades (Rotor 0) for the zero stage. The selection of the number of inlet guide vanes and the number of zero stage vanes (vane/blade cut-off ratio), and the axial gaps between the inlet guide vanes, Rotor 0 and Stator 0 were set by the technical requirements for an ''acoustic cut-off'' in order to prevent higher inlet noise levels. This resulted in larger-than-normal axial gaps on both sides of the zero stage blade, as shown in Fig. 2. These large gaps are detrimental to compressor performance, making the aerodynamic design of the compressor even more challenging.

The following sections summarize the detailed design of the new front stages of the LM2500+ compressor with emphasis on the zero stage and the first stage blade designs. Three-dimensional viscous analysis using the computer program developed by Jennions and Turner [17] was used extensively in the design of the compressor blading.

Front Frame and Inlet Guide Vane Design

The LM2500+ front frame is very similar to the original engine frame. It is a five-strut (four thin struts and one thick strut), 17-4 steel casting and retains the same inner and outer front forward flange configuration for inlet commonality as shown in Fig. 2. The frame's inner and outer flowpath walls were flared to increase the flow area through the frame to prevent a higher pressure loss due to a possible flow restriction. The original front frame struts are bi-convex airfoils, which for the LM2500+ were made more aerodynamic using NACA 65-series airfoils. Thickness and airfoil contour changes lowered the front frame losses as verified by three-dimensional viscous analysis of the frame.

The inlet guide vane (IGV) airfoil design was done with a conventional profile. The correlation of NACA 63-series airfoil cascade data by Dunavant was used with the IGV solidity varying from 0.89 at the tip of 1.2 at the hub. The IGV exit swirl was varied almost linearly from about 18 deg of pre-swirl at the tip to −15 deg of counterswirl at the hub. The tip pre-swirl provided Mach number relief to the downstream rotor at the tip, while the hub counterswirl helped lower the hub Mach number into the zero stage vane. The IGV design was important because it has to deliver the required swirl distribution to the zero stage blade at the design condition and it has to be able to operate adequately at part speed when the airfoil is closed by as much as 60 deg. The IGV airfoil was analyzed at the design point with the three-dimensional viscous analysis. This analysis was done to verify the magnitude and radial distribution of pressure loss assumed in the circumferentially averaged through-flow analysis and its ability to meet the exit swirl requirements.

Table 2 Rotor and stator pitch line design parameters summary

Parameter	IGV	Rotor 0	Stator 0	Rotor 1	Stator 1	Rotor 2
Solidity	1.045	1.582	1.281	1.176	0.974	0.915
Aspect Ratio	6.04	1.390	4.000	2.337	3.708	2.609
Inlet Mach No.	0.489	1.018	0.706	0.826	0.727	0.771
Diffusion Factor		0.423	0.267	0.348	0.353	0.355

Zero Stage Blade Design

Preliminary mechanical design studies showed that dovetail stresses on a traditional zero stage blade design would limit the minimum radius ratio to 0.45. A blisk version of the rotor permitted a reduction in the radius ratio to 0.368. This reduction in radius ratio also provided some aerodynamic performance benefits by lowering the inlet specific flow. The blisk also provided a parts count reduction by replacing 40+ parts with a single part, and eliminated the wear issue of a midspan shroud, blade and disk and dovetails. Although blisk technology has been in existence for 20+ years, its inclusion in the LM2500+ represents the first introduction of a blisk to GE Aircraft Engines' Marine and Industrial engines product line.

Table 3 shows the comparison of the geometric and aerodynamic design parameters between the zero stage rotor for the LM2500+ compressor and the first stage blade from the GE Aircraft Engines E^3 compressor. As illustrated by the thickness comparisons in Table 3, the LM2500+ blades were considerably thicker (ruggedized) to increase foreign object damage (FOD) tolerance. The location of maximum thickness was also moved forward on the LM2500+ airfoil, in a similar manner as illustrated in the paper by Wadia and Law [18], to provide improved resistance to leading edge foreign body impact.

Rotor 0 was designed to the vector diagrams created from a data match of the CF6-80C2 core compressor as reported earlier. Transonic airfoil design principles presented in [18] were applied to custom tailor the mean camber lines to alleviate some of the performance penalties associated with the ruggedization. The detrimental effect on performance due to the large increase in thickness, especially near the hub, was also reduced by scalloping (area-ruling) the hub flowpath within the blade as shown in Fig. 2.

The inlet relative Mach number is transonic over most of the blade span of the LM2500+ Rotor 0. The efficiency of a transonic

Table 3 Zero stage blade key aerodynamic design parameters

Parameter	LM2500+ Rotor 0	GEAE E^3 Rotor 1
Number of Blades	16	28
Inlet Corrected Flow (kg/s)	84.5 (186 lb/s)	54.5 (120 lb/s)
Inlet Specific Flow (lb/s-sq.in.)	36.0	36.2
Stage Pressure Ratio	1.438	1.65
Inlet Corrected Tip Speed (ft/s)	1,363	1,495
Inlet Tip Pre-Swirl (degrees)	18	14
Inlet Hub Counter-Swirl (degrees)	-15	0
Inlet Relative Tip Mach Number	1.19	1.32
Inlet Radius Ratio	0.368	0.52
Aspect Ratio	1.39	1.51
Pitch Solidity	1.59	1.71
Pitch Diffusion Factor	0.44	0.46
Tip, Pitch, Hub Tmax/C	.037, .088, .130	.024, .052, .096

blade is heavily influenced by shock losses, which may exceed the losses due to cascade diffusion and secondary flow effects. The Mach number just ahead of the leading edge passage shock can be influenced by the shape of the blade suction surface ahead of the shock. Increasing the average suction surface angle, as measured from axial, ahead of the shock reduces the average Mach number upstream of the shock through external compression and should reduce the shock losses. However, this type of airfoil can result in a reduced cascade throat area. If the throat is too small, the cascade will not pass the design flow and may not achieve the attached shock pattern desired for minimum loss. The lessons learned in transonic rotor performance studies by Wadia and Copenhaver [19], with different cascade area ratios, were applied to set the throat margin, internal contraction and trailing edge camber of the zero stage blade. The blade was designed with a 5% throat margin.

The design was further analyzed with a three-dimensional viscous code to get more definitive results on the effect of custom tailoring the mean camber lines and to verify that the cascade would pass the design flow and deliver the design intent exit radial profiles of total pressure and temperature.

The flow computed by the three-dimensional analysis was 1.05% higher than the design flow rate. This difference between the design and calculated flow rate is consistent with that between the three-dimensional analysis and measured flow on other similar transonic blade row designs.

The radial profiles of total pressure, temperature and adiabatic efficiency (at Stator 0 leading edge) calculated by the three dimensional viscous analysis (3-D) are illustrated in Fig. 3. The total pressure profile is hub strong and agrees well with the design intent also shown in Fig. 3. The calculated efficiency was slightly higher relative to the design vector diagrams.

Figure 4 shows the isentropic Mach number distribution on the pressure and suction surfaces of the LM2500+ zero stage blade. Figure 5 shows the corresponding calculated shock structure at two immersions along the blade span. Near the tip, a two-shock system was selected over a single leading edge shock pattern to obtain a balance between the efficiency and stability of the blade. It was recognized that the peak efficiency would occur on a slightly higher operating line where the passage shock merged with the leading edge shock. At the midspan, Fig. 5 shows a single passage shock structure with the shock intersecting the pressure and suction surfaces at 30 and 65% axial distance from the leading edge of the airfoil, respectively.

Figure 6 shows the isentropic blade surface Mach number distribution near the hub of the blade. The hub scalloping provided the required relief to the 13% thick hub section by lowering the average Mach number and resulted in a shock-free design by keeping the blade surface Mach numbers below unity. No flow separation at the hub was observed in the three-dimensional calculations.

Figure 7 shows the zero stage blisk used in the first build of the LM2500+ engine.

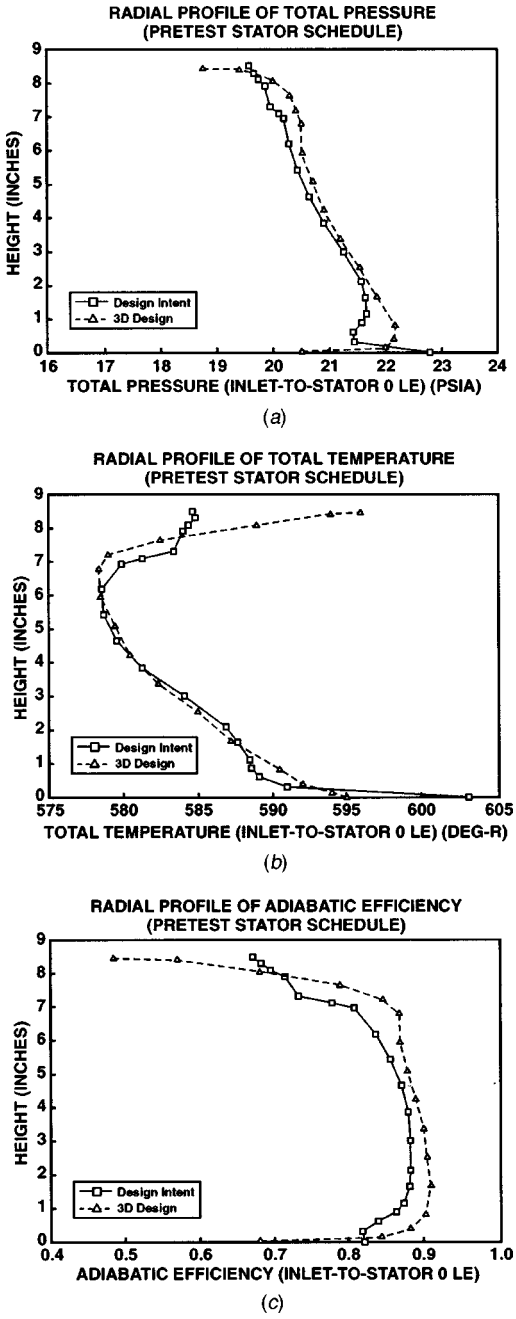

Fig. 3 Comparison of Stage 0 blade exit radial profiles of total pressure, total temperature, and adiabatic efficiency at the aerodynamic design point

Zero Stage Vane Design

Stator 0 on the LM2500+ replaces the inlet guide vane on the base machine but has aerodynamic characteristics similar to the first stage vane in the baseline compressor. As mentioned before, the stator hub loading levels and inlet absolute Mach numbers were controlled by using −15 deg counterswirl into the zero stage blade. Table 4 summarizes the geometric and aerodynamic design parameters for the vane.

Table 4 Zero stage vane key aerodynamic design parameters

Parameters	Zero Stage Vane
Number of Vanes	40
Tip, Pitch, Hub Chord (in.)	2.49, 2.01, 1.7
Tip, Pitch, Hub Tmax/C	.105, .081, .039
Inlet Absolute Hub Mach Number	0.95
Hub Diffusion Factor	0.55

In the paper on three-dimensional relief, Wadia and Beacher [20] have shown that the need to align the inlet metal angle precisely with the skewed inlet flow angles at the endwall (at the risk of placing a significant spanwise twist gradient in the blade surface near the endwall) appears to be less than might be implied from two-dimensional cascade analyses. While some recognition of the high air angles that exist at the endwalls was considered in the design of the zero stage vane, extreme leading edge angle gradients were not required. Figure 8 shows the calculated three-dimensional vane surface isentropic Mach number distribution at the tip, pitch and hub. A shock-free diffusion at the hub was ac-

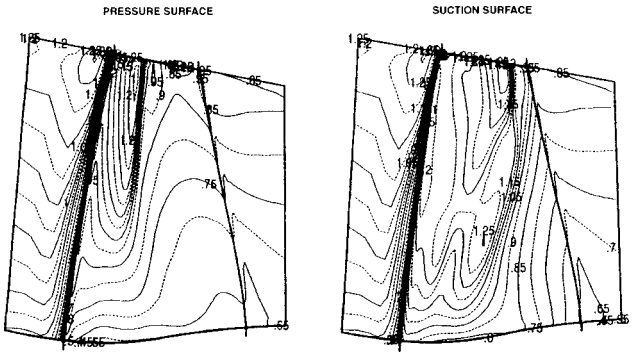

Fig. 4 LM2500+ Rotor 0 isentropic Mach number contours on the pressure and suction surfaces

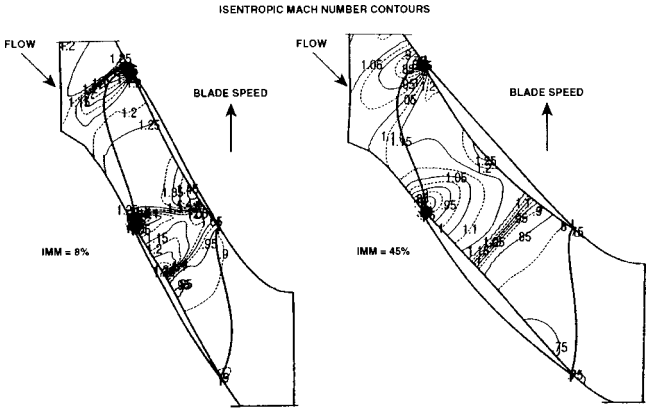

Fig. 5 LM2500+ Rotor 0 blade passage shock structure at 8 and 45% immersions

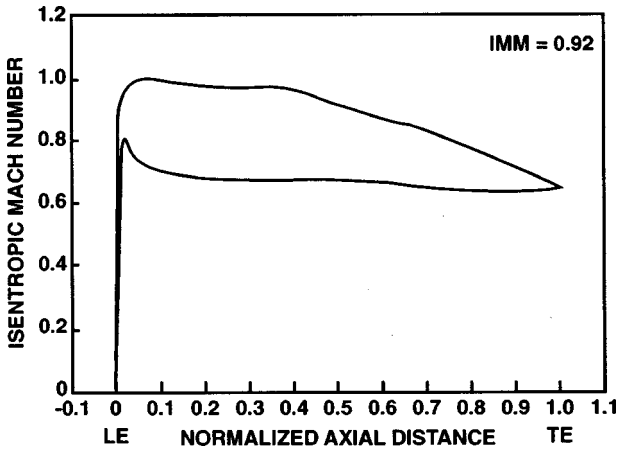

Fig. 6 Axial distribution of blade surface isentropic Mach number near the hub for LM2500+ Rotor 0

complished and the ability of the stator to deliver the required swirl to the following rotor was verified by the three-dimensional analysis.

First Stage Blade Design

CF6-80C2 and LM2500 first stage compressor blades are designs that use midspan shrouds. The LM2500+ first stage blade moved away from the shrouded design to a wide chord rotor design. Some of the key geometric and aerodynamic design parameters for the first stage blade are presented in Table 5.

Similar to the zero stage blade, this airfoil was also ruggedized to improve FOD tolerance. Some amount of hub scalloping was

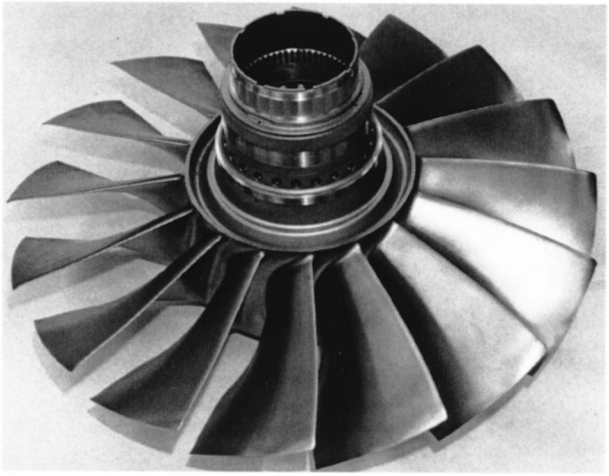

Fig. 7 LM2500+ Rotor 0 blisk

also done to accommodate the large thickness increase in the hub due to the elimination of the midspan shroud and thicker tip sections. Three-dimensional analysis was used extensively in the design, and Fig. 9 illustrates the isentropic Mach number distribution on the blade surface at the tip, pitch and hub immersions. As illustrated by the axial distribution of the blade surface Mach number at the hub and the midspan in Fig. 9, most of the airfoil sections along the span were front loaded. However, the sections locally near the tip were more aft loaded to reduce tip leakage and improve performance as has been demonstrated in low-speed testing by Wisler [21]. As in the zero stage blade analysis, the three-dimensional analysis was used to verify that the desired radial profiles of total pressure and efficiency were achieved by the first stage blade.

Figure 10 shows a photographic comparison of the current production first stage midspan shrouded blade and the new wide chord LM2500+ first stage blade. The LM2500+ blade has about 35% lower aspect ratio and 60% more midspan chord, but approximately the same midspan solidity relative to the first stage blade in the base machine.

First Stage Vane Design

The first stage vane design was only a minor change from that in the CF6-80C2 core compressor. The design incidences on the LM2500+ Stator 1 were patterned after those from the CF6-80C2 Stator 2 as this would be the second stage of the LM2500+ compressor. The vane surface isentropic Mach number distributions on Stator 1 were similar to those reported for the zero stage vane. The required inlet conditions into the next rotor stage, which is identical to the CF6-80C2 airfoil, were verified by the three-dimensional analysis.

LM2500+ Variable Stator System

To ensure stall-free operation at part speed, the inlet guide vanes and the first six stators are variable in the LM2500+ engine. The method of scheduling the variable stators was changed in the LM2500+. Whereas the LM2500 uses a pair of level arms powered by twin actuators, the LM2500+ uses two torque shaft assemblies located 180 deg apart to actuate the compressor variable stator vanes. Each torque shaft, which is cylindrically shaped, is mounted to the compressor casing along the axis of the engine with a bearing at each end to allow for rotation within a forward and aft mounting bracket. A hydraulic actuator attached to a lug near the front end of each shaft rotates the shaft. Additional lugs,

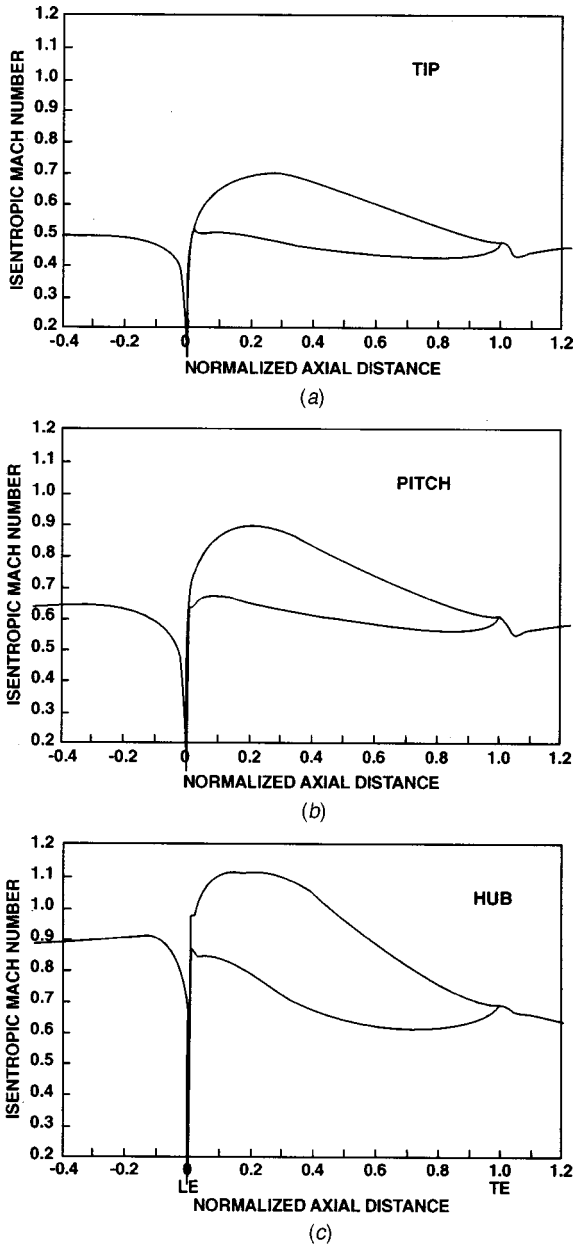

Fig. 8 Axial distribution of Stage 0 vane surface isentropic Mach number

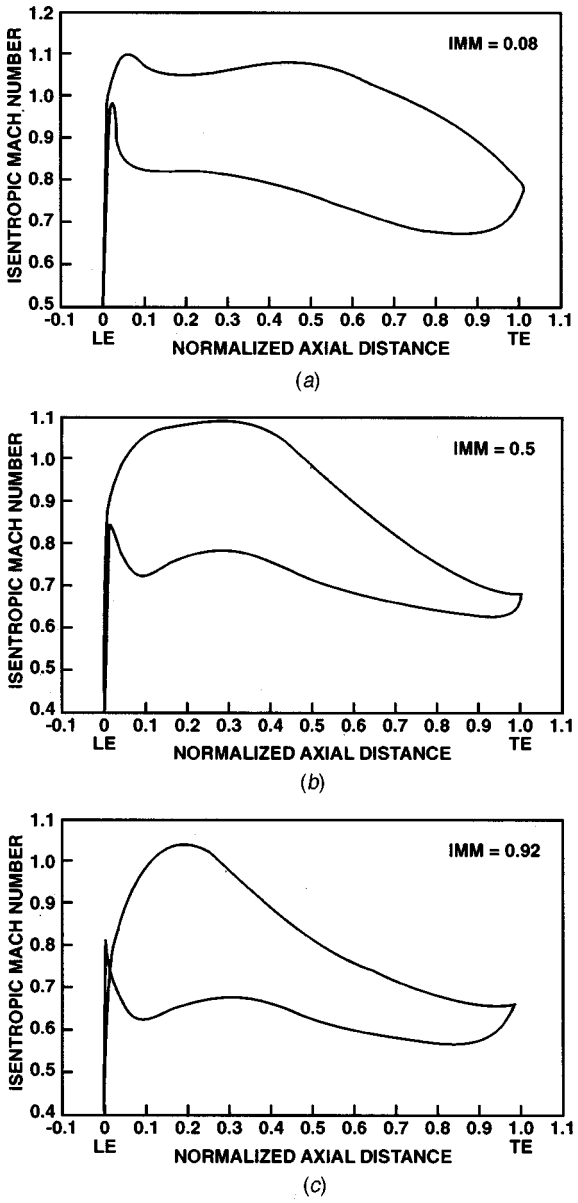

Fig. 9 Axial distribution of blade surface isentropic Mach number for Rotor 1

one for each variable stator stage, are bolted along the length of the shaft. As the shaft turns, a turnbuckle bolted to each lug is pushed or pulled to rotate a multipiece, 360-deg ring to which each stator vane lever arm is connected, opening or closing the VSV. The key benefit derived by using the torque tube is its added flexibility to schedule each stage with stator angle schedules that are nonlinear to each other.

The variable stator schedule is controlled as a function of the compressor inlet corrected speed, with the second stage stator angle used as the reference. Stage characteristic data sets acquired from core engine tests of the CF6-80C2 and the LM2500 compressor were used to assemble a pitch line off-design model of the LM2500+ compressor with the new inlet guide vane and zero stage, and the mixture of airfoils from the CF6-80C2 and LM2500. This model was used to develop a pretest stator schedule for the LM2500+.

The change in Stator 2 angle (pretest) from the design nominal as a function of compressor corrected speed is shown in Fig. 11. The change in the setting angles from design for the inlet guide vanes and Stators 0, 1, and 3–6 are shown in Fig. 12 as a function of the Stator 2 ''master'' angle. While the linear relationship of Stators 0–6 with Stator 2 was retained from the CF6-80C2 and the LM2500 experience, the inlet guide vane relationship was highly nonlinear with respect to the ''master'' stator angle.

Table 5 First stage blade key aerodynamic design parameters

Parameters	Stage 1 Blade
Number of Blades	26
Tip, Pitch, Hub Solidity	.95, 1.29, 1.86
Aspect Ratio	2.337
Inlet Relative Tip Mach Number	0.90
Pitch Inlet Swirl Angle (degrees)	20
Chord (in.)	3.35
Tip, Pitch, Hub Tmax/C	.035, .090, .13

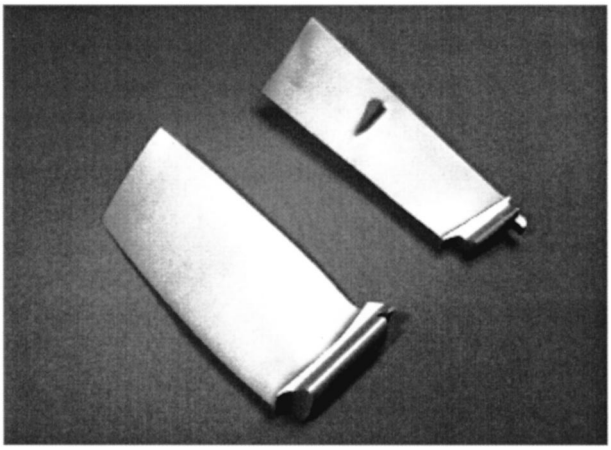

Fig. 10 Comparison between the LM2500+ wide chord Rotor 1 and the LM2500 Rotor 1 with the midspan shroud

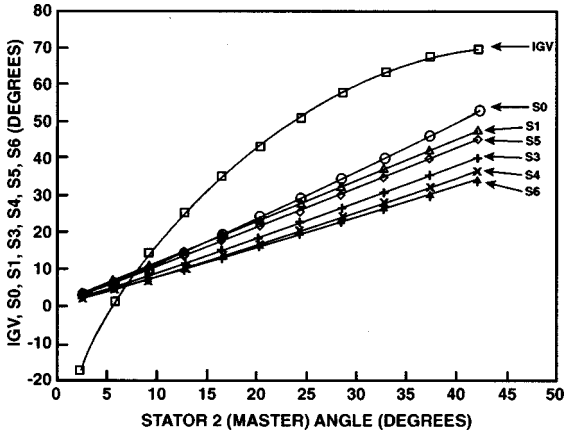

Fig. 12 LM2500+ compressor pretest variable stator gang relation

Test Compressor Instrumentation Summary

The first engine with the LM2500+ compressor was tested as a gas generator with a conic nozzle at GE Aircraft Engines test facilities in Evendale with a dry low emissions (DLE) combustion system.

The overall compressor performance was measured using four five-element combined inlet total pressure and total temperature rakes and three five-element rakes at the compressor discharge. Other performance measurements included the compressor speed and inlet flow, which was measured with a calibrated bellmouth with inlet rakes. All compressor bleed flows were measured using calibrated pipes.

Interstage compressor instrumentation was extensive. Each stage in the compressor had leading edge total pressure and total temperature instrumentation. All the compressor airfoils were instrumented with either flame-sprayed or thin film strain gages, and light probe instrumentation was included over Rotors 0 and 1.

Two vane stem-mounted potentiometers per stage were used on all variable stators to monitor stator position during the test. Trimmer motors were provided for all variable stators to individually vary the stator settings for performance/aeromechanical optimization.

Tip clearance measurements were obtained over the rotors in stages 0, 1, 2, 6, 11, and 16. All the compressor airfoils in the LM2500+ that were common to the base engine were from a lease pool engine (which had about 700 h run time), including the rear compressor case. The measured average clearance to blade height, at design speed, varied between 0.7–1.%, except for stage 16 which had significantly larger clearances (~5%). The clearances on the new airfoils and on the airfoils from the lease pool engine were somewhat larger than one would expect in a new engine.

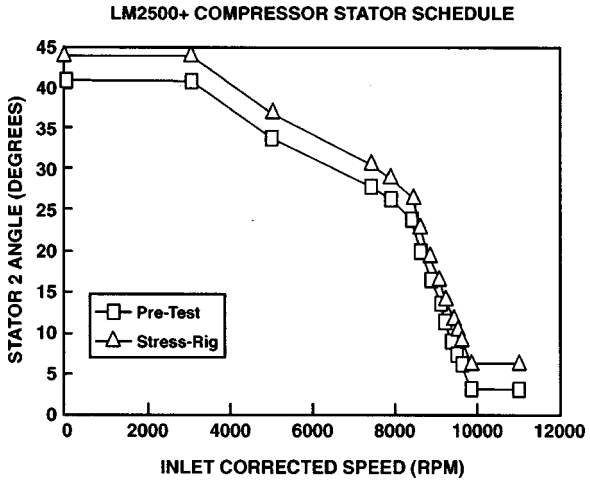

Fig. 11 LM2500+ compressor stator schedule

Compressor Test Performance Results

Figure 13(*a*) shows the comparison of the measured and predicted compressor operating lines with the pretest variable stator schedule. The distinct steps in the compressor operating line represent the different stages of operation of the DLE combustion system, which uses compressor discharge bleed to control the combustion flame temperature. The compressor achieved the design flow at the design speed, and the agreement between the calculated and measured flow at speed with the pretest variable stator schedule as shown in Fig. 13(*b*) was very good. The compressor achieved its peak polytropic efficiency, slightly over 91%, near its aerodynamic design point as shown in Fig. 13(*c*). The test data shown in Fig. 13(*c*) is as measured, while the pretest prediction line includes an estimated 0.5 points derate in target efficiency due to compressor instrumentation, hardware quality and clearances.

The individual performance for the blisk and that of the downstream compressor with the mixture of CF6-80C2 and LM2500 airfoils was separated in the following manner. The zero stage performance was determined by using data from the inlet rakes and the zero stage, vane-mounted probes. In spite of the large clearances and the significant amount of ruggedization in the transonic Rotor 0, the IGV-Rotor 0 combination achieved a peak polytropic efficiency of 90.5%, which was 2.8% better than design intent. The downstream compressor performance with the mixed airfoils, as determined by using the zero stage, vane-mounted probes and the exit rakes (and referred to as the ''rear block'' in this paper), also achieved the desired match point for the flow and efficiency goal relative to the baseline compressor.

The measured radial profile of total pressure and temperature at Rotor 0 exit was in good agreement with the three-dimensional calculations and the measured efficiency was slightly higher than the calculations near the tip.

Aeromechanically, the first two new stages performed per design intent over the entire operating range including vane off-schedule operation. However, among all the other compressor blades, strain gage signals on Rotors 2, 3, and 4 indicated higher than desired stresses between 83–90% design speed. A small variable stator schedule adjustment, using the trimmer motors on the variable stators, provided an acceptable solution to the aerome-

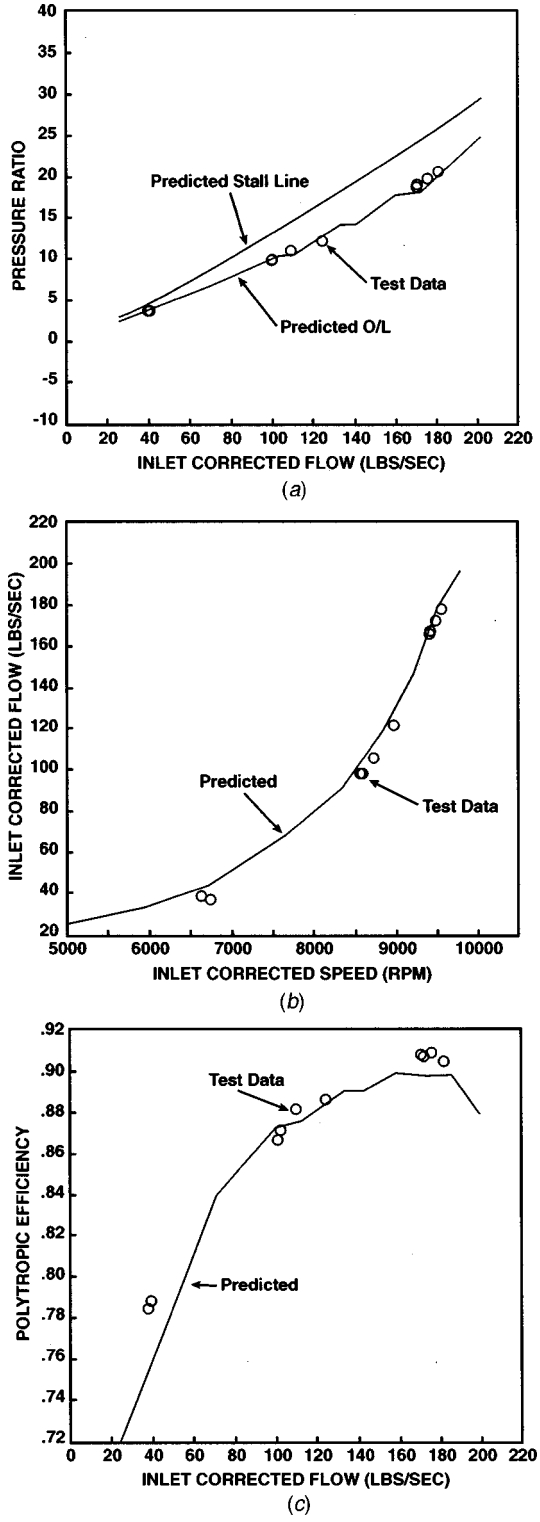

Fig. 13 LM2500+ compressor performance with pretest variable stator schedule

chanical stress issue. The loading on these rotors was reduced by a combination of the change in their upstream and downstream stators, resulting in a significant reduction in aeromechanical response. As a result, the IGV through Stator 2 were closed 3 degrees from nominal (only at part speed), and Stators 5 and 6 were opened by 3 and 5 deg from nominal, respectively. The loading relief on Rotors 2, 3, and 4 came as a consequence of pushing the load forward onto the zero and first stages and onto the downstream side loading up the middle stages (Rotors 5, 6, and 7) of the compressor. The schedule adjustment did not adversely affect compressor operability as supported by data later in this paper.

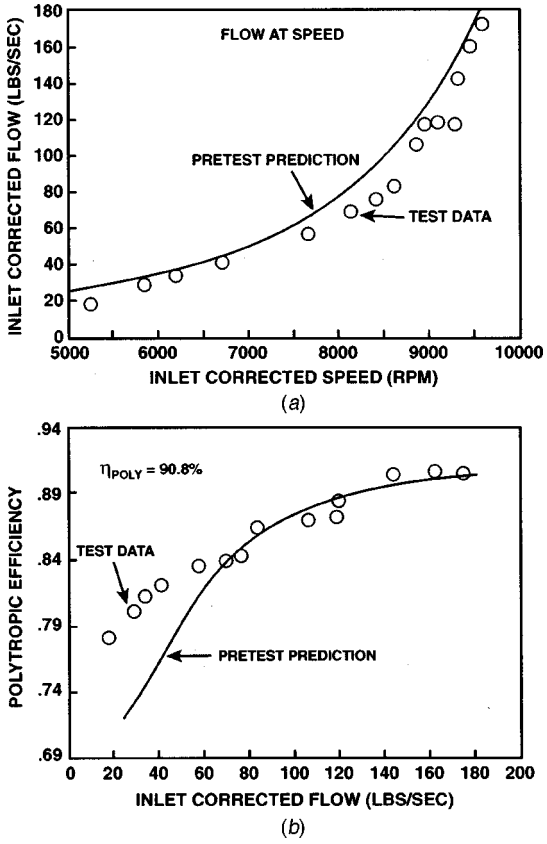

Fig. 14 LM2500+ compressor performance with "stress rig" variable stator schedule

The strain gages on all the compressor vanes indicated low stresses. However, the high aspect ratio inlet guide vanes, which have the largest travel with compressor speed, exceeded acceptable design stresses between 93–101% design speed. The IGV stress issue was resolved by a variable stator gang closure of 3 deg at high speed.

This final production ganging of the stators to the torque tube was defined and mechanically verified while on test. This experimentally determined master stator schedule as a function of inlet corrected speed, labeled as the "stress rig" in succeeding paragraphs, is shown in Fig. 11.

Compressor Performance With "Stress Rig" Stator Schedule

The optimized stator schedule to reduce the stresses in the inlet guide vanes and the front rotors reduced the inlet corrected flow by 6% at design speed. The loss in flow was retrieved by increasing the compressor speed by 1.4%, with about 0.3% loss in peak overall compressor polytropic efficiency.

Figure 14(*a*) shows the reduction in flow at speed along the compressor nominal operating line with the "stress rig" variable stator schedule. The compressor polytropic efficiency along the engine operating line versus compressor inlet corrected flow is shown in Fig. 14(*b*). The compressor achieved a peak polytropic efficiency of 90.8% at 73.6 kg/s (162 lb/s) at 19.8:1 pressure ratio.

The zero stage performance with the "stress rig" was determined using data from the inlet rakes and the zero stage, vane-mounted probes. Figure 15(*a*) shows the pressure ratio at flow achieved by the IGV-Rotor 0 combination along the engine operating line. The corresponding efficiency at flow for the IGV-Rotor

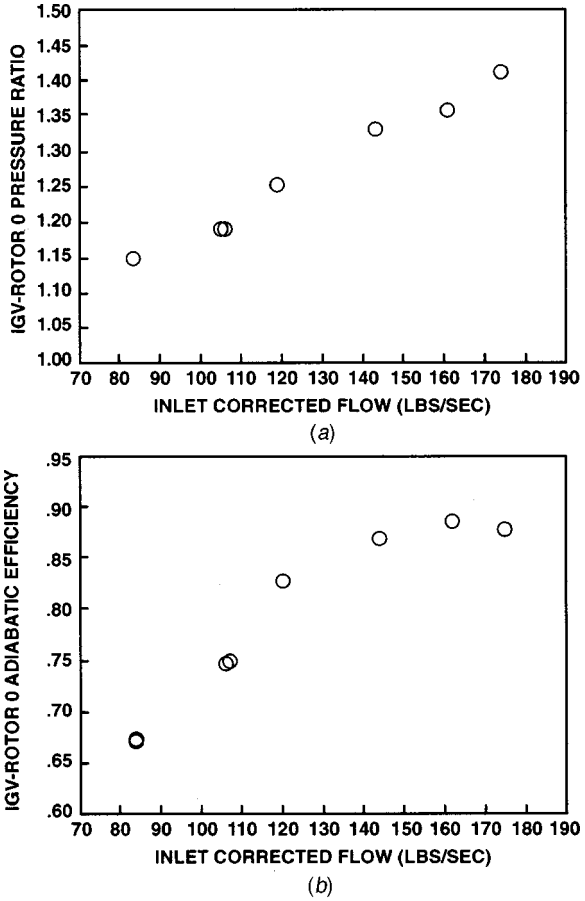

Fig. 15 LM2500+ IGV-Rotor 0 performance

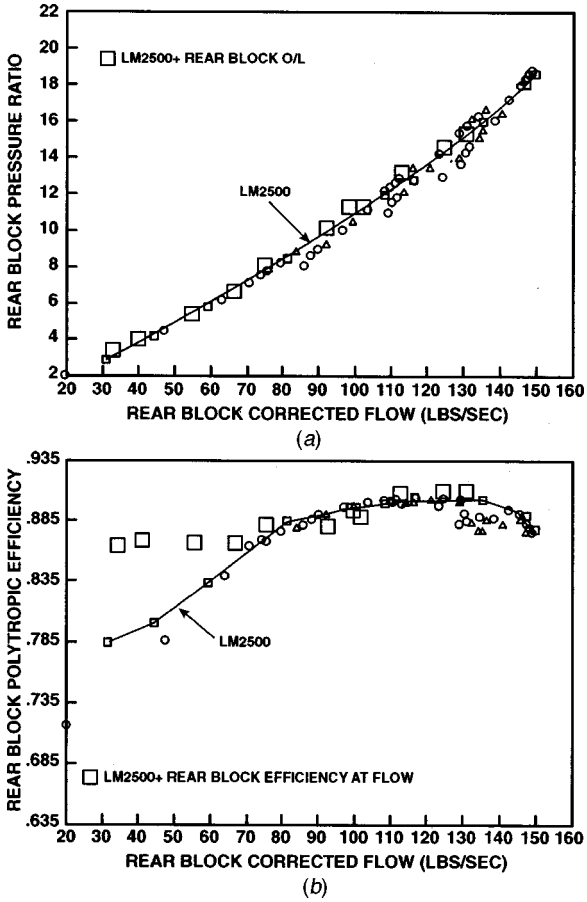

Fig. 16 LM2500+ "rear block" performance

0 combination is shown in Fig. 15(*b*) with the peak polytropic efficiency dropping to 89.5% due to the change in the variable stator schedule.

The downstream compressor performance with the mixed airfoils was determined by using the zero stage, vane-mounted probes and the compressor exit rakes. Figure 16(*a*) shows the comparison between the base LM2500 compressor operating line and the measured distribution of pressure ratio with flow for the "rear block" on the LM2500+. Note that the corrected flow for the LM2500+ "rear block" was calculated using the zero stage, vane-mounted, leading edge measurements for total pressure and total temperature, while that for the base LM2500 compressor truly represents the compressor inlet conditions. The LM2500 (small symbols) and the LM2500+ (large symbols) were both run with the DLE combustion system and hence the "stepped" (for combustor staging) compressor operating line. Data for the base LM2500 engine with the single annular combustion (SAC) system is also shown as a solid line without symbols in the figure. Figure 16(*b*) shows the corresponding comparison of efficiency at flow for the base LM2500 compressor and the LM2500+ compressor "rear block." The LM2500+ "rear block" shows approximately 0.8 points improvement in peak efficiency, which is in agreement with the estimated improvement in efficiency with the custom-tailored CF6-80C2 airfoils. While not a technical requirement, these airfoils also provided a significant improvement in performance at lower corrected flows.

The compressor was not throttled to stall at these high-pressure ratios. Stall-free compressor performance was demonstrated along a 7% high operating line, however, by adding flow blockers ("tabs") to the exhaust nozzle to reduce the area.

Open stator stall testing to determine compressor "open stator stall margin" (defined as the difference between the scheduled VSV angle and the VSV angle at stall) was conducted on the first development test engine. Holding constant speed, the variable stator gang was opened in 1-deg intervals until the compressor stalled. Figure 17 shows the open stator stall test results. The VSV gang based on Stator 2 is shown plotted versus the compressor inlet corrected speed. The stator position at which the compressor stalled as the VSV gang was opened is also shown in Fig. 17. At 90% design speed and beyond, the VSV gang was opened to demonstrate the required margin without stalling the compressor. The LM2500+ compressor demonstrated over 10 deg margin at 9000 rpm and over 5 deg at 5000 rpm, which is adequate. The actual margin at the open stop was not determined, but is enough for stall-free operation of the LM2500+ compressor.

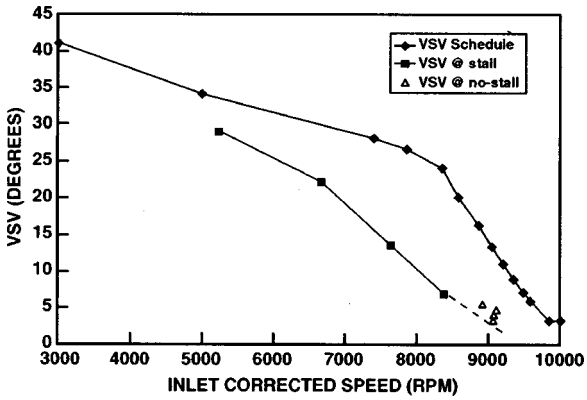

Fig. 17 LM2500+ compressor open stator stall test results

Concluding Remarks

The aerodynamic design of the 17-stage, 23.3:1 pressure ratio single-spool axial compressor for the LM2500+ gas turbine has been reported. The new zero stage and stage 1 compressor blades and vanes were designed using three-dimensional computational methods. Advanced compressor airfoils from the CF6-80C2 compressor were also integrated successfully with the baseline LM2500 compressor airfoils. The compressor achieved a peak polytropic efficiency slightly over 91% and met all its design operability objectives.

In spite of the significant ruggedization of the front-stage airfoils operating in the transonic flow regime, advanced design tools were able to provide accurate guidance during the design phase to achieve the level of compressor efficiency required for the successful field implementation of the LM2500+ at its full mature power rating. Production engine data have duplicated the performance predictions based on the development engine.

Acknowledgment

The authors would like to thank GE Aircraft Engines for permission to publish this paper.

Nomenclature

blisk = bladed disk
C = airfoil section chord
IMM = radial immersion (0 = tip, 1 = hub)
T_{max} = airfoil section max thickness
Z = axial distance (inches)

References

[1] Scalzo, A., and Mori, Y., 1988, "A New 150 MW High Efficiency Heavy Duty Combustion Turbine," ASME, Paper No. 88-GT-162.
[2] Kashiwabara, Y., Katoh, Y., Ishii, H., Hattori, T., Matsura, Y., and Sasada, T., 1990, "Developments Leading to an Axial Flow Compressor for a 25MW Class High Efficiency Gas Turbine," ASME, Paper No. 90-GT-238.
[3] Sehra, A., Bettner, J., and Cohn, A., 1991, "Design of a High Performance Axial Compressor for Utility Gas Turbine," ASME, Paper No. 91-GT-145.
[4] Smed, J., Pisz, F., Kain, J., Yamaguchi, N., Umemura, S., 1991, "501F Compressor Development Program," ASME, Paper No. 91-GT-226.
[5] Janssen, M., Zimmermann, H., Kopper, F., and Richardson, J., 1995, "Application of Aero-Engine Technology to Heavy Duty Gas Turbines," ASME, Paper No. 95-GT-133.
[6] Stringham, G., Cassem, T., Prince, T., and Yeung, P., 1998, "Design and Development of a Nine Stage Axial Flow Compressor for Industrial Gas Turbines," ASME, Paper No. 98-GT-140.
[7] Farmer, R., 1994, "GE Launches LM2500+ Rated at 39 MW and 38% Thermal Efficiency," Gas Turbine World, May/June 1994, pp. 24–32.
[8] Valenti, M., 1998, "Luxury Liners Go Green," ASME Mechanical Engineering, July, pp. 72–73.
[9] Klapproth, J. F., Miller, M. L., and Parker, D. E., 1979, "Aerodynamic Development and Performance of the CF6-6/LM2500 Compressor,"AIAA, Paper No. 79-7030.
[10] Eisenberg, B., 1993, "Development of a New Front Stage for an Industrial Axial Flow Compressor," ASME, Paper No. 93-GT-327.
[11] Katoh, Y., Kashiwabara, Y., Ishii, H., Tsuda, Y., and Yanagida, M., 1993, "Development of a Transonic Front Stage of an Axial Flow Compressor for Industrial Gas Turbines," ASME, Paper No. 93-GT-304.
[12] Van Leuven, V., 1994, "Solar Turbines Incorporated Taurus 60 Gas Turbine Development," ASME, Paper No. 94-GT-115.
[13] Rocha, G., Saadatmand, M., and Bolander, G., 1995, "Development of the Taurus 70 Industrial Gas Turbine," ASME, Paper No. 95-GT-411.
[14] Koch, C. C., 1981, "Stalling Pressure Rise Capacity of Axial Flow Compressor Stages," ASME Journal of Engineering for Power, October 1981.
[15] Koch, C. C., and Smith, L. H., 1975, "Loss Sources and Magnitudes in Axial Flow Compressors," GE Aircraft Engines Technical, Report No. R75AEG344.
[16] Adkins, G. G., and Smith, L. H., 1982, "Spanwise Mixing in Axial Flow Turbomachines," ASME Journal of Engineering for Power, **104**, pp. 97–110.
[17] Jennions, I. K., and Turner, M. G., 1993, "Three-Dimensional Navier Stokes Computations of Transonic Fan Flow Using an Explicit Flow Solver and Implicit k-e Solver," ASME Journal of Turbomachinery, **115**, pp. 261–272.
[18] Wadia, A. R., and Law, C. H., 1993, "Low Aspect Ratio Transonic Rotors: Part 2-Influence of Location of Maximum Thickness on Transonic Compressor Performance," ASME Journal of Turbomachinery, **115**, pp. 226–239.
[19] Wadia, A. R., and Copenhaver, W. W., 1996, "An Investigation of the Effect of Cascade Area Ratios on Transonic Compressor Performance," ASME Journal of Turbomachinery, **118**, October 1996, pp. 760–770.
[20] Wadia, A. R., and Beacher, B. F., 1990, "Three-Dimensional Relief in Turbomachinery Blading," ASME Journal of Turbomachinery, **12**, No. 4, pp. 587–598.
[21] Wisler, D. C., 1985, "Loss Reduction in Axial-Flow Compressors Through Low Speed Model Testing," ASME Journal of Engineering for Gas Turbines and Power, **107**, pp. 354–363.
[22] Dunavant, J. C., "Cascade Investigation of a Related Series of 6 Percent Thick Guide Vane Profile and Design Charts," NACA-TN-3959.

A Solution Strategy Based on Segmented Domain Decomposition Multigrid for Turbomachinery Flows

M. L. Celestina
A. P. Solutions, Inc.,
Cleveland, OH 44135
e-mail: mark.celestina@grc.nasa.gov

J. J. Adamczyk
NASA Glenn Research Center,
Cleveland, OH 44135

S. G. Rubin
University of Cincinnati,
Cincinnati, OH 45221

A Segmented Domain Decomposition Multigrid (SDDMG) procedure was developed for viscous flow problems as they apply to turbomachinery flows. The procedure divides the computational domain into a coarse mesh comprised of uniformly spaced cells. To resolve smaller length scales such as the viscous layer near a surface, segments of the coarse mesh are subdivided into a finer mesh. This is repeated until adequate resolution of the smallest relevant length scale is obtained. Multigrid is used to communicate information between the different grid levels [1]. To test the procedure, simulation results will be presented for a compressor and turbine cascade. These simulations are intended to show the ability of the present method to generate grid independent solutions. Comparisons with data will also be presented. These comparisons will further demonstrate the usefulness of the present work for they allow an estimate of the accuracy of the flow modeling equations independent of error attributed to numerical discretization.
[DOI: 10.1115/1.1451085]

Introduction

To maintain a reasonable number of mesh points while attempting to resolve the wide range of length scales associated with turbomachinery passage flows, mesh stretching is often employed. However, mesh stretching can have an adverse effect on the convergence rate of a solution. This is particularly true if large mesh stretching is used. Another issue which impacts the convergence rate of finite volume discretization formulations is the ratio of the largest surface area of a cell to the smallest surface area of a cell. This ratio is often referred to as cell aspect ratio. It is well known that large values of cell aspect ratio can severely compromise the solution convergence rate.

Code developers, from experience or analysis [1] developed rules which govern the range of mesh stretching and cell aspect ratio to be used with their codes. Users are strongly encouraged to follow these rules in order to attain solution convergence. However, in some applications, strict adherence to the rules is not sufficient to ensure solution convergence nor does it guarantee adequate resolution of flow details.

The motivation for the present work came from attempts at developing a single mesh which is sufficiently fine to accurately capture a number of key flow features which are known to impact the aerodynamic performance of turbomachinery blading. This task becomes quite difficult if the mesh is required to conform to the stretching and aspect ratio rules and the number of mesh points or mesh cells are being held constant in order to control solution times.

This difficulty associated with stretched meshes led to an investigation of alternative meshing strategies. A promising mesh generation strategy which can overcome the stated difficultly is based on a mesh patch strategy known as domain decomposition. Domain decomposition employs a number of mesh segmented domains, i.e., mesh patches, which may or may not overlap. The mesh in each segmented domain is tailored so as to capture the dominant flow features within the domain. Some examples of works in this area are papers by Berger [2]. Another is the CHIMERA method originally developed by Steger [3] and since refined by Liou [4].

Brandt [5] observed that certain forms of domain decomposition can be viewed in the context of a multigrid solution strategy. These particular types of domain decomposition use a multigrid procedure to communicate information between the various mesh patches. The resulting methodology is called segmented domain decomposition multigrid strategy (SDDMG).

The first implementation of a SDDMG procedure to internal flows was by Srinivasan and Rubin [6]. They developed an adaptive approach to achieve optimal mesh resolution of a number of internal flows. Their work showed that the SDDMG method improved the resolution of the flowfield throughout as compared to a solution obtained with a single mesh using the same number of mesh points.

The objective of this work is to develop a segmented domain decomposition multigrid strategy within the framework of a three-dimensional finite volume, cell-centered scheme which solves the Reynolds-averaged form of the Navier-Stokes equations for turbomachinery flows. A key objective being the capability to efficiently generate solutions which are mesh independent. The strategy includes using uniform meshes in the blade-to-blade direction. For a three-dimensional simulation, a stretched mesh is used in the spanwise direction. The uses of a stretched mesh in the spanwise direction allowed a straight forward assessment of the usefulness of the SDDMG procedure prior to a full 3-D implementation.

The main elements of the SDDMG procedure are: a multiblock flow solver; a multigrid solution strategy; a multiblock mesh generation strategy; boundary conditions compatible with a multiblock flow solver; and interface conditions compatible with a multiblock flow solver. The next section discusses these elements in more detail. The SDDMG method is then applied to two cases. The first is a compressor cascade and the second is a turbine cascade. The intent of these simulations is to show the ability of the SDDMG method to converge to the underlying flow features which control the aerodynamic performance of turbomachinery

Contributed by the International Gas Turbine Institute and presented at the International Gas Turbine and Aeroengine Congress and Exhibition, New Orleans, Louisiana, June 4–7, 2001. Manuscript received by the IGTI, January 30, 2001. Paper No. 2001-GT-435. Review Chair: R. A. Natale.

blade rows. Where applicable the simulation results are compared to measurements. The final section presents a summary of this work with conclusions based on the results.

Procedure

The SDDMG procedure in this work solves the Reynolds-averaged Navier-Stokes equations, i.e., mean flow equations, using a cell-centered finite volume formulation. On each mesh, a Runge-Kutta iteration procedure is used to advance the solution [7].

The present work uses the two-equation standard $k-\varepsilon$ turbulence model of Launder and Spalding [8] to estimate the eddy viscosity. This turbulence model is a high Reynolds number model which requires the use of wall functions at solid surfaces and is valid from the beginning of the log-layer to the outer region of a turbulent boundary layer. The k and ε equations are discretized in the same way as the governing mean flow equations. The details of the discretization can be found in Shabbir et al. [9].

A mesh generation code developed by Mulac [10] generated all of the meshes used in this work. The code is a general purpose turbomachinery mesh generator which generates a three-dimensional H-mesh by applying a series of cubic spline fits to the geometric definition of the flowpath and blade.

Multiblock Structure. The multiblock structure for the current work begins with a single global parent mesh. This mesh is comprised of uniform cells and covers the entire computational domain. A global parent mesh is shown in Fig. 1 in computational space.

The first level of refinement subdivides the global parent mesh into sub-domain meshes. These segmented domains, relative to the global parent mesh, are called child meshes. The only rule that must be followed in refining a mesh level is that the boundary mesh lines of a child mesh must be coincident with a mesh line of the parent mesh. Figure 1 shows an example of two child meshes defined within a global parent mesh in computational space. This example shows a refinement in two mesh directions, however, the SDDMG method allows for refinement in a single direction.

Every subsequent level of mesh refinement is done in a similar manner. The child meshes on the previous mesh level are called parent meshes on their mesh level. From within these meshes, new child meshes are defined within the boundary of the parent mesh.

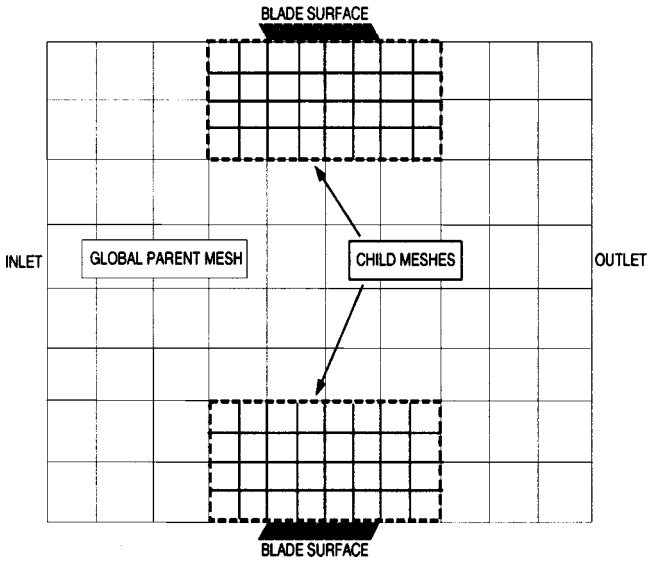

Fig. 1 Global parent mesh with two child meshes in computational coordinates. The dashed line depicts the boundaries of the child meshes.

The information that is needed to facilitate communication between a child mesh and its parent mesh is the location of the child mesh within its parent mesh and the type of refinement strategy used to generate the child mesh. The location of the child mesh within its parent mesh is important as it determines the type of boundary conditions to be applied to the child mesh. If a child mesh boundary is coincident with an external boundary, then the appropriate external boundary conditions is used. If the child mesh boundary is internal to the parent mesh, the appropriate interface condition is applied.

Multigrid Strategy. The present work used multigrid to computationally link a child and parent mesh. Within the context of multigrid, a child mesh defines the fine mesh and the associated parent mesh the coarse mesh. The steps involved with multigrid [5] are: an iteration procedure for solving the governing equations at each mesh level; a prolongation operator for transferring information from the parent mesh to the child mesh, i.e., from a coarse mesh to a fine mesh; a restriction operator for transferring information from the child mesh to the parent mesh. In the present work, a Runge-Kutta iteration procedure is used to advance the solution on each mesh level. A multigrid procedure also requires an estimate of relative truncation error between the child mesh and the associated parent mesh. This truncation error estimate appears as a forcing function in the mean flow equations associated with the parent mesh. Inclusion of the truncation error estimate in the mean flow equations associated with the parent mesh ensures that the spatial accuracy of these equations is consistent with the equations being solved on the child mesh. Further details on the multigrid strategy used in the present work can be found in Celestina [1].

Mesh Generation Strategy. The domain decomposition approach presented here assumes that all meshes for a simulation are generated before the calculation is started. The primary reason for this is to preserve the integrity of the geometry, primarily the blade surface definition, across all mesh levels. For convenience, the first step in this process involves the generation of a very fine mesh with uniform spacing for the entire computational domain using the mesh generation code developed by Mulac [10]. In constructing the finest mesh, one must consider the distance from the solid surfaces defined in terms of boundary layer wall units y^+. This must be consistent with the wall function boundary conditions of the turbulence model. Of equal importance is adequate resolution of the leading edge and trailing edge regions of the turbomachine geometry. For transonic blading, the region over which a shock wave interacts with a boundary layer also requires fine resolution.

As was previously stated, the only direction in which the mesh is stretched is the radial direction. Uniform mesh spacing is maintained in the blade to blade direction.

The fine global mesh is used to generate the global parent mesh and all child meshes by discarding the appropriate number of mesh points. The effect of the mesh generation procedure on the definition of the leading edge region of a high-speed compressor rotor is shown in Fig. 2. The global parent mesh, mesh level 1, generates a wedgelike leading edge. After five levels of mesh refinement, the finest child mesh, mesh level 6, provides a good definition of the leading edge region. The axial definition of mesh levels 3 and 4 are identical because they involve only a refinement in the pitch-wise direction.

Following the generation of all the parent and child meshes, a procedure is applied to all the subdomain meshes to ensure that the interface mesh lines of a child mesh are coincident with a mesh line of the parent mesh. This procedure is important as it simplifies the specification of the interface boundary condition on the child mesh. The direction of the projected area of the child mesh at the interface is identical to the parent mesh and the value of the projected area is half that of the parent mesh.

Boundary Conditions. The external boundary conditions are

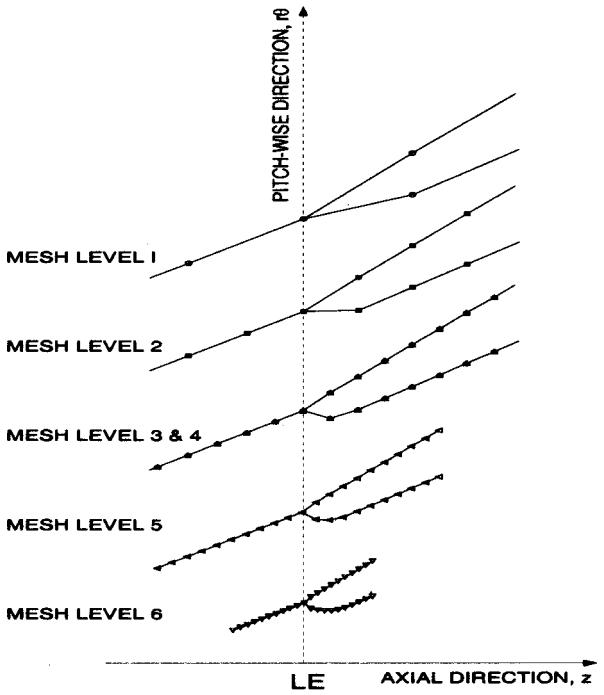

Fig. 2 Resolution of blade surface definition with mesh refinement

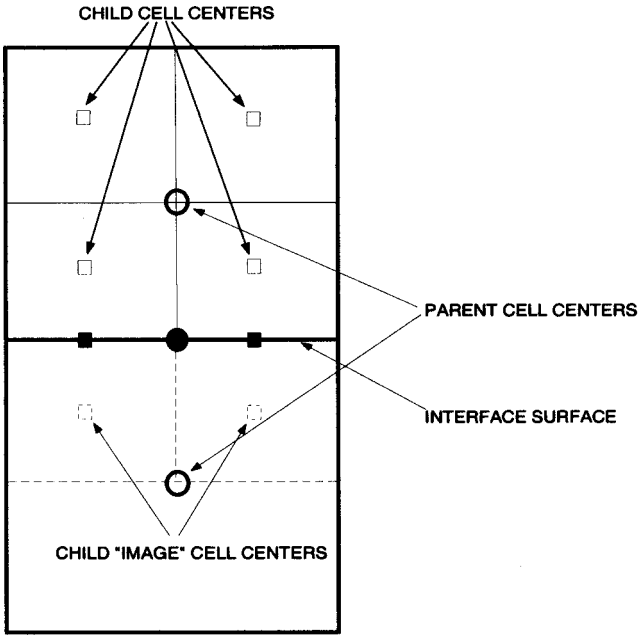

Fig. 3 Schematic of a parent mesh/child mesh interface surface

applied at the boundary of the finest mesh, i.e., parent or child, coincident with the external boundary. At solid surfaces, the external boundary conditions require that there be no heat transfer and that the fluid velocity relative to the surface be zero. At the incoming flow boundary, the external boundary condition sets the fluid total temperature, total pressure and flow direction. At the exit of the flow domain, the external boundary condition sets the static pressure.

At the external boundary for all other mesh levels, the external boundary conditions incorporate terms which reflect the relative truncation error between the parent and child mesh. The details associated with the implementation of external boundary conditions can be found in Celestina [1].

Interface Conditions. To complete the implementation of the domain decomposition procedure, the interface condition needs to be applied at a child mesh boundary not coincident with an external boundary. Hence, these interface conditions are applied at the child mesh boundary coincident with a parent mesh surface. This boundary is a line for two-dimensional flows and a plane for three-dimensional flows. The interface condition must conserve mass, momenta and energy across the interface between the child and parent mesh. The pressure must also be continuous across the interface. These requirements are stated by the following equations:

$$\begin{aligned} \rho_C &= \rho_P \\ [\rho \mathbf{v}]_C &= [\rho \mathbf{v}]_P \\ p_C &= p_P \\ H_{0C} &= H_{0P} \end{aligned} \tag{1}$$

where ρ is density, $\rho\mathbf{v}$ is the momentum vector, p is pressure, and H_0 is the enthalpy.

Figure 3 shows an interface surface between two parent mesh cells. The upper parent cell is within a child mesh domain and contains four child mesh cells. The lower parent mesh cell is outside but adjacent to a child mesh domain and contains the child mesh ''image'' cells. The open circles in Fig. 3 represent the center of the parent mesh cells and the open squares represent the center of the child mesh cells. The open broken line squares represent the center of the child mesh ''image'' cells. The physical location of the right-hand side of Eq. (1) is represented by the shaded circle in Fig. 3. The value of ρ, $\rho\mathbf{v}$, p, and H_0 at this location is the average of ρ, $\rho\mathbf{v}$, p, and H_0 from the centers of the parent mesh cells bordering the interface surface. The physical location of the left-hand side of Eq. (1) is represented by the shaded squares in Fig. 3. The value of ρ, $\rho\mathbf{v}$, p, and H_0 at these squares is set equal to the value of the corresponding variable located at the shaded circle. The value of ρ, $\rho\mathbf{v}$, p, and H_0 at the cell center of the child mesh ''image'' cell is then obtained by linear extrapolation using the value at the child interface surface and the value of the center of the child mesh bordering the child interface surface. The ''image'' cell values along with the interior cell values are then used to compute the viscous stress at the interface surface.

Implementation. The solution procedure is illustrated in the schematic diagram in Fig. 4, and the details can be found in Celestina [1]. The calculation begins on a mesh denoted as GPM (Global Parent Mesh) in Fig. 4. This mesh is covers the entire computational domain and represents mesh level I. The next mesh is the child of GPM and covers a portion of the computational domain. It should be noted that the child mesh domain may be identical to the parent mesh domain. This mesh represents mesh level II. A preset number of Runge-Kutta iterations, indicated as N iters. at the top of the diagram, are performed on GPM. The resulting estimate of the solution is interpolated, indicated as the broken line in the diagram, onto the child mesh (mesh level II). A preset number of iterations are performed on the child mesh. The updated estimate of the solution is passed back to the GPM along with an estimate of the relative truncation error associated with these two meshes. Once again, N iterations are performed on the GPM. The updated estimate of the solution is then passed back to the child mesh. This procedure represents a V-cycle multigrid solution strategy [5].

The next level of mesh refinement is now introduced. The estimate of the solution from the child mesh, level II, is interpolated onto the next mesh level, level III. The child mesh, level II, becomes the parent mesh, while the level III mesh becomes its child

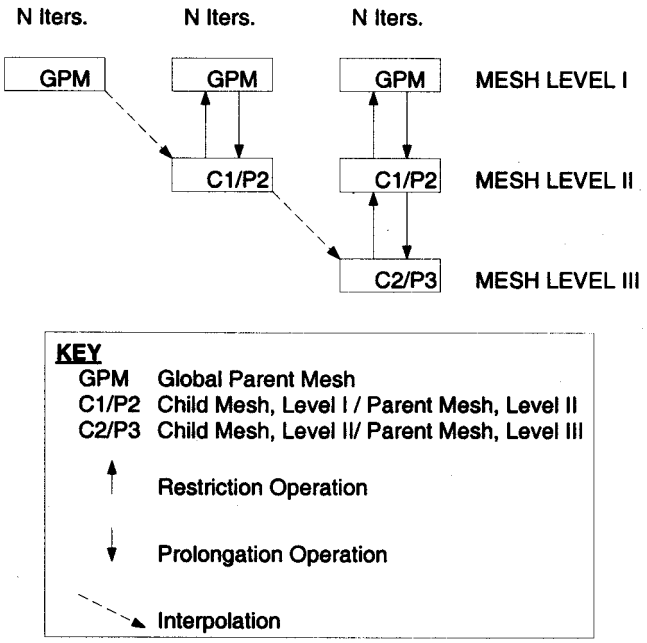

Fig. 4 Schematic of SDDMG procedure

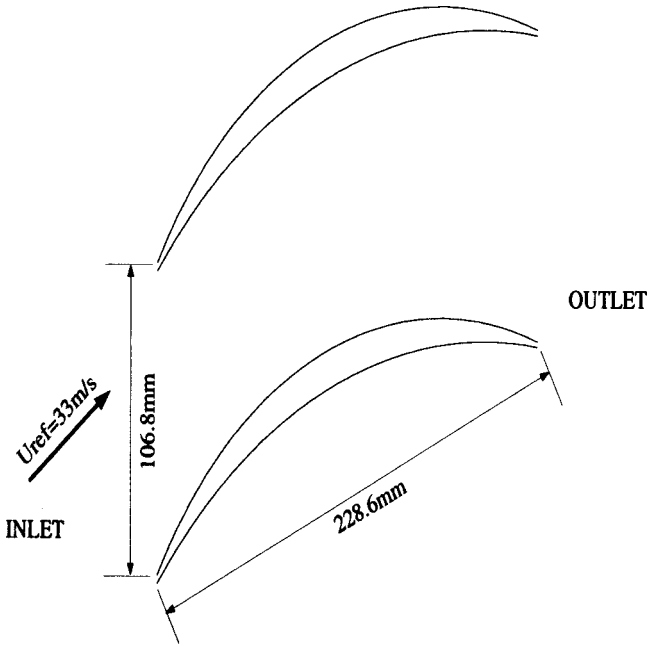

Fig. 5 Schematic of the ARL compressor cascade

mesh. The Runge-Kutta iteration procedure is initiated on the new parent mesh. After a preset number of iterations, *N* iters, the estimate of the solution is interpolated onto mesh level III. A set number of Runge-Kutta iterations are performed at this mesh level. The updated estimate of the solution along with an estimate of the relative truncation error associated with the parent and child mesh is passed back to the parent mesh. A set number of Runge-Kutta iterations are performed on the parent mesh. At the completion of the iteration procedure, the parent mesh is redefined as a child mesh (level II) associated with a parent mesh (GPM). The updated estimate of the solution from the redefined parent mesh is passed back to its parent along with an estimate of the relative truncation error. Once again, *N* Runge-Kutta iterations are performed on the parent mesh. Following a *V*-cycle multigrid strategy, the updated estimate of the solution is passed back to the child mesh, level II. At mesh level II, *N* Runge-Kutta iterations are performed and the subsequent estimate of the solution is passed onto the child mesh (mesh level III) of mesh level II. After a set number of Runge-Kutta iterations are completed on the child mesh, the procedure checks to see if there is another mesh level within mesh level III. If so, the mesh level is advanced and mesh level III becomes the parent mesh for mesh level IV. The foregoing procedure is then repeated involving all the previously defined mesh levels. This procedure is continued until all of the predetermined mesh levels have been included. Upon inclusion of the last mesh level, the solution strategy is terminated when the change in the estimated solution (based on two successive passes through the solution strategy) is within a given tolerance.

If, upon examination of the converged solution, it is felt that more resolution is needed in a given flow region, a finer mesh can be generated spanning the region. This new mesh is introduced at the appropriate mesh level and the solution strategy restarted incorporating the new mesh. An example of this is discussed in the results section, where two additional mesh refinements are added to a converged solution.

Results

Two geometries are presented to test and validate the SDDMG method. The cases are: a compressor cascade and a turbine cascade. The geometry for the two cascade cases include solid end-walls. Both cases have a limited amount of experimental data available. Comparisons to this data are made where possible.

ARL Compressor. The ARL cascade [11] is shown in Fig. 5. This cascade is made up of double-circular-arc airfoils typical of a highly loaded compressor blade. From the test report, the chord length c is given as 228.6 mm and the cascade solidity is 2.14. The aspect ratio is 1.61. The incoming flow is subsonic with a velocity of 33 m/s and the Reynolds number based on airfoil chord is 501,000.

To limit the influence of side-wall and end-wall boundary layer growth on the measurements, suction was applied upstream of the cascade inlet plane on all walls. To simulate the test setup, the aspect ratio of the simulated geometry was set to 8. This is done primarily to limit the impact of the side-wall and end-wall boundary layers on the core flow.

Since the geometry of the cascade airfoils is two-dimensional and the code used in this study is written in cylindrical coordinates, the hub and shroud, representing the cascade side-walls, must be placed at a very large radius. In addition, the ratio of the hub radius, R_h, and the shroud radius, R_s, must be near one. These two requirements yield a radius ratio $R^* = R_s - R_h / R_s$ near zero. In this study, the hub to shroud radius was set to 0.947 yielding a radius ratio of 0.053.

The test report presented data for three incidence angles. The simulation will only consider the data presented for an incidence angle of -1.5 deg.

The meshes used in the simulation of the ARL compressor cascade were of uniform spacing in the cascade plane. In the radial direction, the mesh spacing was non-uniform in order to resolve the side-wall boundary layers. The meshes on a cascade plane located at midspan are shown in Fig. 6. A total of seven mesh levels are used in the present simulation with six subdomain mesh levels. Table 1 gives a summary of the mesh sizes.

The global parent is mesh level 1 and contains 61 axial points with 21 of these points distributed uniformly along the chord of the airfoil. The inlet and outlet flow planes are set one chord length upstream and downstream, respectively, of the cascade inlet and exit planes. The number of radial mesh planes is fixed at 41. The spacing between these radial planes is varied in order to resolve the side-wall boundaries and is maintained for all subdomain meshes. In the global parent mesh, 21 equally spaced

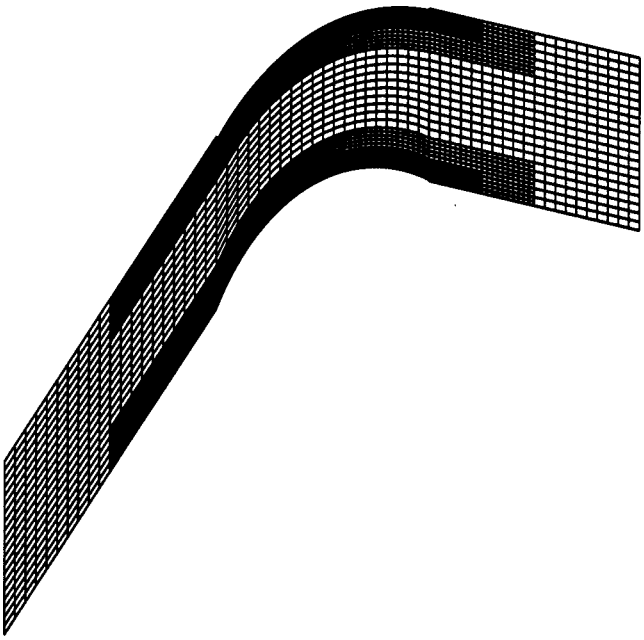

Fig. 6 Sectional view of the ARL compressor SDDMG mesh at midspan with seven mesh levels

planes are distributed across the cascade passage. The first set of subdomain refinements, mesh level II, starts at 50 percent chord upstream of the cascade inlet plane and ends at 50 percent chord downstream of the cascade exit plane. This refinement extends 25 percent of the pitch into the flow passage from either side of the blade surface. The third level of mesh refinement starts at 25 percent chord upstream of the cascade inlet plane and ends at 25 percent chord downstream of the cascade exit plane and extends 12 1/2 percent into the flow passage from either blade surface. This refinement strategy is repeated for the next two mesh levels with mesh level IV, starting at 12 1/2 percent (half of 25 percent) upstream of the cascade inlet plane and ending at 12 1/2 percent (half of 25 percent) downstream of the cascade exit plane and extending half of 12 1/2 percent into the flow passage from either blade surface. Mesh levels 6 and 7 are used to refine the region of flow surrounding the leading edge and trailing edge. These two sub-domains are illustrated in Figs. 7 and 8.

The simulation of the ARL cascade was done for an incidence angle of zero degrees. This incidence angle was established by matching the blade pressure distribution as predicted by a potential flow code [12;13] to that measured. It was felt that this procedure removed any issues associated with flow periodicity in the experiment.

Table 1 Mesh refinement schedule for ARL compressor

Mesh Level	Axial Points	Radial Points	Tangential Points	Number of Meshes
1	61	41	21	1
2	81	41	11	2
3	121	41	11	2
4	201	41	11	2
5	361	41	11	2
6	41	41	11	4
7	41	41	11	4

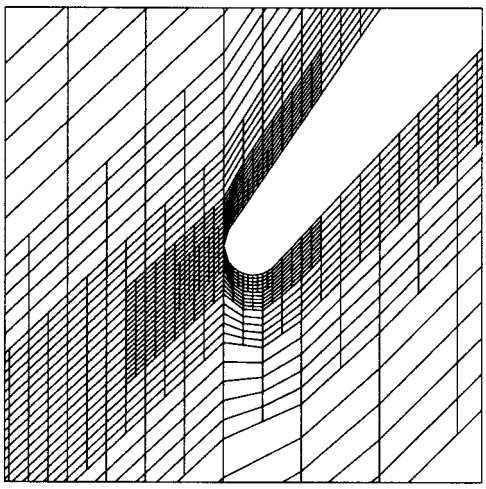

Fig. 7 SDDMG mesh near the leading edge region of the ARL compressor at midspan

Figure 9 shows contours of velocity magnitude at the midspan plane of the cascade. The contours of velocity magnitude remain continuous as they pass between the various mesh levels. The wake is seen to decay in a smooth manner with distance from the trailing edge. Figure 10 shows velocity vectors in the region of the suction surface trailing edge. The flow is separated from the suction surface in this region. The zero velocity line is shown in the figure and is seen passing smoothly through two mesh levels with the separation region extending across three mesh levels. The smooth transition of the flow from one mesh level to another is a direct result of the multigrid procedure.

The SDDMG procedure can converge to a mesh independent solution in critical flow regions such as the region surrounding the leading edge. The pressure field in this region of flow controls the initial development of the blade boundary layers. Another flow region which is important to resolve is the region of flow near the suction surface of the blade trailing edge. The flow in this region plays a major role in establishing the flow blockage and the blade circulation. To show that the solution in the leading edge region for the ARL cascade is independent of mesh, the blade pressure distribution, in terms of a pressure coefficient, C_p, for the various

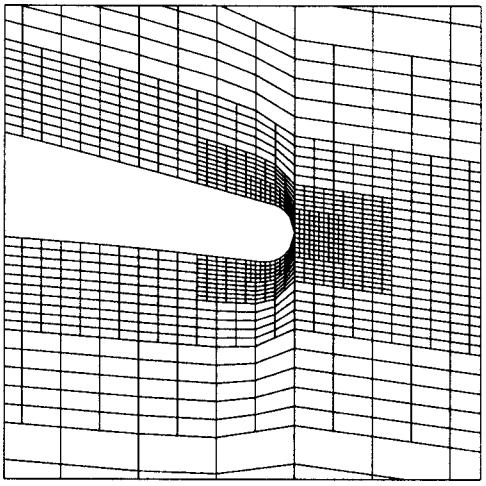

Fig. 8 SDDMG mesh near the trailing edge region of the ARL compressor at midspan

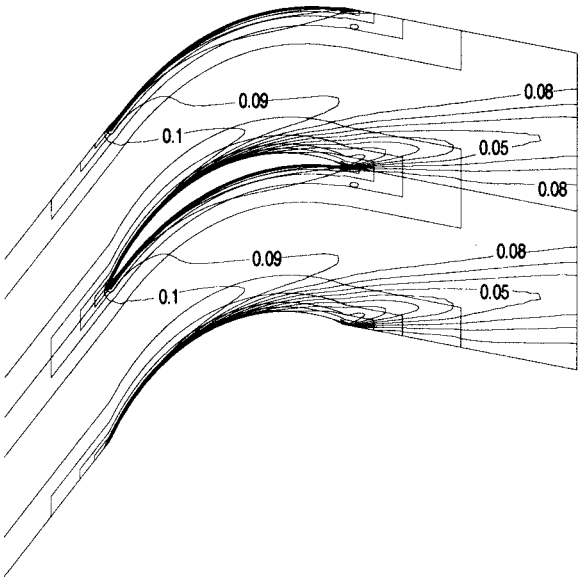

Fig. 9 Contours of velocity magnitude at midspan

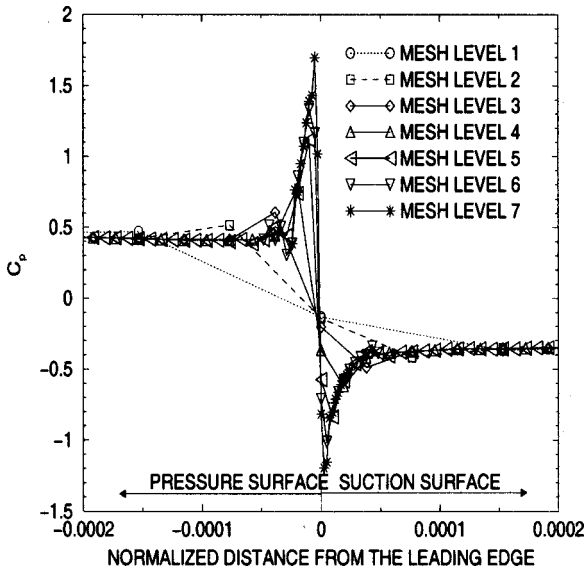

Fig. 11 Convergence of blade surface C_p for all SDDMG mesh levels versus normalized distance from the leading edge at midspan

mesh levels is plotted as a function of distance from the leading edge in Fig. 11. This shows that as the mesh refinement is increased (level 1 being the coarsest and level 7 the finest), the surface pressure distribution asymptotes to a curve which is independent of mesh level, hence a mesh independent result. In addition, note that the distribution associated with all mesh levels coarser than the finest, level 7, appear to be ''smooth'' estimates of the fine mesh result. This being the case even for the coarsest mesh (level 1) in which the leading edge is viewed as a wedge. These ''smooth'' estimates of the fine mesh result is a direct result of the multigrid strategy underpinning the SDDMG procedure.

Figure 12 shows the nondimensional axial velocity plotted as a function of distance from the suction surface for the finest 4 mesh levels. The chordwise location is near the suction surface trailing edge at about 90 percent of chord. The finest mesh is level 5 and the coarsest mesh is level 2. The velocity profiles obtained from the solution on each mesh level form a smooth velocity profile. The profiles on the finest two mesh levels, levels 4 and 5, are nearly identical and indicate that the solution in the region of the suction surface trailing edge is nearly mesh independent.

The next two figures show comparisons with experimental data. Figure 13 shows the blade surface pressure distribution as a function of blade chord as computed and measured. As noted above, the incidence angle for the simulation is zero degrees while that reported by Zierke and Deutsch [11] is −1.5 deg. The difference compensates for incoming flow differences between the simulated cascade with an infinite number of blades and the cascade in the experiment whose blade count is five. The final result for the ARL cascade, Fig. 14, shows the profile of the axial velocity across the pitch of the cascade. The axial location is 32.9 percent of the chord downstream of the cascade exit plane. Both simulation results and measurements are shown in Fig. 14. The simulation results incorporated all seven mesh levels. The wake measure-

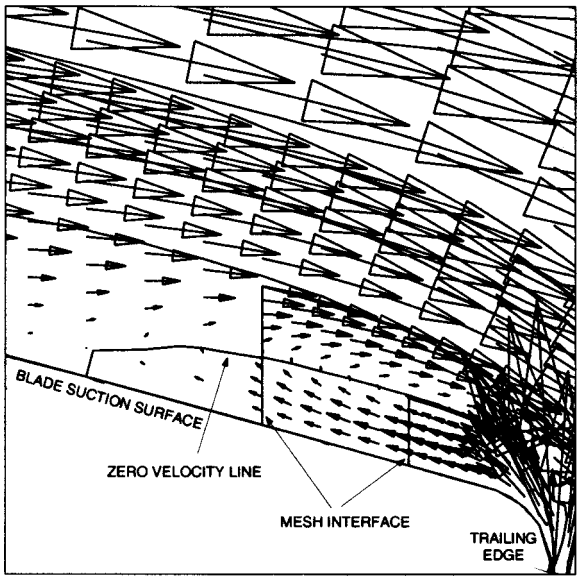

Fig. 10 Velocity vectors near the suction surface trailing edge midspan for SDDMG

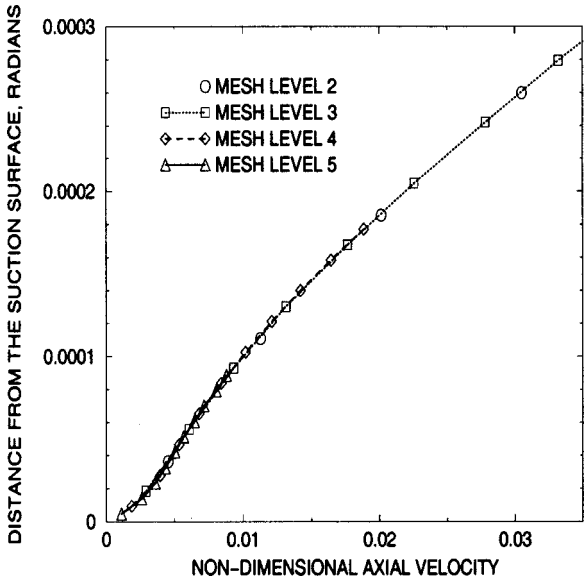

Fig. 12 Nondimensional axial velocity versus distance from the suction surface at midspan

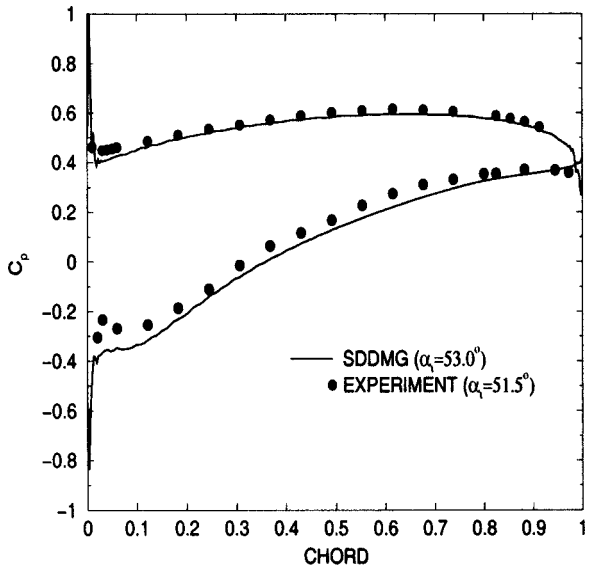

Fig. 13 Comparison of blade surface C_p versus percent chord at midspan for experimental data and SDDMG

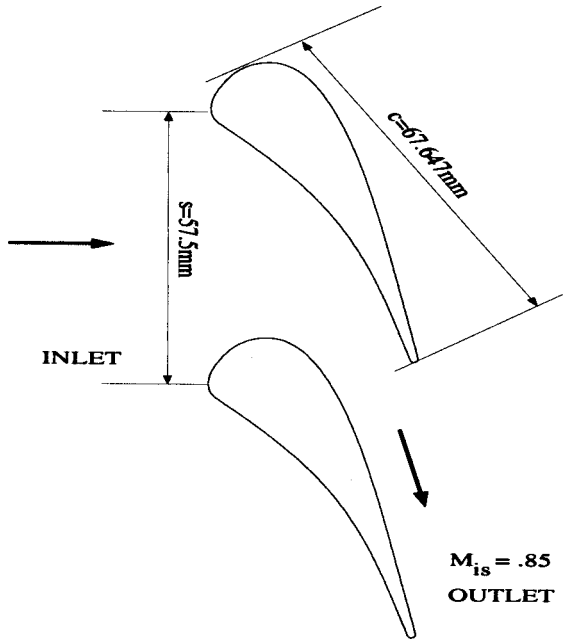

Fig. 15 Schematic of VKI turbine cascade

ments from the experiment were obtained with a five-hole probe. In the figure, two values of the wake velocity from the experiment are shown with error bars. For 95 percent confidence level, the uncertainty bound is about ±6 percent of the inlet velocity within the wake region [11]. Since it was shown that the simulation results are nearly independent of mesh, the difference between the computations and measurement is due to geometric differences between the physical cascade test setup and that specified in the simulation or errors introduced by the turbulence model.

VKI Turbine Cascade. The VKI turbine cascade airfoil geometry is shown in Fig. 15. It is representative of a highly loaded turbine nozzle. The aerodynamic performance [14] of a cascade of these airfoils was assessed in the Von Karman Institute short-duration isentropic light piston compression tube facility. The chord length of the tested airfoils is 67.647 mm and the cascade solidity is 1.176. Additional details of the cascade geometry can be found in Arts et al. [14]. All simulations were performed for an isentropic exit Mach number of 0.85. The experimental setup did not allow for the removal of the side-wall boundary layers. The cascade is simulated with the side walls included. Thus, the simulation is three-dimensional.

A cascade plane perspective of the midspan mesh used in the initial simulation is shown in Fig. 16. On each cascade plane, the mesh has seven mesh levels. These sub-meshes are identical for all cascade planes. In the spanwise direction, there are 41 cascade planes. They are spaced in the spanwise direction so as to resolve the side wall boundary layers. Table 2 gives a summary of the mesh sizes.

Mesh level 1 is the global parent mesh. The first two mesh levels, levels 2 and 3, are axial and pitchwise refinements of the global parent mesh. Mesh levels 4 and 5 are pitchwise refinements

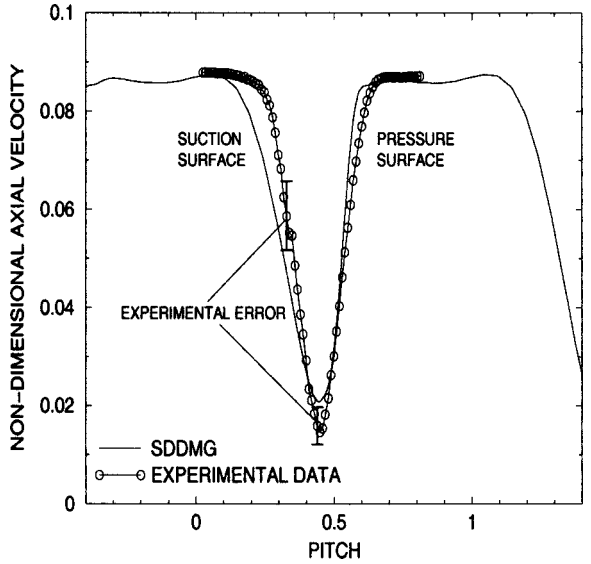

Fig. 14 Comparison of nondimensional axial velocity versus pitch at midspan for experimental data and SDDMG

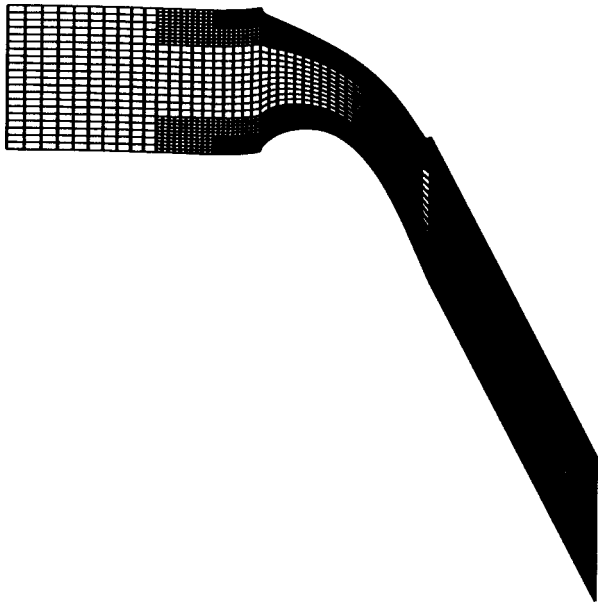

Fig. 16 Sectional view of the VKI turbine SDDMG mesh at midspan with six mesh levels

Table 2 Mesh refinement schedule for VKI turbine

Mesh Level	Axial Points	Radial Points	Tangential Points	Number of Meshes
1	61	41	21	1
2	81	41	11	2
3	121	41	11	2
4	101	41	11	2
5	101	41	11	2
6	21	41	11	4
7	21	41	11	4

only and are employed to resolve the blade boundary layers. Finally, mesh levels 6 and 7 are designed to better define the flow in the neighborhood of the leading and trailing edge.

A series of simulations showed that the flowfield was two-dimensional between 10 and 80 percent of span and thus only results for the midspan cascade plane will be reported. Figure 17 is a plot of the Mach number contours at midspan. The contours remain continuous as they pass through the various mesh levels. Figure 18 shows the velocity vectors in the region of the blade trailing edge. There is no evidence of these velocity vectors being discontinuous. Indeed, one can clearly see two counterrotating vorticies formed by the merger of the flow the suction and pressure surface.

A plot of the local loss coefficient, defined as

$$\chi = \frac{1 - \left(\frac{p_2}{p_{t2}}\right)^{\gamma - 1/\gamma}}{1 - \left(\frac{p_2}{p_{t1}}\right)^{\gamma - 1/\gamma}} - 1$$

(where p is pressure, p_t is the total pressure and the indice 1 denotes the inlet flow plane and 2 the measuring plane at 142 percent chord downstream of the cascade inlet plane) is shown as a function of pitch in Fig. 19. Both simulation and experimental results are shown. The agreement appears good, however, the simulation results overpredict the loss at the center of the wake. To ascertain whether this overprediction of loss is numerical in origin, a further refinement of the flow neighboring the suction surface was attempted. At the location of minimum suction surface pressure, the mesh refinement reduced the value of y^+ at the centroid of the first cell from approximately 75 to approximately 20. The resulting velocity profile through the suction surface boundary layer is shown in Fig. 20. Shown on the figure are plots associated with the three mesh levels. The finest mesh is level 9 and the coarsest mesh is level 5. Mesh level 8 represents the first refinement of mesh level 5 and mesh level 9 is a second refinement of level 5. The plots in Fig. 20 show that the results for mesh levels 8 and 9 are nearly identical. This indicates that the solution through the suction surface boundary layer in the vicinity of minimum pressure is nearly mesh independent. The simulation results presented in Fig. 18 are associated with the velocity profile for

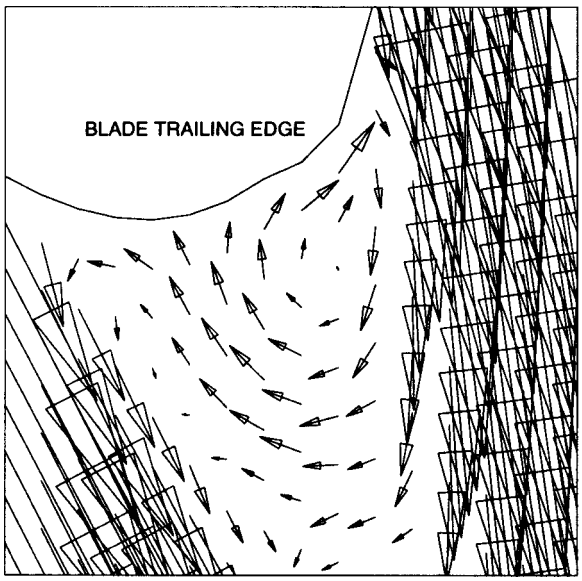

Fig. 18 Flow vectors near the trailing edge at midspan

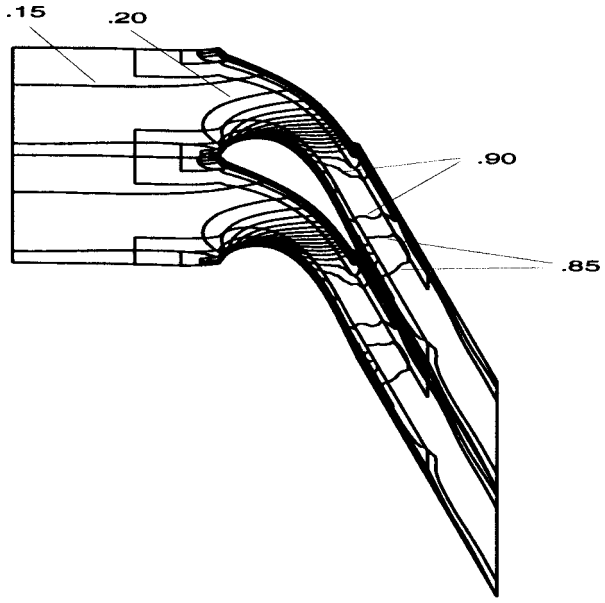

Fig. 17 Mach number contours at midspan in increments of 0.05

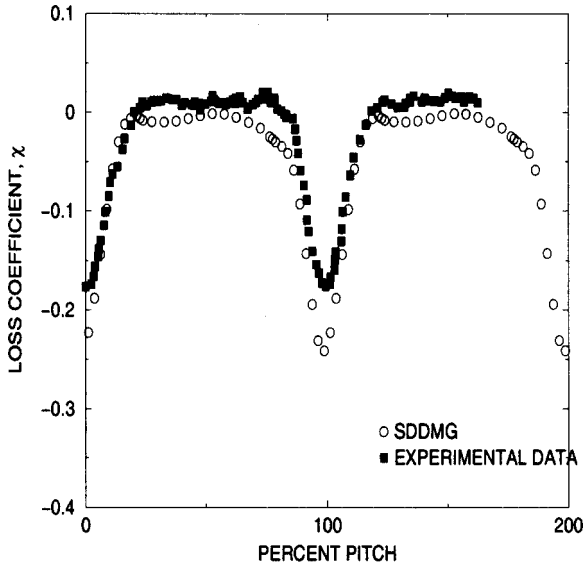

Fig. 19 Loss coefficient at 143 percent chord at midspan

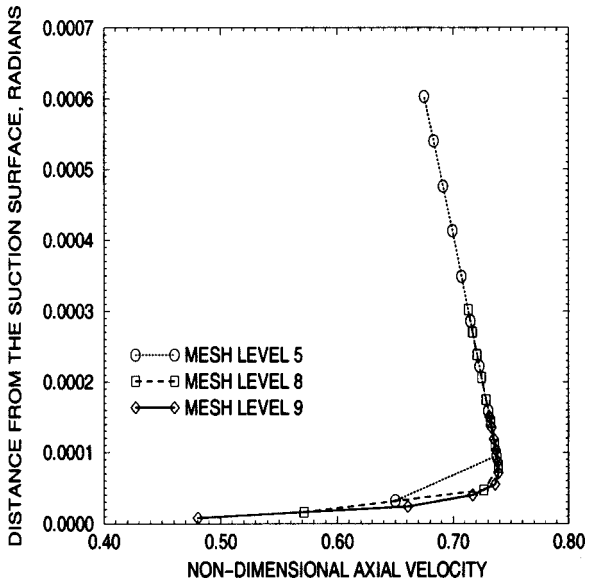

Fig. 20 Nondimensional axial velocity versus distance from the suction surface at midspan

mesh level 5. Note that the results for mesh level 5 fail to resolve the outer region of the suction surface boundary layer. The impact of the refined definition of the suction surface boundary layer on the local loss coefficient is shown in Fig. 21 as a function of pitch. The plots from Fig. 19 are repeated in the figure. The added refinement appears to have little impact on the estimated loss at the center of the wake. The refinement does appear to yield a sharper loss profile with the loss profile for level 8 being nearly that for mesh level 9. Thus, one can state that the loss profiles are nearly mesh independent. Any differences between the simulation and experimental result are due to experimental error (note the experimental loss coefficient is greater than one in the core flow region), a difference between the simulated geometry and that of the experiment, or the modeling of turbulence.

For both the ARL and VKI cascade simulations, the SDDMG procedure did not adversely impact the stability of the Runge-Kutta iteration strategy. On the contrary the stability of the Runge-Kutta procedure appeared to be improved by the SDDMG procedure. This positive impact on stability appears to be related to the elimination of the adverse effects of mesh stretching by the SDDMG procedure.

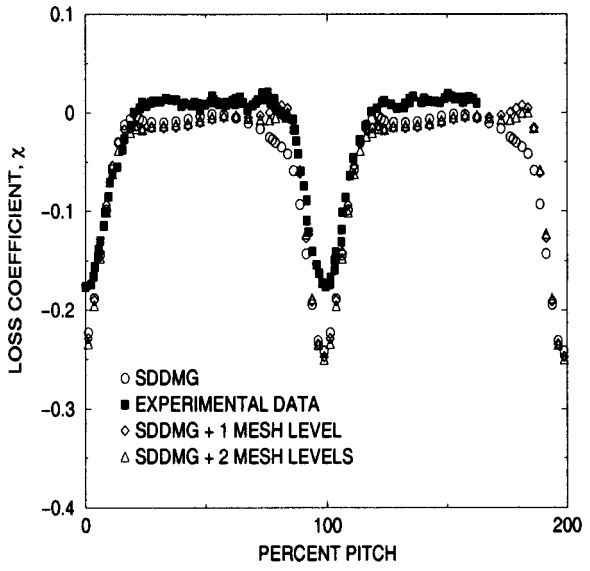

Fig. 21 Comparison of loss coefficient at 143 percent chord at midspan

Summary and Conclusions

Accurate predictions of the aerodynamic performance of turbomachinery blading requires resolution of flow features near the leading and trailing edges of blades, boundary layers, shocks and clearance flows. To obtain the required flow detail, grid cells are clustered in regions of high flow gradients and then stretched to fill in the remaining flow region. This often results in grids with very high aspect ratios. For CFD codes which employ a Runge-Kutta-based iteration strategy, this often leads to numerical stability problems. To circumvent these stability problems and still have the ability to resolve features associated with high flow gradients, a segmented domain decomposition multigrid (SDDMG) procedure was developed. The SDDMG procedure was implemented in 2-D to test its ability to produce grid independent solutions and enhance the stability of a Runge-Kutta-based integration strategy.

The SDDMG procedure was used to simulate a compressor and turbine cascade. Each case was used to show a different feature of the SDDMG procedure. Both simulations yield results which were grid independent. Results were shown that illustrated the ability of the SDDMG procedure to capture the flow details in the neighborhood of a compressor blade leading edge and a turbine blade trailing edge. In addition, it was shown that the SDDMG procedure yielded velocity profiles associated with blade boundary layers which were grid independent.

Comparison of simulation results to experimental data showed the SDDMG procedure was predicting solutions that are consistent with the experimental data. Indeed since the simulation results are, for all practical purposes grid independent, any difference between simulation and experiment is due to geometry differences, experimental error, or the modeling of turbulence.

Comparison of the SDDMG method to a conventional meshing strategy is difficult because the mesh construction of each system is so different. However, such a comparison was reported and discussed in Celestina [1]. A comparison of the convergence history of the two strategies to a time asymptotic solution showed that the SDDMG method converged about 15 percent faster than the conventional stretched mesh method even with about 15 percent more mesh points.

Based on the results from this study, the SDDMG procedure is a viable alternative to grid stretching to resolve the flow features which control the performance of turbomachinery blading. An implementation of the SDDMG procedure in 3-D is recommended.

Acknowledgment

Thanks go to Mr. Richard Mulac for his help with grid generation and Dr. Aamir Shabbir for his help with the implementation of the $k-\varepsilon$ turbulence model in this work.

References

[1] Celestina, M. L., 1999, "Segmented Domain Decomposition Multigrid for 3-D Turbomachinery Flows," Ph.D. dissertation, University of Cincinnati, Cincinnati, OH.
[2] Berger, M. J., and Colella, P., 1989, "Local Adaptive Mesh Refinement for Shock Hydrodynamics," J. Comp. Phys., **82**, pp. 64–84.
[3] Steger, J., and Benek, J. A., 1987, "On the Use of Composite Grid Schemes in Computational Aerodynamics," Comput. Methods Appl. Mech. Eng., **64**, pp. 301–320.
[4] Liou, M.-S., and Kao, K.-H., 1994, "Progress in Grid Generation: From Chimera to DRAGON Grid," NASA TM 106709.
[5] Brandt, A., 1977, "Multi-Level Adaptive Solutions to Boundary-Value Problems," Math. Comput., **31**, 138, pp. 333–390.
[6] Srinivasan, K., and Rubin, S. G., 1997, "Solution Based Grid Optimization Through Segmented Multigrid Domain Decomposition," J. Comp. Phys., **136**, pp. 467–493.

[7] Adamczyk, J. J., Celestina, M. L., Beach, T. A., and Barnett, M., 1990, ''Simulation of Three-Dimensional Viscous Flows Within a Multistage Turbine,'' ASME J. Turbomach., **112**, pp. 370–376.
[8] Launder, B. E., and Spalding, D. B., 1974, ''The Numerical Computation of Turbulent Flows,'' Comput. Methods Appl. Mech. Eng., **3**, pp. 269–289.
[9] Shabbir, A., Zhu, J., and Celestina, M. L., 1996, ''Assessment of Three Turbulence Models in a Compressor Rotor,'' ASME 96-GT-198.
[10] Mulac, R. A., 1986, ''A Multistage Mesh Generator for Solving the Average-Passage Equation System,'' NASA CR-179539.
[11] Zierke, W. C., and Deutsch, S., 1989, ''The Measurement of Boundary Layers on a Compressor Blade in Cascade, Vol. 1,'' NASA CR-185118.
[12] McFarland, E. R., 1982, ''Solution of Plane Cascade Flow Using Improved Surface Singularity Methods,'' ASME J. Eng. Power, **104**, pp. 668–674.
[13] McFarland, E. R., 1984, ''A Rapid Blade-to-Blade Solution for Use in Turbomachinery Design,'' ASME J. Eng. Gas Turbines Power, **106**, pp. 376–382.
[14] Arts, T., Lambert de Rouvroit, M., and Rutherford, A. W., 1990, ''Aero-Thermal Investigation of a Highly Loaded Transonic Linear Turbine Guide Vane Cascade,'' VKI Technical Note 174.

The Effect of Variable Chord Length on Transonic Axial Rotor Performance

William B. Roberts
Mem. ASME
e-mail: byron.far@juno.com

Albert Armin

George Kassaseya

Airfoil Management Co. and
Airfoil Technologies International,
Compton, CA 90220

Kenneth L. Suder
Mem. ASME

Scott A. Thorp

Anthony J. Strazisar
Mem. ASME

NASA Glenn Research Center,
Cleveland, OH

Aircraft fan and compressor blade leading edges suffer from atmospheric particulate erosion that reduces aerodynamic performance. Recontouring the blade leading edge region can restore blade performance. This process typically results in blades of varying chord length. The question therefore arises as to whether performance of refurbished fans and compressors could be further improved if blades of varying chord length are installed into the disk in a certain order. To investigate this issue the aerodynamic performance of a transonic compressor rotor operating with blades of varying chord length was measured in back-to-back compressor test rig entries. One half of the rotor blades were the full nominal chord length while the remaining half of the blades were cut back at the leading edge to 95% of chord length and recontoured. The rotor aerodynamic performance was measured at 100, 80, and 60% of design speed for three blade installation configurations: nominal-chord blades in half of the disk and short-chord blades in half of the disk; four alternating quadrants of nominal-chord and short-chord blades; nominal-chord and short-chord blades alternating around the disk. No significant difference in performance was found between configurations, indicating that blade chord variation is not important to aerodynamic performance above the stall chord limit if leading edges have the same shape. The stall chord limit for most civil aviation turbofan engines is between 94–96% of nominal (new) blade chord. [DOI: 10.1115/1.1459734]

Keywords: Axial Compressor, Variable Chord, Blade Recontour, Performance Restoration

Introduction

Users of gas turbine engines have a vested interest in tracking performance trends with time in service to determine component deterioration and, consequently, maintenance intervals. During the life of any gas turbine, blade erosion is present, especially for those units that are exposed to unfiltered air such as aviation turbofan engines. It has been observed that atmospheric particulate erosion is a serious concern for the fan and the tip regions of high pressure compressors, see Sallee et al. [1], Kramer et al. [2], Covey et al. [3], and the DOE/FAA Symposium [4]. The effect of this erosion is to reduce the blade chord progressively from the midspan to the tip region and to roughen and distort the blade surface.

The effects of roughness on rotor performance have been documented by Suder et al. [5] and Roberts [6]. These papers indicate that the penalty for leading edge roughness and erosion can be significant. Turbofan operators therefore perform chord length restoration at routine maintenance intervals to regain performance before deterioration is too severe to salvage blades.

As the rotor blades erode, the leading edge becomes rough, blunt and distorted from the nominal shape and the aerodynamic performance suffers (Reid and Urasek [7]). Nominal performance can be recovered by recountouring the leading edges as reported by Roberts [8]. A recontouring or reprofiling process similar to that illustrated in Fig. 1 can restore nominal operation for multiple compressor and engine refurbishment cycles until the blade chord erodes to the stall limit. Below this chord length, which varies among engine-compressor types, a decrease of stall margin is likely (Roberts [9,10]).

After compressor blade rework that includes leading edge recontouring, there exists a pool of blades with different chord lengths, ranging from blades that are near nominal chord length down to those near the stall chord limit. Furthermore, as blades erode below the stall limit, they must be replaced with new blades that have the full nominal chord length. A set of compressor blades of varying chord length will therefore be installed into each turbofan engine that goes through a complete maintenance cycle. The current maintenance practice is to distribute blades of varying chord length around the disk with a check for balance. A reassembled engine is then checked on a test stand to insure that it meets rated thrust with sufficient exhaust gas temperature margin before return to an aircraft. Since even 1% of fuel burn can add up

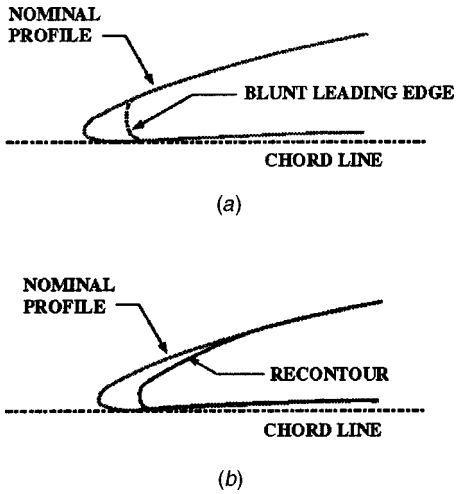

Fig. 1 Schematic of blade leading edge—(*a*) Blunt leading edge due to erosion, (*b*) Recontoured leading edge

Contributed by the International Gas Turbine Institute and presented at the International Gas Turbine and Aeroengine Congress and Exhibition, New Orleans, Louisiana, June 4–7, 2001. Manuscript received by the IGTI, January 18, 2001. Paper No. 2001-GT-498. Review Chair: R. A. Natole.

to several tens of millions of dollars in operator cost per year for a large fleet of engines, the question arises ''Does fan or compressor performance depend on the order in which mixed-chord blades are installed into a fan or compressor disk?'' Investigation of this issue through back-to-back engine tests at an airline maintenance facility is prohibitively expensive in terms of both cost and time. Furthermore, the results would be difficult to interpret due to other changes made to an engine during a shop visit. The purpose of the present investigation is therefore to explore this issue in a carefully controlled compressor research rig environment.

An opportunity to perform the necessary variable-chord rotor testing arose when a NASA-Glenn high-speed compressor rotor was damaged during compressor stability research. During a weld-repair and a recontour of the blade leading edges, one-half of the rotor blades were repaired to nominal chord and one-half were repaired to 95% of nominal chord. This chord length was chosen because the great majority of civil turbofan engines have stall chord limits between 94 and 96% of nominal chord [9,10].

Test Rotor

The test rotor for the present study, shown in Fig. 2, is from a low aspect ratio transonic core compressor inlet stage designated as NASA Stage 35. The results reported here were obtained from a rotor-only configuration with the stator removed. This configuration eliminates blade row interactions and thus allows direct measurement of flow differences between rotor configurations. The rotor design pressure ratio is 1.865 at a massflow of 20.19 kg/s. The inlet relative Mach number is 1.13 at the hub and 1.48 at the tip at the design tip speed of 454 m/s. The rotor has 36 blades, an inlet tip radius of 25.4 cm, a hub-tip radius ratio of 0.70, an aspect ratio of 1.19, a tip solidity of 1.3, and an axial chord of 2.72 cm at the tip and 4.12 cm at the hub. The rotor tip clearance at design speed is 0.40 mm (0.016 in.), which corresponds to 0.7% of chord. Details of the rotor aerodynamic design were reported by Reid and Moore [11]. Overall aerodynamic performance of the stage was reported by Reid and Moore [12].

Instrumentation and Measurement Techniques

All measurements were taken in the NASA-Glenn W8 single-stage axial compressor facility, shown schematically in Fig. 3. A complete description of the facility is given in Moore and Reid [12]. Mass flow is measured using a calibrated orifice located far upstream of the compressor. The orifice measurements are corrected to standard-day conditions at the rotor inlet. Radial distributions of total and static pressure, total temperature, and flow angle are measured at stations 1 and 2 shown in Fig. 4. Stage 35 is a close-coupled stage, and there is not sufficient space for a survey station between the rotor and stator. Since additional survey stations were not added in the present work, Station 2, which is normally used to survey the stator outlet flow, is the first available aerodynamic survey station downstream of the rotor. The measurement uncertainties are: massflow, ± 0.3 kg/s; flow angle, ± 0.5 deg; total pressure ± 0.01 N/cm^2; total temperature, ± 0.6 K. The probe measurements are corrected for Mach number and streamline slope based on a calibration of each probe used and on

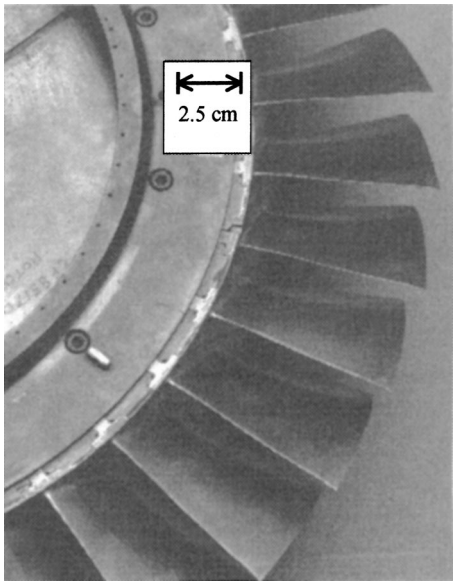

Fig. 2 NASA rotor 35

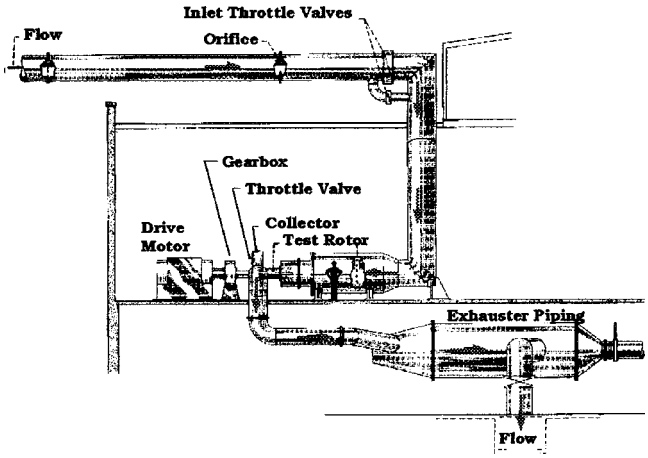

Fig. 3 NASA-Glenn single-stage transonic compressor test facility

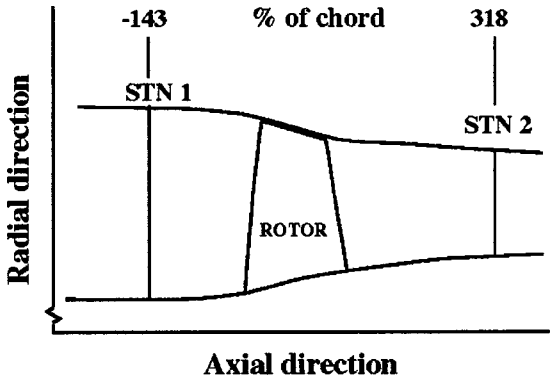

Fig. 4 Location of aerodynamic survey stations

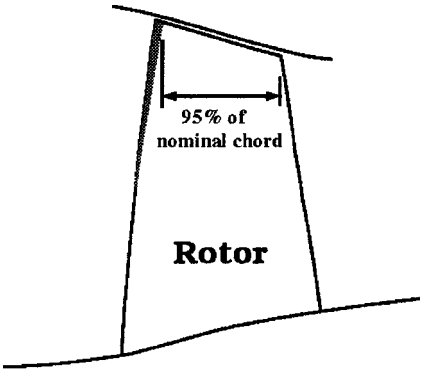

Fig. 5 Simulated erosion of 5% of chord over the outer 50% of span

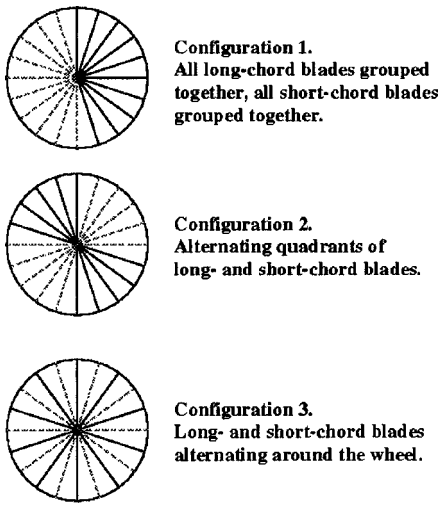

Fig. 6 Schematic of tested blade installation configurations

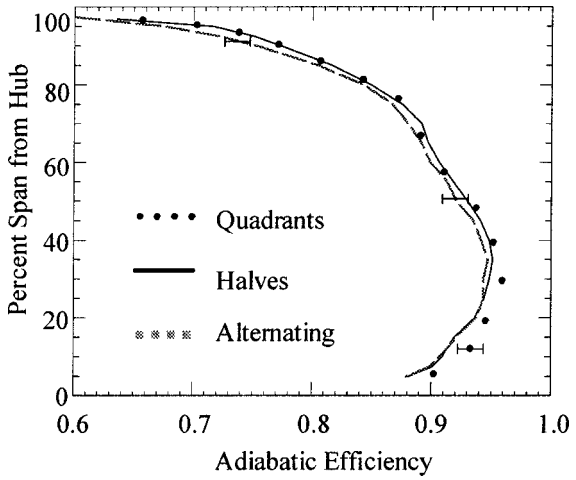

Fig. 8 Radial profiles of efficiency for 80% speed at a massflow rate of 17.5 kg/s

the design streamline slope. All measurements are corrected to sea-level standard-day conditions at the rotor inlet. Radial distributions of total temperature are mass averaged across the annulus. Radial distributions of total pressure are energy averaged by converting them to their enthalpy equivalents and then mass averaging them across the annulus.

Experimental Procedure

Figure 5 shows the simulated erosion applied to one-half of the Rotor 35 blades during leading edge repair. Starting at mid-span, these blades were blended back to 95% of nominal chord at the tip and then recontoured as shown in Fig. 1 using a procedure described by Roberts [8] and Model and Roberts [13]. The remain-

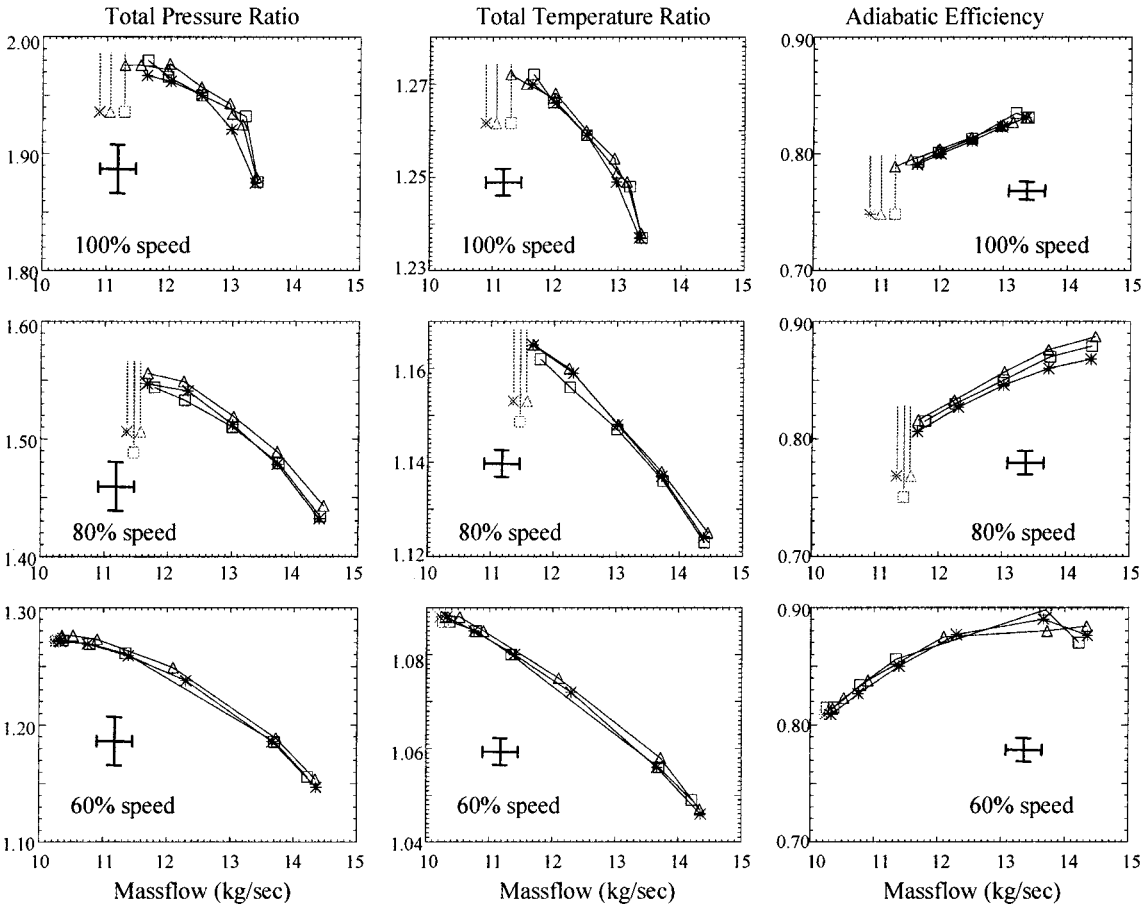

Fig. 7 Rotor overall performance at 60, 80, and 100% speed for three blade installation configurations. Stalling massflow denoted by vertical bars. Crosses denote error bars. □, halves; △, quadrants; ∗ alternating.

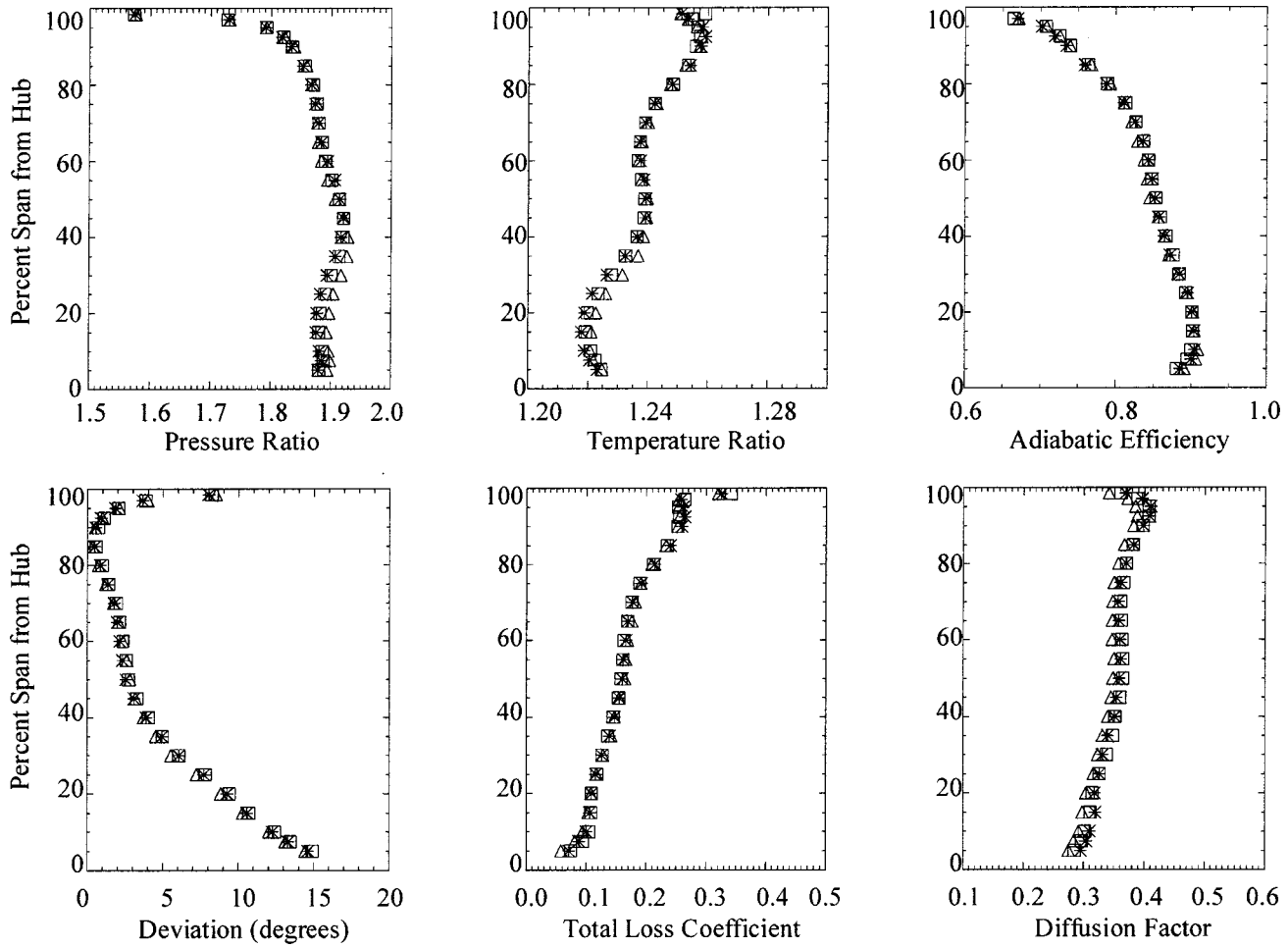

Fig. 9 Rotor performance at 100% speed, maximum massflow operating point—□, halves; △, quadrants; ∗, alternating

ing half of the blades were weld repaired back to the full nominal chord length, and the leading edges were then also recontoured using the same process.

The rotor was tested using the three blade installation configurations of nominal and short-chord blades illustrated in Fig. 6:

1. HALVES: 18 nominal-chord blades followed by 18 short-chord blades;
2. QUADRANTS: four 90-deg. segments around the compressor disk, each containing nine blades of the same chord length;
3. ALTERNATING: nominal-chord and short-chord blades alternating around the disk.

These configurations were chosen to investigate the range of possible blade installation configurations that might be encountered when reinstalling mixed-chord blades into a fan or compressor during an engine shop maintenance visit.

All configurations were tested at 100, 80, and 60% of design speed. These speeds yield tip relative Mach numbers of 1.48, 1.18, and 0.89, respectively. These speeds were chosen to cover the range of tip speeds encountered within modern fans and the front, middle, and rear stages of core compressors. Full spanwise probe surveys were taken to provide detailed performance data over the annulus height as well as mass averaged performance parameters.

Test Results

Figure 7 summarizes the rotor performance characteristics at 100, 80, and 60% speed for the three configurations tested. Full-span aerodynamic performance surveys were acquired at each point plotted in Fig. 7. The error bars shown in each figure indicate the estimated error in the data based on uncertainties in pressure and temperature measurement, probe calibration, and probe positioning. The stalling massflow for each configuration tested at 80 and 100% speed is noted by a vertical bar. At 60% speed the stalling massflow was not significantly different than the lowest massflow at which full surveys were acquired.

The maximum massflow achieved at design speed does not correspond to rotor choke, but is set by choking of the diffuser downstream of the rotor, which was not designed for the exit flow swirl present when the stator is removed. In addition, the pressure rise and efficiency for all three configurations at design speed are lower than previously measured for rotor 35 [11]. This results from the fact that the leading edge recontour process for both the short-chord and nominal-chord blades did not preserve a slight end bend at the leading edge in the outer 10% of the blade span. The repair process is fully capable of preserving the end-bend found in the original Rotor 35 airfoil. However, the time and resources available for the ''one-off'' repair of Rotor 35 did not justify the cost of the tooling required to preserve this feature in the repaired blades. Since the end-bend helps to adjust the blade leading-edge incidence to the lower axial velocity within the end-wall boundary layer, its elimination during blade repair resulted in lower pressure rise and efficiency due to increased loss and blockage at the tip. These differences between the repaired blade and original blade performance are significantly reduced at 80% and 60% of blade speed. The authors feel that the differences between original and repaired blade performance do not compromise the

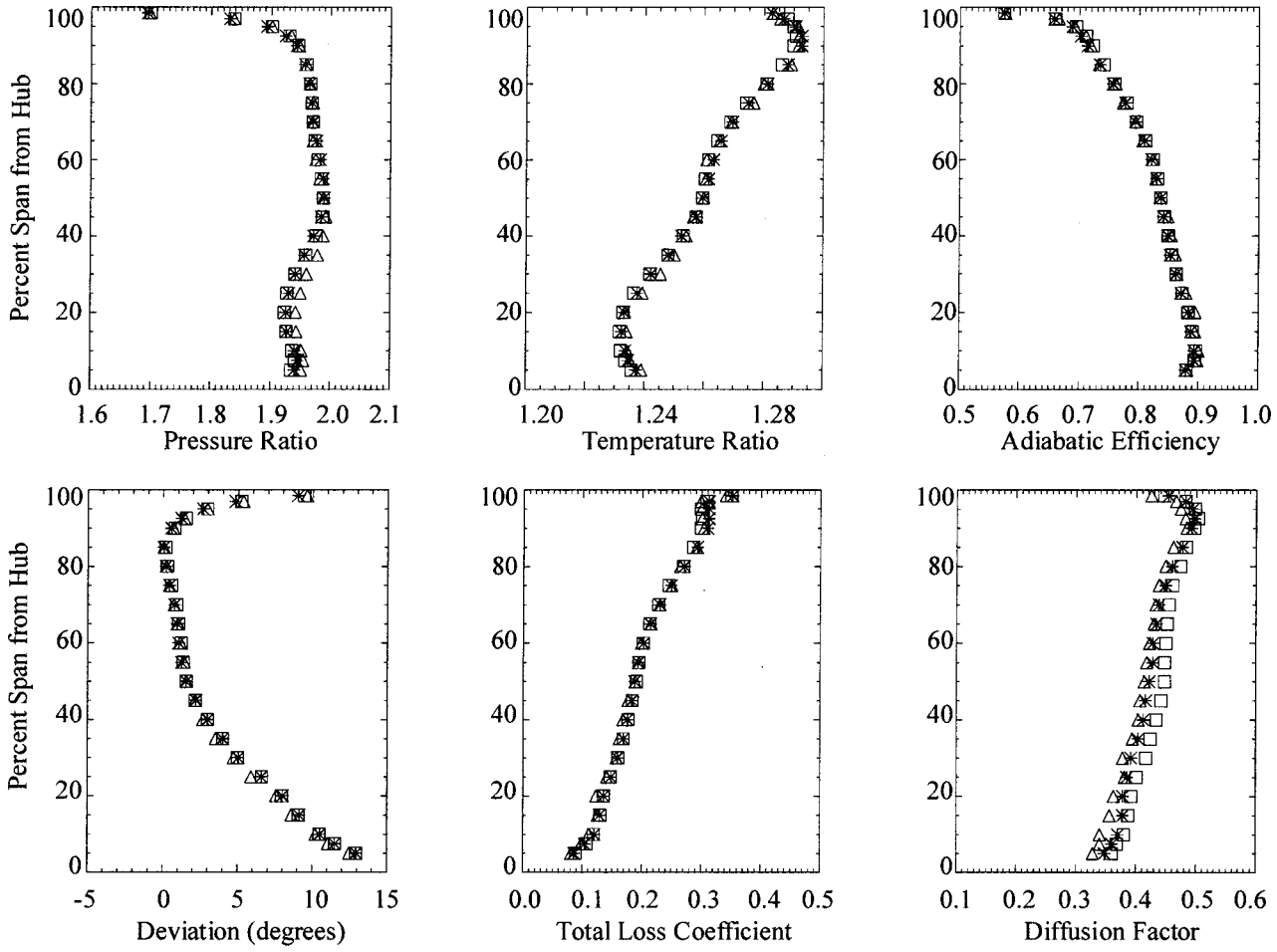

Fig. 10 Rotor performance at 100% speed, midway between maximum and near-stall operating points—□, halves; △, quadrants; ∗, alternating

results of this investigation, which is focussed on differences in blade performance as a function of how mixed-chord blades are loaded into the compressor disk.

It can be seen from Fig. 7 that, within the measurement error, there are only two significant differences in performance for the different blade installation configurations. First, the ''alternating'' blade installation (Configuration 3) consistently delivers the largest stall margin. At design speed the stall margin for the ''alternating'' blade configuration is 18.4% compared to 16.4% for the ''halves'' configuration. This seems reasonable since the short-chord blades have a higher aspect ratio and can be expected to have less stable operating range. By grouping these blades together (as in the ''halves'' configuration), stall precursive disturbances have an opportunity to grow in amplitude as they rotate around the short-chord half of the wheel, thus triggering stall. By contrast, in the ''alternating'' configuration, the wheel consists of pairs of long- and short-chord blades, and the long-chord blades apparently serve to stabilize their short-chord neighbors.

The second notable difference in overall performance shown in Fig. 7 is a consistent spread in efficiency between the three blade installation configurations at 80% of design speed. Two reasons for this spread can be seen in Fig. 8, a plot of the spanwise profiles of efficiency at the highest massflow. The data symbols have been removed in order to more clearly see the differences between profiles. The ''quadrant'' configuration is approximately 2 points higher in efficiency than the other two configurations over the lower 40% of span. Although masked by the steep radial gradient in efficiency near the tip, a close look at the data also reveals that the ''alternating'' configuration is 2–4 points lower in efficiency than the other two configurations at any given location outboard of 80% span. While the efficiency differences shown in Figs. 7 and 8 are not much greater than the uncertainty of the measurements, they are consistently evident across the massflow range and are therefore probably real. Survey data was often acquired at 60 and 100% speed during the same rig run as the data shown in Fig. 8 and inspection of the data acquired at these other speed does not show the same trends as observed at 80% speed. One explanation for the lower efficiency of the ''alternating'' configuration near the tip is that at 80% speed the rotor is operating in the transonic regime, with a tip relative Mach number of 1.18 and a midspan relative Mach number of 1.01. Since the flow around the leading edge is extremely sensitive to geometry in this Mach number regime, it is possible that the lower efficiency is due to the imperfect repair and the impact of adjacent long-chord and short-chord blades on the bow wave system.

Civil aviation gas turbines operate at or near design speed for much of each mission. Since the majority of mission fuel burn therefore occurs near design speed, it is instructive to look for differences in blade element performance between the three blade installation configurations at design speed. Spanwise distributions of total pressure ratio, total temperature ratio, adiabatic efficiency, deviation, total loss coefficient and diffusion factor are presented at design speed for three massflows that cover the stable operating range of the rotor in Figs. 9–11. The spanwise performance comparisons show no performance difference, within measurement error, attributable to changes in the blade installation configuration. A final comparison of detailed performance for the three installation configurations is shown in Fig. 12, where the tip static pres-

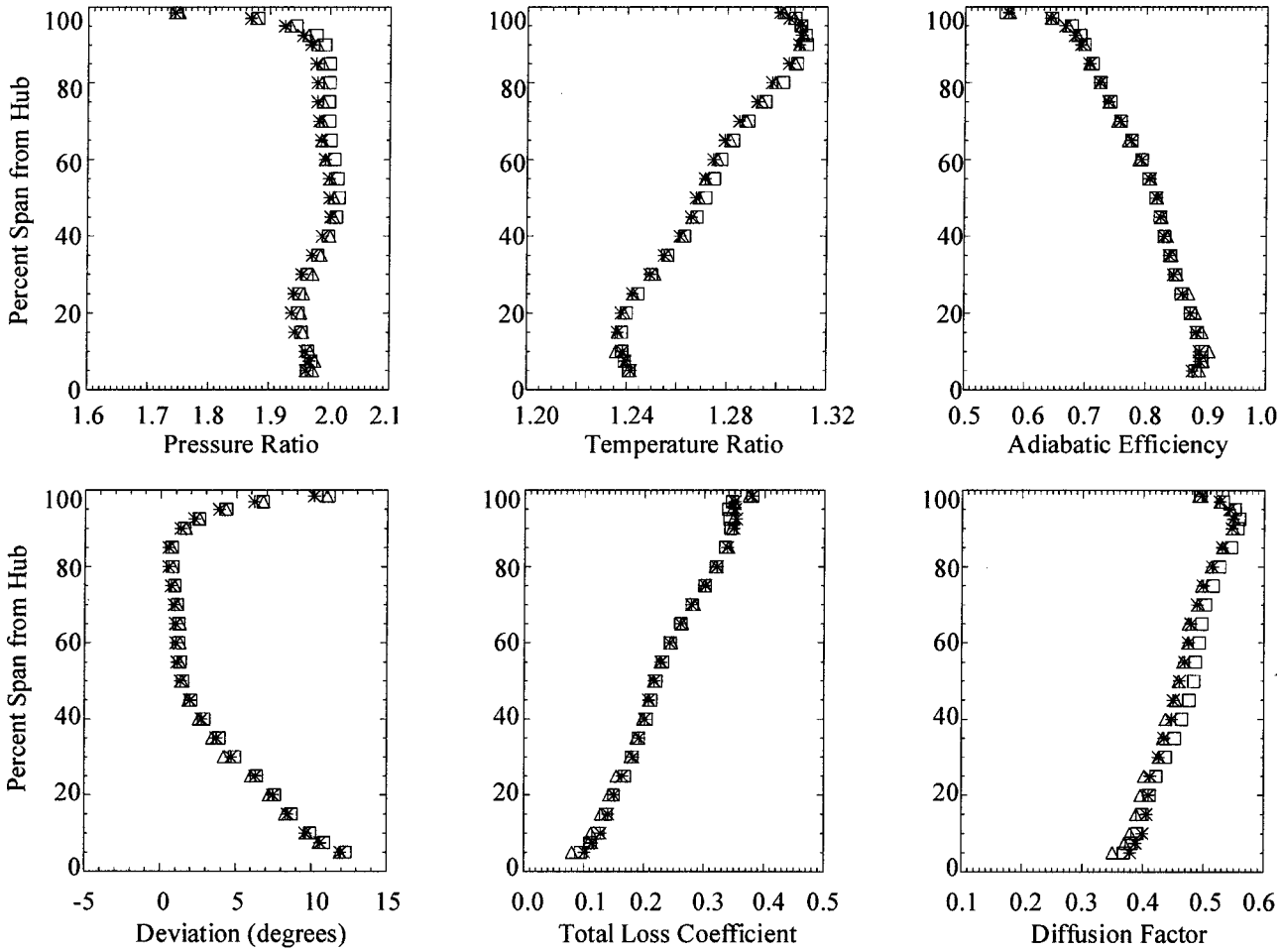

Fig. 11 Rotor performance at 100% speed, near-stall operating point—□, halves; △, quadrants; ∗, alternating

sure rise across the rotor measured by an array of static pressure taps in the casing is presented for 100% speed at the same three operating points as shown in Figs. 9–11. Once again, there is no measurable difference in performance between the three installation configurations.

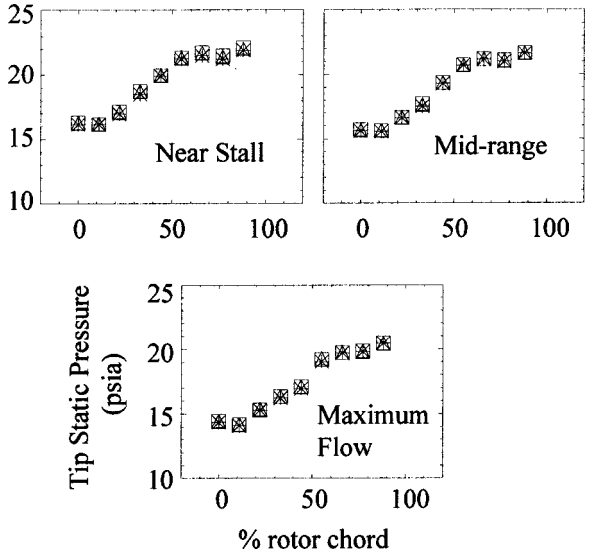

Fig. 12 Static pressure distributions over the blade tip for three operating conditions at 100% design speed

Discussion

One might ask to what degree the rotor insensitivity to chord length measured in the present work is a result of the relatively poor performance of the repaired blade. In other words, if the tip end-bend featured in the original rotor had not been lost during the repair process, and the repaired rotor had an efficiency more typical of a new rotor, would the results have been the same. While the imperfect restoration of the leading edge was not ideal, repair of this blade did provide a unique opportunity to investigate performance differences in a series of back-to-back tests in a carefully controlled compressor research rig environment. In the authors experience, if the leading edge of a used, eroded blade is recontoured to a shape that delivers near nominal performance across the span, i.e., the same loss and turning as a nominal blade, then there is no discernible difference in performance between the new and refurbished blade.

A second question is whether or not tight manufacturing tolerances need to be held for blades if performance is not sensitive to blade chord variation. The authors feel that not only should the present tolerances be held for overall blade manufacture, but that leading edge tolerances should be tightened so as to force blade vendors to err on the small side of the tolerance band, thus creating a bias toward thin leading edges rather than thick leading edges.

Summary and Conclusions

The test results presented above for three radically different configurations of rotor blade chord mismatching indicate that, for

blade chords down to 95% of nominal, there are only two measurable performance differences between configurations for the tested rotor. First, there is a 2% difference in stall margin, with the ''alternating'' blade installation configuration providing the best stall margin. Second, there is a 2 point difference in efficiency at 80% speed, with the ''alternating'' blade configuration providing the lowest efficiency. This spread in efficiency may be caused by the imperfect repair and by the rotor operating at transonic relative inlet Mach numbers at this speed.

Since the three installation configurations tested cover the extremes of possible chord mismatch, it can be concluded that mismatching is not important to aerodynamic performance above the stall chord limit, which for most civil aviation engines is between 94–96% of nominal (new) chord length. This statement applies *only* to blades that have been refurbished with a leading edge recontour.

Furthermore, in that the mismatched Rotor 35 was tested at 100% design speed—corresponding to ''fan'' tip speeds, 80% speed—corresponding to ''front compressor'' tip speeds, and 60% speed—corresponding to ''rear compressor'' tip speeds, the authors believe that the insensitivity to blade installation configurations observed in the present work applies to fans, low pressure compressors, and the rear stages of high pressure compressors alike.

Acknowledgments

The authors would like to thank NASA Glenn Research Center for supporting the research effort reported herein, and Mr. David Williams and Mr. Randy Thomas for their continuing excellent mechanical and electronic test support in the W-8 facility. The first authors would particularly like to thank Mr. Andrew Lewis of Airfoil Management Company and Mr. Ian Coats of Airfoil Technologies International for their blade refurbishment support during this research.

References

[1] Sallee, G. P., Kruckenburg, H. D., and Toomey, E. H., 1978, ''Analysis of Turbofan Engine Performance Deterioration and Proposed Follow-on Tests,'' NASA CR-134769.
[2] Kramer, W. H., Paas, J. E., Smith, J. J., and Wulf, R. H., 1980, ''CF6-6D Engine Short-term Performance Deterioration,'' NASA CR-159830.
[3] Covey, R. R., Mascetti, G. J., and Roessler, W. U., 1978, ''Examination of Commercial Aviation Operational Energy Conservation Strategies,'' The Aerospace Corporation, Aerospace Report No. ATR-79 (7761)-1, Vol. 2.
[4] *Proc., DOE/FAA Symposium on Commercial Aviation Energy Conservation Strategies*, Apr., 1981.
[5] Suder, K. L., Chima, R. V., Strazisar, A. J., and Roberts, W. B., 1994, ''The Effect of Adding Roughness and Thickness to a Transonic Axial Compressor Rotor,'' ASME J. Turbomach., **117**, pp. 491–505.
[6] Roberts, W. B., 1995, ''Advanced Turbofan Blade Refurbishment Technique,'' ASME J. Turbomach., Tech. Brief, **117**, pp. 666–667.
[7] Reid, L., and Urasek, D. C., 1973, ''Experimental Evaluation of the Effects of a Blunt Leading Edge on the Performance of a Transonic Rotor,'' ASME J. Eng. Power, **95**, pp. 199–204.
[8] Roberts, W. B., 1984, ''Axial Compressor Performance Restoration by Blade Profile Control,'' ASME Paper No. 84-GT-232.
[9] Roberts, W. B., 1995, ''A Study of the Performance and Stalling Behavior of JT8D Short Chord Compressor Blade Elements,'' Airfoil Management-Airfoil Technologies International Internal Note (Oct.).
[10] Roberts, W. B., 1996, ''A Study of the Performance and Stalling Behavior of CF6-80C2 Short Chord Compressor Blade Elements,'' Airfoil Technologies International Internal Note (May).
[11] Reid, L., and Moore, R. D., 1978, ''Design and Overall Performance of Four Highly-Loaded, High-Speed Inlet Stages for an Advanced High-Pressure-Ratio Core Compressor,'' NASA Tech. Memo., 1337.
[12] Reid, L., and Moore, R. D., 1978, ''Performance of a Single-Stage Axial-Flow Transonic Compressor with Rotor and Stator Aspect Ratios of 1.19 and 1.26, Respectively, and with Design Pressure Ratio of 1.82,'' NASA Tech. Memo., 1338.
[13] Model, D., and Roberts, W. B., 1997, ''A New Lease of Life for Gas Turbine Airfoils,'' Aircraft Technology Engineering and Maintenance Engine Yearbook, 1996–1997.

3-D Transonic Flow in a Compressor Cascade With Shock-Induced Corner Stall

Anton Weber
e-mail: anton.weber@dlr.de

Heinz-Adolf Schreiber
e-mail: heinz-a.schreiber@dlr.de

Reinhold Fuchs

Wolfgang Steinert

German Aerospace Center (DLR),
Institute of Propulsion Technology,
51170 Köln, Germany

An experimental and numerical study of the transonic flow through a linear compressor cascade with endwalls was conducted. The cascade with a low aspect ratio of 1.34 was tested at an inlet Mach number of 1.09 and a Reynolds number of 1.9×10^6. Detailed flow visualizations on the surfaces and five-hole probe measurements inside the blading and in the wake region showed clearly a three-dimensional boundary layer separation on the blade surface and the sidewall, and a severe corner stall induced by a strong 3-D shock system at blade passage entrance. The experimental data have been used to validate and improve the 3-D Navier-Stokes code TRACE. Results showed an excellent resolution of the complex flow field. Surface pressure distributions on the entire blade surface and the endwalls, flow angle and total pressure contours within the blade passage and the wake are compared with the experimental results. An analysis of the secondary flow of this highly staggered cascade did not show the classical corner vortex. Instead, a severe flow deviation and partly reverse flow near the walls is seen. The flow solver helped to identify a weak ring vortex that originates from the passage sidewall. Surface oil flow pictures on the blade contour and the sidewall are in qualitatively good agreement to numerical surface streaklines. A considerable improvement of the numerical results could be achieved by a gradual grid refinement, especially in the corner region and by successive code development. [DOI: 10.1115/1.1460913]

Introduction

Enormous efforts are devoted to improving the efficiency of gas turbine components. One part is to design and employ custom-tailored blade profiles with minimum losses and controlled blade boundary layers. The second and even more complex part is to minimize losses resulting from secondary flows near hub and casing. Recent three-dimensional blading design concepts, which for example apply sweep and dihedral, help to control secondary flows, to reduce or suppress corner stalls and try to avoid adverse transports of low-momentum fluids inside of the blade rows [1,2]. These complex flows can only be resolved and understood by making use of fully three-dimensional Navier-Stokes flow solvers. However, their reliability, and thus the progress of the new design approach, strongly depends on the ability to predict the flow field and the design parameters as accurately as possible, and not only to give qualitatively good results. Especially the mass flow rate, pressure rise, and efficiency strongly depend on the ability to simulate the boundary layers on blade and endwalls including 3-D separations.

Thus, there is a significant interest in thorough validations of the new Navier-Stokes solvers, especially for highly loaded flows present in compressor blade rows. Especially for transonic compressors with embedded shock waves and shock-induced separations, only a few test cases from real compressors are available, however, with limited information on viscous flow regions [3,4]. Most of the code validations have been performed with lower loaded test cases of turbine configurations with accelerated flows. Decelerated flows and separation in the corner regions are even more critical for an accurate numerical simulation.

Because of a simple geometry, steady flow, and easy experimental accessibility cascade tests allow a deep insight into the viscous flow regions and provide detailed experimental data for a thorough code validation process. Therefore, Kang and Hirsch [5], for example, analyzed a subsonic cascade with high flow turning and corner stall. They gave a detailed description of the secondary flow field and compared the results to their Navier-Stokes solutions. At very high supersonic inlet Mach numbers, Osborne et al. [6] recently provided test results of a cascade, but for compressor flows this blade had an atypical favorable pressure gradient.

The present work deals with a cascade that is typical for a transonic compressor blade section with relatively low flow turning, low supersonic inflow velocities, but a strong normal shock wave at blade passage entrance. The interaction of this shock wave with the blade boundary layer and the incoming endwall boundary layer leads to a complex flow field with shock-induced separations on the blade and the corner region.

The work presented here has two main objectives: The first objective is to analyze and understand the shock induced secondary flow from both the experiment and the numerical simulation. The second, but main, objective is to use the detailed experimental data to validate and improve the numerical algorithm, the type and density of the computational mesh, and to select suitable turbulence models of our Navier-Stokes solver. Some existing shortcomings of the simulation are discussed, although most details of the flow structure are clearly revealed.

Experimental Setup

The experiments were performed in the Transonic Cascade Tunnel of DLR Cologne. It is a closed loop, continuously running facility with an upper transonic wall and variable test section height. The air supply system enables an inlet Mach number range from 0.2 to 1.4 and a Mach number independent variation of the Reynolds number. For the present tests, in which the influence of endwall and secondary flow should be dominant, a cascade with enlarged blade chord ($c=125$ mm, $s/c=0.70$) and a relatively low aspect ratio of 1.34 was installed. Figure 1 shows the test section with four compressor blades fixed between perspex endwalls. To control inlet and exit flow of the cascade, the exit flow is guided by two tailboards combined with throttles which are hinged to the outermost blades. Although there are only four

Contributed by the International Gas Turbine Institute and presented at the International Gas Turbine and Aeroengine Congress and Exhibition, New Orleans, Louisiana, June 4–7, 2001. Manuscript received by the IGTI, October 2, 2000. Paper No. 2001-GT-345. Review Chair: R. A. Natole.

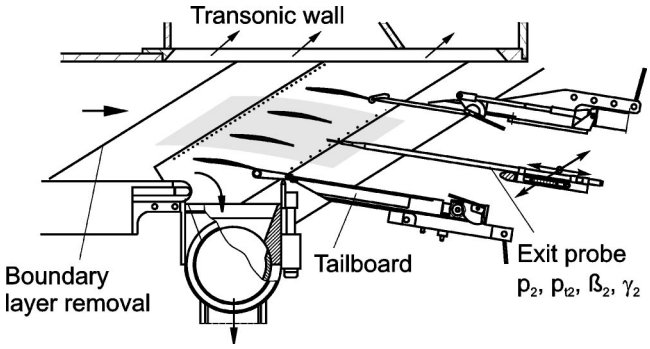

Fig. 1 Test section of DLR transonic cascade wind tunnel

blades, an acceptable periodic cascade flow could be established with suction through the outer bypass channels and a suitable throttle setting in the rear.

The blade and cascade geometry corresponds to a cascade, that has been tested extensively at DLR under 2D- and Q3D-conditions with a blade aspect ratio of 2.4 (see, for example, [7,8]) and served also as geometry in a 3-D study on blade sweep [9].

Two center blades were instrumented with static taps to measure the static pressure distribution in four spanwise sections. Furthermore, endwall static pressure distributions were recorded from 130 taps along the center blade passage (see Fig. 9). Within the blade passage and in the exit planes three and five-hole probes measured pitot- and static pressure and flow angle distributions. The 5-hole probe had a conical head with 2.6 mm in diameter. Additional laser-2-focus (L2F) readings checked inlet and exit planes and confirmed the probe results even inside of the wake regions [10].

Test Conditions. The tests were run at an inlet Mach number of 1.09, a total pressure of 1.1 bar, giving a blade chord Reynolds number of 1.9×10^6. The turbulence level of the inlet flow is approximately 0.6 percent, the thickness of the incoming sidewall boundary layer is 5 mm. Inlet flow conditions were determined from total pressure, sidewall static pressure taps and additional L2F measurements at midspan.

Description of Test Case

At a fixed inlet Mach number of 1.09 the cascade was tested at different incidence angles ranging from choked flow condition ($\beta_1=147.0$ deg) to 2.5 deg higher incidence with higher loading and stronger boundary layer separation. The test point presented here was operated with an experimental pressure ratio of 1.45, a condition at which the cascade just choked at an inlet flow angle of 147.1 deg (see Fig. 6).

Flow Structure. With the corresponding back-pressure a nearly normal shock wave establishes in front of the blade passage, but the back-pressure is high enough to avoid local reaccelerations to supersonic flows and a second normal shock. Figure 2 shows a Schlieren picture of the test section. The blade surface Mach number distributions together with the integrated midspan flow parameters are provided in Fig. 8. The Schlieren picture in reality shows integral values of the density gradients along the blade span. Dominant in this picture is the midspan location of the quasi normal shock wave ahead of the blade passage, although the shock surface near the windtunnel sidewall boundary layer is slightly bent upstream. The real three-dimensionality of the shock surface can be estimated from the simulated footprint of this shock wave which is plotted in the lower part of Fig. 3. This figure also shows the Mach contours on the sidewall and the blade suction surface.

Due to the high preshock Mach number of 1.4 near the blade surface, the shock is strong enough to induce separations. In the

Fig. 2 Schlieren photo at $M_1=1.09$, $\beta_1=147.1$ deg

blade center region a shock-induced laminar separation bubble is observed between 49 and 69 percent of chord and in the wall region a severe corner stall can be seen.

Oil flow pictures from both, the suction surface and the wall provided in Fig. 4, clearly show the region of separation, the reattachment line ($x/c=0.7$) in the center part of the blade, and the area of reverse corner flow close to the sidewalls. A sketch of the cascade and an interpretation of these surface streak lines is given in Fig. 5.

The sidewalls do not show the classical crossflow from pressure to suction side with nearwall overturning, but clearly visualize a tremendous deviation around the trailing edge and a separation line together with a focus on the rear part of the endwall. This strong deviation near the endwall in combination with a wall stall seems to be typical for cascades with high stagger angles as it was already shown in a similar, but subsonic test of Stark and Bross [11].

Simulated suction surface streak lines are plotted in the right-hand side of Fig. 4 in comparison to the experimental oil streak lines. This first comparison reveals, that the corner stall in the simulation is more extended and the footprint of the shock wave is more bowed in spanwise direction than in the experiment. Further explanations and other details in relation to the numerical result will be discussed in the forthcoming.

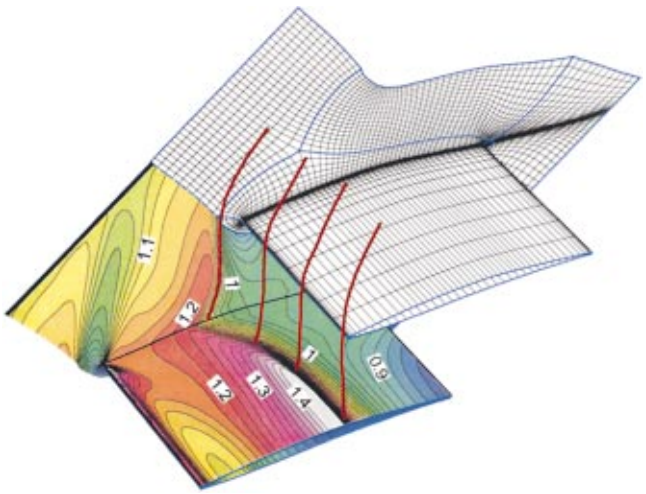

Fig. 3 Computational grid (50 percent blade span, skip=2), inlet plane: $x/c_{ax}=-0.81$, outlet plane: $x/c_{ax}=1.59$, and simulated surface iso-Mach contours at test conditions

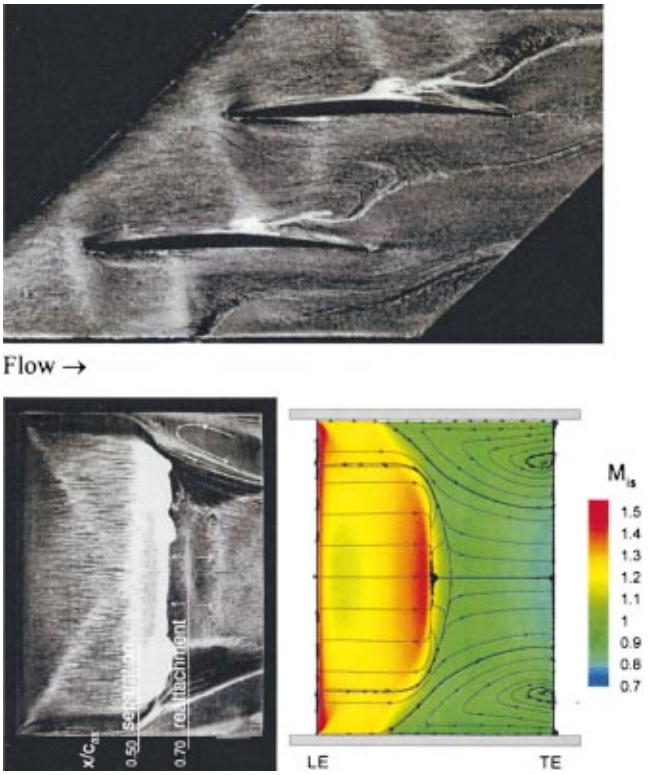

Fig. 4 Oil streak lines on sidewall (top) and suction surface (bottom, left) and TRACE simulation, $M_1=1.09$, $\beta_1=147.1$ deg

An interesting flow feature in the entrance region of this transonic flow case can be observed in the leading edge endwall corner region. The detached bow shock ahead of the leading edge interacts with the endwall boundary layer and initiates a 3-D disturbance with a slight over-expansion at the endwall leading edge corner and a weak oblique shock which both travel under about 60–65 deg toward the cascade center. The suction surface Mach number contours of the NS simulation in Fig. 4, bottom right, slightly indicate this overexpansion with peak Mach numbers in the leading edge corner region.

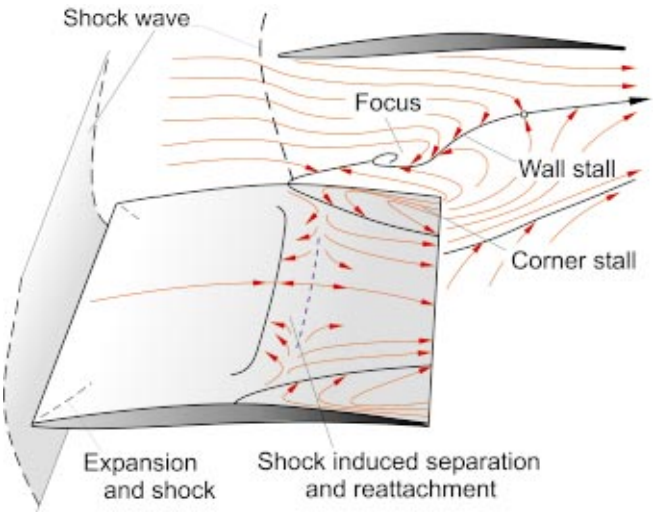

Fig. 5 Interpretation of oil streak lines

Flow Solver

The flow solver used in the numerical analysis is the 3-D Navier-Stokes code TRACE developed since 1991 at DLR Cologne for steady and unsteady turbomachinery flow simulation [12–16]. The main topics of TRACE are:

- Multi-block solver on general structured grids
- Time integration: Explicit or implicit scheme (using ILU decomposition)
- Spatial discretization: Jameson-type central differences with eigenvalue damping or Roe-upwind TVD
- Full multigrid method (FMG)—not used here.
- Steady and unsteady multistage capability using either mixing plane approach (Giles) or sheared cell technology
- Turbulence models: Baldwin & Lomax, Spalart & Allmaras, standard and low-Reynolds k-ε (Kato & Launder extension), high and low-Reynolds k-ω (extension for compressible flows, Suga, Craft & Launder approach)
- Transition modeling: Abu-Ghannam/Shaw criterion as an additional correlation—not used here.

Computational Approach

In the context of this paper the ability of the code to determine transition was not applied. All calculations were run by assuming a fully turbulent steady flow throughout the blade passage. Before starting the numerical analysis, a high-quality five-block structured grid has been generated by Yamamoto [17] and the author. Special emphasis was placed on a high degree of overall grid orthogonality and to get an ideal wake resolution, shown in Fig. 3. In order to achieve the desired inlet flow conditions M_1 and β_1 at the inlet reference plane ($x/c_{ax}=-0.25$), a constant backpressure was imposed at the outlet boundary of the computational domain at $x/c_{ax}=1.59$. Inlet and exit boundaries are treated by nonreflecting boundary conditions according to Giles and Saxer. To simulate the inlet turbulence level a mixing length of 1 percent of blade chord was imposed at the inlet plane.

The first series of calculations were performed on a relatively coarse grid having 383.823 nodal points overall, using an explicit Jameson cell-centered scheme for time integration and the standard k-ε turbulence model with wall functions. For all calculations in this mode only the relatively low loaded choked flow conditions allowed a stable and converged 3-D solution. In general, the calculated losses dominated by the strong corner stall were too high in comparison to the experiments. Therefore, the overall exit pressure level decreased by more than 5 percent—compared to the experiment—in terms of the static pressure ratio p_2/p_1. In subsequent attempts finer grids, different solution schemes as well as low-Reynolds turbulence models were applied. A major step regarding stability could be done by using an implicit upwind scheme on the basic grid. In the end, only a much finer grid with 707.119 nodal points overall ($y^+=1\ldots3$, 49 points for resolving half of the span) together with a low-Reynolds k-ω model and an implicit upwind scheme (TVD) yielded exit static pressure levels near experimental ones and stable as well as converged solutions over the whole working range. All operating points in this mode could be run with a CFL number of 100.

In contrast to the standard k-ε model with wall functions, the k-ω model used here has extensions to count for pressure dilatation, compressible dissipation, and effects of rotation. It was found that for highly loaded compressor flows the k-ω model, even with wall functions, has advantages over the standard k-ε model. Going from coarse to fine grids ends up with the same code stability and convergence behavior but less total pressure losses and higher pressure rise. Furthermore, it was found to be important to have the same fine near-surface grid spacing in the corner region, for both the blade and endwall surface.

In Fig. 6 top, the mean static pressure ratio p_2/p_1 for a constant inlet Mach number is shown as a function of the inlet flow angle

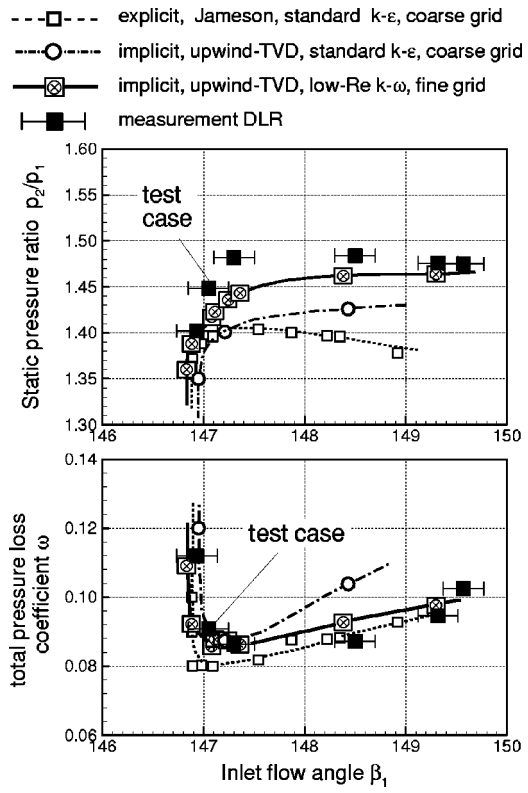

Fig. 6 Achieved overall pressure ratio and midspan total pressure losses for crucial code development steps, $M_1 \cong 1.09$.

β_1. This figure clearly illustrates the achieved static pressure ratios of the simulation for three code development steps in relation to the experimental data. The corresponding total pressure loss coefficients at blade midspan are shown in Fig. 6 bottom. In contrast to the static pressure, which is nearly constant over the whole exit plane, the total pressure varies in spanwise direction. This can be seen in Fig. 13, where for test case conditions the numerical results are compared to the experiments, one solution for a coarse grid and the other for the finest one. The largest discrepancy obviously exists in the endwall region, where the coarse grid solution (standard k-ε model, explicit scheme) shows significant higher losses. Due to higher corner losses and corresponding blockage, the coarse grid solutions provide lower overall pressure rise. It should be mentioned that the ad-hoc use of the present (up-to-date) experimental windtunnel data for code validation gave a tremendous contribution onto the code development.

Using the implicit upwind TVD scheme and the low-Reynolds k-ω turbulence model for the finest grid, the simulations for all operating points, even the near stall cases, were stable. All results presented in the forthcoming were obtained applying these latter options of the Navier-Stokes solver.

Results

For the test point, already described, with choked flow condition ($M_1 = 1.09$, $\beta_1 = 147.1$ deg) and an experimental static pressure ratio of 1.45, detailed data were collected within the blade passage and the exit plane. A second set of detailed data closer to stall exists for $\beta_1 = 148.5$ deg, but the results, which show similar agreement to the corresponding numerical simulations, are not presented here [10]. In the following sections we will concentrate on this special operating point at $\beta_1 = 147.1$ deg and compare the experimental data to the numerical analysis.

Inlet Flow. The incoming sidewall boundary layer upstream of the cascade was measured to have a thickness of 5 mm and a

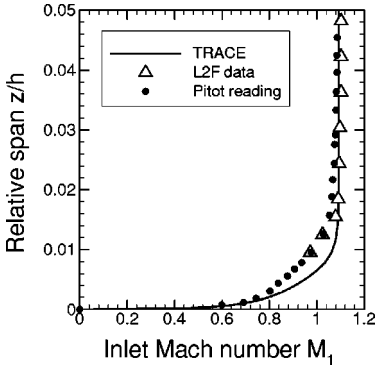

Fig. 7 Measured and simulated incoming sidewall boundary layer profiles ahead of the cascade at $x/c_{ax} = -0.25$. 3-D-NS simulation: pitchwise averaged, $M_1 = 1.09$, $\beta_1 = 147.1$ deg.

form factor of $H_{12} = 1.88$. Figure 7 shows the experimental distributions of Laser-2-Focus and pitot probe readings in comparison to the numerical simulation at a distance of 25 percent axial chord upstream of the leading edge plane. The pitchwise averaged wall boundary layer from the 3-D Navier-Stokes results shows a more ample boundary layer profile, i.e. in the simulation there is a slightly higher momentum of the incoming wall boundary layer. Nevertheless, all calculations were performed with no sidewall boundary layer imposed far upstream at the computational inlet plane ($x/c_{ax} = -0.84$), but this was done to achieve a nearly similar boundary layer thickness at the station where the wall boundary layer was measured. Imposed at the computational inlet plane were total pressure p_{t1}, total temperature T_{t1}, a constant inlet turbulent intensity of 1 percent, and the pitchwise velocity component v_1, which is known via the target values M_1 and β_1.

Mach Number Contours. In Fig. 8 calculated and measured blade surface Mach numbers are compared in 4 spanwise sections at 7.1, 16.7, 27.4, and 50 percent span from the sidewall. At the top of Fig. 8 inlet and exit mean values at midspan are listed. Here, the overall agreement is quite good. Differences occur in the static pressure ratio, where the simulation could not just reach the experimental value of $p_2/p_1 = 1.45$ and the exit flow angle β_2, where in the experiment a 0.8 deg higher flow turning is measured. In the lower part experimental (left) and simulated (right) profile Mach numbers in 4 cuts are presented. It is clearly shown that from mid-span toward the sidewall the shock front moves upstream for both, theory and experiment. The theory, however, slightly overpredicts this upstream movement of the 3-D shock surface, which can be seen in the footprints of the shock in the lower part of Fig. 4. On the pressure side there is only little variation in the isentropic Mach number distribution in spanwise direction due to a local incidence increase when approaching the wall.

In the center of Fig. 8, experimental and numerical surface Mach numbers are compared in a section near the sidewall and at midspan. In general, there is a good agreement for both cuts. Both show a higher local incidence close to the wall in relation to the midspan section and both have less pressure increase near the wall. But as the simulation achieves a lower back-pressure than the experiment, there is a slight difference between the simulated and measured isentropic Mach number levels in the rear part of the passage. At midspan, the flow acceleration on the suction side leads to a so-called preshock overshoot ($M_{max} = 1.46$), whereas in the experiment there is a flattening of the distribution caused by a laminar shock-induced separation with a maximum Mach number of only 1.34. The shock-induced (laminar) separation extends from 49–69 percent with a turbulent reattachment indicated by vertical dotted lines. In contrast to that the numerical turbulent simulation found a short turbulent separation bubble from 50–54 percent of chord. An additional experiment outside of this project,

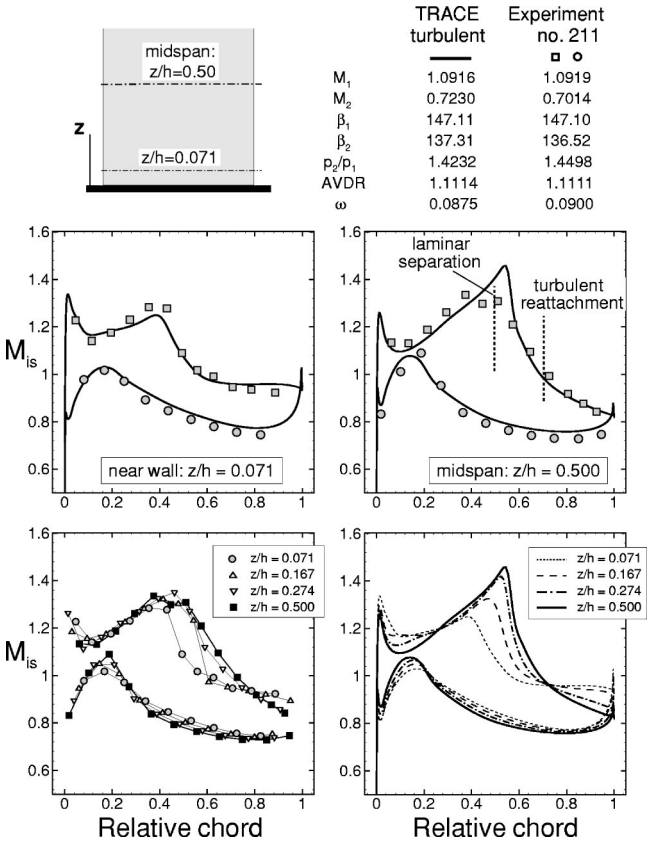

Fig. 8 Isentropic profile Mach number distribution in 4 spanwise cuts. Top: averaged data at midspan; center: near-wall and midspan distributions; bottom: spanwise development in experiment and 3-D simulation.

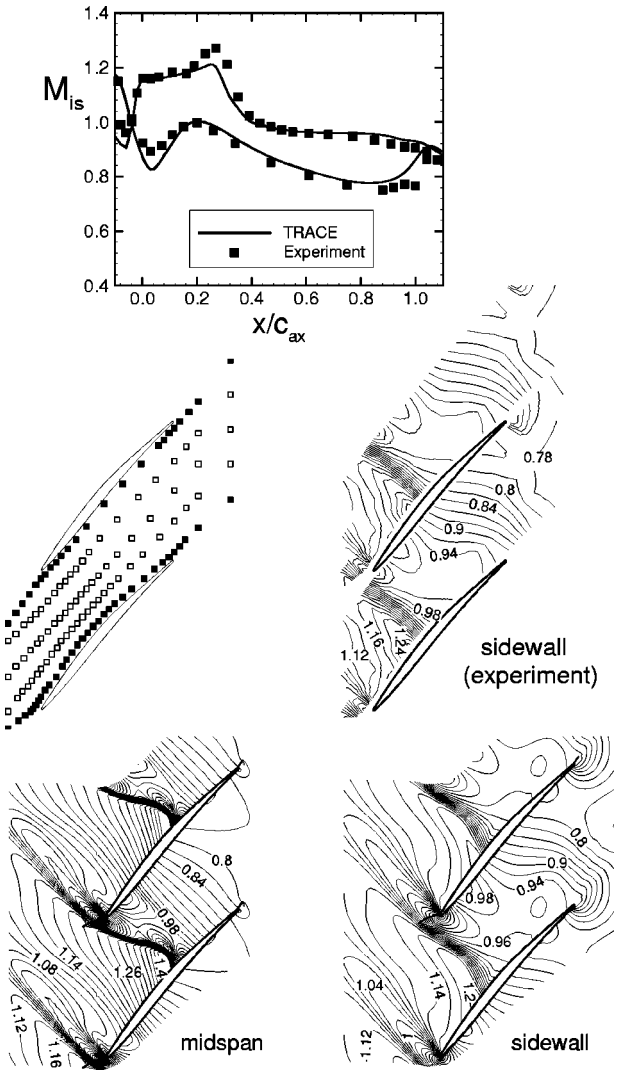

Fig. 9 Isentropic Mach number. Top: distribution near SS and PS sidewall/corner (full symbols in pressure tap locations); center right: experimental contours from sidewall pressure taps; bottom: 3-D simulation at midspan and sidewall.

in which the suction surface boundary layer was forced to become turbulent ahead of shock impingement, showed less upstream influence underneath the shock, and thus a slightly higher preshock Mach number similar to the presented numerical result. Improvements in calculating the present laminar shock induced separation are achieved by assuming a laminar profile boundary layer together with a transition model, a first result of which is presented by Kügeler et al. [15].

In the experiment the sidewall of one blade passage was equipped with 130 static pressure taps, as can be seen at the center of Fig. 9 left. At right, the measured isentropic Mach number contours are plotted. The experiment shows a nearly normal shock which meets the suction surface at 40 percent of chord. In contrast to that, the numerical analysis (bottom, right) shows a curved shock front with more upstream influence near the blade surface. In the trailing edge region again the theoretical Mach number level is slightly higher—compare, for example, $M_{is}=0.94$ at the sidewall. At midspan, the simulated iso-Mach lines can be seen at bottom, left. The shock front is shifted more downstream in comparison to the sidewall, especially near the shock impingement point at the suction surface and the shock front is strongly bowed. At the top of Fig. 9 the wall Mach number distribution along two near-blade cuts (full symbols at center, left) is shown and the corresponding numerical results are interpolated into the experimental pressure tap locations. In the simulation, again, the near-wall shock position is slightly shifted more upstream with lower preshock Mach numbers in comparison to the experiment.

S_3 Traverses. Figure 10 shows total pressure contours from two S_3 traverse planes ($x=$constant) inside of the cascade at $x/c_{ax}=0.71$ and 0.86 and one plane in the wake region at $x/c_{ax}=1.43$, which is identical to the denoted cascade exit plane 2. Inside of the cascade a large separation in the suction side corner with a symmetrical quarter-circle-like shape can be seen in the numerical analysis. Unlike in the experiment the low total pressure zone is more extended along the wall in pitchwise direction toward the pressure side and less extended in spanwise direction; i.e., there is a more triangularlike shape, measured also by Stark and Bross [11]. In both passage traverses the spatial extension of the reverse flow region is marked with a dotted line in the simulation. The thickness of the calculated suction side boundary layer decreases slightly from midspan toward the region about 20 percent from the wall. This region of minimal viscous losses is accompanied by minimal shock losses (blue areas in Fig. 10), a region in which the main shock wave is pushed forward and becomes oblique due to the interaction with the endwall boundary layer. Both effects, less shock losses and even more clearly, less viscous losses around $z/h=0.2$ are also recognized by the pitot probe measurements.

Downstream of the trailing edge plane, both theory and experiment show a similar mixing behavior of blade wake. Due to a tremendous deviation in the near-wall region, the wake center line is curved and shifted toward the pressure side. However, as the corner stall was more pronounced in the simulation, the region of low total pressure is still more concentrated in this area.

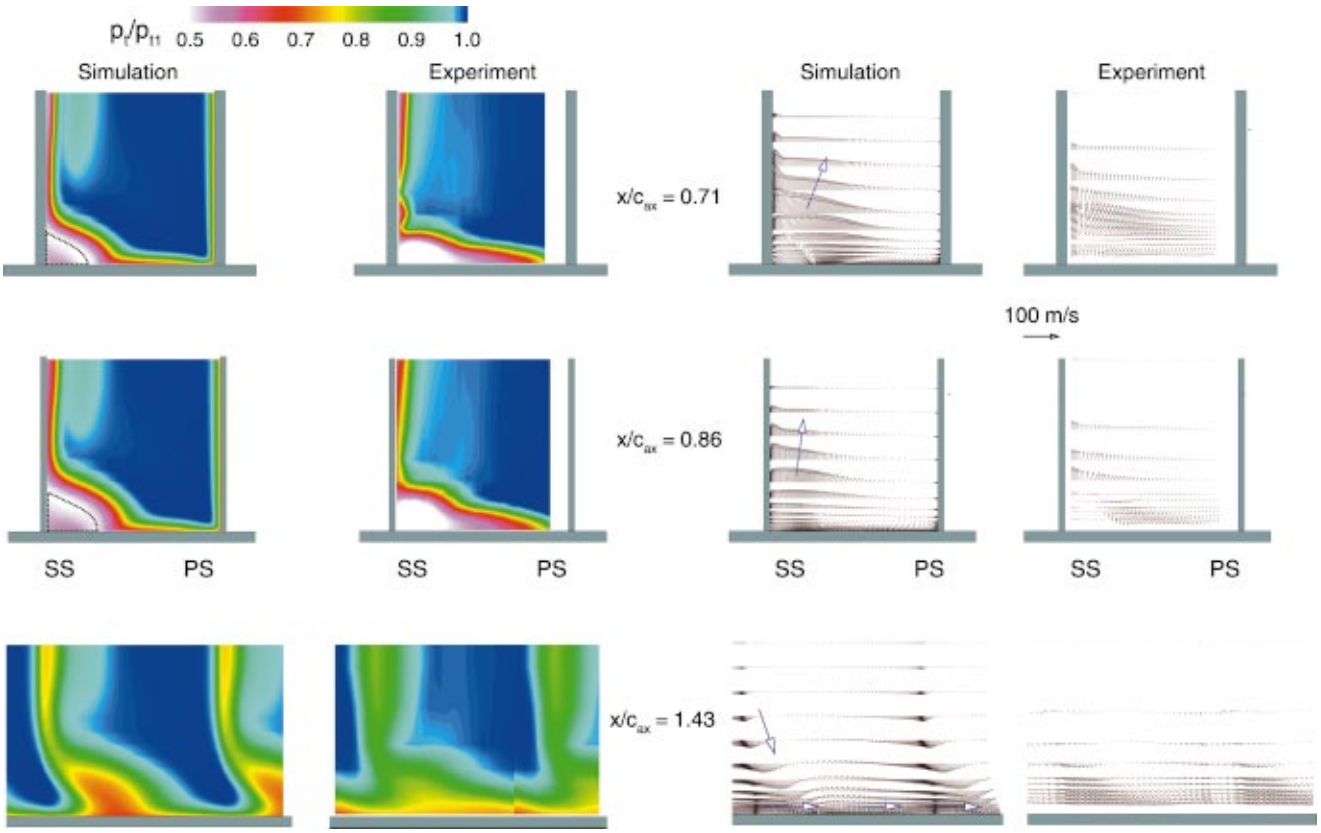

Fig. 10 Development of total pressure in streamwise direction and extension of reverse flow region (dotted line), left 3-D simulation, right experiment (Pitot probe)

Fig. 11 Development of secondary velocity in streamwise direction, right-hand side: five-hole probe experiment

In the same axial positions calculated and measured secondary flow charts are shown in Fig. 11. Neither inside of the cascade nor in the wake traverse can a classical passage vortex pattern be detected. The dominant secondary flow inside of the blading takes a direction away from the suction side corner; i.e., mass is transported mainly toward midspan. In the exit traverse plane there are two dominant secondary flow directions. Globally, the mixing of the low-momentum blade wake forces the mean flow to fill up the blade wake, and especially the former suction side corner region. Therefore, there is a mass transport toward the sidewall, but in the direct vicinity of the sidewall the secondary flow is directed in bladewise direction from suction to pressure side which is just the opposite direction of a classical passage vortex. This phenomenon was already analyzed experimentally by Stark and Bross [11] for highly staggered compressor cascades. The comparison theory versus experiment shows an overall similar flow pattern, but the magnitude of the secondary velocity vectors is at least 20 percent higher in the numerical simulation.

Intrablade Spanwise Sections. For a quantitative comparison of local experimental and simulated flow data Fig. 12 shows a series of plots with total pressure, pitchwise and spanwise flow angle distributions (β and γ) along z=constant cuts in the rear part of the blade passage ($x/c_{ax}=0.86$). For the total pressure both Pitot and five-hole probe readings are compared with the numerical analysis. At midspan position and 29.8 percent span away from the wall, the 3-D simulation and the experimental data agree quite well. Significant differences are observed at $z/h=0.149$ in the total pressure distributions and the spanwise flow angle distributions γ. This is due to the fact that in the numerical analysis this cut is placed already within the corner stall region, whereas in the experiment this cut is just aside. Because of more corner blockage in the simulation there is also more spanwise mass transport toward the blade center, indicated by higher values in the γ-distribution at $z/h=0.149$. At the wall-nearest cut at $z/h=0.071$, the flow angle determinations of the numerical simulation, both β and γ, are doubtful, because this cut is located just near the center of the corner stall and in a region of partly reverse flow, where the data analysis fails. This uncertainty is true also for the flow angle measurements within this reverse flow region. Also, the near suction surface five-hole probe measurements of the β-angle are imperfect and had to be corrected.

Spanwise Flow Quantities. Figure 13 shows spanwise distributions for conservatively averaged total pressures and flow angles β at the exit plane at $x/c_{ax}=1.43$. This was done by mixing out pitchwise variations in flow properties via solving the conservation equations for mass, momentum, and energy for both theory and experiment. The total pressure has a slight minimum around 20–25 percent of span before it increases toward the wall (see again center of Fig. 10). Approaching the sidewall, the exit flow angle shows a continuous increase of deviation up to more than 15 deg. As already mentioned before, a comparable result was obtained by Stark and Bross [11], who measured a similar flow angle distribution also behind a highly staggered compressor cascade. The classical overturning near the cascade endwalls, that normally results from crossflow emerging from pressure to suction side and the corresponding passage vortex, obviously exists only with compressor cascades of low stagger angle and higher overall flow turning, which can be seen for example in Kang and Hirsch [5]. In the present highly staggered cascade, the boundary layer separation on the sidewall effectively suppresses the cross flow and the corresponding local overturning. Both the oil flow traces on the sidewall in Fig. 4 and their interpretation in Fig. 5 show this line of wall separation diagonally in the rear part of the passage.

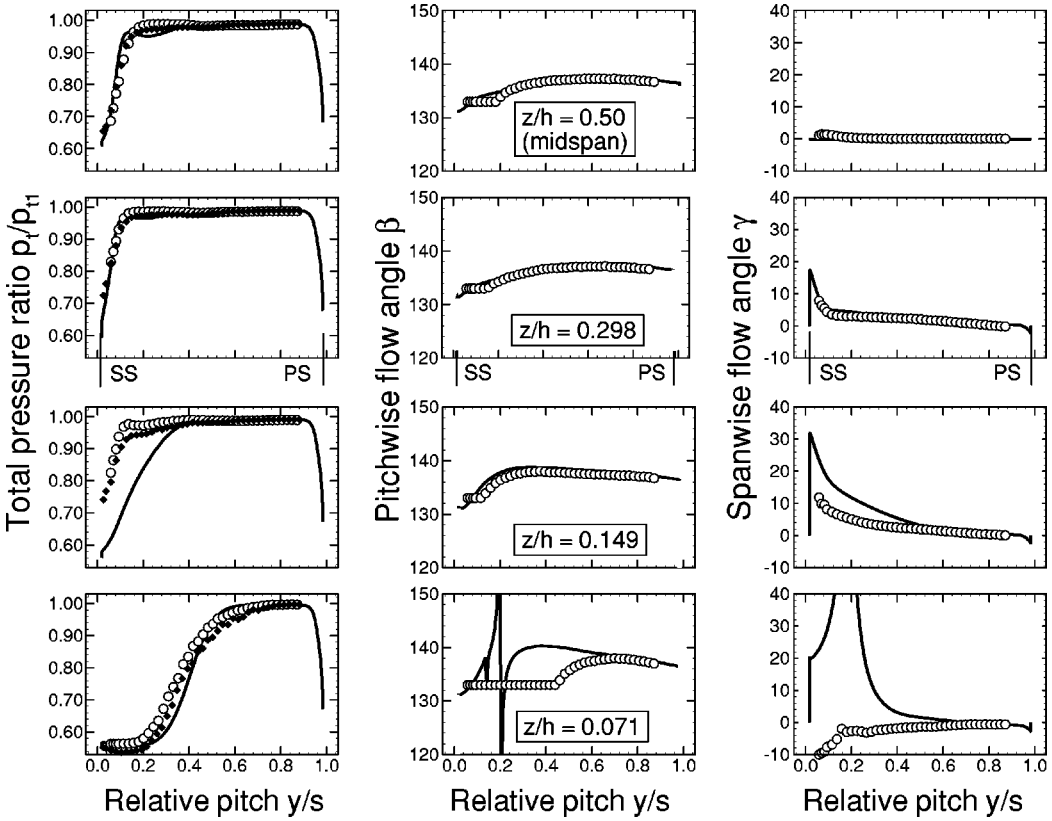

Fig. 12 Pitchwise distribution of total pressure and flow angles β and γ inside the blade passage ($x/c=0.86$) at four spanwise positions. 3-D-simulation compared to experimental data from 5 hole probe (hollow) and extra Pitot readings (solid symbols).

Structure of Corner Stall

The typical horseshoe vortex that normally forms around the blade leading edge is practically not visible and seems to have no significant influence on the endwall- and global passage flow. The flow ahead of the leading edge is just primarily influenced by the interaction of the detached bow shock with the incoming endwall

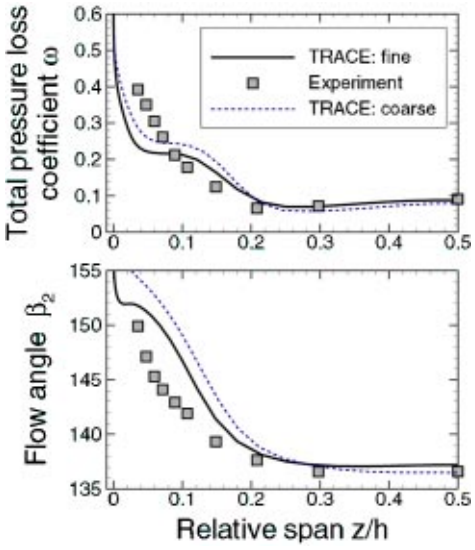

Fig. 13 Spanwise distributions in exit plane at $x/c_{ax}=1.43$, pitchwise averaged. Coarse grid: standard k-ε model with wall functions; fine grid: low Reynolds k-ω model.

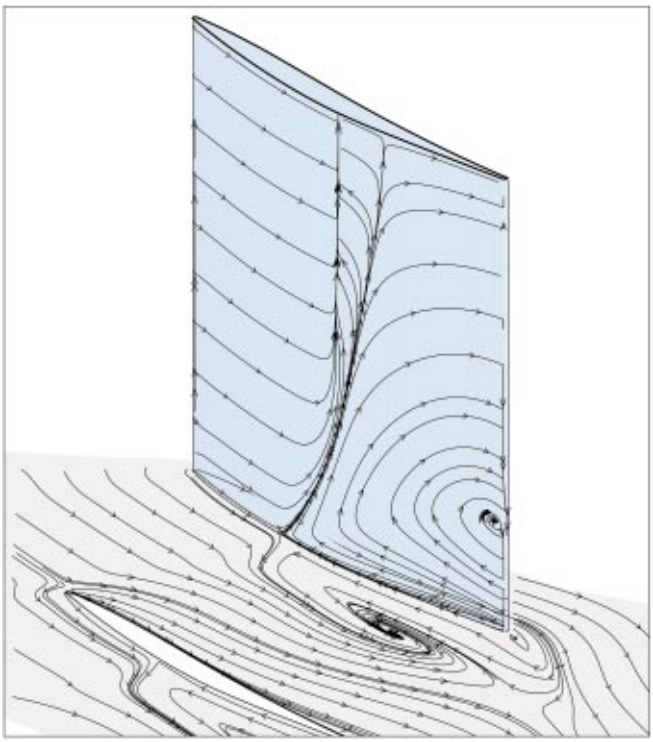

Fig. 14 Simulated surface streak lines on blade and sidewall

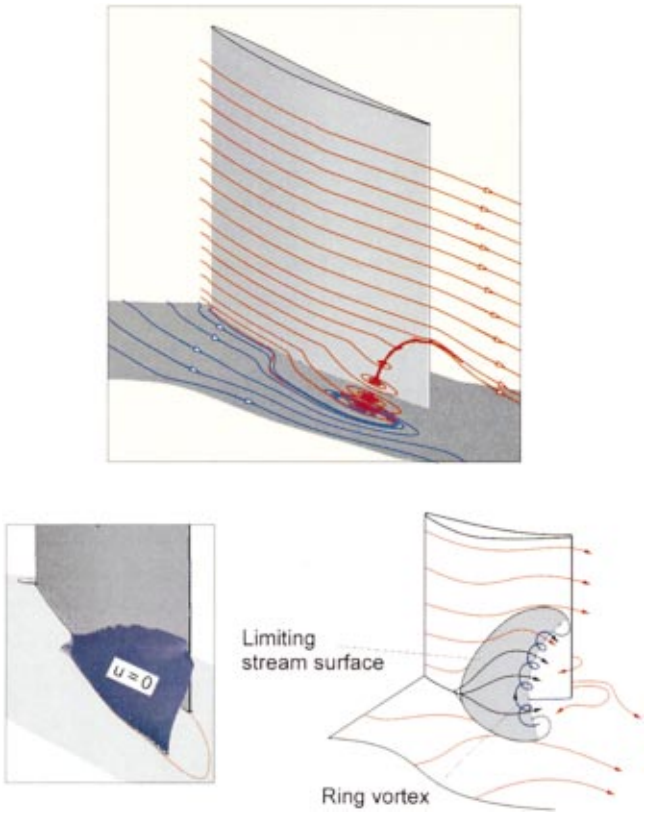

Fig. 15 Simulated near-wall streamlines on suction surface and sidewall—bottom left: calculated structure of reverse flow

boundary layer, the effect of which is hardly visible as a slight disturbance on the wall and suction surface oil traces in Fig. 4. The rear part of the blade passage, however, is dominated by the corner stall and associated wall stall. The experimental Oil streak lines on sidewall and suction surface in Fig. 4 clearly show the reverse flow regions and the stall line on the wall. The numerical Navier-Stokes simulation of surface flow traces shown in Fig. 14 provides very similar results. Experiment and simulation both visualize the endwall separation line that rolls up into a focus and the reverse flow around the trailing edge. On the suction surface, especially in the corner region, the streaklines are somewhat different. Again, the stall region in the simulation is a bit more extended and shows a small focus at the trailing edge which is not visible in the experiment (Fig. 4, bottom).

For a better and complete understanding of the complex flow pattern, especially away from the surface and inside the separation region, solely flow visualizations of the surface streak lines are not sufficient. Probes and even laser anemometers are in most cases unsuitable tools to study the complex stall regions and vortex structures. A thorough analysis of the three-dimensionally simulated flow field can fill this gap. Therefore, particle traces were generated from the numerical solutions which started at the entrance region of the cascade. For an optimal visualization of the vortex topology it was necessary to start the sidewall traces just inside the boundary layer and the blade surface traces just outside of the shear layer. Within the corner stall region the corresponding traces from both sides roll up to a vortex shown in the upper part of Fig. 15. One end of this vortex originates from the sidewall and the outer leg just hits the trailing edge. In further experiments and numerical simulations, however, we observed that the detailed structure of this vortex strongly depends on the operating condition and especially on the back pressure, as was also discussed in a similar work of Hah and Loellbach [18], who analyzed a corner stall in a compressor stator hub region and a similar corner stall in the hub region of the NASA rotor 37. In the present experiments the ring-like vortex is shifted upstream when the back-pressure is increased and with lower back pressure it seems that the outer branch of the vortex away from the wall points downstream.

In contrast to the present Navier-Stokes simulation (see Fig. 4, bottom right), in the experiment shown here the outer branch of the vortex does not meet the profile trailing edge (Fig. 4, bottom left), but probably drifts toward the wake region. Basically, however, the topology of this shock-induced corner stall is well predicted and very similar to the topology already suggested by Schulz et al. [19]. The sketch in the lower part of Fig. 15 right again illustrates the limiting stream surface above the separation zone and the ring vortex that originates from the wall. On the left-hand side of this figure, the extension of the reverse flow region of the present test case is demonstrated by the calculated stream-surface with $u=0$.

Conclusions

A detailed experimental and numerical study on shock-induced corner and wall stall in a linear compressor cascade has been presented. The Navier-Stokes simulation provided an excellent resolution of the flow field, showing up many details like surface streaklines, shock-induced separation and the vortex structure within the corner region. Simulation and experiment both showed clearly that with this highly staggered cascade there is no cross-flow on the sidewall from pressure to suction side and no corresponding overturning near the wall. Thus, no classical passage vortex exists, but instead a weak ring vortex originates from a separation region on the rear part of the sidewall.

During the code validation process, the numerical results of the Navier-Stokes solver were improved by:

- grid refinements especially in the corner regions,
- applying a low-Reynolds k-ω turbulence model,
- introducing an implicit upwind scheme (TVD)

Although the results were improved considerably, the simulation still slightly overpredicts the extension of the corner stall and the resulting blockage effect. Because of that, the simulation achieved less static pressure rise than the experiment. Further improvements are expected by considering laminar flow on the blade front and transition in the shock interaction region.

Overall, the work presented above demonstrated the fruitful interplay between computational and experimental fluid mechanics. In this context, the present Navier-Stokes solver was improved and validated especially for flows in compressors with strong decelerations and complex corner separations.

Remarks. A collection of selected data of this test case is published in a short report of Weber et al. [20] and available via Internet: http://www.dlr.de/~toni/tsg97.htm.

Acknowledgments

This work was partially supported by Arbeitsgemeinschaft Hochtemperatur-Gasturbine (AG Turbo), Bundesministerium für Wirtschaft und Technologie, BMWi, Förderkennzeichen 0327040B5.

Nomenclature

AVDR = axial velocity density ratio: AVDR$=(\rho_2 u_2)/(\rho_1 u_1)$
c = chord length
h = blade height
M = Mach no.
p = pressure
Re = Reynolds no.
s = blade spacing
u,v,w = cartesian velocity components

x,y,z = cartesian coordinates (x: axially, y: pitchwise, z: spanwise)
β = pitchwise flow angle: $\beta = \text{atan}(v/u) + 90$ deg
γ = spanwise flow angle $\gamma = \text{atan}(w/u)$
ρ = density
ω = total pressure loss coefficient: $\omega = (p_{t1} - p_t)/(p_{t1} - p_1)$

Subscripts

1 = inlet plane upstream of leading edge: $x/c_{ax} = -0.25$
2 = exit plane downstream of trailing edge: $x/c_{ax} = 1.43$
ax = axially
is = isentropic entity
LE = leading edge
t = total
TE = trailing edge

References

[1] Weingold, H. D., Neubert, R. J., Behlke, R. F., and Potter, G. E., 1997, "Bowed Stators: An Example of CFD Applied to Improve Multistage Compressor Efficiency," ASME J. Turbomach., **119**, pp. 161–168.

[2] Gümmer, V., Wenger, U., and Kau, H. P., 2001, "Using Sweep and Dihedral to Control Three-Dimensional Flow in Transonic Stators of Axial Compressors," ASME J. Turbomach., **12**, Paper No. 2000-GT-491.

[3] Fottner, L., 1990, "Test Cases for Computation of Internal Flows in Aero Engine Components," AGARD-AR-275.

[4] Dunham, J., 1998, "CFD Validation for Propulsion System Components," AGARD-AR-355.

[5] Kang, S., and Hirsch, Ch., 1991, "Three Dimensional Flow in a Linear Compressor Cascade at Design Conditions," ASME Paper No. 91-GT-114, Orlando, FL.

[6] Osborne, D. J., Ng, W. F., and Tweedt, D. L., 1998, "Studies of Secondary Flow at Endwall of a Supersonic Compressor Cascade," AIAA J., **36**, No. 2, pp. 128–133.

[7] Steinert, W., Schreiber, H. A., and Weber, A., 1996, "Experimente am transsonischen Verdichtergitter DLR-TSG-89-5 bei $M_1 = 0.90$ und $M_1 = 1.09$," DLR-IB-325-10-96, DLR Köln, Germany.

[8] Fuchs, R., Steinert, W., and Starken, H., 1993, "Transonic Compressor Rotor Cascade with Boundary-Layer Separation: Experimental and Theoretical Results," ASME Paper No. 93-GT-12-405.

[9] Weber, A., and Nicke, E., 1997, "A Study of Sweep on the Performance of a Transonic Cascade with and without Endwall Influence," Proc., 13th Int. Symp. Air Breathing Engines, ISABE, Chattanooga, TN, Vol. 2, pp. 877-888.

[10] Weber, A., Schreiber, H. A., Fuchs, R., and Steinert, W., 2000, "Räumliche Strömungen in transsonischen Verdichtergittern sehr hoher Belastung," Abschlußbericht zum HTGT-Turbotech Vorhaben 1.131 der Arbeitsgemeinschaft Hochtemperatur-Gasturbine (AG-Turbo), DLR Köln, Germany.

[11] Stark, U., and Bross, S., 1996, "Endwall Boundary Layer Separations and Loss Mechanisms in Two Compressor Cascades of Different Stagger Angle," AGARD-CP-571, Paper No. 1.

[12] Vogel, D. T., 1994, "Navier-Stokes Calculation of Turbine Flows with Film Cooling," 19th Congress of the International Council of the Aeronautical Sciences, ICAS-94-12-253.

[13] Vogel, D. T., 1999, "A Simulation Package for Turbomachinery Components," Proc. First ONERA-DLR Aerospace Symposium, Paris, France.

[14] Kügeler, E., 2000, "Numerische Untersuchung der Filmkühlung aus einer Reihe von Fan-shaped Bohrungen auf der Saugseite einer Turbinenschaufel und Vergleich mit Experimenten," DGLR Jahrestagung 2000, Leipzig, DGLR-JT2000-139, Bonn, Germany.

[15] Kügeler, E., Weber, A., and Lisiewicz, S., 2001, "Combination of a Transition Model with a Two-Equation Turbulence Model and Comparison with Experimental Results," Proc. 4th European Turbomachinery Conference, Florence, Italy, Paper No. ATI-CST-076/01.

[16] Eulitz, F., Engel, K., Nürnberger, D., Schmitt, S., and Yamamoto, K., 1998, "On Recent Advances of a Parallel Time-Accurate Navier-Stokes Solver for Unsteady Turbomachinery Flow," *Computational Fluid Dynamics '98*, Proc., 4th ECCOMAS, eds., Papailiou et al., Vol. 1, Part 1, pp. 252–258, John Wiley & Sons, New York, NY.

[17] Yamamoto, K., and Engel, K., 1997, "Multiblock Grid Generation Using an Elliptic Differential Equation," AIAA Paper No. 97-0201, 35th Aerospace Sciences Meeting & Exhibit, Reno, NV.

[18] Hah, C., and Loellbach, J., 1999, "Development of Hub Corner Stall and Its Influence on the Performance of Axial Compressor Blade Rows," ASME J. Turbomach., **121**, pp. 67–77.

[19] Schulz, H. D., Gallus, H. E., and Lakshminarayana, B., 1989, "Three-Dimensional Separated Flow Field in the Endwall Region of an Annular Compressor Cascade in the Presence of Rotor-Stator Interaction—Part I: Quasi-Steady Flow Field and Comparison with Steady-State Data," ASME Paper No. 89-GT-76.

[20] Weber, A., Steinert, W., Fuchs, R., and Schreiber, H. A., 1999, "3D Flow in a Transonic Compressor Cascade (DLR TSG-97)," DLR-IB-325-06-99.

An Experimental and Numerical Investigation Into the Mechanisms of Rotating Instability

Joachim März
Mem. ASME
STN Atlas Elektronik GmbH,
Bremen 28305, Germany

Chunill Hah
Fellow ASME
NASA Glenn Research Center,
Cleveland, OH 44135
e-mail: chunhill.hah@grc.nasa.gov

Wolfgang Neise
Mem. ASME
DLR, Institute of Propulsion
Technology,
Berlin, Germany

This paper reports on an experimental and numerical investigation aimed at understanding the mechanisms of rotating instabilities in a low speed axial flow compressor. The phenomena of rotating instabilities in the current compressor were first identified with an experimental study. Then, an unsteady numerical method was applied to confirm the phenomena and to interrogate the physical mechanisms behind them. The experimental study was conducted with high-resolution pressure measurements at different clearances, employing a double phase-averaging technique. The numerical investigation was performed with an unsteady 3-D Navier-Stokes method that solves for the entire blade row. The current study reveals that a vortex structure forms near the leading edge plane. This vortex is the result of interactions among the classical tip-clearance flow, axially reversed endwall flow, and the incoming flow. The vortex travels from the suction side to the pressure side of the passage at roughly half of the rotor speed. The formation and movement of this vortex seem to be the main causes of unsteadiness when rotating instability develops. Due to the nature of this vortex, the classical tip clearance flow does not spill over into the following blade passage. This behavior of the tip clearance flow is why the compressor operates in a stable mode even with the rotating instability, unlike traditional rotating stall phenomena. [DOI: 10.1115/1.1460915]

Introduction

Rotating instability is a phenomenon that occurs in the tip flow region of axial compressor stages during stable operation. It can be observed in highly staggered rotors with significant tip clearance and is strongest at high-load operating points where the characteristic levels off.

In this condition, the single-stage fan under investigation radiates an audible, whistling tone, and wall pressure spectra in the vicinity of the rotor disk exhibit nonrotational components. These form a characteristic hump at roughly half of the blade passing frequency (BPF), as can be seen in Fig. 1.

Previous work on the axial fan test stand at DLR Berlin focused on the effects of varying tip clearance and blade number on rotating instability. Circumferential mode analysis was performed and led to the model of a rotating source mechanism that moves relative to the blade row at a fraction of the shaft speed, not unlike rotating stall cells but with higher mode orders (Kameier and Neise [1], Liu et al. [2], März et al. [3]).

Spectra similar to those seen in Fig. 1 were encountered in pressure measurements in the first stage of an axial multistage compressor, as reported by Baumgartner et al. [4]. Structural vibrations excited by this non-rotational source added to the relevance of the phenomenon.

The effect could also be reproduced in the third stage of the low-speed research compressor at TU Dresden after enlarging the stage's tip clearance sufficiently (Müller and Mailach [5]).

Experimental Study

Test Facility and Instrumentation. The present investigation was performed on the axial fan test stand of DLR Berlin. This rig is a low-speed single-stage fan with outlet guide vanes. Its design parameters are given in Table 1. The tip clearance can be varied by exchanging casing segments with the impeller diameter remaining constant. Fan characteristics at different tip clearances are shown in Fig. 2. Characteristics were recorded by closing and opening the throttle and thus exhibit hysteresis in the stalled region.

An access window incorporating 40 piezo-resistive pressure sensors was installed. The sensors were spaced as closely as possible to provide adequate resolution of the pressure field in the region of interest. Transducers needed to be staggered to achieve an axial resolution of 1.33 mm (see Fig. 3). In addition, a pressure sensor was installed on the blade tip suction side at 36% chord and 3 mm inwards from the blade tip.

Frequency response of the amplifier/transducer/tap combination was verified and found to be within 3 dB up to 17 kHz bandwidth with a linear phase relationship. To correct for transducer drift, the dc component of the signals was corrected against a row of 20 static pressure taps. These were periodically sampled with a scanivalve during measurements. Trigger pulses for ensemble averaging were derived from a shaft encoder.

Together with rotor position/operating point signals, 48 channels were acquired at 51.2 kSamples/s. At a suitably chosen rotor speed of 2560/min, this sample rate results in a resolution of 40×50 (axial $\times$ circumferential) pressure samples per blade passage.

Data acquisition was performed using a VXI front-end, sampling 60 seconds of time data at 16-bit resolution onto throughput disks. The resulting 590 megabytes per operating point configuration could be stored on one CDROM each.

Measured Flow Characteristics of Rotating Instability. The current compressor was investigated extensively to identify rotating instability along the fan operating lines with four different clearance gaps. The rotating instability was most clearly observed near the maximum fan loading at the two largest tip gaps of 2.8 and 5.6% of tip axial chord. In the following sections, overall

Contributed by the International Gas Turbine Institute and presented at the International Gas Turbine and Aeroengine Congress and Exhibition, New Orleans, Louisiana, June 4–7, 2001. Manuscript received by the IGTI, February 12, 2001; revised Manuscript received November 7, 2001. Paper No. 2001-GT-536. Review Chair: R. A. Natole.

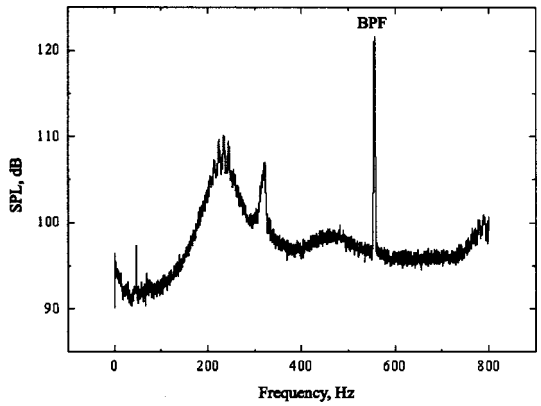

Fig. 1 Wall pressure spectrum with rotating instability components $n=1400$/min, BPF=560 Hz

Table 1 Axial fan test stand

rotor blade #	24
stator blade #	17
stator airfoil	flat circular arc
rotor diameter	452.4 mm
tip clearance	0.3, 0.6, 1.2 or 2.4 mm (ζ=0.7, 1.4, 2.8, 5.6 percent of tip chord)
design point	3000/min, ϕ=0.230
hub-to-tip ratio	0.62
tip stagger angle	27°

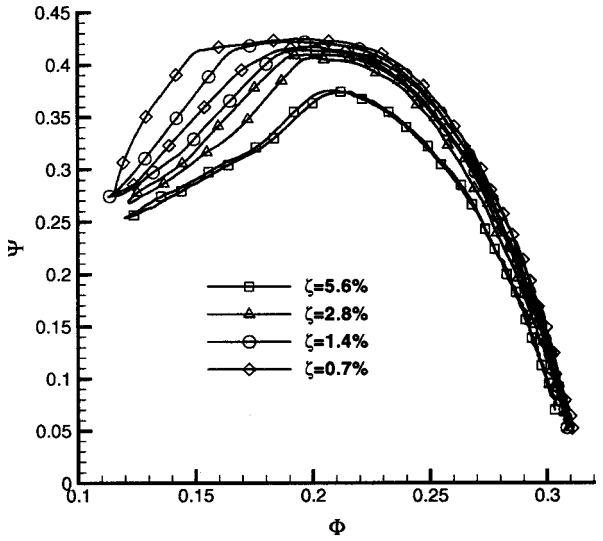

Fig. 2 Fan characteristics at different tip clearances

observations will be presented first. More detailed flow features for the 2.8% tip clearance case near maximum loading will then be shown, since this case was also analyzed numerically to study the flow mechanisms.

Pseudo-Spatial Correlation. A line of sensors located across the rotor disk and sampled simultaneously delivers instantaneous scan lines of the wall pressure field. The rotor's motion results in a sweep across subsequent passages. Thus, with a sufficient sampling rate, a highly resolved picture of the pressure field can be

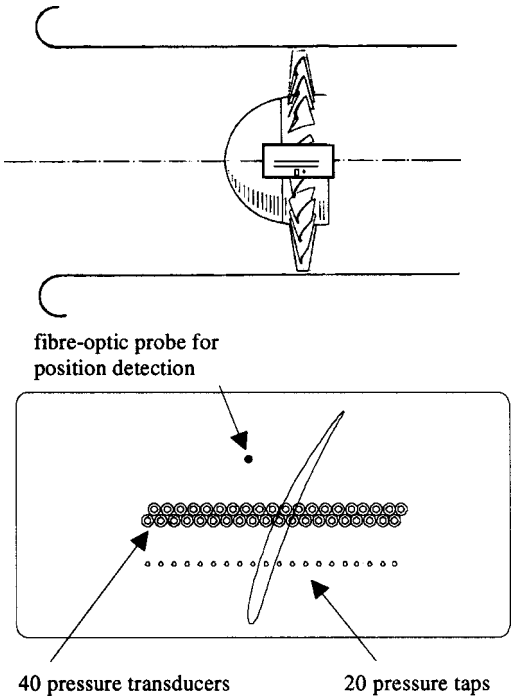

Fig. 3 Position and layout of the access window

obtained by mapping pressure time histories onto the rotor circumference. This "pseudo-spatial correlation" is done under the assumption that the pressure field is steady in the relative frame.

Unsteadiness in the relative frame will result in an aliasing phenomenon. The spatial correlation between neighboring scan lines breaks up when the relative frame pressure field is unsteady on a time scale comparable to 1/BPF. Thus, once the flow becomes unsteady in the relative frame, this technique will only show a convolution of the unsteady pressure field with the blade passing frequency.

Figure 4 shows time-lapse plots for four different tip clearances, with operating points suitably chosen to show rotating instability in the latter two cases. Steady flow dominates the endwall region in the cases with tip clearances of $\zeta=0.7$ and 1.4%. In addition to the potential flow field, the roll-up and trajectory of the tip clearance vortex can clearly be seen. Some disturbances are introduced by the blade wake and in the area between the blade and the departing tip clearance vortex.

At tip clearances of $\zeta=2.8$ and 5.6%, highly unsteady flow takes over. The potential flow field varies in its intensity from blade to blade. While, for the aforementioned reasons, these structures cannot be interpreted as an instantaneous spatial pattern, the presence of a rather localized low-pressure spot can be noticed at seemingly random positions in the rotor entry plane. Instantaneous pressure values at the spot's location go down to $C_p=-3$.

Ensemble Averaging. Ensemble averaging overcomes the aliasing problem by eliminating any non-rotational components in the pressure signals. The ensemble-averaged contour plots look very similar to the steady flow patterns at smaller tip clearance, but detail is reduced considerably. In Fig. 5, a blade-to-blade average is taken over 150 samplings of one blade passage using a trigger signal from the shaft encoder.

Standard Deviation. As a by-product of ensemble averaging, the standard deviation can be plotted as a measure of the "local unsteadiness" in the passage. Standard deviation is computed here as

$$p'_{\mathrm{rms}}=\sqrt{\overline{(p_{ij}-\mu_{ij})^2}}$$

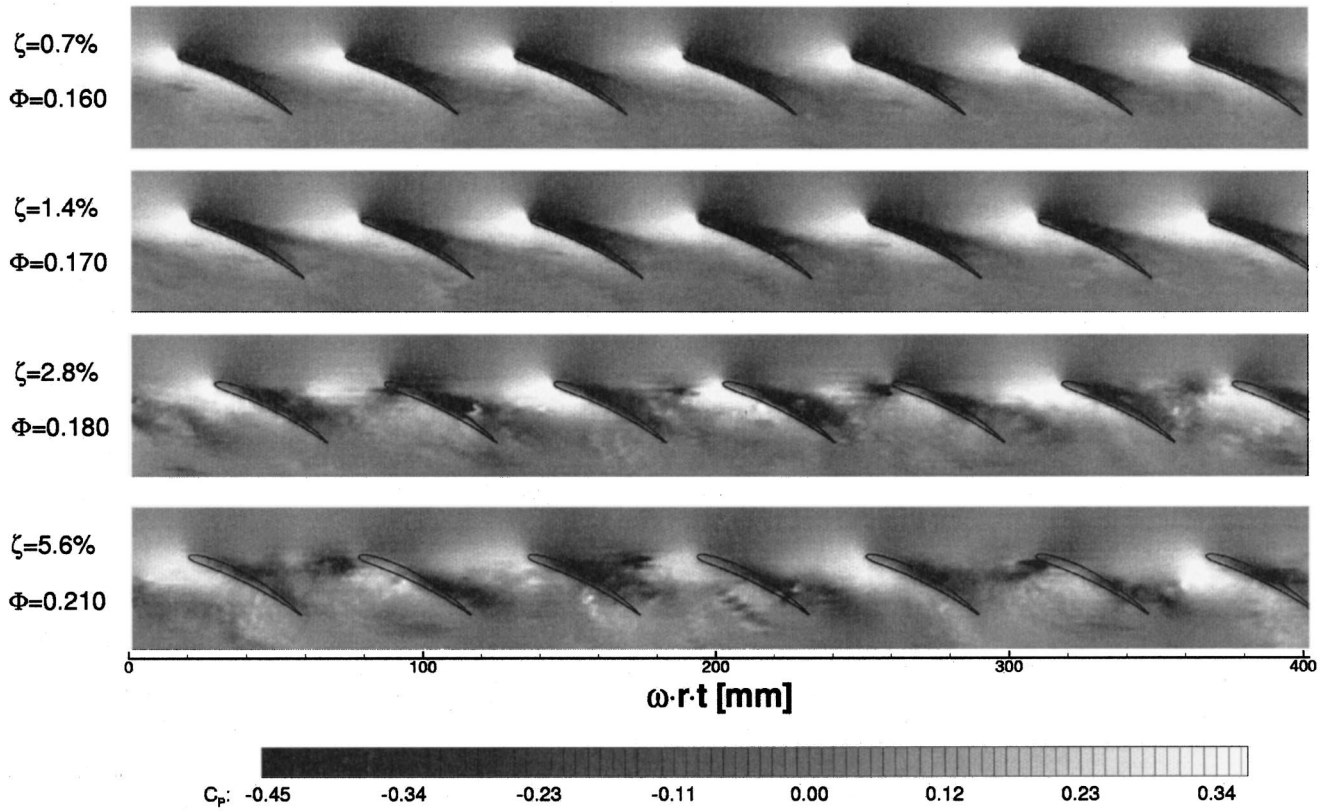

Fig. 4 Time-lapse plots of casing wall pressure at different tip clearances

with the instantaneous pressure value p_{ij} and the ensemble-averaged pressure μ_{ij} at location (i,j) within the passage. While not an immediate physical quantity, it maps the locus of unsteadiness in the passage.

Unfortunately, a ± 0.5 sample uncertainty in acquiring the trigger pulse lets steep gradients in the pressure field appear as fluctuations. High values of p'_{rms} underneath the airfoil/tip gap position as shown in Fig. 5 must be attributed to this effect.

It can be seen that there is a high fluctuation content in the entry plane of the rotor. In particular, maximum fluctuation amplitude can be found just ahead of the blade leading edge, stretching to the neighboring blade's suction side.

At the near maximum loading conditions with the two large clearances shown in Fig. 4, the phenomena of rotating instability were identified with the whistling tone from the compressor and also through pressure spectra. For the current study, the third case with the nominal tip gap of 2.8% at the flow coefficient of 0.18 is investigated in detail. The measurements correspond to the upper branch of the characteristic in Fig. 2.

Double Phase Averaging. To gain a closer physical understanding of the mechanism of this unsteadiness, it would be necessary to ''de-convolute'' the pressure time traces and ''transform'' them into the relative frame in order to see the unsteady process as does an observer in the relative frame.

After more closely examining the blade sensor signal in the presence of rotating instability, a double phase averaging algorithm was developed allowing display of the rotating instability cycle as an animation virtually in the relative frame.

It turns out that the blade sensor signal has a strong periodic content (see Fig. 6). Such a period can be regarded as one ''cycle'' of rotating instability.

To assemble an animation of this cycle, pressure samples must be collected

(a) for all locations in the blade passage (axial and circumferential),
(b) for all phase bins within one period of the blade pressure signal.

The wall pressure signals are only correlated to the blade sensor signal when the instrumented blade passes underneath the access window. These ''position coincidences'' are collected, evaluated by phase, and then re-sorted into phase bins (see Fig. 7). Thus, the double phase averaging now consists of averaging stripes of equal phase and circumferential position, i.e. belonging to the same ''bin.'' In this way, 60 s of data were split into ''position coincidences,'' assigned a phase value, and averaged, yielding about 70 averages per 10 deg phase bin. This procedure is based on two assumptions:

(a) The observed phenomenon must not have a circumferential preference; i.e., it must rotate freely in the rotor and must not be bound to some upstream disturbance such as stators or other inlet distortions.
(b) The observed phenomenon is correlated over some extent in the circumferential direction, at least over the width of the data window being averaged.

Figure 8 shows pressure contours in the relative frame during one period of rotating instability. Apart from substantial fluctuations in the potential flow field, the most prominent feature is a low-pressure spot that travels continuously from the middle blade's suction side to the following blade's pressure side. This low-pressure spot is interpreted as the footprint of a radial vortex. It is created much like a starting/unstarting vortex from the airfoil, travels across the blade passage, and interacts with the following blade, giving rise to a new ''starting vortex.'' However, in order to

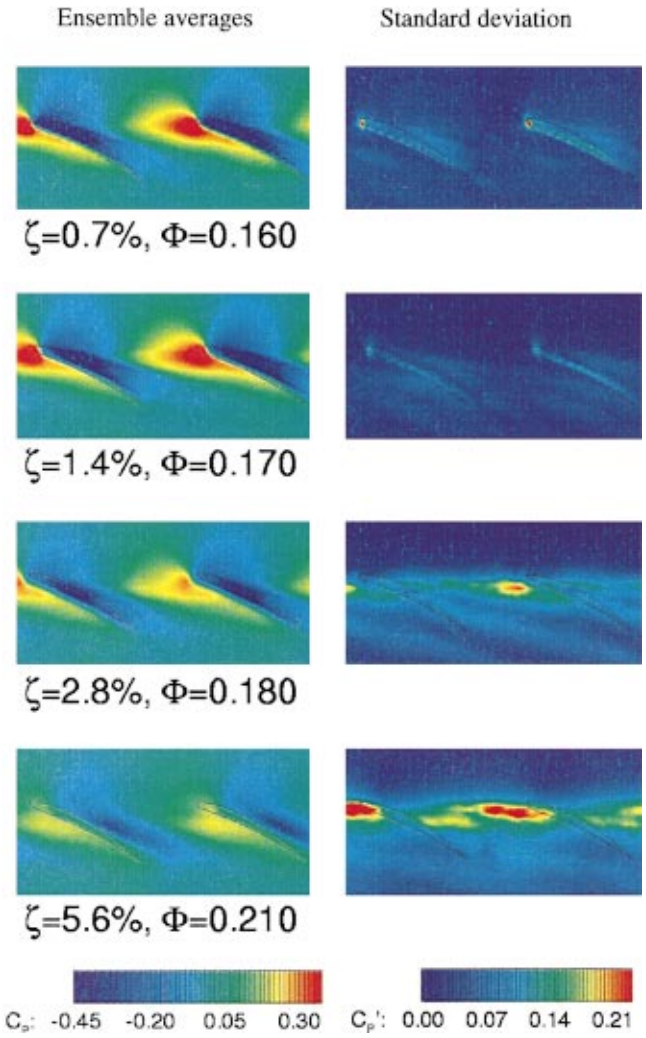

Fig. 5 Ensemble averages and standard deviation plots for varying tip clearance and selected operating points

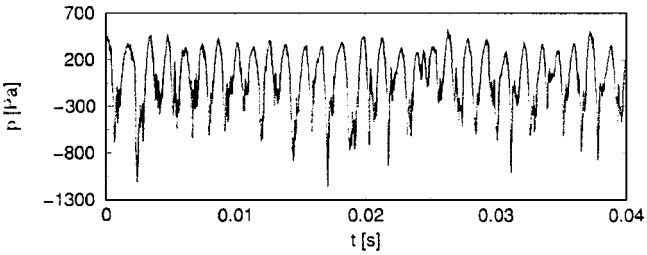

Fig. 6 Time history of blade pressure signal

fully understand this unsteady endwall flow, knowledge of flow quantities in the deeper layers of the endwall flow would be required.

Numerical Study

The experimental study presented in the previous section provides evidence of rotating instabilities and a description of the unsteady behavior through measurements and analysis of casing and blade tip pressures. A numerical investigation was performed to examine detailed flow structures so that the physical mechanisms behind the unsteady phenomena could be adequately explained. The rotor with a tip gap of 2.8% and a flow coefficient of 0.18 was numerically analyzed.

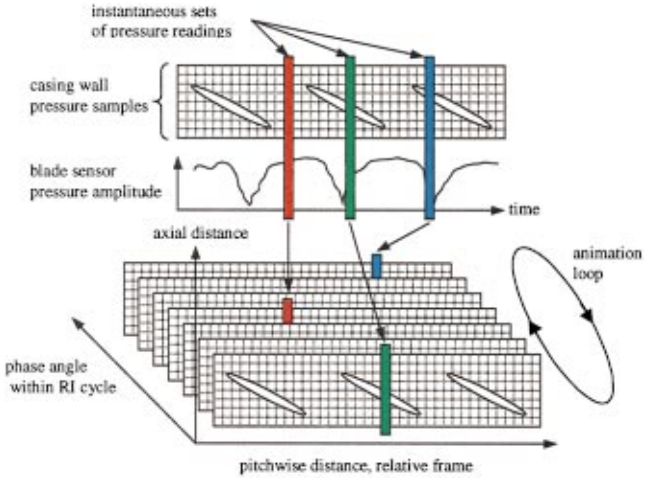

Fig. 7 Sorting algorithm for double phase averaging

Numerical Method. A three-dimensional steady Navier-Stokes code that has been successfully tested for a wide range of turbomachinery flows (Hah [6,7]) was modified to execute a time-accurate simulation of the full annulus of the compressor. The downstream stator was not included in the numerical analysis since the measurements showed that the influence of the stator on the rotating instability was negligible. At each time step, the governing equations are solved with an implicit relaxation method using a fully conservative control volume approach. Previous studies (Cho et al. [8], Hah et al. [9]) have shown that high-order discretization schemes are necessary in both space and time to avoid excessive numerical dissipation. A third-order accurate interpolation scheme is used for the spatial discretization of the convection terms, and central differencing is used for the diffusion terms. The method is of second-order spatial accuracy with smoothly varying grids. For the time-dependent terms, an implicit second-order scheme is used. For unsteady flow calculations, the size of the time step is primarily determined by the requirement for physical accuracy. However, the time step is also restricted by numerical stability. For the current implicit time integration approach, a subiteration is performed at each time step. Residuals of each finite difference equation are integrated over the entire flow domain at each sub-iteration. When the integrated residuals of all the equations are reduced by four orders of magnitude from their initial values during the subiteration, the solution is advanced to the next time step. A modified two-equation model is used to estimate Reynolds stresses. The turbulence model applies either a wall function or a low-Reynolds-number correction near the wall depending on the flow and grid resolution near the wall.

At the inlet of the computational domain, the total pressure, total temperature, and two velocity components are specified. Since no unsteady measurements of static pressure or other flow variables were available downstream of the rotor, circumferentially averaged static pressure was specified on the shroud at the outlet of the computational domain. Nonreflective procedures are used at the exit to minimize the influence of upstream effects. Further details of the computational procedures for the unsteady flow analysis are given by Hah et al. [9, 10].

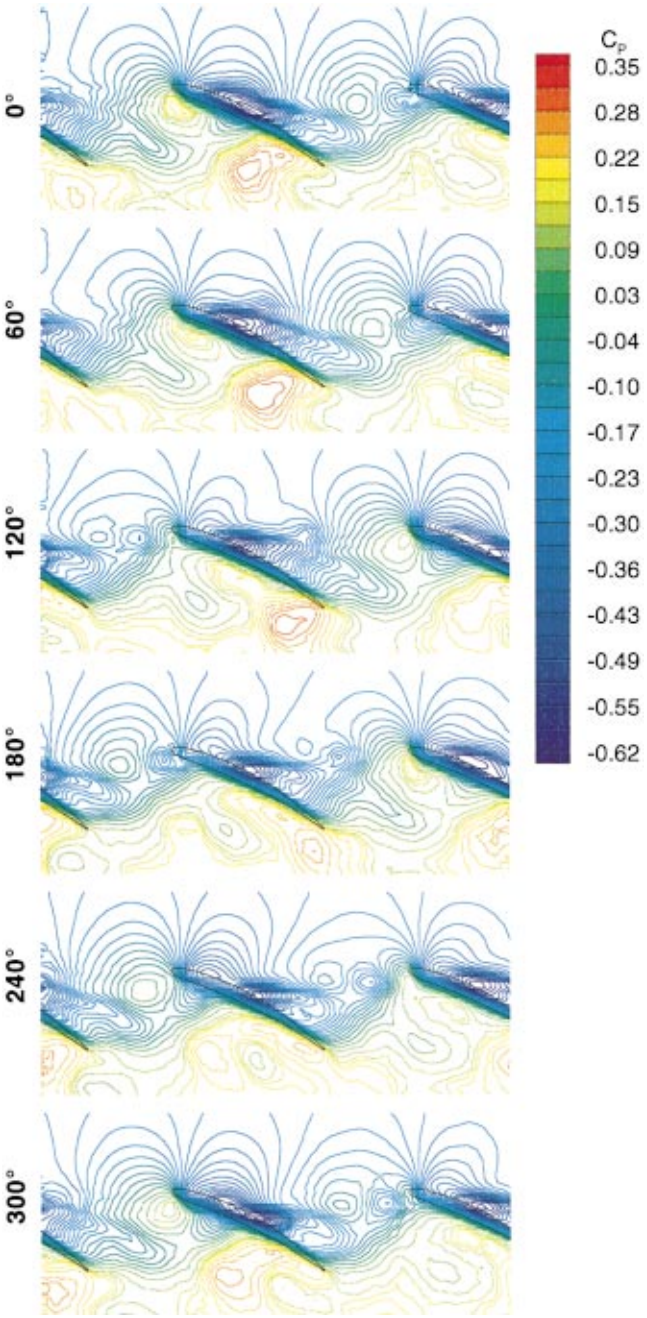

Fig. 8 Relative frame pressure field during one cycle of rotating instability

The rotor consists of 24 blades. To minimize the computational resources required, a coarse grid consisting of 40 nodes in the blade-to-blade direction, 36 nodes in the spanwise direction, and 102 nodes in the streamwise direction was used for each blade passage in the unsteady full-annulus simulation. Four spanwise grid nodes describe the tip clearance. The grid contains a total of 3.5 million nodes.

Because the total number of grid points was restricted to achieve a practical computational turn-around time, the grid was clustered near the tip region. The current grid resolves the main flow feature, namely the interaction between the tip clearance flow and the incoming flow in a low-speed regime, reasonably well. The calculation was executed on a CRAY C-90 computer, requiring roughly ten single-CPU hours to advance the time-accurate solution by one blade pitch revolution on the current computational grid.

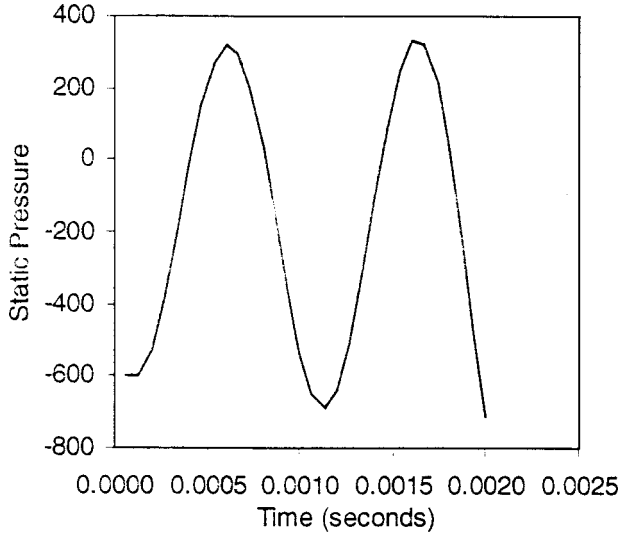

Fig. 9 Calculated time history of blade pressure

Calculated Characteristics of Rotating Instability. To obtain an initial flow field for the unsteady full-annulus calculation, a steady single-passage calculation was first performed. However, the steady calculation does not provide converged solutions below a flow coefficient of 0.2. Therefore, the steady single-passage solution at a flow coefficient of 0.2 was used as an initial solution for the unsteady full-annulus calculation. The rotor exit pressure at the casing was then gradually raised by an increment of 0.001 psi to obtain a flow rate of 0.18.

The unsteady full-annulus calculated flow field becomes unsteady at mass flow rates below 0.2. The unsteadiness is mainly due to unsteady movement of the tip clearance vortex, which is amplified by an increase in the tip gap. Unsteady wandering of the tip clearance vortex for relatively large tip gaps was also observed by Zierke et al. [11].

At the flow rate of 0.18, a rotating instability was observed in the numerical solution. After about two rotor revolutions, an almost periodic unsteady solution was observed. The fan characteristics in Fig. 2 show hysteretic behavior for the two largest tip clearances. Computations were performed for operating conditions from choke to stall and compared with measurements at the same conditions. Figure 9 shows calculated static pressure variation at a location on the rotor suction surface 36% axial chord downstream of the leading edge and 3 mm inboard of the blade

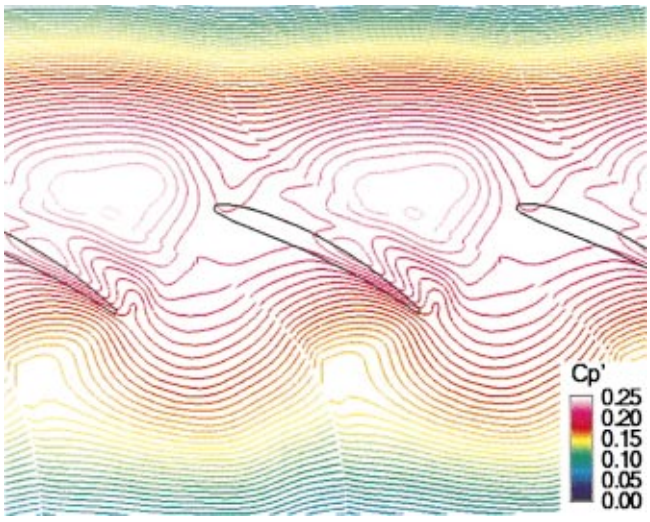

Fig. 10 Calculated standard deviation of pressure on casing

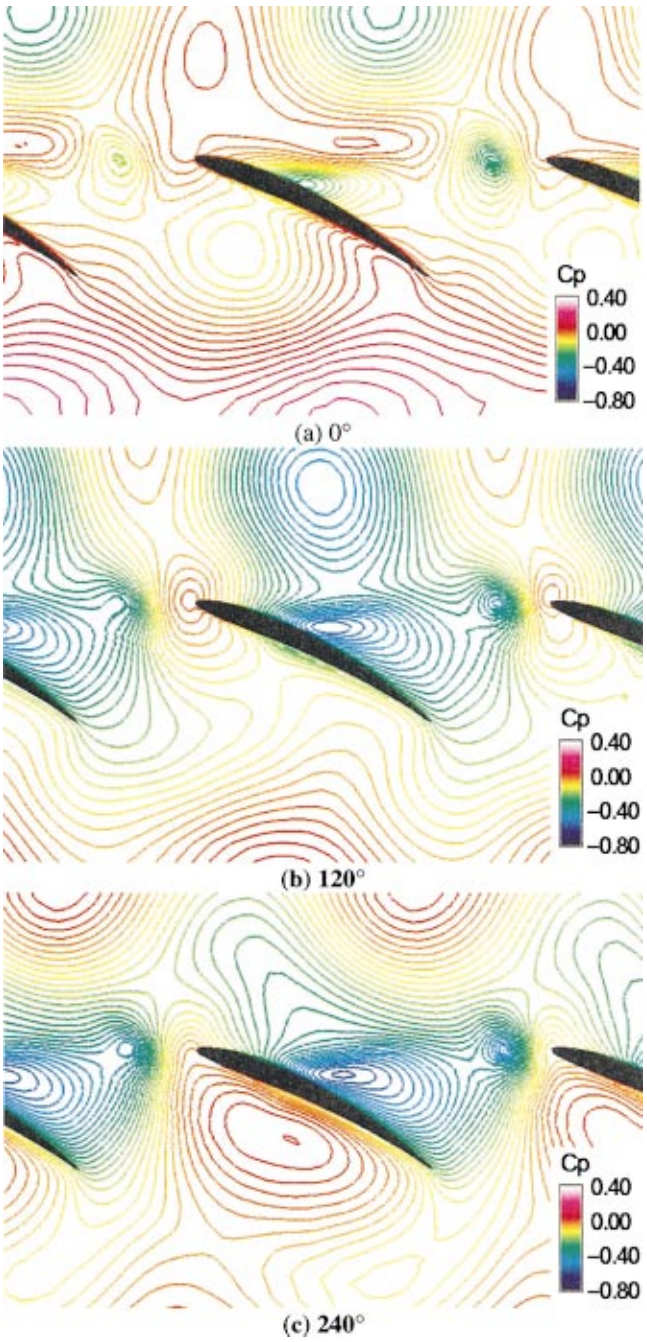

Fig. 11 Calculated instantaneous pressure field during one instability cycle

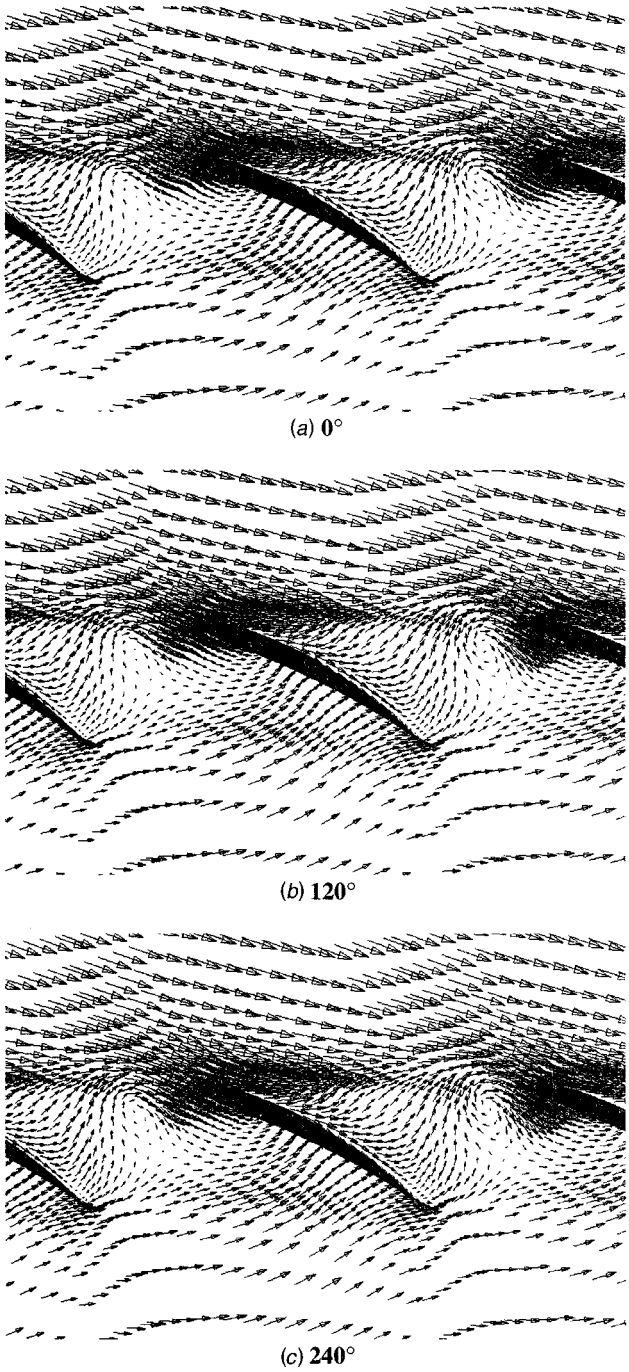

Fig. 12 Calculated instantaneous velocity vectors during one instability cycle

tip. The almost periodic variation in static pressure indicates the instability cycle. The measured pressure signal shown in Fig. 6 exhibits very similar behavior with more complex variation during each cycle.

Figure 10 shows the calculated distribution of the standard deviation of static pressure on the casing. The standard deviation was calculated from instantaneous flow solutions during one instability cycle. Passage-to-passage variations of the standard deviation were negligible in the numerical solution. The peak value of the calculated standard deviation is located further away from the pressure side of the blade and further upstream than that of the measurements in Fig. 5. This difference may be due to the relatively coarse computational grid and/or inadequacy of the currently applied turbulence model.

Figure 11 shows the calculated instantaneous static pressure distribution on the casing at three instants during one instability cycle. As seen in the measurements (Fig. 8), the calculation also shows a region of low static pressure moving from the suction side of the passage to the pressure side at roughly half the rotor speed.

To investigate the mechanism behind this observation, the calculated flow field was examined further. Figure 12 shows instantaneous velocity fields at the rotor tip at three instants during the instability cycle. Axially reversed flow extending over the entire circumferential direction is observed near the trailing edge. Calculated instantaneous streamlines are shown in Fig. 13. Both Figs. 12 and 13 show a vortex in the middle of the blade passage moving from the suction side of the passage to the pressure side at roughly half the rotor speed. The strength of the vortex varies

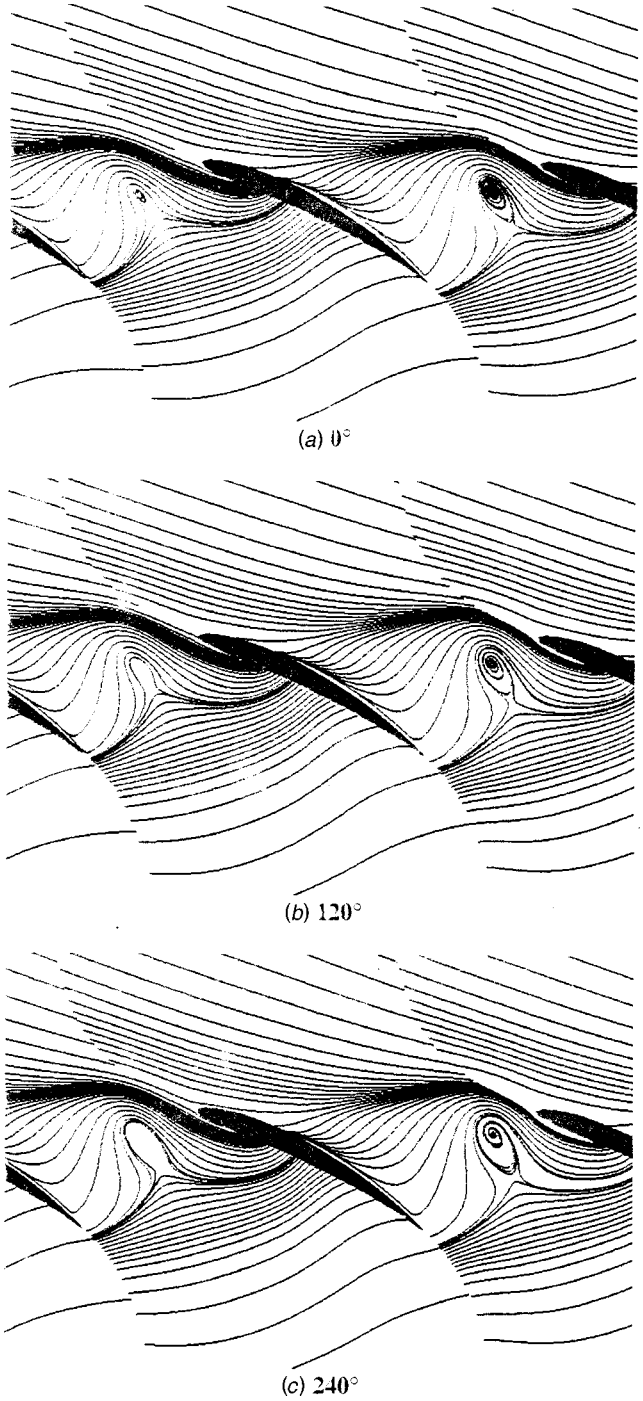

Fig. 13 Calculated instantaneous streamlines during one instability cycle

between different passages at different times. As this vortex moves in the tangential direction, the local pressure field also changes due to the change in blockage.

A three dimensional view of the vortex is shown in Fig. 14 with particle traces in an instantaneous three-dimensional flow field. This vortex, denoted as the rotating instability vortex in Fig. 14, seems to be different from the classical tip clearance vortex. Flow near the trailing edge is pushed forward by the axially reversed flow seen in Fig. 12. It then interacts with the tip clearance flow and the incoming flow and results in the rotating instability vortex. This vortex is formed periodically mid-way between the blades and moves toward the pressure side of the passage. Unsteady behavior of this vortex structure is the main mechanism of the rotating instability.

The calculated static pressure history near the blade tip in Fig. 9 shows periodic behavior. This is due to the movement of the rotating instability vortex shown in Fig. 14. The current numerical solution does not show clear periodic variation of flow properties across blade passages, as suggested by Mailach et al. [12]. Instead, the flow structure varies among blade passages in a rather random fashion. The number of instability cells can be determined either by circumferential mode analysis [1], or from frequencies in the relative and absolute frames (shown in Figs. 9 and 1, respectively) which was kindly suggested to the authors by Smith [13]. For the current operating condition, both methods indicate that there are about 30–35 cells, which is more than the number reported by Mailach et al. [12] for a different compressor. It seems that the number of instability cells depends on the specific design of the rotor and its operating condition.

Figure 15 shows a close-up of calculated velocity vectors inside the tip clearance near the rotating instability vortex and the blade leading edge. Previous studies (Smith [14], Koch [15]) have indicated that instability arises when the tip clearance flow spills into the adjacent blade passage from the pressure side at the leading edge. The results in Fig. 15 show that the tip clearance flow does not spill into the next blade passage at the leading edge. Instead, the flow follows the pressure side of the leading edge. The flow structure seen in Fig. 15 seems to be the reason why the compressor operates in a very stable mode even with the rotating instability.

Concluding Remarks

Summary. Experimental and numerical studies were conducted to understand the mechanisms of a rotating instability observed in a compressor operating near stall with a large tip clearance.

To detect the rotating instability, unsteady pressures were measured with high-resolution pressure transducers on the casing and near the blade tip. Ensemble-averaged plots of the casing pressures and their deviations suggest that the flow field becomes unsteady with large tip clearances. The measured data indicate that an intermittent low-pressure region traverses the blade passage near the tip. Therefore, two distinct trajectories of tip clearance flow exist near the casing: one that leaves the passage, and the other that impacts the following blade's pressure side.

A three-dimensional unsteady calculation was performed for the full annulus of the rotor to examine the nature of this flow structure and the rotating instability. The unsteady calculation captures the measured flow features well enough to explain the underlying physics of the flow field. With a large tip clearance, the blockage becomes very large near the casing, and axially reversed flow develops over the entire circumferential direction with a decrease in the flow rate. The tip clearance flow coming directly over the blade tip is pushed further upstream by the reversed endwall flow.

What We Learned. The present study shows that the tip clearance flow does not spill into the next blade passage when a rotating instability occurs; instead, the incoming flow follows the pressure side of the leading edge. Consequently, the tip clearance flow, the axially reversed flow near the casing, and the incoming flow interact near the leading edge and form a distinctive vortex structure. This vortex structure moves from the suction side of the passage to the pressure side at roughly half of the rotor speed. The vortex formation in the middle of the passage and its relative pitchwise movement are the main mechanisms of the rotating instability. The compressor operates in a very stable mode even when rotating instability is observed. This is because the tip clearance flow does not spill over into the following blade passage. If

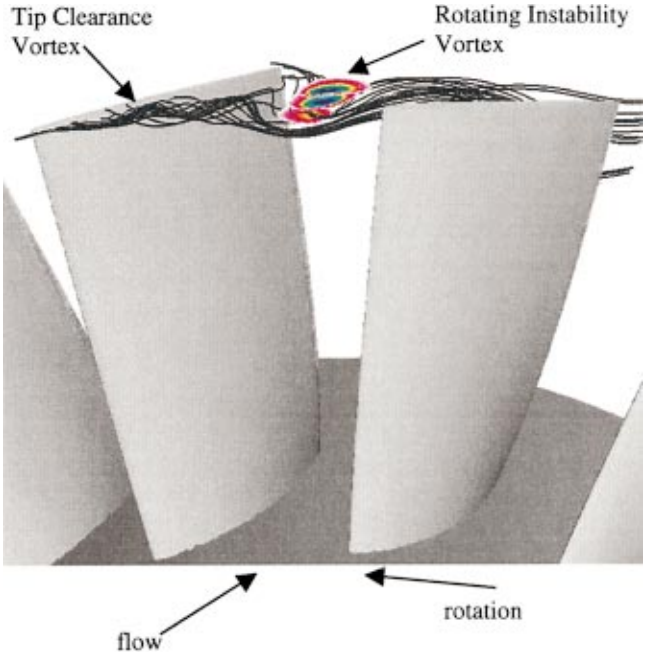

Fig. 14 Structure of instantaneous flow field

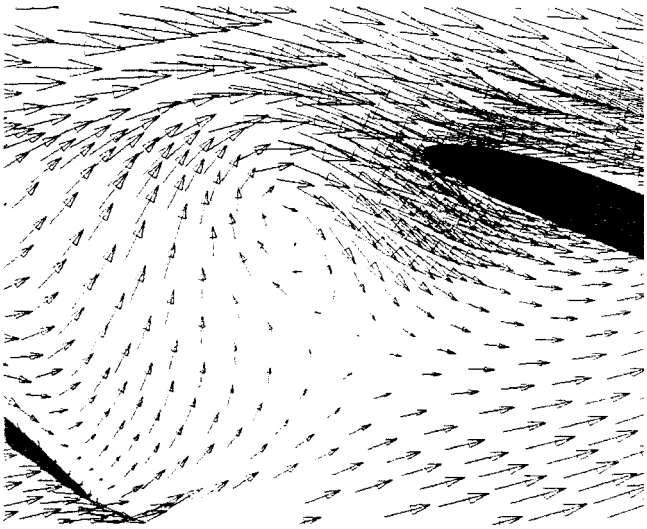

Fig. 15 Flow field near leading edge

the flow rate is further reduced and the in-passage vortex moves upstream of the leading edge, the tip clearance flow spills into the following blade passage and traditional rotating stall occurs.

Acknowledgments

The experimental part of this work was supported by the German Ministry for Research and Technology (BMBF) within the framework of AG Turbo Turbotech II (Teilprojekt 1.245, Förderkennzeichen 0327040D). The study was continued within ''Sonderforschungsbereich 557, Beeinflussung komplexer turbulenter Scherströmungen, TU Berlin'' of the German National Science Foundation. The authors would like to acknowledge the contribution of J. Loellbach of ICOMP during the course of the current study, and to thank Dr. L. H. Smith Jr. of G.E. Aircraft Engines for providing a method of calculating the number of instability cells with measured frequencies and helping to clarify related flow physics.

Nomenclature

n = rotor speed (1/min)
BPF = blade passing frequency
ϕ = flow rate
ψ = pressure coefficient
ζ = tip clearance, nondimensionalized by tip chord
C_P = static pressure coefficient, nondimensionalized by dynamic head of rotor tip speed
C'_P = static pressure fluctuation coefficient, nondimensionalized by tip stagnation pressure
μ = ensemble average of static pressure
p'_{rms} = standard deviation of pressure
i = index in axial direction
j = index in circumferential direction

References

[1] Kameier, F., and Neise, W., 1997, ''Experimental Study of Tip Clearance Losses and Noise in Axial Turbomachines and Their Reduction,'' ASME J. Turbomach., **119**, pp. 460–471.
[2] Liu, J.M., Holste, F., and Neise, W., 1996, ''On the Azimuthal Mode Structure of Rotating Blade Flow Instabilities in Axial Turbomachines,'' AIAA Pap., 96-1741, 2nd AIAA/CEAS Aeroacoustics Conference.
[3] März, J., Gui, X., Neuhaus, L., and Neise, W., ''Circumferential Structure of Rotating Instability Under Variation of Flow Rate and Solidity,'' VDI-Ber., **1425**, pp. 189–198.
[4] Baumgartner, M., Kameier, F., and Hormouziadis, J., 1995, ''Non Engine Order Blade Vibration in a High Speed Compressor,'' ISABE 95-7094, Twelfth Int. Symp. on Airbreathing Engines, Melbourne, Australia.
[5] Müller, R, and Mailach, R., 1998 ''Experimentelle Untersuchung von Verdichterinstabilitäten am Niedergeschwindigkeitsverdichter Dresden,'' VDI-Berichte 1425, pp. 167-176, VDI-GET-Tagung Turbokompressoren im industriellen Einsatz, Hannover, Germany.
[6] Hah, C., 1984, ''A Navier-Stokes Analysis of Three-Dimensional Turbine Flows Inside Turbine Blade Rows at Design and Off-Design Conditions,'' ASME J. Eng. Gas Turbines Power, **106**, pp. 421–429.
[7] Hah, C., 1987, ''Calculation of Three-Dimensional Viscous Flows in Turbomachinery with an Implicit Relaxation Method,'' AIAA J. Propul. Power, **3**, No. 5, pp. 415–422.
[8] Cho, N.-H., Liu, X., Rodi, W., and Schonung, B., 1992, ''Calculation of Wake-Induced Unsteady Flow in a Turbine Cascade,'' ASME Paper 92-GT-306.
[9] Hah, C., Puterbaugh, S.L., and Copenhaver, W.W., 1993, ''Unsteady Aerodynamic Phenomena in a Transonic Compressor Stage,'' AIAA Pap., 93-1868.
[10] Hah, C., Schulze, R., Wagner, S., and Hennecke, D. K., 1999, ''Numerical and Experimental Study for the Short Wavelength Stall Inception in a Low-Speed Axial Compressor,'' Proc. Fourteenth ISABE Conference, IS-234.
[11] Zierke, W.C., Farrell, K.J., and Straka, W.A., 1994, ''Measurements of Tip Clearance Flow for a High Reynolds Number Axial-Flow Rotor: Part 1—Flow Visualization,'' ASME Paper 94-GT-453.
[12] Mailach, R., Lehmann, I., and Vogeler, K., 2000, ''Rotating Instabilities in an Axial Compressor Originating from the Fluctuating Blade Tip Vortex,'' ASME Paper 2000-GT-506.
[13] Smith, L. H., 2001, private communication.
[14] Smith, L.H., 1970, ''Casing Boundary Layers in Multistage Axial-Flow Compressors,'' *Flow Research and Blading*, Elsevier, Amsterdam The Netherlands.
[15] Koch, C. C., 1981, ''Stalling Pressure Rise Capability of Axial Compressor Stage,'' ASME J. Eng. Power, **98**, pp. 411–424.

Discussion: "An Experimental and Numerical Invesitgation Into the Mechanism of Rotating Instability" (Maerz, J., Hah, C., and Neise, W., 2002, ASME J. Turbomachinery, 124)

Nick Cumpsty
Rolls-Royce plc.
e-mail: nick.cumpsty@rolls-royce.com

There is a lot to admire in this paper and I congratulate the authors in using experiment and CFD to contribute to the understanding of a complicated phenomenon. Once a flow becomes

nonuniform, as it does for the flow described here, there are many more degrees of freedom and the flow can establish itself in many different ways. In consequence, flow that is stalled (in the sense that this takes for rotating stall in compressors) can exhibit many different arrangements. I would like to suggest that the rotating disturbance found here is a particular type of rotating stall corresponding to the special circumstances of an isolated rotor with large tip clearance.

The problem that I have with this paper and with others that have come from Germany over the last few years is the term ''rotating instability.'' One of the useful conclusions from the present paper, referred to in the section ''What We Learned,'' is that the flow is actually very stable. In fact, a condition of instability is very hard to observe, since it is by its very nature transient: A pencil standing vertically on its point is in a condition of instability, but the moment it is microscopically perturbed it ceases to be in the state of instability but is falling toward its new stable condition. The compressor will similarly be unstable at the instant before it moves from being unstalled to being in rotating stall; similarly, for a compressor in rotating stall, there will be an instantaneous condition of instability as the throttle is opened and it moves from stalled to unstalled. The stalled condition, however, is normally very stable.

I have been told that the term ''rotating instability'' is well established and it is implied by this that it should remain in circulation. The term gained currency in Germany a few years ago to describe the type of rotating disturbance described in this paper. It was an unfortunate choice then and remains unfortunate now. It is a widely recognized feature of the English language that words can be created, adapted, and re-used to suit needs. One of the most famous of English quotations is ''What's in a name? that which we call a rose by any other name would smell as sweet'' (*Romeo and Juliet*: Shakespeare). While accepting the spirit of this quotation, it is also true that it would be confusing to refer to a rose using the word ''thorn,'' or even the word ''garlic.'' Put another way, if we want to choose a new use for a word, we should make sure that it does not have a prior meaning that could be confusing, by implying properties that do not apply. Such is the case for ''rotating instability,'' which strictly has no clear meaning, but which implies a special condition that is inconsistent with the stable behavior of the rotating stall flow pattern that is the subject of this paper.

Closure to ''Discussion of 'An Experimental and Numerical Investigation into the Mechanisms of Rotating Instability' '' (2002, ASME J. Turbomach., 124)

J. Maerz

C. Hah
e-mail: chunhill.hah@aki.lerc.nasa.gov

W. Neise

NASA Glenn Research Center, 21000 Brookpark Rd., Cleveland, OH 44135

The authors would like to thank Prof. Cumpsty for sharing his insight and his view of the flow phenomena we investigated.

We agree that the stage's overall behavior in rotating instability is indeed stable. This implies that the observed phenomenon, rather than being of transient nature, exhibits constant statistical properties (frequencies, amplitudes, etc.). On a smaller scale, looking at the flow in an individual blade passage, complex three-dimensional events take place periodically which this paper aims to identify.

The fact that the overall performance of the turbomachine is stable does not contradict the existence of flow instabilities in certain regimes, as is the case in a free jet flow which is fully stable globally, but undisputedly exhibits flow instabilities in the intrinsic flow of the free shear layer.

In earlier work, the first proposed cause of the observed behavior was periodic flow separation. Looking at the simplified example of 2-D flow around an airfoil, separation certainly fulfills the requirements of flow instability: the flow departs into a different state with a recirculation region.

In the case of rotating stall, the blades communicate their stalled state by inducing a different angle of attack on neighboring blades. If turbomachines were not round one might call this ''propagating stall,'' and having identified individual blade stall as a flow instability, we might as well call it, more generally, ''propagating flow instability.'' Is it, in the absence of further knowledge, inadequate to generalize an unknown propagating disturbance of the local tip flow as ''rotating instability''?

Thus, we assume that on a blade-pitch scale we are dealing with a flow instability that is triggered/phase locked by its neighboring blades into a periodic pattern (which must satisfy the condition of 2π-periodicity), and therefore becomes regular. The phase-locked phenomenon, on a global (stage) scale, exhibits steady periodic behavior.

Not knowing the detailed flow pattern, the term rotating/propagating flow instability is therefore the more cautious term, as we do not positively know that the flow really ''stalls'' in the tip region (though a recirculation region of some kind almost certainly occurs). There is more evidence that ''rotating instability'' and ''rotating stall'' are different, though related, phenomena: the number of ''cells'' involved in rotating instability is larger by an order of magnitude than in the case of rotating stall. We have observed rotating instability alone near design point operation, rotating instability plus rotating stall simultaneously when approaching the stall line, and, of course, rotating stall alone when the machine is throttled further.

Incidentally, the term ''rotating instability'' was not coined in Germany: Bent et al.[1] investigated the generation of broadband noise in centrifugal pump impellers and called the observed disturbance of the discharge flow ''rotating stall-like instability'' as well as a ''rotating flow instability.''

The authors agree with Prof. Cumpsty that perhaps the phenomena could be described with a different term (like ''rotating tip vortex instability'' or ''rotating tip vortex disturbance''). However, the term ''rotating instability'' has been used to describe the phenomenon in earlier studies, in consideration of particular features of the flow. We, therefore, used the same terminology to identify the flow phenomenon in our paper.

[1]Bent, McLaughlin, Thompson: ''The Influence of Discharge Configuration on the Generation of Broadband Noise in Centrifugal Turbomachinery.'' DGLR/AIAA Aeroacoustics Conference 1992, 92-02-099.

Short and Long Length-Scale Disturbances Leading to Rotating Stall in an Axial Compressor Stage With Different Stator/Rotor Gaps

M. Inoue
e-mail: ino@mech.kyushu-u.ac.jp

M. Kuroumaru

S. Yoshida

M. Furukawa

Department of Energy and Mechanical Engineering,
Kyushu University,
Fukuoka, Japan

The transient processes of rotating stall evolution have been investigated experimentally in a low-speed axial compressor stage with three stator-rotor gaps. The pressure traces at eight circumferential locations on the casing wall near the rotor leading edge have been analyzed by the wavelet transforms. With the appropriate mother wavelets, the evolution of short and long length-scale disturbances leading to the stall can be captured clearly. Behavior of these disturbances is different depending on the stator-rotor gap. For the large and middle gap, the stall inception is detected by a spiky short length-scale disturbance, and the number of spiky waves increases to generate the high frequency waves. They become the short length-scale part-span stall cells at the mild stall for the large gap, while they turn into a big stall cell with growth of a long length-scale disturbance for the middle gap. In the latter case, therefore, the stalling process was identified with "high-frequency stall inception." For the small stator-rotor gap, the stalling process is identified with "long wavelength stall inception" and supported the recent computational model for the short wavelength stall inception by showing that closing the rotor-stator gaps suppressed the growth of short length-scale disturbances. From the measurement of the pressure field traces on the casing wall, a hypothesis has been developed that the short length-scale disturbance should result from a separation vortex from a blade surface to reduce circulation. The processes of the stall evolution are discussed on this hypothesis. [DOI: 10.1115/1.1458022]

Introduction

In the last decade, the investigation of rotating stall inception was highlighted in axial flow compressors from a view point of active control. As a result, it is generally accepted that two types of stall inception occur [1–3]. One is long wavelength stall inception (also called modal wave inception) in which a long length-scale disturbance (LLSD) grows in amplitude gradually under an unstable condition of the whole compression system [4]. Another is short wavelength stall inception (also called spike-type inception), in which a short length-scale disturbance (SLSD) grows in size rapidly under a condition of high rotor incidence angles [5]. However, there are other routes of stall evolution according to a report of the European collaborative project for investigating the generic features of stall inception in aero-engine type compressors [6]. In this report, it was concluded that just being able to detect modes and spikes would not be sufficient in a high speed compressor, and a whole range of other low and high-frequency disturbances need to be taken into consideration.

So-called high-frequency stall inception is one of the other routes which were observed by Day et al. [6] in two compressors operating at full speed, and considered that the high-frequency waves resulted from multiple short length-scale part-span stall cells. Similar phenomena were observed in the low speed compressor test rigs [7–9]. Structure of the multiple short length-scale part-span stall cells was elucidated by Inoue et al. [10] who pointed out dangerousness of their occurrence. In evolution process of this type of stall, a spiky SLSD appeared and disappeared sporadically at first, the number of the SLSDs increased with the flow rate decreasing, and the high-frequency waves were generated [8,9]. With further throttling, a long length-scale wave overlapped the multiple spiky waves and finally turned into a big stall cell in a deep stall condition [9]. Cumpsty (Discussion of reference [9]) pointed out that a LLSD could be detected at the beginning of the stall evolution process. Obviously, both SLSD and LLSD seem to be associated with this process. However, it has not been made clear how the SLSD and LLSD behave in this process.

Moreover, factors which determine the route of stall evolution have not been clarified yet. There are too many factors to be considered such as hub/tip ratio, tip clearance, configuration of the rotor and stator, presence of other structures near the stage, etc. Gong et al. [11] made the 3-D inviscid flow simulation with a body-force model in the blade region to capture development of rotating stall via SLSD, and showed that reduction of inter-blade row gaps suppressed the growth of SLSDs. Although such a numerical simulation may have potential to determine the route of stall evolution in the future, further experimental studies will be necessary to get to the final goal.

The first purpose of this paper is to present an experimental method for elucidating the behavior of SLSD and LLSD in the transient stalling process. Wavelet analysis is applied to the pressure traces measured on the casing wall near the rotor leading edge.

The second purpose is to show how the SLSD and LLSD behave in process of the high frequency stall inception (in response to the Discussion of reference [9]), and to show the effect of stator-rotor gap on the stalling process.

Contributed by the International Gas Turbine Institute and presented at the International Gas Turbine and Aeroengine Congress and Exhibition, New Orleans, Louisiana, June 4–7, 2001. Manuscript received by the IGTI, January 2001. Paper No. 2001-GT-341. Review Chair: R. A. Natole.

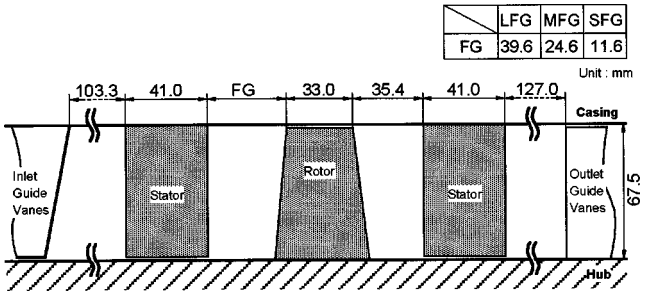

Fig. 1 A schematic view of test section

Experimental Facility and Measurement Method

The experimental study has been conducted in a low-speed research compressor of Kyushu University. A schematic view of the test section is shown in Fig. 1. It consists of an inlet guide vane row, a front stator, a test rotor, a rear stator, and an outlet guide vane row. The diameter, the hub/tip ratio, the number of blades and the tip clearance of the rotor are 449, 0.7, 24, and 0.5 mm, respectively. The two stators have 22 cantilevered blades with tip clearance of 0.5 mm. The compressor stage is designed for a constant whirl angle of absolute flow at the rotor inlet (stator exit) and 0.5 reaction at the midspan. The inlet guide vanes are designed for the same exit flow angle distribution as the rotor to simulate a middle stage of a compressor. Although the front and the rear stator were geometrically identical in the previous paper [9], the rear stator is replaced by the endbend/swept blades to suppress corner stall inside the stator which occurred prior to the rotor stall inception. The details are shown in Inoue et al. [9] for the design specifications and in Inoue et al. [12] for the endbend/swept blades.

The experiments have been conducted for three axial gaps between the rotor and front stator: the ratios of gap to axial chord length at the rotor tip are 1.203, 0.747, and 0.352, which are denoted by LFG (large front gap), MFG (middle front gap), and SFG (small front gap), respectively, in the following discussion. The experiment in the previous papers was conducted for LFG, where the multiple short length-scale stall cells revealed significantly low-pressure bubbles on the casing wall under a mild stall condition [9,10]. The locations of the front stator trailing edge for MFG and SFG are set up at the upstream edge and the center of the low pressure bubble, respectively, which existed in the mild stall for the LFG. The gap between the rotor and the rear stator is kept to be 1.075 times of the axial chord length.

The stage performance has been evaluated for the combination of the rotor and the rear stator. Usually the total-to-static pressure rise is used to evaluate the compressor stage performance. In the present study, however, it is difficult to estimate the downstream static pressure because the casing wall pressure becomes higher than the averaged value due to the swirling flow which changes with flow rate. Therefore, the total pressure rise of the stage has been evaluated from the pressure difference between the inlet and outlet chamber by subtracting the aerodynamic losses of other elements which were obtained in a preliminary experiment without the rotor and the rear stator.

Evolution of short length-scale disturbance (SLSD) and long length-scale disturbance (LLSD) was examined by simultaneous measurement with eight pressure transducers (Kulite XCS-062) mounted on the casing wall 4.1 mm upstream of the rotor leading edge at intervals of 45 deg in the circumferential direction. The blade passing frequency was removed through a low-pass filter. In order to distinguish behavior between SLSD and LLSD, the low-pass filtered pressure traces were analyzed by wavelet transforms.

Transient event near the rotor tip was estimated by simultaneous measurement of the casing wall pressure with seven pressure transducers (Kulite XCS-062) which were mounted on the casing wall along the axial direction to cover the rotor region. A hot-wire survey was made 8 mm upstream of the rotor to get the correlation with the casing wall pressure.

Experimental Results and Discussions

Performance Characteristic Curve. The pressure-rise characteristic curve of the stage performance changed slightly depending on the gaps. However, the difference was so small in comparison with the accuracy of measurement that the meaningful results could not be obtained. On the other hand, the behavior of the pressure rise and flow rate in process of stall evolution changed clearly depending on the gaps.

Figure 2 shows the total-to-total pressure-rise characteristics of the compressor stage for LFG and SFG. For reference, the total-to-static pressure coefficients were estimated by subtracting the dynamic pressure evaluated by the averaged axial velocity (flow rate), and are shown below the total-to-total characteristic curves. In every case, the total-to-static pressure characteristic seems to have negative pressure gradient at the stall point.

For LFG, the stall inception of the rotor is detected at point A when the flow rate is reduced. At a moment of the stall inception, the flow rate and pressure rise coefficient decrease by itself (without throttling) from point A to B, and the compressor rotor falls into mild stall. When the throttle is closing carefully from point B, the flow rate decreases to point C, and then, jumps suddenly to point D where the compressor falls into deep stall. This behavior is the same as the previous experiment [9], although the rear stator is replaced by the end-bend/swept blades. Only the difference is in the transient time from point A to B: the flow rate and pressure rise coefficient drop in several tens of rotor rotations (more rapidly than the previous case: about a hundred rotations of rotor).

For SFG, the flow-rate and pressure-rise coefficient decrease by itself from point A to D in dozens of rotor rotations and the compressor falls into deep stall directly. For MFG, the characteristic curve was almost the same as SFG (the figure omitted), but the transient time from point A to D was much longer than SFG.

Wavelet Transform of Casing Wall Pressure Trace. The transient stalling processes of the axial compressor stage with three stator/rotor gaps have been studied using the pressure fluctuation on the casing wall. In general, a spiky short length-scale disturbance (SLSD) appears locally and can be captured near the rotor leading edge, while a long length-scale disturbance (LLSD) is detected over a wide range of axial direction. Therefore, eight

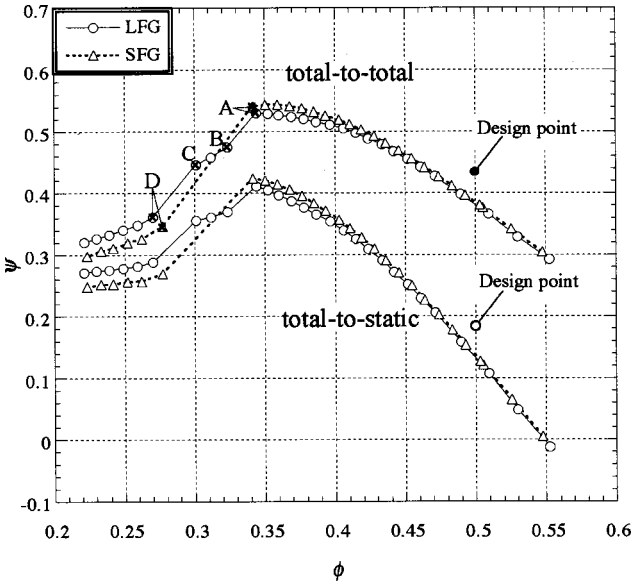

Fig. 2 Pressure rise characteristics of compressor stage

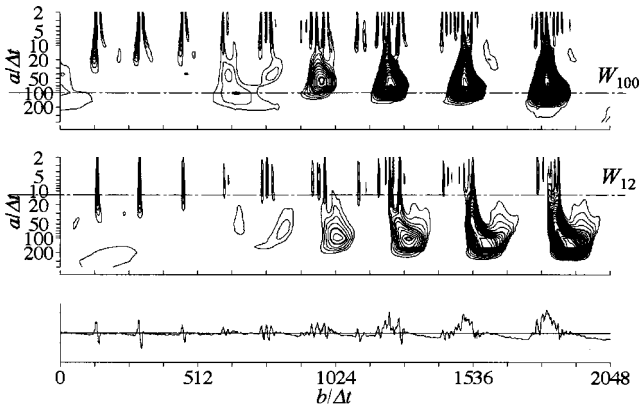

Fig. 3 Wavelet transforms of a low-pass filtered pressure trace with the mother wavelets of Eqs. (2) and (3)

pressure transducers were mounted on the casing wall 4.1 mm upstream of the rotor leading edge at intervals of 45 deg in the circumferential direction to examine behavior of both disturbances in the stalling process. In the previous study [9] using a single transducer, occurrence of spiky SLSDs could be seen clearly in the pressure trace when the blade passing frequency was removed through a low-pass filter. However, the behavior of LLSD with small amplitude could not be captured when the number of SLSDs was increasing. Although the LLSD can be captured by taking a discrete Fourier transform in space about the circumference of the compressor [2], this technique cannot be used for SLSD. On the other hand, a wavelet transform is useful to look into a transient event of disturbances with different scale and is used recently for investigating the compressor stalling process [9,13].

In this study, therefore, in order to look into the behavior of SLSD and LLSD simultaneously, the eight pressure traces are analyzed with the following wavelet transforms.

The wavelet transform of a pressure signal $p(t)$ is defined by

$$W(a,b)=\frac{1}{\sqrt{a}}\int \Psi(T)p(t)dt \tag{1}$$

where $\Psi(T)$ is a mother wavelet, a is the scaling parameter, b implies translation, and $T=(t-b)/a$. When an appropriate function is chosen as $\Psi(T)$, a large value of $W(a,b)$ implies that the disturbance with scale a exists locally around b. The most widely used is the Marr wavelet (also called the ''Mexican hat'') written by

$$\Psi(T)=(1-T^2)\exp(-T^2) \tag{2}$$

However, it is effective to use the point-symmetrical mother wavelet of

$$\Psi(T)=-\sin(2T)\exp(-T^2) \tag{3}$$

for capturing a spiky SLSD which is characterized by the rapid increase followed by rapid decrease in the pressure.

Figure 3 shows an example of the wavelet transforms in the transient stalling process. The low-pass filtered pressure trace to which Eq. (1) was applied is shown on the bottom of the figure. The data shown here are not for the LFG, MFG, and SFG, but for the additional experiment described later. They are employed for convenience of explanation because this event includes both a spiky SLSD and a LLSD in a relatively short temporal scale. The upper and middle frame are the contour maps of $W(a,b)$ calculated with the mother wavelets of Eqs. (2) and (3), respectively. Only the positive values of $W(a,b)$ are represented in each figure to show the phenomenon more clearly. The abscissa is $b/\Delta t$ and the ordinate is a logarithmic scale of $a/\Delta t$ in the opposite direction, where Δt is taken to be 1/120 of a rotor rotation. That is, $b/\Delta t=120$ on the abscissa corresponds to the period of a rotor rotation, and $a/\Delta t=120$ on the ordinate implies that the length-scale of disturbance is identical to a rotor circumference. It is found that a spiky SLSD occurring on the left side of the low-pass filtered pressure trace reveals a high value area of the middle map near $a/\Delta t\approx 12$, although two areas appear for one spiky wave in the upper map. This implies that behavior of a spiky wave cannot be captured by the Marr wavelet. The point-symmetrical wavelet should be used for the spiky wave.

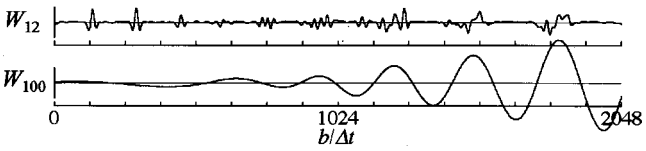

Fig. 4 Variation of wavelet transforms for specified scales of SLSD and LLSD

On the other hand, the both wavelet transforms are capable of capturing the disturbance with scale of $a/\Delta t\approx 100$ which develops with time, although presence of a LLSD is hardly distinguished in the low-pass filtered pressure trace. However, it should be noted that the point-symmetrical wavelet brings about phase shift of 90 deg for the sinusoidal LLSD because of its form. Namely, a location of the maximum $W(a,b)$ shifts from a high part of the LLSD where the SLSDs are crowded on the pressure trace. Therefore, the Marr wavelet of Eq. (2) should be used for looking into behavior of LLSD without phase shift.

When the wavelet transform was made for the raw pressure trace including the blade passing frequency, the contour maps of $W(a,b)$ were almost the same as in Fig. 3 except the range of $a/\Delta t<5$ (the figure is omitted). This is natural since the wavelet transform has essentially the nature of filters in scale. Therefore, the wavelet analysis was applied to the low-pass filtered pressure traces in this study.

In order to look into the transient stalling process in detail, it is necessary to arrange the eight $W(a,b)$ maps of pressure traces at eight circumferential locations each for the point-symmetrical and Marr wavelet. However, it is hard to present them in a compact and understandable way in the limited space of the paper. On the other hand, behavior of disturbance with a specified scale can be seen clearly in the variation of $W(a,b)$ with time at the fixed

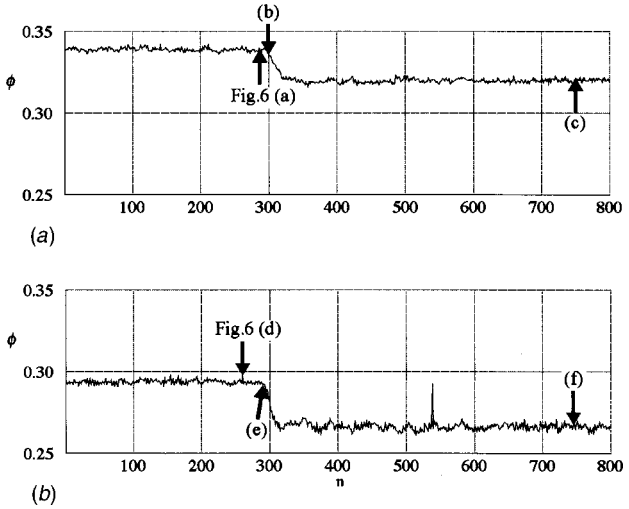

Fig. 5 Variation of flow-rate coefficient with the rotor rotation in transient stalling process for large front gap—(*a*) stalling process of mild stall (A→B), (*b*) stalling process of deep stall (C→D)

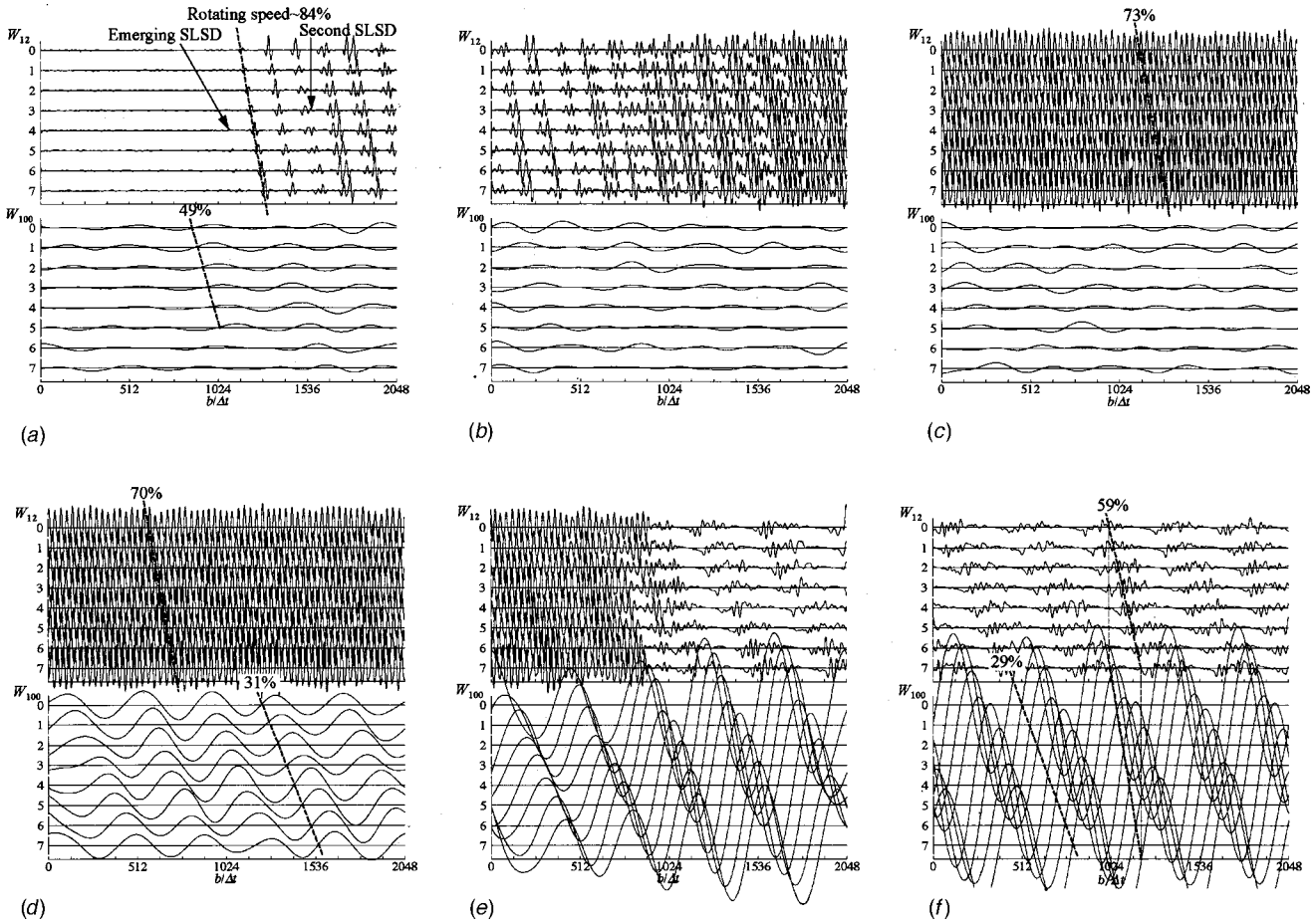

Fig. 6 Evolution of short and long length-scale wave for large front gap—(*a*) transient process from point (a) in Fig. 5(*a*), (*b*) transient process from point (b) in Fig. 5(*a*), (*c*) transient process from point (c) in Fig. 5(*a*), (*d*) transient process from point (d) in Fig. 5(*b*), (*e*) transient process from point (e) in Fig. 5(*b*), (*f*) transient process from point (f) in Fig. 5(*b*)

values of $a/\Delta t$. In this paper, therefore, the variation of $W(a,b)$ at a fixed value of $a/\Delta t$ is presented each for SLSD and LLSD. The values at $a/\Delta t=12$ and 100 are chosen for representing SLSD and LLSD, and denoted by W_{12} and W_{100}, respectively. Figure 4 shows the variation of W_{12} along $a/\Delta t=12$ in the middle frame of Fig. 3 and W_{100} along $a/\Delta t=100$ in the upper frame. This kind of representation is considered to be a wave through a simplified wavelet filter for the disturbance with scale of $a/\Delta t=12$ or 100. It is found how the SLSD and LLSD behave in the stalling process in Fig. 4.

Evolution of Rotating Stall for Large Front Gap. As mentioned before, the stall occurs in two steps in the case of LFG. According to the previous paper [10], the first step was the mild stall with multiple short-length scale part-span stall cells and the second one was the deep stall with a big stall cell.

Figures 5 (*a*) and (*b*) are the variation of flow-rate coefficient with rotor rotation in process of the mild and deep stall. In each cace, the flow-rate decreases in several tens of rotor rotations. The behavior of SLSD and LLSD in each process has been examined by the wavelet analysis for the low-pass filtered pressure traces at eight circumferential locations on the casing near the rotor leading edge. The small letters (a) to (f) indicated by arrows in Fig. 5 are corresponding to the start points of the pressure traces which are analyzed by the wavelet transforms in Figs. 6(*a*) to (*f*).

Figures 6(*a*) to (*c*) show the variation of W_{12} and W_{100} for the eight pressure traces in process of the mild stall. It can be seen on the W_{12}-traces of Fig. 6(*a*) that a spiky SLSD appears and rotates nearly at 80 percent of the rotor speed. The stall inception (point A in Fig. 2) is detected with the formation of this disturbance. It is attenuated after one rotor rotation, the second SLSD is generated next to it, and the two disturbances grow in amplitude. The number of SLSDs increases in similar manner (Fig. 6(*b*)) from point A to B in Fig. 2, and finally the multiple short length-scale stall cells appear at intervals of 4.8 times of a blade spacing the waves of which are shown in Fig. 6(*c*). They rotate nearly at 70 percent of the rotor speed. On the W_{100}-traces of Fig. 6(*a*) a LLSD is appreciable prior to the formation of the SLSD, but it never keeps up for long time. Near the stall inception it seems to rotate at constant speed, but it does not grow in amplitude nor rotate at constant speed once the spiky SLSD is generated and increases in the number as shown in Figs. 6(*b*) and (*c*). For the first step of stall, LLSD is not predominant for the stall evolution.

Figures 6(*d*) to (*f*) show the variation of W_{12} and W_{100} in pro-

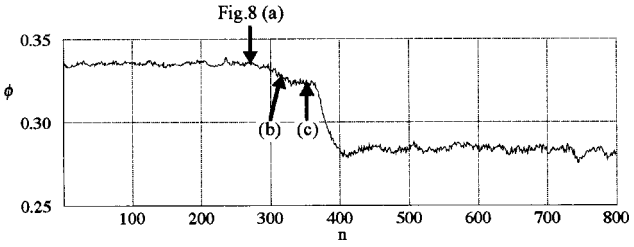

Fig. 7 Variation of flow-rate coefficient with the rotor rotation in transient stalling process for middle front gap

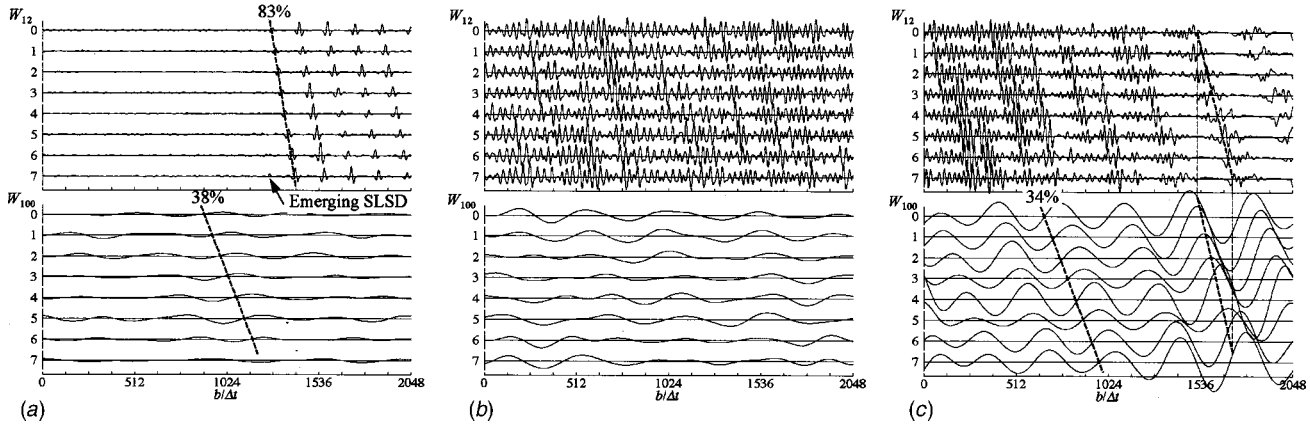

Fig. 8 Evolution of short and long length-scale wave for middle front gap—(*a*) transient process from point (a) in Fig. 7, (*b*) transient process from point (b) in Fig. 7, (*c*) transient process from point (c) in Fig. 7

cess of the deep stall. When the compressor is throttled near point C in Fig. 2, the LLSD grows in amplitude and rotates nearly at 30 percent of the rotor speed as shown in Fig. 6(*d*), while the multiple spiky SLSDs are still rotating nearly at 70 percent of the rotor speed. At point C of Fig. 2, the SLSDs are attenuated suddenly with growth of the LLSD (Fig. 6(*e*)), and the compressor falls into the deep stall with a big stall cell. For the second step of stall, LLSD is predominant for the stall evolution.

At deep stall, the SLSDs still exist in the high pressure range of the strong LLSD (Fig. 6(*f*)). The high and low pressure range of LLSD correspond to the big stall cell and the unstalled blades, respectively, [14]. Presence of the SLSDs in the stall cell was discussed in the previous paper [10]. As shown in Fig. 6(*f*), they are rotating nearly at 60 percent of the rotor speed. They seem to develop in the right side of the long wave where the blades enter stall, and degenerate in the left side where the blades go out of stall. This trend agrees with behavior of so-called ''sub-cell vortices'' in the stall cell which were found by Outa and Kato [15] on the bases of their hot-film probe measurement and unsteady 2D numerical simulation.

Evolution of Rotating Stall for Middle Front Gap. Figure 7 shows the variation of flow-rate coefficient with rotor rotation in the stalling process of MFG. The small letters (a) to (c) indicated by arrows denote the start point of pressure traces which are analyzed by the wavelet transforms in Figs. 8(*a*) to (*c*). The flow rate decreases gradually from (a) to (c) in the first half of stalling process, and rapidly in the latter half.

Figures 8(*a*) to (*c*) show the variation of W_{12} and W_{100} for the eight pressure traces in the stalling process of MFG. A LLSD with small amplitude is rotating nearly at 40 percent of the rotor speed just before the stall inception, but it does not grow in amplitude nor rotate once a spiky SLSD is generated (Fig. 8(*a*)). Then, in the first half stalling process, the number of SLSDs increases to generate the high-frequency waves which are sporadically increasing and decreasing in amplitude as shown in Fig. 8(*b*). When the LLSD grows and rotates at about 30 percent of rotor speed, the SLSDs are attenuated and concentrate in the high pressure range of the LLSD as shown in Fig. 8(*c*). In the latter half stalling process, the LLSD grows in dozens of rotor rotations to form a big stall cell where behavior of the SLSDs are similar to Fig. 6(*f*). The evolution process of disturbances is similar to that of LFG, but the amplitude of high-frequency waves is not so large as that in the mild stall for LFG. The compressor rotor stalls in one step. This behavior seems to resemble the phenomenon of the high-frequency stall inception observed by Day et al. [6].

Evolution of Rotating Stall for Short Front Gap. Figures 9(*a*) and (*b*) show the variation of W_{12} and W_{100} for the eight pressure traces in the stalling process of SFG. The start point of traces in each figure is also indicated by the corresponding small letter in Fig. 10 which shows the variation of flow-rate coefficient with the rotor rotation. A LLSD with small amplitude is rotating nearly at 30 percent of the rotor speed about a hundred rotor rotations prior to the stall inception (the figure is omitted). As it grows, several SLSDs with small amplitude appear in the high

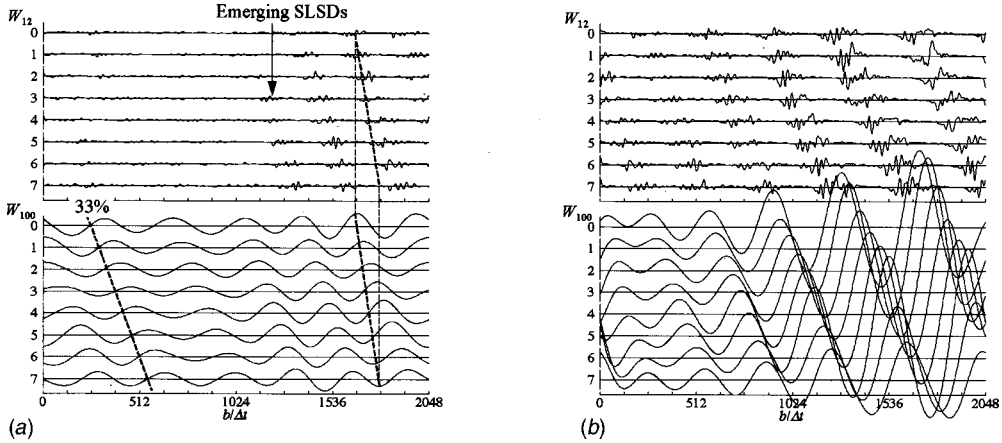

Fig. 9 Evolution of short and long length-scale wave for small front gap—(*a*) transient process from point (a) in Fig. 10, (*b*) transient process from point (b) in Fig. 10

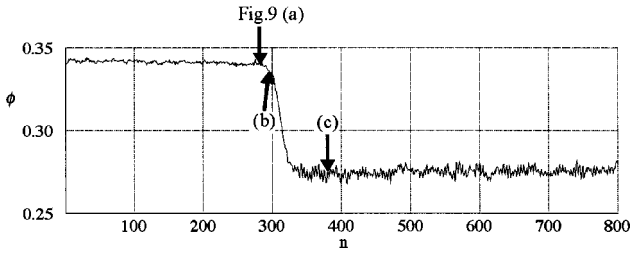

Fig. 10 Variation of flow-rate coefficient with the rotor rotation in transient stalling process for small front gap

pressure range of LLSD (Fig. 9(*a*)). They increase in the number and the amplitude with rapid amplification of the LLSD (Fig. 9(*b*)), and a big stall cell is generated in dozens of rotor rotations. The SLSDs behave similarly to Fig. 6(*f*) after the big stall cell develops (at (c) in Fig. 10). Although the SLSDs exist at the stall inception, their amplitude is smaller than that of the spiky SLSD appearing at the stall inception of LFG (Fig. 6(*a*)). For this case, LLSD is predominant for the stall evolution.

Trace of Pressure Field on Casing Wall. In the previous papers [9,10], the authors succeeded in elucidating the structure of the multiple short length-scale stall cells in the mild stall for LFG using a so-called ''double phase-locked averaging technique'' with which the measurement data could be averaged synchronously with both the rotor and stall cell rotation. It was found that the short length-scale stall cell consisted of a tornadolike vortex which spanned from a blade suction surface to the casing wall ahead of the rotor as illustrated in Fig. 11. A physical interpretation for this phenomenon was made in terms of bound circulation and vortices around a blade. That is, the tornadolike vortex is a three dimensional separation vortex from the blade suction surface to reduce the circulation near the tip region. On the other hand, from observation of the low-pass filtered pressure near the rotor leading edge, the size, shape and rotating speed of a spiky wave appearing at the stall inception quite resembled those of the multiple short length-scale stall cells for LFG [9]. Therefore, it was considered that the spiky SLSD at stall inception should have the structure similar to that of the multiple short length-scale stall cell.

In the present study, the further measurements have been conducted to elucidate the difference in structure between the spiky SLSD at inception and the short length-scale stall cell in the mild stall.

First, the traces of pressure field on the casing wall have been obtained by simultaneous measurements with seven axially arranged pressure transducers. Figures 12(*a*) and (*b*) show the pressure field traces for the spiky disturbance at inception and for the multiple short length-scale stall cells in the mild stall. As the pressures are measured at fixed locations and the blades rotate from left to right, the time proceeds from right to left in the figure. On the top of the figure, the raw and low-pass filtered pressure traces 4.1 mm upstream of the rotor leading edge are shown for reference. Short vertical lines in the top figure indicate blade passings and correspond the short vertical lines on the bottom of the figure. It should be noted that this pressure field is different from the instantaneous pressure distribution relative to the rotor because the time goes from right to left in the figure.

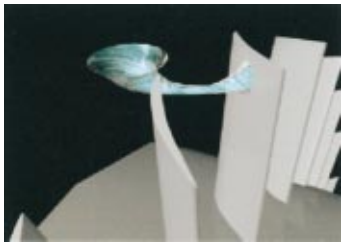

Fig. 11 Illustrations for flow structure of short length-scale stall cell

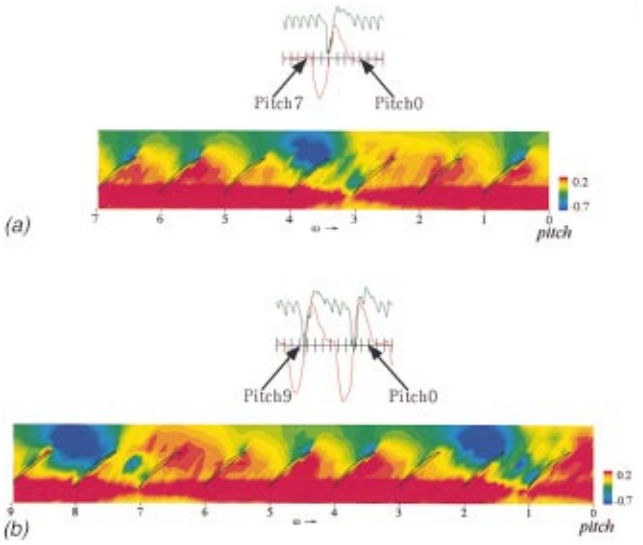

Fig. 12 Pressure field traces on casing wall for large front gap—(*a*) stall inception, (*b*) mild stall condition

In Fig. 12(*a*), the significantly low pressure area can be seen at the right of the considerably high pressure area upstream of the rotor. This phenomenon causes the spiky wave pattern which is characterized by rapid increase followed by rapid decrease in pressure. The low-pass filtered pressure trace upstream of the rotor leading edge captures this feature well although its phase delays from the raw pressure wave. At the mild stall, similar low pressure areas can be observed although they are somewhat larger than at the inception as shown in Fig. 12(*b*). These area were caused by the separation vortices spanning to the casing wall [10] as illustrated in Fig. 11.

Comparing Fig. 12(*a*) with Fig. 12(*b*), the spiky SLSD at inception is considered to result from the separation vortex from the blade. This consideration seems to be in line with the idea of Camp and Day [5] who mentioned that the spike type inception was three-dimensional breakdown of the flow field associated with high rotor incidence angle. On the other hand, Hoying et al. [16] made a 3-D viscous-inviscid hybrid numerical simulation, and found that the spike was caused by a tip clearance vortex spilling upstream of the rotor. However, his calculation does not conflict with the separation vortex model illustrated in Fig. 11 in a broad sense. According to the vortex theory, the tip clearance vortex is nothing but a kind of separation vortex which consists of vortex lines separated from blade tip instead of suction surface. The multiple SLSCs are in a developed state, while the stall inception is a transient event. Although the vortex separates from near midspan at the mild stall, the separation may be located near the tip at the onset. It could be located at blade tip surface when the tip clearance is large.

In order to verify the above remarks, the correlation is evaluated between the casing wall pressure fluctuation and the output fluctuation of a hot-wire inserted 8 mm upstream of the rotor. The correlation function is written by

$$R(r)=\overline{p'\cdot\nu'(r)}/\sqrt{\overline{p'^2}\cdot\overline{\nu'^2(r)}} \tag{4}$$

where p' = fluctuation of the casing wall pressure
ν' = fluctuation of the hot-wire output
r = radial location of the hot-wire

Figure 13(*a*) shows the correlation function $R(r)$ in process of the mild stall for LFG. The abscissa is the nondimensional radial

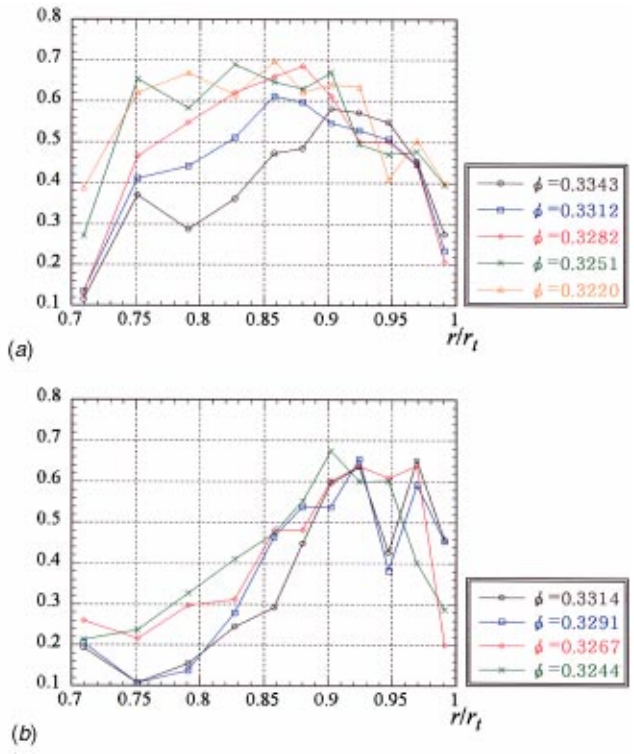

Fig. 13 Correlation functions between the casing wall pressure and the hot-wire signal 8 mm upstream of the rotor—(*a*) process of mild stall evolution for large front gap, (*b*) first half process of stall evolution for middle front gap

location of hot-wire. The flow rate coefficients as parameters should refer to the values on the ordinate of Fig. 5(*a*). In the early process of stall of LFG (Fig. 13(*a*)), the correlation is high near the casing; but, the high correlation area extends to the whole flow passage in the mild stall condition. Figure 13(*b*) shows the correlation function in the first half process of stall for MFG where the number of SLSDs was increasing and the amplitude of high-frequency waves were sporadically increasing and decreasing before the LLSD grew and rotated. The flow rate coefficients as parameters are corresponding to the ordinate of Fig. 7. In this case, the high correlation area is restricted near the casing. This fact implies that the separation vortex is restricted only the blade tip region unless the multiple short length-scale stall cell are fully developed in the mild stall.

On the other hand, the SLSDs still existed in the stall cell at deep stall, as shown in Fig. 6(*f*). They were generated by attenuating the amplitude of spiky SLSDs in the mild stall for LFG (Fig. 6(*e*)), and by appearing in the high pressure range of LLSD for SFG (Figs. 9(*a*) and (*b*)). To look into what the SLSDs is, the pressure field trace on the casing wall at deep stall is presented in

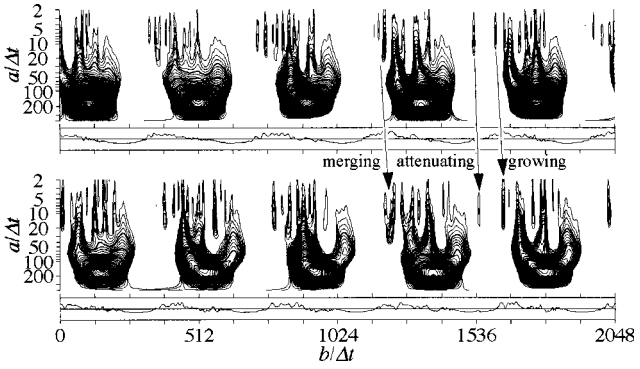

Fig. 15 Wavelet transforms of low-pass filtered pressure traces at two locations 45 deg apart in the circumferential direction at deep stall condition

Fig. 14. The raw and low-pass filtered pressure traces upstream of the rotor leading edge are shown on the top of the figure in the same manner as Fig. 12. The traces in the two rotor rotations are shown in the figure, although the period of a long wave due to a big stall cell is longer than three rotor rotations since it rotates at about 30 percent of the rotor speed. The stall cell covers the blades from the upper row to the right part of lower row of the pressure field trace (three quarters on the right side of the top figure). The low pressure areas can be observed ahead of the rotor in the stall cell. They correspond to SLSDs according to the wavelet transform. They are more clearly seen on the right side of the lower frame of the pressure field trace where the blades are entering to the stall cell. By comparing them with the low pressure areas in Fig. 12, they also seem to result from the separation vortices from the blade suction surfaces. It is considered that the blade releases the separation vortex to reduce the circulation in the active stall cell.

Looking into the results of the wavelet transform, however, their behavior is different from the spiky SLSDs at mild stall. Figure 15 shows the wavelet transform maps for two low-pass filtered pressure traces at 45 deg apart in the circumferential direction. The contour lines distributed around $a/\Delta t = 5 \sim 15$ correspond to the SLSDs. Their size and intervals are irregular although they are rotating about 60 percent of rotor speed. Some SLSDs diminish and some ones grow in amplitude as shown by arrows in Fig. 15. This behavior may be caused by upstream movement of the separation vortex since the pressure traces were obtained at a fixed axial location. In some cases, the merging of separation vortices may occur to grow in size as shown by the left arrow in the figure.

Additional Discussions. From the experimental results shown in the previous section, it is reasonable to develop a hypothesis that the SLSD results from a separation vortex from a blade surface to reduce circulation. The processes of stall evolution are discussed on this hypothesis in this section.

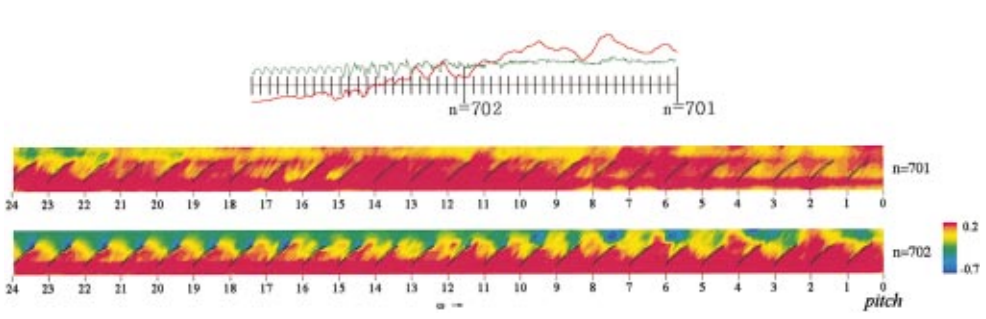

Fig. 14 Pressure field traces on casing wall at deep stall condition for large front gap

For LFG, the stalling process was in two steps. In the first step, a spiky SLSD appeared at the stall inception, the number of spiky waves increased, and the compressor ran at a fixed flow rate in the mild stall condition where the multiple short length-scale stall cells revealed the high-frequency waves. These facts imply that the stall initiates with formation of a three-dimensional separation vortex near the tip of a blade and the number of blades with three dimensional separation vortex increases. The vortex spans from the casing wall to blade suction surface very near the tip at the inception, then the separation point on the blade moves to mid-span. At the mild stall, comparatively stable condition is maintained by a sufficient front space for spanning the separation vortices which constitute the short length-scale part-span stall cells with tornadolike structure at equal intervals. In the second step, growth of a long wavelength breaks the stable condition to gather the separated blades in a big stall cell.

The stalling process of MFG was similar to LFG. However, the process from inception to deep stall went on by itself in about a hundred of the rotor rotations. In this process, the separation point of the three-dimensional vortex is restricted near the blade tip region. A long wavelength grows without formation of the multiple short length-scale part-span stall cells. This process is considered to be identified with the high frequency stall inception observed in two aeroengine-type compressors operating at full speed [6].

On the other hand, the stalling process of SFG is identified with 'long wave-length stall inception' although several small-size SLSDs existed in the high pressure range of LLSD at the stall inception. The number and the amplitude of SLSD increased in the stall evolution process. In this case, the separation vortices occur in the low velocity region of LLSD and seem to play a role for increasing the amplitude of LLSD to lead to deep stall.

The present experimental result supports the computational model for the short wave-length stall inception proposed by Gong, et al. [11], who showed that bringing the IGV close to the first rotor suppressed the development of spikes. Physical explanation of this effect can be made based on the hypothesis of the separation vortex: the small gap upstream of the rotor leading edge arrests the growth of a vortex spanning to the casing wall ahead of the rotor. The separation vortices from the rotor blades interact with the front stator blades. The low-energy fluid is redistributed circumferentially near the casing and a long length-scale wave is generated. It is very interesting that Gongs' model is capable of predicting this effect, although the number of blades is assumed to be infinitive.

The stall inception for LFG and MFG was detected by formation of a spiky SLSD. In this sense, this process seems to be a kind of short wavelength stall inception (also called spike-type inception). However, the process of stall evolution is quite different from usual spike-type inception process reported so far. In the usual case, a spiky wave grows rapidly in size. A spiky wave seems to be caused by the separation vortex from the blade, as shown in Fig. 12. If so, vortices from several blades must be merged in the usual spike-type inception process in order to grow in size. In the present study, an additional experiment was made by reducing the gap between the rotor trailing edge and the rear stator for LFG to examine the effect of the rear stator. The rear gap ratio was 0.620 based on the axial chord length at the rotor tip. In this case, a small LLSD was appreciable prior to formation of a spiky SLSD, but it never kept up for long time nor rotated. Immediately after the formation of a spiky SLSD the LLSD grew rapidly. At the same time, the SLSD was attenuated and the number of the SLSDs increased in the high pressure range of the LLSD to grow in amplitude in dozens of rotor rotations, as shown in Figs. 3 and 4. This process may look like spike-type inception if the LLSD grow more rapidly. However, the merging of vortices could not be observed in the stall evolution process. What conditions enable to make a spiky disturbance grow in size should be elucidated in the future.

Conclusions

The process of rotating stall evolution was studied experimentally in a low-speed axial compressor stage by changing the stator/rotor gap. The pressure traces at 8 circumferential locations on the casing wall near the rotor leading edge were analyzed with the wavelet transforms. The pressure field traces on the casing wall covering the rotor region were examined to imagine the transient event in stalling process. The results are summarized as follows.

1 Behavior of short and long length-scale disturbances leading to rotating stall can be captured clearly by the wavelet analysis with the appropriate mother wavelet. The point-symmetrical mother wavelet is available for a spiky short length-scale disturbance which is characterized by rapid decrease following rapid increase in the low-pass filtered pressure trace, while the Marr wavelet is available for a long length-scale disturbance. Evolution of each disturbance can be examined simply by observing the variations of the wavelet transforms at a fixed scale corresponding to each disturbance.

2 The behavior of short and long length-scale disturbances is different depending on the stator/rotor gap. In the case of large gap the stalling process was in two steps. In the first step, a spiky short length-scale disturbance was generated at the stall inception, and the number of spiky waves increased to have the multiple short length-scale stall cells in the mild stall condition. In this process a long length-scale disturbance was appreciable, but did not play a predominant role. In the second step, the long length-scale disturbance grew with attenuation of the short length-scale disturbances and the compressor fell into a deep stall.

3 The stalling process for the middle gap is considered to be identified with the high frequency stall inception which was observed in two aeroengine-type compressors operating at full speed [6]. The stall inception was detected by a spiky short length-scale disturbance, then, the number of spiky waves increased sporadically to generate the high frequency waves, and turned into a deep stall cell with growth of a long length-scale disturbance. Although the process was similar to the large gap, the stall developed in one step (without throttling) from inception to deep stall.

4 The stalling process for the small gap is identified with ''long wavelength stall inception.'' A long length-scale disturbance with small amplitude was rotating nearly at 30 percent of the rotor speed prior to the stall inception. As it grew, several short length-scale disturbances with small amplitude appeared in the high-pressure range of long length-scale disturbance. They increase in the number and the amplitude with rapid amplification of the long length-scale disturbance to generate a big stall cell.

5 The experimental result supported the computational model for the short wavelength stall inception proposed by Gong et al. [11], who showed that closing the rotor-stator gaps suppressed the growth of short length-scale disturbances.

6 In the present experiments, the usual spike-type inception process in which a spiky wave grows rapidly in size did not occur. However, when the rear stator was close to the rotor trailing edge in the additional experiment, a long length-scale disturbance grew rapidly with increasing the number of short length-scale disturbances immediately after appearance of a spiky wave at the stall inception (Fig. 3).

7 From the comparison of the pressure field traces on the casing wall between the transient stalling process and the mild stall condition, a hypothesis was built up that the short length-scale disturbance should result from a separation vortex from a blade surface to reduce circulation. The processes of stall evolution were discussed in this hypothesis.

Acknowledgments

The authors are extremely grateful to Prof. Cumpsty for his useful discussion in the previous paper [9] which motivated to start the present work. They also appreciate to Mr. Iwakiri for helping the experimental work.

References

[1] McDougall, N. M., Cumpsty, N. A., and Hynes, T. P., 1990, ''Stall Inception in Axial Compressors,'' ASME J. Turbomach., **112**, pp. 116–125.

[2] Garnier, V. H., Epstein, A. H., and Greitzer, E. M., 1991, ''Rotating Waves as a Stall Inception Indication in Axial Compressors,'' ASME J. Turbomach., **113**, pp. 290–301.

[3] Day, I. J., 1993, ''Stall Inception in Axial Flow Compressors,'' ASME J. Turbomach., **115**, pp. 1–9.

[4] Moore, F. K., and Greitzer, E. M., 1986, ''A Theory of Post-Stall Transients in Axial Compression Systems: Parts I, II,'' ASME J. Eng. Gas Turbines Power, **108**, pp. 68–76, pp. 231–239.

[5] Camp, T. R., and Day, I. J., 1998, ''A Study of Spike and Modal Stall Phenomena in a Low-Speed Axial Compressors,'' ASME J. Turbomach., **120**, pp. 393–401.

[6] Day, I. J., Breuer, T., Escuret, J., Cherrett, M., and Wilson, A., 1999, ''Stall Inception and the Prospects for Active Control in Four High Speed Compressors,'' ASME J. Turbomach., **121**, pp. 18–27.

[7] Mathioudakis, K., and Breugelmans, F. A. E., 1985, ''Development of Small Rotating Stall in a Single Stage Axial Compressor,'' ASME Paper, 85-GT-227.

[8] Silkowski, P. D., 1995, ''Measurement of Rotor Stalling in a Matched and a Mismatched Multistage Compressor,'' GTL Report, No. 221, Gas Turbine Laboratory, Massachusetts Institute of Technology, Cambridge, MA.

[9] Inoue, M., Kuroumaru, M., Tanino, T., and Furukawa, M., 2000, ''Propagation of Multiple Short Length-Scale Stall Cells in an Axial Compressor Rotor,'' ASME J. Turbomach., **122**, pp. 45–54.

[10] Inoue, M., Kuroumaru, M., Tanino, T., Yoshida, S., and Furukawa, M., 2000, ''Comparative Studies on Short and Long Length-Scale Stall Cell Propagating in an Axial Compressor Rotor,'' ASME Paper, 2000-GT-0425, pp. 1–9; to be published in ASME J. Turbomach.

[11] Gong, Y., Tan, C. S., Gordon, K. A., and Greitzer, E. M., 1999, ''A Computational Model for Short Wavelength Stall Inception and Development Multistage Compressors,'' ASME J. Turbomach., **121**, pp. 700–700.

[12] Inoue, M., Kuroumaru, M., Furukawa, M., Kinoue, Y., Tanino, T., Maeda, S., and Okuno, K., 1997, ''Controlled-Endwall-Flow Blading for Multistage Axial Compressor Rotor,'' ASME Paper No. 97-GT-248, pp. 1–11.

[13] Cheng, X. B., Chen, J. G., and Nie, C. Q., 1999, ''Comparative Study of the Method for Detecting and Analyzing Rotating Stall Inception in Compressors,'' Proc., Int. Gas Turbine Congr., Kobe, Japan, pp. 541–546.

[14] Day, I. J., and Cumpsty, A. N., 1978, ''Measurement of Interpretation of Flow within Rotating Stall Cells in Axial Compressors,'' J. Mech. Eng. Sci., **20**, No. 2, pp. 101–114.

[15] Outa, E., and Kato, D., 1998, ''N-S and Experimental Aspects of a Developed Part-Span Stall in an Axial Stage of a Rotor and Stator Cascades,'' Proc., US-Japan Seminor, Abnormal Flow Phenomena in Turbomachinery, Osaka, Japan.

[16] Hoing, D., Tan, C. S., Huu, Duc Vo, and Greitzer, E. M., 1999, ''Role of Blade Passage Flow Structures in Axial Compressor Rotating Stall Inception,'' ASME J. Turbomach., **121**, pp. 735–742.

Boundary Layer Development in the BR710 and BR715 LP Turbines—The Implementation of High-Lift and Ultra-High-Lift Concepts

R. J. Howell
e-mail: rjh@eng.cam.ac.uk

H. P. Hodson

V. Schulte

R. D. Stieger

Whittle Laboratory,
Cambridge University,
Cambridge CB3 0DY, United Kingdom

Heinz-Peter Schiffer

F. Haselbach

Rolls-Royce Deutschland,
GmbH,
Dahlewitz 15827, Germany

N. W. Harvey
Turbine Systems,
Rolls-Royce plc,
Derby DE24 8BJ, UK

This paper describes a detailed study into the unsteady boundary layer behavior in two high-lift and one ultra-high-lift Rolls-Royce Deutschland LP turbines. The objectives of the paper are to show that high-lift and ultra-high-lift concepts have been successfully incorporated into the design of these new LP turbine profiles. Measurements from surface mounted hot film sensors were made in full size, cold flow test rigs at the altitude test facility at Stuttgart University. The LP turbine blade profiles are thought to be state of the art in terms of their lift and design philosophy. The two high-lift profiles represent slightly different styles of velocity distribution. The first high-lift profile comes from a two-stage LP turbine (the BR710 cold-flow, high-lift demonstrator rig). The second high-lift profile tested is from a three-stage machine (the BR715 LPT rig). The ultra-high-lift profile measurements come from a redesign of the BR715 LP turbine: this is designated the BR715UHL LP turbine. This ultra-high-lift profile represents a 12 percent reduction in blade numbers compared to the original BR715 turbine. The results from NGV2 on all of the turbines show "classical" unsteady boundary layer behavior. The measurements from NGV3 (of both the BR715 and BR715UHL turbines) are more complicated, but can still be broken down into classical regions of wake-induced transition, natural transition and calming. The wakes from both upstream rotors and NGVs interact in a complicated manner, affecting the suction surface boundary layer of NGV3. This has important implications for the prediction of the flows on blade rows in multistage environments.
[DOI: 10.1115/1.1457455]

Introduction

Since the fan of a high bypass ratio turbo fan engine produces up to 80 percent of the total thrust of an engine it is vital that the low pressure turbine that drives it is efficient. A 1 percent increase in LP turbine efficiency gives rise to a 0.7–0.9 percent increase in engine efficiency; see Wisler [1]. In over 50 yr of extensive research the efficiency of the LP turbine has risen just 10 percentage points to today's efficiency levels of over 90 percent. The development of the gas turbine as a whole, and the LP turbine in particular, has therefore reached a stage where rises in efficiency are increasingly hard to obtain. Manufacturers are therefore looking for other ways to make their products more competitive.

Engine weight reductions provide financial benefits to both the airlines and to the engine manufacturers. The LP turbine can be up to one third of the total engine weight. A way of decreasing its weight and manufacturing costs is to reduce the number of blades. In doing this for a given stage loading, each blade must carry a greater aerodynamic load. The main loss generation mechanism in the LP turbine is that due to profile loss in the boundary layers. When increasing the lift of a profile, it is therefore vital to understand the boundary layer development. The data presented in this paper validates the design concepts used in producing these high-lift profiles.

This paper is organized so that it clearly shows the development of both the understanding of wake-boundary layer interactions and the development of high and then ultra-high-lift LP turbine blades. After an introduction to the subject, the experimental methods are then presented. Hot film results are then presented from LP turbines that represent conventional, high lift and finally ultra-high-lift designs. Each turbine design represents a step in the evolution of our understanding of the aerodynamics of these turbines and the results show the increasing complexity of the flows.

The Mach number distribution for conventional lift blading in Fig. 1 has a large and continual acceleration over the leading part of the suction surface and up to the peak Mach number. Although not shown in these inviscid predictions, soon after the peak Mach number, the flow separates under the adverse pressure gradients. Up to the peak Mach number, the acceleration is high enough and the momentum thickness Reynolds number low enough to keep the boundary layers laminar, despite the effects of periodic wake turbulence. A boundary layer is unstable when it is being decelerated. Therefore, the turbulence from the periodic passing of wakes is likely to cause transition from laminar to turbulent flow. However, as is often the case (see Howell et al. [2]) this transition does not occur until very near the position where the laminar flow starts to detach from the blade surface. The exact reason for this is not fully understood, but it could simply be that a separated shear layer (or a boundary layer near separation) is highly unstable. It therefore transitions easily when the wake turbulence is above it.

Curtis et al. [3] showed, through a loss-lift parametric study involving a large number of profiles, that it was possible, with steady flow, to increase the lift of a datum profile by approximately 20 percent without an increase in profile loss. Those studies were carried out at a higher Reynolds number than those presented in this paper. The increased lift profile (a so-called high-lift profile) resulted in a Zweifel coefficient of 1.05. Some of these

Contributed by the International Gas Turbine Institute and presented at the International Gas Turbine and Aeroengine Congress and Exhibition, New Orleans, Louisiana, June 4–7, 2001. Manuscript received by the IGTI, December 18, 2000. Paper No. 2001-GT-441. Review Chair: R. A. Natole.

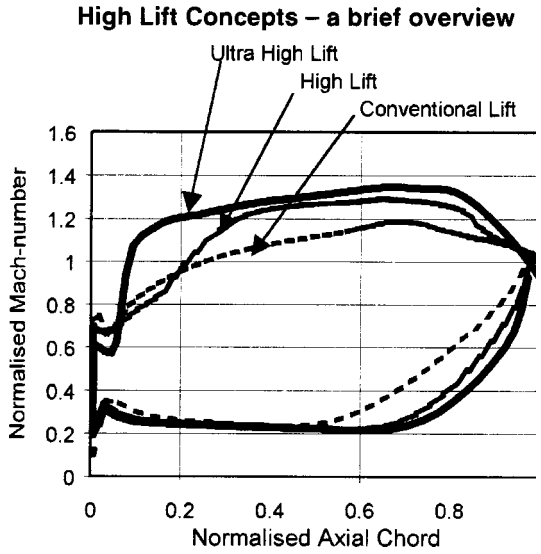

Fig. 1 Comparison of predicted conventional lift. High-lift, and ultra-high-lift Mach number distributions (normalized); after Haselbach et al. [13]

profiles produced separation bubbles on the rear of the suction surface. The results suggested an optimum profile would be something similar to that shown in Fig. 1.

Wakes shed from upstream blade rows travel over downstream blades disturb their boundary layers; see Hodson [4] and Ladwig and Fottner [5]. As a boundary layer becomes more receptive to disturbances, the high turbulence in the wakes eventually causes the formation of turbulent spots through the mechanism of bypass transition. Schauber and Klebanoff [6] showed that these spots travel down stream in a characteristic manner. An ST diagram is a contour plot of, for example shear stress, with time on the *y*-axis and surface distance on the *x*-axis; see Fig. 2. The different celerities of the leading and trailing edges of the turbulent spots mean that the regions of high shear seen in ST diagrams diverge in time. This is because the leading and trailing edge velocities of turbulent spots are reported to travel at approximately 90 and 50 percent of the local free stream velocity for zero pressure gradient flow. Behind the spot is a calmed region of flow that has a full velocity profile, which is shown in Fig. 2 as region C. This profile

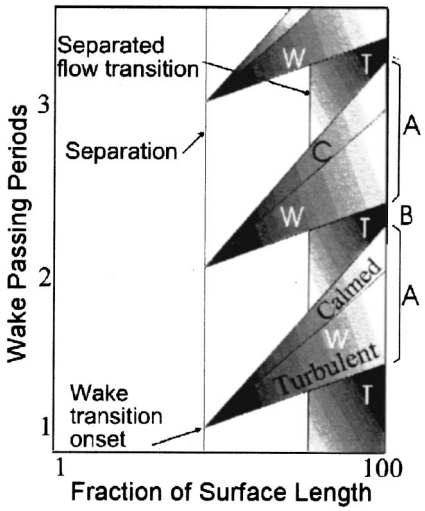

Fig. 2 A schematic diagram of wake-induced transition and separated flow transition

(which is almost linear out to the freestream, Cumpsty et al. [7]) is very stable to disturbances and will not so easily separate in an adverse pressure gradient, as a laminar profile would. The value of the trailing edge velocity is highly dependent on the local pressure gradient, but the leading edge velocity is almost unaffected by it. The ends of calmed regions that trail turbulent spots are variously reported to travel at approximately 30 percent of the local free stream velocity; see Gostelow et al. [8]. The effect of variable pressure gradient on the velocity of the calmed region has not been documented.

Schulte [9] showed the details of how the losses were controlled at a Reynolds number of 130,000. He showed that it was the interaction of the calmed regions of turbulent spots (formed by wake passing) that suppressed the separation bubble. This separation bubble suppression is the reason for the control of the losses on the high lift turbine profiles. Howell [10] and Howell et al. [2] showed that this understanding could be taken further. Still higher lift blades were investigated in cascade tests: the so-called ultra-high-lift profiles.

The control of the separation bubbles and their losses is dependent on wake-induced transition occurring around the separation location. Wake-induced transition usually starts at the position where flow separation would occur with steady inflow. This is true in all the cases presented in this paper. The Reynolds number tested here ranged from 60,000 to 120,000. The low-speed measurements taken at the Whittle Laboratory on a variety of profiles and at a variety of Reynolds numbers above 130,000 also indicate the same onset location of wake-induced transition. In many of the low-speed tests carried out, the Reynolds number based on momentum thickness was approximately 250 just before separation. This obviously changes slightly depending on the pressure distribution. However, for the ultra-high-lift profiles (the BR715UHL) part of the design specification was actually to achieve a momentum thickness Reynolds number of at least 250, by the position of separation. This helped to guarantee that wake induced transition occurs at the separation location. This in turn keeps the performance of ultra-high-lift profile at similar levels to previous generations of high-lift or low-lift designs.

From these Whittle Laboratory tests, Rolls-Royce Deutschland designed the profiles employed on the BR715UHL LP turbine. To control losses the profiles were aft loaded. Wakes and their effects were used to control the losses generated by the separation bubbles present in these designs. Howell [10] also showed that it is also the wake turbulence and not just the effect of the calmed region that helps to suppress the losses generated by the bubbles on ultra-high-lift profiles.

Cobley et al. [11] describe the many parts of the design process leading to the development of the LP turbines in the BR700 series of engines. They also describe some of the design methodologies used to develop the high-lift profiles. Harvey et al. [12] showed that the efficiency of these LP turbines is approximately the same as previous generations. In particular, the BR715 actually achieved an efficiency above previous generation LP turbines as well as 20 percent reduction in blade numbers. Figure 3 (taken from Haselbach et al. [13]) shows the increased lift obtained for the three profiles shown here as compared to current Rolls-Royce designs. These levels of performance were obtained without a loss penalty.

The BR715UHL LP turbine is the most highly loaded turbine ever tested by Rolls Royce Deutschland—formally BMW Rolls Royce. No unsteady design tools were available at the time for this design. Rolls Royce carried out the design in collaboration with the Whittle Laboratory.

The main objective of this research was to validate the understanding of suction side boundary layers under the influence of wakes. The data presented in this paper clearly illustrate that the presence of wakes shed from upstream blade rows dominates the boundary layer development. Under no circumstances can the boundary layer development be considered a steady process. This

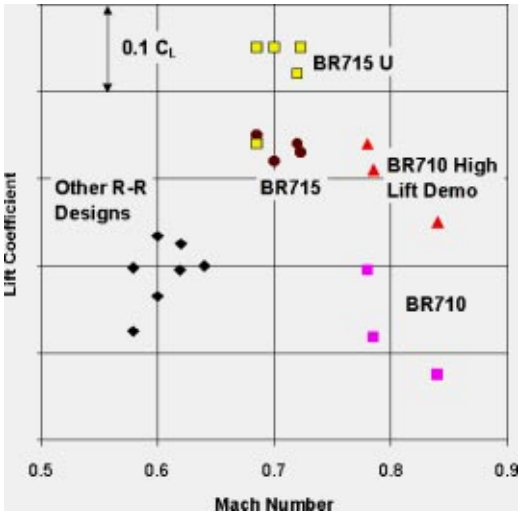

Fig. 3 Lift coefficient versus Mach number for a variety of blade profiles, including the high-lift profiles of the BR715 and BR710 demonstrator. The BR715UHL turbine achieves even high lift coefficients. After Haselbach et al. [13].

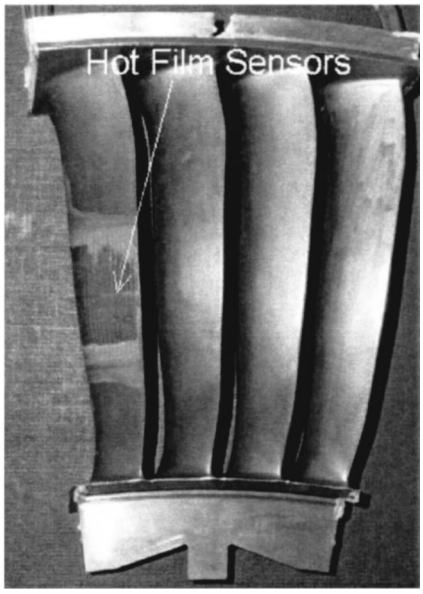

Fig. 4 NGV2 of the BR715UHL LP turbine showing the hot film array of sensors on the right hand aerofoil

paper shows that the understanding of wake boundary layer interactions has been successfully employed in the new designs of the BR700 series LP turbines.

Experimental Details

The measurement of wall shear stress using hot films was developed by Bellhouse and Schultz [14], and is now a well-established technique. It is possible to calibrate hot films, but this is a difficult and time-consuming process; see Hodson [15] and Davies and O'Donnell [16]. Also, errors of 20 percent or more arise when hot films calibrated in a laminar flow are used to measure a turbulent flow. The hot film sensors were used on the aft part of suction surfaces and were therefore likely to see laminar, turbulent, calmed, and separated flow at different positions of the upstream rotor, see Halstead et al. [17] or Banieghbal et al. [18]. Calibration for all these conditions would be extremely difficult and quite probably impossible. It is for these reasons that the hot film sensors are used in an uncalibrated form, which yields a pseudo shear stress. When used in an uncalibrated manner, the absolute level of the shear stress is unknown, but it is the relative magnitude of the shear stress level from sensor to sensor that is obtained. With careful analysis, this relative or ''quasi''-shear stress is all that is required to obtain information regarding the state of the boundary layers.

The highest frequencies associated with turbulent fluctuations are thought to be of the order of 300 kHz, whereas the frequency response of the hot film sensors is around 30–40 kHz. Therefore, the majority of the turbulent fluctuations in the boundary layer cannot be measured. However, laminar, turbulent and separated boundary layers have very different shear stress levels. The changes in the levels occur at frequencies of the order of the wake passing of upstream rotors. This means that the hot film sensors can detect the passage of turbulent spots and their calmed regions as well as separated flows. The ability to measure these differing flow conditions and their relative robustness makes the hot film sensors a powerful measurement tool in a rig environment. No other instrumentation capable of unsteady measurement was available upstream of the NGVs. Therefore, all the interpretation in this paper is made solely from CFD predictions (not shown) and the hot film measurements.

Past investigations into the development of blade surface boundary layers indicated that most of the interesting physics occurs from peak suction to the trailing edge of the profile. It is between these positions that the hot film sensors were located. The hot films were located at 40 percent span for NGV2 the BR710, BR715 and BR715UHL turbines. The films are located at 50 percent span for NGV3s on the BR715 and BR715UHL LP turbines. The occasional sensor failure is common on highly three-dimensional profiles due to difficulties with securing the hot film arrays to the curved surface of the blades. Figure 4 shows the NGV2 of the BR715UHL LP turbine with the hot film in position. Data from faulty sensors has not been shown, but the analysis of the flows was not hampered to any significant extent by such failures.

The data was ensemble averaged over 200 revolutions of the upstream rotor and logged at the rate of 125 kHz for the BR710 and BR715 turbine tests. For the BR715UHL tests, 256 ensembles were taken at a rate of 80 kHz for each sensor.

A variety of data processing techniques were employed to reduce the data. As well as the raw quasi shear stress τ_w, time mean values were also calculated. The ensemble RMS of a signal is a measure of the deviation from the ensemble mean of that signal. The ensemble skew of a signal distinguishes the positive or negative deviation of the signal at a particular time (measured relative to the reference time) from the mean of the signal at the same time. With hot film measurements, the skew of a signal is useful for detecting how far the boundary layer has progressed through transition (Hodson et al. [19]). If a boundary layer is completely laminar then the skew of the signal will be near zero. If it is predominantly laminar with the occasional turbulent component then the skew of a signal will be small, but positive. Where the RMS is maximum (at an intermittency of approximately 50 percent) then the skew would be approximately zero. As the signal becomes turbulent with a smaller laminar component, the skew becomes negative. As the boundary layer becomes completely turbulent, the skew of a signal approaches zero. It is a characteristic of hot film gage signals from transitional flows, that the positive skew, early in transition, is more obvious than the later negative skew.

Results

BR710 High-Lift Demonstrator Rig: Stage 2 Nozzle Guide Vane—CRUISE. The time history of the raw quasi-wall shear stress measurements taken at the cruise condition are shown in Fig. 5. The uppermost plot shows the measurements at 71 percent surface length. The lowest plot shows data from nearest the trail-

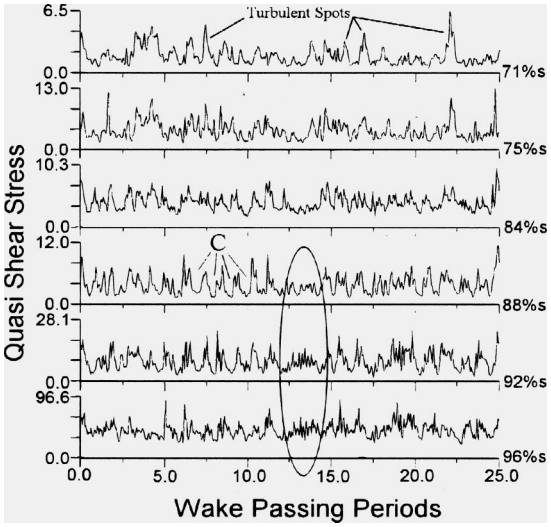

Fig. 5 Time history traces of quasi wall shear stress for the cruise condition of the BR710 LP turbine

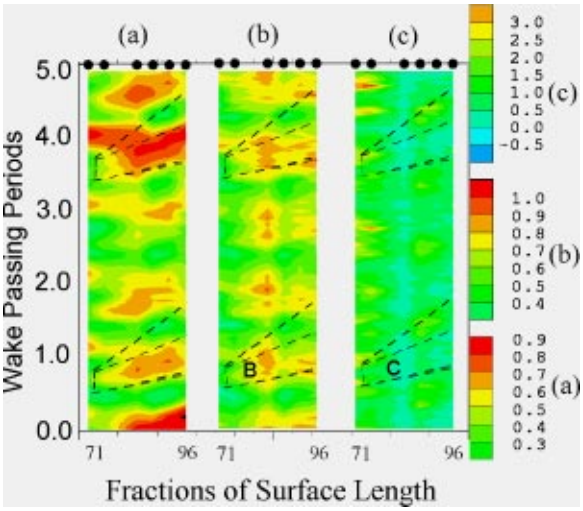

Fig. 6 ST diagrams of (*a*) nondimensional ensemble mean quasiwall shear stress, (*b*) nondimensional ensemble RMS, and (*c*) ensemble skew

ing edge of the blade at 96 percent. The large upward spikes in shear stress are due to turbulent spots traveling over the sensors. The signals at 71 percent *s*, show turbulent spots, but little evidence of calmed flow. The quasi-wall shear stress between these wakes (while not zero) probably indicates that this is near the position of separation. There are large fluctuations in the boundary layer at the final sensor indicating that transition is not complete at this Reynolds number. Calmed regions of flow can be seen at some locations, particularly those regions marked C, however, these calmed flow regions do not survive until the trailing edge of the profile.

The measurements within the ellipse show an interesting feature. There seems to be an absence of turbulent spots at the first sensor around the thirteenth wake. This allows separated flow transition to occur as wake-induced spots are not present to disturb this process. The wake turbulence will obviously be present, so this separated flow transition cannot be considered to occur as it would in a steady environment. A frequency doubling of the fluctuations can be seen as the flow travels from the sensor at 88 to 92 percent *s* which is often seen in separated flow transition; for example, see Gostelow and Hong [20].

Figure 6 shows the ST diagrams. The black circles at the top of such plots indicate the position of the functional sensors. Plot (a) shows the nondimensional ensemble mean quasi wall shear stress, (b) shows the ensemble RMS, and (c) shows the ensemble skew. The relevant scales for each plot are located on the right hand side of the figure. The shear stress is made nondimensional by the maximum value of shear stress measured by each sensor, i.e., $\tilde{\tau}(s,t)/\tilde{\tau}_{\max}(s)$, where t is time. This serves to enhance the periodic fluctuations in shear stress, but at the expense of their overall level. The RMS of the data is made nondimensional by the maximum value of RMS measured at each sensor, i.e., $\tilde{\tau}'(s,t)/\tilde{\tau}'_{\max}(s)$.

Figure 6(*a*) shows a wedge shape region of high shear starting at approximately 71 percent *s* (within the dashed lines). The trailing edge of this wedge travels at approximately 50 percent of the local freestream velocity, while the leading edge travels faster at around 90 percent. The dashed lines on the figure correspond to these velocities and were calculated from a predicted velocity distribution. The final line (with the steepest gradient) corresponds to the probable celerity of the calmed region. The calmed region is variously reported to travel at 30 percent U. The velocity distribution (not shown) also showed that boundary layer separation occurs at approximately 70 percent *s*, which is where wake-induced transition starts to occur.

At the same phases and surface positions as regions of high quasi-wall shear, one can see regions of high RMS, see (*b*) and some regions of slightly negative skew in Fig. 6(*c*). This is consistent with the interpretation that these regions are caused by transitional flow and are caused by the movement of turbulent spots over the sensors.

BR715 Engine Stage 2 Nozzle Guide Vane—TAKEOFF. The raw signals from the hot film sensors of the NGV2 of the BR715 LP turbine are presented in Fig. 7. The signal from the sensor at 78 percent *s* is characteristic of a disturbed laminar (and mostly separated) boundary layer. Occasionally, a passing rotor wake causes transition to occur via the formation of a turbulent spot, but only in about one in five wake passings, at this Reynolds number and surface position. The sensors further downstream indicate that more turbulent spots have formed as the boundary layer becomes more receptive to the wake disturbances.

Figure 8 presents data from this NGV as ST diagrams similar to those in Fig. 6. Wake-induced transition occurs, on average, at 82 percent *s* as indicated by a wedge-shaped region of high quasi-wall shear (contours gray to black). The trajectories drawn onto the figure are those that correspond to the leading and trailing edges of turbulent spots. The final trajectory is the approximate velocity of the end of the calmed region. These trajectories have been calculated from predicted blade surface pressure distributions assuming constant values for the convection rates.

It is noted that near the leading edge the contours of ensemble mean, RMS and skew seem to travel faster than the local free

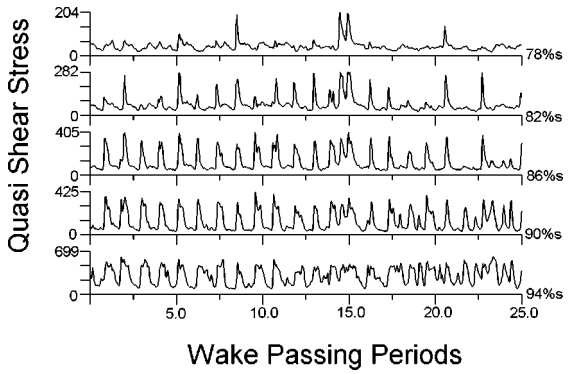

Fig. 7 Raw hot film data from NGV2 of the BR715 LP turbine

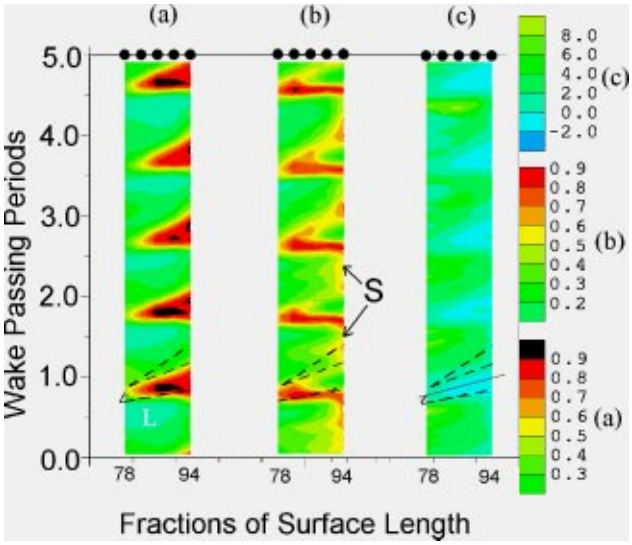

Fig. 8 ST diagrams of (*a*) nondimensional ensemble mean quasi-wall shear stress, (*b*) nondimensional ensemble RMS, and (*c*) ensemble skew. Data is taken from NGV2 of the BR715 LP turbine.

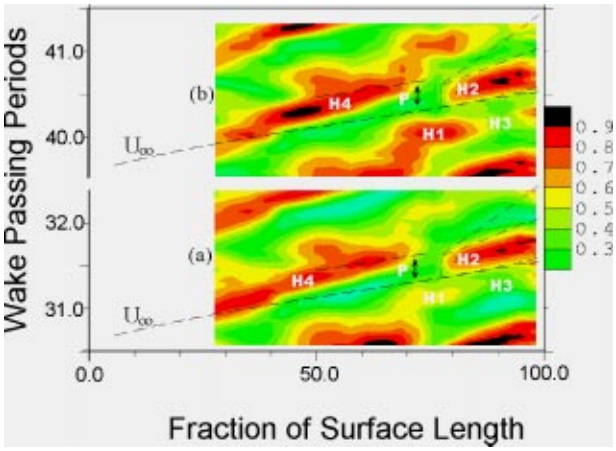

Fig. 10 ST diagrams of nondimensional ensemble mean quasi-wall shear stress from NGV3 of the BR715 LP turbine; CRUISE conditions

stream velocity. It is believed that the wake causes transition by causing the formation of turbulent spots under its path. The wake convects at the local freestream velocity, but the spot's leading edge travels at approximately 0.9 U. Therefore, the wake overtakes the spots it has formed, allowing it to form further spots ahead of the original ones. The wake then finds itself further downstream and over a region of flow that is more receptive to disturbances. Spots may also form under regions of the wake where the turbulence level is lower, that is, ahead of the wake centerline. In this way, the leading edge of the wake-affected zone may seem to travel faster than the free stream. Regions of high ensemble RMS (Fig. 8(*b*)) and negative skew occur at the same positions in time and space as those of high shear. This is consistent with the interpretation of wake-induced transition occurring at 78 percent *s*. Regions of high ensemble RMS seem to occur just before the arrival of each wake. This could be separated flow transition starting to occur as it starts after the calmed region of the previous spots have passed, see regions marked "S."

Both NGVs of the BR710 and BR715 engines show classical wake induced transitional behavior of the boundary layers. NGV2 of the BR715UHL also shows this behavior, but the data has not been presented for brevity.

BR715 Engine Stage 3 Nozzle Guide Vane—CRUISE. Figure 9 shows the variation in time mean quasi-wall shear stress

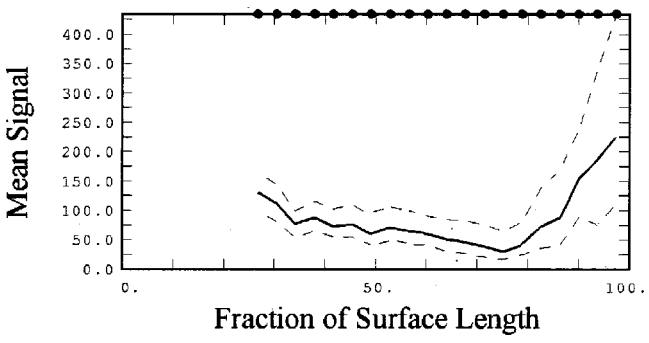

Fig. 9 Variation of time mean (solid lines) and the envelope of the ensemble mean quasi-wall shear stress for NGV3 of the BR715 LP turbine

variation over the surface of NGV3 of the BR715 LP turbine at the cruise condition. The shear stress starts relatively high and drops as the boundary layer thickens despite the flow acceleration. After the minimum at 75 percent *s*, the shear stress increases due to the boundary layer undergoing transition. This increases the amount of turbulent flow at each sensor location and therefore the mean level of quasi wall shear stress. Computational predictions showed that time mean position of boundary layer separation occurs at approximately 65 percent *s*.

Figure 10(*a*) shows regions of high ensemble mean quasi-wall shear (marked "H2") originating at 75 percent *s*. These are caused by (and occur at the wake passing frequency of) the wakes shed from Rotor 2. The regions marked "H4" are not in fact regions caused by the high shear in turbulent spots. They are simply the response of the laminar boundary layers to the passage of wakes in the freestream. Because of the method of making the data nondimensional, the levels of the regions H4 and H2 are the same color, however, they are very different levels. The mean quasi wall shear stress in Fig. 8 shows that the mean shear stress is decreasing in this region. The RMS (not shown) of this data is almost constant up to peak suction in these locations and the skew (also not shown) is also near zero. The conclusion is that wake transition occurs in the region of laminar separation and not before.

Figure 10(*b*) shows data for the same condition but at a different position of the upstream rotor. Again the regions marked H2 are seen, but there are also other regions marked H1, which are stronger than those in Fig. 10(*a*), and are of only a slightly lower quasi-wall shear that those marked H2. They show that transitional activity occurs at these surface positions, for certain positions of the upstream rotor. Therefore, there are two regions of transitional activity and which occur at Rotor 2 blade passing frequency. A possible explanation for this is the following. The first transition region seen in the ST diagrams (H2) is caused by Rotor 2 and occurs at 75 percent *s*. The other transition region is caused by wakes from NGV2 that pass through Rotor 2 (region H1). Rotor 1 in turn modulates NGV2 wakes. The difference in blade counts for Rotors 1 and 2 leads to the low-frequency beating (modulation), whereby at some Rotor 2 positions the strength of the second transition region is diminished. The amplitude-modulated wakes are distorted as they travel through NGV3, which makes interpreting the data more difficult.

This beating in this data is similar to that measured by Arndt [21]. In that investigation Arndt showed that Rotors 1 and 2 interactions gave rise to amplitude modulations of the strength of the wakes that entered NGV3. Regions marked H1 reduce in strength

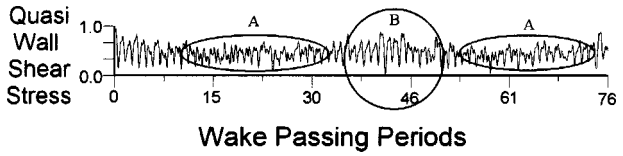

Fig. 11 Ensemble mean data for one revolution of Rotor 2 of the BR715 LP turbine

as they reach the start of regions H3 because they are older turbulent boundary layer. New turbulent boundary layer is formed at H2, which has a higher quasi-wall shear stress.

Figure 11 shows the variation of quasi-wall shear stress for a hot film sensor located at 71.5 percent *s* on NGV3 for a complete revolution of Rotor 2. It can be seen that there is a variation in the amplitude of shear stress from the interference in region A, to the reinforcement that occurs in regions B. The variation of shear stress is a consequence of the changes in turbulent spot production rates that occur because of the beating effect. Wakes with high turbulence intensity are likely to cause the higher shear stress regions circled in region B. Arndt [21] carried out measurements with a hot film probe traversed upstream of the inlet of NGV3 from an MTU LP turbine and observed a similar beating of the inlet turbulence field.

BR715U Engine Stage 3 Nozzle Guide Vane—CRUISE. The final hot film measurements are taken from the BR715U LP turbine. These show similar results as from the 3rd-stage NGV in the BR715 turbine but it should be remembered that blades on this LP turbine generate 12 percent more lift than the BR715 turbine.

The measured and predicted pressure distributions for this profile are shown in Fig. 12. The measured static pressures show at pressure plateau and therefore boundary layer separation starting at approximately 82 percent axial chord. This is a little later than the hot film measurements will have us believe. However, given the few static pressure tappings available in this rig, it is not unreasonable that there is a difference.

The time history of the raw data for various sensors along the surface can be seen in Fig. 13. There is no obvious evidence of individual turbulent spots or indeed calmed regions. Other data (Ramesh [22]) taken in low-speed tests have also shown that the boundary layers on ultra-high-lift profiles do not seem to exhibit as much calmed flow near the trailing edge as lower-lift profiles. This does not necessarily mean that calmed regions do not exist in these flows: it just means that they are not obvious from raw data. Further examination of these figures shows that there is little periodicity in the raw data, however wake-passing events can be seen in some of the data presented in the skew data in Fig. 14. The lack of periodicity in the flows on this turbine is believed to be

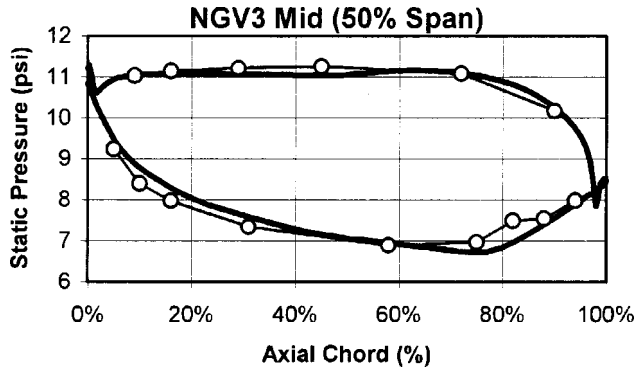

Fig. 12 Predicted (solid line) and measured (circles) static pressures on NGV3 of the BR715U LP turbine; CRUISE conditions. After Haselbach et al. [13]

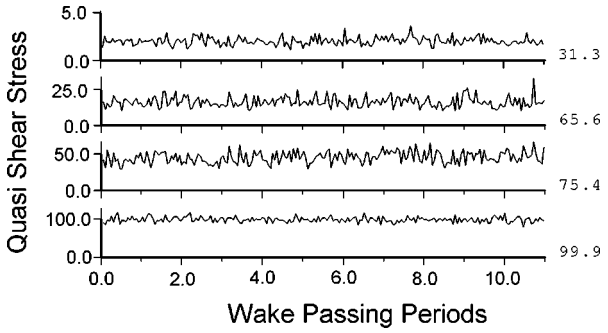

Fig. 13 Time history of the raw data

caused by the strong separated flow transition present. Cascade measurements on ultra-high-lift LP turbines have shown that the separation bubbles and their transition can dominate the flows on these blades, Howell et al. [2] and Ramesh [22]. It is believed that in this case, the wakes simply modulate the separated flow transition process and so the wake-induced transition is not easily seen from hot film measurements alone.

The ST diagrams of this data show wake-induced transition occurring more clearly than the raw data of previous plots. For example, see the ensemble mean quasi-wall shear stress data in Fig. 15 and in particular regions marked H1 and H2—these mark the onset of wake induced transition. This occurs at approximately the separation location of the boundary layer.

The blade numbers for this turbine are different from the previous one and no beating could be seen in the data. Again, this is

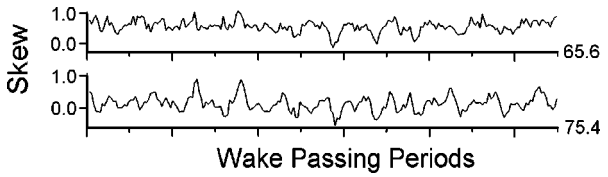

Fig. 14 Ensemble mean skew for to sensors showing the change in periodicity of the data as the flow travels downstream

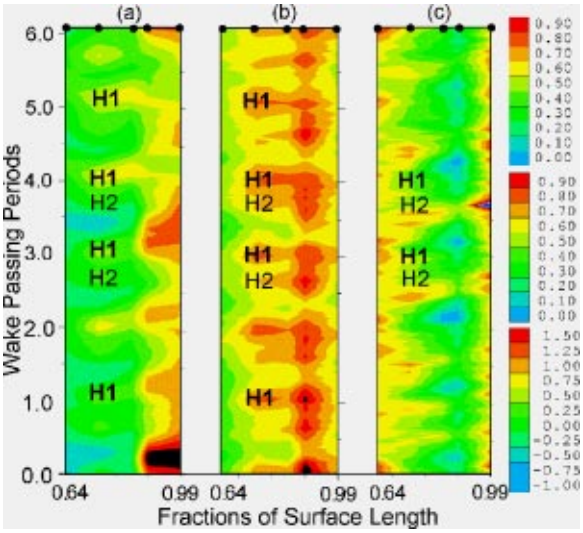

Fig. 15 ST diagrams of (*a*) nondimensional ensemble mean quasi-wall shear stress, (*b*) nondimensional ensemble RMS, and (*c*) ensemble skew. Data is taken from NGV3 of the BR715U LP turbine.

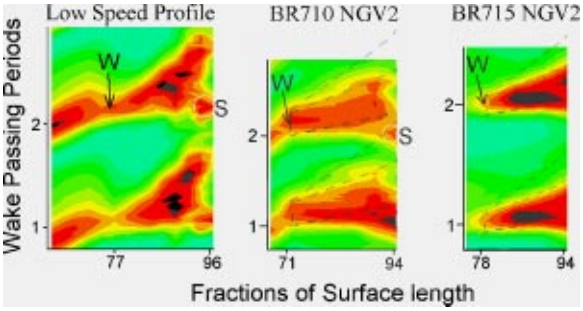

Fig. 16 A comparison of low-speed and high-speed measurements of ensemble quasi-wall shear stress from various profiles

not to say that beating does not occur, but it could be that it is disguised by the separated flow transition, which seems to be the dominant transition mechanism.

The doubling of the wake passing reduced frequency (seen in Figs. 10 and 15), which the 3rd-stage NGVs are subjected can be considered beneficial, particularly for the ultra-high-lift profiles. Higher Reynolds numbers occur in the first stages of the LP turbine, while lower Reynolds numbers occur in later stages. This is fortuitous as high reduced-frequencies (caused by multistage interactions) occur in later stages in the LP turbine where the larger separations (due to lower Reynolds numbers) are likely to be better controlled, see Howell et al. [2]. In the first few stages, there are fewer blade row interactions; but as Howell et al. [2] showed, one does not desire reduced frequency doubling as this increases losses.

Comparison With Low-Speed Data. Having described some of the salient details of the data from the high-speed rigs, it is now appropriate to compare these measurements to some take from a low-speed facility designed to simulate the presence of an upstream rotor.

Figure 16 shows ST diagrams of non-dimensional ensemble mean quasi wall shear stress data from both second stage NGVs from the LP turbines already discussed and also from a low-speed high-lift blade. The low-speed profile is described by Curtis et al. [3] and is denoted profile H. Measurements from the low speed profile capture all the important features that are seen in the high-speed measurements. The onset location of wake-induced transition is shown as a region of high shear stress denoted W. This region forms a wedge shape that is bounded by the trajectories of the leading and trailing edge of turbulent spots.

Separated flow transition can be seen occurring (between the wakes) on the low-speed profile and BR710 profile. The last sensor on the BR710 profile was located at 94 percent *s*, whereas the last sensors on the other profiles were at around 96 percent *s*. If separated flow transition occurs late on the blade, then the sensors on BR715 profile may not be far enough back along the surface to measure this. The data from NGV2 of the BR715UHL turbine show very similar features to NGV2 of the BR715 turbine, and so have therefore not been shown.

The low shear regions caused by the spot's calmed regions can be seen in the raw data of all measurements. The wake passing frequency of the high-speed rigs was of the order of 3 kHz, but for the low-speed measurements the frequency is just 60 Hz. The frequency response of the hot films was the same for both regimes. The low-speed measurements therefore allow a much larger number of samples to be taken per wake passage. This gives better quality data, allows much better analysis and illustrates the advantage of taking measurements in low speed rigs. This type of moving bar wake generator cannot simulate an upstream stator row because the moving bars do not turn the flow. However, their use in gaining the highest quality data with relative ease and allowing parametric studies is obvious.

Conclusions

Boundary layer separation occurs on NGV2 of the 710 LP turbine rig soon after peak Mach number, and reattach before the trailing edge. At cruise Reynolds numbers, wake-induced transition starts at around the separation position, but separated flow transition is not complete by the trailing edge. Calmed regions can be seen in much of the data of this conventional lift LP turbine.

Results from NGV2 of the BR715 LP turbine rig show periodic wake-induced transition starting at around 71 percent *s*. Flow separation occurs near the same position, but only between wake-induced transition regions. Calmed regions can be seen in much of the data, even at the trailing edge. It is possible that there is an open separation at the trailing edge at some rotor positions and at the Reynolds number shown, but on average (in time) the trailing edge flow is attached.

The results from NGV3 of the BR715 LP turbine are far more complicated than those for NGV2 of the same turbine. This blade row is subjected to a more disturbed flow, as there is another stage ahead of it. Wake-induced transition (caused by Rotor 2) occurs at around 75 percent *s*. A wake transition region occurs between those caused by rotor 2, and is probably caused by NGV2 and a combination of NGV1, and Rotor 1 causing a beating frequency with Rotor 2. RMS and skew data are consistent with this interpretation.

The results from NGV3 of the BR715 LP turbine are similar to those of the same NGV on the BR715 LP turbine, except that the separated flow transition seems to dominate the flow. This is probably due to the increased deceleration used on these profiles used to generate the increased lift. There is an absence of the beating in the BR715U turbine data. The beating is almost certainly present, but could be that the separated flow transition tends to disguise this.

The most important features of the measurements from the second stage NGVs of all the high-speed turbine rigs are present in the low-speed rigs. It is with results from low-speed rigs tests that the physical understanding of wake boundary layer interactions has been obtained. This in turn has provided the firm base on which to develop the high and ultra-lift profiles presented.

None of the flows on these NGVs can be considered steady. Therefore, design methods that neglect the unsteady effects of wakes are completely incapable of predicting the flows. As design envelopes are pushed further (in terms of lift) it will be a requirement that design methods can predict these unsteady features.

This paper has shown that through a program of mainly low-speed experimental research, a good understanding of the interactions of wakes turbulence and boundary layers has been developed. From this knowledge, incremental steps have been taken that has allowed the development of ultra-high-lift profiles. The effects of multistage interactions have also been understood, and it is believed that this understanding can help in the design of future multistage machines, particularly at low Reynolds numbers.

Acknowledgments

Rolls Royce Deutschland GmbH and Rolls Royce plc are acknowledged for funding this research and granting permission to publish this information.

Nomenclature

τ_w = quasi-wall shear stress
τ'_w = RMS of signal
$\tilde{\tau}_w$ = nondimensional ensemble mean quasi-wall shear stress
$\tilde{\tau}'_w$ = nondimensional ensemble mean RMS
s = surface length

t = time
δ^* = boundary layer displacement thickness
θ = boundary layer momentum thickness
∞ = local free stream

References

[1] Wisler, D. C., 1997, ''The Technical and Economic Relevance of Understanding Boundary Layer Transition in Gas Turbine Engines,'' NASA Minnowbrook II proceedings.
[2] Howell, R. J., Ramesh, O. N., Hodson, H. P., Harvey, N. W., and Schulte, V., 2000, ''High Lift and Aft Loaded Profiles for Low Pressure Turbines,'' ASME Paper No. 2000-GT-261, accepted for publication in ASME J. Turbomach.
[3] Curtis, E. M., Hodson, H. P., Banieghbal, M. R., Denton, J. D., Howell, R. J., and Harvey, N. W., 1996, ''Development of Blade Profiles for Low Pressure Turbine Applications,'' ASME J. Turbomach.
[4] Hodson, H. P., 1993, ''Modelling Unsteady Transition and Its Effects on Profile Loss,'' ASME Paper No. 1989.
[5] Ladwig, M., and Fottner, L., 1993, ''Experimental Investigations of the Influence of Incoming Wakes on the Losses of a Linear Turbine Cascade,'' ASME Paper No. 93-GT-394.
[6] Schubauer, G. B., and Klebanoff, P. S., 1955, ''Contributions on the Mechanics of Boundary Layer Transition,'' NACA TN 3489 (1955) and NACA Rep. 1289.
[7] Cumpsty, N. A., Dong, Y., and Li, Y. S., 1995, ''Compressor Blade Boundary Layers in the Presence of Wakes,'' International Gas Turbine Congress.
[8] Gostelow, J. P., Walker, G. J., Solomon, W. J., Hong, G., and Melwani, N., 1996, ''Investigation of the Calmed Region Behind a Turbulent Spot,'' ASME Paper No. 96-GT-489.
[9] Schulte V., 1995, ''Unsteady Wake Boundary Layer Interaction,'' Ph.D. thesis, Cambridge University, Cambridge, UK.
[10] Howell R. J., 1999, ''Wake Separation Bubble Interactions in Low Reynolds Number Turbomachinery,'' Ph.D. thesis, Cambridge University, Cambridge, UK.
[11] Cobley, K., Coleman, N., Siden, G., and Arndt, N., 1997, 'Design of the new three stage Low Pressure Turbine for the BMW Rolls-Royce BR715 Turbofan Engine,' ASME Paper No. 97-GT-419.
[12] Harvey, N. W., Cox, J., Howell, R. J., Hodson, H. P., and Schulte, V., 1998, ''The Role of Research in the Aerodynamic Design of an Advanced Low-Pressure Turbine,'' 3rd European Conference on Turbomachinery Fluid Mechanics and Thermodynamics, Vol. A, IMechE Conf. Trans.
[13] Haselbach, F., Schiffer, H.-P., Horsman, M., Dressen, S., Harvey, N., and Read, S., 2001, ''The Application of Ultra-High Lift Blading in the BR715 LP Turbine,'' submitted to the IGTI:
[14] Bellhouse, B. J., and Schultz, D. L., 1966, ''Determination of Mean and Dynamic Skin Friction, Separation and Transition in Low-Speed Flow With a Thin-Film Heated Element,'' J. Fluid Mech. **24**, 2.
[15] Hodson, H. P., 1983, ''Boundary layer and Loss Measurements on the Rotor of an Axial flow Turbine,'' ASME Paper No. 83-GT-4.
[16] Davies, M., and O'Donnell, F., 1998, ''Local Measurement of Loss Using Heated Thin Film Sensors,'' International Gas Turbine Congress.
[17] Halstead, D. E., Wisler D. C., Okiishi, T. H., Hodson, H. P. and Shin, H., 1995, ''Boundary Layer Development in Axial Compressors and Turbines, Part 1: Composite Picture, part 2: Compressors, Part 3: Turbines, Part 4: Computations and Analysis,'' presented at the IGTI Comference, Houston, TX.
[18] Banieghbal, M. R., Curtis, E. M., Denton, J. D., Hodson, H. P., Huntsman, I., and Schulte, V., 1995, ''Wake Passing in LP Turbines,'' Paper No. 23, AGARD conference. Loss Mechanisms and Unsteady Flows in Turbomachines, Derby, May.
[19] Hodson, H. P., Huntsman, I., and Steele A. B., 1993, ''An investigation of boundary layer development in a multistage LP turbine,'' ASME Paper No. 93-GT-310.
[20] Gostelow, J. P., and Hong G., 1995, ''Representation of Boundary-Layer Transition and Turbulent Spots in Temporal and Frequency Domains,'' *Flow Visualisations VII*, Begell House, New York, NY, pp. 218–223.
[21] Arndt, N., 1991, ''Blade Row Interaction in a Multistage Low Pressure Turbine,'' ASME Paper 91-GT-283.
[22] Ramesh, O. N., 2000, private communication.

Pressure Surface Separations in Low-Pressure Turbines—Part 1: Midspan Behavior

Michael J. Brear[1]
e-mail: mjbrear@unimelb.edu.au

Howard P. Hodson
e-mail: hph@eng.cam.ac.uk

Whittle Laboratory,
Cambridge University,
Cambridge, UK

Neil W. Harvey
Rolls-Royce, plc,
Derby, UK
e-mail: neil.harvey@rolls-royce.com

This paper describes an investigation into the behavior of the pressure surface separation at midspan in a linear cascade. It is found that the pressure surface separation can be a significant contributor to the profile loss of a thin, solid, low-pressure turbine blade that is typical of current engine designs. Numerical predictions are first used to study the inviscid behavior of the blade. These show a strong incidence dependence around the leading edge of the profile. Experiments then show clearly that all characteristics of the pressure surface separation are controlled primarily by the incidence. It is also shown that the effects of wake passing, freestream turbulence and Reynolds number are of secondary importance. A simple two-part model of the pressure surface flow is then proposed. This model suggests that the pressure surface separation is highly dissipative through the action of its strong turbulent shear. As the incidence is reduced, the increasing blockage of the pressure surface separation then raises the velocity in the separated shear layer to levels at which the separation can create significant loss.
[DOI: 10.1115/1.1450764]

Introduction

The intense competition within the airline industry creates sustained pressure to achieve reductions in both the cost of manufacture and the weight of modern aircraft engines. The low-pressure turbine accounts for roughly one third of the gross weight of the Rolls-Royce ''RB211'' and ''Trent'' series of aircraft engines [1]. As a result, there is significant demand for low pressure turbine blades that are both light and inexpensive. For the designer, reduced engine weight implies a choice between thin, solid, and thick, hollow low-pressure turbine blades. However, thin, solid blades are substantially cheaper to manufacture than equivalent thick, hollow blades and are, therefore, used in most modern designs.

Of course, the aerodynamic performance of a low-pressure turbine blade must also be acceptable. In particular, thin, solid blades often have a separation bubble near the leading edge on the pressure surface *at design conditions*. This separation is referred to as the ''pressure surface separation.'' Given that thick, hollow blades can be designed to avoid this phenomenon, the relative aerodynamic performance of thin, solid blades is dependent on the loss that the pressure surface separation produces.

The behavior of the pressure surface separation inside the rotating rig is complex and appears to be affected by both centrifugal and radial pressure gradient effects [2–4]. However, it is generally found that separation occurs close to the leading edge and the location of reattachment moves further downstream with reduced flow coefficient (or incidence). Pressure surface separations in linear cascade also exhibit a strong dependence on incidence [5–7]. However, only Yamamoto and Nouse [6] performed measurements of the pressure surface boundary layer. Their results suggested that the pressure surface separation could produce significant loss although this was not quantified.

The main aims of this investigation are therefore to quantify the loss produced by the pressure surface separation, to identify the mechanisms that give rise to this loss and to develop a prediction method that can be used in the preliminary stages of design. Experiments are performed at midspan on a thin, solid, low-pressure turbine blade in linear cascade. In keeping with studies such as Curtis et al. [1], the effect of a more ''engine representative'' disturbance environment is also investigated. A complementary study concerning the effect of the pressure surface separation on the secondary flow is presented in Brear et al. [8].

Experimental Methods

All experiments were performed in low-speed, open-return wind tunnels at the Whittle Laboratory. Further details are given in Brear [9]. The ''moving bar cascade,'' discussed in more detail by Curtis et al. [1], was used to simulate the wakes shed from an upstream blade-row. Wakes were generated by circular bars of 2-mm diameter which translate circumferentially along a plane located 50 percent C_x upstream of the cascade leading edge. This choice of bar diameter and axial location was shown by Howell et al. [10] to generate wakes that are representative of those inside the low-pressure turbine. The cascade consisted of seven blades (Fig. 1) with circular leading edges and parameters given in Table 1. It is noted that He [7] studied the same profile, but on a cascade with a lower aspect ratio.

The behavior of the pressure surface separation was studied in three disturbance environments: steady inflow (SI), with wake passing (W) and with a turbulence grid in place (G). RMS intensities are given in Table 2. The steady inflow and grid investigations were performed at +10 deg, 0 and −10 deg incidence. The wake passing investigation was only performed at 0 deg incidence, for which the flow coefficient ($\phi = V_X/U$) was fixed at 0.73 and the reduced frequency, $\bar{f} = 0.29, 0.58, 1.16$, was varied by changing the spacing of the bars. The range of Re_2 (based on blade chord) was from 100,000 to 300,000, although most results were obtained at a cruise Re_2 of 130,000. In all cases, the suction surface boundary layer was tripped at 73 percent C_x with a 0.41-mm-diam stainless steel trip. This limited the effect of variations in the suction surface flow during the present study, but increased the overall profile loss considerably.

The turbulence grid was specifically chosen so as to create an ''engine representative'' turbulence intensity. It was placed approximately 870 mm upstream of the central cascade blade and was composed of a square array of 12.7-mm circular bars with

[1]Present address: Department of Mechanical and Manufacturing Engineering, University of Melbourne, Australia

Contributed by the International Gas Turbine Institute and presented at the International Gas Turbine and Aeroengine Congress and Exhibition, New Orleans, Louisiana, June 4–7, 2001. Manuscript received by the IGTI, October 20, 2000. Paper No. 2001-GT-437. Review Chair: R. A. Natole.

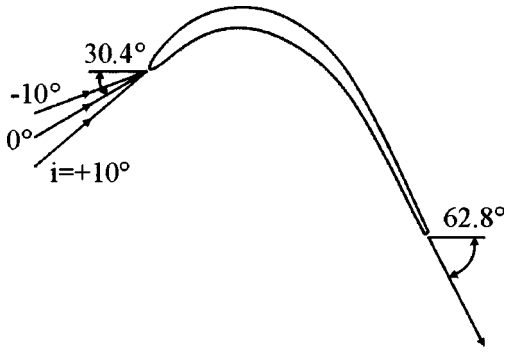

Fig. 1 Blade A and the angles of incidence studied

76.2 mm pitch. RMS intensities are given in Table 2. The streamwise integral length-scale of the turbulence was approximately 21 mm at 0 percent C_x and midpitch.

Hotwire measurements along the pressure surface and at inlet to the cascade were performed with "Dantec" single, normal hotwires and Dantec constant temperature anemometry equipment. A total of 8192 samples were measured at a 2-kHz logging frequency, with the low-pass filter set to 1 kHz cut-off. The entire pressure surface flow was mapped out with 19 circumferential traverses from 95 to 5 percent C_x along the pressure surface in 5 percent C_x increments and a further traverse at 1 percent C_x. All traverses extended from 0.1 mm circumferentially above the pressure surface to one third of the blade pitch. Details of the calibration procedure are given in Brear [9]. Uncertainty of $\overline{u}$ was estimated to be $\pm 0.1\ \overline{u}$ in the separated shear layer and $\pm 0.03\ \overline{u}$ in the freestream and attached flow.

The surface static pressure was measured around the blade with a "Scanivalve" differential pressure transducer of ± 35 mbar range. Uncertainty of V/V_2 is estimated to be ± 0.02.

A single pitot probe was used for measurements of the pressure surface loss (Y_{PS}) and profile loss (Y_P). The probe tip had 0.5 mm o.d. and 0.3 mm i.d. The small diameter was required for reasonable resolution of the pressure surface boundary layer. The wake traverses were performed at 125 percent C_x and the pressure surface traverses were performed at 95 percent C_x. The pressure surface loss coefficient (Y_{PS}) was defined as

$$Y_{PS}=\frac{P_{01}-P_{0.95\ \text{percent}CX}}{P_{01}-P_2} \tag{1}$$

where $P_{0.95\ \text{percent}CX}$ is the stagnation pressure measured at 95 percent C_x. Similarly, the profile loss (Y_P) coefficient was defined as

Table 1 Parameters of blade A

chord, C (mm)	148.3
axial chord, C_X (mm)	126.8
pitch, s (mm)	103.8
span, h (mm)	375.0
inlet flow angle at i=0°, α_1 (°)	30.4
design exit flow angle, α_{2D} (°)	62.8

Table 2 RMS intensities at 0 percent C_x and midpitch

	steady inflow	wake passing			turb. grid
		$\bar{f}$ =0.29	$\bar{f}$ =0.58	$\bar{f}$ =1.16	
u_{RMS}/V_1	0.6	4.0	5.8	7.4	4.0

$$Y_P=\frac{P_{01}-P_{02}}{P_{01}-P_2} \tag{2}$$

where P_{02} is the stagnation pressure measured at 125 percent C_x. In order to obtain a mass averaged pressure surface loss coefficient ($\overline{Y_{PS}}$), the flow at 95 percent C_x was assumed to be at the blade design exit angle (α_{2D}) and with uniform static pressure equal to ambient pressure. Both of these assumptions are closely satisfied at 125 percent C_x, meaning that $\overline{Y_{PS}}$ is a reasonable measure of the contribution by the pressure surface to the overall mass averaged profile loss at 125 percent C_x. Y_{PS} and Y_P were measured using a "Zoc" differential pressure transducer of $\pm 10''$ H_2O range. The uncertainty of measuring both Y_P and Y_{PS} is estimated to be ± 0.0017 at $Re_2=130{,}000$, which is a considerable fraction of Y_{PS}.

Smoke-wire flow visualization was used to reveal the structure of the pressure surface separation at midspan. A wire made of "80/20 Vacrom" was placed upstream of the cascade. It was 0.12 mm in diameter and had 88.3 Ω/m impedance. "Shell Ondina Oil EL" oil coated the wire and a DC voltage was applied between its two ends. A 1 kW columnated Halogen lamp was placed downstream of the cascade. This produced a sheet of light that was positioned to illuminate the midspan section. A high-speed, digital video camera (Kodak Ektapro, model 4540) was positioned next to the cascade. A perspex cascade endwall allowed viewing of the pressure surface flow.

Numerical Predictions

The numerical predictions were performed with a steady, two-dimensional, viscous/inviscid coupled solver named "Mises" [11]. This was only used in its fully inviscid mode in the present study and predictions were performed at a cascade exit Mach number of 0.2. Special attention was paid to the resolution of the leading edge flow and grid independence was achieved easily.

Results and Discussion

Stagnation Pressure Loss. Figure 2(*a*) shows typical wake traverses performed at three incidences. The wake profile is essentially symmetrical at +10 deg incidence. As the incidence is reduced, an extended region of stagnation pressure loss develops on the pressure side of the wake. Figure 2(*b*) shows that this region of pressure side loss originates upstream of the trailing edge: at a given incidence, the magnitude of the asymmetry in Fig. 2(*a*) is matched by the traverses in Fig. 2(*b*).

The variation of pressure surface loss with Reynolds number is shown in Fig. 3. The effect of the turbulence grid was within the experimental uncertainty. Furthermore, the pressure surface loss when wake passing was included could not be measured directly because the loss associated with the wakes could not be separated from that generated along the pressure surface. As an estimate of the significance of the data in Fig. 3, the mass-averaged values at $Re_2=130{,}000$ correspond to approximately 0.5, 0.6, and 1.2 percent of the isentropic efficiency of a modern low pressure turbine operating at +10, 0, and −10 deg incidence, respectively. This suggests that the pressure surface flow can have a significant impact on the performance of the low pressure turbine.

Isentropic Velocities. Figure 4 shows the predicted effect of incidence on the flow around the leading edge. The stagnation point moves from near the pressure surface blend point at +10 deg incidence to approximately coinciding with the suction surface blend point at −10 deg incidence. The stagnation points are also accompanied by peaks in velocity (indicated by the second arrow extending from the leading edge center) which will be called leading edge "spikes" [12]. The varied location of these spikes shows that they are *not* associated with any discontinuities in curvature, but instead suggest that they arise in the smooth flow around a surface with a small radius of curvature.

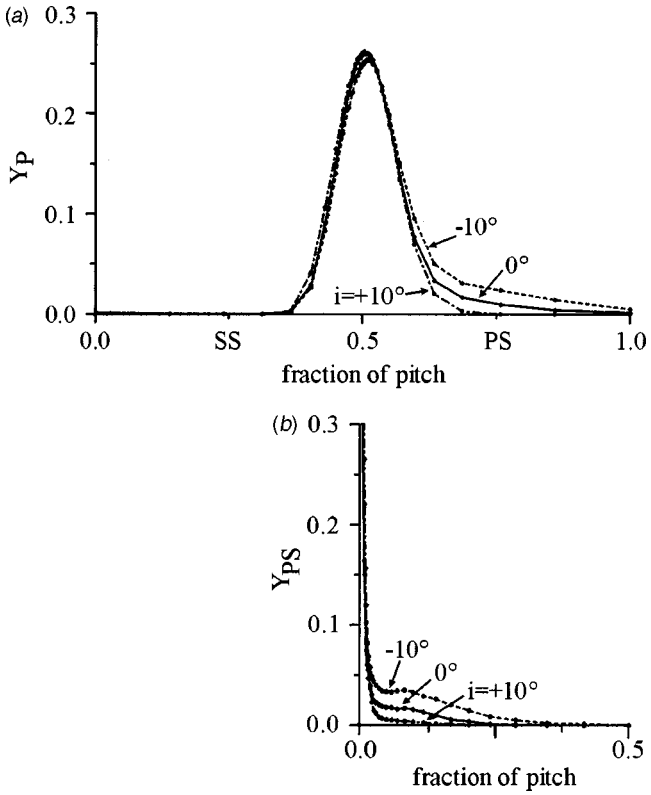

Fig. 2 (*a*) Wake at 125 percent C_x, and (*b*) pressure surface stagnation pressure loss traverses at 95 percent C_x (Re_2 =130,000, steady inflow)

As the incidence is reduced, the leading edge spikes from the start of an extended region of deceleration on the pressure surface (Fig. 5(*a*)). Furthermore, Fig. 4 suggests that there must be a spike on the leading edge and that the magnitude of the inviscid deceleration on the pressure surface is controlled by the location of the

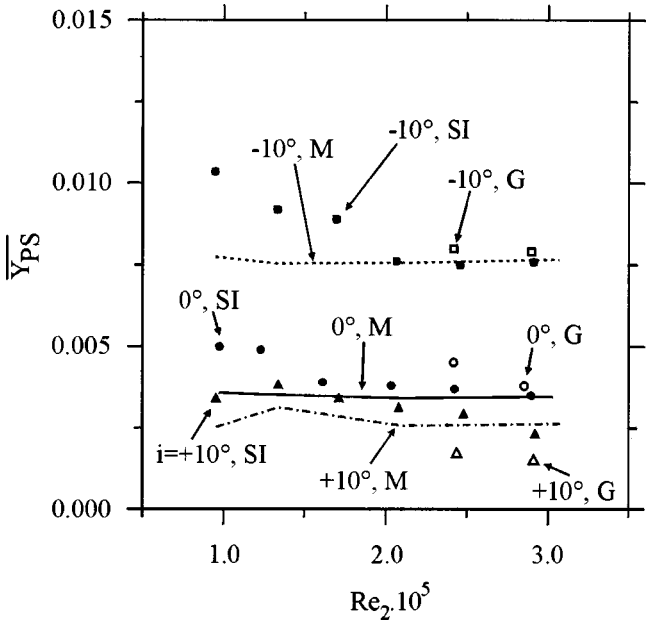

Fig. 3 Pressure surface stagnation pressure loss variation with Re_2 (no wake passing, SI=steady inflow, G=grid, M=model)

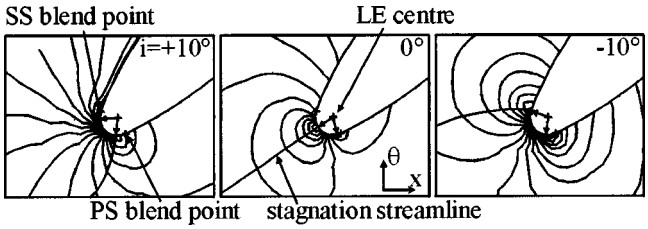

Fig. 4 Predicted contours of isentropic velocity around the leading edge

leading edge stagnation point. Given that the magnitude of these leading edge spikes primarily determines the intensity of the inviscid deceleration downstream of the leading edge, it appears that the leading edge flow gives rise to the strong incidence dependence of the pressure surface separation.

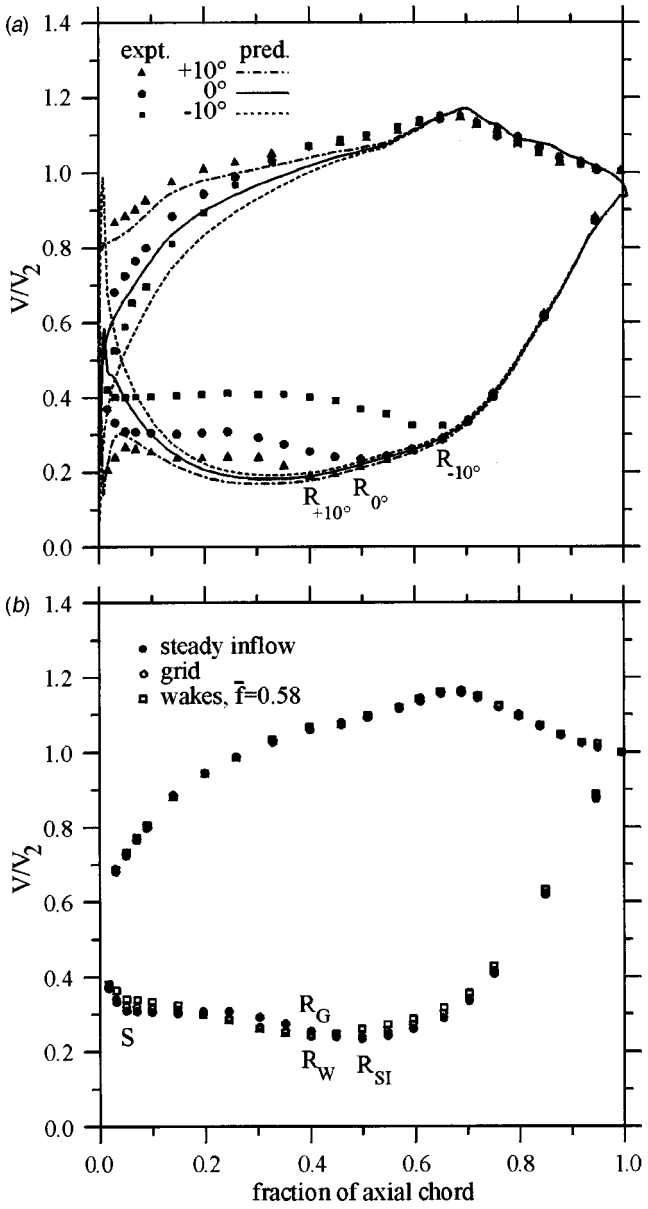

Fig. 5 Isentropic velocities from numerical prediction and experiment (*a*) under steady inflow (Re_2=130,000), and (*b*) at 0 deg incidence (Re_2=130,000)

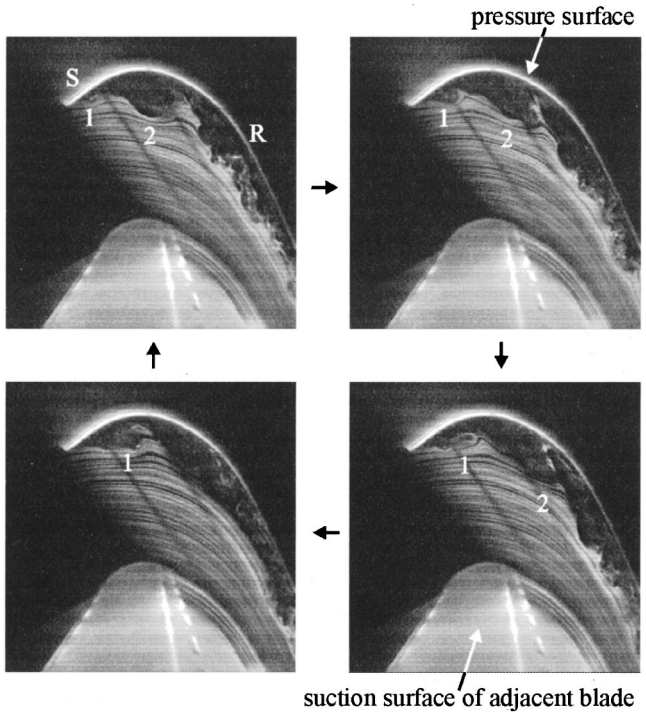

Fig. 6 Smoke wire visualization at $i=-10$ deg ($Re_2=130{,}000$, steady inflow)

For a given blade, the location of the leading edge stagnation point is controlled by the incidence. In design, the location of the stagnation point at a given incidence can be controlled, for example, by variations in the inlet metal angle of the blade. Of course, careful placement of the stagnation point can only be done at one incidence. This suggests that leading edge spikes cannot always be avoided on thin turbomachinery blades that operate over a large range of incidences.

While leading edge spikes may form the start of the inviscid deceleration along the pressure surface, the extended region of deceleration from 0 to 30 percent C_x occurs because the profile in question is relatively thin. Brear et al. [8] show that thickening the blade profile removes this extended region of adverse pressure gradient, and hence the pressure surface separation. However, this may be undesirable due to the cost reasons described earlier.

Figure 5(*a*) shows that the pressure surface separation significantly modifies the static pressure distribution around the leading edge and foreblade (0 to 50 percent C_x). The magnitude of the peak velocity in experiment is smaller than that found in the inviscid numerical predictions. This is in keeping with Walraevens and Cumpsty [12], who suggest that the differences between the inviscid and experimental isentropic velocity distributions is because the leading edge separation increases the radius of curvature followed by the flow.

The location of reattachment (identified as *R* with appropriate subscripts) is shown in Figs. 5(*a*), (*b*) as occurring at the local maximum of static pressure. This method of locating the reattachment point is shown by Brear et al. [8] to be reasonable using surface flow visualizations obtained both from experiments and numerical predictions on blade A. In an inviscid flow, a point of attachment is, of course, a local maximum in static pressure (eg., the leading edge stagnation points in Fig. 4). Furthermore, the mean velocity profiles presented in Fig. 8(*a*) suggest that this method is valid. Figure 5(*a*) is therefore clear evidence that the size of the pressure surface separation increases considerably with reduced incidence.

Smoke-Wire Flow Visualization. Smoke wire visualization at -10 deg incidence illustrates the behavior of the pressure surface flow (Fig. 6). At midspan vortices of spanwise sense form periodically: the structure labeled 1 can be seen to be relatively small in the first image (top left) and then undergo a rapid growth as it travels downstream. By the fourth image (bottom left), it is approaching the scale that structure 2 had in the first image. The frequency of this process matches that observed in the hotwire measurements discussed later. Similar behavior to Fig. 6 was also observed at $+10$ and 0 deg incidence. This suggests that transition within the pressure surface separation is characterized by the growth, transport and eventual breakdown of vortices. Significant unsteadiness continues downstream of the mean reattachment point (*R*).

Hotwire Measurements. Figure 7 is in qualitative agreement with the smoke-wire visualization presented in Fig. 6. Furthermore, Fig. 7 shows the incidence dependence of the entire pressure surface flow. The trend seen in Fig. 7 therefore agrees with those presented in the stagnation pressure loss measurements (Fig. 2(*b*)) and the isentropic velocity distributions (Fig. 5(*a*)). Since unsteadiness must take its kinetic energy from the mean flow, regions of unsteadiness are often coincident with regions of stagnation pressure loss. Therefore, Fig. 7 suggests that the added loss created by reducing the incidence (Fig. 2(*b*), Fig. 3) originates mainly within the pressure surface separation.

Mean velocity profiles throughout the pressure surface separation at 0 deg incidence are shown in Fig. 8(*a*). Reversed flow is not indicated since a stationary, single hotwire cannot determine the flow direction. The velocity profiles are inflectional within the separated shear layer. Although not shown, there is also a trend for the point of inflection to move further away from the pressure surface with a reduction in incidence. Thus, the pressure surface separation becomes thicker as it becomes longer. In order to pass a given massflow through the bladerow, it follows that the veloci-

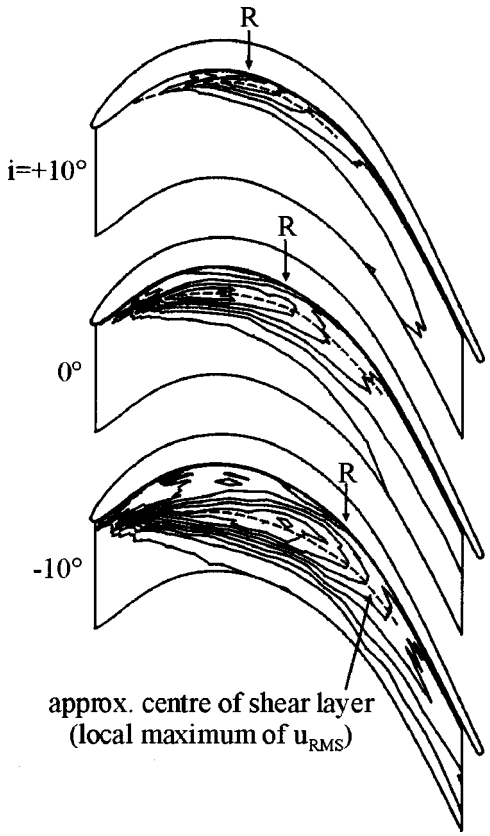

Fig. 7 Contours of u_{RMS}/V_2 along the pressure surface (contour level$=0.01V_2$, $Re_2=130{,}000$, steady inflow)

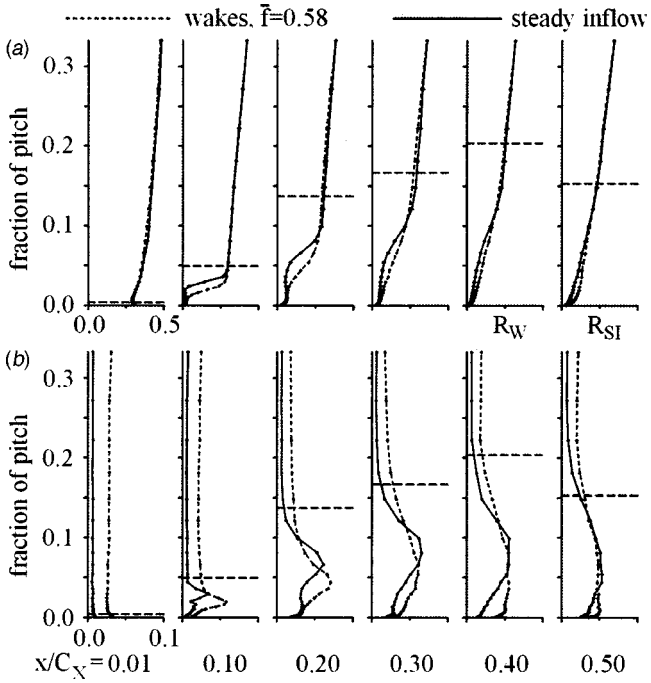

Fig. 8 Profiles of (*a*) $\bar{u}/V_2$ and (*b*) u_{RMS}/V_2 throughout the pressure surface separation ($i=0$ deg, $Re_2=130{,}000$, no grid)

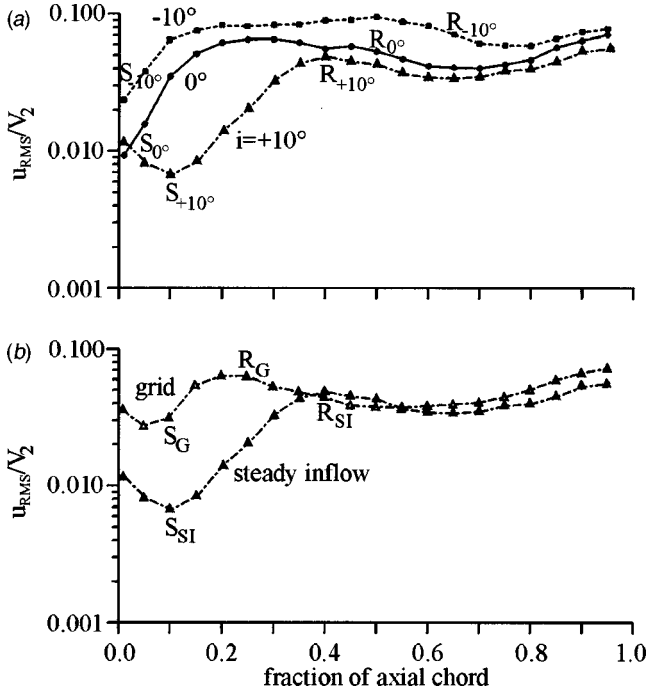

Fig. 9 Maximum u_{RMS} along the pressure surface for (*a*) steady inflow ($Re_2=130{,}000$, steady inflow), and (*b*) $i=+10$ deg ($Re_2=130{,}000$, no wake passing)

ties through the separated shear layer must increase as the incidence is reduced. The consequences of this are discussed later.

Figure 8(*a*) also shows that the point of inflection of the mean velocity profiles moves closer to the pressure surface with the addition of wake passing. The reattachment point (R_W), again identified as a local maximum in static pressure (Fig. 5(*b*)), also moves upstream. Therefore, wake passing makes the pressure surface separation smaller. This was also true of the addition of the turbulence grid: the location of reattachment at 0 deg incidence with the turbulence grid in place was the same as that shown for the wake passing case in Fig. 8(*a*). Indeed, the addition of the turbulence grid or wake passing always reduced the size of the pressure surface separation regardless of the wake passing frequency or the incidence.

Figure 8(*b*) shows profiles of u_{RMS} that are typical of hotwire measurements in separation bubbles [13,14]. There is a peak value of u_{RMS}, which will be defined as occurring at the center of the separated shear layer. In keeping with Fig. 8(*a*), the peak value of u_{RMS} moves closer to the pressure surface with the addition of wake passing. Once again, similar behavior always occurred irrespective of whether wake passing or the turbulence grid was used.

In all disturbance environments, the peak value of u_{RMS} coincided with the point of inflection of the mean velocity profiles over most of the separation (eg., Figs. 8(*a*), (*b*)). This has been observed in several studies of separation bubbles, and strongly suggests that the dominant transitional mechanism of the pressure surface separation was the Kelvin-Helmholtz instability [13–15].

Figure 9(*a*) shows that the maximum u_{RMS} grows rapidly under steady inflow. This is particularly clear at +10 deg incidence, with approximately exponential growth occurring over nearly the entire length of the pressure surface separation and ceasing near reattachment. The growth at 0 and −10 deg incidence appears to be more rapid than at +10 deg incidence and ends well before reattachment. In keeping with the results of several other studies, Fig. 9(*a*) is therefore evidence that spatially linear stability theory can be used to describe the transition of the separated shear layer in the low disturbance environment [13,15].

Spatially linear stability theory shows that inflectional mean velocity profiles are unstable to a finite range of frequencies and have a "most amplified frequency" [15]. This most amplified frequency should be evident in raw traces: as Fig. 10(*a*) shows at $Re_2=130{,}000$ and +10 deg incidence, there is a strongly periodic disturbance with a frequency of approximately 90 Hz at 10 percent C_x. Further into the region of exponential growth, this frequency can still be seen in the trace at 20 percent C_x, although it is partially masked by unsteadiness of other timescales. By 40 percent C_x, exponential growth has ended, the shear layer is reattaching and the raw trace exhibits unsteadiness with a range of timescales including that of the most amplified frequency. This final trace can be considered turbulent. Under steady inflow, the raw signals at 0 and −10 deg incidence also exhibited clearly periodic behavior, with similar frequencies to that observed at +10 deg incidence (Table 3).

Table 3 shows that the length/time-scales of the wake passing and the turbulence grid are of the same order as the "most amplified" scales present within the separated shear layer under steady inflow (the length-scales associated with the most amplified frequencies observed under steady inflow were calculated by assuming a convective velocity of half the shear layer edge velocity). Since the separated shear layer should be unstable to a range of frequencies around its most amplified frequency, it is reasonable to expect that the separated shear layer responds to these various forms of freestream disturbance. Figure 10(*b*) is evidence of this: the wake passing frequency can be seen in the "freestream" raw velocity trace as well as in the earlier stages of transition along the center of the separated shear layer. As Fig. 8(*b*) shows, this results in a more rapid rise in the unsteadiness within the separated shear layer. The turbulence grid has similar effect, with its excitation most clear at +10 deg incidence (Fig. 9(*b*)).

Most authors consider that increasing the entrainment of the separated shear layer draws the dividing streamline towards the wall, thereby shortening the separation [12,16]. If this is the case, wake passing in the present study has a qualitatively similar effect to that of the freestream turbulence: both forms of disturbance excite an earlier/stronger transition of the separated shear layer, and hence reduce the size of the pressure surface separation. This also suggests that wake passing may have a similar effect to the

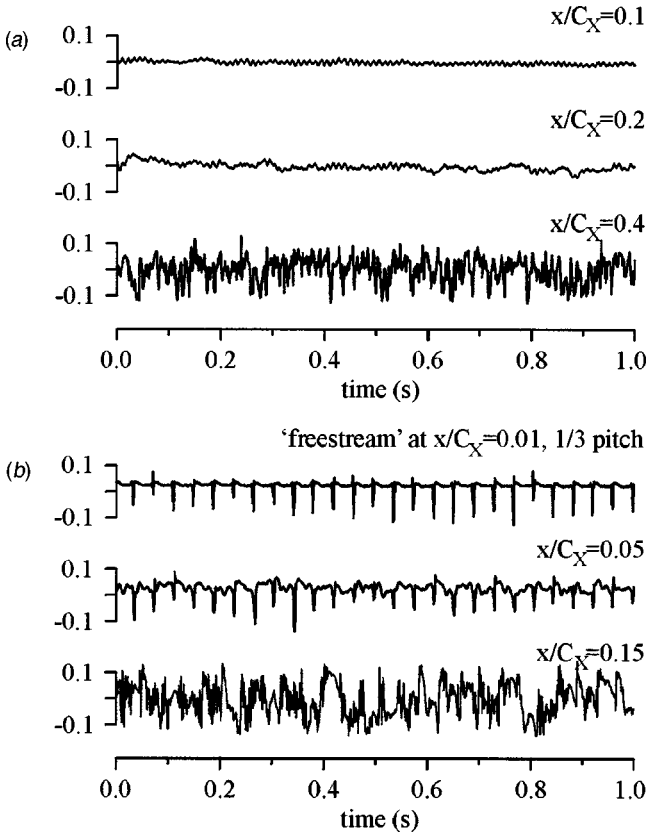

Fig. 10 Time traces of $(u_{RAW}-\bar{u})/V_2$ along the center of the separated shear layer for (*a*) $i=+10$ deg ($Re_2=130{,}000$, steady inflow), and (*b*) $i=0$ deg, $f=0.29$ ($Re_2=130{,}000$, wake passing)

turbulence grid on the loss generated by the pressure surface. Table 4 shows, however, that the turbulence grid appears to have a less significant effect in reducing the length of the pressure surface separation as the incidence is reduced. This is perhaps because the location of turbulent onset, indicated reasonably by the completion of exponential growth in Fig. 9(*a*), moves further upstream with reduced incidence: if transition occurs earlier, there is less unstable, laminar shear layer to excite. Nonetheless, this basic argument explains the commonly observed result that an ''engine representative'' disturbance environment can reduce the size of separated regions in the turbomachine.

Table 3 Length/time-scales under steady inflow, wake passing frequencies and the streamwise integral length-scale of the grid generated turbulence ($Re_2=130{,}000$)

i (°)	steady inflow		wake passing			turb. grid (mm)
	(Hz)	(mm)	$\bar{f}$ =0.29 (Hz)	$\bar{f}$ =0.58 (Hz)	$\bar{f}$ =1.16 (Hz)	
+10	90	18	n/a	n/a	n/a	21
0	87	23	26	52	103	21
-10	83	32	n/a	n/a	n/a	21

Table 4 Mean reattachment locations (x/C_x) of the pressure surface separation on blade A ($Re_2=130{,}000$)

incidence (°)	steady inflow	wake passing			turb. grid
		$\bar{f}$ =0.29	$\bar{f}$ =0.58	$\bar{f}$ =1.16	
+10°	0.4	n/a	n/a	n/a	0.25
0°	0.5	0.40	0.40	0.40	0.40
-10°	0.65	n/a	n/a	n/a	0.60

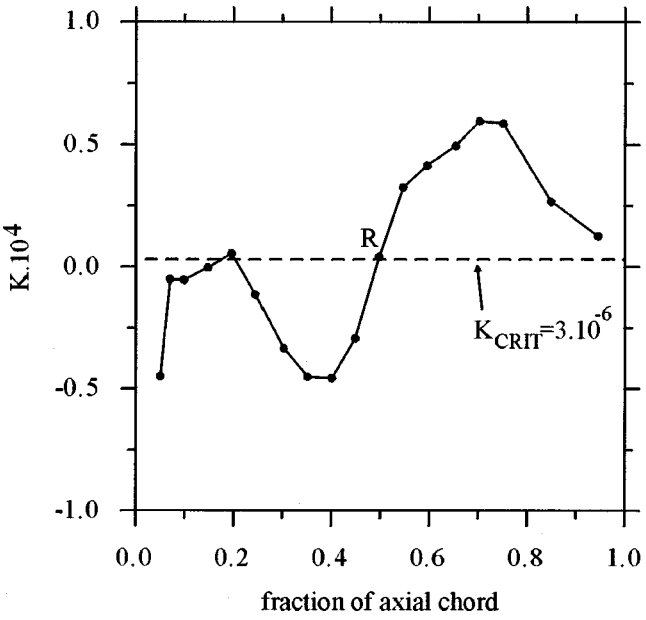

Fig. 11 Acceleration parameter along the pressure surface for $i=0$ deg ($Re_2=130{,}000$, steady inflow)

Downstream of Reattachment. Figures 6 and 7 suggest that the development of the boundary layer downstream of reattachment will be significantly affected by the pressure surface separation. More fundamental studies generally show that structures created within a separation bubble are long lived [17]. The isentropic velocity distributions in Figs. 5(*a*), (*b*) showed a strong favorable pressure gradient along the pressure surface from reattachment to the trailing edge. This suggests the possibility of relaminarization [18]. Using the experimental results in Fig. 5, the acceleration parameter along the pressure surface was calculated using

$$K=\frac{\nu}{V^2}=\frac{dV}{ds} \tag{3}$$

and is shown in Fig. 11. It can be seen that once reattachment occurs, the acceleration parameter exceeds the critical acceleration parameter (3.10^{-6}) that is commonly used to indicate whether relaminarization should occur [18]. The fluid therefore experiences a complex set of possible influences downstream of reattachment: both the history of the separated flow from upstream and that of the strong acceleration should be significant.

Figure 12 shows u_{RMS} profiles from reattachment to 95 percent C_x at 0 deg incidence. From the reattachment point onwards the

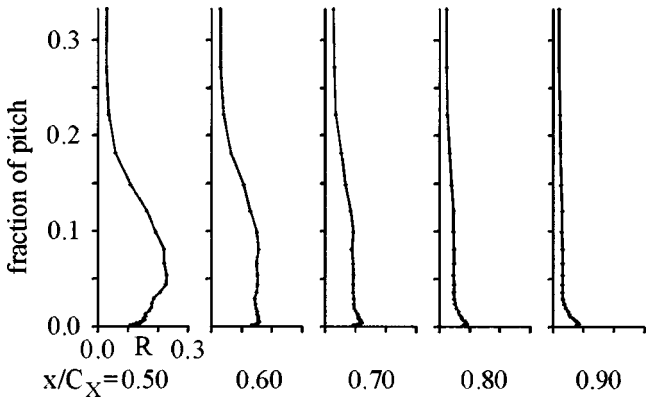

Fig. 12 u_{RMS}/V from reattachment to 95 percent C_x ($i=0$ deg, $Re_2=130{,}000$, steady inflow)

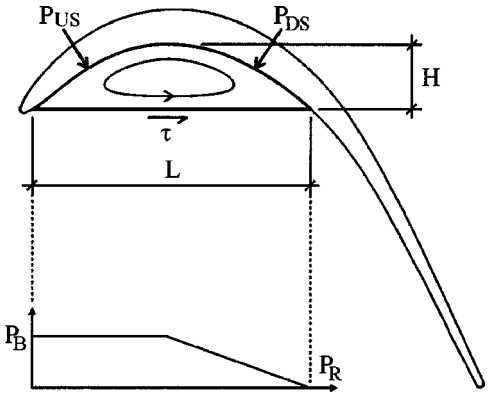

Fig. 13 The model of the pressure surface separation

u_{RMS} produced in the separated shear layer appears to dissipate and/or diffuse. However, a peak in u_{RMS} develops nearest the wall. In keeping with other studies, the general tendency of the boundary layer downstream of reattachment is to allow the unsteadiness produced upstream to diminish while a new ''inner layer'' develops along the pressure surface [17]. In all the cases studied, the absolute peak u_{RMS} of the inner layer increased with axial distance (eg., Figs. 9(*a*), (*b*)). However, Fig. 12 shows that when u_{RMS} is nondimensionalized by the local isentropic velocity, the peak associated with the inner layer decreases with axial distance. The behavior of the inner layer is therefore an example of a ''weak'' relaminarization [18]. The continued increase in absolute levels of unsteadiness with axial distance suggests that the mean flow does not act to promote turbulent dissipation over turbulent production. The flow is relaminarizing simply because the rate of turbulent production inside the inner layer is less than the rate at which the freestream velocity increases.

Modeling the Pressure Surface Separation. It has been shown that the pressure surface separation can be a significant contributor to the profile loss. This section presents a model of the pressure surface separation and hence suggests mechanisms by which this loss is produced. Furthermore, this model uses only the isentropic velocity distribution and the mean velocity profiles throughout the pressure surface separation. By using viscous, numerical predictions, it can therefore also be used as a predictive model in the preliminary stages of design.

The model of the pressure surface separation considers that the fluid bounded by the dividing streamline and the surface is in static equilibrium [19] (Fig. 13). The dividing streamline is assumed to be axial, meaning that the pressure forces acting normal to the dividing streamline do not contribute to the axial equilibrium. Laminar shear stresses throughout the pressure surface separation are neglected because they are considered to be small.

The axial balance between the three imposed forces is

$$H(P_{US}-P_{DS})+L\tau=0 \tag{4}$$

where H is the maximum circumferential thickness of the separation and L is its axial length. P_{US} is the average static pressure from the separation point to the maximum separation thickness and was found to be approximately equal to the pressure in the dead air region (P_B). P_{DS} is the average static pressure from the maximum separation thickness to reattachment. A linear variation over the pressure recovery region results in

$$P_{DS}=\frac{(P_B+P_R)}{2} \tag{5}$$

which Fig. 5 suggests is a reasonable approximation.

Substituting Eq. (5) into Eq. (4) gives

$$\overline{C_\tau}=\frac{(C_{PB}-C_{PR})}{4\overline{C_P}}\frac{H}{L} \tag{6}$$

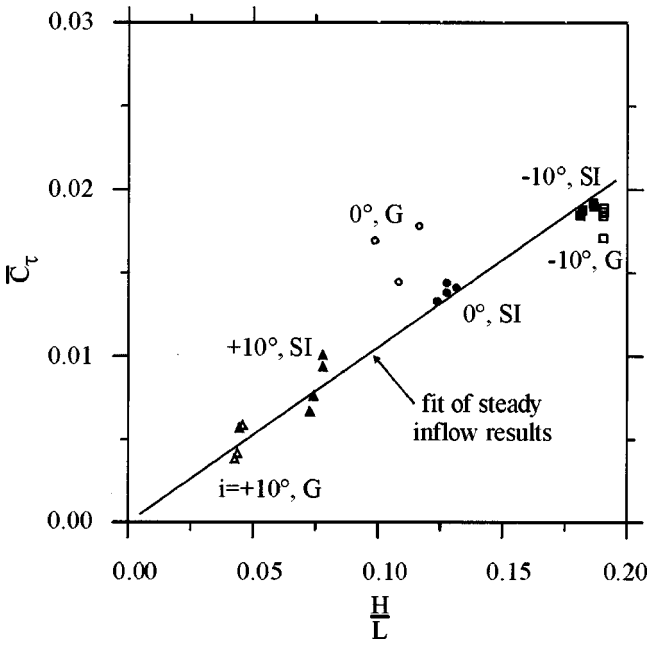

Fig. 14 Turbulent shear stress coefficient versus aspect ratio of the pressure surface separation (no wake passing)

where C_{PB} and C_{PR} are the static pressure coefficients in the dead air region and at reattachment and $\overline{C_P}$ is the average static pressure along the separation. $\overline{C_\tau}$ is the average turbulent shear stress coefficient along the dividing streamline

$$\overline{C_\tau}=\frac{\int-\rho\overline{u'v'}dL}{\int\rho V^2 dL} \tag{7}$$

where V is the velocity at the edge of the separated shear layer. The isentropic velocity distribution in Fig. 5(*a*) at 0 deg incidence has been superimposed onto the mean profiles in Fig. 8 as dashed lines. This shows that the isentropic velocity is a reasonable shear layer edge velocity. Similar results are found at other incidences.

Equation (6) relates the turbulent shear along the dividing streamline to two nondimensional groups. The first relates the pressure difference over the separation to the local average dynamic head and was determined experimentally from the blade surface static pressure measurements. The second is the aspect ratio of the pressure surface separation (H/L). The axial length (L) of the separation is also determined from the blade surface static pressure measurements. The maximum height of the separation (H) is estimated from the mean velocity profiles such as Fig. 8(*a*) by assuming that the velocity along the dividing streamline at maximum height is half that of the local freestream velocity. Thus, all terms in Eq. (6) are obtained solely from experimental results.

Figure 14 shows the values of $\overline{C_\tau}$ obtained from Eq. (6) against the aspect ratio of the pressure surface separation. The three clusters of points at low, medium, and high aspect ratio represent data taken at +10, 0, −10 deg incidence respectively, with each cluster composed of results at Re_2 between 100,000 to 300,000. The straight line through the data is a line of best fit of the steady inflow data only. While this approximately linear variation may suggest some deeper significance, the authors feel that it is more likely to be particular to the present study. The actual value of $\overline{C_\tau}$ along the dividing streamline could not be measured because a stationary, single hotwire was used. However, the range shown in Fig. 14 is within those found in the literature for laminar separation bubbles, which suggests that the values of $\overline{C_\tau}$ found in the present study are reasonable.

Neglecting the laminar shear, the dissipation coefficient can be written as

$$C_d = \frac{1}{\rho V^3} \int_0^{\delta} -\rho \overline{u'v'} \frac{d\overline{u}}{dy} dy \tag{8}$$

At reattachment, Horton [20] puts forward several arguments to suggest that his ''universal'' mean velocity profile is similar to a wake and thus has constant turbulent viscosity. In Horton's [20] formulation, Eq. (8) becomes

$$C_d = \frac{\delta}{\delta^*} \overline{C_{\tau,\delta}} \int_0^{\delta/\delta^*} \left[d\left(\frac{\overline{u}}{V}\right) / d\left(\frac{y}{\delta^*}\right) \right]^2 d\left(\frac{y}{\delta^*}\right) \tag{9}$$

where $\overline{C_{\tau,\delta}}$ is the average turbulent stress across the reattaching shear layer, δ/δ^* equals 2.14 and the integral equals 0.554. The dissipation coefficient is then simply

$$C_d = 1.19\overline{C_{\tau,\delta}} \tag{10}$$

which Horton [20] applies to the entire turbulent portion of the separated shear layer. Given the usual early transition in the present study, Eq. (10) will therefore be applied over the entire separated shear layer.

The dividing streamline is expected to lie between the center of the separated shear layer and the blade surface [13]. This is certainly the case at separation and reattachment, and suggests that the turbulent shear on the dividing streamline at a given axial location will be less than the maximum turbulent shear in the shear layer. The turbulent shear on the dividing streamline is therefore assumed to be equal to the average across the shear layer ie. $\overline{C_\tau} = \overline{C_{\tau,\delta}}$. It follows that

$$C_d = 1.19\overline{C_\tau} \tag{11}$$

giving a mean dissipation coefficient for the separation and completing the model.

Comparing the Model With Experiment. The pressure surface loss coefficient can be written as

$$Y_{PS} = \frac{2S_0}{s \cos \alpha_2} \int_0^{0.95S_0} C_d \left(\frac{V}{V_2}\right)^3 d\left(\frac{s}{S_0}\right) \tag{12}$$

which requires the isentropic velocity and values of C_d from reattachment to 95 percent C_x. The model provides C_d along the pressure surface separation. Given the complex nature of the relaminarizing flow downstream of reattachment, a suitable choice of C_d in this region is not clear. A value of 0.002 is used downstream of reattachment, which is a typical value for turbulent boundary layers [21].

Figure 3 shows a comparison between the predicted and measured values of Y_{PS} for the steady inflow results. The model agrees closely with experiment at higher Reynolds numbers. Because the dissipation coefficient downstream of reattachment was estimated, it cannot be determined whether this improvement is due to the modeling of the pressure surface separation or the region downstream of reattachment. Nonetheless, the trend of increased Y_{PS} with a reduction in incidence is evident.

Figure 15(*a*) reveals the behavior of the model. The pressure surface separation is predicted to create an order of magnitude more loss at -10 deg incidence than at $+10$ deg incidence. At $+10$ deg incidence, the pressure surface separation is a small contributor to Y_{PS} and the attached boundary layer downstream produces most of the pressure surface loss. However, at -10 deg incidence, most of the pressure surface loss is produced by the pressure surface separation. The pressure surface separation at this incidence is almost as dissipative as the flow at the trailing edge.

Given that Fig. 14 predicted that $\overline{C_\tau}$ for the pressure surface separation at -10 deg incidence was only approximately 2.5 times that at $+10$ deg incidence, the order of magnitude difference in the predicted dissipation of the pressure surface separation at

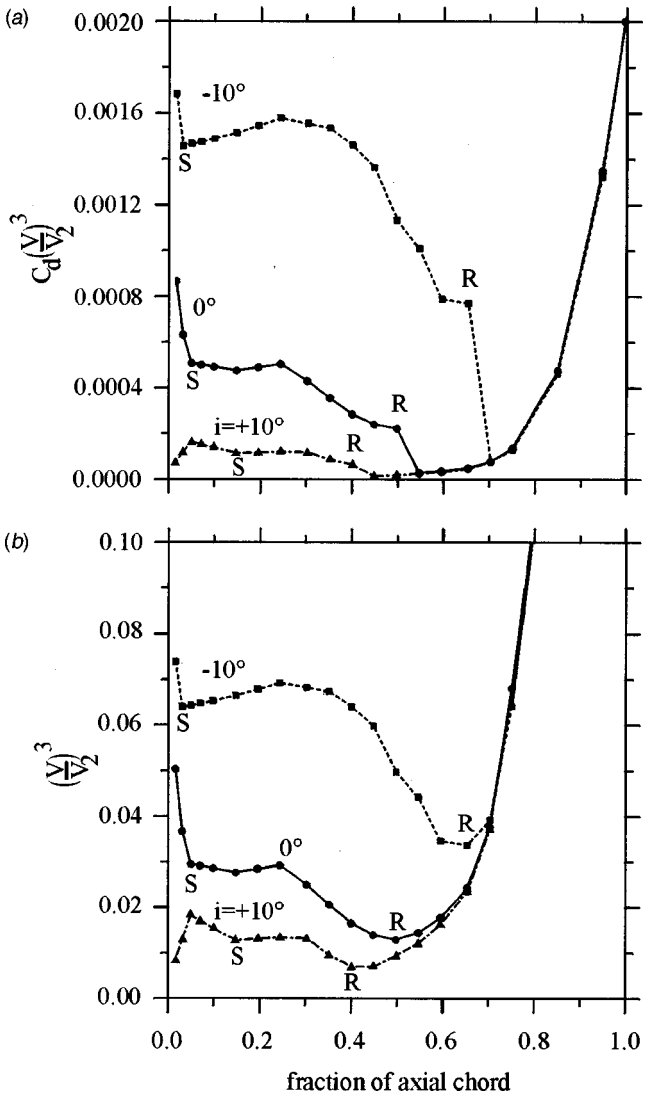

Fig. 15 (*a*) Modeled dissipation rate, and (*b*) cube of isentropic velocity along the pressure surface (Re_2=130,000, steady inflow)

these two incidences cannot solely be due to the difference in C_d. Instead, the dissipation of the pressure surface separation is also dependent on the blockage that the separation produces. This can be seen in Fig. 15(*b*), where the cube of the shear layer edge velocity of the pressure surface separation at -10 deg incidence is approximately five times that at $+10$ deg incidence. Combining the added blockage with the increased value of C_d therefore gives the required order of magnitude difference in dissipation between these two incidences.

The dependence of the pressure surface loss on the pressure surface separation is therefore twofold. A separation with increased aspect ratio will be more dissipative. However, higher aspect ratio separations also present greater blockage to the flow, thereby increasing the velocity in the separated shear layer. The present study showed that this blockage effect is significant, since loss production scales with the cube of the shear layer edge velocity. In the authors' view, this ''twofold'' nature of loss production should be of general relevance to separated, internal flows.

The presented model also sheds light on the designer's choice between thick, hollow, and thin, solid blades. Equivalent, thicker airfoils could possibly be designed in which a given isentropic velocity distribution, such as those shown in Fig. 5, is realized without separating the pressure surface boundary layer. This

would reduce C_d considerably while maintaining the effect of the blockage. However, Fig. 15(*a*) showed that, in terms of the overall profile loss (Y_P), the loss produced by the pressure surface separation at +10 deg and 0 deg incidence is relatively small. This suggests that design operation near 0 deg incidence is reasonable on blade A, and that little improvement in Y_P around 0 deg incidence is expected from an equivalent, thicker profile.

Conclusions

The pressure surface separation can be a significant contributor to the profile loss of thin, low-pressure turbine profiles. This has been shown at negative incidence on a linear cascade of blades that are typical of current engine designs.

The pressure surface separation arose because an adverse pressure gradient existed in the inviscid flow from the leading edge and along the foreblade of the pressure surface. The intensity of this adverse pressure gradient was largely determined by the incidence, which strongly controlled the magnitude and location of ''spikes'' in velocity on the leading edge. All characteristics of the pressure surface separation were therefore mainly dependent on the incidence. The strong acceleration downstream of reattachment was observed to initiate a ''weak'' relaminarization of the pressure surface flow in all cases.

The transitional, separated shear layer appeared to experience the Kelvin-Helmholtz instability. ''Engine representative'' unsteadiness, in the form of either wake passing or grid generated freestream turbulence, was of an appropriate scale to excite the unstable, separated shear layer. This encouraged earlier and/or stronger transition, thereby reducing the size of the pressure surface separation. However, both forms of unsteadiness were suggested to have only a marginal effect on the profile loss.

A simple model of the pressure surface flow was then proposed, in which the mechanism by which the pressure surface separation created its loss was twofold. The pressure surface separation was highly dissipative through the action of its strong turbulent shear. As the incidence was reduced, the increasing blockage of the pressure surface separation then raised the velocity in the separated shear layer to levels at which the separation could create significant loss. This model used only the surface static pressure distribution and the mean velocity profiles inside the pressure surface separation. It can therefore be used as a predictive method in the preliminary stages of design.

Acknowledgments

The authors would like to thank Rolls-Royce, plc and the Defence Evaluation and Research Agency (MOD and DTI CARAD) for their generous financial support and permission to publish the work contained in this paper.

Nomenclature

C_d = dissipation coefficient
C_x = axial chord (m)
$C_P=(P_{01}-P)/(P_{01}-P_2)$ = static pressure coefficient
$f=fC/V_2$ = reduced frequency of bars
h = span (m)
i = incidence (deg)
R = reattachment point
s = blade pitch (m)
s = ordinate along pressure surface (m)
S = separation point
S_0 = pressure surface length (m)
$\overline{u}$ = mean velocity (m/s)
u_{RAW} = raw velocity (m/s)
u_{RMS} = root-mean-square velocity (m/s)
$V=V_2\sqrt{C_P}$ = isentropic velocity (m/s)
$Y=(P_{01}-P_0)/(P_{01}-P_2)$ = stagnation pressure loss coefficient
α = yaw angle
δ = shear layer thickness (m)
δ^* = displacement thickness (m)
ρ = density (kg/m^3)
ν = kinematic viscosity (m^2/s)

Subscripts

1 = cascade inlet
2 = cascade exit
$2D$ = design at cascade exit

References

[1] Curtis, E. M., Hodson, H. P., Banieghbal, M. R., Denton, J. D., Howell, R. J., and Harvey, N. W., 1996, ''Development of Blade Profiles for Low Pressure Turbine Applications,'' ASME J. Turbomach., **119**, pp. 531–538.
[2] Yamamoto, A., Tominaga, J., Matsunuma, T., and Outa E., 1994, ''Detailed Measurements of Three-Dimensional Flows and Losses Inside an Axial Turbine Rotor,'' ASME Paper No. 94-GT-348.
[3] Hodson, H. P., and Addison, J. S., 1988, ''Wake-Boundary Layer Interactions in an Axial Flow Turbine Rotor at Off-Design Conditions,'' ASME Paper No. 88-GT-233.
[4] Scrivener, C. T. J., Connolly, C. F., Cox, J. C., and Dailey, G. M., 1991, ''Use of CFD in the Design of a Modern Multistage Aero Engine LP Turbine Design,'' I. Mech. E. Paper No. C423/056.
[5] Hodson, H. P., and Dominy, R. G., 1987, ''The Off-Design Performance of a Low-Pressure Turbine Cascade,'' ASME J. Turbomach., **109**, pp. 201–209.
[6] Yamamoto, A., and Nouse, H., 1988, ''Effects of Incidence on Three-Dimensional Flows in a Linear Turbine Cascade,'' ASME J. Turbomach., **110**, No. 4, pp. 486–496.
[7] He, L., 1998, ''Unsteady Flow in Oscillating Turbine Cascades—Part 1: Linear Cascade Experiment,'' ASME J. Turbomach., **120**, pp. 262–268.
[8] Brear, M. J., Hodson, H. P., Gonzalez, P., and Harvey, N. W., 2002, ''Pressure Surface Separations in Low Pressure Turbines—Part 2: Interactions With the Secondary Flow'' (2001-GT-438), ASME J. Turbomach., **124**, pp. 402–409.
[9] Brear, M. J., 2000, ''Pressure Surface Separations in Low Pressure Turbines,'' Ph. D dissertation, Cambridge University, Cambridge, UK.
[10] Howell, R. J., Ramesh, O. N., Hodson, H. P., Harvey, N. W., and Schulte V., 1999, ''High Lift and Aft Loaded Profiles for Low Pressure Turbines,'' ASME Paper No. 2000-GT-261, to appear in the ASME J. Turbomach.
[11] Drela, M., and Youngren, H., 1995, ''A User's Guide to Mises 2.3,'' MIT Computational Aerospace Sciences Laboratory Report.
[12] Walraevens, R. E., and Cumpsty, N. A., 1995, ''Leading Edge Separation Bubbles on Turbomachine Blades,'' ASME J. Turbomach., **117**, pp. 115–125.
[13] Watmuff, J. H., 1999, ''Evolution of a Wave Packet Into Vortex Loops in a Laminar Separation Bubble,'' J. Fluid Mech., **397**, pp. 119–169.
[14] Hazarika, B. K., and Hirsch, C., 1997, ''Transition Over C4 Leading Edge and Measurement of Intermittency Factor Using PDF of Hot-Wire Signal,'' ASME J. Turbomach., **119**, July, pp. 412–425.
[15] Dovgal, A. V., Kozlov, V. V., and Michalke, A., 1996, ''Laminar Boundary Layer Separation: Instability and Associated Phenomena,'' Prog. Aerosp. Sci., **30**, pp. 61–94.
[16] Fiedler, H. E., and Fernholz, H. H., 1990, ''On Management and Control of Turbulent Shear Flows,'' Prog. Aerosp. Sci., **27**, pp. 305–387.
[17] Castro, I. P., and Epik, E., 1998, ''Boundary Layer Development After a Separated Region,'' J. Fluid Mech., **374**, pp. 91–116.
[18] White, F. M., 1991, *Viscous Fluid Flow*, McGraw-Hill, 2nd Edition, New York, NY.
[19] Roshko, A., 1993, ''Perspectives on Bluff Body Aerodynamics,'' J. Wind. Eng. Ind. Aerodyn., **49**, pp. 101–120.
[20] Horton, H. P., 1969, ''A Semi-Empirical Theory for the Growth and Bursting of Laminar Separation Bubbles,'' ARC current papers No. 1073.
[21] Denton, J. D., 1993, ''Loss Mechanisms in Turbomachines,'' ASME J. Turbomach., **115**, pp. 621–656.

Michael J. Brear[1]
e-mail: mjbrear@unimelb.edu.au

Howard P. Hodson
e-mail: hph@eng.cam.ac.uk

Whittle Laboratory
Cambridge University
Cambridge, UK

Paloma Gonzalez
Industria de Turbo Propulsores, S.A.
Madrid, Spain
e-mail: paloma.gonzalez@itp.es

Neil W. Harvey
Rolls-Royce, plc,
Derby, UK
e-mail: neil.harvey@rolls-royce.com

Pressure Surface Separations in Low-Pressure Turbines—Part 2: Interactions With the Secondary Flow

This paper describes a study of the interaction between the pressure surface separation and the secondary flow on low-pressure turbine blades. It is found that this interaction can significantly affect the strength of the secondary flow and the loss that it creates. Experimental and numerical techniques are used to study the secondary flow in a family of four low-pressure turbine blades in linear cascade. These blades are typical of current designs, share the same suction surface and pitch, but have differing pressure surfaces. A mechanism for the interaction between the pressure surface separation and the secondary flow is proposed and is used to explain the variations in the secondary flows of the four blades. This mechanism is based on simple dynamical secondary flow concepts and is similar to the aft-loading argument commonly used in modern turbine design.
[DOI: 10.1115/1.1450765]

Introduction

The designer of the low pressure turbine in a modern aircraft engine is commonly faced with the choice between thick, hollow and thin, solid blades. Brear et al. [1] point out that thin, solid blades can be preferable since they are considerably less expensive to manufacture. However, separation bubbles often occur near the leading edge on the pressure surface of these thin profiles *at design conditions*. This separation is referred to as the 'pressure surface separation' and, as Brear et al. [1] show, can significantly increase the profile loss.

Several previous studies have observed some interaction between the pressure surface separation and the secondary flow [2–4]. These studies were primarily concerned with the effects of incidence. As such, they were not able to quantify the interaction between the pressure surface separation and the secondary flow because incidence affects both the size of the pressure surface separation and the stage loading. However, one observation of Yamamoto et al. [4] is of particular interest to the present study. In certain cases, reductions in incidence decreased the strength of the secondary flows only up to a particular value of negative incidence. At incidences lower than this the secondary flow became stronger. Yamamoto et al. [4] explained this as resulting from fluid within the pressure surface separation migrating to the tip of their rotor blade, over the casing and into the secondary flow. However, Yamamoto et al. [4] did not investigate this further.

The continued trends towards reduced blade counts and increased stage loading [5] both infer that secondary flows are becoming more significant in limiting the performance of the modern low pressure turbine. This paper is therefore intended to complement Brear et al. [1] by studying the effect of the pressure surface separation on the secondary flow. A family of four blades, named A, B, C, and D, are examined (Fig. 1). Blade A is also studied in Brear et al. [1]. Blades B, C, and D all have the same suction surface profile and pitch as blade A, but different pressure surface profiles. At midspan and 0 deg incidence, blade A has a large pressure surface separation which extends from the leading edge to approximately 50 percent C_x. Blade D is also spanwise uniform, although this profile has been thickened in order to remove the pressure surface separation (Fig. 2). Blades B and C are three-dimensional designs. Both are the same as blade A in the central third of span, but are blended out to a thicker profile at the endwalls. Blade C has the same profile at the endwall as blade D, while blade B is thinner at the endwalls.

Experimental Methods

The experiments were performed in a linear cascade without varying the inlet boundary layer or blade incidence. Any variations in the secondary flows of the four blades must therefore only be due to the differing pressure surface geometries. The same cascade and tunnels as those presented in Brear et al. [1] are used. Further details are given in Brear [6]. All experiments were performed at 0 deg incidence and a Re_2 (based on chord) of 210,000. The cascade consisted of seven blades with parameters given in Table 1.

Blades B, C, and D were formed by placing an insert on the pressure surface of blade A. These inserts were fixed in place on the pressure surface and allowed a quick change between cascade geometries during a given set of experiments. At all times, an aerodynamically smooth transition between the inserts and the blade surface was maintained. However, the inserts also prevented measurement of the static pressure on the pressure surface of blade D at midspan and at 1 percent span on blades B, C, and D. The suction surface boundary layer on all four blades was tripped at 60 percent surface length (73 percent C_x) with a 0.31-mm stainless steel tube in order to limit the effect of variations in the suction surface flow.

Care was taken not to vary overall tunnel conditions throughout the experiments. The inlet boundary layer was measured 200 mm (158 percent C_x) upstream of the leading edge of the central cascade blade. Integral parameters are shown in Table 2. The shape factor agrees closely with that of a zero pressure gradient, turbulent boundary layer.

Area traverses were performed with a conical tip, 90-deg included angle, five-hole probe with 0.3 mm forward facing probe holes. The probe tip had an outer diameter of 1.7 mm. Pressure measurements were taken with an eight-channel, ''Scanivalve Zoc'' differential pressure transducer of ± 10 H_2O range. The probe was calibrated over the range ± 30 deg in both yaw and

[1]Present address: Department of Mechanical and Manufacturing Engineering, University of Melbourne, Australia

Contributed by the International Gas Turbine Institute and presented at the International Gas Turbine and Aeroengine Congress and Exhibition, New Orleans, Louisiana, June 4–7, 2001. Manuscript received by the IGTI, October 20, 2000. Paper No. 2001-GT-438. Review Chair: R. A. Natole.

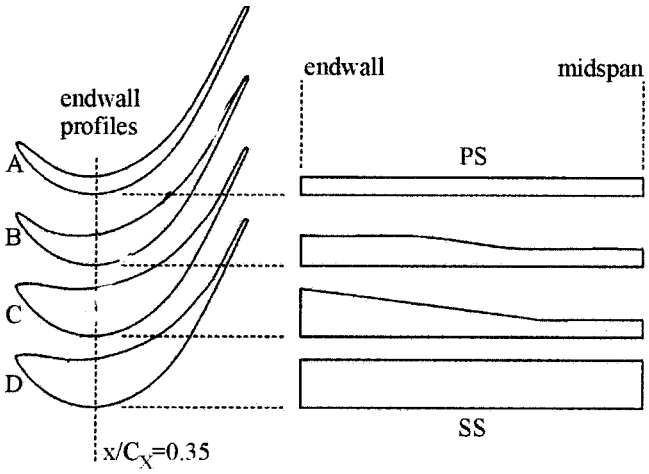

Fig. 1 Endwall and sectional profiles of blades A, B, C, and D

pitch and applied to the experimental data using the methods presented in [7]. The measurement grid consisted of 39 evenly spaced pitchwise points and 50 radial points. The radial points extended from 2.7 to 50 percent span and were concentrated nearer the endwall in order to obtain better resolution of the secondary flow region. In Table 3, the loss coefficient (Y_3) and exit yaw angle (α_3) were obtained from mass averaging from 2.7 to 50 percent span. The profile loss coefficient (Y_P) is a mass average from 30 to 50 percent span, which is the approximate extent of two-dimensional flow in Fig. 3.

Blade surface static pressure measurements were measured with a "Scanivalve" differential pressure transducer of ±35 mbar range.

Langston and Boyle's [8] method of flow visualization was used on blades A and D. This method uses a liquid to dissolve and

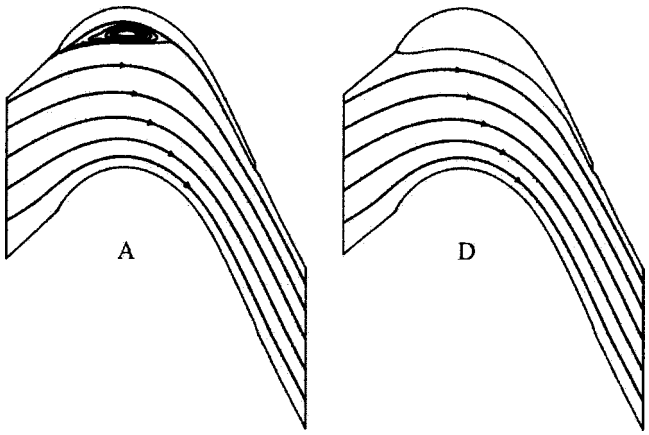

Fig. 2 Predicted streamlines at midspan for blades A and D

Table 1 Parameters of blades A, B, C, and D

chord, C (mm)	148.3
axial chord, C_X (mm)	126.8
pitch, s (mm)	103.8
span, h (mm)	375.0
inlet flow angle at i=0°, α_1 (°)	30.4
design exit flow angle, α_{2D} (°)	62.8

Table 2 Integral quantities of the inlet boundary layer 158 percent upstream of the cascade

δ*/h	θ/h	H
0.00611	0.00421	1.45

Table 3 Mass-averaged results of blades A, B, C, and D at 125 percent C_x from experiment and numerical predictions

	α_3 (°)		Y_3		Y_P	
	expt.	**pred.**	**expt.**	**pred.**	**expt.**	**pred.**
A	62.3	62.4	0.0450	0.0347	0.0282	0.0250
B	62.4	62.6	0.0418	0.0334	0.0286	0.0248
C	62.5	62.8	0.0404	0.0312	0.0282	0.0245
D	62.5	62.7	0.0403	0.0300	0.0281	0.0244

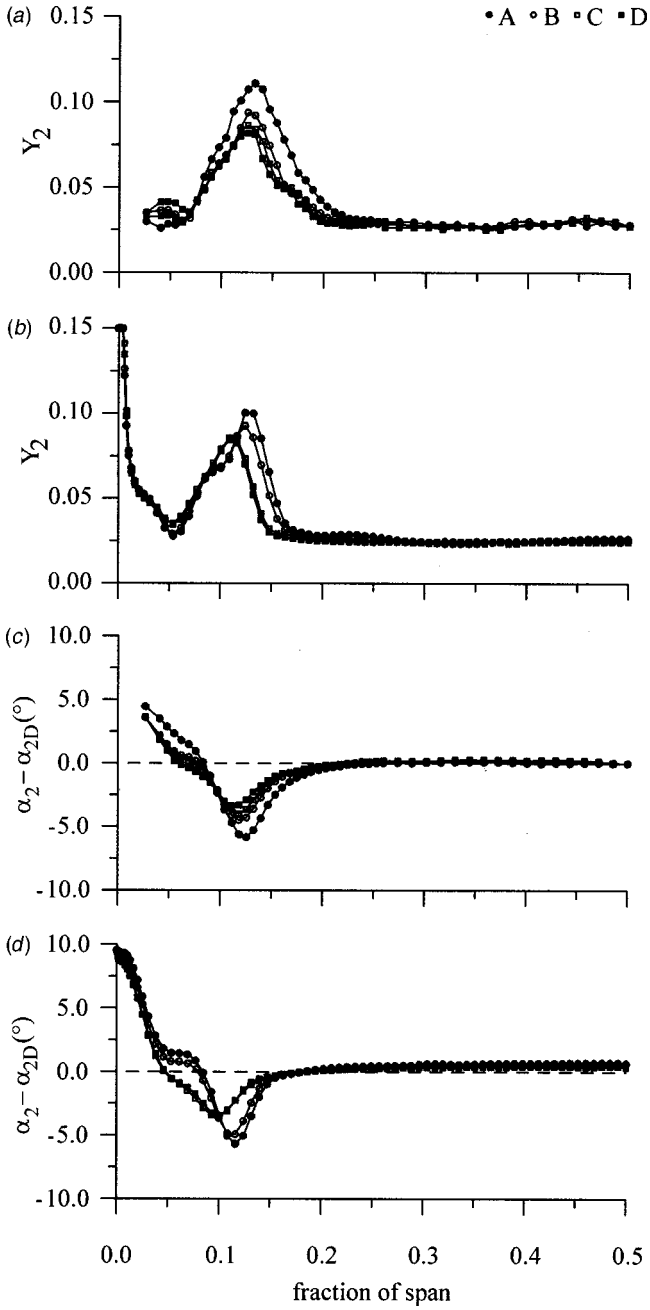

Fig. 3 Pitchwise mass-averaged (*a*) stagnation pressure loss (experiment), (*b*) stagnation pressure loss (predicted), (*c*) exit yaw angle (experiment), and (*d*) exit yaw angle (predicted) for blades A, B, C, and D at 125 percent C_x

transport dots of ink in the local direction of the skin friction. When the tunnel is turned on, the dots of ink become short streaks that reveal the structure of the surface streamlines. Synthetic oil of wintergreen (methyl salicylate) was used to dissolve the ink dots produced with a ''Staedler Permacolor 317'' pen drawn on a drafting film backing. This method of flow visualization is, of course, least accurate in regions of zero shear. It is therefore emphasized that the results obtained in regions of separated flow should be interpreted with great care. It is also noted that the suction surface trip wire was removed for these experiments only.

Numerical Predictions

The numerical predictions were performed using ''Multip99,'' which solves a thin shear layer form of the Reynolds averaged, Navier-Stokes equations supplemented by a mixing length turbulence model [9]. The predictions were performed at a cascade exit Mach number of 0.3 in order to accelerate convergence.

Other than their differing pressure surface geometries, all four blades had the same basic computational mesh. This mesh extended from 33 percent C_x upstream of the blade-row to 33 percent C_x downstream and had 109 axial, 49 circumferential, and 73 radial points. Preliminary numerical predictions showed that this axial extent of the mesh was effectively outside the potential field of the bladerow and that the quality of the solution was not compromised. A plane of symmetry was enforced at midspan with an inviscid boundary condition. Several numerical predictions were performed on coarser meshes and, in keeping with Hildebrant and Fottner [10], mesh independent predictions of the secondary flow were never observed. However, the mesh used in the present study appears to have produced results of sufficient accuracy for the arguments put forward.

Turbulent onset on the pressure surface was fixed at 25 percent C_x, which was the approximate location of turbulent onset in experiments (see Brear et al. [1]). On blade A, this gave a reattachment location of 59 percent C_x compared with the experimental result of 50 percent C_x. It is also noted that specifying transition onset at the pressure surface leading edge completely removed the pressure surface separation. Transition on the suction surface was specified at the same location as the boundary layer trip in experiments (73 percent C_x). The transition locations were then fixed for all subsequent predictions on the four blades. The endwall boundary layer was considered turbulent throughout the computational domain. Since the measurement of the inlet boundary layer was performed 158 percent C_x upstream of the bladerow, the boundary layer at the inlet to the computational domain was ''grown'' from the measured inlet boundary layer using zero pressure gradient, turbulent boundary layer relations. Thus, the integral quantities given in Table 2 were increased by 20 percent when used as inlet boundary conditions for the numerical predictions.

Results and Discussion

Area Traverses. Pitchwise mass averaged experimental and computational results for the area traverses are shown in Fig. 3. These show that from approximately 25 to 50 percent span, the exit yaw angle is effectively the same on all four blades and matches the design intent closely. Of note are the spanwise uniform profiles A and D. Even though blade D is considerably thicker than blade A, both blades have the same exit yaw angle and hence loading at midspan. It therefore follows that any spanwise uniform profile made from any section of the four blades studied will have the same loading since the profiles of blades B and C fall between those of blades A and D. The observed variations from 0 to 25 percent span are therefore not due to an intentional spanwise variation of loading. In this sense, this work differs from most three-dimensional design studies where spanwise variations in loading are deliberately introduced. Thus, the present work is not a typical three-dimensional design study even though blades B and C are three-dimensional designs.

Table 3 shows that the variations in pressure surface geometry have not changed the profile loss significantly. Therefore, the added thickness of blade D serves little aerodynamic purpose around midspan at 0 deg incidence in addition to the blade being considerably more costly to manufacture than blade A. This supports the findings of Brear et al. [1] and highlights the motivation behind the use of thin, solid blades; if aerodynamic requirements do not dictate the use of a thick blade, a thin blade is preferable because they are less costly.

The importance of achieving realistic predicted transition onset locations should be emphasized. Specifying transition at the leading edge on the suction surface resulted in profile losses of approximately 0.04. Other studies of turbine profiles that compared numerical predictions with experiments showed similar behavior [10,11]. Specifying transition at the leading edge on the suction surface is clearly physically unrealistic as the acceleration from the leading edge to peak suction on low-pressure turbine blades should keep the boundary layer laminar [12]. The considerable extent of laminar flow on low-pressure turbine blades therefore necessitates the use of realistic transition modeling if reasonable predictions of profile loss, and hence efficiency, are sought.

Figure 4 shows that the structure of the secondary flow at 125 percent C_x is the same as that reported in other studies of low-pressure turbine blades in linear cascade [2,3,10,11]. Furthermore, Fig. 3 and Fig. 4 show that there is considerable variation in stagnation pressure loss and exit yaw angle in the secondary flow region (from approximately 0 to 20 percent span). A trend is clearly apparent in Fig. 3: the peaks in stagnation pressure loss and underturning reduce in magnitude and move closer to the endwall as the blade thickness is increased. Experiments show that blade D, which has the lowest loss, achieved 10.2 percent lower mass averaged stagnation pressure loss (Table 3) and approximately 2 deg less peak underturning than blade A. Numerical predictions behave similarly, although the predicted stagnation pressure loss in the secondary flow region is significantly less than that found in experiment. It is emphasized, however, that even though the absolute value of the mass averaged stagnation pressure loss is significantly underpredicted, Table 3 shows that the relative variation between the results for blades A and D (0.0047) is the same as that found in experiment.

Entropy Generation Rates. The entropy generation rate throughout the entire computational domain was calculated for each of the four blades. The entropy generation rate per unit volume ($\rho\dot{s}$) was calculated from the rate of shear work performed by the fluid:

$$\rho\dot{s} = \frac{1}{T}(\mu+\mu_t)\left[\left(\frac{\partial v_\theta}{\partial x}+\frac{1}{r}\frac{\partial v_x}{\partial \theta}\right)^2+\left(\frac{1}{r}\frac{\partial v_r}{\partial \theta}+\frac{\partial v_\theta}{\partial r}\right)^2+\left(\frac{\partial v_x}{\partial r}+\frac{\partial v_r}{\partial x}\right)^2\right] \tag{1}$$

Figure 3 shows that the secondary flow region extends from approximately 0 to 20 percent span. This region was divided into a number of volumes that are defined in Fig. 5. The pitchwise extent of the ''pressure surface'' (PS) region was chosen such that this volume would contain the pressure surface separation on blades A and B. Similarly, the radial extent of the ''endwall'' (EW) region contained the inlet boundary layer. The circumferential extent of the ''suction surface'' (SS) and ''core'' regions were less important as the core region contained nearly isentropic flow. The remaining region is termed the 'downstream' (DS) region. Since the flow is steady and adiabatic, the total entropy generated in each of these domains can be expressed as an exit stagnation pressure loss coefficient

$$Y = \frac{2T_{01}}{\rho s h V_2^3 \cos\alpha_2}\int_V \rho\dot{s}\,dV \tag{2}$$

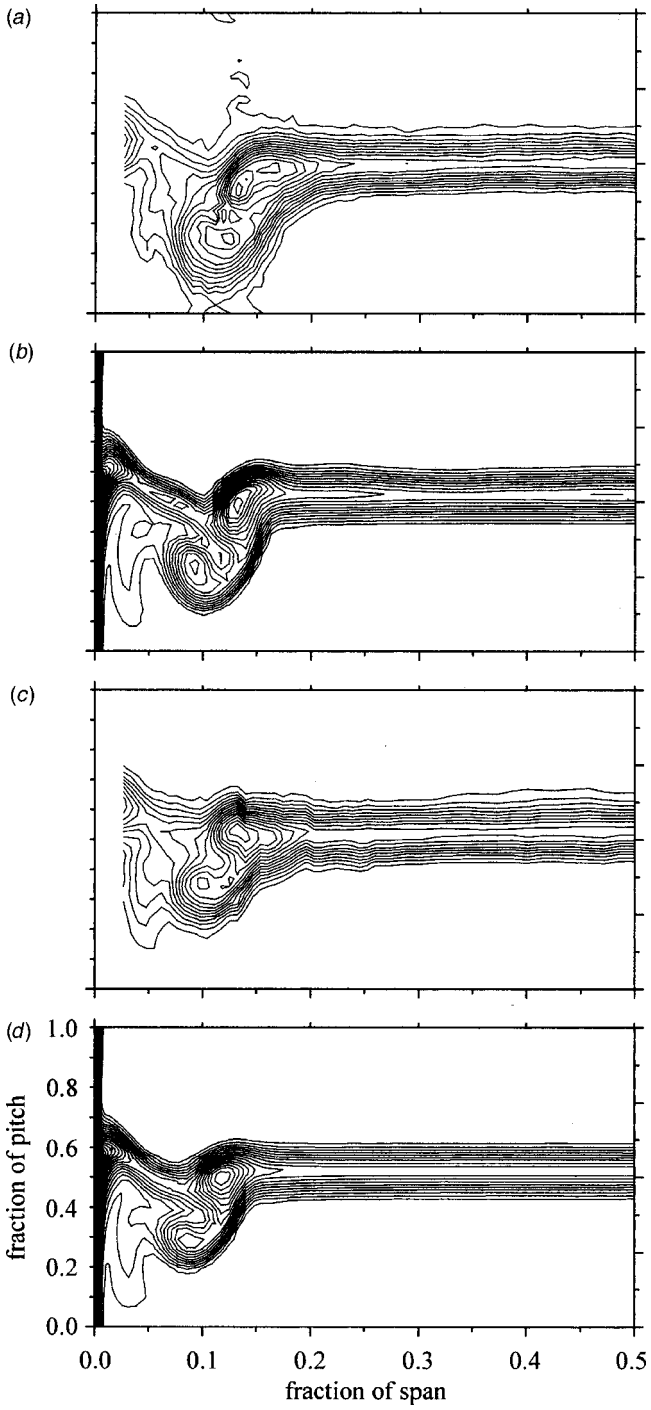

Fig. 4 Contours of loss coefficient (Y) at 125 percent C_x for (*a*) blade A (experiment), (*b*) blade A (predicted), (*c*) blade D (experiment), and (*d*) blade D (predicted) (contour level=0.025)

Results of this analysis are shown in Table 4. The total loss reduction from blade A to blade C is 0.0044, which is similar to the relative variations in both the experimental and predicted area averaged loss results in Table 3 (0.0047). However, it is also noted that this method of analysis predicts that blade D has a slightly larger loss than blade C. This is not in keeping with the results presented in Table 3 and is thought to expose the limitations of the numerical modeling in discriminating between the expected small differences in loss for these two designs.

Table 4 shows that the variations in the loss generated by the four different blades is not restricted to a particular region of the

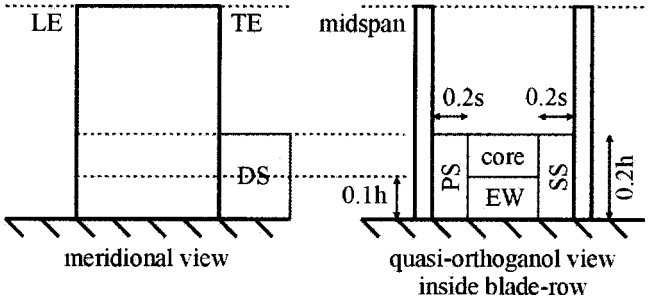

Fig. 5 Schematic of the regions defined in the entropy generation rate analysis

secondary flow. Instead, the reduction in loss from blades A through to D is achieved by reducing the loss created throughout the entire secondary flow region. Interestingly, the most significant reduction in loss generation is not the pressure surface region, but the suction surface region. This is perhaps expected as the suction surface region will contain the highest velocity fluid: it is generally the case in turbomachinery that the state of the surface flow near peak suction will be most significant in determining the total loss produced by the bladerow [13].

In order to reveal the mechanisms that cause these variations in entropy generation rate, a dissipation coefficient for the flow near the endwall was calculated

$$C_d = \frac{T_{01}}{\rho V_2^3} \int_0^{0.1h} \rho \dot{s} dr \tag{3}$$

where the spanwise extent of the integration was chosen to include the entire inlet boundary layer. It is noted that this quantity is normalized by the exit velocity of the cascade, and is therefore an indicator of the absolute entropy generation rate from 0 to 10 percent span at a given (x, θ) location.

Figure 6 shows contours of this dissipation coefficient on blades A and D. As discussed earlier transition onset on the pressure surface was specified to occur at 25 percent C_x. Figure 6 shows that there is a clear peak in dissipation coefficient at this axial location on blade A. As with the model presented in Brear et al. [1], numerical predictions therefore show that the pressure surface separation dissipates mean flow energy primarily through turbulent shear. The added thickness of blade D has removed the pressure surface separation, thereby removing a loss production mechanism. The loss produced in the PS region in Table 4 correspondingly decreases. The dissipation at mid-pitch is also noticeably different on blades A and D. On blade A, the region of high dissipation near the pressure surface extends across the blade passage and towards the suction surface. In contrast to this, the mid-pitch flow on blade D is characterized by lower levels of dissipation. Given that the entropy generation rate (Eq. (1)) is defined as a function of shear strain rates only, the variations shown in Fig. 6 must arise from variations in shear strain rates. Surface flow visualizations presented in the next section suggest the mechanisms by which this occurs.

Surface Flow Visualization. The pressure surface flow is strongly modified by the different blade designs (Figs. 7 and 8). Experiments and numerical predictions show that the pressure sur-

Table 4 Predicted stagnation pressure losses in each region of the secondary flow on blades A, B, C, and D

	EW	SS	PS	core	DS	total
A	0.0013	0.0169	0.0026	0.0001	0.0037	0.0247
B	0.0011	0.0167	0.0023	0.0001	0.0036	0.0237
C	0.0009	0.0145	0.0018	0.0001	0.0029	0.0203
D	0.0009	0.0151	0.0014	0.0001	0.0033	0.0209

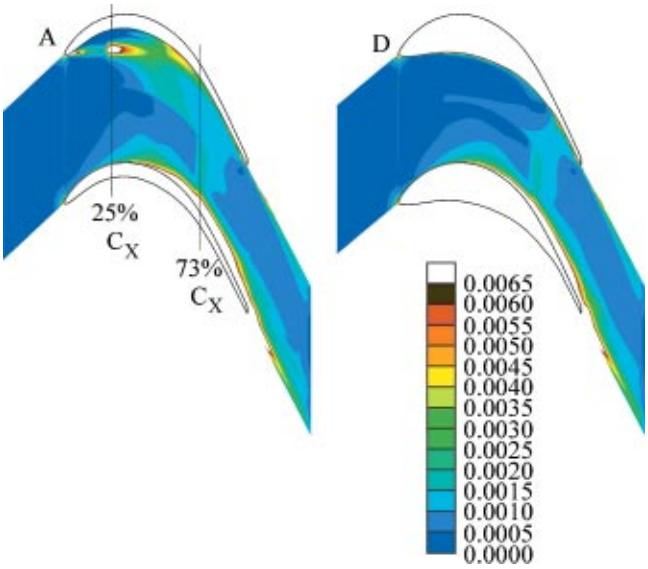

Fig. 6 Predicted dissipation coefficient for 0 to 10 percent span on blades A and D

face separation on blade A reattaches at 50 and 59 percent C_x, respectively, at midspan. In comparison to this, blade D has no pressure surface separation and most of the pressure surface flow follows approximately straight lines. Blades B and C, because of their increasing thickness, tend to suppress the pressure surface separation near the endwall.

Blade A also has the most circumferential endwall motion (Figs. 9 and 10). Although less obvious in experiments, the results for blade A show a region of the endwall flow near the pressure surface with negative axial velocity. The passage vortex separation line also impinges onto the suction surface slightly further downstream as the blade thickness increases. These trends suggest that the passage vortex becomes weaker from blades A through to D.

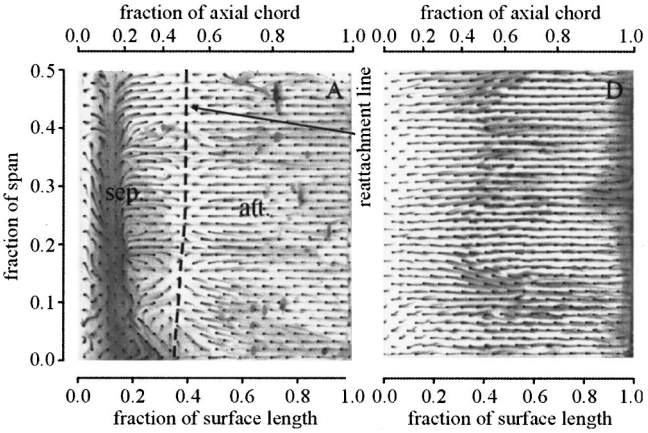

Fig. 7 Experimental flow visualization on the pressure surfaces of blades A and D

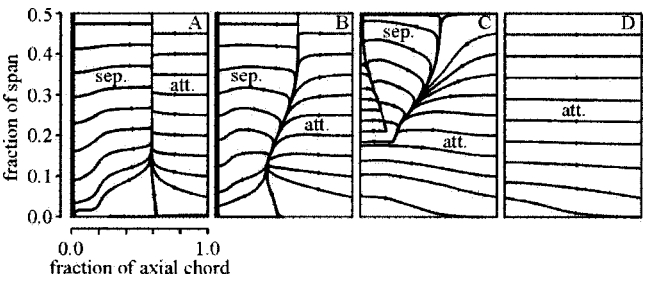

Fig. 8 Predicted flow on the pressure surfaces of blades A, B, C, and D

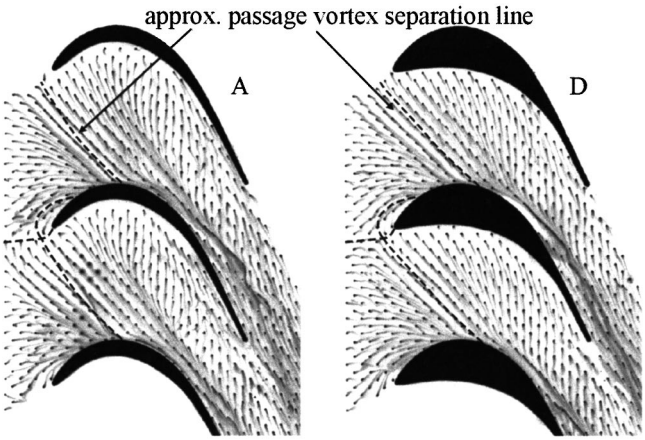

Fig. 9 Experimental flow visualization on the endwalls of blades A and D

There are also significant variations in the suction surface flow (Fig. 11). As in Figs. 9 and 10, the passage vortex separation line intersects with the suction surface earliest on blade A. This line reaches the trailing edge at approximately 15 and 10 percent span on blades A and D, respectively. The difference in the area of surface flow bounded by these separation lines on the two blades is considerable.

The structure of the interaction between the pressure surface separation and the passage vortex is now apparent. On blade D, the surface flow is typical of many turbines [2,3] and suggests that the inlet boundary layer and some of the attached pressure surface flow roll up into the passage vortex. In contrast to this, blade A has a more complex flow structure. Figure 12 shows streamlines that originate away from the endwall impinging onto the pressure surface near the reattachment point of the pressure surface separation. As a part of the recirculating flow, these streamlines then travel along the pressure surface and upstream while migrating radially towards the endwall. Once they have reached the endwall, these streamlines cross towards the suction surface and roll up into the passage vortex. This overall process gives rise to the surface flow visualizations presented in Figs. 7–11 and shows that the flow within the passage vortex is composed of fluid from both the inlet boundary layer *and the pressure surface separation.*

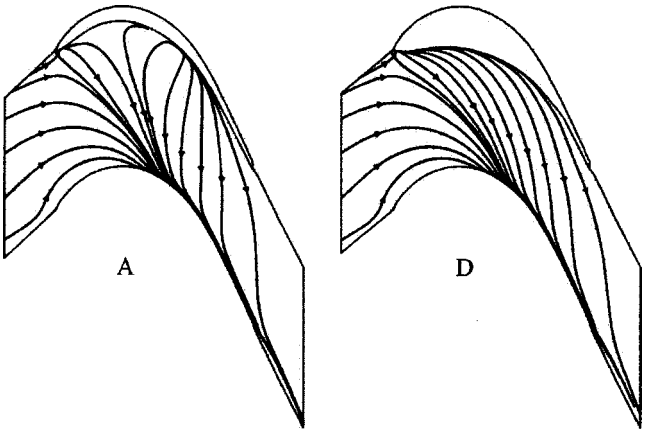

Fig. 10 Predicted flow on the endwalls of blades A, B, C, and D

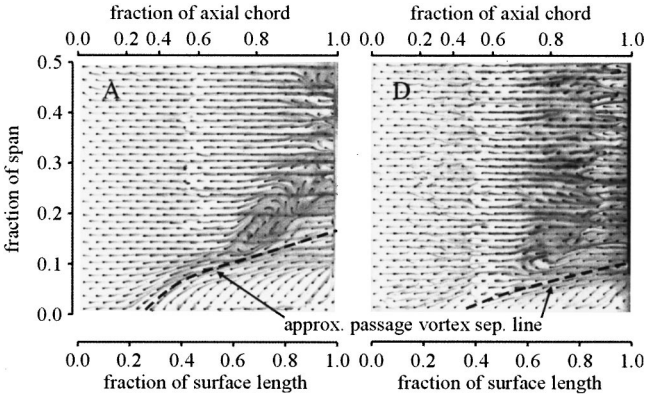

Fig. 11 Experimental flow visualization on the suction surfaces of blades A and D

The trend of reduced secondary flow strength with increased blade thickness is also in agreement with the area traverses presented earlier (Fig. 3). Furthermore, the surface flow visualizations also give a qualitative understanding of the physical mechanisms responsible for the variations in loss production. For example, the strongly circumferential endwall motion observed on blade A in Figs. 9 and 10 suggests that, relative to the other blades, the endwall boundary layers will be more highly skewed. As Fig. 6 showed, the entropy generation rate over the endwall on blade A is correspondingly increased. Table 4 showed that the most significant loss reduction occurs in the suction surface region defined in Fig. 5. Figure 11 also suggests a reduction in boundary layer skew from blades A through to D. Therefore, the secondary flow strength and the loss produced within the bladerow appear to be directly related.

Static Pressure Distributions. Figure 13 shows experimental and predicted isentropic velocity distributions of the four blades. At midspan, the isentropic velocities along the suction surface foreblade (0 to 50 percent C_x) become higher as the blade thickness increases. This is thought to be due to blockage effects. As discussed in Brear et al. [1], the location of the local minimum in the isentropic velocity on the pressure surface is close to the reattachment point of the pressure surface separation at midspan. Comparison of the local minima in Fig. 13 with the reattachment points in Figs. 7 and 8 confirm this both experimentally and in the numerical predictions. This also suggests that the overprediction

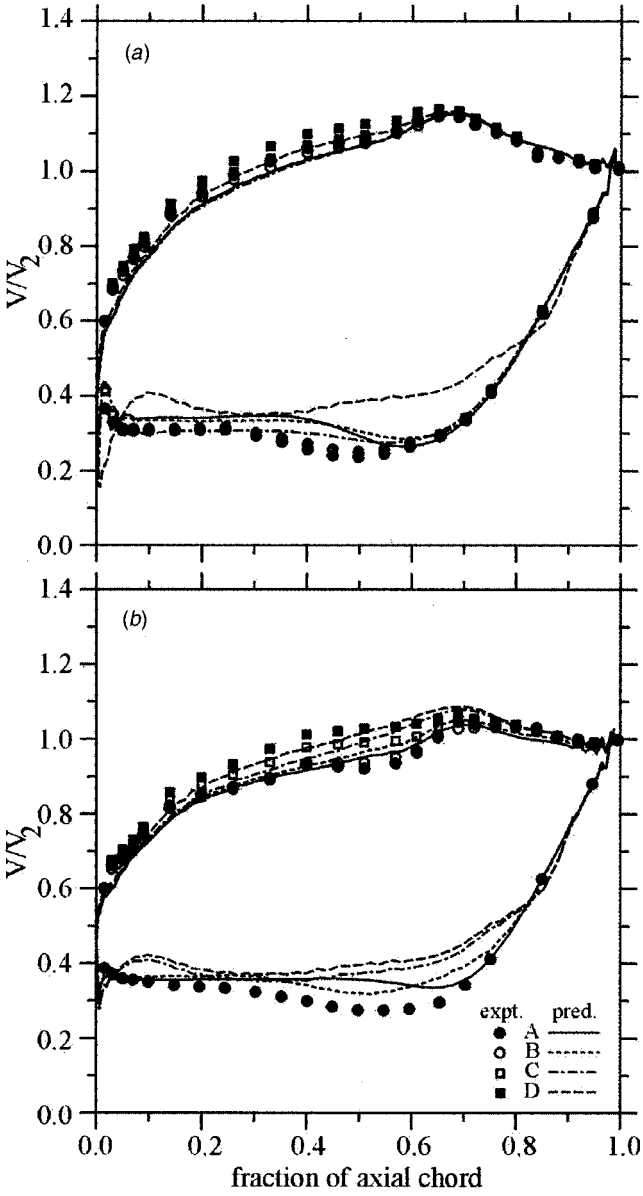

Fig. 13 Experimental and predicted isentropic velocity distributions of blades A, B, C, and D at (*a*) midspan, and (*b*) 1 percent span

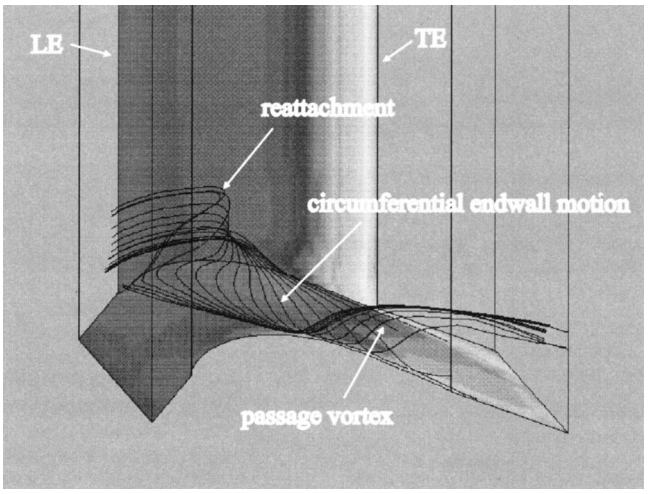

Fig. 12 Predicted streamlines close to the endwall on blade A

of the length of the pressure surface separation is the main cause of the different experimental and predicted isentropic velocities along the pressure surface.

All four blades have similar loading at midspan (Table 5). This is expected as the blades have the same pitchwise mass-averaged yaw angle at midspan (Fig. 3). Table 5 shows that predictions of both the foreblade loading and overall loading at 1 percent span increase with a decrease in secondary flow strength. As a result, the blade loading cannot be the determinant of the observed variations in secondary flow because all four blades have nominally the same loading at midspan and the trend in the loading at the endwalls is of the opposite sense to that required for secondary flows to strengthen.

A number of investigators have found that the overall development of the secondary flow in a turbine is particularly sensitive to the flow around the intersection of the foreblade and the endwall [11,14]. This can be explained using simple dynamics. Because the boundary layer momentum on the endwall and pressure surface is at its lowest around the foreblade, the flow is most easily

Table 5 Loading coefficients at midspan and 1 percent span from experiment and numerical predictions (fb is the foreblade from 0 to 50 percent C_x ov is the overall blade from 0 to 100 percent C_x)

	midspan				1% span			
	$C_{L,fb}$		$C_{L,ov}$		$C_{L,fb}$		$C_{L,ov}$	
	expt	pred	expt	pred	expt	pred	expt	pred
A	0.36	0.35	0.84	0.80	0.27	0.26	0.64	0.62
B	0.35	0.34	0.82	0.80	n/a	0.27	n/a	0.63
C	0.37	0.34	0.85	0.80	n/a	0.28	n/a	0.65
D	n/a	0.34	n/a	0.80	n/a	0.29	n/a	0.67

forced towards the suction surface of the adjacent blade by a given blade-to-blade pressure gradient. For a given blade loading, it is therefore best to impose the largest blade-to-blade pressure gradient in regions that are most resistant to cross-passage transport, i.e., regions where the flow has highest momentum. This is commonly referred to as ''aft-loading'' since, for a given amount of turning, profiles designed using this argument will tend to have as much loading as possible in the aft region of the blade.

Given that the blade loading cannot be responsible for the observed trend in secondary flow, the aft-loading philosophy suggests that the only other likely determinant is the momentum of the fluid close to the endwall. However, the usefulness of the endwall isentropic velocity distributions in the present argument is not clear. For example, several authors have found that the isentropic velocity along the suction surface near the endwall is strongly modified by the impingement of the secondary flow from across the blade passage [11,14]. Therefore, the causal link between endwall loading and secondary flow strength is not one way: the endwall loading drives the secondary flow, but the secondary flow also modifies the endwall loading. Using endwall isentropic velocities to explain some observed variation in secondary flow may result in a circular argument.

This difficulty can be avoided by using the isentropic velocity distribution of the two-dimensional blades A and D at midspan (Fig. 13(*a*)). Because of its added thickness, blade D has higher isentropic velocities over most of its surface. Near the endwall, blade D still represents the greater blockage to the incoming flow. The momentum of the fluid through the bladerow should therefore be higher on blade D. Fluid passing blade D is therefore less likely to be turned toward the suction surface and the secondary flow should be weaker.

Figures 7 and 8 showed clearly that the progressive increase in blade thickness from blades A through to D is matched by a decrease in the size in the pressure surface separation. This is expected since the blockage added onto the pressure surface should tend to reduce the intensity of the deceleration around the pressure surface foreblade and hence encourage the pressure surface boundary layer to remain attached. The existence or suppression of the pressure surface separation is therefore inseparable from the choice of isentropic surface velocity. Because the argument put forward makes no reference to whether any of the boundary layers are separated or attached, the pressure surface separation should then be viewed as part of an overall low momentum flow near the endwall. The results for blades B and C are also easily explained using this argument. Because they represent intermediate blockage of blades A and D, the momentum of the fluid near the endwall on blades B and C will lie between that on blades A and D. The observed trend in secondary flow over the four blades then follows.

Conclusions

The interaction of the pressure surface separation with the secondary flow can significantly affect the development of the secondary flow and the loss that it creates. This has been shown in a series of experiments performed on a family of four low-pressure turbine blades in linear cascade. Numerical predictions of these four blades show the same trend as that found experimentally.

A mechanism for this interaction has been suggested. This employs simple dynamics and is similar to the aft-loading argument commonly used in modern turbine design. The foundation of this argument rests on the momentum of the flow near the endwall. In particular, the existence of a pressure surface separation near the endwall is an indicator that the flow in this region has low momentum and will therefore respond to the imposed blade-to-blade pressure gradient by migrating strongly across the endwall. The strength of the secondary flow and the skewing of the blade surface boundary layers are therefore increased. Since the entropy generation rate is a function of the varying shear strain rates inside these skewed boundary layers, the loss production throughout the secondary flow region varies with the strength of the secondary flow.

Using this argument, the secondary flow strength and loss production can be reduced by raising the momentum of the fluid near the endwall. This has been shown by progressively thickening the blade on the pressure surface. As part of an overall increase in the momentum of the fluid near the endwall, additional blade thickness has the inevitable effect of reducing the size of the pressure surface separation, thereby suppressing the interaction between the pressure surface separation and the secondary flow.

Acknowledgments

The assistance of Prof. John Denton and Dr. Liping Xu of the Whittle Laboratory is most gratefully acknowledged. The authors would also like to thank Rolls-Royce, plc and the Defence Evaluation and Research Agency (MOD and DTI CARAD) for their generous financial support and permission to publish the work contained in this paper.

Nomenclature

C_d = dissipation coefficient
C_x = axial chord (m)
$C_L = \oint C_P d(x/C_X)$ = circumferential loading coefficient
$C_P = (P_{01}\text{-}P)/(P_{01}\text{-}P_2)$ = static pressure coefficient
h = span (m)
$H = \delta^*/\theta$ = boundary layer shape factor
s = blade pitch (m)
$\dot{s}$ = specific entropy generation rate (J/kg.K.s)
$V = V_2\sqrt{C_P}$ = isentropic velocity (m/s)
$Y = (P_{01}\text{-}P_0)/(P_{01}\text{-}P_2)$ = stagnation pressure loss coefficient
α = yaw angle
δ^* = displacement thickness (m)
μ = dynamic viscosity (kg/m.s)
θ = momentum thickness (m)
ρ = density (kg/m^3)

Subscipts

P = profile
t = turbulent
1 = cascade inlet
2 = pitchwise mass average at 125 percent C_x
$2D$ = design at cascade exit
3 = area mass average at 125 percent C_x

References

[1] Brear, M. J., Hodson, H. P., and Harvey, N. W., 2001, ''Pressure Surface Separations in Low-Pressure Turbines—Part 1: Midspan Behavior,'' ASME J. Turbomach., **124**, pp. –.
[2] Hodson, H. P., and Dominy, R. G., 1987, ''Three-Dimensional Flow in a Low-Pressure Turbine Cascade at Its Design Condition,'' ASME J. Turbomach., **109**, pp. 177–185.

[3] Hodson, H. P., and Dominy, R. G., 1987, ''The off-design performance of a low-pressure turbine cascade,'' ASME J. Turbomach., **109**, pp. 201–209.
[4] Yamamoto, A., Tominaga, J., Matsunuma, T., and Outa E., 1994, ''Detailed Measurements of Three-Dimensional Flows and Losses Inside an Axial Turbine Rotor,'' ASME Paper No. 94-GT-348.
[5] Curtis, E. M., Hodson, H. P., Banieghbal, M. R., Denton, J. D., Howell, R. J., and Harvey, N. W., 1996, ''Development of Blade Profiles for Low Pressure Turbine Applications,'' ASME J. Turbomach., **119**, pp. 531–538.
[6] Brear, M. J., 2000, ''Pressure surface separations in low pressure turbines,'' Ph. D dissertation, Cambridge University, Cambridge, UK.
[7] Dominy, R. G., and Hodson, H. P., 1993, ''An investigation of factors influencing the calibration of five-hole probes for three-dimensional flow measurements,'' ASME J. Turbomach., **115**, pp. 513–519.
[8] Langston, L., and Boyle, M. T., 1982, ''A New Surface-Streamline Flow-Visualisation Technique,'' J. Fluid Mech., **125**, pp. 53–57.
[9] Denton, J. D., 1992, ''The Calculation of Three-Dimensional Viscous Flow Through Multistage Turbomachines,'' ASME J. Turbomach., **114**, pp. 18–26.
[10] Hildebrant, T., and Fottner, L., 1999, ''A Numerical Study of the Influence of Grid Refinement and Turbulence Modelling on the Flow Field Inside a Highly Loaded Turbine Cascade,'' ASME J. Turbomach., **121**, pp. 709–716.
[11] Duden, A., Raab, I., and Fottner, L., 1998, ''Controlling the Secondary Flow in a Turbine Cascade by 3-D Airfoil Design and Endwall Contouring,'' ASME J. Turbomach., **121**, pp. 191–199.
[12] Halstead, D. E., Wisler, D. C., Okiishi, T. H., Walker, G. J., Hodson, H. P., and Shin, H. W., 1997, ''Boundary Layer Development in Axial Flow Compressors and Turbines—Part 3: LP turbines,'' ASME J. Turbomach., **119**, pp. 225–237.
[13] Denton, J. D., 1993, ''Loss Mechanisms in Turbomachines,'' ASME J. Turbomach., **115**, pp. 621–656.
[14] Weiss, A. P., and Fottner, L., 1995, ''The Influence of Load Distribution on Secondary Flow in Straight Turbine Cascades,'' ASME J. Turbomach., **117**, pp. 133–141.

Investigation of Unsteady Aerodynamic Blade Excitation Mechanisms in a Transonic Turbine Stage—Part I: Phenomenological Identification and Classification

Björn Laumert
KTH—The Royal Institute of Technology,
Heat and Power Technology,
100 44 Stockholm, Sweden
e-mail: laumert@egi.kth.se

Hans Mårtensson
Volvo Aero Corporation,
Propulsion Systems,
Military Engines Division,
461 81 Trollhättan, Sweden

Torsten H. Fransson
KTH—The Royal Institute of Technology,
Heat and Power Technology,
100 44 Stockholm, Sweden

Based on the results of time-dependent 3-D viscous computations the aerodynamic mechanisms that cause the unsteady pressure fluctuations on the vane and rotor blade surface of a high-pressure transonic turbine are identified and separately classified in a phenomenological manner. In order to be able to describe separately the influence of wake, potential and shock distortions on the blade surface pressure at design operation conditions, the stator exit Mach number is increased as to enhance the shock distortions and lowered as to enhance potential and wake distortions. In a comprehensive approach the observations from the off-design conditions are utilized to classify every major perturbation observed in the perturbation space-time maps at design operation conditions. The spanwise variations caused by the inherent 3-D nature of the flow field and promoted by the 3-D shape of the rotor blade are addressed. [DOI: 10.1115/1.1458577]

Introduction

In modern fan and turbine design, where great effort is put on lowering weight and raising performance, the challenge is to optimize for conflicting aerodynamic and structural demands. For example in the case of forced response it might be necessary to allow frequency crossings in the Campbell diagram as reported by Manwaring et al. [1]. In this case it is crucial to have knowledge about the blade pressure amplitudes and their relative phase to be able to foresee the structural response in order to avoid high cycle fatigue. Furthermore, in order to be able to influence the unsteady blade pressure characteristics in the design process it is necessary to have a deep understanding of the distortion sources and the aerodynamic interaction mechanisms.

In high-pressure transonic turbine stages the deterministic flow distortions seen by a blade row stem from upstream wakes, upstream and downstream potential field and shock impingement and reflection. Mayer [2] and Lefcourt [3] conducted very early analytical studies on the convection of wakes through airfoil rows and made predictions on the interaction with the airfoil surface. Later, Hodson [4] broadened the understanding of wake motion and wake generated unsteadiness in turbine rotor passages with flow field and blade pressure measurements in a large-scale low-speed test turbine stage. He also conducted computations with unsteady wake gust boundary conditions [5]. Doorly and Oldfield [6], Ashworth et al. [7] and Johnson et al. [8] investigated the impact of both wakes and shocks on downstream transonic rotor blades in a linear cascade facility, where the flow distortions were generated with upstream moving bars. With the help of Schlieren photographs, a complex shock reflection pattern was captured. Giles [9] and Saxer and Giles [10] also observed the presence of a complex shock reflection pattern in their numerical studies of high-pressure transonic turbine stages.

Contributed by the International Gas Turbine Institute and presented at the International Gas Turbine and Aeroengine Congress and Exhibition, New Orleans, Louisiana, June 4–7, 2001. Manuscript received by the IGTI, October 24, 2000. Paper No. 2001-GT-258. Review Chair: R. A. Natole.

A number of research groups have investigated different aspects of rotor stator interaction with measurements in realistic rotating test facilities, often accompanied with numerical computations: Lakshminaryana et al. [11] and Chernobrovkin and Lakshminaryana [12] investigated wake and potential distortions in a subsonic test facility. Dunn et al. [13] and Rao et al. [14] quantified the unsteady loading on the vane and the rotor blade of a transonic turbine stage. On the same facility Venable et al. [15] and Busby et al. [16] conducted studies on the impact of different axial gaps on the unsteady aerodynamics and turbine performance. As Dunn did in his investigations, Hilditch et al. [17] concluded that the large pressure fluctuations on the front rotor blade suction surface were caused by the direct impact of the vane trailing edge shock. It was also noted that the pressure side fluctuations were caused by the impact of the vane potential field. Three-dimensional aspects were investigated by Moss et al. [18]. They observed large pressure fluctuations at the rotor suction side near the root, which were associated with the impact of a stator wake loss core.

The aim of the present study is a detailed identification of the distortion sources that causes the pressure perturbations on the vane and rotor blade surface in a transonic test turbine with the help of 3-D viscous nonlinear time-dependent computations. The computational results have earlier been validated against experimental data and the agreement between measured and predicted unsteady blade pressures was good and allows the conclusion that the important unsteady phenomena were captured (Laumert et al. [19]). As only few studies so far have investigated the influence of 3-D effects, great care is taken to describe and explain radial variations. One novelty of the present investigation is the utilization of operation point variations to enhance shock, potential and wake effects to aid to and reassure the understanding of the observed surface pressure perturbations. In Part II of the paper, the connection between the identified distortions and the characteristics of the forcing function is established and force and moment amplitudes promoting model blade excitation modes are examined. In this sense this two-part paper establishes a link between flow distortions and possible blade excitations.

Table 1 Boundary and flow conditions for the computed test cases

Boundary Conditions	Design OP	Low M_2 OP	High M_2 OP
P_{01} [bar]	1.628	1.628	1.628
P_3 hub [bar]	0.533	1.185	0.48
T_{01} [K]	441.6	441.6	441.6
T_w [K]	293	293	293
Rotor speed [RPM]	6500	4250	7350
Vane t/e coolant	Inj. Slot, 3% coolant	Round, 0% coolant	Round, 0% coolant
A2/A1	1.0	1.0	1.04
A3/A1	1.09	1.09	1.24
Flow Conditions			
M_2 abs.	0.95	0.58	1.1
M_2 span 15% | 85%	1.0 | 0.92	0.61 | 0.56	1.17 | 1.05
M_3 rel.	0.92	0.36	0.85
$\dot{m}$ [kg/s]	10.62	8.98	10.42
P_2 [bar]	0.868	1.267	0.716
α_2 [deg]	-72.6	-72.6	-72.9
β_2 [deg]	-41	-39.2	-41.23
β_3 [deg]	63.1	60.4	61.4

Test Turbine

The computations were performed on the VKI BRITE EURAM test turbine geometry. This turbine is designed to simulate correctly the aerodynamic conditions in a modern HP aero-engine stage operating at transonic conditions with a design stator exit Mach number of 1.03 at 6500 RPM rotor speed. A large experimental program investigating the effects of rotor speed variations, cooling flow ejection and axial gap variations on the unsteady aerodynamics in the rotor blade row has been conducted and reported by Denos et al. [20,21]. They also presented a more detailed description of the turbine, including a 3-D view of the stage geometry. The computational predicted rotor blade surface pressures presented in this paper were earlier validated against Kulite measurements of the unsteady blade pressure at midspan on this test turbine [19].

Test Cases and Boundary Conditions

Starting point for the investigation of the blade pressure excitation mechanisms has been the computations at the test facility design operating conditions. The boundary conditions for the considered test case are listed in Table 1. A detailed description can be found in Laumert et al. [19].

As this investigation aims towards establishing the connection between the observed pressure perturbation on the blade surface and the excitation source, two additional test cases were studied in order to enhance the wake and the shock distortion by lowering and raising the vane exit Mach number to $M_2=0.58$ and $M_2=1.1$, respectively (computed, time and mass averaged at $0.23c_{ax}$ behind the stator trailing edge). At design operation conditions the vane is choked and the rotor is close to choking which made it necessary to increase the stator exit to throat area ratio and increase the rotor through-flow area in order to increase M_2. This was accomplished by increasing the casing-to-hub distance by 4% at the stator exit and 13% at the rotor exit for the high Mach number case. The boundary conditions for the off design test cases were chosen such as to preserve the blade loading characteristics by maintaining the relative flow angles.

Only for the base test case the nominal stator trailing edge geometry with ejection slot and cooling gas ejection was utilized. For the other cases a round trailing edge was used as it was shown earlier by Laumert et al. [19] that this simplification only had minor influence on the rotor unsteady aerodynamics.

The computations were performed with pressure-based boundaries specified at stage inlet and outlet. Inlet conditions were given as radial profiles of total pressure and temperature. At the stage outlet a radial pressure equilibrium condition was imposed. Temperature walls were employed with a nonslip boundary condition. The turbine rotor is not shrouded and the tip gap was included in the computational model. The tip gap was estimated to 0.3% of the rotor span. It has to be mentioned that the number of blades was reduced from 43 stator and 64 rotor blades to 42 and 64, respectively, in order to facilitate the periodicity requirements. This was done in a simple fashion without any modification to the airfoil geometry. Two stator and three rotor passages were utilized in the computations.

The boundary conditions and the computed time and mass averaged flow conditions for all test cases are summed in Table 1.

Flow Solver Description

Numerical Method. The equations used to model the viscous flow are the Favre-averaged Navier Stokes equations for compressible flow expressed in the cartesian coordinate system. The equations are extended to turbulent flow using the k-ε turbulence model formulation with standard wall functions.

The 3-D Navier Stokes flow solver VOLSOL developed at Volvo Aero Corporation was used. The numerical method to solve the governing equations is based on an explicit, time-marching, cell-centered finite-volume procedure. The convective fluxes are reconstructed with a third order upwind biased scheme, which is based on the characteristic variables and associated characteristic velocities. The viscous fluxes are computed with a compact second order accurate centered flux scheme. Time integration is handled with an explicit three-stage Runge-Kutta procedure. Eriksson [22] provided a detailed description of the numerical method.

A second-order sliding grid interface method was employed to pass flow information between the stator and the rotor frame of reference.

Gas Injection Model. An integral film cooling injection model simulates gas injection by adding the influence of the penetrating jets as source terms in the governing equation. The injection region, mass flow, Mach number and temperature of the injected gas are specified as user input based on empirical basis or experience. Details of the method have been presented by Dahlander et al. [23].

Grids and Boundary Layer Treatment

The flow solver uses structured multi-block grids. The grid generation code uses a parameter-controlled module-script, designed for turbine blades. The grids are nonorthogonal body-fitted. A picture of the computational grid has been presented by Laumert et al. [19]. The grid size was typically 759039 nodes for the unsteady computations. Five radial nodes were used to model the rotor tip gap.

An O-grid was used around the blades with controlled stretching in the direction normal to the wall. The boundary layers were resolved down to a $y+$ mean value of 28 for the standard wall function computations.

Computational Approach

The PVM software package was used for code parallelization. Steady state solutions were used as initial conditions for the un-

steady computations, which needed 4400 time steps per period. The size of the maximum deviation in static pressure on the rotor blade at midspan between two periods served as convergence criteria. Convergence was reached after eight periods, when the deviation was less then 0.1%. Due to the nonlinear processes convergence to exactly zero in this sense cannot be expected, as sub harmonics and/or portions of uncoherent flow may be present.

Data Evaluation

Space-Time Maps. The blade surface pressure perturbations were analyzed with the help of time-space maps at three radial positions, namely 15, 50, and 85% span. The contour levels in the time-space maps represent the perturbation from the time mean static pressure normalized with the stage inlet total pressure $(P - P_{\text{time-mean}})/P_{01}$. The abscissa represents the pressure variation in time where the time is normalized by the stator blade passing period. At time=0, the stator and rotor leading edge are axially aligned at midspan. The ordinate represents the pressure variation along the blade wetted surface (arc length) from the leading edge (zero) along suction (negative half) and pressure (positive half) side to the trailing edge. The arc length is normalized by the total blade arc length.

Distortion Tracking. The phenomenological linking of the blade pressure perturbations with flow distortions is accomplished by comparing instantaneous pressure perturbation contour plots of the blade passages with contour plots that enable to track the movement of a specific distortion through the stage. The shock motion is captured with contours of the pressure gradient modulus $|\nabla P|$. Information about the relative position of wakes and shocks is gathered in contour plots of the density gradient modulus $|\nabla \rho|$. Additionally the wake distortion appears as a negative jet with counter-rotating vortices in the perturbation velocity flow vector field.

Results and Discussion

Shock Motion. Before specifically discussing the surface pressure perturbation events it is helpful to have established the shock motion in the turbine stage. As the stator trailing edge shock is weak and rather difficult to capture at design operation conditions, the shock motion is presented for the high M_2 test case, featuring a stronger shock. Though the shock angles as well as characteristic speeds differ for the two operation conditions, conclusions about the shock influence at design operation conditions can still be drawn in the comparative discussion of the surface pressure perturbations.

The shock motion is visualized with contour plots of the pressure gradient modulus at midspan. The study was supported with pressure perturbation contour plots that are not shown here due to space limitations. Figure 1 shows the blade passage at 10 successive time steps during one vane passing period in the rotor frame of reference. The time t is related to the position of the marked rotor blade relative to the marked stator blade. The stator trailing edge shock position and reflections are marked with solid and dotted lines, respectively. The arrows indicate the shock wave movement. The discussion starts with the picture of the blade passage in the upper left corner at $t=-0.06$. At this instant in time the vane trailing edge shock (S) is in contact with the front suction side of the rotor blade close to the leading edge and a shock reflection formation (S-R1) is evident. The open end of the reflection bows around the rotor blade suction side towards the lower rotor blade pressure side, while the wave front travels upstream towards the vane lower suction surface (see $t=0.06-0.24$). The downstream part of the wave hits the lower rotor blade pressure surface, is partly reflected (S-RR1) and distorted (see $t=0.24$). The wave bulk hits the vane suction surface at approximately $t=0.30$ and is reflected (S-RR2) towards the rotor blade passage (see $t=0.34$). This last reflected wave is rather weak and hardly notable in the perturbation pressure.

When the trailing edge shock passes the rotor leading edge, the high pressure behind induces a Mach wave (M) to travel along the rotor blade pressure surface (see $t=0.44$). The shock front itself stretches into the rotor blade passage until it hits the adjacent rotor blade suction surface, where it is partly reflected (see $t=0.54-0.64$). The reflected wave (S-R2) travels towards the lower rotor blade's aft pressure surface where it again is reflected (see $t=0.74$). It should be noted that the present shock motion is very similar to the one observed by Johnson et al. [8] in a linear cascade facility.

Blade Surface Pressures. The surface pressure perturbations are analyzed for both the vane and the rotor blade. The investigation starts at midspan, where the subsonic and high stator exit Mach number case aid to the understanding of the design condition test case. Thereafter, spanwise variations are reported and discussed for the design case only.

Vane at 50% Span. Space-time surface pressure perturbation maps for the subsonic, the high M2 case and the design case are shown in Figs. 2, 3, and 4, respectively. All three show a characteristic pattern of three high/low pressure regions (peaks are marked P-SS, SR-SS in the figures) on the aft suction side of the stator blade corresponding to three rotor blade passing events during the presented time. The subsonic case shows excitation levels of an order of magnitude lower compared to the other cases. In the subsonic case the perturbations are caused by the direct impact of the alternating passing of the high and low pressure regions of the downstream rotor potential field. In the high Mach number case the perturbation is caused by the impact of the stator trailing edge shock reflection on the rotor front suction surface, denoted S-R1 in Fig. 1. The same mechanism is responsible for the perturbations at design operation conditions.

In the high Mach number case the influence of the downstream unsteadiness is limited to the region downstream the choking line, which is located at arc length $L_a=-0.3$ on the vane suction side. At this position, a second narrow band of high/low pressure regions is located. The peaks are denoted S-SS in Fig. 3. The passing rotor increases the passage blocking periodically and causes a termination of the expansion through the vane nozzle. The termination is featured by the formation of a vane pressure side trailing edge shock that hits the neighboring vane suction side, causing the pressure peak S-SS in the throat region. The shock formation is indicated in Fig. 1, time instants $t=-0.04-0.24$. The shock is designated SP in the figure.

At design conditions the formation of a vane pressure side trailing edge shock is not evident. As earlier described in [19] the shock formation is inhibited due to the cooling gas injection. The pressure variations (peaks are designated SP-SS in Fig. 4) in the throat area between arc length $L_a=-0.2$ and -0.3 are associated with the upstream movement of a sonic pocket that is located downstream the choking line. The movement is indicated with an arrow in Fig. 4.

In the subsonic and the high Mach number cases no pressure variations are evident on the vane pressure side. These cases were computed with a round stator trailing edge geometry without cooling gas ejection. In the design case, pressure variations are observed at the ejection slot location. See Fig. 4. It should be noted that these could have a considerable influence on the cooling performance.

Vane Spanwise Variations at Design Conditions. The vane pressure perturbation space-time maps for design operation conditions at 15 and 85% span are shown in Figs. 5 and 6, respectively.

The same characteristic perturbation pattern is observed as the map at 50% span. Though the pattern is the same, the perturbation strength differs slightly. As the stator exit Mach number increases from casing to hub, the trailing edge shock (S in Fig. 1) and the associated reflection (S-R1 in Fig. 1) increases in strength and

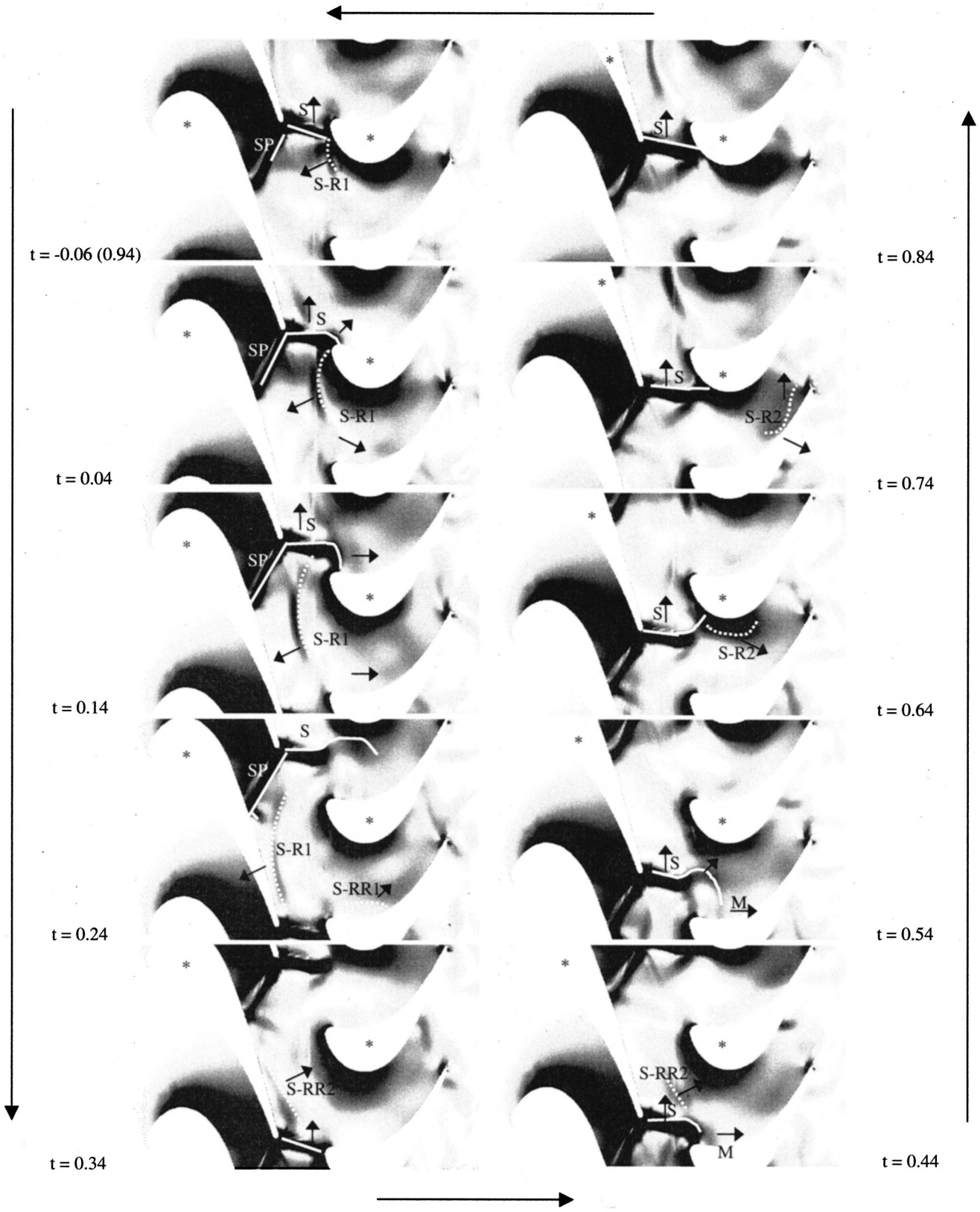

Fig. 1 Contour plots of the pressure gradient modulus showing the stage passage at midspan. High Mach number OP.

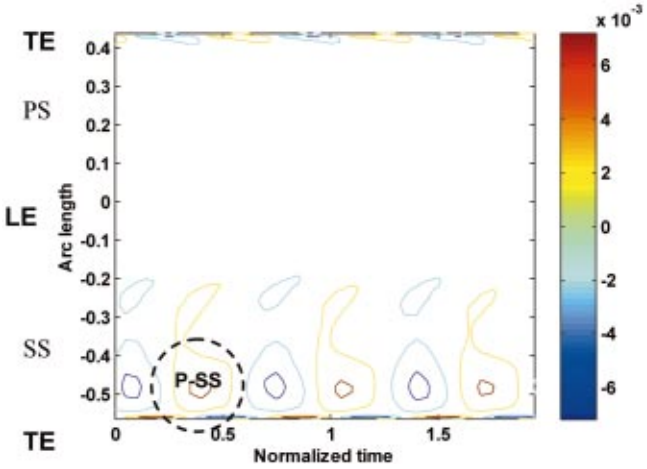

Fig. 2 Space-time map of the vane surface pressure perturbations for the subsonic test case at 50% span

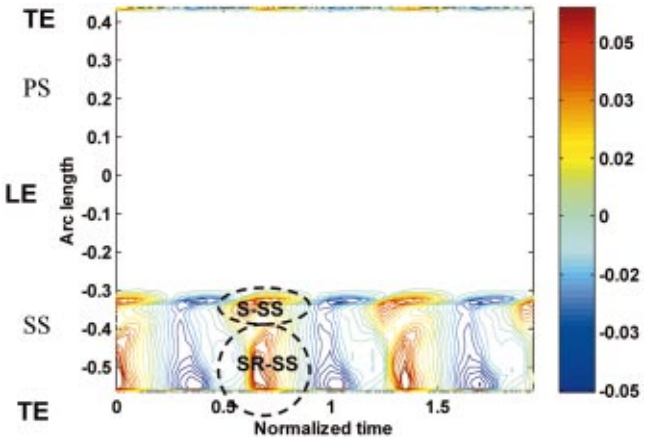

Fig. 3 Space-time map of the vane surface pressure perturbations for the high M2 case at 50% span

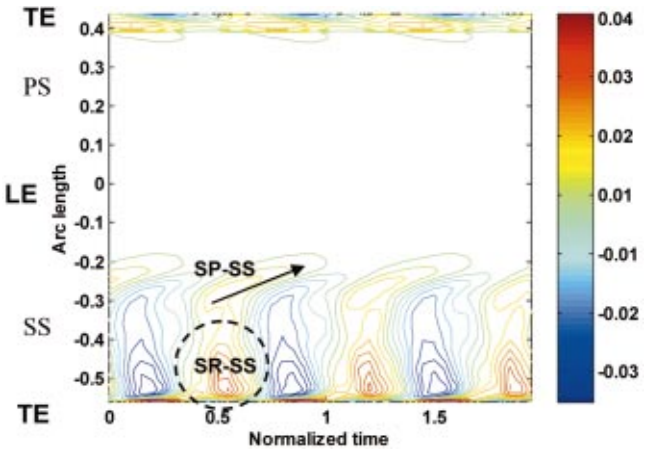

Fig. 4 Space-time map of the vane surface pressure perturbations for the design test case at 50% span

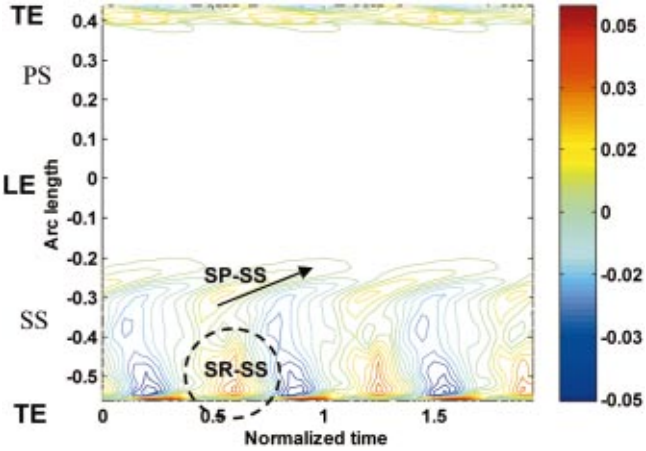

Fig. 5 Space-time map of the vane surface pressure perturbations for the design test case at 15% span

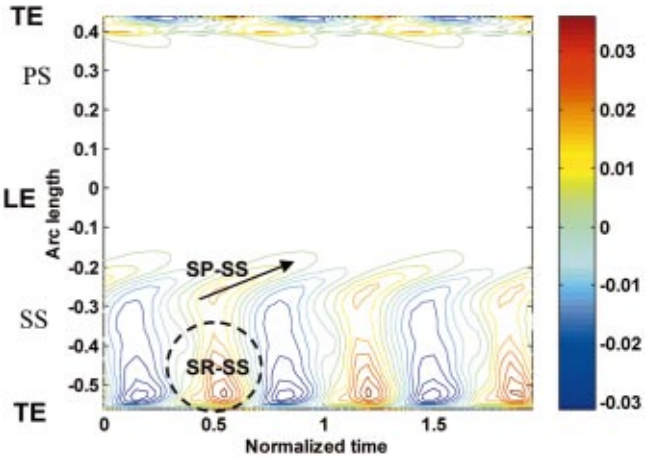

Fig. 6 Space-time map of the vane surface pressure perturbations for the design test case at 85% span.

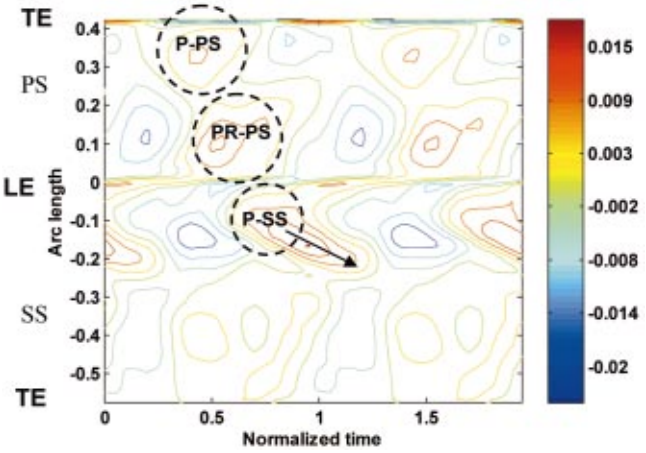

Fig. 7 Space-time map of the rotor surface pressure perturbations for the subsonic test case at 50% span

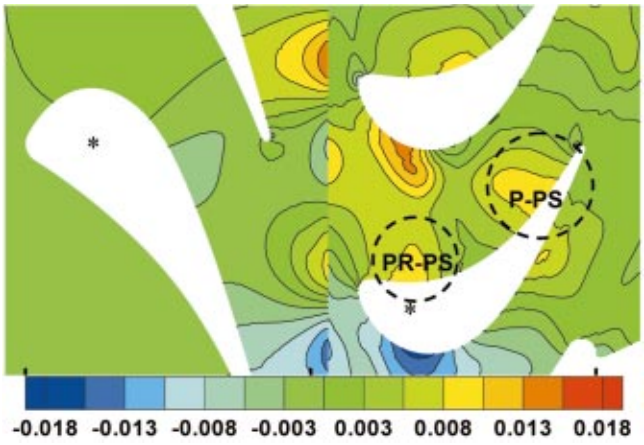

Fig. 8 Contour plot of the pressure perturbations for the subsonic test case at $T=0.43$. Stage passage at 50% span.

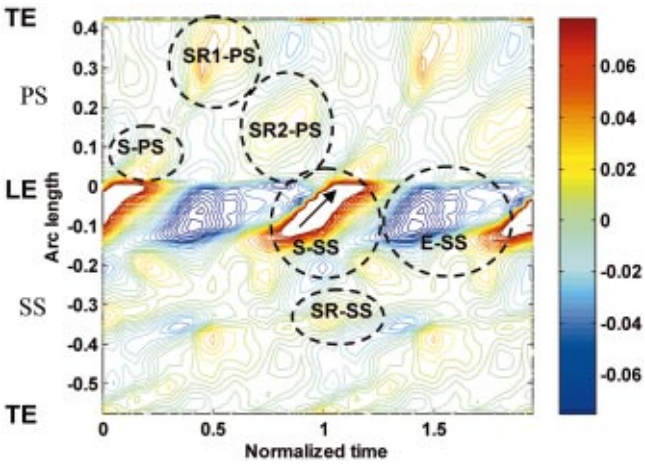

Fig. 9 Space-time map of the rotor surface pressure perturbations for the high M2 test case at 50% span

thus the perturbation SR-SS, caused by the shock reflection, is stronger towards the hub and weaker towards the tip.

Rotor at 50% Span. The discussion will start with the subsonic case. As there is no trailing edge shock present in this test case the rotor blade pressure excitations are related to the impact of the upstream potential field and the wake travelling through the rotor blade passage. Figure 7 shows the pressure perturbation space-time map of the rotor blade surface. During the presented time a rotor blade ''sees'' two vanes passing.

The pressure side perturbations are mainly connected with the alternating impact of the high and low pressure region of the vane potential field. They are not associated with any characteristic velocity relative to the blade surface. The pressure perturbation P-PS at the aft is caused by the direct impact of the potential field. The perturbation PR-PS towards the front appears later than P-PS though the front region passes the vane trailing edge earlier than the aft. PR-PS is most likely caused by a reflection of the potential field on the neighboring rotor blade suction surface. The time delay is associated with the wave front traveling across the passage. This excitation mechanism is illustrated in Fig. 8, showing a pressure perturbation contour plot of the stage blade passage at midspan. The marked rotor blade has a relative position to the marked vane corresponding to a normalized time $t=0.43$. Note that the pressure perturbations are not frame independent. Therefore a discontinuity is seen at the rotor-stator interface.

The pressure perturbation P-SS at the front suction side of the rotor blade is also strongly influenced by the direct impact of the vane potential field. But the pressure peak is also governed by the wake passing, causing the perturbation to travel with the wake downstream along the suction side. The wake-induced movement is indicated with an arrow in Fig. 7. Lakshminarayana et al. [11] and Chernobrovkin and Lakshminarayana [12] have earlier described the wake excitation mechanism in detail. Downstream the rotor blade crown at $L_a=-0.2$, the pressure perturbations are relatively weak and will not be addressed any further.

In the next section the high stator exit Mach number case will be discussed in order to relate the earlier discussed shock motion to pressure events on the rotor blade surface. Compared to the subsonic case the excitation level is almost an order of magnitude higher in the case.

The pressure perturbation space-time map of the rotor blade surface is shown in Fig. 9. The three pressure peak events designated S-PS, SR1-PS and SR2-PS on the pressure side are all related to the vane trailing edge shock motion in the rotor blade passage. When the vane trailing edge shock passes the rotor leading edge it bows around and influences the pressure side for a short time period. The shock motion is visualized in Fig. 1, $t=0.14$. This mechanism causes the pressure rise S-PS in Fig. 9. The peak SR1-PS origins from the shock reflection S-R2 as it impinges on the aft pressure side of the rotor blade. See also Fig. 1 at $t=0.74$. Pressure perturbation SR2-PS is caused by the impact of the shock reflection that bows around the rotor leading edge and impinges on the pressure surface of the neighboring blade. This shock reflection path can be followed in Fig. 1, time $t=-0.06-0.24$.

When the stator trailing edge shock sweeps the rotor suction surface from the blade crown to the leading edge a strong pressure peak follows its path. This pressure peak is designated S-SS in Fig. 9 and the motion is indicated with an arrow. The shock is followed by an expansion causing the pressure to fall. The pressure minimum is designated E-SS in Fig. 9, and the motion is indicated with an arrow.

The impact of the shock reflection S-R2 in Fig. 1 ($t=0.74$) on the rotor suction surface is the cause of the pressure peak in the rotor throat region designated SR-SS in Fig. 9. The other peaks on the aft suction surface are most likely connected with shock wave reflections, but they could not be followed in the pressure gradient contour plots.

The foregoing observations lead to the conclusion that the stator trailing edge shock is the dominant pressure perturbation source in the high Mach number case. Potential field and wake excitations are certainly present but their influence is negligible.

The pressure perturbation excitation mechanisms at design test conditions are discussed in the light of the observations and knowledge from the subsonic and the high Mach number test case. Relations between the observed pressure perturbations in the design case and the other cases are established by the study of three characteristics of the pressure fluctuations: location in time and space, shape (or movement along the blade surface) and perturbation strength. During a blade passing period, three major pressure events are observed on the rotor blade's pressure surface: Pressure peak P-PS in Fig. 10 has the same origin as peak P-PS in Fig. 7 in the subsonic case, namely the direct rotor potential field on the aft pressure surface. Pressure peak PR-PS in Fig. 10 has its counterpart in pressure Peak PR-PS for the subsonic case visualized in Fig. 7. It has its origin in the reflection of the vane potential field on the front rotor suction side. In the high Mach number case this event is certainly present, but hidden by the shock reflection based excitation SR2-PS. As the shock reflection is present in the design case as well, a corresponding perturbation SR-PS is seen in Fig. 10, though it is located slightly further downstream on the rotor pressure surface.

The front suction side of the blade at design conditions is—as earlier described in the high Mach number case—dominated by

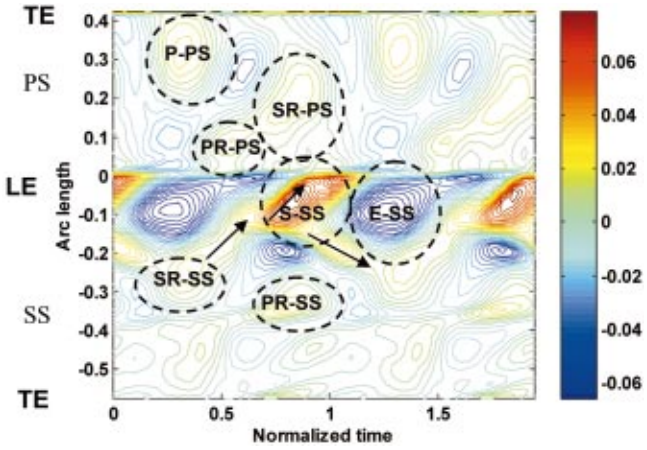

Fig. 10 Space-time map of the rotor surface pressure perturbations for the design test case at 50% span

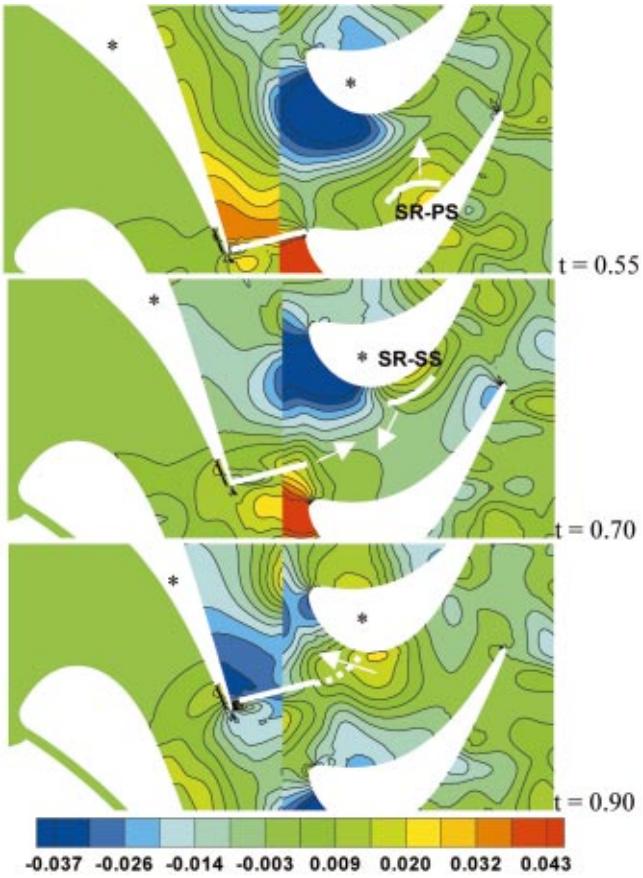

Fig. 11 Contour plot series of the pressure perturbations for the design test case. Stage passage at 50% span.

the direct impact of the stator trailing edge shock. The associated pressure peak and minimum are designated S-SS and E-SS in Fig. 10. The pressure peak PR-SS at the blade throat region is caused by a potential field reflection analogously to the shock reflection that causes the peak SR-SS in the high Mach number case. See Figs. 9 and 10.

Between the blade position $L_a = -0.15$ and the blade throat region at position $L_a = -0.3$ an upstream and a downstream moving perturbation is observed. The fluctuation movements along the blade surface are depicted with arrows in Fig. 10. The downstream travelling pressure perturbation is associated with the wake movement in the blade passage (compare with the subsonic case in Fig. 7). The upstream travelling perturbation is not fully understood, but the following explanation is suggested: In the design operation condition test case, the shock reflection S-RR1 in Fig. 1 at time $t = 0.24$ hits the rotor pressure side slightly downstream the position that is observed in the high Mach number case, causing the perturbation SR-PS in Fig. 10. At this position on the blade surface the pressure side is turned to face more in axial direction and the wave is re-reflected and travels towards the neighboring suction side where it causes the pressure peak SR-SS in Fig. 10. It then refracts with the trailing edge shock and is swept around the crown of the blade, following the shock motion towards the leading edge of the blade. The mechanism is illustrated in the series of pressure fluctuation contour plots of the blade passage in Fig. 11. The suggested wave motion and the location of the trailing edge shock as well as the associated pressure perturbations are marked in the figure. The time t is related to the position of the marked rotor blade relative to the marked stator blade.

Rotor Spanwise Variations at Design Conditions. In principle all pressure perturbation events observed at midspan are also present at 15% span, though their location in the time space-map is slightly changed. Compare Figs. 10 and 12. There are additional perturbations seen at 15% that will be addressed in the following. Due to the increased shock strength and the change in rotor geometry towards the root, a first shock reflection emanates shortly after the vane trailing edge shock impact on the rotor suction side. The shock reflection travels across the blade passage and hits the aft pressure side of the neighboring blade, causing the pressure peak SR2-PS in Fig. 12. The periodical appearance and movement of a weak suction side trailing edge shock causes the pressure peak S2-SS near the trailing edge on the blade suction side.

At 85% span it is observed, that the potential field perturbations are less pronounced compared to the lower span positions. On the pressure side the potential influence is only seen in pressure peak P-PS. The pressure peak SR-PP in Fig. 13 corresponds to the shock reflection peak SR-PP in Fig. 10 at 50% span. Furthermore it can bee seen that the vane trailing edge shock directly influences the front pressure side at 85% span. The resulting pressure peak is depicted S-PS in Fig. 13. On the suction side the pressure events observed at 50% span are present at 85% apart from the potential reflection PR-SS in Fig. 10, which is missing in Fig. 13. The different location of the pressure peaks in the space-time map between the 50% span and the 85% position are mainly attributed to the three dimensional shape of the rotor blade which results in a variation of the relative position of the spanwise rotor sections relative to the stator trailing edge.

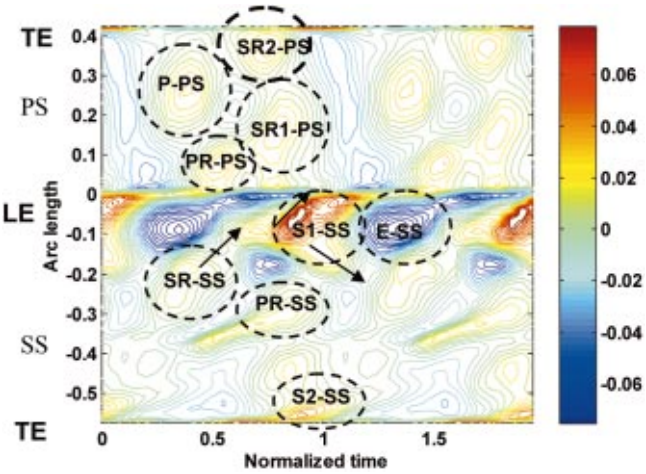

Fig. 12 Space-time map of the rotor surface pressure perturbations for the design test case at 15% span

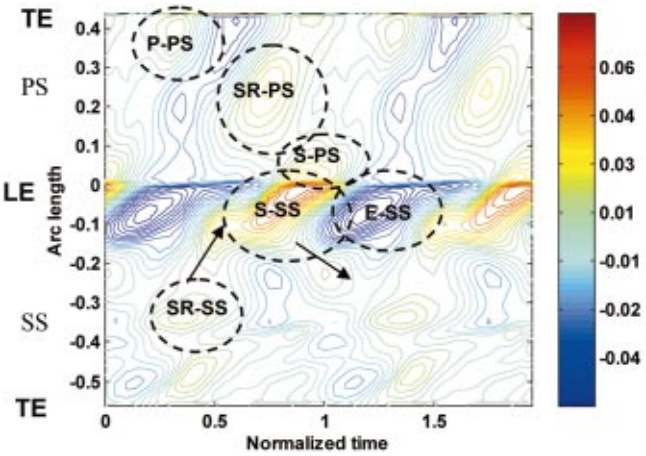

Fig. 13 Space-time map of the rotor surface pressure perturbations for the design test case at 85 % span

Conclusions

A 3-D computational study has been performed to investigate the vane and rotor blade pressure fluctuations in a transonic turbine stage. The goal was to establish the connection between the excitation source and the observed pressure perturbations on the blade surface.

In the investigations of the vane surface pressure fluctuations it is concluded that the blade at suction surface is periodically affected by the downstream rotor potential field at the subsonic operation conditions.

At the flow conditions with the high stator exit Mach number and the design case on the other hand, the pressure perturbations are caused by the periodical impact of the stator trailing edge shock reflection on the rotor suction surface. In these cases the excitation level is an order of magnitude higher than in the subsonic test case. There are no significant excitations observed upstream of the throat area in any case, as the stator is choked at the high Mach number and design conditions and the influence zone of the downstream potential field is limited in the subsonic case. On the pressure side pressure perturbations are observed at the stator ejection slot. It is postulated that these can have a considerable influence on the cooling performance. The investigation of the spanwise variations at design conditions did not reveal any new excitation features, but the excitation level decreases from hub to tip.

In the study of the rotor blade surface pressure fluctuations it is observed that the pressure side is affected by the stator potential field and the suction surface by both potential and wake distortions in the subsonic case. In the high Mach number case the dominating excitation source is the stator trailing edge shock motion in the blade passage on both pressure and suction surface. At design operation conditions it is shown that the combination of shock, potential and wake excitation is responsible for the blade pressure perturbation pattern. The investigation of spanwise variations revealed that the radial variation in vane trailing edge shock strength and the three-dimensional rotor shape considerably changes the appearance of the pressure perturbations on the rotor blade surface.

In this investigation every major surface pressure perturbation appearing on the vane and the rotor has been addressed and linked to its excitation source.

Acknowledgments

This research was funded by Sweden's National Flight Research Program (NFFP). The authors wish to acknowledge this financial support as well as the support from KTH—the Royal Institute of Technology and Volvo Aero Corporation.

Nomenclature

A = annulus area
c = chord
L = length
$\dot{m}$ = mass flow
M = Mach number
P = static pressure
P_0 = total pressure
T = static temperature
T_0 = total temperature
t = time
α = stator relative angle
β = rotor relative angle

Subscripts

a = arc
ax = axial
s = stator
w = wall
1 = stator inlet condition
2 = stator outlet, rotor inlet
3 = rotor outlet

Abbreviations

E = expansion
OP = operation point
P = potential
R = reflection
RR = re-reflection
S = shock

References

[1] Manwaring, S. R., Rabe, D. C., Lorence, C. B., and Wadia, A. R., 1997, "Inlet Distortion Generated Forced Response of a Low-Aspect-Ratio Transonic Fan," ASME J. Turbomach., **115**, pp. 724–740.
[2] Meyer, R. X., 1958, "The Effects of Wakes on the Transient Pressure and Velocity Distributions in Turbomachines," ASME J. Basic Eng., Oct., pp. 1544–1552.
[3] Lefcort, M. D., 1965, "An Investigation Into Unsteady Blade Forces in Turbomachines," ASME J. Eng. Power, Oct., pp. 345–354.
[4] Hodson, H. P., 1985, "Measurements of Wake-Generated Unsteadiness in the Rotor Passages of Axial Flow Turbines," ASME J. Eng. Gas Turbines Power, **107**, pp. 467–476.
[5] Hodson, H. P., 1985, "An Inviscid Blade-to-Blade Prediction of a Wake-Generated Unsteady Flow," ASME J. Eng. Gas Turbines Power, **107**, pp. 337–344.
[6] Doorly, D. J., and Oldfield, M. L. G., 1985, "Simulation of the Effects of Shock Wave Passing on a Turbine Rotor Blade," ASME J. Eng. Gas Turbines Power, **107**, Oct., pp. 998–1006.
[7] Ashworth, D. A., LaGraff, J. E., Schultz, D. L., and Grindrod, K. J., 1985, "Unsteady Aerodynamic and Heat Transfer Processes in a Transonic Turbine Stage," ASME J. Eng. Gas Turbines Power, **107**, Oct., pp. 1022–1030.
[8] Johnson, A. B., Rigby, M. J., and Oldfield, M. L. G., 1989, "Unsteady Aerodynamic Phenomena in a Simulated Wake and Shock Wave Passing Experiment," AGARD-CP-468.
[9] Giles, M. B., 1988, "Calculation of Unsteady Wake Rotor Interaction," J. Propul. Power, **4**, pp. 356–362.
[10] Saxer, A. P., and Giles, M. B., 1994, "Predictions of Three-Dimensional Steady and Unsteady Inviscid Transonic Stator/Rotor Interaction With Inlet Radial Temperature Nonuniformity," ASME J. Turbomach., **116**, pp. 347–357.
[11] Lakshminarayana, B., Chernobrovkin, A., and Ristic, D., 2000, "Unsteady Viscous Flow Causing Rotor-Stator Interaction in Turbines. Part I: Data, Code, and Pressure Field," J. Propul. Power, **16**, No. 5, pp. 744–750.
[12] Chernobrovkin, A., and Lakshminarayana, B., 2000, "Unsteady Viscous Flow Causing Rotor Stator Interaction in Turbines. Part 2: Simulation, Integrated Flow Field and Interpretation," J. Propul. Power, **16**, No. 5, pp. 751–759.
[13] Dunn, M. G., Bennet, W., Delaney, R., and Rao, K., 1992, "Investigation of Unsteady Flow Through Transonic Turbine Stage: Data/Prediction Comparison for Time-Averaged and Phase-Resolved Pressure Data," ASME J. Turbomach., **114**, pp. 91–99.
[14] Rao, K. V., Delaney, R. A., and Dunn, M. G., 1994, "Vane-Blade Interaction in a Transonic Turbine: Part I—Aerodynamics," J. Propul. Power, **10**, No. 3, May–June, pp. 305–311.
[15] Venable, B. L., Delaney, R. A., Busby, J. A., Davis, R. L., Dorney, D. J., Dunn,

M. G., Haldemann, C. W., and Abhari, R. S., 1999, ''Influence of Vane-Blade Spacing on Transonic Turbine Stage Aerodynamics: Part I—Time-Averaged Data and Analysis,'' ASME J. Turbomach., **121**, Oct., pp. 663–672.
[16] Busby, J. A., Davis, R. L., Dorney, D. J., Dunn, M. G., Haldemann, C. W., Abhari, R. S., Venable, B. L., and Delaney, R. A., 1999, ''Influence of Vane-Blade Spacing on Transonic Turbine Stage Aerodynamics: Part II—Time-Resolved Data and Analysis,'' ASME J. Turbomach., **121**, Oct., pp. 673–685.
[17] Hilditch, M. A., Smith, G. S., and Singh, U. K., 1998, ''Unsteady Flow in a Single Stage Turbine,'' ASME Paper No. 98-GT-531.
[18] Moss, R. W., Ainsworth, R. W., Sheldrake, C. D., and Miller, R., 1997, ''The Unsteady Pressure Field Over a Turbine Blade Surface: Visualization and Interpretation of Experimental Data,'' ASME Paper No. 97-GT-474.
[19] Laumert, B., Mårtensson, H., and Fransson, T. H., 2000, ''Investigation of the Flowfield in the Transonic VKI BRITE EURAM Turbine Stage with 3D Steady and Unsteady N-S Computations,'' ASME Paper No. 2000-GT-0433.
[20] Denos, R., Sieverding, C. H., Arts, T., Brouckaert, J. F., Paniagua, G., and Michelassi, V., 1999, ''Experimental Investigation of the Unsteady Rotor Aerodynamics of a Transonic Turbine Stage,'' IMECH Conf. Trans., 3. European Conference on Turbomachinery, pp. 271–287.
[21] Denos, R., Arts, T., Paniagua, G., Michelassi, V., and Martelli, F., 2000, ''Investigation of the Unsteady Rotor Aerodynamics in a Transonic Turbine Stage,'' ASME Paper No. 2000-GT-0435
[22] Eriksson, L.-E., 1990, ''A Third Order Accurate Upwind-Biased Finite Volume Scheme for Unsteady Compressible Flow,'' VFA Report 9370-154, Volvo Aero Corporation, Trollhättan, Sweden.
[23] Dahlander, P., Abrahamsson, H., Mårtensson, H., and Håll, U., 1998, ''Numerical Simulation of a Film Cooled Nozzle Guide Vane Using an Injection Model,'' ASME Paper No. 98-GT-439.

Investigation of Unsteady Aerodynamic Blade Excitation Mechanisms in a Transonic Turbine Stage—Part II: Analytical Description and Quantification

Björn Laumert
KTH—The Royal Institute of Technology,
Heat and Power Technology,
100 44 Stockholm, Sweden
e-mail: laumert@egi.kth.se

Hans Mårtensson
Volvo Aero Corporation,
Propulsion Systems,
Military Engines Division,
461 81 Trollhättan, Sweden

Torsten H. Fransson
KTH—The Royal Institute of Technology,
Heat and Power Technology,
100 44 Stockholm, Sweden

This paper presents a study of the blade pressure perturbation levels and the resulting blade forces in a high-pressure transonic turbine stage based on 3-D time dependent viscous computations. Globally, the blade pressure unsteadiness is quantified with the RMS of the pressure perturbations integrated in both time and along the blade surface. Operation point as well as spanwise variations are addressed. Locally, the relative strength of the pressure perturbation events on the vane and rotor blade surface is investigated. To obtain information about the relative strength of events related to the blade passing frequency and higher harmonics, the pressure field is Fourier decomposed in time at different radial positions along the blade arc-length. The amplitude peaks are then related to the pressure events in space-time maps. With the help of the observations and results from the blade pressure study, the radial variations of the unsteady blade force and torque acting on a constant span blade profile section are investigated. The connection between the first and second vane passing frequency pressure amplitudes on the rotor blade surface and the resulting force and the torque amplitudes for three selected blade modes was investigated in detail. In this investigation the pressure was integrated over defined rotor blade regions to quantify local force contributions. Spanwise as well as operation point variations are addressed. [DOI: 10.1115/1.1458579]

Introduction

The knowledge of the forcing function, i.e., the Fourier decomposed amplitude and phase of the surface blade pressure associated with the base distortion frequency and higher harmonics, is important in order to foresee and avoid undesired vibratory stresses in the blade structure early in the design process of compressor and turbine stages.

A number of studies have been conducted on the issue of aerodynamic forcing of turbine blades. Korakianitis [1,2] used a 2D non-linear computational method to evaluate the influence of varying stator-rotor pitch ratios and axial gap on the blade force. Freudenreich et al. [3] also used comprehensive numerical parameter studies of varying axial gap, stator rotor pitch, stator exit Mach number and operation points to investigate the influence of design parameters on the forcing function. Clark et al. [4] conducted a sensitivity study on the influence of blade scaling on the numerical prediction of the blade forcing. In a combined experimental and numerical investigation of the unsteady blade loads in a vaneless counter-rotating turbine facility Haldemann et al. [5] concluded that the presented numerical methods were conservative in the predicted excitation levels.

Though the evaluation of the forcing function provides answers to the question of the level of possible excitations, it gives no guidance in the search for a better aerodynamical design, as the information about the physical mechanism of the aerodynamical excitation is lost in the Fourier decomposition. The establishment of a link between the excitation source and the actual pressure fluctuation prior any Fourier analysis of the flow field is therefore of great value. This concept is the basic idea of this two-part paper: In Part I the link between excitation source and blade pressure perturbation is, established in a phenomenological approach, and in Part II the forcing function is analyzed based on the knowledge of the excitation sources. The objective is to quantify the local pressure perturbations and their relative contribution to the blade force and torque for three model vibratory blade modes. Care is taken to describe and analyze radial and operation point variations.

Contributed by the International Gas Turbine Institute and presented at the International Gas Turbine and Aeroengine Congress and Exhibition, New Orleans, Louisiana, June 4–7, 2001. Manuscript received by the IGTI, October 24, 2000. Paper No. 2001-GT-259. Review Chair: R. A. Natole.

Test Cases and Numerical Approach

The computations were performed on the VKI BRITE EURAM test turbine geometry. In addition to the design operation conditions, a high and a low stator exit Mach number test case was computed in order to study the effect of pronounced shock and wake distortions. The test conditions are listed in Table 1. The computations were conducted with the Volvo Aero Corporation in-house developed flow solver Volsol. The code is a 3-D viscous solver utilizing the k-ε turbulence model closure with standard wall functions. The numerical method is based on an explicit, time-marching, cell centered finite-volume procedure. The accuracy of the Runge-Kutta time integration is second order. The convective fluxes are computed with a third order upwind biased scheme, based on the characteristic velocities. The viscous fluxes are computed with a compact, second order accurate, centered flux scheme.

A comprehensive description of the turbine test facility has been presented by Denos et al. [6]. Details of the computational test cases, numerical methods and computational grids have been presented by Laumert et al. in [7] and [8].

Data Evaluation

Fourier Decomposition. To obtain information about the relative strength of pressure perturbation events related to the

Table 1 Boundary and flow conditions for the computed test cases

Boundary Conditions	Design OP	Low M_2 OP	High M_2 OP
P_{01} [bar]	1.628	1.628	1.628
P_3 hub [bar]	0.533	1.185	0.48
T_{01} [K]	441.6	441.6	441.6
T_w [K]	293	293	293
Rotor speed [RPM]	6500	4250	7350
Vane t/e coolant	Inj. Slot, 3% coolant	Round, 0% coolant	Round, 0% coolant
A2/A1	1.0	1.0	1.04
A3/A1	1.09	1.09	1.24
Flow Conditions			
M_2 abs.	0.95	0.58	1.1
M_2 span 15% | 85%	1.0 | 0.92	0.61 | 0.56	1.17 | 1.05
M_3 rel.	0.92	0.36	0.85
$\dot{m}$ [kg/s]	10.62	8.98	10.42
P_2 [bar]	0.868	1.267	0.716
α_2 [deg]	-72.6	-72.6	-72.9
β_2 [deg]	-41	-39.2	-41.23
β_3 [deg]	63.1	60.4	61.4

blade passing frequency and higher harmonics, the pressure field was Fourier decomposed in time at 15, 50, and 85% span along the blade arc-length. The Fourier figures show the amplitude of one harmonic at different spanwise positions along the pressure and suction surface of the blade.

Pressure Perturbation RMS. A global measure for the total pressure perturbation strength on the blade surface at a defined blade span position is defined by the RMS of the local blade pressure perturbation integrated in time and along the blade arc.

$$\mathrm{RMS}_{\mathrm{tot}} = \sqrt{\frac{\int_{\mathrm{arc}}(\Sigma_{i=1}^{n} p_i^2)ds}{n\int_{\mathrm{arc}} ds}} \tag{1}$$

A global measure for the pressure perturbation strength in a specific vane passing frequency at a defined blade span position is defined as follows:

$$\mathrm{RMS}_n = \sqrt{\frac{\int_{\mathrm{arc}} p_{n\text{-amp}}^2 ds}{2\int_{\mathrm{arc}} ds}} \tag{2}$$

where $p_{n\text{-amp}}$ is the arcwise local pressure amplitude of the nth blade passing frequency obtained by a Fourier decomposition of the unsteady pressure field.

Rotor Blade Force and Torque. The pressure was integrated around the rotor blade profile at defined blade span positions to give the unsteady force and torque components that promote selected model vibratory blade modes, namely a flex mode, an edgewise bending mode and a torsion mode. The flex mode promoting force part acts perpendicular to the blade chord, the edgewise bending mode promoting force part acts chordwise. The chord line center was chosen as torsion axis.

The force amplitude of the nth vane passing frequency was normalized with the RMS_n level and the blade chord length. This provides a relative measure of the force realization degree of the pressure perturbation unsteadiness in the nth vane passing frequency. Similarly, the torque amplitude was normalized with the RMS_n level and the square of the half chord length.

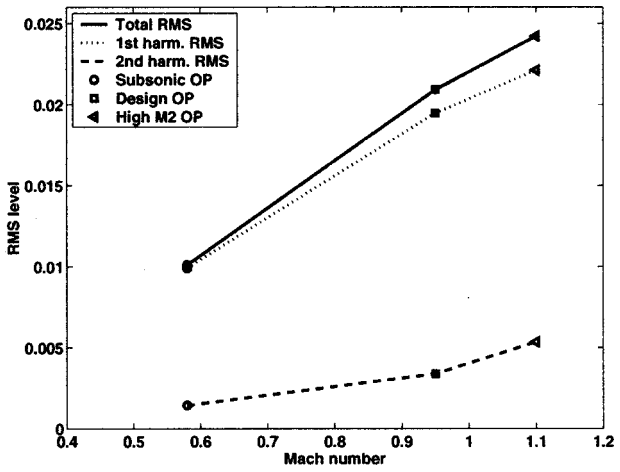

Fig. 1 RMS/Q versus M_2 for the vane at midspan

Results and Discussion

Analysis of the Pressure Perturbation Levels. In this first part of the result section two main issues are addressed: Firstly, the analysis and discussion of the pressure excitation levels with respect to operation point variations at midspan. Secondly, the investigation of the spanwise excitation level variations for the design test conditions. The study is conducted for both the vane and the rotor, but focusing on the rotor.

Vane at 50% Span. In Fig. 1, the pressure perturbation RMS scaled with the vane exit dynamic pressure is plotted against the vane exit Mach number. The normalized RMS levels for the first and second rotor blade passing frequencies are also shown. It can be seen that the normalized total RMS rises with increasing Mach number. In this operation area the level doubles. The observed trend is not an obvious fact, as the normalized pressure RMS is constant with respect to vane exit Mach number variations for low subsonic operation conditions. The explanation for the rise at higher subsonic and transonic operation conditions is probably the presence of shocks. Furthermore it is observed that the slope of the first harmonic normalized RMS level slightly flattens, while the slope of the second harmonic level slightly ascends, as higher harmonics become more important with increasing Mach number. Figures 2 and 3 show the perturbation amplitude along the vane surface at midspan for the first and second blade passing fre-

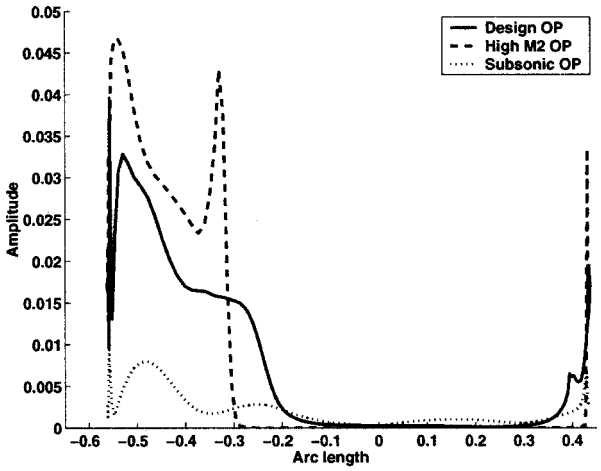

Fig. 2 Pressure amplitude of the 1st rotor passing frequency along the vane surface at 50% span

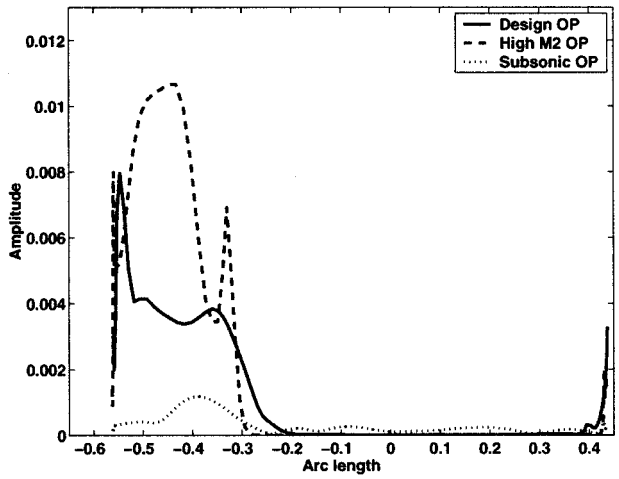

Fig. 3 Pressure amplitude of the 2nd rotor passing frequency along the vane surface at 50% span

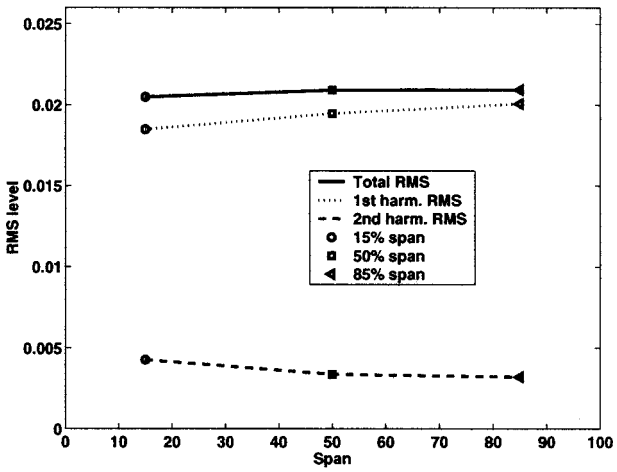

Fig. 4 RMS/Q versus span for vane at design conditions

quency, respectively. The excitation levels of higher harmonics are relatively low and will not be discussed here. At all operation conditions the region of major pressure excitations is located at the aft suction side of the vane. In the design and high Mach number case the region of influence of flow distortions is limited upstream by the choking line. In the design case a stator geometry with a trailing edge ejection slot was utilized, whereas in the high Mach number case a round stator trailing edge was used. With the ejection slot geometry the choking area is located further upstream and therefore pressure perturbations are noticed further upstream. In Part I of this paper [7], it was observed that the pressure excitation source in the subsonic case was the periodical impact of the downstream rotor potential field. In the design and the high Mach number cases the main excitation source is the impingement of a reflected shock wave from the rotor suction side. This leads to considerably higher perturbation amplitudes in the design and high Mach number case compared to the subsonic case. Probably due to increasing shock strength, the second harmonic shows relatively higher amplitude levels in the high Mach number case compared to the design case. In Part I [7] it was stated that a pressure side trailing edge shock from the neighboring stator periodically impinges on the vane suction surface in the high Mach number case. This explains the amplitude peak close to the choking line, at arc length $L_a = -0.3$ for the high Mach number operation conditions.

Vane Spanwise Variations at Design Conditions. In Fig. 4, the normalized pressure perturbation RMS levels for the design case are plotted versus the radial position. It is observed that the total normalized RMS is nearly constant with respect to the radial position. The normalized RMS of the first blade passing frequency slightly increases with increasing radius. On the other hand, the normalized RMS level decreases slightly for the second blade passing frequency, due to the fact that the Mach number and with it the shock reflection strength decreases from hub to shroud.

The variations of the local pressure amplitudes with respect to the spanwise position are only minor and are not further discussed for the vane.

Rotor at 50% Span. The normalized perturbation pressure RMS at rotor blade midspan is plotted against the stator exit Mach number in Fig. 5. As for the vane, the total normalized RMS increases and the unsteadiness is distributed to higher harmonics with increasing Mach number as shocks and shock reflections start to appear.

Predicted pressure perturbation amplitude levels along the blade surface at midspan are shown in Figs. 6 and 7, for the first and second vane passing frequency, respectively, together with measurement data obtained at design conditions.

In connection with the space time maps in Figs. 8, 9, and 10, the relative strength of the local pressure events at rotor blade midspan are illustrated for the tree operation conditions in the following. The contour levels in the time-space maps represent the perturbation from the time mean static pressure normalized with the stage inlet total pressure $(P - P_{\text{time-mean}})/P_{01}$. To aid the reader, the pressure signal abbreviations are explained in Table 2.

At subsonic conditions three pressure peaks of comparable strength are evident in the first vane passing frequency. They are located at the front suction side and along the pressure side of the blade and correspond to the vane potential field perturbations P-SS, P-PS and PR-PS depicted in Fig. 8. At design conditions (transonic) the impact of the vane trailing edge shock gives rise to a significant and dominating amplitude rise at the rotor front suction side. Furthermore the appearance of both potential and shock reflection (SR-SS, PR-SS in Fig. 9) affect the aft suction side and give rise to amplitude peaks in the same order of magnitude as the potential field distortions on the pressure side. The increased shock strength at the high Mach number operation conditions significantly increases the perturbation amplitude at the front suction side. Furthermore the increasing number of shock reflection

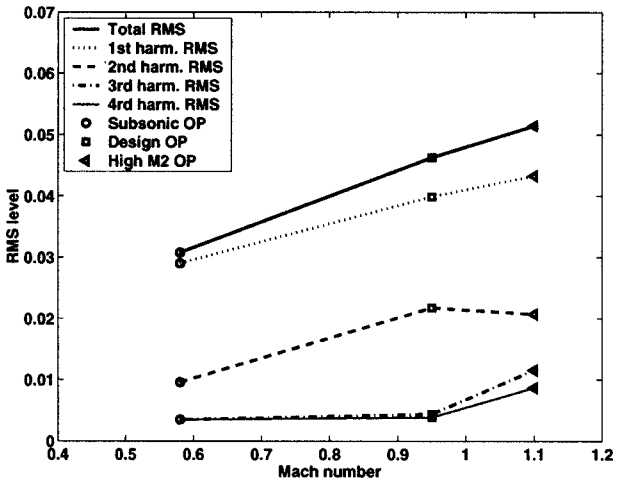

Fig. 5 RMS/Q versus M_2 for the rotor at midspan

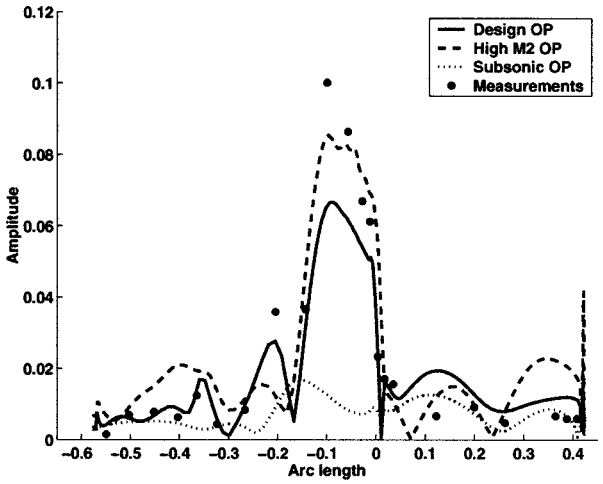

Fig. 6 Pressure amplitude of the 1st vane passing frequency along the rotor surface at 50% span

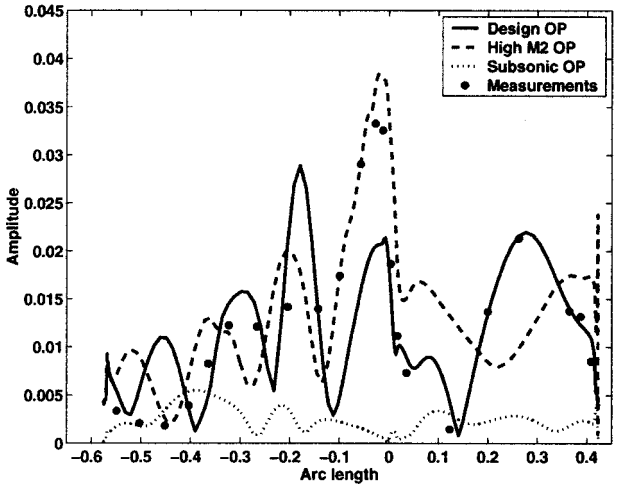

Fig. 7 Pressure amplitude of the 2nd vane passing frequency along the rotor surface at 50% span

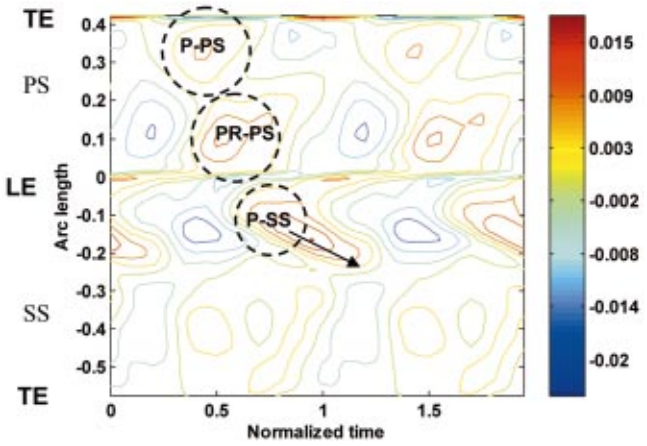

Fig. 8 Space-time map of the rotor surface pressure perturbations for the subsonic test case at 50% span

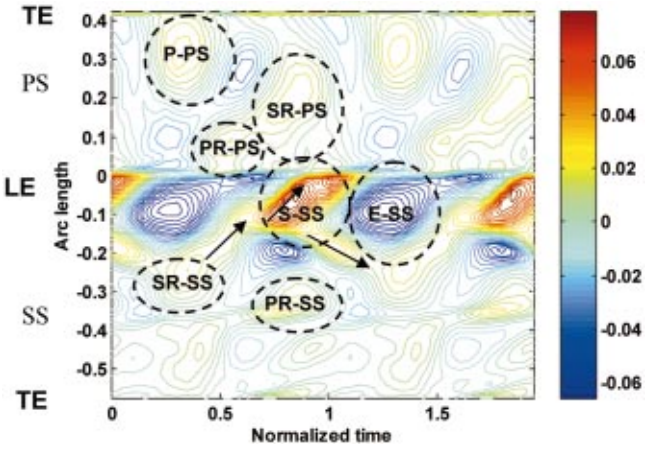

Fig. 9 Space-time map of the rotor surface pressure perturbations for the design test case at 50% span

events (see Fig. 10) leads to higher amplitudes towards the rotor blade trailing edge on both the pressure and the suction side of the blade.

As is observed in Fig. 7, the subsonic test case shows comparably low levels in the perturbation amplitude along the rotor blade surface for the second vane passing frequency. The peak amplitude levels of the design and high Mach number case are in the same order of magnitude as the potential field and shock reflection excitation levels in the first vane passing frequency. Apart from the region of direct impact of the trailing edge shock on the front rotor suction side, the second harmonic amplitude peaks at transonic conditions are caused by two pressure events occurring

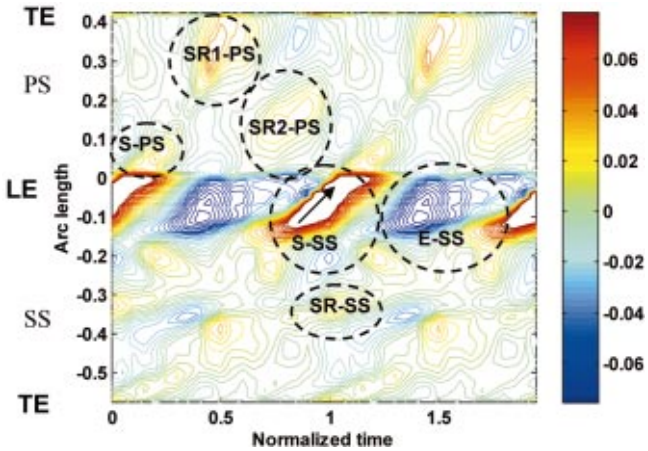

Fig. 10 Space-time map of the rotor surface pressure perturbations for the high M2 test case at 50% span

Table 2 Pressure signal abbreviations and explanations

Abbreviation	Explanation
P-PS	Vane potential field impact – on press. side
PR-PS	Potential field reflection – on pressure side
S-PS	Vane trailing edge shock impact – "-"
SR-PS	Shock reflection impact – on pressure side
P-SS	Vane potential field impact – on suction side
PR-SS	Potential field reflection – on suction side
E-SS	Expansion – on suction side
S-SS	Vane trailing edge shock impact – "-"
SR-SS	Shock reflection impact on suction side

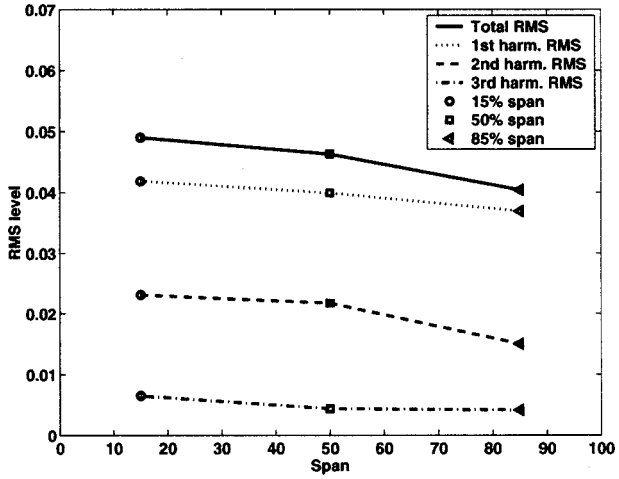

Fig. 11 RMS/Q versus span for rotor at design conditions

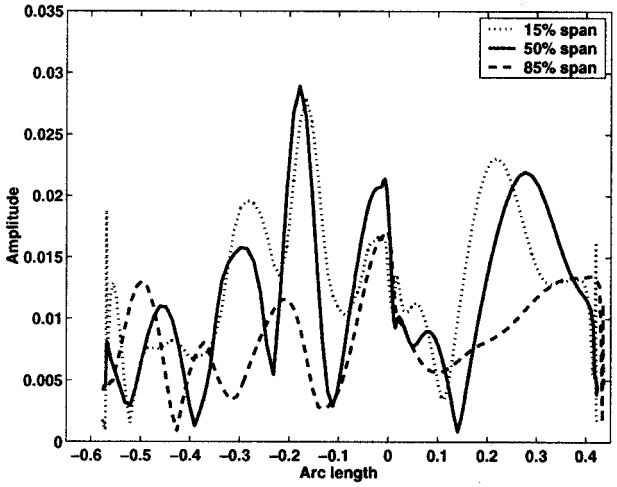

Fig. 13 Pressure amplitude of the 2nd vane passing frequency along the rotor surface; design OP

successively during a vane passing period. While at design conditions the events generally are of different physical origin (wake traveling and shock reflection on the suction side, potential field impact and shock reflection on the pressure side), at high Mach number conditions the events are related to the direct or reflected shock impact.

It is observed in Figs. 6 and 7, that the agreement between the measured amplitudes and the design case predictions generally is very good apart from the front suction side region where the amplitude is lower, thus indicating that the stator trailing edge shock is under-predicted.

Rotor Spanwise Variations at Design Conditions. The Mach number decreases from the hub to the casing (see Table 1), thus the strength of dominant distortion source namely the stator trailing edge shock decreases. As a result, the normalized pressure perturbation RMS levels visualized in Fig. 11 slightly decrease from hub to shroud along the rotor blade. The most prominent decrease is observed in the second vane passing frequency.

As already indicated by the almost constant level of pressure distortions in the first vane passing frequency in Fig. 11, the local variation of the pressure amplitude along the blade surface shown in Fig. 12 is similar at all studied span positions. Some local differences are addressed in the forthcoming in connection with the corresponding space-time maps in Figs. 9, 13, 14, and 15. In the region of the direct vane trailing edge shock impact on the

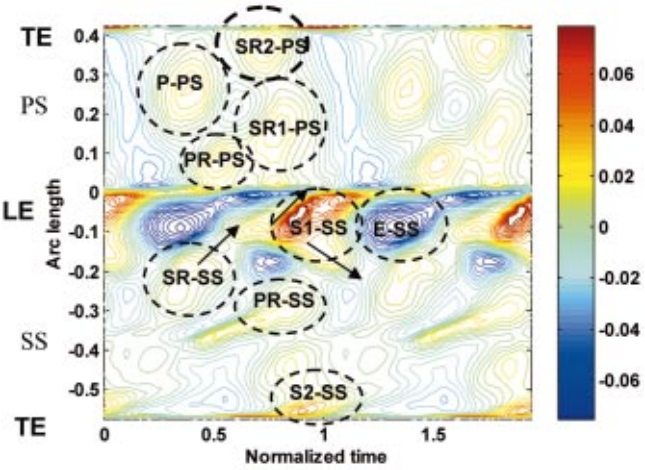

Fig. 14 Space-time map of the rotor surface pressure perturbations for the design test case at 15% span

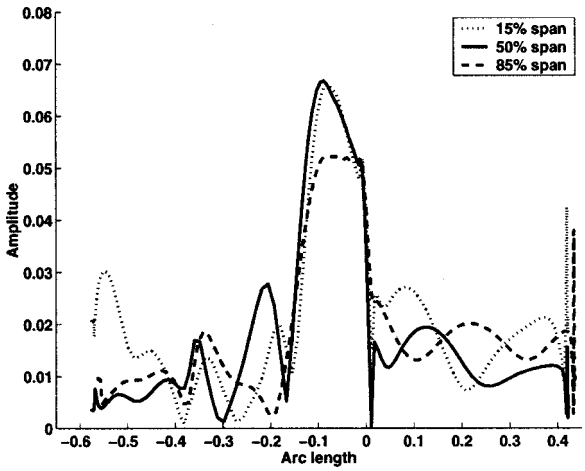

Fig. 12 Pressure amplitude of the 1st vane passing frequency along the rotor surface; design OP

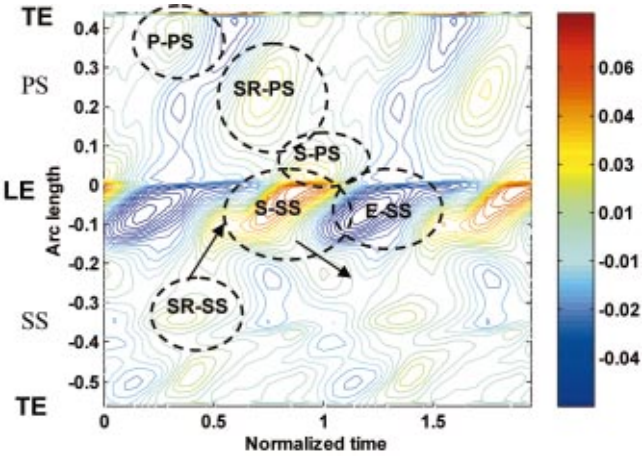

Fig. 15 Space-time map of the rotor surface pressure perturbations for the design test case at 85% span

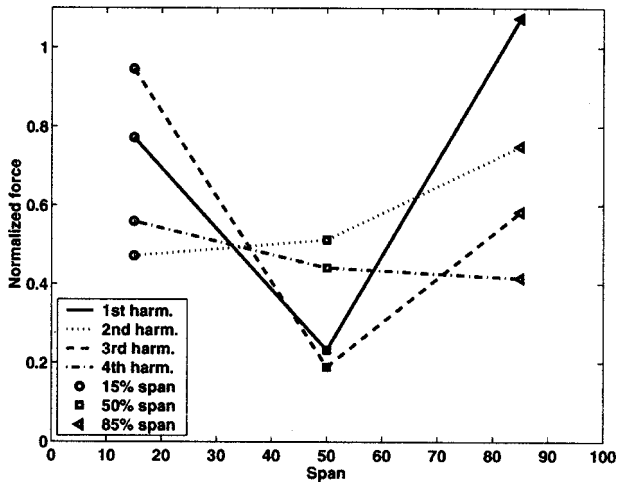

Fig. 16 Amplitude of the normalized force perpendicular to the rotor blade chord versus span; design OP

front blade suction side ($L_a = -0.1$ in Fig. 12) the pressure amplitude is lower at 85% span as the shock strength decreases towards the tip. The local appearance and movement of a weak shock on the aft suction side causes the high perturbation amplitude at $L_a = -0.55$ at 15%.

On the pressure side the trend is similar for the 15 and 50% position, but the perturbation amplitude is larger at 15% span. The reason is twofold: Firstly, as the stator exit Mach number is higher towards the hub, the potential field perturbations are stronger and secondly, the additional shock reflection peak depicted SR2-PS in Fig. 14 promotes the amplitude level of the first vane passing frequency towards the aft. The single shock reflection depicted SR-PS in Fig. 15 gives the additional peak on the pressure side at 85% span at $L_a = 0.22$ in Fig. 12. At 15 and 50% two events per period affect this location thus promoting the amplitude level in the second harmonic rather than the first.

In the second vane passing frequency the pressure perturbation amplitude distribution along the blade surface is very similar for the 15 and 50% span positions. There are only minor differences observed in the amplitude strength and position along the blade surface in Fig. 13. For the 85% span position on the other hand considerable differences are observed. Governed by the 3-D rotor blade shape and the decreasing strength of the rotor trailing edge shock, there are fewer potential field and shock reflections present at 85% span (compare Fig. 15 with Figs. 9 and 14). Two events per vane passing period at the same location are therefore rarely seen at 85% span. This in turn leads to lower second harmonic perturbation amplitudes on both mid to aft suction side and the pressure side of the blade. This is consistent with the pronounced decrease in the second harmonic RMS level in Fig. 11 at 85% span.

Mode Analysis for Design Operation Conditions. In this section the unsteady forces and torque promoting three model rotor blade mode shapes, namely a flex mode, an edgewise bending mode and a torsion mode are investigated for the design operation condition. The observed spanwise variations are also addressed.

Flex Mode: 1st Vane Passing Frequency. Figure 16 shows the amplitude of the normalized unsteady force acting perpendicular to the blade chord at 15, 50, and 85% span. The normalized force is a measure of the degree of force realization of the pressure unsteadiness connected with the first vane passing frequency. It was earlier concluded, that the spanwise RMS variation is weak for the first vane passing frequency. Figure 16 reveals on the other hand that the amplitude variation of the normalized force for the first vane passing frequency with respect to the spanwise position is very strong. In fact, the degree of force realization is less than a third the degree of force realization at 15 and 85% span. The pressure amplitude variations along the blade surface, shown in Fig. 12, do not reveal the reason for the strong radial variation in the force, as the amplitude pattern is similar for all positions along the blade span.

To aid to the understanding of the spanwise force variations and to investigate the relative influence of the different pressure events along the blade surface on the force, the pressure was separately integrated over three regions along the blade arc. When examining Fig. 12, the subdivision of the arc appears naturally, as the vane trailing edge shock induced pressure perturbation for all span positions dominates a defined region at the front suction side of the rotor and therefore can be viewed separately. The three areas were defined as follows: firstly, the aft suction side, stretching from the blade trailing edge to $L_a = -0.155$; secondly, the front suction side stretching from $L_a = -0.155$ to the leading edge and thirdly, the blade pressure side. The forces acting on the individual blade regions and the summed forces are visualized in Fig. 17 for 15, 50, and 85% span. The forces are depicted in polar coordinates, where the length of the arrow represents the amplitude of the force and the angular position represents the relative phase. The blue arrow represents the force contribution of the front suction side (the trailing edge shock), the green is the contribution of the aft suction side and the black is the contribution of the pressure

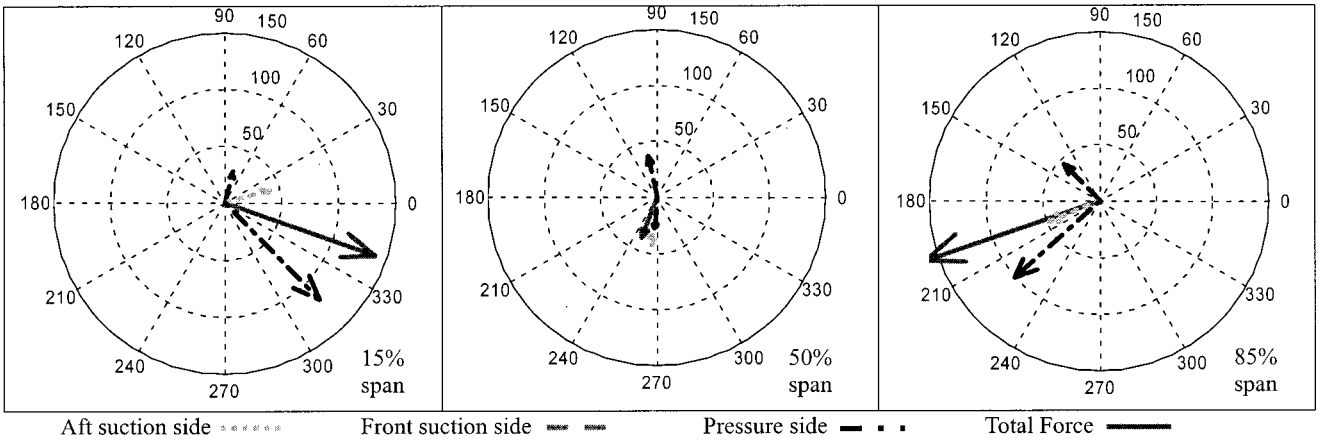

Fig. 17 Flex mode: 1st harm. amplitude and phase of the force acting on the front suction side, the aft suction side and the pressure side at 15, 50, and 85% span. The summed total force acting on the whole blade arc is also shown.

side. The local arrows' vector sum form the red arrow, which represents the total force acting over the blade arc at a defined spanwise position.

It is observed that the force amplitude due to the influence of the shock on the front rotor suction side (blue arrow) almost doubles from 15–85% span, although the pressure amplitude in this area decreases (see Fig. 12). The force increases as the projection of the front suction side arc length on the chord increases from hub to shroud (the curvature decreases). As the rotor blade leans in the direction of the blade rotation, the arrow turns counterclockwise, indicating that the impact of the shock occurs earlier towards the shroud. Comprising the observations, the direct shock influence on the force normal to the chord is defined by four parameters: firstly, the stator exit Mach number, defining the pressure amplitude; secondly, the blade stagger-angle; and thirdly, the curvature of the blade, which together quantify the degree of force realization of the pressure distortion for the present mode shape. Fourthly, the blade leaning, influencing the phase.

The examination of the green arrow reveals that the contribution of the pressure perturbations on aft suction side to the force is in the same order of magnitude as the shock perturbation on the front suction side. The force amplitude variation with respect to the spanwise position appears to be small. The phase shift is almost 180 deg from hub to shroud, rotating clockwise, thus indicating that the pressure events that contribute to the force appear half a period earlier at 15% span compared to the 85% span position. The change in phase is a result of the earlier mentioned appearance of different perturbation events along the aft suction side in spanwise direction and their relative phase along the blade surface, governed by the radial Mach number variation and the 3-D blade shape.

The contribution of the pressure side perturbations (black arrow in Fig. 17) to the force perpendicular to the chord varies strongly in both phase and amplitude in spanwise direction. At 15 and 85% span, the force amplitude is more than twice the amplitude of the front suction side (shock) and the aft suction side. At 50% it is in the same order of magnitude. The phase shift is about 90 deg in clockwise direction from hub to shroud, thus indicating that the pressure events that contribute to the force appear a quarter of a vane passing period earlier at 15% span than at 85% span. As in the case of the aft suction side, the spanwise variations in phase and amplitude can be explained with the varying appearance and importance of different pressure perturbation events on the pressure side of the rotor blade. At 50% span, the dominating perturbation events are P-PS and PR-PS in Fig. 9 and as they are in opposing phase during a vane passing period the resulting force amplitude is comparably low.

When looking at the resulting total force in Fig. 17 (the red arrow), it is observed that the unsteady force acting on the pressure side is the dominant contributor at 15 and 85% span. The phase movement of the local forces is from the left half to the right half from hub to shroud, where the aft suction side and the pressure side force move clockwise and the front suction side counterclockwise. This leads to a 150-deg phase shift from hub to shroud in the total force. At 50% span the front suction side and the aft suction side and pressure side forces are in opposing phase and counteracting. This fact, together with the relative small amplitude of the pressure side force at 50% span, explains the total force amplitude minimum and the low degree of force realization depicted in Fig. 16.

2nd Vane Passing Frequency. It has earlier been described that the shock impact on the front suction side causes a pressure perturbation amplitude in the second vane passing frequency in the same order of magnitude as the other perturbations observed on the pressure and suction side of the rotor (see Fig. 13). The perturbation amplitude is not as dominating as in the first vane passing frequency. The local contribution of the front suction side perturbations to the force acting perpendicular to the chord becomes therefore negligible. The local contributions of the aft suction side and pressure side decrease from hub to tip as the level of second harmonic perturbations decrease in this region. As the phase difference of the local force contributions from the aft suction side and the pressure side decreases from hub to shroud, the degree of force realization increases slightly in the second vane passing frequency, as is observed in Fig. 16. The phase variation of the total force is less than 60 deg from hub to shroud. For the sake of brevity the local force contributions for the second vane passing frequency are not shown here.

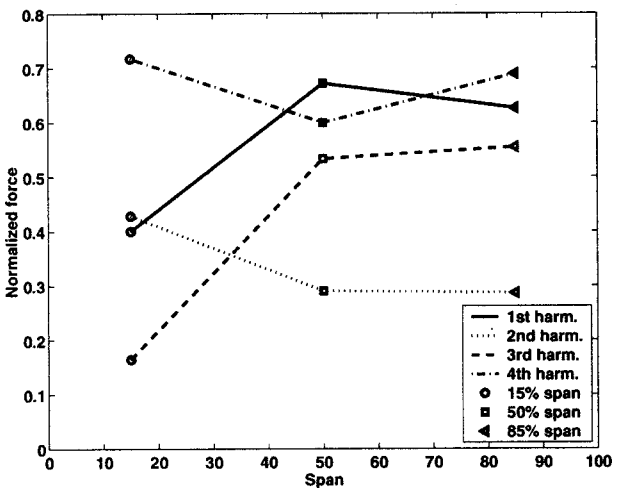

Fig. 18 Amplitude of the chordwise acting normalized force versus span; design OP

Edgewise Bending Mode: 1st Vane Passing Frequency. Figure 18 reveals that the spanwise variation of the chordwise acting normalized force is not as strong as observed for the perpendicular acting force seen in Fig. 16. As for the flex mode, the investigation of the total force in chordwise direction at a specific spanwise position is viewed in the perspective of the local force variation at the front suction side (shock influence), aft suction side and the pressure side. When examining Fig. 19, it is observed that the force due to pressure perturbations on the front suction surface (the direct impact of the stator trailing edge shock, blue arrow) is the dominating contribution to the total force at 50% span.

This is true for all spanwise positions. In fact in this particular case it would be conservative to assume that the total force amplitude equals the force contribution by the shock distortion on the front suction side. The force amplitude due to the shock perturba-

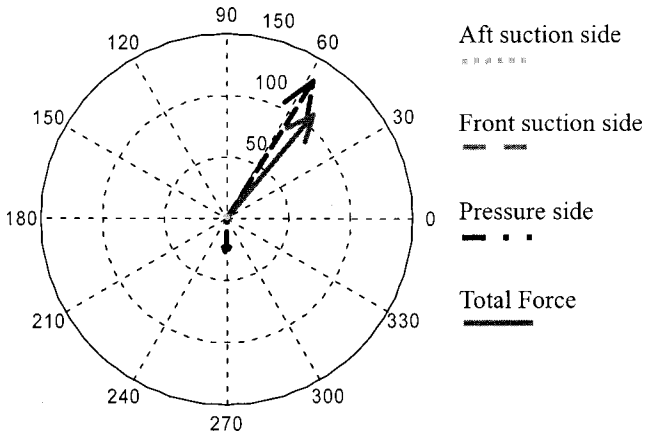

Fig. 19 Bending mode: 1st harm. amplitude and phase of the force acting parallel to the chord at 50% span

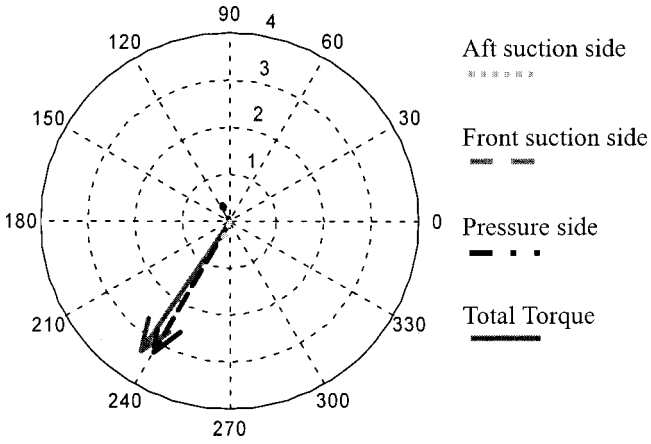

Fig. 20 Torsion mode: 1st harm. amplitude and phase of the torque at 50% span

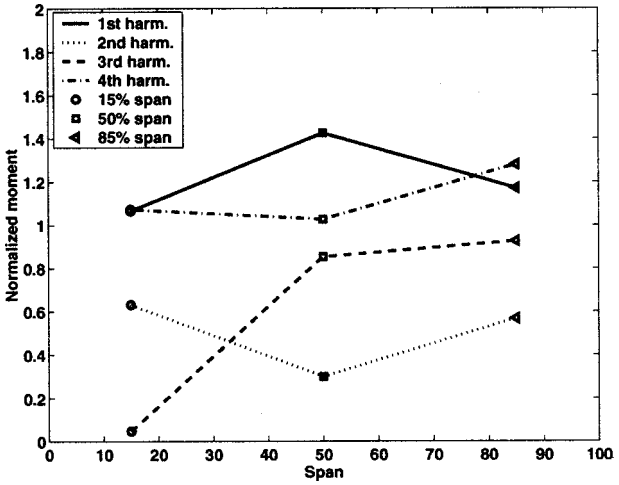

Fig. 21 Amplitude of the normalized torque versus span; design OP

tion decreases slightly from hub to tip and exhibits a counterclockwise phase shift of 60 deg, indicating that the perturbation appears earlier at the hub than at the shroud. As the shock strength decreases from hub to shroud the amplitude of the pressure perturbation on the front suction side decreases from hub to shroud. Furthermore the projection of the front suction side arc length perpendicular to the chord decreases from hub to shroud (the curvature decreases). This explains the decrease in the force amplitude. The phase shift is connected to the blade leaning as earlier explained for the flex mode.

2nd Vane Passing Frequency. The local contribution of the pressure perturbations on the aft and front suction and the pressure side to the chordwise acting second harmonic force amplitude are all in the same order of magnitude for the investigated spanwise positions. At 50% span the three local force contributions have a phase shift of 120 deg relative to each other and cancel out to a high extent. Therefore, the total normalized force depicted in Fig. 18 shows a minimum at 50% span. The phase shift of the total force that promotes the edgewise bending mode is about 150 deg from hub to shroud.

Torsion Mode: 1st Vane Passing Frequency. The investigation of the unsteady torque acting on the chord center axis shows very similar trends as the investigation of the chordwise force. The normalized torque amplitude for the first vane passing frequency varies moderately with the spanwise position. The examination of the local contributions in Fig. 20 reveals that the shock induced perturbation on the front suction side (blue arrow) is the by far the largest contributor to the total torque as it is a strong perturbation acting at a large distance to the center of rotation.

2nd Vane Passing Frequency. As observed in the investigations of the chordwise acting force, the local contribution of the pressure perturbations on the aft and front suction and the pressure side to the second harmonic torque amplitude are all in the same order of magnitude.

At 50% span the local torque contributions are canceling out to a high extent as they exhibit a 120 deg phase shift relative to each other and thus a minimum is observed in the total normalized torque in Fig. 21 at 50% span.

Mode Analysis for Varying Operation Conditions. In this section the observed variations in relative force and torque strength for the three operation conditions will be addressed for the rotor blade midspan location.

Flex Mode: 1st Vane Passing Frequency. The amplitude of the unsteady force acting perpendicular to the rotor blade chord for the subsonic, the design and high Mach number operation conditions is shown in Fig. 22. In contrast to the edgewise bending and torsion mode (Figs. 23 and 24), the flex mode promoting force of the first vane passing frequency does not increase with increasing Mach number at 50% span. In fact, the force amplitude shows a minimum at design conditions. The explanation is the earlier shown low degree of force realization at 50% span at design operation as the effect of the force promoting pressure perturbation events cancel out to a high extent as they appear with opposing phase during a vane passing period. This is also the case for the high Mach number conditions. At subsonic operation conditions on the other hand, where complex shock and potential field reflections are not present, the spanwise variations in the force realization are smaller. More detailed, the flex mode promoting potential field disturbances on the blade pressure side, depicted P-PS and PR-PS in Fig. 8, are in phase and the suction side contribution is at the most 90 deg phase shifted, thus not rescinding the pressure side contribution to the force.

Flex Mode: Higher Harmonics. The appearance of two perturbation events per vane passing period on the aft suction and pressure side in the transonic regime leads to second harmonic force amplitudes in the same order of magnitude as in the first harmonic for design and high Mach number operation conditions

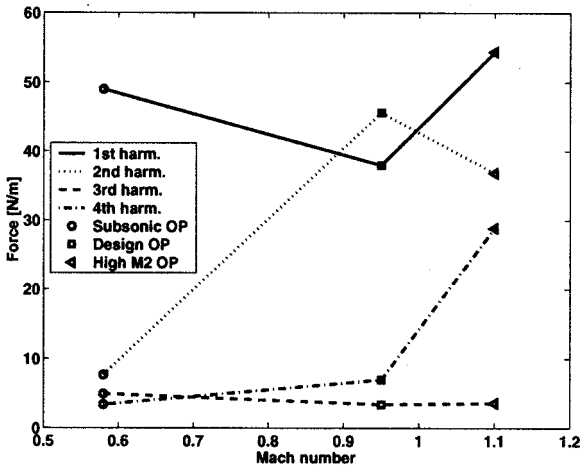

Fig. 22 Amplitude of the force perpendicular to the rotor blade chord versus M_2 at midspan

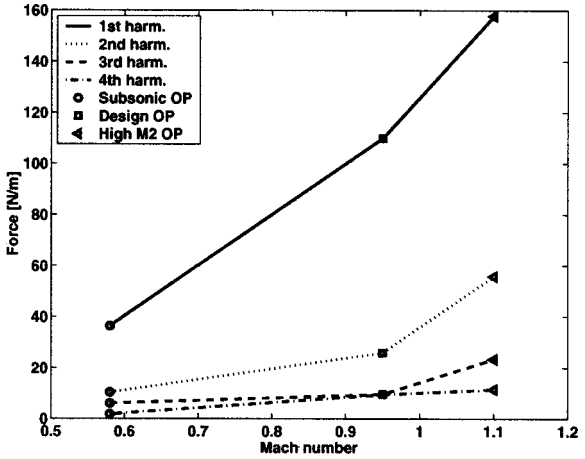

Fig. 23 Amplitude of the chordwise acting force versus M_2 at midspan

at 50% span. As the physical origin of the two events per period merely is shock related with strong pressure gradients at high Mach number conditions, multiples of the second vane passing frequency are governed, resulting in the strong fourth harmonic force amplitude seen in Fig. 22.

Edgewise Bending and Torsion Mode: 1st Vane Passing Frequency. At all operation conditions, the pressure perturbations located at the front suction side give the major contribution to the chordwise acting force and torque variations. The influence of perturbations at other blade regions on this force is weak. In the case of the subsonic operation conditions the vane potential field (P-SS in Fig. 8) influences this region. At design conditions the stator trailing edge shock (S-SS in Figs. 9 and 10) induces a stronger perturbation at this location, which strengthens with increasing Mach number. Therefore the first harmonic amplitude of the force and torque shown in Figs. 23 and 24 rises from subsonic to high Mach number conditions.

Edgewise Bending and Torsion Mode: Higher Harmonics. At design operation conditions the local force and torque contribution of the front and aft suction side and the pressure side to the edgewise bending and torsion mode are in the same order of magnitude and cancel out to a high extent as they exhibit a phase shift of about 120 deg relative to each other. Therefore the amplitude rise of the second vane passing frequency in Figs. 23 and 24 from subsonic to design operation conditions is small, even though the second harmonic pressure perturbation amplitude along the blade surface is considerably stronger at design conditions. At high Mach number operation on the other hand, the local contribution of the shock-influenced region at the blade front suction side is dominating, and therefore the amplitude of higher harmonics increases considerably.

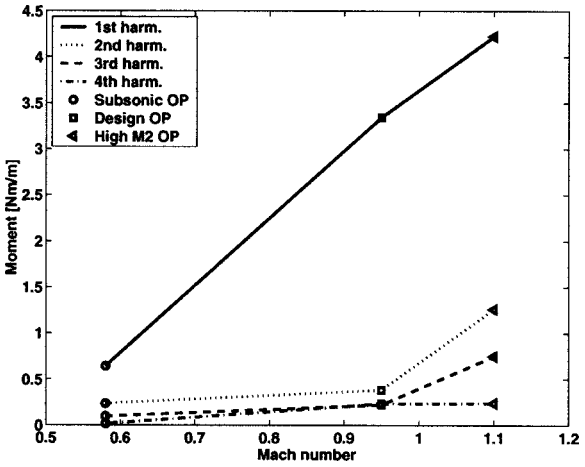

Fig. 24 Amplitude of the torque versus M_2 at midspan

Conclusions

In the analysis of the pressure perturbation levels on the vane and rotor blade surface, it is concluded that the RMS levels increase considerably faster than the dynamic pressure with increasing stator exit Mach number due to the appearance of shocks in the transonic flow regime. Furthermore, the presence of shocks and shock reflections increase the portion of higher frequencies in the unsteady pressure signal. The spanwise variation of the RMS levels at design operation conditions is rather small. The slight decrease towards the shroud is explained with the decreasing strength of the vane trailing edge shock.

In the study of the Fourier decomposed blade pressure signals it is concluded that the first harmonic pressure amplitude peaks along the rotor blade surface at 50% span are in the same order of magnitude on the pressure and the suction side. At design and higher Mach number operation conditions the pressure amplitude due to the direct shock impact on the rotor front suction side is more than twice as large as the other amplitude peaks along the blade surface in the first vane passing frequency. The presence of shock reflections at transonic conditions governs second harmonic perturbation amplitudes that are in the same order of magnitude as first harmonic amplitudes along the pressure and the aft suction side of the rotor blade. At subsonic operation conditions second harmonic perturbations are generally an order of magnitude smaller than first harmonic perturbations.

In the analysis of the first vane passing frequency force and torque amplitudes at design operation conditions, it is concluded that the flex mode promoting force is influenced by the pressure perturbations at all separately investigated blade regions, namely the front and aft suction side and the pressure side. The spanwise force variation is strong at transonic conditions with a force minimum at midspan as a result of the inherent phase shifts of the pressure peak signals relative to each other. At subsonic conditions the spanwise variations are small, which in fact results in a stronger flex mode promoting force at midspan compared to the transonic conditions.

The strong shock-induced pressure perturbation on the front rotor suction side gives the dominating contribution to the edgewise bending and torsion mode promoting force and torque at design conditions and the spanwise amplitude variations are relatively small. The force and torque amplitude increases with increasing stator exit Mach number. It is concluded that the force contribution due to the shock impact is defined by four design parameters: the stator exit Mach number, the blade lean, the blade stagger angle and the blade suction side curvature.

For all investigated blade modes it is observed that higher harmonic force and torque amplitudes increase with increasing Mach number.

Acknowledgments

This research was funded by Sweden's National Flight Research Program (NFFP). The authors wish to acknowledge this financial support as well as the support from KTH—the Royal Institute of Technology and Volvo Aero Corporation.

Nomenclature

c = chord
L = length
$\dot{m}$ = mass flow
M = Mach no.
n = discrete time step number

p = local static pressure perturbation
P = static pressure
P_0 = total pressure
Q = dynamic pressure
T = static temperature
T_0 = total temperature
t = time
α = stator relative angle
β = rotor relative angle

Subscripts

a = arc
ax = axial
s = stator
w = wall
1 = stator inlet
2 = stator outlet, rotor inlet
3 = rotor outlet

Abbreviations

E = expansion
P = potential
R = reflection
RR = re-reflection
S = shock

References

[1] Korakianitis, T., 1992, ''On the Prediction of Unsteady Forces on Gas Turbine Blades: Part 1—Description of the Approach,'' ASME J. Turbomach., **114**, pp. 114–122.

[2] Korakianitis, T., 1992, ''On the Prediction of Unsteady Forces on Gas Turbine Blades: Part 2—Analysis of the Results,'' ASME J. Turbomach., **114**, pp. 123–131.

[3] Freudenreich, K., Jöcker, M., and Fransson, T. H., 2000, ''Gust and Forcing Function in a Transonic Turbine,'' submitted for the 4th European Conference on Turbomachinery—Fluid Dynamics and Thermodynamics Firenze, 20th–23rd Mar.

[4] Clark, J. P., Stetson, G. M., Magge, S. S., Ni, R. H., Haldemann, C. W., and Dunn, M. G., 2000, ''The Effect of Airfoil Scaling on the Predicted Unsteady Loading on the Blade of a 1 and 1/2 Stage Transonic Turbine and a Comparison with Experimental Results,'' ASME Paper No. 2000-GT-0446.

[5] Haldemann, C. W., Dunn, M. G., Abhari, R. S., Johnson, P. D., and Montesdeoca, X. A., 2000, ''Experimental and Computational Investigation of the Time-Averaged and Time-Resolved Pressure Loading on a Vaneless Counter-Rotating Turbine,'' ASME Paper No. 2000-GT-0445.

[6] Denos, R., Sieverding, C. H., Arts, T., Brouckaert, J. F., Paniagua, G., and Michelassi, V., 1999, ''Experimental Investigation of the Unsteady Rotor Aerodynamics of a Transonic Turbine Stage,'' IMECHE Conf. Trans., 3. European Conference on Turbomachinery, pp. 271–287.

[7] Laumert, B., Mårtensson, H., and Fransson, T. H., 2001, ''Investigation of Unsteady Aerodynamic Blade Excitation Mechanisms in a Transonic Turbine Stage—Part I: Phenomenological Identification and Classification,'' submitted to the ASME TURBO EXPO Land, Sea and Air Conference.

[8] Laumert, B., Mårtensson, H., and Fransson, T. H., 2000, ''Investigation of the Flowfield in the Transonic VKI BRITE EURAM Turbine Stage with 3-D Steady and Unsteady N-S Computations,'' ASME Paper No. 2000-GT-0433.

Numerical Unsteady Flow Analysis of a Turbine Stage With Extremely Large Blade Loads

Markus Jöcker
e-mail: markus@egi.kth.se

Francois X. Hillion

Torsten H. Fransson

Royal Institute of Technology,
Chair of Heat and Power Technology,
S-10044 Stockholm, Sweden

Ulf Wåhlén
Volvo Aero Corporation,
Space Propulsion Division,
S-46181 Trollhättan, Sweden

This paper presents the detailed numerical analysis including parametric studies on the aerodynamic excitation mechanisms in a turbine stage due to the unsteady stator-rotor interaction. The work is part of the predesign study of a high-pressure subsonic turbine for a rocket engine turbopump. The pressure level in such turbines can be remarkably high (in this case 54 MPa inlet total pressure). Hence, large unsteady rotor blade loads can be expected, which impose difficult design requirements. The parameter studies are performed at midspan with the numerical flow solver UNSFLO, a 2-D/Q3-D unsteady hybrid Euler/Navier-Stokes solver. Comparisons to 2-D and steady 3-D results obtained with a fully viscous solver, VOLSOL, are made. The investigated design parameters are the axial gap (~8–29 percent of rotor axial chord length) and the stator vane size and count (stator-rotor pitch ratio ~1–2.75). For the nominal case the numerical solution is analyzed regarding the contributions of potential and vortical flow disturbances at the rotor inlet using rotor gust computations. It was found that gust calculations were not capable to capture the complexity of the detected excitation mechanisms, but the possibility to reduce excitations by enforcing cancellation of the vortical and potential effects has been elaborated. The potential excitation mechanism in the present turbine stage is found dominant compared to relatively small and local wake excitation effects. The parameter studies indicate design recommendations for the axial gap and the stator size regarding the unsteady rotor load. [DOI: 10.1115/1.1458023]

Keywords: Unsteady Flow Computation, Forced Response, Turbomachinery, Turbine, Turbopumps, CFD, Design

Introduction

Turbines for liquid rocket engine applications are extreme in many aspects depending on the engine type and application. To reach high rocket engine performance, the goal is to maximize the pressure levels, which can be achieved by using closed cycles, e.g., staged combustion cycles or full-flow staged combustion cycles. Such cycles are demanding for high-performance—high-output power turbines in order to drive the high-pressure head pumps. This also implies that in some cases the turbine is working at very extreme pressure levels. As a consequence of the high pressure levels in this type of turbine, the absolute unsteady pressure variation and the induced unsteady load will be large. This represents a significant challenge for the designer. Possibilities to understand and reduce the dominant influencing parameters are therefore of high interest.

Today, it is possible to analyze in detail the unsteady aerodynamic flowfield in turbomachines with computational fluid dynamics (CFD). The rapid computing power development entails that unsteady CFD analyses are more commonly used in the design of turbomachinery. Since the unsteady flow influences the performance and contributes to the loads, improvements in these fields can be achieved together with better understanding of the flow physics.

Numerical approaches to study aerodynamic blade row interactions can be distinguished by models which apply unsteady inlet and exit boundary conditions on a single blade row, e.g., [1,2] and models, which include several blade rows in the computational domain, e.g., [3–5].

The single blade row approach, in the following called gust method, is computationally cheaper, but the specification of the unsteady inlet and outlet boundary conditions requires usually assumptions on the flow distortion. On the other hand it allows the isolated study of the distortions, which can be of potential, vortical and entropical type. Several publications aimed at studying the influence of these perturbation contributions to the blade excitations [6,7]. Lakshminarayana [8] presented a subsonic turbine stage study focusing on the influence of numerical parameters and operating conditions on the blade excitation, for which Chernobrovkin [9] described and analyzed the contributions of vortical and potential effects to the blade excitation.

The consideration of a complete stage (stage method) seems to become increasingly necessary in cases of more complex distortions, which can occur in transonic turbine stages and in cases with narrow vane-blade spacing. The complex interaction mechanisms in the vane-blade gap of such cases can probably not be described sufficiently with inlet boundary conditions as used in gust methods.

Only a few studies are known to the authors, which concentrate on the examination of design parameters and their influence on the unsteady turbine blade excitation. Korakianitis [10,11] used gust approach to investigate in detail the influences of axial gap and stator blade count and blade size on the excitations of a rotor blade row in a subsonic turbine stage. He found an optimum axial gap, where vortical and potential excitation effects cancel out partly. Furthermore, he demonstrated the increased potential and decreased wake influence on the blade excitation level with enlarged stator-rotor pitch ratios. In [12,13] a comprehensive experimental and numerical study of the shock blade interaction in a transonic turbine stage with varying axial gap is presented with conclusions how the unsteadiness influences the stage performance. [14] studied the influence of axial gap on a subsonic high-pressure turbine stage using a commercial 2-D method and succeeded to derive a geometrical design rule for the axial gap.

Contributed by the International Gas Turbine Institute and presented at the International Gas Turbine and Aeroengine Congress and Exhibition, New Orleans, Louisiana, June 4–7, 2001. Manuscript received by the IGTI, October 13, 2000. Paper No. 2001-GT-260. Review Chair: R. A. Natole.

Table 1 Design point data

Total inlet pressure	[MPa]	54
Total inlet temperature	[K]	760
Rotational speed	[rpm]	14 000
Power level	[MW]	190
Mass flow	[kg/s]	1700

Jöcker [15] presented the results of a comprehensive parameter study of axial gap and stator vane design in a transonic turbine, where rotor inlet gust measurements were compared to numerical results and related to the predicted unsteady blade forces.

The authors believe that 2-D and Q3-D tools are very valuable for parametric studies of the physical phenomena, especially when computational costs, data processing effort and time are taken into account. 3-D computational methods are needed for realistic predictions of the flow behavior [16], or at least a correct specification of the Q3-D streamtube (see, e.g., [17]).

The overall objective of this study is to find methods to optimize the design of a highly loaded turbine working at extreme pressure levels. For this purpose, a new one-stage subsonic turbine, typical for a high-pressure rocket engine application, was designed at Volvo Aero Corporation. This design was thereafter used in the various flow simulations and parametric studies described in this paper with the specific objective to quantify and understand the influence of these parameters on the unsteady blade load.

The present study shows, for the first time as far as the authors are aware, comparisons of rotor excitation levels obtained for a predesign study with results from different methods (gust versus stage) and on different cascades found in literature. It proposes several design recommendations regarding the reduction of unsteady blade excitation forces in the turbine stage and it is believed that this work is a further step towards the incorporation of unsteady flow analysis in the design process.

Turbine Stage Description and Varied Parameters

The investigated turbine is a one-stage subsonic turbine designed to operate at pressure levels corresponding to what can be considered in an extreme closed-cycle rocket engine. The stator is designed with constant vane profiles with a high subsonic outlet Mach number. The rotor is designed with radial variation in the blade profiles taking into account the variation of the stator outlet condition and with a small outlet swirl angle, the blades are therefore twisted. The blades are also shrouded. No outlet guide vane is used in the design. The main design data are given in Table 1. The nominal flow conditions at stator inlet (1), in the gap region (2), and at rotor outlet (3) as obtained from the axisymmetric design are given in Table 2.

Starting from nominal design parameter studies have been performed investigating the axial gap influence and the stator influence on the unsteady rotor excitation level. Figure 1 shows the stage configuration with the nominal axial gap, the range of investigated axial gaps and the various stator-rotor configurations investigated. Table 3 gives an overview of the presented cases. The axial gap was varied between 8 percent and 29 percent of rotor axial chord. The stator count was varied such that the pitch ratio R is between 1 and 3. To achieve a pitch ratio of 2.75 two

Table 2 Design flow data at stage inlet (1), stage outlet (3), and in the gap between stator and rotor (2)

Position	1/stat	2/stat	2/rot	3/rot
M	0.17	0.732	0.274	0.83
α [°]	0	-72.01	-30.66	66.23
p [kPa]	52540	36498	36498	24275

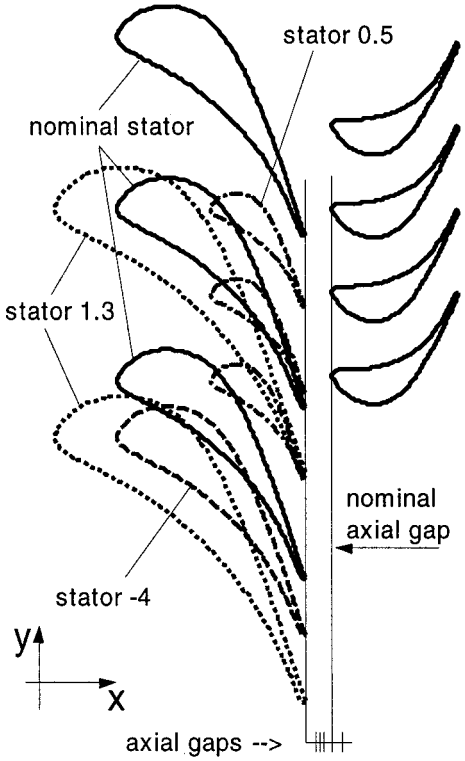

Fig. 1 Description of investigated turbine stage configurations

methods of modification were applied: in case (−4), the stator pitch was increased by removing 4 vanes, in case (1.3) the stator was additionally scaled by a factor 1.3 to maintain the steady aerodynamics.

Short Description of Numerical Methods

Two numerical methods were applied and their results were compared. Both numerical methods assume perfect gas despite the large pressure level.

2-D Viscous/Inviscid Method (UNSFLO). UNSFLO [3] is a 2-D/Q3-D unsteady flow solver computing explicitly the nonlinear Euler equations on unstructured grids. It takes into account viscosity with a thin layer approach using an implicit method on an O-type grid containing the boundary layer around the vanes and blades. For the present results a one-equation k-l turbulence model as documented in [18] was used.

The code can either be run in the stage calculation mode or in the single blade row mode. In case of stage calculations two blade

Table 3 Overview of investigations

Name	g_{ax} [%]	# vanes	# blades	R
Nominal	21.4	16	33	2.063
Axial gap study				
8	8.0	16	33	2.063
10	9.9	16	33	2.063
12	11.8	16	33	2.063
16	15.6	16	33	2.063
29	28.6	16	33	2.063
Stator study				
0.5	21.4	32	33	1.0313
1.3	21.4	12	33	2.75
-4	21.4	12	33	2.75

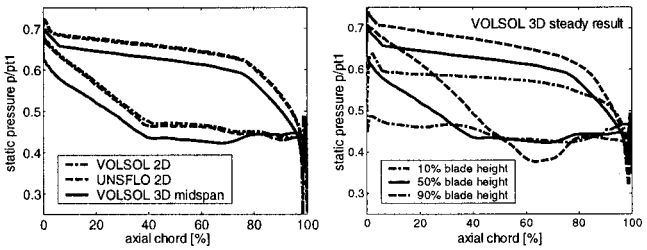

Fig. 2 Steady rotor surface pressure, VOLSOL and UNSFLO results, $g_{ax}=29$ percent

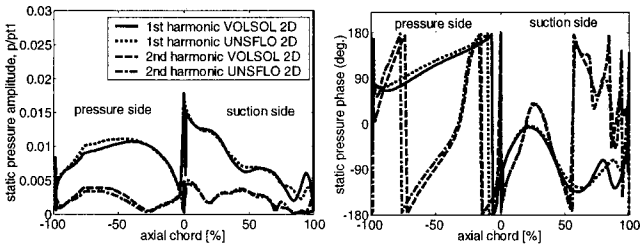

Fig. 3 Unsteady rotor surface pressure, Volsol 2-D—Unsflo 2-D, $g_{ax}=29$ percent

rows are modeled. The method applies a mixing plane between the blade rows to establish a steady solution, for the unsteady solution the blade rows are moved relative to each other during the computation. Otherwise, an unsteady single blade row calculation can be performed, where the unsteady flow is induced by the moving gust specified at the inlet flow boundary. This gust is prescribed in terms of pressure and velocity amplitudes of the flow disturbance. In the present study the velocity disturbance is given with a spatially Gaussian distribution in pitchwise direction. The pitchwise pressure variation is prescribed with a sinusoidal function. Both distributions are periodic with the stator vane pitch. During the unsteady computation the prescribed rotor inlet flow disturbance is moved with the rotational speed relative to the rotor blade. Both methods (stage and gust) apply the time inclination concept by Giles [3] to allow periodic solutions.

For all UNSFLO calculations, a mesh sensitivity study has been performed. Coarser inviscid meshes lead to comparable results in terms of the 1st harmonic unsteady rotor pressure, a drastic refinement of the present grid gave a prediction of vortex shedding from the rotor trailing edge, for which this code is not capable. Hence, full mesh independence cannot be claimed.

2-D and 3-D Fully Viscous Method (VOLSOL). VOLSOL, developed at Volvo Aero Corporation, is a general 3-D unsteady flow solver, which solves the Euler equations or the Reynolds-averaged Navier-Stokes equations. For the present investigation the standard k-ε turbulence model with standard wall functions was applied. The numerical method [19,20] is an explict three stage Runge Kutta, time marching finite volume approach with optional local time stepping. The convective fluxes are calculated with a third order upwind biased scheme, the viscous fluxes are computed with a second order centered scheme. The code applies structured multiblock H-type and O-type meshes and can be used for 2-D and 3-D computations.

For steady stage calculations the stator-rotor interface is of mixing plane type, for unsteady stage calculations a sliding grid technique is applied. In difference to UNSFLO the circumferential extensions of the stator and rotor mesh domains must be identical to allow periodic solutions. To achieve this the rotor has been up-scaled by 3.1 percent. This increases the steady load of the blade through a higher steady pressure on the pressure side tail (locally 1–2 percent of p_{t1}). The scaling effect on the unsteady load could not be quantified, because the necessary unsteady calculation with non-scaled blades for comparison can not be performed with this code.

Results

Comparison of Numerical Methods (Validation). Several publications have demonstrated the ability of UNSFLO to predict the unsteady flow behavior in turbine stages by comparison to experimental data (e.g., [16,17]). However, due to lacking experimental data for the present case the predictions were compared to results obtained with another code, VOLSOL, which has been used for design analysis of turbines at Volvo Aero Corporation with good results for several cases. Figure 2 shows a comparison of the steady blade surface pressures obtained with UNSFLO, VOLSOL 2D and VOLSOL 3-D with an axial gap of 29 percent.

The comparison demonstrates a good agreement of the 2-D methods and points out the differences to a 3-D computation. The main observation is that the blade surface pressure distribution is shifted to a higher pressure level in the 2-D calculation compared to the 3-D prediction. In the right part of Fig. 2, the blade pressure distribution is shown at three blade heights, 10, 50, and 90 percent of span. It shows that the design foresees a moderately distributed steady blade load over the blade span with increasing pressure level from hub to casing.

Both the 2-D and 3-D predictions expand to the same back pressure at midspan, which is given by the boundary conditions, but a 3-D flow stream sheet experiences a radial displacement outwards from the stator inlet to the rotor outlet. This causes the observed increased pressure differences (2-D–3-D) in upstream direction. The stream sheet displacement could be modeled with the Q3-D method by specification of a streamtube expansion. In the present 2-D calculations no effort has been made to calculate on the correct stream sheet and purely 2-D calculations have been performed. The authors believe that this is justified in the case of the performed parameter studies, because only the relative changes are investigated but in the comparison to 3-D results differences are inevitable.

Figure 3 compares the unsteady blade surface pressures obtained with UNSFLO and VOLSOL 2-D in terms of 1st and 2nd harmonic of the perturbation pressure. Good agreement can be seen on most parts of the blades both in amplitude and phase.

Small differences are seen on the pressure side, 30–70 percent of axial chord, and on suction side, 70–100 percent axial chord. It could be that this is related to the difference in rotor geometry, which occurs from the necessary scaling of the VOLSOL rotor: the different geometrical positions of the neighboring blades can cause different propagation of the pressure waves through the passage. However, the differences are so small compared to the studied variations that it gives sufficient confidence in the results.

Analysis of the Unsteady Flow, Nominal Case. The following analysis of the nominal flow by using UNSFLO will be the basis for the parameter studies evaluation. The nominal case is characterized by a dominant potential rotor excitation caused by the upstream stator with local maximum stator exit Mach numbers up to 0.9. The rotor excitation due to the stator wake has a minor influence and contributes only very locally to the excitation (see following section ''Identification of Vortical and Potential Effects, Nominal Case''). The wake influence is discussed with help of the perturbation velocity field, which forms a negative jet in the rotor frame of reference creating two counter-rotating vortices when chopped by the rotor. This phenomenon is well described in [21].

Figure 4 shows the harmonics 1–4 of the rotor surface pressure amplitudes, the phase is only shown exemplary for the 1st harmonic. Six important excitation regions are highlighted which are analyzed with help of the analysis of the instantaneous flow field (Fig. 5) and a time space plot of the blade surface pressure (Fig. 6). In Fig. 5 a discontinuity occurs between stator and rotor perturbation flowfield, because time averages are taken in the stator

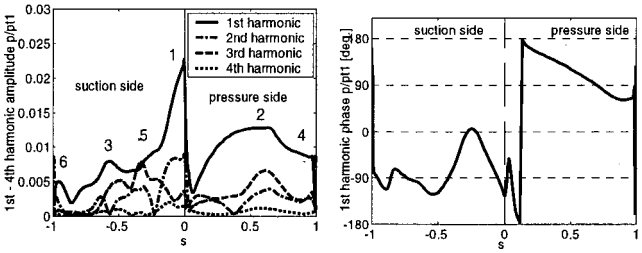

Fig. 4 Harmonics 1–4 of rotor surface perturbation pressure, UNSFLO, nominal case

fixed- and rotor fixed coordinate system and subtracted from the instantaneous values. These time averages are not continuous.

In the time-space plot the blade positions of the maxima 1, 2, 3, 3b, and 5 observed in the pressure harmonics are marked with vertical lines. Where these lines cross the time of maximum excitation a horizontal line is drawn, which indicates the times of the instantaneous flow field plots discussed in Fig. 5. The peaks 1, 3, and 3b are the main excitations on suction side and can clearly be related to the potential excitation. They appear as pressure peaks moving upstream on the rotor blade with the passing frequency of the stator. It is obvious that the excitations 3 and 3b are at very close locations on the blade, but occur at different times.

The excitation 6 on suction side is hard to identify. It coincides with the sweeping of the wake over the aft part of the blade suction side. This might induce the small variation of a transonic pocket observed at the rotor trailing edge leading to a 1st harmonic excitation.

The main excitations on the pressure side (2 and 4) are due to the reflected pressure wave from the neighboring blade suction side and hence also of potential type. At position 2 also the wake excitation influences the pressure, when the velocity perturbation vortex downstream of the wake center line attaches to the pressure side. This induces a negative pressure distortion on the surface at a time around $t=0.2$, which will thereafter be overlaid by the negative potential wave. Obviously, at this position wake and pressure wave excitations are in phase and increase the contribution to the 1st harmonic excitation.

The first harmonic phase indicates, when the 1st harmonic excitations occur in time relative to the reference time (which corresponds here to aligned leading edges of stator and rotor). On suction side the phase is about zero in the wake influence region (5) and otherwise phase shifted by about -90 deg. The pressure side phase is characterized by a continuous change from about 180 to 90 deg beside the variations at the leading and trailing edge. It is seen in the time space plot of the perturbation pressure (Fig. 6) that the excitations on pressure side due to wave reflections form a pattern as if the maxima were moving from the leading edge to the trailing edge during the period. This explains the 1st harmonic phase behavior.

The blade forces and moment presented in Fig. 7 show a sinusoidal trend, the first harmonic amplitude is clearly dominating. The main excitation is due to the passing potential flow field of the stator as discussed in the foregoing and the sinusoidal pattern is mainly induced by the strong 1st harmonic pressure side excitation. A disturbance of the sinusoidal behavior is seen at a time around 0.2, which is due to the potential interaction between stator and rotor flow field at the rotor leading edge. This will increase drastically when reducing the axial gap, which will be discussed in detail.

Identification of Vortical and Potential Effects, Nominal Case. For the study of vortical and potential effects rotor only calculations were performed with varying amplitudes of wake velocity deficit (D) and pressure wave amplitude (P) at the inlet to

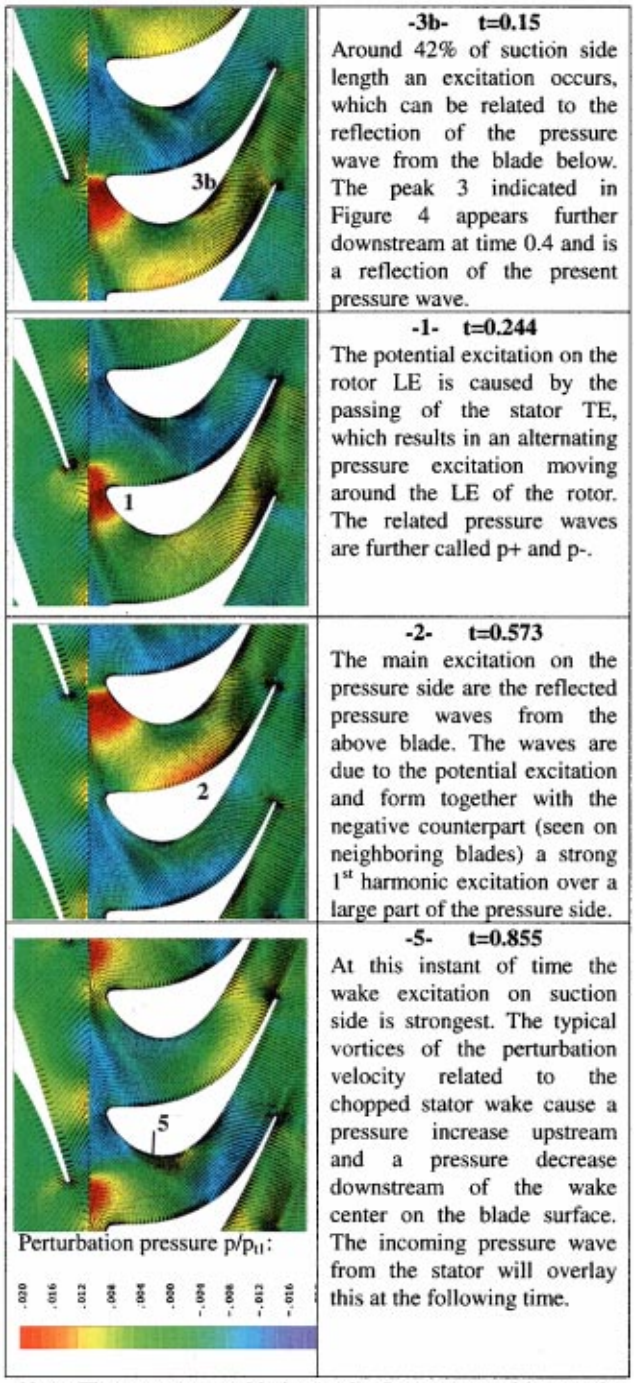

Note: The center rotor blades in the figures are subject to the enclosed discussion.

Fig. 5 Perturbation pressure and velocity flow field at four instants in time, UNSFLO, nominal case

the rotor 15.3 percent of $C_{ax,rotor}$ in front of the blade. Table 4 provides an overview of the specified parameters, which will be explained in the following section.

Splitting into vortical and potential effects builds on the following fundamental splitting theorem by Goldstein [22], which states that the velocity disturbance is composed of a vortical part and a potential part, each related to different physical phenomena

$$\partial\vec{w} = \partial\vec{w}_w + \partial\vec{w}_p \tag{1}$$

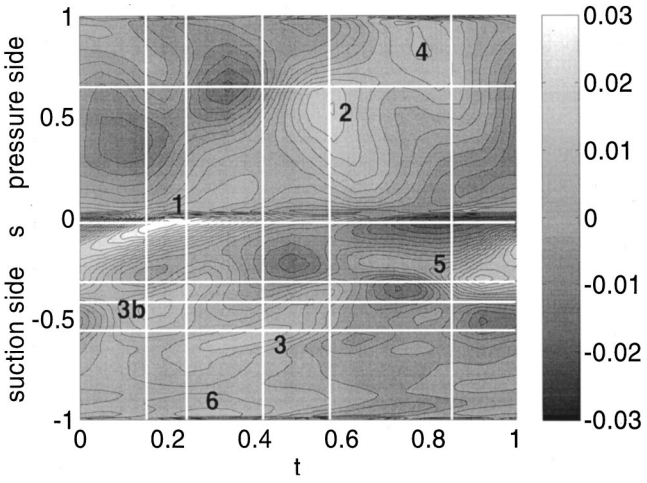

Fig. 6 Time space plot of rotor surface perturbation pressure p/pt1, UNSFLO, nominal case

where $\partial\vec{w}$ is the spatial velocity perturbation vector in the wake frame of reference. The vortical perturbation (rotational velocity) results from the wake of the upstream blade row and the potential perturbation (irrotational velocity) results from the pressure field of the upstream and downstream blade rows. The velocity disturbance in the wake is characterized by the inlet angle α_w and by the maximum amplitude of the velocity defect, which is defined as

$$D = \frac{w_{Fw} - w_{\min}}{w_{Fw}} \tag{2}$$

With these parameters and the wake width W a Gaussian distribution of the velocity field $\vec{w}_w$ in tangential direction (y) can be described

$$\vec{w}_w = |\vec{w}_{Fw}| \cdot \left[1 - D \cdot e^{-1/2(y/S_s \cdot W)^2}\right] \cdot \begin{pmatrix} \cos\alpha_w \\ \sin\alpha_w \end{pmatrix} \tag{3}$$

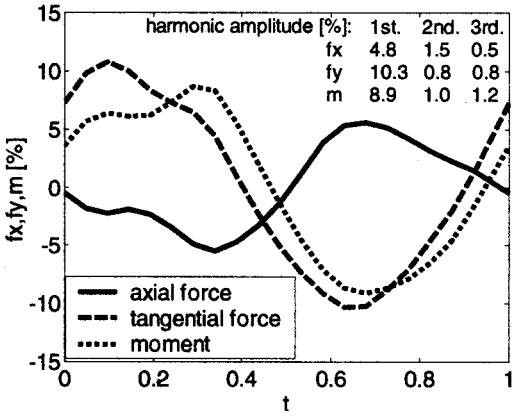

Fig. 7 Blade forces and moment in percent of time average, UNSFLO, nominal case

Table 4 Parameters of vortical and potential effects study, UNSFLO

D [%]	P [%]	R
0, 2, 4, 6, 8	2	2.063
4	0, 1, 2, 3, 4	2.063

Table 5 Spatial 1st harmonic gust amplitudes

	Splitting result	"best fit"	Steady stator exit flow
D	0.075	0.08	0.0517
P	0.011	0.02	0.0167

For subsonic flows it can be expected that the potential-flow disturbance is sinusoidal in the y direction and that it decays in x direction. A general wave like solution of the potential flow equation for such a flow is

$$\Phi(x,y) = A \cdot e^{(i \cdot k \cdot y + \lambda \cdot x)} \tag{4}$$

where A is the amplitude, λ governs the axial decay and $k = 2\pi/S_s$ dictates the periodicity of the potential Φ. The potential disturbance is described by a pressure amplitude ∂p, which also induces the velocity amplitude $\partial\vec{w}_p$. These are related in the present method by

$$\partial p = -\rho_{Fw} \cdot (\vec{w}_{Fw} \cdot \partial\vec{w}_p) \tag{5}$$

The potential pressure wave is shifted in space so that the disturbance maximum is placed in the wake centerline. More details on the method can be found in [3].

In order to specify the amplitudes of wake and pressure disturbance necessary to reproduce the stage calculation result a splitting of the predicted steady velocity field as documented in [6] and extended in [23] has been performed. Table 5 shows the obtained 1st harmonic amplitudes compared to the spatial 1st harmonic of the steady stator exit flow. The 'best fit' result comes closest to the stage calculation result in terms of 1st harmonic unsteady rotor blade pressures (see Fig. 8). When regarding the results of the parameter studies on the potential amplitude (left side of Fig. 8) it becomes obvious that the potential amplitude of 0.011 estimated with the splitting method leads to a very different excitation than the stage calculation result.

The steady stator exit pressure distribution comes closer to the "best-fit" parameter but is still too low to give comparable results to the stage calculation. The splitting estimation of the wake amplitude is satisfactory. This result demonstrates the difficulty to correctly estimate the simplified inlet gust conditions. It was also found that the gust calculations gave only 1st harmonic responses. This is important, as the higher harmonics become increasingly dominant for decreased g_{ax} (see following section).

The 1st harmonic blade surface pressures due to the varied inlet pressure and wake amplitudes in Fig. 8 show the relative importance of these two excitation contributions as well as their influence locations. Obviously, the largest excitation part for the present case results from the potential interaction. In the right part of Fig. 8 the wake influence can be identified at mainly two blade positions:

1. On the pressure side between 20–70 percent blade length. Here, also the potential part has a strong influence.

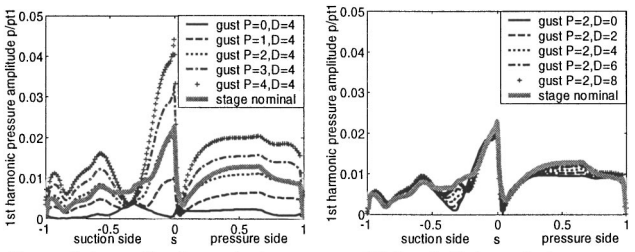

Potential amplitude variation P=0 – 4 %

Wake deficit variation D=0 - 8%

Fig. 8 Vortical and potential influence on 1st harmonic rotor surface perturbation pressure, UNSFLO

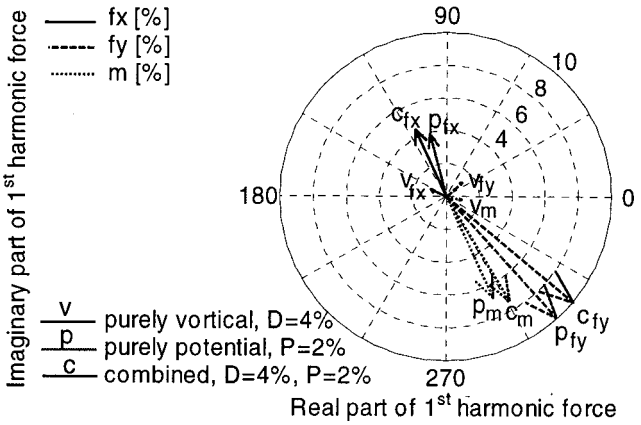

Fig. 9 Unsteady forces normalized with time average in the complex plane, UNSFLO

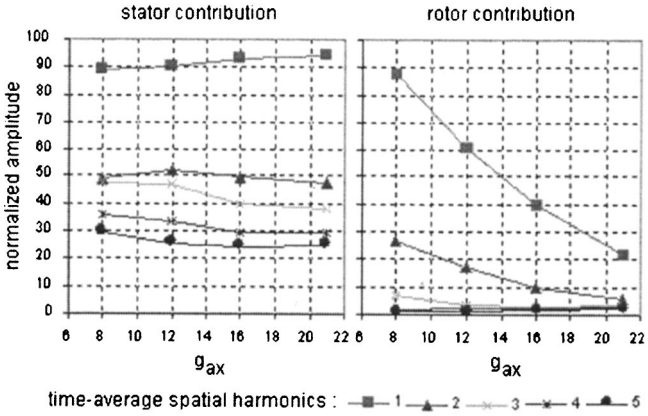

Fig. 10 Evolution with axial gap of the stator row and rotor row contributions to the pressure distribution at their interface

2. On suction side at about 30 percent blade length. The potential excitation part is very small at this location.

These wake influence regions at positions 2 and 5 in Fig. 4 are also characterized by local maxima in the 2nd and 3rd harmonic of the pressure.

The analysis of the blade forces and moment is shown in Fig. 9. The excitation components are presented in the complex plane, which allows viewing the differences in magnitude and phase. It has been found that the excitation obtained with the gust analysis behaves linear in the investigated range so that the combined excitation is the linear superposition of vortical and potential excitation force vectors. An interesting finding is that the forces due to vortical and potential interaction are phase shifted. This indicates the possibility to optimize the design by modification of the sources to obtain an optimum cancellation of the contributions.

Axial Gap Study. The following investigation extends the work presented in [10, 11] where the axial gap varies between 20 and 60 percent of the rotor axial chord. It focuses on the aerodynamic excitation of the rotor (though the stator experiences also an unsteady acoustic excitation at very small gap).

The axial gap is an obvious key parameter to reduce both weight and size of the machines but it has also a strong impact on the aerodynamics. Since the wake propagates in respect with the flow angle and decays slowly downstream while the pressure disturbance generally spreads in a different direction and decays exponentially, a variation of the axial gap means a variation of the relative importance of these excitation sources and their phase shift. The ideal gap would see the two sources cancel out each other as much as possible.

Moreover, while the wake is generated by viscosity at the trailing edge of the stator, the pressure field at the interface is influenced both by the stator and the rotor rows and thus this excitation source depends much more on the axial gap. Its features can only be fully grasped through unsteady simulations of the flow in the complete stage. Figure 10 provides an illustration: the tangential pressure distribution was recorded along a line at a constant axial distance downstream of the stator (4.6 percent of $c_{ax,rotor}$) over one period relative to the stator and Fourier decomposed both in time and y direction. Time averaging in the stator frame (resp. rotor frame) cancels the influence of the rotor row (resp. stator row). The figure shows how the normalized time-average spatial harmonic amplitude vary with the axial gap, when time averaging is performed in the stator frame (left figure) and rotor frame (right figure). In the stator frame, the small variations could partly be of numerical origin, because the generation of a suitable mesh becomes difficult for small axial gap configurations: there is not enough space to define different combinations of H-mesh cells at the stator outlet and at the rotor inlet. Furthermore, for stage calculations some dummy cells are inserted between the two grids and tend to distort their boundary cells. The right part of Fig. 10 shows the increasing influence of the rotor row on the upstream pressure field, when the rotor comes closer to the stator. For the smallest axial gap, the first spatial harmonic of the rotor becomes as strong as the stator one.

Five variations of axial gap were performed in addition to the nominal case (Table 3). For each one, the x and y components of the instantaneous aerodynamic force, on the blade are reported. As previously noticed in [13] the time-average force does not vary significantly with the axial gap. In the present study the maximum deviation from the nominal time averaged load is -1.7 percent (for $g_{ax}=12$ percent).

The perturbation part of the force in x and y directions (after non-dimensionalization by their respective time-average) are plotted in Fig. 11 over one period relative to the stator pitch for all the studied gaps. As these perturbations are re-scaled by a similar quantity for all axial gaps, they are comparable in the magnitudes of excitation. In terms of Fourier analysis, the axial gaps differ by the number of harmonics involved (Fig. 12).

Increasing g_{ax} from 21 percent (nominal) to 29 percent leads to minor differences on f_y and more visible differences on f_x. It is mainly due to the variation of the phase shift between the potential and wake excitations. The blade experiences the pressure dis-

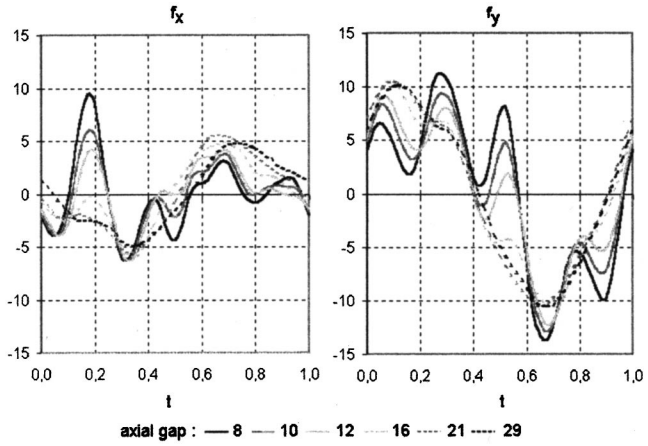

Fig. 11 Instantaneous aerodynamic force on the rotor blade for all the gaps

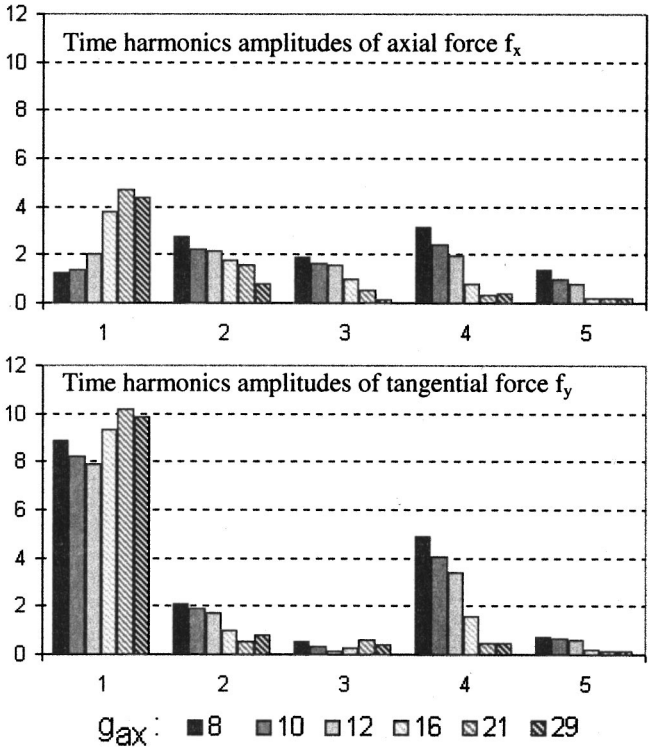

Fig. 12 Amplitude of the time harmonics of the aerodynamic force for all the gaps

turbance at approximately the same time (peak 1 at time 0.2) but it crosses the stator wake later with a gap of 29 percent (time 0.85 instead of 0.7).

On the contrary, decreasing the axial gap results in more unsteadiness. The first harmonic of f_x does not further increase for g_{ax} below 21 percent, whereas its higher harmonics become stronger. The first harmonic of f_y fluctuates but still prevails, while its fourth harmonic is nevertheless remarkably high. Therefore, at very small axial gaps, at least up to four harmonics of the force must be taken into account. The small gap case (8 percent) is now analyzed in detail.

The amplified peak 1 of the small gap cases (at time 0.2 in Fig. 11) is due to the increasing influence of the positive pressure wave p^+, which hits the rotor blade 0 leading edge when this one is passing in front of the stator trailing edge (Fig. 13). This wave p^+ is stronger than in the nominal case (9.14 percent of p_{t1} instead of 3.2 percent). Its spatial location is wider and its successive reflections are delayed ($t=0.2$ instead of 0.25). The mechanism of reflected pressure waves between pressure and suction side is illustrated in Fig. 14.

The second pressure wave p^-, negative, occurs in the middle of the passage. It hits the suction side leading edge stronger (-3.0 percent of p_{t1} instead of -2.3 percent) and sooner ($t=0.85$ instead of 0.9) and reflects to hit the pressure side of blade $+1$.

The wake, seen as a negative jet sucking mass from the pressure side to the suction side [21], is convected through the rotor passage and only influences clearly the pressure distribution when it is impinging on the rotor leading edge (w around $t=0.45$ at $s=0.2$, pressure deficit -4.2 percent). Then one peak w^+ on the suction side and one sink w^- on the pressure side appear like traveling between the wake vortices, but cannot be surely related to the wake; their amplitude is yet less than the potential disturbances.

According to the geometry of the rotor, peak 1 has mainly an influence on f_x and is strong enough to break its sinusoidal shape

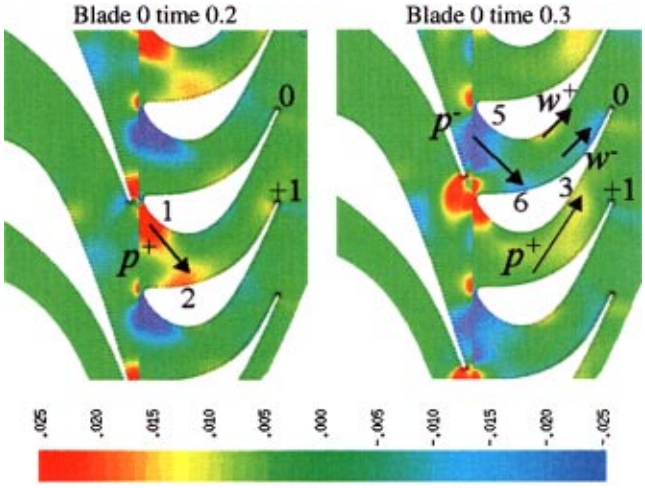

Fig. 13 Perturbation pressure field at $g_{ax}=8$ percent, at times 0.2 and 0.3

(decrease of the first harmonic). The rest of the disturbances are weaker and add higher harmonic to the fundamental sinusoidal.

This parametric study showed that, below axial gap 21 percent, not only the first harmonic but also the second to the fourth harmonics should be taken into account. This requirement originates in the potential interaction, which presents several pressure wave reflections in addition to the sinusoidal excitation.

Vane Study. The results presented in [10,11] suggested that the pitch ratio had a major influence on the excitation and a corresponding variation was performed for the present case. As expected, the scaling of the vanes leaves the mean rotor flow conditions non-effected whereas the pure reduction of the vane number (case -4) increases the mean stator load and rotor load. The unsteady blade excitation will be the subject of the following discussion. Figure 15 shows the comparison of rotor blade surface pressures due to the studied vane configurations.

The amplitude shows that the vane scale has a significant influence on the 1st harmonic blade excitation. The small stator leads to a reduction of the excitation level by more then 50 percent at almost all blade locations, the increase of the stator as well as the removal of stator blades leads to a significant increase of excita-

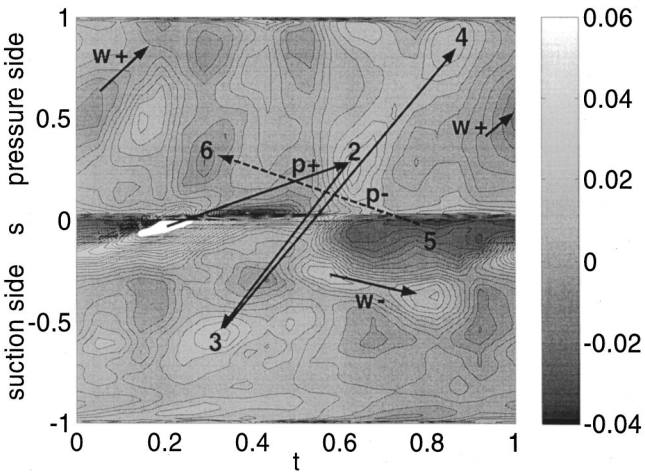

Fig. 14 Time space plot of the rotor surface perturbation pressure at $g_{ax}=8$ percent

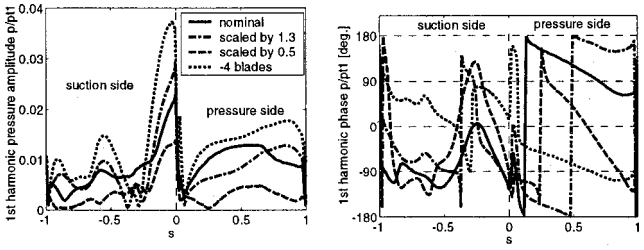

Fig. 15 1st harmonic of Rotor surface perturbation pressure, UNSFLO, vane study

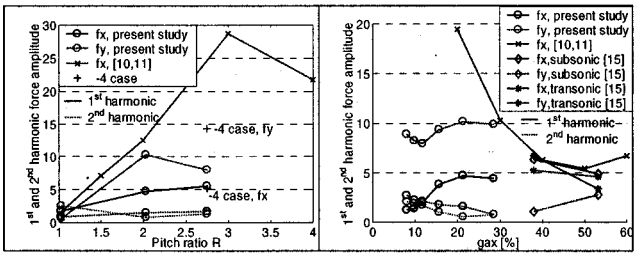

Korakianitis [10,11]:	*HP turbine $M_{2/stat}$=0.96 (maximum), single blade row study, UNSFLO*
Jöcker [15]	*HP turbine, $M_{2/stat}$=0.8/ 0.94 (subs./trans.), 2D stage study, UNSFLO*
Present:	*$M_{2/stat}$=0.73, stage study, UNSFLO*

Fig. 17 Comparison of present results to studies found in literature

tion level. With the geometrical differences of the cases in mind (see also Fig. 1) the following influences of the vane on the rotor excitation can be explained.

Phase Relations. For the presentation of these results the reference time ($t=0$) is always related to the geometrical alignment of the leading edges of vane and rotor. The change in vane pitch leads to an absolute phase difference between the cases of events, which are caused by similarly spread disturbances. The change of vane pitch also changes the relative time between the potential effects and the wake effects, because they spread in different directions. Hence, it is a tool to tune the phase between these effects. In the present study the wake influence is comparably small for the large vane cases, so that such a tuning effect has no significant influence.

Potential Field Strength. Larger vanes will necessarily be accompanied by stronger potential fields and stronger wake defects. In the present study the variation of the potential field is the main reason for the large differences in excitation. The 1st harmonic pressure amplitude varies strongly in the peaks on the suction side related to the unsteady potential pressure wave into the rotor (Fig. 15). For the large vane cases a shift of the pressure side excitation maximum towards the trailing edge can be seen in Fig. 15, probably because the stronger pressure wave propagates differently through the rotor passage. The small vane case has a significantly reduced potential excitation. The differences between the up- and down scaled vane cases (0.5 and 1.3) are pointed out in the time-space plots of unsteady surface pressure in Fig. 16.

The large vane case shows a comparable excitation pattern to the nominal (Fig. 6) dominated by reflected pressure waves in the passage. The small vane case is characterized by the wake influence on most parts on the blade, which are indicated by the pressure extrema in Fig. 16 (right side) traveling downstream with time. The potential influence is mainly limited to the leading edge region, the maxima due to the pressure wave of the large vane (left part of Fig. 16) are comparably weak for the small vane case.

Removal of Vanes. The (-4) case demonstrates that not only the size of the vane determines its potential excitation strength. This case produces a larger steady load and a larger excitation (relative to the steady load) due to the removal of four vanes. Both the pressure side excitation as well as the peaks on suction side are strongly increased (Fig. 15).

Wakes of Small Vanes. If the vane is small enough two (or more) consecutive wakes can influence the flow in one rotor passage at the same time. This is the case for the present small stator (0.5), which shows clearly the influence of two wakes on the pressure side (Fig. 16, right side), which results in a 2nd harmonic dominance in the excitation.

Excitation Frequency. The change of vane count changes also the excitation frequency, which is not visible in the presented figures. This is an important factor concerning the design because of the resonance danger at the blade eigenfrequencies.

Comparison to Other Studies. Figure 17 shows a comparison of the present results to a selection of results found in literature, which presented a comparable measure of excitation.

The fundamental study in [10,11] shows the trends to be expected when varying the parameters axial gap and vane pitch. The comparison to the present results and to results obtained by Jöcker [15] demonstrates that the unsteady excitation in a stage varies significantly due to the different geometries and operating conditions. In particular, expected trends might be violated in dependence of the actual conditions, as experienced in the present study for extremely small axial gaps. The comparison shows also that the present configuration is subjected to half the axial excitation levels of the case studied in [10,11] at the 30-percent axial gap. One reason for this is probably the difference in stator exit Mach number, which has a sensitive influence on the excitation when so close to transonic conditions. Both studies obtained similar trends in the axial force behavior in the range of 40–50 percent axial gap. However, as described in [15] the excitation can behave very differently in the force components and the moment, and the judgement of the excitation can only be done with the knowledge of the blade mode shapes.

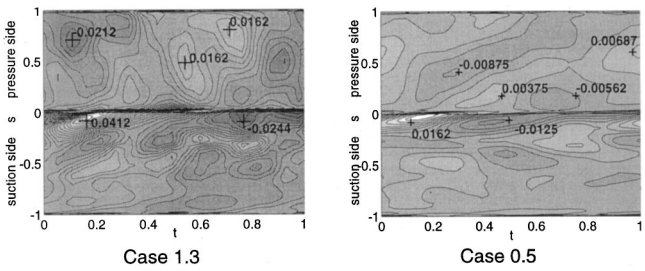

Fig. 16 Time space plots of blade surface perturbation pressure, scaled cases

Conclusions

In the context of a pre-design study for a subsonic turbine stage with extremely large blade loads, the unsteady rotor blade excitation and its dependence on design parameters could be estimated with a 2-D numerical method. The unsteady results of the nominal case could be reproduced with a different 2-D numerical method, but the 3-D results showed expected deviations in the steady flow predictions. The present 2-D study can probably not give the exact blade excitation but only the trends due to the parameter variation.

The blade excitation in the nominal case is dominated by potential effects, which appear in perturbation pressure wave reflections in the rotor passage. The influence of the wake in the nomi-

nal case on the excitation could be quantified and localized with help of gust calculations, which showed a very local and relatively small influence.

It was demonstrated that gust calculation methods, which apply simplified unsteady boundary conditions at the rotor inlet, are not sufficient to find the complex excitation mechanisms described in the present study. This is valid regarding higher harmonics in the excitation due to pressure wave reflections as well as regarding the correct prescription of the boundary conditions, as shown in the present gust study. It turned out that usual approaches to determine the gust amplitudes would give values leading to very different excitation predictions.

Comparisons to studies found in the literature showed that the excitation magnitude and trend with respect to the investigated parameters could vary significantly depending on the geometry and flow range.

To optimize the present design with regard to the blade excitation several recommendations can be given:

- When potential and vortical excitations are of same magnitude a phase tuning of the effects can result in a minimized excitation. Tools to change the relative phase are the axial gap and the stator pitch.
- The reduction of the axial gap does not necessarily lead to an increase of the 1st harmonic excitation level, when the involvement of higher harmonics disturb the basic sinusoidal excitation.
- The increase of axial gap beyond the nominal gives reduced blade excitations due to the decrease of potential stator influence and is suggested to reduce the high unsteady load.
- The size of the stator has a major influence on the excitation, especially when potential effects are dominant, and should be chosen as small as frequency and material integrity allow.
- The vanes number reduction does not only increase the stator and rotor steady load, but also the relative unsteady load. Hence, more vanes should be preferred if possible.

Acknowledgments

The work was carried out in collaboration between the Royal Institute of Technology (KTH) and Volvo Aero Corporation (VAC). The authors would like to thank for the fruitful support from Hans Mårtensson (VAC). The Swedish National Space Board supported this work. The opportunity to use the code UNSFLO provided by Rolls Royce (Dr. Peter Stow) is gratefully acknowledged.

Nomenclature

A = potential amplitude [percent]
$C_{ax,stator}$ = stator axial chord [m]
$C_{ax,rotor}$ = rotor axial chord [m]
D = wake velocity deficit $(w_{max}-w_{mean})*100/w_{mean}$ [percent]
f = perturbation blade forces in percent of time average [percent]
g_{ax} = axial gap in percent of rotor axial chord [−]
k = tangential wave no. [1/m]
M = Mach no. [−]
m = perturbation blade moment about $(x_{min},y_{min})_{Rotor}$ in percent of time average [percent]
p = pressure [Pa]
P = pressure wave amplitude $(p_{max}-p_{mean})*100/p_{t2/rot}$ [percent]
R = pitch ratio S_s/S_r [−]
s = normalized curvilinear distance on blade [−]
S_r = rotor pitch [m]
S_s = stator pitch [m]
T = temperature [K]
t = time/vane passing time [−]
$w,\vec{w}$ = relative velocity [m/s]
W = wake width normalized with S_s [−]
Φ = velocity potential $(=\nabla\vec{w})$ [m^2/s]
α = flow angle [deg]
$\partial(..)$ = spatial disturbance [−]
λ = axial wave no. [1/m]
ρ = density [kg/m^3]

Subscripts

1 = stage inlet
2 = between stator and rotor
3 = stage outlet
ax = axial
F = flux-averaged value
min, max, mean = minimum, maximum, average
t = total flow value
/rot = rotor frame of reference
/stat = stator frame of reference
W = wake frame of reference
x = axial direction
y = tangential direction

Abbreviations

2-D,Q3-D,3-D = two-, quasi-three- and three dimensional
LE, TE = leading edge, trailing edge

References

[1] Holmes, D. G., Mitchel, B. E., and Lorence, C. B., 1997, "Three Dimensional Linearized Navier-Stokes Calculations for Flutter and Forced Response," *8th Int. Symp. on Unsteady Aerodynamics and Aeroelasticity in Turbomachines*, Stockholm, Sweden.
[2] Silkowski, P. D., and Hall, K. C., 1997, "A Coupled Mode Analysis of Unsteady Multistage Flows in Turbomachinery," ASME Paper No. 97-GT-186.
[3] Giles, M., 1991, "UNSFLO: A Numerical Method For The Calculation Of Unsteady Flow In Turbomachinery," GTL Report No. 205.
[4] Jung, A. R., Mayer, J. F., and Stetter, H., 1996, "Simulation of 3D-Unsteady Stator/Rotor Interaction in Turbomachinery Stages of Arbitrary Pitch Ratio," ASME Paper No. 96-GT-69.
[5] He, L., 1999, "Three-Dimensional Unsteady Navier-Stokes Analysis of Stator-Rotor Interaction in Axial-Flow Turbines," Paper No. 557/049/99, *3rd European Conf. on Turbomachinery*, London, UK.
[6] Manwaring, S. R., and Wisler, D. C., 1993, "Unsteady Aerodynamics and Gust Response in Compressors and Turbines," ASME J. Turbomach., **115**, pp. 724–740.
[7] Chung, M.-H., and Wo, A. M., 1997, "Navier Stokes and Potential Calculations of Axial Spacing Effect on Vortical and Potential Disturbances and Gust Response in an Axial Compressor," ASME J. Turbomach., **119**, pp. 472–481, July.
[8] Lakshminarayana, B., Chernobrovkin, A., and Ristic, D., 2000, "Unsteady Viscous Flow Causing Rotor-Stator Interaction in Turbines, Part 1: Data, Code, Pressure," J. Propul. Power, **16**, No. 5.
[9] Chernobrovkin, A., and Lakshminarayana, B., 2000, "Unsteady Viscous Flow Causing Rotor-Stator Interaction in Turbines, Part 2: Simulation, Integrated Flowfield and Interpretation," J. Propul. Power, **16**, No. 5.
[10] Korakianitis, T., 1992, "On the Prediction of Unsteady Forces on gas Turbine Blades: Part 1—Description of the Approach," ASME J. Turbomach., **114**, pp. 114–122.
[11] Korakianitis, T., 1992, "On the Prediction of Unsteady Forces on gas Turbine Blades: Part 2—Analysis of the Results," ASME J. Turbomach., **114**, pp. 123–131.
[12] Busby, J. A., Davis, R. L., Dorney, D. J., Dunn, M. G., Haldeman, C. W., Abhari, R. S., Venable, B. L., and Delaney, R. A., 1999, "Influence of Vane-Blade Spacing on Transonic Turbine Stage Aerodynamics Part II: Time-Resolved Data and Analysis," ASME J. Turbomach., **121**, pp. 673–682.
[13] Venable, B. L., Delaney, R. A., Busby, J. A., Davis, R. L., Dorney, D. J., Dunn, M. G., Haldeman, C. W., and Abhari, R. S., 1999, "Influence of Vane-Blade Spacing on Transonic Turbine Stage Aerodynamics Part I: Time-Averaged Data and Analysis," ASME J. Turbomach., **121**, pp. 663–672.
[14] Von Hoyningen-Huene, M., and Hermeler, J., 1999, "Time-Resolved Numerical Analysis of the 2-D Aerodynamics in the First Stage of an Industrial Gas Turbine for Different Vane-Blade Spacings," ASME Paper No. 99-GT-102.
[15] Jöcker, M., Freudenreich, K., and Fransson, T., 2000, "Parametric Studies of the Aerodynamic Excitation in High Pressure Turbines," *9th Int. Symp. on Unsteady Aerodynamics, Aeroacoustics and Aeroelasticity of Turbomachines (ISUAAAT) Lyon, France*, September 4–7.
[16] Moss, R. W., Ainsworth, A. W., Sheldrake, C. D., and Miller, R., 1997, "The Unsteady Pressure Field Over a Turbine Blade Surface: Visualization and In-

terpretation of Experimental Data,'' ASME Paper No. 97-GT-474.
[17] Hilditch, M. A., Smith, G. C., and Singh, U. K., 1998, ''Unsteady Flow in a Single Stage Turbine,'' ASME Paper No. 98-GT-531.
[18] Birch, T., 1987, ''Navier-Stokes Predictions of Transition, Loss and Heat Transfer in a Turbine Cascade,'' ASME Paper No. 87-GT-22.
[19] Eriksson, L.-E., 1990, ''A Third Order accurate Upwind-Biased Finite Volume Scheme for Unsteady Compressible Flow,'' *VFA Report 9370-154, Volvo Aero Corporation*, Trollhättan, Sweden.
[20] Eriksson, L. E., 1995, ''Development and Validation of Highly Modular Flow Solver Versions in G2DFLOW and G3DFLOW Series for Compressible Viscous Reacting Flow,'' *Technical Report 9970-1162 Volvo Aero Corporation, Sweden*.
[21] Hodson, H. P., and Dawes, W. N., 1998, ''On the Interpretation of Measured Profile Losses in Unsteady Wake-Turbine Blade Interaction Studies,'' ASME J. Turbomach., **120**, Apr..
[22] Goldstein, M. E., 1978, ''Unsteady Vortical and Entropic Distortions of Potential Flows Round Arbitrary Obstacles,'' J. Fluid Mech., **89**, Part 3, pp. 433–468.
[23] Feiereisen, J. M., Montgomery, M. D., and Fleeter, S., 1993, ''Unsteady Aerodynamic Forcing Functions—A Comparison Between Linear Theory and Experiment,'' ASME Paper No. 93-GT-141.

Development and Evaluation of a High-Resolution Turbine Pyrometer System

Torsten Eggert[1]
e-mail: torsten.eggert@de.bosch.com

Bjoern Schenk[2]

Helmut Pucher

Technical University Berlin,
Institute of Combustion Engines,
10587 Berlin, Germany

Optical pyrometers provide many advantages over intrusive measuring techniques in determining the spatial and time varying temperature distribution of fast rotating components in gas turbines. This paper describes the development and evaluation of a versatile high-resolution pyrometer system and its application to radial turbine rotor temperature mapping as has been done in a R&D project at the Technical University Berlin under funding from Siemens Power Generation (KWU). The development goal was a pyrometer system with a temporal resolution of 1 μs, a minimum field of view of 1 mm, and a measurement range from 600 to 1500°C. A prototype of the pyrometer system has been built and tested at the small gas turbine test facility of the Technical University Berlin. The system yielded excellent results with respect to measurement uncertainty, resolution, and reliability. Finally, measurement results obtained with the new system on a radial turbine rotor and on a heavy duty industrial gas turbine are compared with measurements conducted with a commercially available turbine pyrometer system.
[DOI: 10.1115/1.1452245]

Introduction

The thermal efficiency of gas turbine engines has been steadily climbing over the past three decades. However, the tradeoff for greater efficiency has been significantly higher gas temperatures at turbine inlet and increasingly severe combinations of temperature and stress on the rotating components. The determination of the thermal loading of gas turbine blades implies the accurate knowledge of the actual surface temperature distribution of the vanes and rotating blades. The capacity to accurately measure temperature in the turbine's rotating components has thus become an integral part of the development and monitoring phases of these machines. A comprehensive review of the developments and applications in fast-response noncontact radiation thermometry applied to gas turbines which have been conducted worldwide over the past three decades, has already been presented elsewhere; see Schenk and Raake [1]; Eggert [2].

Fundamentals of Radiation Pyrometry

In general, an optical device is used to define the sampling area on the target surface and relay collected radiation to a light-sensitive detector, typically a photodiode (Fig. 1). The low-level photosignal produced by the detector is amplified and then often conditioned to give an output signal linear with target temperature. Calibration of the instrument is obtained by sighting it onto targets (usually blackbody furnaces) at known temperatures and recording the output signal.

Radiation Model. Depending on the application (location of the pyrometer probe and optical sight path) and the engine design (combustor alignment), pyrometer measurements may require a computer model to accurately interpret the signals as discussed by De Lucia and Lanfranchi [3]. This is due to the fact that in nonisothermal systems such as cooled axial turbine stages, or even uncooled radial turbine stages, the total sensed (exitent) radiation comprises two major components:

- radiation produced as the result of the target surface temperature (emittent radiation);
- radiation reflected due to inter-reflection between the target surface and its surroundings (adjacent blades, nozzle guide vanes, combustor liner).

Assuming that the transmission characteristic of the optical system is independent of the wavelength within the wavelength range of interest (given by the detector), the signal output of the pyrometer can be expressed as

$$U = Z \cdot \tau_{\text{system}} \cdot \omega_T \cdot A_T \cdot \int_{\Delta\lambda} \epsilon_a(\lambda, T) \cdot L_b(\lambda, T_T) \cdot R(\lambda) d\lambda \quad (1)$$

with

$$\epsilon_a = \frac{L_{\text{ex}}(\lambda, T)}{L_b(\lambda, T_T)} \quad (2)$$

where

$$L_{\text{ex}_i} = L_{\text{em}_i} + L_\eta = \epsilon_{m_i} L_{b_i} + \frac{(1-\epsilon_{m_i})}{A_i} \cdot \sum_{j=1}^{n} A_j L_{\text{ex}_j} F_{ij} \quad (3)$$

and according to Planck's law

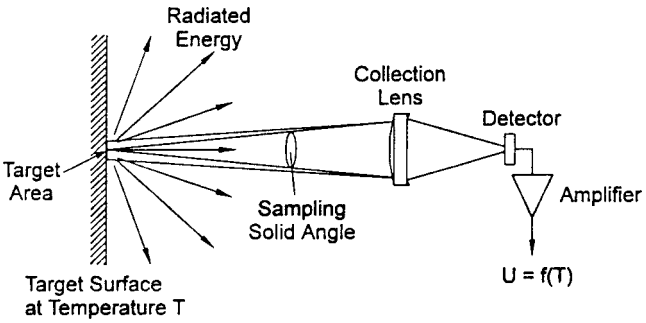

Fig. 1 Measurement principle

[1]Since 1999 with Robert Bosch GmbH, Stuttgart, Germany.
[2]Since 1997 with Honeywell Engines & Systems (former AlliedSignal Engines), Phoenix, AZ.

Contributed by the International Gas Turbine Institute and presented at the International Gas Turbine and Aeroengine Congress and Exhibition, New Orleans, Louisiana, June 4-7, 2001. Manuscript received by the IGTI, January 24, 2001. Paper No. 2001-GT-578. Review Chair: R. A. Natole.

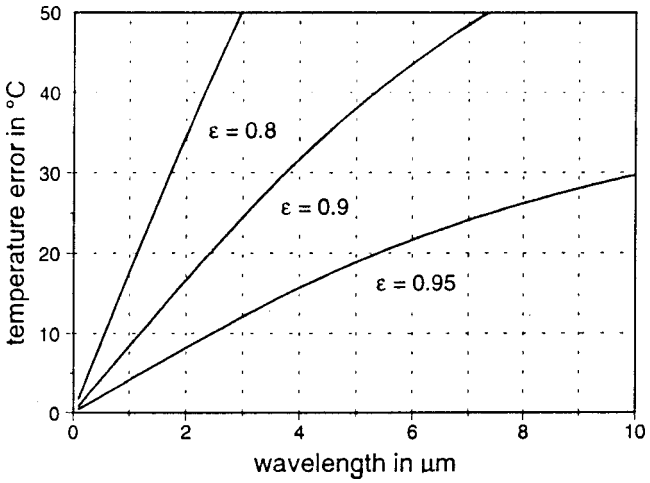

Fig. 2 Temperature measurement error due to unknown target emissivity

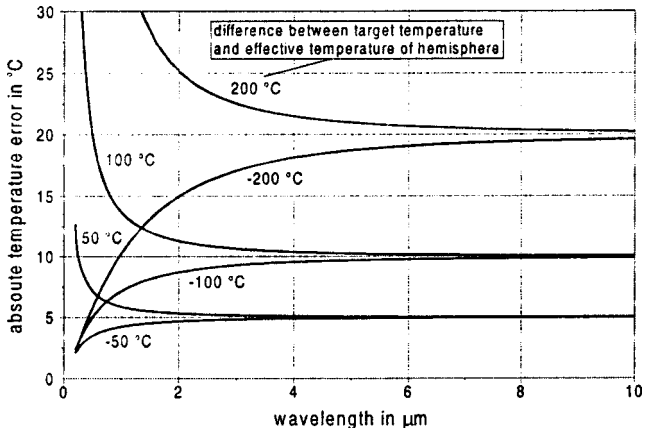

Fig. 3 Temperature measurement error due to environmental irradiation (T_M=1000°C, ϵ=0.9)

$$L_b(\lambda,T)=\frac{c_1}{\lambda^5\cdot(e^{c_2/\lambda T}-1)} \tag{4}$$

An approximation often used to simplify the calculation of radiative heat transfer is Wien's law, whose validity is limited by the condition $(\lambda T)\ll c_2$, so that

$$L_b(\lambda,T)=\frac{c_1}{\lambda^5\cdot e^{c_2/\lambda T}} \tag{5}$$

Since the pyrometer reads the global target radiation, the reflected component could represent an irritating source of error. Consequently, one first has to estimate and then to subtract the reflected radiation L_η (which is related to the surface temperature distribution and the geometry) from the measured radiation $L_{ex,i}$, before proceeding to convert Wien's law. To overcome the estimation problem, De Lucia and Masotti [4] proposed a scanning radiation technique that requires no prior knowledge of the theoretical temperature distribution. The final error of this method strongly depends on the angular calibration, the positioning of the pyrometer probe, and the target emissivity.

Measurement Uncertainties. Figure 2 describes the measurement error for a spectral pyrometer that was calibrated on a black body and is used to detect thermal radiation from a target of unknown emissivity. Given the simplification that the influence of environmental irradiation can be neglected in Eq. (3), the measured temperature value is always smaller than the true target temperature for target emissivities $\epsilon<1$. Moreover, it is apparent from Fig. 2 that pyrometer systems using detectors, which operate at smaller wavelengths, are less sensitive to changes in target emissivity.

Since the target in a typical turbine is surrounded by a hemisphere of potentially higher or lower effective temperature than the target temperature itself, Fig. 3 illustrates the temperature measurement error of a spectral pyrometer viewing a target of 1000°C and a known emissivity ϵ of 0.9 for selected differences between the target temperature and the effective hemisphere temperature. The resulting measurement error is shown as an absolute value.

Figure 3 emphasizes that the accuracy of pyrometers operating at small wavelengths is greatly impacted by environmental irradiation, especially if the effective temperature of the hemisphere surrounding the target is significantly greater than the target temperature.

Turbine Pyrometer System Requirements

Spatial and Temporal Resolution. Sufficient spatial resolution of the observed target (small target spot compared with visible black width) is an important turbine pyrometer system requirement in order to highly resolve the temperature gradients around cooling holes and to accurately detect the step change in temperature once a new blade enters the optical path of a turbine pyrometer. On the other hand, for a given passing speed of the blades, the target spot size might be limited by the response time of the detector/amplifier unit and the maximum feasible amount of data to be processed and stored. Since the target application of the new pyrometer system is a heavy-duty gas turbine, a target spot size of 1 mm in diameter has been selected as a reasonable objective.

Given a blade tip speed of about 500 m/s, a point on the blade would completely pass through a 1 mm target spot in 2 μs. This translates into a frequency requirement of 500 kHz for the detector/amplifier unit. In order to achieve a temperature resolution of 1°C, maximum damping of 1% of the electrical signal is allowed.[3] This equals an allowable damping of -0.2 dB, which in turn translates into a required -3 dB frequency response of about 1 MHz for the system. However, it has been shown that this consideration is only valid for an infinitesimal small radiation (point) source. Due to the averaging effect of a finite target spot size, the required frequency response of the system is only half of the foregoing, if the radiation source (target) moving into the optical sight path of the system is at least as big as the target spot diameter [2]. Therefore, a frequency response of 1 MHz has been selected as a conservative objective, resulting in a more than adequate dynamic system characteristic for the chosen target spot diameter.

Other important system requirements which arose from the designated application (turbine geometry, combustion gas composition, etc.) include:

- mountable probe geometry;
- given measuring distance;
- opacity of sight path (emission and absorption of combustion gas);
- optical access to target object;
- insensitive to contamination of the optical system;
- expected blade surface temperature range (600–1500°C, depending on application).

[3]The nonlinear relationship between target temperature and detector output signal is extremely dependent on the wavelength of the detected radiation. Therefore, the cited value is valid for a wavelength of about 1 μm, which is representative for the effective wavelength of the pyrometer system.

System Design

An optical turbine pyrometer system usually consists of:

- the optical probe (so-called sight tube);
- the detector/amplifier unit;
- the signal conditioner and data acquisition unit.

Probe Design. It is the sight tube's task to hold the optical system in the proper geometric relationship to the target and to provide an interface between the optics and the engine. Major design considerations regarding the optical probe were:

- miniaturization to avoid significant flow disturbance;
- highly effective cooling scheme to protect the probe in the severe hot gas environment for the duration of the measurement;
- design for simple exchange of (damaged) optical components;
- design for manufacturability.

The indirect viewing method (Fig. 4) has been chosen, since it is especially applicable to research and development projects, because the radial access to the turbine casing allows measurements at varying radii by simply moving the sight tube into and out of the turbine casing. By turning the sensor along its center axis it is possible to explore areas which would be inaccessible for rigid sensors. A 45-deg deviation mirror or prism has to be installed in the lower section of the sight tube reflecting the thermal radiation by 90 deg towards the optical system. These sight tubes are usually made of a high-temperature nickel-base alloy (or eventually even an ODS-alloy) and are additionally internally air or water-cooled.

Due to the high thermal loading of the probe, a double-wall, water-cooled, cylindrical design has been chosen (Fig. 5). The probe head features a removable prism fixture, which allows easy access to the prism for cleaning or exchange purposes. This feature also enables the use down-looking prisms or the use of an optical component, which is suitable for measurements at a different wavelength. The probe head of the prototype system, which is intended to be applied to a small radial turbine rotor, has an outer diameter of 18 mm, while the probe head of the sight tube for use in heavy duty gas turbine features a 22-mm outer diameter. Once the water-cooling capability reaches its limit, an additional plasma-sprayed yttria-stabilized-zirconia (YSZ) thermal barrier coating (TBC) can be applied for further improvement in probe protection, if required for future applications in even more severe environments.

The mechanical probe design included heat transfer calculations to determine the thermal loading to optimize the cooling scheme of the probe, thermo-mechanical stress analysis including probe bending to ensure probe integrity during operation, as well as vibration analysis. Although this work has been conducted at

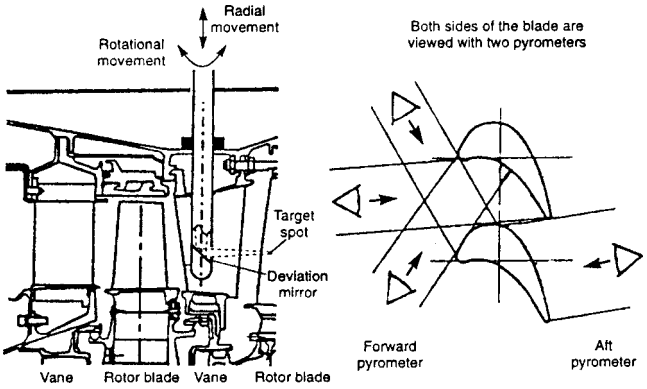

Fig. 4 Mirror viewing access (indirect viewing method)

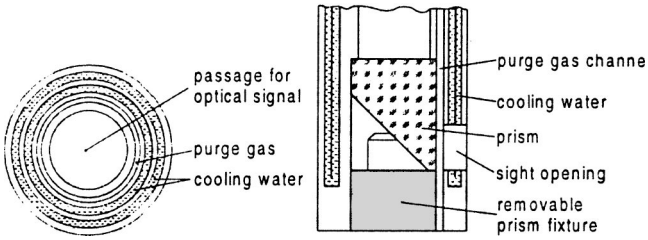

Fig. 5 Cooling scheme and optical probe head design

the Technical University Berlin by the authors, a detailed description of the work has already been presented by Siemens Power Generation (KWU) elsewhere [5], and therefore will not be repeated in this paper for the sake of brevity.

Optical System. Figure 6 illustrates the entire optical system which is incorporated in the probe and outlines the main optical components and design features in a detailed fashion. The optical system consists of a quartz prism having a gold coating with a diamond top coat on its backface, a quartz glass lens, an array of apertures to minimize incidence of irradiation, and an adjustable light guide, which allows adjustment of the field of view (distance to target for sharp image) over a wide range. Figure 6 also emphasizes another important feature of the modular probe design, i.e., the use of down-looking prisms (104.6 deg maximum ray deflection) in order to scan areas close to the blade root, which would not be accessible with a standard 90-deg prism. Figure 7 shows the final probe of the prototype pyrometer system.

Detector and Amplifier. The goals in the design of the detector system are to achieve the maximum signal-to-noise ratio as the photo current conversion, a fast time response, small linear and nonlinear distortions and a sufficient slew rate reserve in order to exclude transient intermodulation at high signal dynamics [6].

For small changes in target temperature the rate at which radiant energy varies with the target temperature is inversely proportional to the wavelength of the radiation. Therefore, it is clearly advantageous to employ a detector which responds only to extremely short wavelengths. Silicon-PIN-photodiodes are usually applied to turbine pyrometer systems to detect the thermal radiation. They are responsive only to radiation in the 0.4–1.2 μm range, have response times below 1 μs, and most importantly, absorption of radiation by the combustion gas (CO_2 and water vapor, which are normally present in turbine engines) is of no consequence since this occurs only for wavelengths longer than 1.5 μm. Unfortunately, relying on this short spectrum of radiation which is far removed from the emission peak of thermal radiation at lower temperatures (below 1000°C) gives insufficient signal below about 600°C for typical turbine pyrometer optical systems as discussed by several authors, e.g., [7,8]. A more useful parameter among the minimum detectable temperature is the achievable temperature resolution. This is the incremental change in target temperature that will cause an incremental change in radiation energy input to the detector that is just equal to the noise-equivalent-power to the detector/amplifier unit. That means it is quite possible to detect a relatively low temperature without being able to achieve a sufficient temperature resolution. Therefore, a silicon avalanche photodiode (Si-APD) has been selected for the new pyrometer system. Si-APDs provide the advantage of internal signal amplification and are responsive to radiation in the same range as silicon-PIN photodiodes (0.4–1.2 μm). The APD selected for the system is illustrated in Fig. 8. It is equipped with an internal temperature control circuit and achieves an internal signal amplification factor of 300.

The quality of the signal-to-noise ratio and the dynamic sensor performance depend strongly on the detector operating mode and the detector circuit. It can be stated that the best results concerning

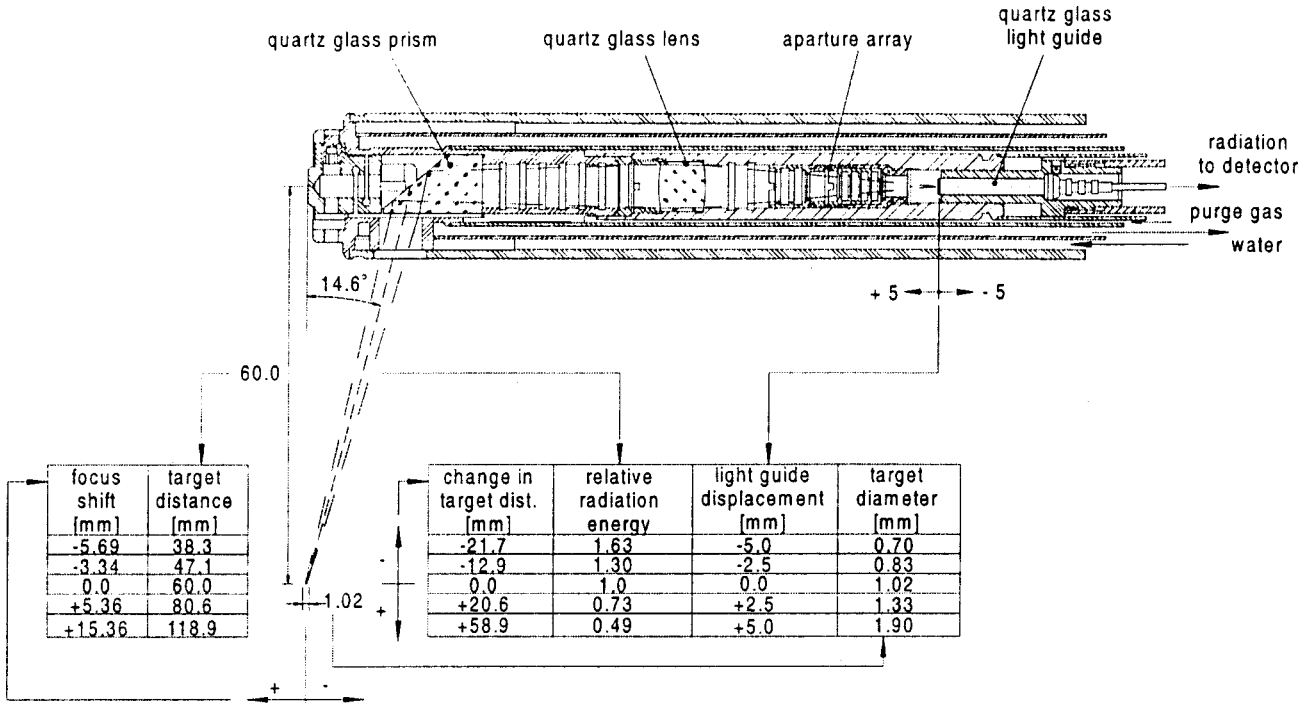

Fig. 6 Modular and flexible design of optical system

the noise and distortion reduction have been obtained by the choice of a transimpedance photoamplifier. It turned out that in this case the dominant noise is produced by the amplifier elements. By a proper selection of low-noise operational amplifiers, a high signal-to-noise ratio can be achieved. Figure 9 shows a schematic of the complete electrical system of the prototype pyrometer system, featuring a silicon APD and a low-noise transimpedance amplifier. The system was designed to achieve −3 dB frequency response of 1 MHz.

To prevent saturation of the amplifier, a range switch in terms of changing the high voltage bias of the APD has been incorporated in order to allow temperature measurements over the requested broad range of 600 to 1500°C. The significantly improved temperature resolution capability of this Si-APD/transimpedance amplifier setup compared with conventional turbine pyrometer detector/amplifier units is shown in Fig. 10.

Signal Processing. The amplifier system has been equipped with an in-house developed analog eight-pole Butterworth anti-aliasing filter to prevent misinterpretation of high frequency noise during the subsequent A/D conversion. The filter has a cut-off frequency of 500 kHz, which is given by the maximum frequency of the radiation signal obtained from the target. In order to satisfy the Shannon-theorem (sampling theory), the system contains a 12-bit A/C converter with a frequency response of 1 MHz. A/D conversion is triggered by a one-per-revolution signal provided by a fast-response optical speed sensor located close to the engine shaft. This trigger pulse is also used to establish the angular po-

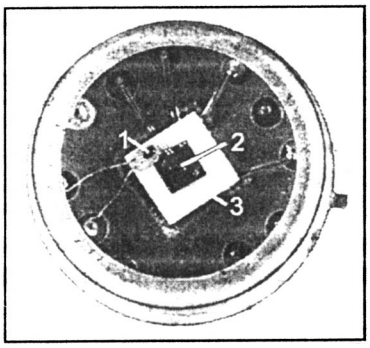

Fig. 8 Si-APD with temperature sensor and Peltier-cooler. 1: Temperature sensor, 2: detector element, 3: Peltier cooler.

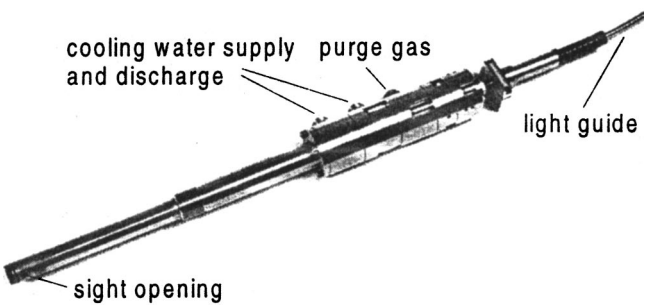

Fig. 7 Probe of the prototype pyrometer system

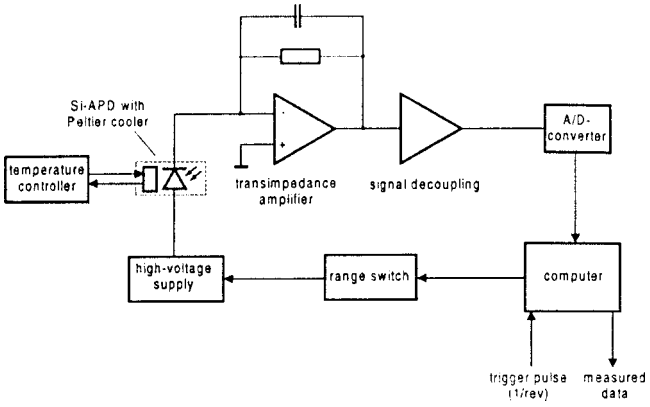

Fig. 9 Schematic of signal processing system

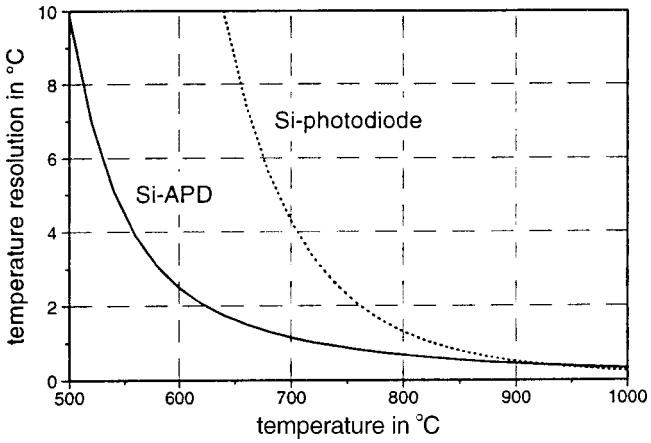

Fig. 10 Temperature resolution of silicon-based detectors operating with a transimpedance amplifier

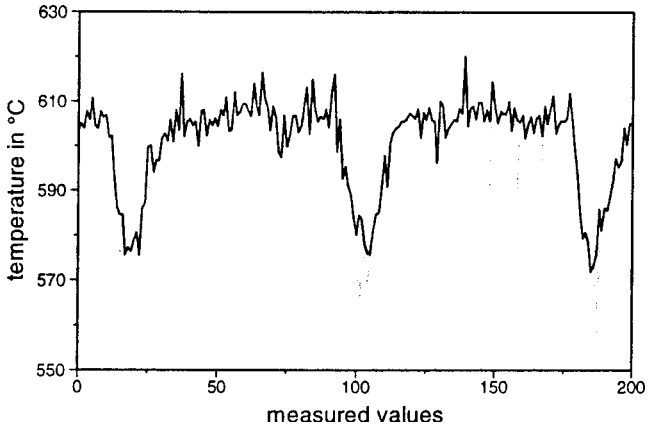

Fig. 11 Comparison of two different digital signal averaging methods

sition of each discrete digital value on the rotor. Values are typically recorded for one revolution per radial probe position. It is recommended to record over multiple revolutions for digital filtering purposes though, i.e., minimizing noise by averaging the measured values from multiple revolutions. This method is especially beneficial for measurements of low-target temperatures, which in turn result in relatively small signal-to-noise ratios. Figure 11 compares two methods of averaging the values obtained over multiple revolutions. The gray curve results from averaging the values of five-revolutions, while for generation of the black curve sometimes only four values were averaged, if the fifth value deviated significantly from the other four values. The latter method represents the preferred way of digital filtering.

Averaging over more than five revolutions has proven to only marginally improve the signal quality any further , and would also result in significant memory requirements.

System Evaluation

Prior to system evaluation in real gas turbine engine environments, the new pyrometer system has been optimized and extensively evaluated in a laboratory environment. Using very fast light emitting diodes, the dynamic system response and signal-to-noise ratio has been optimized especially for low target radiation (simulating target temperatures below 700°C). Upon completion of these tests, the system has been calibrated at a black body furnace prior to assembly in the small gas turbine test bed.

Gas Turbine Test Bed Evaluations. Figure 12 illustrates the

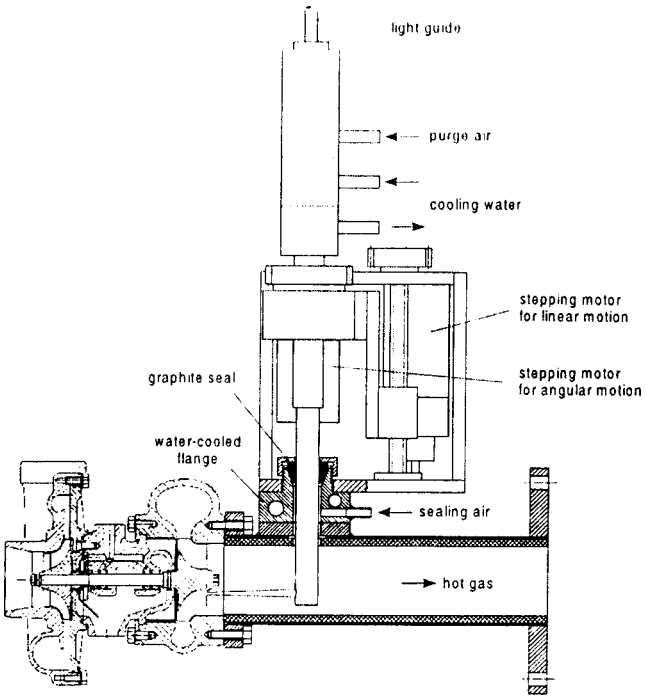

Fig. 12 Application of new pyrometer system to small gas turbine test bed

application of the pyrometer probe and traversing unit to the small gas turbine test bed of the Technical University Berlin [9], in this case equipped with a standard automotive turbocharger. The linear and angular positioning accuracy of the traversing system is 0.1 mm and 0.1 deg, respectively. For complete mapping of the temperature distribution of the radial turbine rotor (65-mm tip diameter, and 55-mm visible diameter), the probe was moved radially inwards in 0.5 mm steps. At each radial position the system recorded target radiation over five revolutions.

The same surface temperature measurement was repeated using

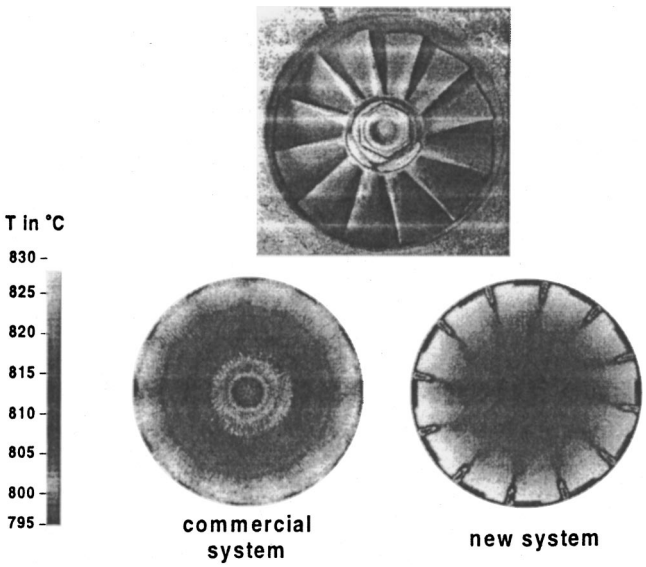

Fig. 13 Radial turbine rotor temperature distribution measured by two different pyrometer systems at 100,000 rpm and 900°C turbine inlet temperature

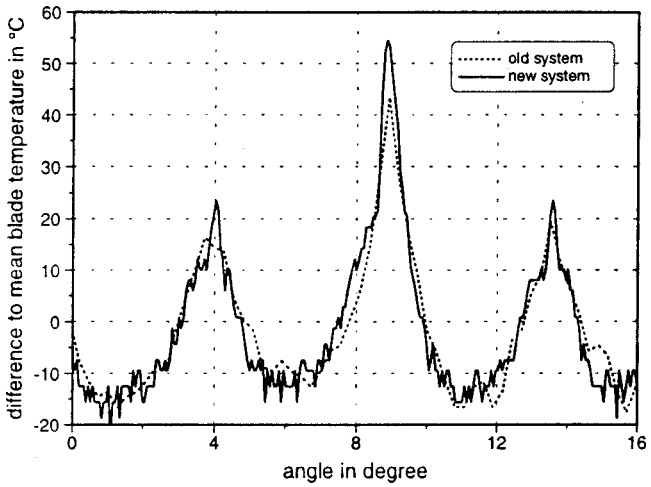

Fig. 14 Temperature distribution of axial turbine blades measured by two different pyrometer systems

a commercially available turbine pyrometer system, which features a target spot diameter of 4 mm, and a −3 dB frequency response of 150 kHz.

Figure 13 shows a comparison of the results obtained from the two systems, which emphasizes the dramatic improvement in temporal and spatial resolution achieved by the new system.

The same comparison was performed on the second stage turbine blades of a 90-Hz Siemens V64. 3A heavy duty gas turbine in the Siemens gas turbine test facility in Berlin. Figure 14 again illustrates the superior performance and fidelity of the new pyrometer system. The measured temperature trace of three adjacent blades at a given radial position is shown. The blade experiencing the highest surface temperature was equipped with strain gages, which resulted in a changed temperature distribution compared to the noninstrumented standard blades.

Summary and Conclusions

A novel advanced mapping turbine pyrometer system with a nominal target spot diameter of 1 mm, a −3 dB frequency response of 1 MHz, for use over a broad target temperature range from 600–1500°C, has been successfully developed and evaluated. This valuable instrument offers improved measurement accuracy for turbine blade cooling research and field inspection, since it provides sufficient spatial and temporal resolution to accurately detect the temperature gradients around cooling holes, which has been a major challenge for commercially available state-of-the-art turbine pyrometers.

The modular design of the probe enables the use of optical components, which are suitable for measurements at a different wavelength. This is particularly important, since application of currently existing turbine pyrometry to ceramic-coated components is limited by the radiative properties of these materials. As noted earlier, the standard technique requires all surfaces to have high emissivity within the spectral band of the detector to avoid large measurement uncertainties. Ceramic thermal barrier coatings do not meet these requirements. Coatings such as yttria-stabilized zirconia deposited on a metallic underlayer, itself deposited on a metal substrate, generally have low spectrally dependent emittance in the wavelength of interest. High emissivity values just exist in the 8–12-μm band, which requires the use of different detectors and optical components. A design study of a novel fast-response, high-resolution pyrometer system for such applications has already been completed at the Technical University Berlin and will be presented in a separate publication in the near future.

Acknowledgments

The authors gratefully acknowledge the financial support provided by Siemens Power Generation (KWU), the technical contributions and excellent cooperation of Dr. Raake of Siemens Power Generation (KWU) over the course of the project, as well as the significant contributions of Mr. Federau of Schaefter and Kirchhoff Opto-Sensorik und Messtechnik (Hamburg, Germany) with respect to design and manufacturing of the optical probes.

Nomenclature

A = area, m^2
c_1 = first radiation constant, W μm^4 m^{-2} sr^{-1}
c_2 = second radiation constant, μm K
e = base of natural logarithm
F = angle factor
L = radiance, W m^{-2} sr^{-1}
n = no. of surfaces
R = spectral responsivity of detector, A/W
T = temperature, K
U = output signal, V
Z = transimpedance, V/A
ϵ = emissivity
λ = wavelength, μm
ω = solid angle, sr
τ = transmittance

Subscripts

a = apparent
b = blackbody conditions
ex = exitent
em = emittent
i,j = ith and jth elements
m = material
r = reflected
system = optical system
T = target

References

[1] Schenk, B., and Raake, D., 1995, "Fast Response Turbine Pyrometry for High Temperature Gas Turbine Applications—Present State of Technology and Future Demand," Proc. Int. Symp. "Local Strain and Temperature Measurements in Non-Uniform Fields at Elevated Temperatures," High Temperature Mechanical Testing Committee, Berlin, Germany.
[2] Eggert, T., 2000, "Turbine Pyrometry with High Spatial and Temporal Resolution," (in German), Ph.D. dissertation, Technical University Berlin (1999), Wissenschaft & Technik Verlag, Berlin, Germany.
[3] De Lucia, M., and Lanfranchi, C., 1992, "An Infrared Pyrometry System for Monitoring Gas Turbine Blades: Development of a Computer Model and Experimental Results," ASME-Paper No. 92-GT-80.
[4] De Lucia, M., and Masotti, G., 1994, "A Scanning Radiation Thermometry Technique for Determining Temperature Distribution in Gas Turbines," ASME-Paper No. 94-GT-39.
[5] Frank, S. F. L., Holt, T. O., Eisenlohr, H., and Raake, D., 2001, "Application of a High Resolution Turbine Pyrometer to Heavy Duty Gas Turbines," presented at 46th ASME Turbo Expo, New Orleans, LA, June 4–7.
[6] Koschel, W., Salden, D., and Hoch, T., 1986, "Turbine Rotor Blade Measurements Using Infrared Pyrometry," AGARD-CP 399, Philadelphia, PA.
[7] Beynon, T. G. R., 1981, "Turbine Pyrometry—An Equipment Manufacturer's View," ASME-Paper No. 81-GT-136.
[8] Kirby, P. J., 1989, "Some Considerations Relating to Aero Engine Pyrometers," AGARD-CP 399.
[9] Schenk, B., Eggert, T., and Pucher, H., 1998, "A Unique Small Gas Turbine Test Facility for Low-Cost Investigations of Ceramic Rotor Materials and Thermal Barrier Coatings," ASME-Paper No. 98-GT-554.

Three Component Velocity Field Measurements in the Stagnation Region of a Film Cooled Turbine Vane

Marc D. Polanka[1]
e-mail: marc.polanka@wpafb.af.mil

J. Michael Cutbirth[2]
e-mail: CutbirthJM@nswccd.navy.mil

David G. Bogard
e-mail: dbogard@mail.utexas.edu

Mechanical Engineering Department,
University of Texas at Austin,
Austin, TX 78712

The showerhead region of a film-cooled turbine vane in a gas turbine engine involves a complex interaction between mainstream flow and coolant jets. This flow field was studied using three component laser Doppler velocimeter measurements in a simulated turbine vane test facility. Measurements were focused around the stagnation row of holes. Low and high mainstream turbulence conditions were used. The spanwise orientation of the coolant jets, typical for showerhead coolant holes, had a dominating effect. Very high levels of turbulence were generated by the mainstream interaction with the coolant jets. Furthermore, this turbulence was highly anisotropic, with the spanwise component of the turbulent fluctuations being twice as large as the other components. Finally, there was an interaction of the high mainstream turbulence with the coolant injection resulting in increased turbulence levels for the spanwise velocity component, but had little effect on the other velocity components. [DOI: 10.1115/1.1459733]

Introduction

Cooling of gas turbine blades and vanes using discrete hole film cooling has been, and remains, a mainstay technology for gas turbine designs. There have been numerous studies of film cooling performance on many different test geometries from flat plates to circular cylinders to full airfoils. For most of these studies, the goal has been to understand the effects of the film cooling flow on such measurable quantities as the film-cooling adiabatic effectiveness and the surface heat transfer. However, there has been little study of the velocity field associated with coolant jet and mainstream interaction, and the resulting turbulence.

The greatest heat load on a turbine airfoil generally occurs at the leading edge. There have been a number of studies of airfoil leading edge film cooling using cylinders or cylindrical models with flat afterbodies. In general, cylinders simulate a turbine blade geometry, and film cooling hole patterns have been representative of those found on a blade. However, there are important differences between turbine blades and vanes. The stagnation point on a blade occurs at a point on the airfoil that can be reasonably modeled as a cylindrical surface with a somewhat symmetrical pressure distribution. For a turbine vane, the stagnation line is located well beyond the geometric leading edge towards the pressure side of the airfoil. The stagnation streamline is strongly curved as it approaches the vane airfoil, and the pressure distribution is highly nonsymmetric. Consequently, cylindrical models are not well suited for simulating a turbine vane.

There is also a significant difference in the film cooling hole configurations for the leading edge of turbine blades and vanes. The blade typically has two or three rows of holes symmetrically positioned around the stagnation line. These rows are usually fairly far apart with spacing between rows of the order of five hole diameters, and a pitch between holes of about seven hole diameters. In contrast, the vane has five to seven rows of holes positioned closer together (often termed the ''showerhead'' region). Consequently, the interaction among coolant holes will be significantly different for vane and blade leading edge cooling.

Studies of the velocity and turbulence fields associated with film cooling on the leading edge of a blade have been presented in a series of publications from Universität der Bundeswehr München, i.e., Ardey and Fottner [1,2], and Ardey et al. [3]. The configuration consisted of two rows of holes, one on the suction side and one on the pressure side of the stagnation line. The coolant jets on the suction side remained attached, and maximum turbulence levels were found in the core of the jets. On the pressure side, the coolant jets were separated from surface, and maximum turbulence was generated in the wake region below the separated jets. In both cases the turbulence was found to be highly anisotropic.

Showerhead film cooling configurations were incorporated in the simulated turbine vane models used by Abuaf et al. [4] and Ames [5]. However, the emphasis of these studies was the overall airfoil cooling, and no detail of the film cooling performance was obtained within the showerhead region. Studies of showerhead cooling designs were conducted by Bohn et al. [6] who showed movement of the stagnation line due to influence by film cooling jets. The emphasis of the current study was to obtain detailed velocity field measurements in the showerhead region of a film cooled turbine vane. These results complement measurements of the adiabatic effectiveness in the showerhead region published previously (Polanka et al. [7], and Witteveld et al. [8]). These measurements have also been supplemented by further work presented in Cutbirth and Bogard [9].

A large-scale turbine vane model was used in a cascade facility designed to correctly simulate the flow about the turbine vane. Special attention was placed on the effect of high mainstream turbulence levels, and on the impact of blowing ratio on the incoming stagnation line. This study represents the first attempt at highly detailed three component velocity measurements within the near-wall region of a film cooled showerhead. These details provide important validation data to the engine designers for development and evaluation of 3-D CFD simulations of this film cooling flow.

[1]Currently at the Air Force Research Laboratory-Wright Patterson AFB
[2]Currently at Naval Surface Warfare Center-Carderock Division

Contributed by the International Gas Turbine Institute and presented at the International Gas Turbine and Aeroengine Congress and Exhibition, New Orleans, Louisiana, June 4–7, 2001. Manuscript received by the IGTI, October 28, 2000. Paper No. 2001-GT-402. Review Chair: R. A. Natole.

Experimental Facility

To correctly model the flowfield surrounding a turbine airfoil vane, a simulated three vane cascade test section was built. A complete description of this facility can be found in Polanka [10]. The test section contained a central airfoil and two simulated neighboring airfoil surfaces. It was located in one corner of the closed loop wind tunnel as shown in Fig. 1. A 4:1 contraction ratio inlet nozzle preceded the inlet to the test section which was 1.02 m wide by 0.55 m tall. The side walls of the inlet section diffused slightly to maintain the freestream velocity constant as the boundary layers grew along the side walls. The flow then passed through two main passages around the central airfoil, and two bypass passages on the outside of the inner and outer airfoils. Flow rates through the bypass passages were controlled using adjustable throats. Adjustment of the flow through the bypass passages, along with a movable tailboard, allowed the stagnation streamlines on each of the three leading edges to be correctly positioned. This resulted in equal inlet flows (within 1%) for the two main passages.

A secondary flow loop was used to remove air from the main wind tunnel flow for use as the film cooling flow. This secondary air was driven by a single 7.5 hp, centrifugal blower. The blower brought air in from the wind tunnel just upstream of the fan and directed it into the primary film cooling heat exchanger. For these investigations the film cooling flow was run at the same temperature as the freestream so minimal cooling was needed in the secondary loop. Upon existing this heat exchanger, the coolant was split into three independent lines to feed the three airfoil cavities. The flow rates into the airfoil plenums were monitored via in-line orifices.

Airfoil and Film Cooling Configuration. The airfoil geometry was a large-scale model of a modern commercial turbine first stage vane. The Reynolds number ($Re = 1.2 \times 10^6$, based on chord length and exit velocity) was matched to that of the actual turbine operation. Dimensions for the model vane were a chord length of about 59.4 cm, a span of 54.9 cm, and a leading edge diameter of nominally 15 cm. The airfoil was built out of a polyurethane foam with a low thermal conductivity (0.048 W/mK). The forward section was machined to an even wall thickness of 1.37 cm to maintain the proper film cooling hole length to diameter ratio. The interior of the forward section was divided into three chambers, as shown in Fig. 2. This allowed independent control of cooling to the showerhead, suction side, and pressure side of the airfoil. For this investigation, only the showerhead coolant was utilized.

At the leading edge of the airfoil there was a six row showerhead film cooling configuration. Each row contained 11 holes each with diameter $D = 4.11$ mm. These holes had an injection angle of 25 deg with respect to the surface and were orientated 90 deg from the streamwise direction. The showerhead configuration consisted of one row on the design stagnation line with two rows toward the pressure side and three rows on the suction side. These rows were spaced $3.33D$ apart and the holes were positioned with a spanwise pitch of $P/D = 5.55$.

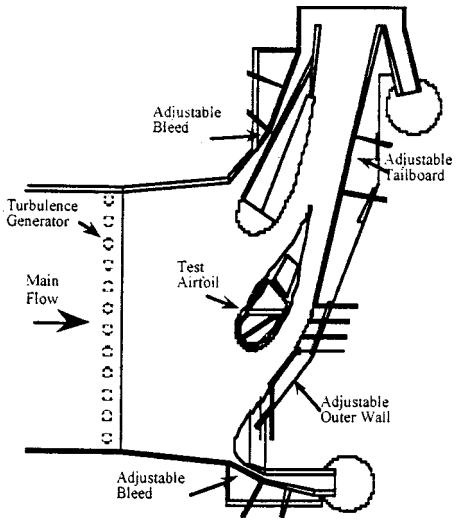

Fig. 1 Test section of turbine vane facility

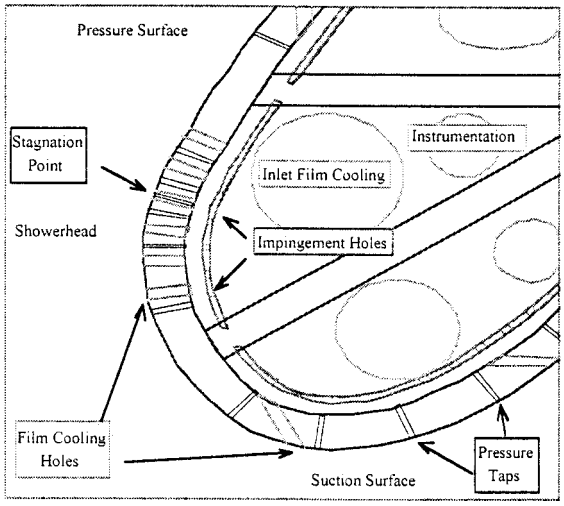

Fig. 2 Schematic of vane internal geometry

Impingement plates were installed inside the airfoil to correctly simulate the actual inlet flow to the film-cooling holes. Each impingement plate consisted of a nominally 1-mm-thick aluminum plate fixed into place with a 5.5-mm gap between the impingement plate and the inner airfoil wall. The impingement plates contained 7.8-mm-dia holes with the same pitch/film cooling hole diameter ratio of 5.55. The rows of impingement holes were located directly between the entrances to the film cooling holes in both the streamwise and spanwise directions. There were then 12 impingement holes per row to maintain the periodicity. Figure 2 shows the location of the impingement plate and holes along with the film cooling holes.

Measurements, Data Processing, and Uncertainty. The primary measurements for this investigation were three component velocities made with an LDV. The LDV was a standard TSI system modified to incorporate three components with side-scatter collection optics. TSI correlator processors incorporating sample bias corrections were used. The sample size used for these velocity measurements was 2000 points, which was typically acquired over a time period of about one minute, depending on the data rate. Precision uncertainties for these measurements were determined from statistical analysis of multiple samples at a given measurement location. Precision uncertainties were less than $\pm 2\%$ for the mean velocities for most of the measurements. Very near the surface of the airfoil a higher uncertainty for the mean velocities of $\pm 4\%$ was obtained because of the higher turbulence levels for the near wall region. The turbulence rms fluctuation measurements away from the airfoil surface had a precision uncertainty of $\pm 2\%$, increasing to $\pm 8\%$ near the wall.

Experimental Conditions

A series of tests were performed investigating the interaction of the showerhead cooling with the mainstream flow. To establish a baseline, a no-showerhead blowing condition was created with the showerhead holes covered with tape. This was compared to the velocity field for showerhead blowing ratios of $M = 1.0$ and 2.0. For all tests reported here, the stagnation line was positioned to impinge directly on the stagnation row of holes (the Stag row).

For this investigation the density ratio was maintained at DR $=1.0$. This was primarily due to refraction problems with the LDV laser beams. Ideally, the density ratio would have been DR $=1.8$ to make direct comparisons with the adiabatic effectiveness measurements taken on this airfoil [7]. However, at this density ratio, LDV measurements were not possible due to refraction effects interfering with the beams. In a separate study film cooling adiabatic effectiveness measurements were obtained at density ratios of 1.1, 1.2, and 1.8 [10]. These results showed that the adiabatic effectiveness were similar for all density ratios, suggesting a similar interaction of the jets with the mainstream.

All experiments were conducted with a mainstream approach velocity of $U_\infty = 5.8$ m/s, which established a Reynolds number matching that of actual engine operation. These tests were run with low and high mainstream turbulence. The low mainstream turbulence level was $Tu_\infty \approx 0.5\%$. The high mainstream turbulence generator, described by Polanka [10], consisted of 12 vertical, 3.8 cm diameter bars located 12.2 rod diameters upstream of the vane leading edge. At $x/c = 0.14$ upstream of the airfoil the turbulence intensity was $u_{\text{rms}}/U_\infty = 0.20$, with an integral length scale of $\Lambda_f = 4.2$ cm or $\Lambda_f/D = 10$. The mean velocity profile at high turbulence, shown in [10], was within 1% of the low turbulence profile and did not have any indication of wakes from the bar grid at this position. For high mainstream turbulence, the turbulence was uniform within $\pm 10\%$ across inlet to the vane passages [11].

Results

Three component velocity field measurements are presented for both low and high freestream turbulence in the showerhead region. This data is presented in the form of planes of data focused around the stagnation row of holes. The region of velocity measurements extended from six hole diameters in front of the stagnation row to the second hole on the pressure surface (PS2), streamwise. In the cross-stream direction, the measurement plane extended from about 14 hole diameters toward the inside of the tunnel to the first row of holes on the suction side (SS1). This box defined the region around the stagnation line and the stagnation row of holes. In the figures that follow the U and V components are shown as vectors while the W component is displayed as a contour plot.

The planes were taken at discrete locations along the span of the airfoil. The baseline height was at a $z/D = 48.9$ where $z = 0.0$

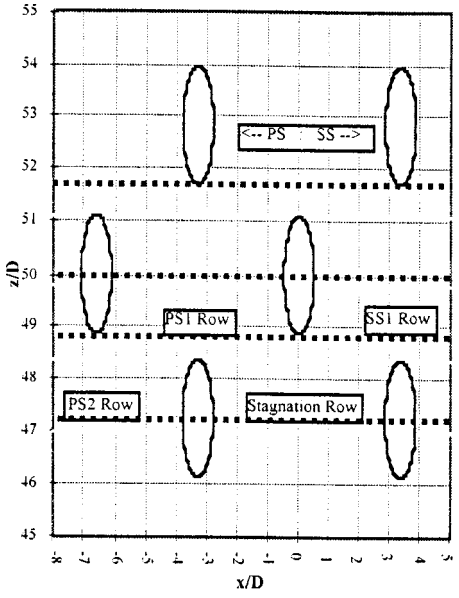

Fig. 3 Schematic showing positions of data planes relative to hole locations

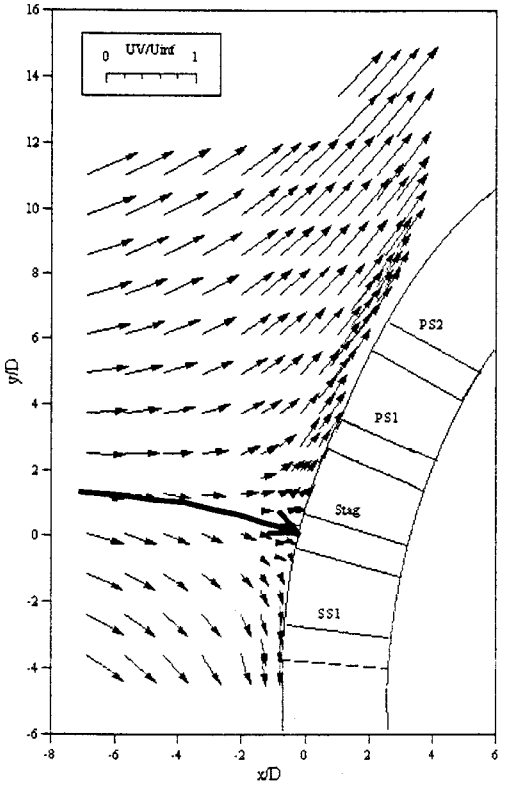

Fig. 4 Mean velocity field, no coolant injection, $Tu_\infty = 0.5\%$

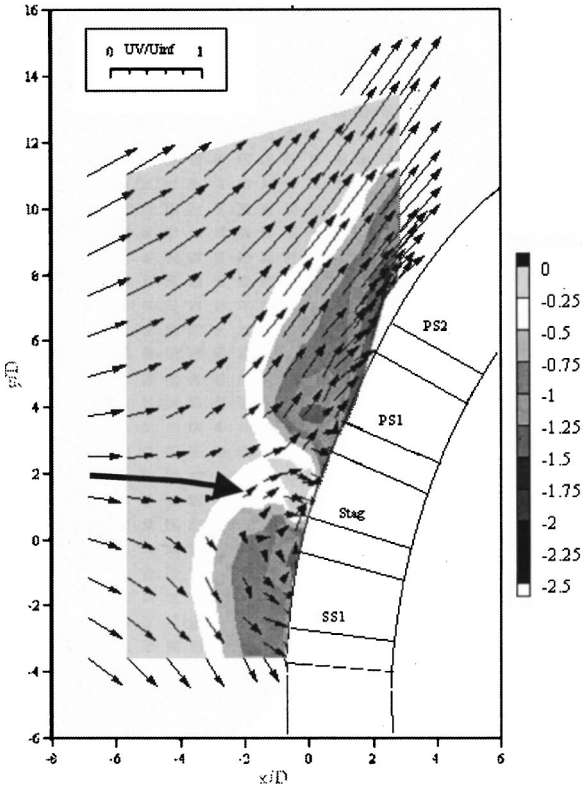

Fig. 5 Mean velocity field, $M = 2.0$, $Tu_\infty = 0.5\%$

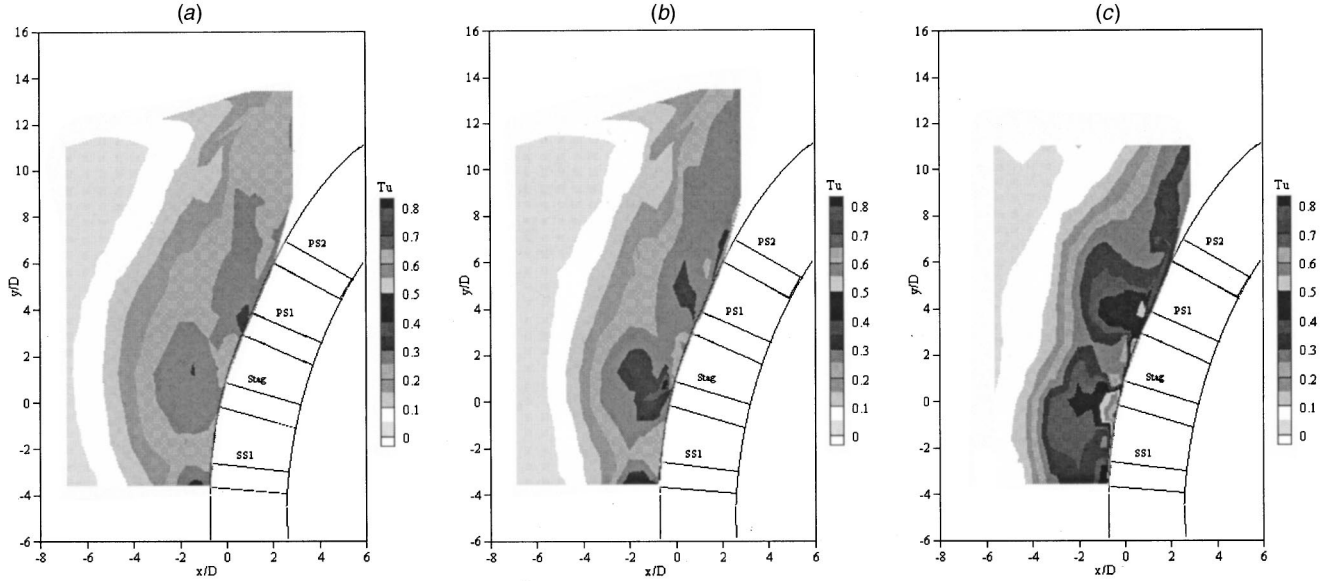

Fig. 6 Rms turbulence fields for $Tu_\infty = 0.5\%$—(*a*) u'/U_∞, (*b*) v'/U_∞, (*c*) w'/U_∞

was specified as the center of the Stag hole at the base of the vane (see [9]). This location was chosen because it was in the middle of the region utilized for film cooling effectiveness experiments reported on previously [7]. The position relative to the hole was chosen since it was where the peak W velocity was found for the nearest coolant hole in the showerhead row of holes. This position was very near the bottom of the coolant hole. Figure 3 shows a two dimensional projection of the region utilized for these measurements where the horizontal lines show the locations of the measurement planes to be discussed in the following paragraphs.

Low Turbulence. With low mainstream turbulence the velocity field was measured with the film cooling rows taped over to obtain a baseline undisturbed by film cooling injection. These measurements established a baseline flow to determine how coolant injection from the showerhead affected the stagnation region. The velocity field without coolant injection is presented in Fig. 4, showing a stagnate region encompassing the stagnation (Stag) row hole, but relatively strong cross-flows over the rows of holes on either side of the Stag row. The velocity field with coolant injection, with a blowing ratio of $M = 2.0$, is shown in Fig. 5. The plane of the velocity field presented in Fig. 5 was located at the bottom of a coolant hole in the stagnation row ($z/D = 48.9$ shown in Fig. 3). Contrasting the velocity fields in Figs. 4 and 5, it is evident that coolant injection causes a displacement of the stagnation streamline at least $2D$ from the surface.

Also shown in Fig. 5 are contours indicating the magnitude of the mean W velocity component. Relatively strong W component velocities are evident due to the spanwise orientation of the coolant holes. Velocity magnitudes in excess of $|W/U_\infty| = 0.5$ extend beyond $y/D = 2$ from the surface. This may be attributed to coolant flow from holes located farther up the row of holes. Between rows Stag and PS1 the magnitude of the W component velocity was low indicating that interaction of the mainstream with coolant jets caused the coolant jet from the Stag row of holes to flow primarily towards the suction side of the airfoil. In general the coolant flow from the stagnation row of holes was found to be very sensitive to the position of the approach stagnation streamline, with a slight shift in the streamline causing a shift in coolant flow from one side of the vane to the other.

Also evident in Fig. 5 is a displacement of the peak W velocity from the surface for the coolant jet originating from the PS1 row of holes. The core of this coolant jet appears to be $1D$ from the surface. Thermal field measurements reported in the companion study, Cutbirth and Bogard [9] showed that all the coolant jets in the showerhead region were separated from the surface.

Of particular interest was the turbulence levels generated by the interaction of the showerhead coolant jets with the mainstream. Contours plots showing the distribution of the three components u'/U_∞, v'/U_∞, and w'/U_∞, are presented in Figs. 6(*a*), (*b*), and (*c*), respectively. Immediately obvious from these contour plots is that the jet interaction with the mainstream causes significant turbulence levels, and that the turbulence is highly anisotropic. Peak levels for the three components were $u'/U_\infty = 0.3$, $v'/U_\infty = 0.4$, and $w'/U_\infty = 0.6$. These peak levels are extremely high turbulence levels; furthermore, for all three components the turbulence levels exceeded 0.25 at distances more than $2D$ from the surface. For

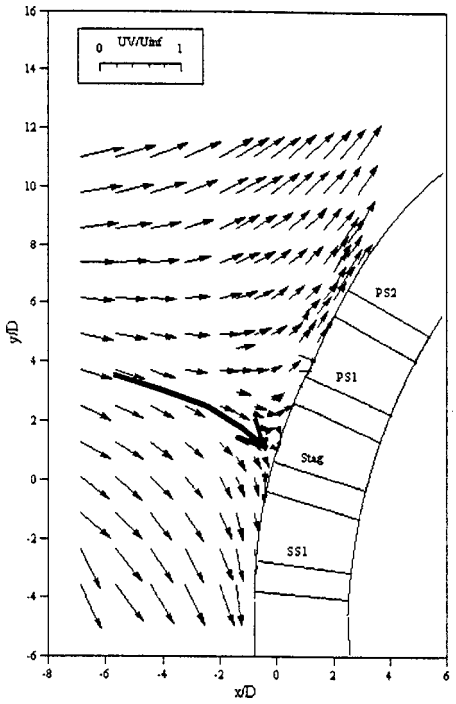

Fig. 7 Mean velocity field, no coolant injection, $Tu_\infty = 20\%$

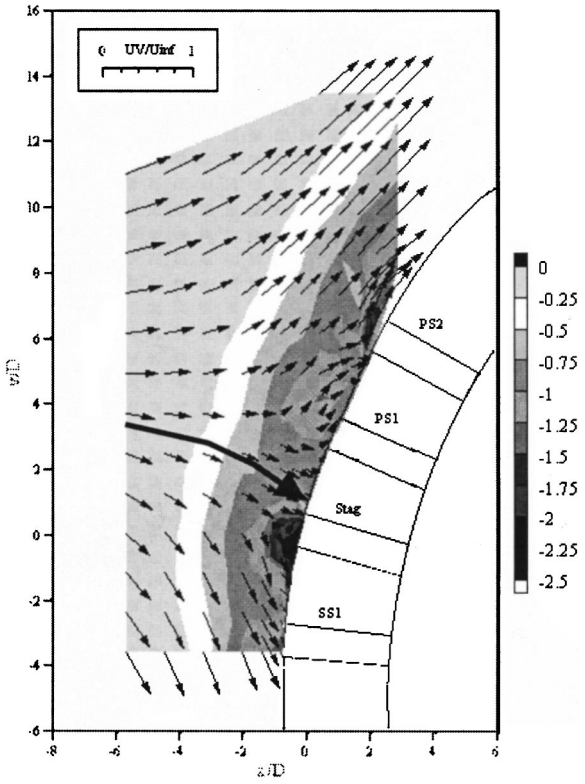

Fig. 8 Mean velocity field, $M=20$, $Tu_\infty=20\%$

comparison, the peak turbulence levels for a free jet would be $w'/U_{centerline}=0.3$, (see Hinze [12]). Furthermore, Pietrzyk et al. [13] measured turbulence levels along the centerline of a coolant jet with 35 deg injection angle on a flat surface. For a blowing ratio of $M=1.0$ and unit density ratio, the maximum turbulence levels were 0.2. Comparison to these cases highlights the relatively large turbulence levels generated in the showerhead region.

High Turbulence. Mean and turbulence velocity field measurements were repeated with a highly turbulent mainstream flow, without and with film cooling injection. For these experiments the turbulence level of the approach flow was $Tu_\infty=20\%$ with an integral length scale of $\Lambda_f=10D$. The mean velocity fields without and with coolant injection are presented in Figs. 7 and 8, respectively. The mean velocity field without coolant injection was very similar to the low mainstream turbulence case discussed previously (Fig. 4). However, there was noticeable difference when coolant injection with a blowing ratio of $M=2.0$ was used. Comparing Figs. 7 and 8, the mean velocity field appears to be essentially the same without and with coolant injection. In particular, there does not appear to be any displacement of the stagnation point away from the surface as occurred for the low mainstream turbulence case. This indicates that the high mainstream turbulence enables greater penetration of the mainstream through the coolant jets in the showerhead region.

Mean W component contours for the high mainstream turbulence case were similar to the low mainstream turbulence case (Fig. 5), except the high mainstream turbulence case had a more uniform distribution and extended farther from the wall.

Measurement of the turbulence field, u'/U_∞ and v'/U_∞ (not shown), without coolant injection showed that the streamwise component rms fluctuations, u', were suppressed close to the vane leading edge, i.e. within $3D$ of the surface. The v' fluctuations were amplified slightly in the same region. The suppression of the u' component was expected since this component is normal to the surface, and the amplification of the v' component was expected due to a reorientation of the turbulent fluctuations.

The turbulence field with high mainstream turbulence and coolant injection was of particular interest to determine whether the high mainstream turbulence disrupts the turbulence generated by the coolant jet interaction with the mainstream. Turbulence fields for the u'/U_∞, v'/U_∞, and w'/U_∞, turbulence fields with high mainstream turbulence are presented in Figs. 9(*a*), (*b*), and (*c*), respectively. Peak levels were found to be $u'/U_\infty=0.3$, $v'/U_\infty=0.35$, and $w'/U_\infty=0.6$, which were essentially the same as for the low mainstream turbulence case. However, there were some differences in the distributions of the rms turbulence fields. The u'/U_∞ fields for low and high mainstream turbulence were quite similar showing extended areas around the holes with $u'/U_\infty>0.25$. For the v'/U_∞ fields, the high mainstream turbulence case had slightly larger regions of $v'/U_\infty>0.3$ than the low turbulence case. However, for the w'/U_∞ field, there was a distinct difference

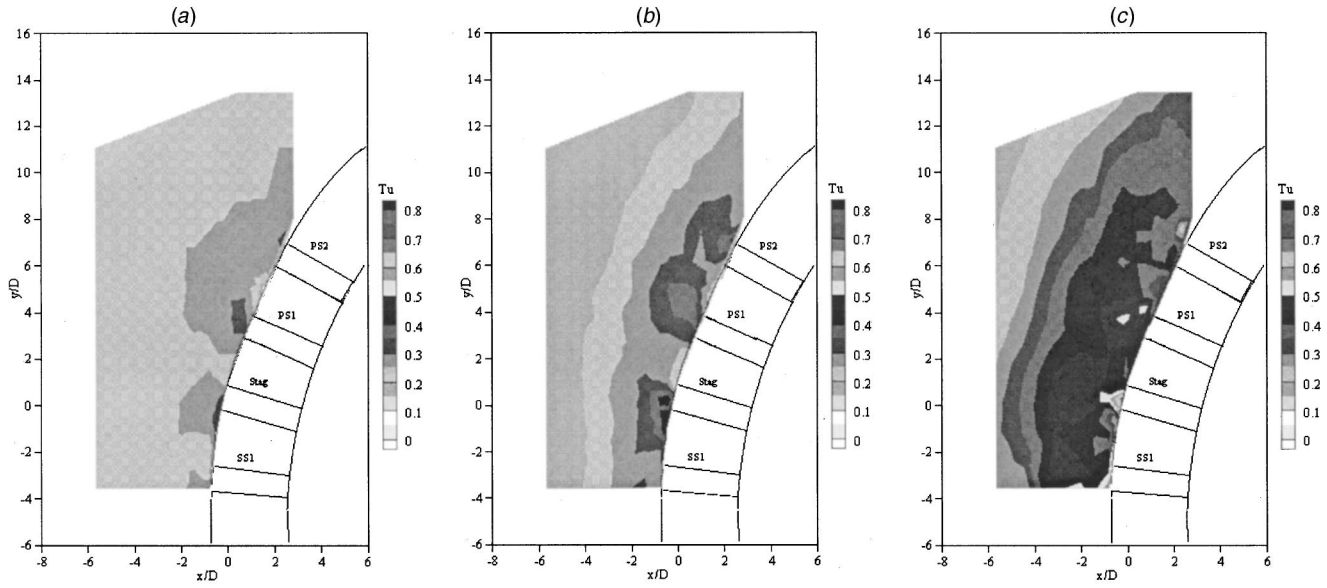

Fig. 9 Rms turbulence fields for $Tu_\infty=20\%$—(*a*) u'/U_∞, (*b*) v'/U_∞, (*c*) w'/U_∞

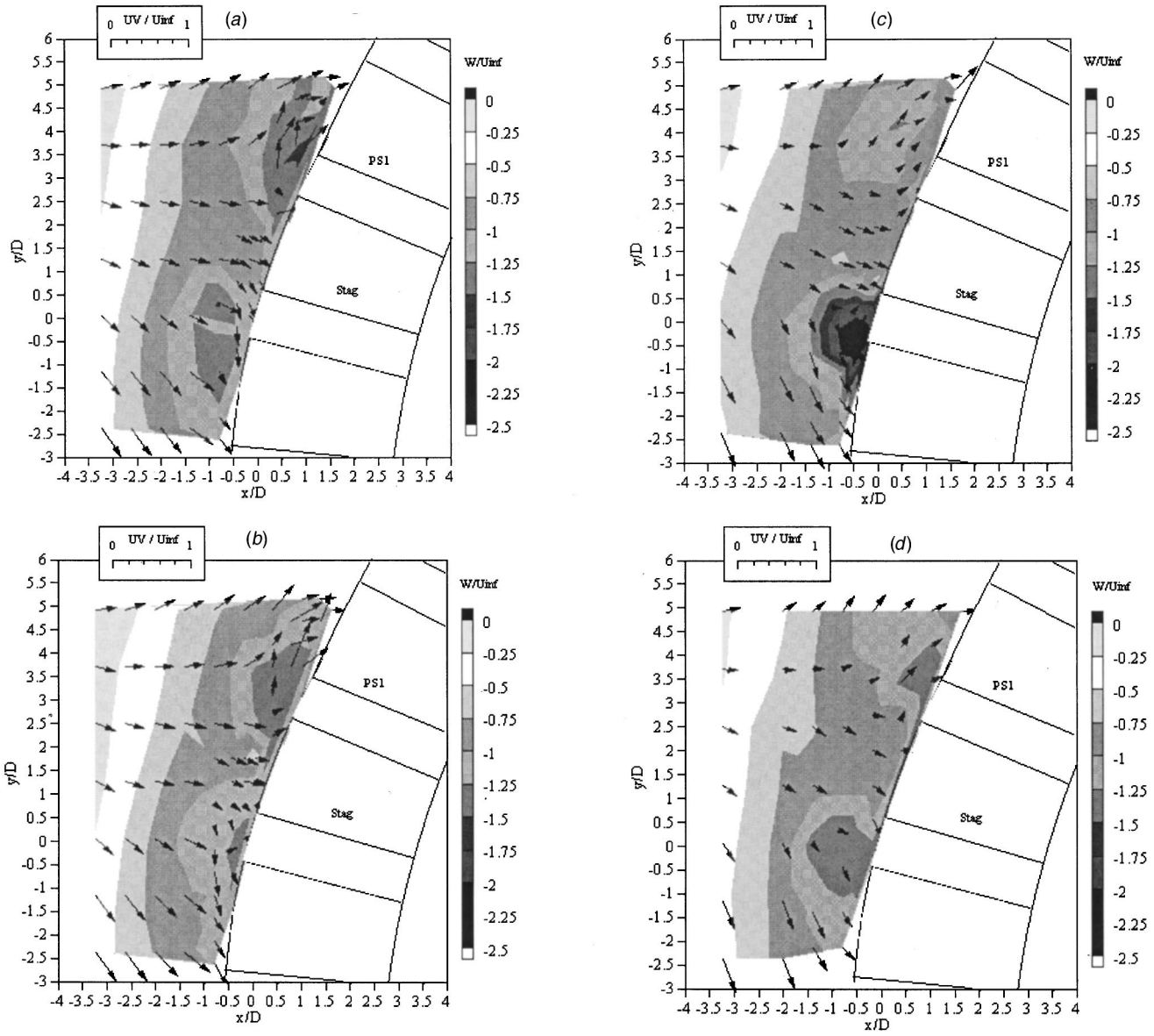

Fig. 10 Variations of mean velocity field with spanwise position; coolant injection with $M=2.0$ and mainstream $Tu_\infty=20\%$ —(*a*) $z/D=51.7$, (*b*) $z/D=50.0$, (*c*) $z/D=48.9$, (*d*) $z/D=47.3$

between the high and low mainstream turbulence cases. For low mainstream turbulence, levels of $w'/U_\infty>0.4$ were confined to regions around the hole exits extending $2D$ from the surface. For high mainstream turbulence, levels of $w'/U_\infty>0.4$ covered the leading edge area and extended to $3D$ from the surface. This larger region of high w'/U_∞ levels for the high mainstream turbulence case can be attributed to oscillations of the coolant jets by the large-scale mainstream turbulence. The coolant jets have a large W velocity component, and movement of the coolant jets about a point in the flow will result in large fluctuations in the w component, while having relatively little effect on the u' and v' components.

The spanwise variations of the mean velocity field for the high mainstream turbulence case are shown in Fig. 10(*a*)–(*d*) for lateral positions of $z/D=51.7$, 50.0, 48.9, and 47.3. These positions range over a complete pitch between holes so that the flow field at $z/D=51.7$ is also representative of the flow field expected at 46.1 due to the periodicity between holes. For the stagnation row of holes the position $z/D=48.9$ corresponds to the bottom exit of the hole, which is the baseline position presented previously in Fig. 8. At this position the exit velocity from the stagnation row was greater than $|W/U_\infty|=2.0$ in a jet core which was adjacent to the wall. At the next position, $1.5D$ farther in the spanwise direction, the maximum mean spanwise velocity reduced to less than $|W/U_\infty|=1.5$. At the farther spanwise positions there was little decrease in the maximum lateral velocity of the coolant from the stagnation row of holes. For all four lateral positions relatively strong lateral velocities extended $3d-5d$ from the surface, showing the influence of the accumulated blowing from the showerhead.

As noted previously, the maximum rms fluctuations occurred for the w component of velocity. The variations of w'/U_∞ for different spanwise positions are shown in Figs. 11(*a*)–(*d*). At $z/D=48.9$, immediately below the hole exit for the Stag row hole, the peak w' occurred very close to the wall and below the core of the coolant jet as identified by the maximum W shown in Fig. 10(*c*). At the next spanwise position, $z/d=47.3$, the peak w' level was not diminished; moreover, the area over which $w'/U_\infty\geqslant 0.6$ increased significantly. The increase in extent of high w' levels

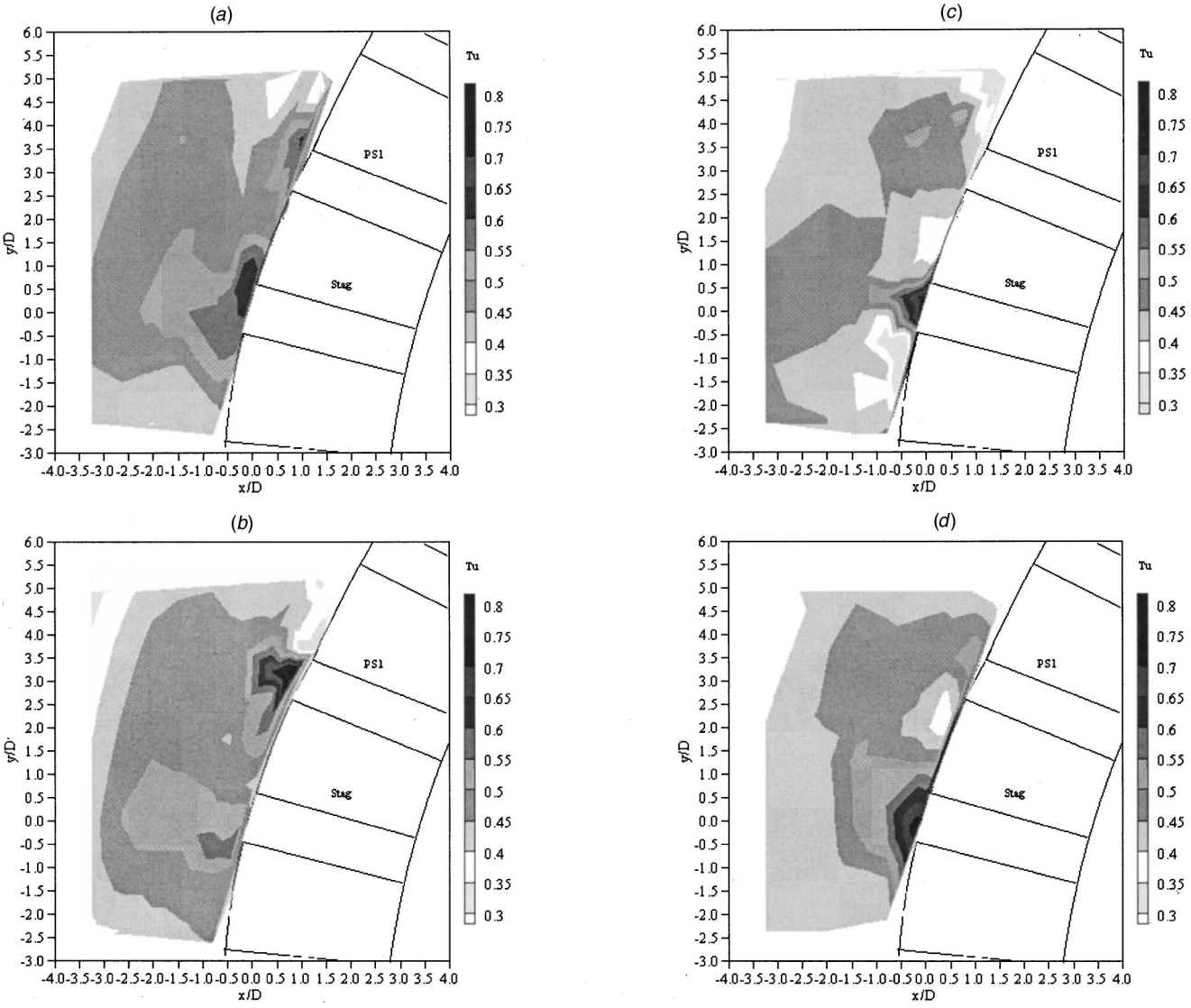

Fig. 11 Variations of w'/U_∞ turbulence levels with spanwise position; with $M=2.0$ and mainstream $Tu_\infty=20\%$—(*a*) $z/D=51.7$, (*b*) $z/D=50.0$, (*c*) $z/D=48.9$, (*d*) $z/D=47.3$

indicates that the high w' levels were not generated within the coolant hole, but by the interaction of the coolant jet with the mainstream external to the hole. Again the high w' levels were distinctly below the core of the coolant jet indicating that the turbulence was produced in the shear layer below the separated coolant jet. Farther in the spanwise direction, equivalent to positions $z/D=51.7$ and 50.0, w' levels diminish in the region around the Stag row of holes. In the region around the PS1 row of holes, the maximum w' levels occurred at $z/D=50.0$ with a peak level of $w'/U_\infty=0.8$. This position is $\Delta z/D=1.5$ below the exit of the PS1 row hole. Furthermore, the high turbulence levels occurred below the core of the coolant jet. Consequently, this high turbulence appears to also be produced by the shear layer below the separated coolant jet. The high w' levels around the PS1 row of holes diminished quickly in succeeding spanwise positions.

Conclusions

As industry comes to rely more on CFD predictions for turbine design, there is need to provide data for the more complex flow fields associated airfoil leading edge cooling. One of the goals of this program was to obtain comprehensive experimental measurements of the flow field associated with showerhead film cooling on a vane that could be used to validate and improve CFD prediction for this complex flow. These velocity field data complement earlier studies of the adiabatic effectiveness for the showerhead region. The inherent three-dimensionality of this flow field dictated that all three velocity components be measured to accurately represent this flow.

Several results from this study indicate the computational prediction of the showerhead flow will be exceedingly difficult. First, the flow in the showerhead region clearly involved a build-up of coolant along the span of the airfoil. Consequently CFD predictions would need to account for the cumulative effect of a large number of holes along the span, requiring a much larger computational domain. A second complexity was the very high levels of turbulence generated by the mainstream interaction with the coolant jets, with turbulence levels that far exceed that found in boundary layer or free jet flows. Furthermore, this turbulence was highly anisotropic, with the spanwise component of the turbulent fluctuations being twice as large as the other components. Finally, there was an interaction of the high mainstream turbulence with the coolant injection resulting in increased turbulence levels. This

result suggests that the mainstream causes an unsteady oscillation of the coolant jets, which further complicates CFD simulations.

Acknowledgments

We would like to acknowledge our sponsors for this work: the Texas Advanced Technology Program, the Advanced Gas Turbine Systems Research Consortium, and Pratt and Whitney. We further thank Pratt and Whitney for supplying the specifications for the vane and film cooling configuration used in this investigation. Finally thanks to Joel Wagner at Pratt & Whitney for review of the manuscript.

Nomenclature

D = hole diameter
DR = density ratio (ρ_c/ρ_∞)
M = blowing ratio based on average velocity from showerhead and approach mainstream velocity ($\rho_c U_c/\rho_\infty U_\infty$)
P = pitch of cooling holes
S = streamwise coordinate along surface
PS1 = 1st row of holes on pressure side
PS2 = 2nd row of holes on pressure side
Stag = row of holes on stagnation line
SS1 = 1st row of holes on suction side
T = temperature
Tu = turbulence level
U, V, W = flow velocity in x, y, and z directions
u, v, w = fluctuating velocities in x, y, and z directions
x = approach stream direction
y = cross-stream direction
z = spanwise direction
Λ_j = integral length scale
η = adiabatic effectiveness
$\overline{\eta}$ = spanwise averaged adiabatic effectiveness
ρ = density

Subscripts

$'$ = root-mean-square
sh = conditions of the coolant jet existing showerhead
∞ = conditions of the approach mainstream.

References

[1] Ardey, S., and Fottner, L., 1997, ''Flow Field Measurements on a Large Scale Turbine Cascade with Leading Edge Film Cooling by Two Rows of Holes,'' ASME Paper No. 97-GT-524.
[2] Ardey, S., and Fottner, L., 1998, ''A Systematic Experimental Study of the Aerodynamics of Leading Edge Film Cooling on a Large Scale High Pressure Turbine Cascade,'' ASME Paper No. 98-GT-434.
[3] Ardey, S., Wolff, S., and Fottner, L., 2000, ''Turbulence Structures if Leading Edge Film Cooling Jets,'' ASME Paper No. 2000-GT-255.
[4] Abuaf, N., Bunker, R., and Lee, C. P., 1997, ''Heat Transfer and Film Cooling Effectiveness in a Linear Airfoil Cascade,'' ASME J. Turbomach., **119**, pp. 302–309.
[5] Ames, F. E., 1998, ''Aspects of Vane Film Cooling with High Turbulence: Part II—Adiabatic Effectiveness,'' ASME J. Turbomach., **120**, pp. 777–784.
[6] Bohn, D. E., Becker, V. J., and Rungen, A. U., 1997, ''Experimental and Numerical Conjugate Flow and Heat Guide Vane,'' ASME Paper No. 97-GT-15.
[7] Polanka, M. D., Witteveld, V. C., and Bogard, D. G., 1999, ''Film Cooling Effectiveness in the Showerhead Region of a Gas Turbine Vane Part I: Stagnation Region and Near-Pressure Side,'' ASME Paper No. 99-GT-48.
[8] Witteveld, V. C., Polanka, M. D., and Bogard, D. G., 1999, ''Film Cooling Effectiveness in the Showerhead Region of a Gas Turbine Vane Part II: Stagnation Region and Near-Suction Side,'' ASME Paper No. 99-GT-49.
[9] Cutbirth, J. M., and Bogard, D. G., 2001, ''Thermal Field and Flow Visualization within the Stagnation Region of a Film Cooled Turbine Vane,'' ASME Paper No. 2001-GT-401.
[10] Polanka, M. D., 1999, ''Detailed Film Cooling Effectiveness and Three Component Velocity Field Measurements on a First Stage Turbine Vane Subject to High Freestream Turbulence,'' Ph.D. dissertation, The University of Texas at Austin, Austin, TX.
[11] Ethridge, M. I., Cutbirth, J. M., and Bogard, D. G., 2000, ''Effects of Showerhead Cooling on Turbine Vane Suction Side Film Cooling Effectiveness,'' ASME IMECE Conference, Orlando. FL.
[12] Hinze, J. O., 1975, *Turbulence*, McGraw-Hill, New York, NY.
[13] Pietrzyk, J. R., Bogard, D. G., and Crawford, M. E., 1989, ''Hydrodynamic Measurements of Jets in Crossflow for Gas Turbine Film Cooling Applications,'' ASME J. Turbomach., **111**, pp. 139–145.

J. E. Sargison
Mem. ASME
School of Engineering,
University of Tasmania,
Hobart, Tasmania 7001, Australia
e-mail: jane.sargison@utas.edu.au

S. M. Guo

M. L. G. Oldfield
Mem. ASME

Department of Engineering Science,
University of Oxford,
Oxford OX1 3PJ, UK

G. D. Lock
Department of Mechanical Engineering,
University of Bath,
Bath BA2 7AY, UK

A. J. Rawlinson
Rolls Royce plc,
Derby DE24 8BJ, UK

A Converging Slot-Hole Film-Cooling Geometry—Part 1: Low-Speed Flat-Plate Heat Transfer and Loss

This paper presents experimental measurements of the performance of a new film-cooling hole geometry—the converging slot-hole or console. This novel, patented geometry has been designed to improve the heat transfer and aerodynamic loss performance of turbine vane and rotor blade cooling systems. The physical principles embodied in the new hole design are described, and a typical example of the console geometry is presented. The cooling performance of a single row of consoles was compared experimentally with that of typical 35-deg cylindrical and fan-shaped holes and a slot, on a large-scale, flat-plate model at engine representative Reynolds numbers in a low-speed tunnel with ambient temperature main flow. The hole throat area per unit width is matched for all four hole geometries. By independently varying the temperature of the heated coolant and the heat flux from an electrically heated, thermally insulated, constant heat flux surface, both the heat transfer coefficient and the adiabatic cooling effectiveness were deduced from digital photographs of the color play of narrow-band thermochromic liquid crystals on the model surface. A comparative measurement of the aerodynamic losses associated with each of the four film-cooling geometries was made by traversing the boundary layer at the downstream end of the flat plate. The promising heat transfer and aerodynamic performance of the console geometry have justified further experiments on an engine representative nozzle guide vane in a transonic annular cascade presented in Part 2 of this paper.
[DOI: 10.1115/1.1459735]

Introduction

This paper presents low-speed flat plate heat transfer and aerodynamic efficiency measurements of a new console cooling geometry. A companion Part 2 paper [1] extends these measurements to compressible flow on an engine representative nozzle guide vane (NGV).

Film cooling is widely applied in gas turbines to protect engine components from gas temperatures above the melting point of component materials. A considerable amount of research has been conducted in order to gain an understanding of the mechanisms involved in film cooling so that the design of film-cooling systems can be optimized to produce the most effective film cooling with a minimum amount of coolant.

Minimizing the aerodynamic loss associated with film cooling is also very important. Denton [2] suggests that, despite an estimated increase in turbine entry temperature of 100 K per 1% coolant mass flow, a reduction of approximately 1% in turbine efficiency per 1% coolant flow can have a large effect on the overall cycle efficiency. This reduction is a viscous effect due to irreversible mixing of the coolant and mainstream flows.

Early work concentrated on the use of slots (e.g., Eckert and Drake [3]), which had the advantage of providing a uniform film that flowed along the downstream surface and did not introduce lateral thermal gradients, which can cause significant thermal stresses in engine components, reducing the life of the component. Farmer et al. [4] have presented data for both straight and shaped inclined slots. Due to the practical structural difficulties associated with the use of slots on engine nozzle guide vanes and turbine blades, research and engine design practice have concentrated on using arrays of discrete holes to provide the most uniform film possible, without compromising the aerodynamic efficiency of the nozzle guide vane. Cylindrical holes, in single or double rows (Ligrani et al. [5]), are often used with the holes directed downstream or with a compound angle in the plane perpendicular to the flow direction such as presented by Sen et al. [6] and Schmidt et al. [7]. Shaped film-cooling holes are also used. Gritsch et al. have presented heat transfer [8], and adiabatic effectiveness [9] measurements and Thole et al. [10] have presented flow-field measurements for film cooling holes that expand laterally and/or forward near the hole exit. The purpose of the expansion is to increase the lateral spread of the coolant film downstream of the holes and to minimize the penetration of the coolant flow into the mainstream. While this shape improves the uniformity of the film over the surface compared with cylindrical holes, the hole expansion causes separation in the hole and inefficient diffusion, which reduce the aerodynamic efficiency of the NGV (Day et al. [11]).

Console

The new converging slot hole, or console, film-cooling hole (patent applied for) described in this paper, has been designed to offer the improved cooling and aerodynamic performance of slot geometry, whilst retaining the mechanical strength of a row of discrete holes.

The cross section of the console changes from a near circular shape at inlet to a slot at exit. In side view (Fig. 1(*a*)) the walls of the console converge and in plan view (Fig. 1(*b*)) the walls diverge, but the convergence is greater than the divergence so that the cross-sectional area decreases and the flow accelerates from inlet to outlet. The minimum hole area (throat) and hence maximum flow velocity are at the hole exit.

It has been widely established (e.g., [12]) that for accelerated flows, such as the console internal flow, the boundary layer generally remains laminar or turbulent boundary layers relaminarize,

Contributed by the International Gas Turbine Institute and presented at the International Gas Turbine and Aeroengine Congress and Exhibition, New Orleans, Louisiana, June 4–7, 2001. Manuscript received by the IGTI, October 23, 2000. Paper No. 2001-GT-126. Review Chair: R. A. Natole.

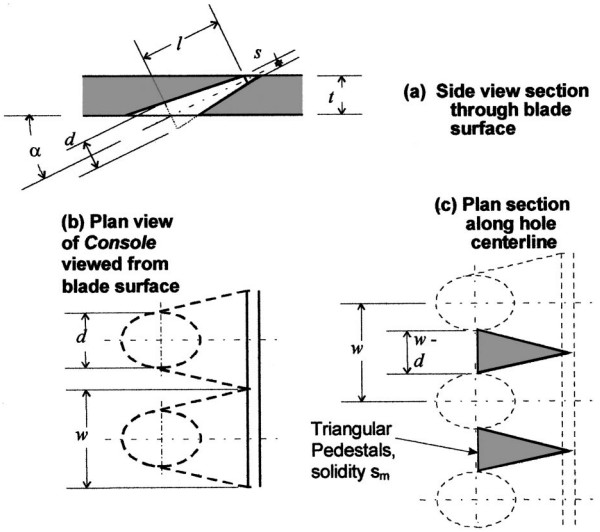

Fig. 1 Basic console configuration—(*a*) side view section through blade surface; (*b*) plan view of console viewed from blade surface; (*c*) plan section along hole centerline

while even a small amount of diffusion generally induces transition to turbulent flow. The losses due to turbulent flow are significantly higher than laminar flow. This is in contrast to conventional fan-shaped or expanded holes where the flow is diffused and slowed down in an attempt to spread the flow of the coolant onto the surface with low momentum. The separations in the fan-shaped hole [10], which reduce the aerodynamic efficiency of the fan-shaped holes, will be significantly reduced in the accelerating console flow. The low-turbulence exit flow from the console should lay a more stable layer of cooling air onto the external blade surface downstream of the exit and should reduce mixing of the coolant and the hot mainstream.

Individual holes in a row of consoles are positioned such that adjacent holes intersect just below the surface as shown in Fig. 1, and a continuous slot is formed on the outside blade surface. The advantage of joining the hole exits is that the ejected coolant film is continuous in the span-wise direction (in contrast to cylindrical holes) and the film therefore benefits from the Coanda effect [12] and will not lift off from the blade surface at typical blowing rates. Evidence of the Coanda effect is described later in this paper.

The roughly triangular pedestals between holes (Fig. 1) maintain the strength of the blade. To compare the structural integrity of the different cooling hole shapes, the minimum cross-sectional area of 25% for the particular console design used in the current work is reduced from 52% for the fan-shaped holes, and 67% for the cylindrical holes. The residual strength of the material with consoles should be sufficient, but further studies of the mechanical design of the console are required to verify this.

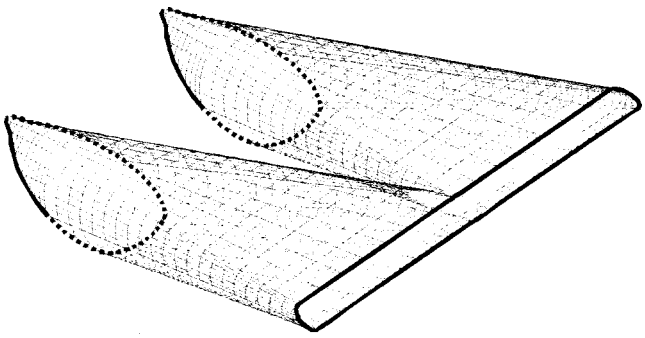

Fig. 2 Uni graphics surface definition of two console film-cooling holes

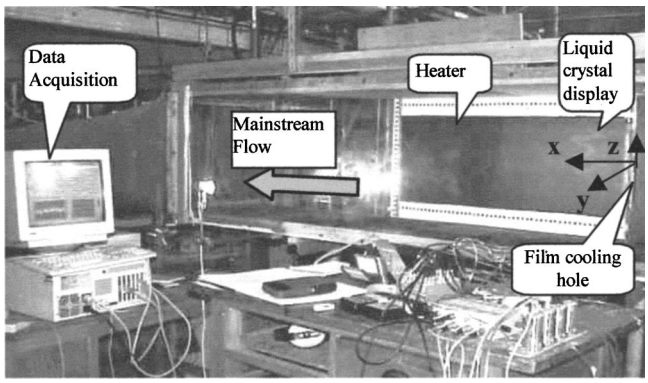

Fig. 3 Osney laboratory low-speed wind tunnel

The geometry of the basic console configuration has been designed to be generated from a family of straight lines as can be seen in Fig. 2, and hence can be manufactured by available drilling (mechanical or laser) techniques. The hole entrance is nominally circular, but due to the way that the experimental consoles were generated, using straight lines, the hole entrance of the actual shape has a slight ''pen nib'' effect as shown in Fig. 2. As precision casting becomes more accurate, it will be possible to modify the basic console shape to further improve performance, such as detailed shaping of the hole entry and exit. The console patent application covers such improvements.

Experimental Program

As outlined in the foregoing, heat transfer and aerodynamic loss measurements were carried out to quantify the performance of the console. The heat transfer experiments will be presented first, followed by the aerodynamic loss measurements.

Heat Transfer Measurement

Experimental Technique. The experiments were performed in a 500×500-mm cross section low-speed, suck down wind tunnel [13] in the Osney Laboratory at the University of Oxford, shown in Fig. 3. The mainstream (primary flow) air speed and temperature were measured upstream of coolant injection and these parameters were independent of the coolant flow. All measurements presented were conducted at engine representative Reynolds number (based on cylindrical hole diameter and mainstream flow) of 36,000, ideal coolant to mainstream momentum flux ratio of 1.1 and density ratio of 1. The Reynolds number for every hole configuration was based on the cylindrical hole diameter for consistency in the presentation of results. The cylindrical hole diameter was 20 mm, the fan-shaped hole inlet diameter was 24 mm, the slot height for the slot and console was 5 mm. By setting the hole pitch to be 60 mm for the cylindrical holes ($3d$), 84 mm for the fan-shaped holes ($3.5d_{\text{fan}}$), and 50 mm for the consoles ($2d_{\text{console}}$) equal throat area per unit width for each hole shape was achieved. For all data presentation, which required a hole diameter, the equivalent cylindrical hole diameter of 20 mm was used. For comparison with slot results, the Reynolds number based on the console and slot, slot height was 144,000.

The ideal mainstream momentum flux ratio is equal to a pressure difference ratio $I_{\text{ideal}}=(P_{0c}-P_m)/(P_{0m}-P_m)$, and this was used as the basis for comparing coolant flows because it is this parameter that is set in the engine. The coolant total pressure P_{0c} is the total pressure measured in the coolant plenum, P_{0m} is the

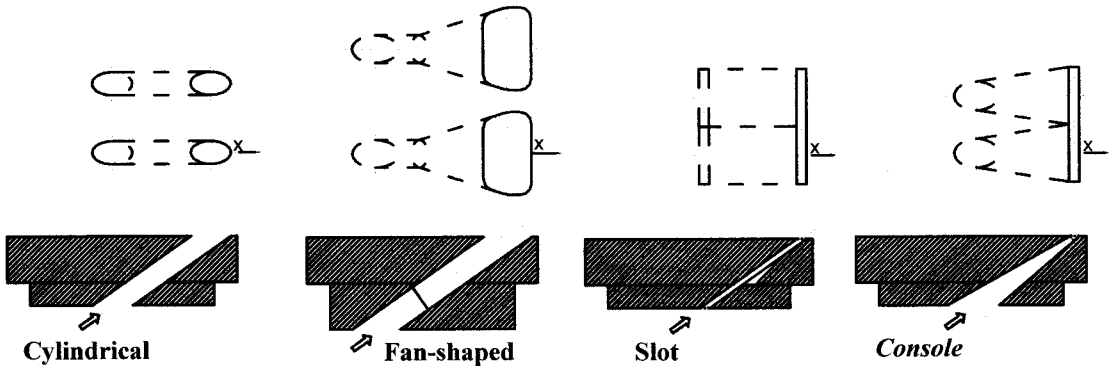

Fig. 4 Typical film-cooling hole configurations

total pressure of the mainstream flow measured upstream of coolant injection, and P_m is the static pressure of the mainstream measured at a wall static pressure tapping.

Although all holes were tested at the same pressure ratio, each hole geometry had a different discharge coefficient. This caused the mass flow rate, and hence velocity ratio and actual mass and momentum flux ratios to be different for each hole. The cylindrical hole mass flow rate was considered to be the standard mass flow rate and a hypothetical diameter, d_{hyp}, was defined for the other film cooling holes, which would produce the same mass flow rate as the cylindrical hole. For both adiabatic effectiveness and heat transfer coefficient, the x parameter was corrected using

$$x_{\text{cor}} = x\left(\frac{d_{\text{hyp}}}{d}\right) \tag{1}$$

since the x scale for the effectiveness and heat transfer for a larger hole diameter would be equivalent when plotted against (x/d).

The equation for heat transfer from a flat plate in uniform, turbulent flow [14] was manipulated to produce the following expression relating h and x, assuming that all other parameters are constant:

$$h \propto x^{-0.2} \tag{2}$$

Since x is corrected as outlined in the foregoing, the consequent correction in h can be written

$$h_{\text{corrected}} = h\left(\frac{d_{\text{hyp}}}{d}\right)^{-0.2} \tag{3}$$

The effectiveness scale does not require correction.

The mainstream flow velocity was 26 m/s and the freestream turbulence intensity was low, of the order of 1%.

The cooling air was supplied from the laboratory compressed air source and the mass flow rate of the air supplied to the plenum chamber was measured through a British Standard BS 1042 orifice plate (17.96 mm dia). The air was heated using a variable power inline heater and fed into a plenum chamber to settle and mix the air before it exited through film-cooling holes mounted in the side of the wind tunnel.

The film-cooling holes were machined in cooling hole plates made from *Rohacell*-type 51G—a closed pore, structural foam, manufactured by Rohm GMBH, with low thermal conductivity of 0.028–0.034 W/mK at 20°C, compared with air at 0.025 W/mK. A series of plates with the different film-cooling hole geometries investigated were produced, and these could be easily changed in the experiment. There were five cylindrical holes and consoles, three fan-shaped holes and a single slot. The main geometrical features of the film-cooling holes are shown in Fig. 4.

A uniform heat flux flat plate, 1000 mm long, 600 mm wide, and 30 mm thick (Fig. 5) was produced from a large sheet of Rohacell backed with fibreboard for stiffness and covered with a 350-mm-wide electrically heated thin film of aluminized Mylar, which was bonded to the surface with high-strength double-sided tape. The resistance of the thin film-heating element quoted by the manufacturer was 2 Ω per square, but it varied slightly with temperature, so the voltage and current were measured in order to calculate the power supplied to the plate. The total resistance of the plate was 5.4 Ω at 18°C and the maximum heater power used was 200 W. The heat flux was uniform to within 3% over the surface of the plate. This plate was situated downstream of the film-cooling holes.

The heating surface was painted black and narrow-band thermochromic liquid crystals were used to measure constant temperature contours on the surface. Changing the coolant temperature or heat flux to the plate and allowing the system to settle to steady-state conditions facilitated construction of a map of temperature contours.

A suite of Matlab routines were written to automatically calculate the heat transfer coefficient and adiabatic effectiveness at each point on the plate from the temperature contours. The temperature contours were extracted using the hue signal in the digital image, which was calibrated against temperature. The contour at a particular value of hue (where hue was most sensitive to temperature) was captured using a Matlab routine, to obtain the temperature contour.

Film Cooling Analytical Technique. In the following discussion, total and recovery temperatures, appropriate to compressible flow, are used in order to present generally applicable equations and for consistency with the compressible experiments described in Part 2 of this paper [1]. Of course, in the incompressible experiments presented here, the total, recovery and static temperatures are equivalent.

The heat transfer coefficient, h, is defined following Jones

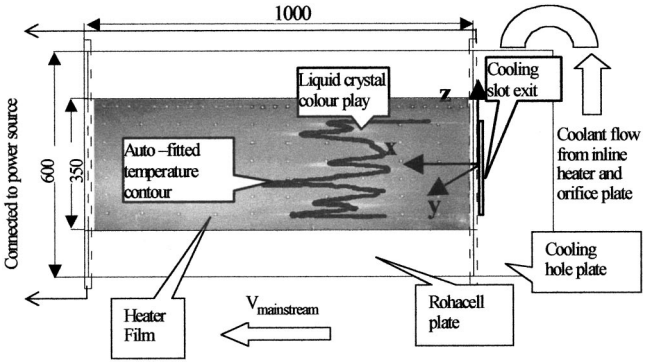

Fig. 5 Tunnel wall showing layout of cooling holes and heated flat plate, overlaid with typical liquid crystal display with processed temperature contour

[14,15] as the constant of proportionality between the local heat flux q and the difference between the wall temperature T_w and convection driving temperature of the gas T_{aw}, or adiabatic wall temperature at that point

$$q = h(T_w - T_{aw}) \tag{4}$$

For film cooling where there are two flows present, T_{aw} is intermediate between the coolant T_{0c} and mainstream T_{0m} total temperatures and depends on these temperatures, the geometry and degree of mixing between the gases upstream of the point of interest on the surface. To eliminate the temperature dependence, a dimensionless adiabatic film effectiveness is defined according to the definition of Jones [14,15]

$$\eta = \frac{T_{aw} - T_r}{T_{0c} - T_{0m}} \tag{5}$$

Here, T_r is the mainstream recovery temperature, which is defined using the recovery factor, $r = \mathrm{Pr}^{1/3}$, suggested by Kays and Crawford [16]

$$T_r = T_{0\infty}\left(\frac{1 + r\dfrac{\gamma-1}{2}M^2}{1 + \dfrac{\gamma-1}{2}M^2}\right) \tag{6}$$

The cooling effectiveness and heat transfer coefficients are primarily functions of cooling geometry, the state of the oncoming boundary layer, freestream turbulence intensity, surface curvature, and ratios of the coolant-to-mainstream density, mass and momentum fluxes, and specific heats [14]. Note the use of the recovery temperature T_r rather than T_{0m}.

To reduce the three controlling temperature variables in the experiment to a single parameter, a dimensionless temperature, θ, is defined

$$\theta = \frac{T_{0c} - T_{0m}}{T_w - T_r} \tag{7}$$

In experiments, an overall heat transfer coefficient h_{mw} based on the mainstream and wall temperatures is measured. If Eqs. (2) and (3) are substituted into Eq. (1), then

$$h_{mw} = \frac{q}{T_w - T_r} = h(1 - \eta\theta) \tag{8}$$

This expression indicates that the variable h_{mw} is linear in θ. Furthermore, for a line relating h_{mw} to θ, h is the slope of the line and the intercept on the θ axis is $1/\eta$. A set of experimental points in (θ, h_{mw}) can be produced by varying the plate heat flux and coolant temperature. The linearity of h_{mw} with θ was tested as part of the Matlab analysis sequence, by plotting h_{mw} against θ, for a number of positions on the plate. The typical results in Fig. 6 show that good linearity was obtained.

Downstream of a row of cooling holes, the effectiveness η varies periodically and previous workers (e.g., [5]) have simply arithmetically averaged η. Since h also varies, this is not technically correct and the correct method to calculate the lateral average is obtained by taking the average of both sides of Eq. (5)

$$\overline{\left[\frac{q}{T_w - T_r}\right]} = \overline{h} - \overline{h\,\eta}\,\theta \tag{9}$$

Thus, the two properties of the film cooling heat transfer that are required for the average heat transfer prediction are $\overline{h}$ and $\overline{h\,\eta}$. The correct way to calculate the laterally averaged effectiveness from the contour data, if it is to be used to determine the average heat transfer is

$$\overline{\eta} = \frac{\overline{h\,\eta}}{\overline{h}} \tag{10}$$

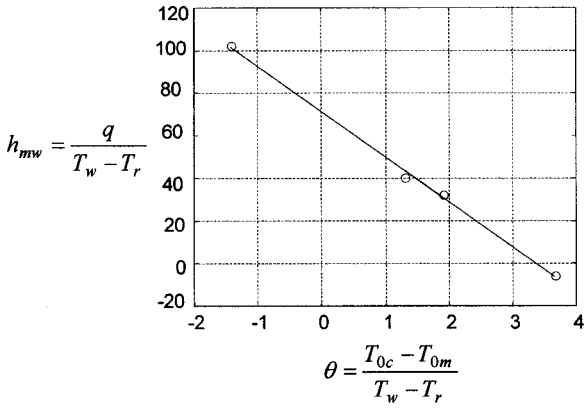

Fig. 6 Typical set of data points and fitted straight line used in Matlab data manipulation

In practice, for moderate levels of heat transfer coefficient, the difference between this definition and spatially averaged η is less than 5%.

Results and Discussion. Experimental results were compared with previously published data to validate the current measurement technique. Good agreement between the current work and published results was obtained such as shown in Figs. 7 and 8 for the cylindrical holes. The validation of the experimental technique by comparison with published results gives confidence in the subsequent console results. Note that the results are compared using the actual momentum flux ratio, I_{actual}, where the momentum flux of the coolant flow is defined:

$$\rho_c v_c^2 = \frac{\dot{m}^2}{\rho} \tag{11}$$

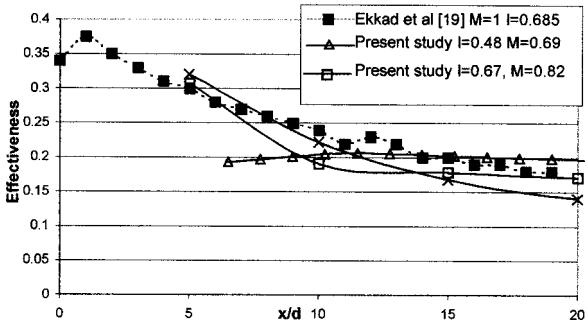

Fig. 7 Cylindrical hole effectiveness compared with published data

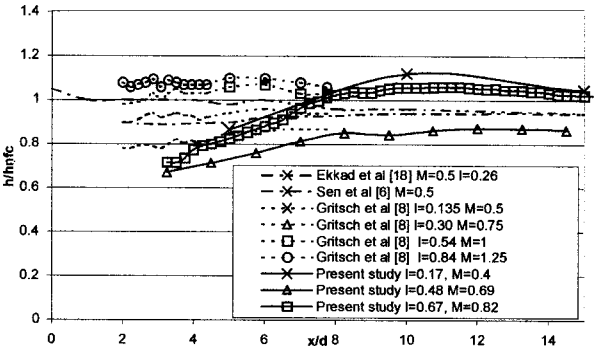

Fig. 8 Cylindrical hole heat transfer coefficient compared with published data

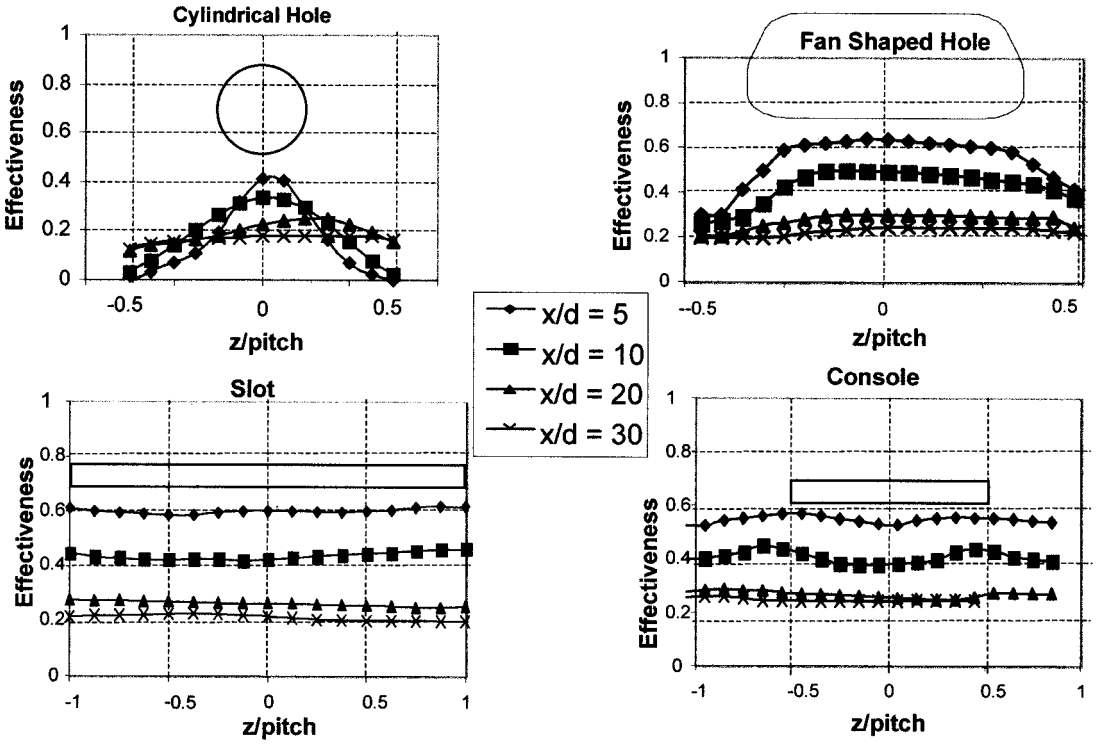

Fig. 9 (*a*)–(*d*) **Lateral variation in adiabatic effectiveness, $I_{IDEAL}=1.1$, $Re_d=36{,}000$**

Throughout Figs. 7–12, the diameter, *d*, used for dimensionless distance is the equivalent cylindrical hole diameter of 20 mm. The dimension *z* for the lateral results in Figs. 9 and 11 is made dimensionless by dividing by the hole pitch. The nominal slot pitch was made equal to the console pitch.

From a perturbation analysis of the effect of uncertainties in the measured parameters on the results of the curve-fitting techniques, the uncertainty in *h* was estimated to be 8%, and the uncertainty in η was estimated to be 7%.

The lateral variation in adiabatic effectiveness for each film-cooling geometry is presented in Figs. 9(*a*)–(*d*). As shown in Fig. 5, the downstream distance *x* is measured from the downstream edge of the cooling hole or slot. The hole exit area is shown to scale on the graph. In this and all following charts, the *x* dimension is divided by the cylindrical hole diameter to provide consistency with the convention set by previous experimenters.

The cylindrical results show a pronounced peak in adiabatic effectiveness, η downstream of the hole center. The peak is more spread for the fan-shaped hole, as would be expected with the lateral expansion near the hole exit. The console result demonstrates a more uniform profile of η slightly enhanced at the intersection of two consoles. This enhancement is most likely due to interaction between vortices formed by the jets from adjacent consoles.

The slot effectiveness is similar to the fan and console peak effectiveness, which accounts for the similarity in the laterally averaged results for these film-cooling holes (Fig. 10). The peak η values for the cylindrical holes are lower and reduce rapidly away from the holes, which accounts for the considerably lower laterally averaged effectiveness results.

The level of the lateral heat transfer coefficient shown in Figs. 11(*a*)–(*d*) is similar for the slot and the console film-cooling holes, and relatively uniform across the hole.

This demonstrates that the console flow is acting similarly to the slot flow. The heat transfer coefficient at exit from the fan-shaped hole demonstrates only a small variation over the hole exit, and the level is markedly lower than for the slot and console. The cylindrical hole peak value is higher than the other cooling configurations; however, *h* is lower between the holes, which contributes to the low laterally averaged heat transfer coefficient shown in Fig. 12.

The laterally averaged heat transfer results in Fig. 12 demonstrate that the slot and console do not significantly change the boundary layer flow compared with no film cooling, and hence the heat transfer coefficient is similar. The fan-shaped and cylindrical film-cooling holes appear to thicken the boundary layer and reduce the heat transfer coefficient compared with no film cooling.

The heat transfer performance of the console has been shown to be similar to the slot and fan film-cooling performance. Aerodynamic loss measurements presented in the following sections are required in order to fully demonstrate the benefits of the console.

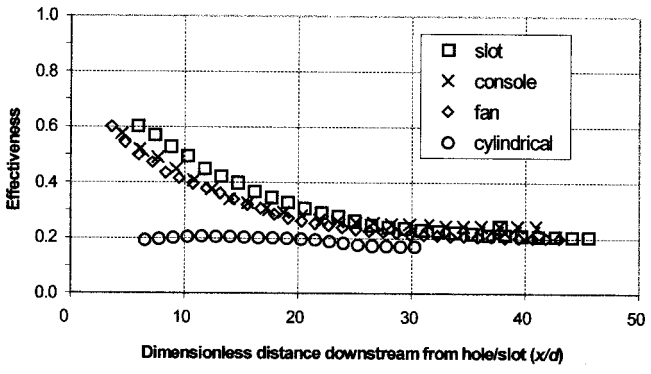

Fig. 10 Laterally averaged adiabatic effectiveness, $I_{IDEAL}=1.1$, $Re_d=36{,}000$

Aerodynamic Loss

Experimental Technique. The measurement of aerodynamic loss was conducted using the tunnel equipment outlined above for the heat transfer measurement, except that there was no heat ap-

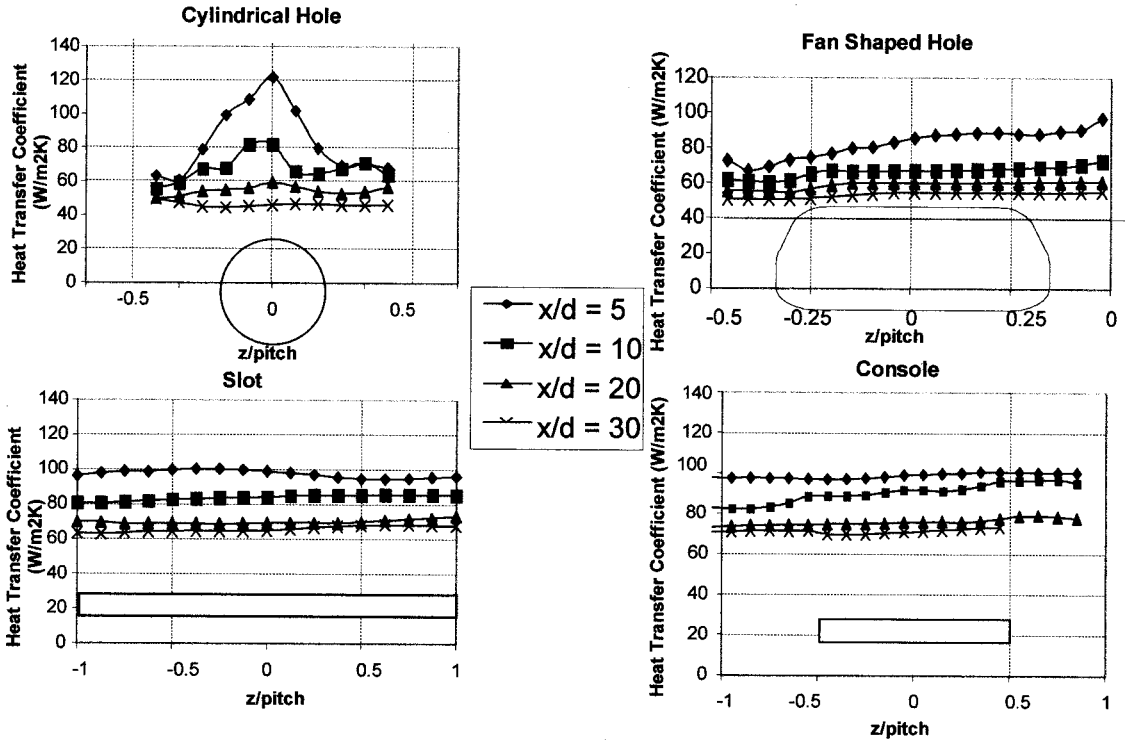

Fig. 11 (*a*)–(*d*) Lateral variation in heat transfer coefficient, $I_{IDEAL}=1.1$, $Re_d=36{,}000$

plied to either the heater film or the coolant. The boundary layer velocity and total pressure profiles were measured with a horizontally traversing pitot probe at the downstream edge of the plate, at positions downstream of a hole center and halfway between two holes.

Analytical Technique. Aerodynamic loss is defined as $(1-\varepsilon)$, [11], where the aerodynamic efficiency, ε, is defined:

$$\varepsilon=\frac{\{\text{Actual Kinetic Energy}\}_{\text{mixingplane}}}{\{\text{Theoretical Kinetic Energy}\}_{\text{available}}} \tag{12}$$

The mixing plane is defined as the hypothetical plane at which the coolant and mainstream flows are fully mixed and the velocity, pressure and temperature are uniform. It is mathematically equivalent to the measurement plane and the velocity, static pressure and temperature at this plane are found by applying the laws of conservation of mass, momentum and energy between the measurement plane and the mixing plane.

The boundary layer traverse at the measurement plane is extended to the width of the wind tunnel, less the boundary layer thickness on the far side as shown in Fig. 13. Although the results of this measurement are dependent on the dimensions of this wind tunnel, the purpose of the current experiments is to produce comparative data only. In the engine, the height of a downstream traverse required to measure aerodynamic efficiency is one blade pitch.

Applying conservation of mass from the measurement plane to the hypothetical mixed out plane in Fig. 13, assuming constant density (low-speed flow)

$$\int_0^H \nu dy = H\nu_2 \tag{13}$$

Applying conservation of momentum

$$P_1+\rho\int_0^H \nu^2 dy = P_2+\rho H\nu_2^2 \tag{14}$$

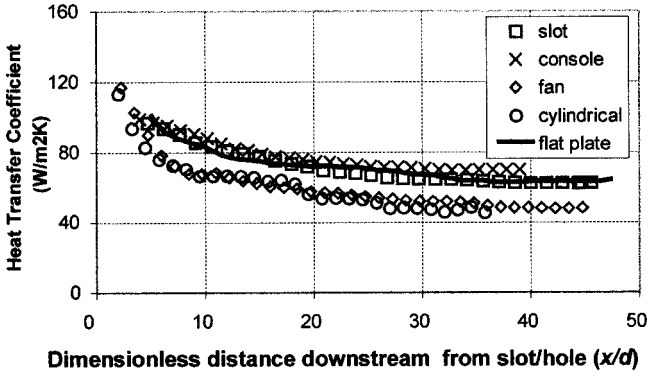

Fig. 12 Laterally averaged heat transfer coefficient, $I_{IDEAL}=1.1$, $Re_d=36{,}000$

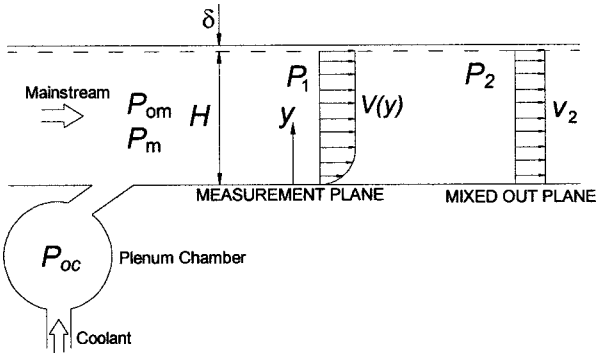

Fig. 13 Measurement and calculation planes for aerodynamic loss

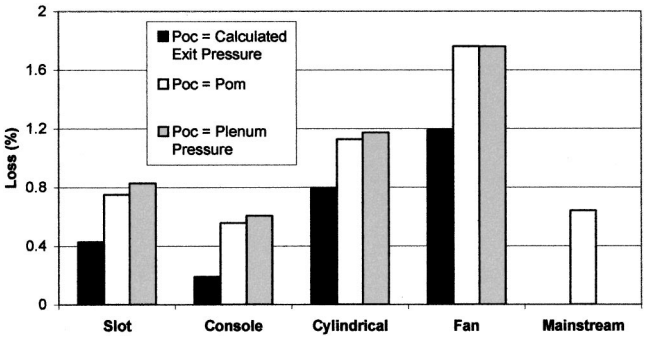

Fig. 14 Comparison of aerodynamic loss of four cooling configurations, $I_{IDEAL}=1.1$, $Re_d=36{,}000$

From these two relationships, the actual kinetic energy flux of the flow at the mixed out plane can be calculated

$$\mathrm{KE}_{\mathrm{actual}}=\frac{1}{2}m\nu_2^2=\frac{1}{2}\rho_2\nu_2^3 \tag{15}$$

For incompressible flow, the theoretical kinetic energy flux, based on the initial total pressure and the calculated static pressure at the mixing plane can be written

$$\mathrm{KE}_{\mathrm{theoretical}}=\frac{\dot{m}_m}{\rho_m}(P_{0m}-P_2)+\frac{\dot{m}_c}{\rho_c}(P_{0c}-P_2) \tag{16}$$

such that the loss is finally written

$$\mathrm{Loss}=1-\frac{\frac{1}{2}\rho\nu_2^3}{\frac{\dot{m}_m}{\rho_m}(P_{0m}-P_2)+\frac{\dot{m}_c}{\rho_c}(P_{0c}-P_2)} \tag{17}$$

Results and Discussion. The usual coolant total pressure used for the calculation of aerodynamic loss is that measured in the cooling plenum. Day et al. [11] point out that there are arguments for using either the coolant exit total pressure or the mainstream total pressure of which all three are presented here. The coolant total pressure at the hole exit was calculated by Day et al. [11] for the compressible case, which requires an iterative solution technique. For the incompressible case, an equation for P_{0c} can be written

$$P_{0c}=P_m+\frac{1}{2}\rho\nu_{\mathrm{exit}}^2=P_m+\frac{1}{2}\frac{\dot{m}^2}{\rho} \tag{18}$$

where P_m is the mainstream static pressure, the mass flux, $\dot{m}$ = measured mass flowrate/A_{exit}, and A_{exit} is the exit area of the hole. For the fan shaped holes, the calculation of coolant exit total pressure is based on the nominal cross-sectional area of the expanded part of the hole at the hole exit plane, unlike Day et al. [11] who use the hole throat area.

The aerodynamic loss measurements presented in Fig. 14 clearly show the advantage of the console over the cylindrical and fan-shaped film-cooling holes. The aerodynamic loss for the console is less than the slot and is even less than the no film-cooling case. This is because the converging console hole flow has less internal loss than the straight slot. The cylindrical and fan-shaped film-cooling holes have considerably higher aerodynamic loss.

The difference between the calculated loss based on exit pressure and the total loss or loss based on plenum pressure is a measure of the loss through the film-cooling hole. This is largest for the fan-shaped hole, at 0.6% and smallest for the console at 0.35%. The large difference between these two results is due to the large loss associated with the inefficient diffusion process in the fan compared to the efficient, accelerating flow in the console. The two straight holes, the slot and cylindrical hole, exhibit a similar difference of 0.4%.

The uncertainty in these measurements was estimated to be 20% based on a 95% confidence level. The trends in loss outlined above remain valid with this level of uncertainty.

Coanda Effect Investigation

Evidence of the Coanda effect has been obtained in flow visualization experiments using a nylon mesh coated with liquid crystals [17], which was positioned across the wind tunnel, one cylindrical hole diameter downstream of the film-cooling holes. The experiment was conducted with jets in crossflow at the same $I_{\mathrm{ideal}}=1.1$ as the other experiments presented in this paper, and jets without crossflow at the same pressure ratio across the hole. The contours extracted from images of the jet shown in Figs. 15 and 16, clearly show that with no crossflow, the cylindrical hole jets lift off from the surface (located at $y/d=0$ in the figures) and with crossflow, the jets penetrate into the flow. For both situations, the console jets from the central three holes remain attached to the surface.

Conclusions

The novel console film-cooling hole shape has been presented and the thermal and aerodynamic performance has been compared with other conventional film cooling hole shapes. The coolant flow from a row of consoles shows good lateral uniformity of adiabatic effectiveness, with regions of slightly enhanced cooling occurring between the consoles due to the interaction of vortices from adjacent holes.

The laterally averaged adiabatic effectiveness results demonstrate that the console approaches the slot effectiveness, as does the fan-shaped hole effectiveness.

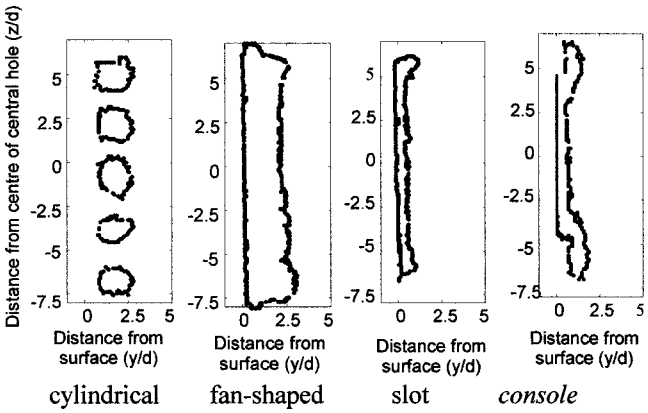

Fig. 15 Film-cooling hole jets contour without crossflow

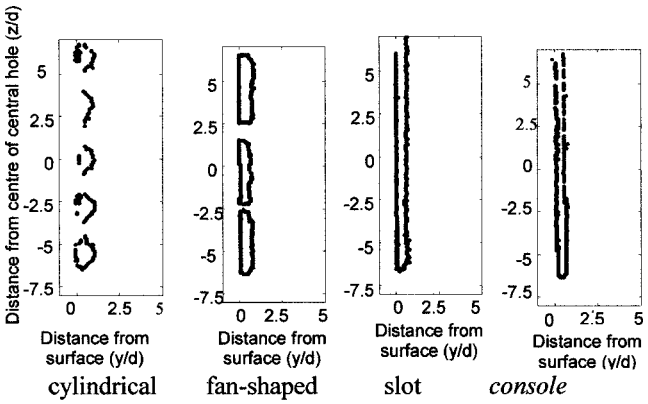

Fig. 16 Film-cooling hole jet contour with crossflow

The console laterally averaged heat transfer coefficient was similar to the slot, and higher than the cylindrical and fan-shaped hole results. The slot and console do not significantly change the boundary layer flow compared with the case of no film cooling, and hence the heat transfer coefficient is similar. The fan-shaped and cylindrical film-cooling holes appear to thicken the boundary layer and reduce the heat transfer coefficient compared with no film cooling. There is an aerodynamic penalty associated with this thickening.

The aerodynamic performance of the console was also investigated, and it was shown that the aerodynamic loss due to a console is significantly less than for fan-shaped or cylindrical film-cooling holes.

Hence, although these results indicate that the thermal performance of the *console* is similar to the fan-shaped film-cooling holes currently in use, the console has a great advantage in terms of aerodynamic performance.

The promising results obtained from the flat plate experiments justify further experiments using the console geometry on a fully cooled nozzle guide vane under engine representative conditions which are presented in Part 2 of this paper [1].

Acknowledgments

This work is supported by Rolls-Royce plc, DERA, DTI CARAD and MOD ARP26c.

Nomenclature

d = hole diameter
h = heat transfer coefficient
h_{mw} = heat transfer coefficient based on wall and mainstream temperatures
h_{nfc} = heat transfer coefficient without film cooling
H = boundary layer traverse distance
I_{actual} = actual momentum flux ratio $=\rho_c v_c^2/\rho_m v_m^2$
I_{ideal} = ideal momentum flux ratio $=(P_{0c}-P_m)/(P_{0m}-P_m)$
KE = kinetic energy flux $=1/2\dot{m}v^2=1/2\rho v^3$
$\dot{m}$ = mass flux $=\rho v$
M = mass flux ratio, blowing ratio $M=\rho_c v_c/\rho_m v_m$
P = pressure
p = hole pitch
q = heat transfer rate from surface to flow
Re_d = Reynolds no. based on hole diameter and mainstream flow conditions, $\mathrm{Re}_d=\rho v d/\mu$
T = temperature
v = flow velocity
x, y, z = Cartesian coordinates
δ = displacement boundary layer thickness
η = film-cooling effectiveness $\eta=(T_{aw}-T_r)/(T_{0c}-T_{0m})$
ρ = density
θ = dimensionless temperature $\theta=(T_{0c}-T_{0m})/(T_w-T_r)$

Subscripts

aw = adiabatic wall
c = coolant
m = gas, mainstream
nfc = no film-cooling condition
o = total, stagnation conditions
r = recovery
w = wall

Abbreviations

console = converging slot-hole
NGV = nozzle Guide Vane

Console Geometric Parameters

s = exit throat slot height, controls coolant mass flow
w = exit slot width, or console hole pitch
d = inlet hole diameter
s_m = solidity ratio, proportion of metal left after hole has been drilled $s_m=1/2(1-d/w)$
α = hole inclination to surface
t = wall thickness
l = hole length $l=t/\sin\alpha$

References

[1] Sargison, J. E., Guo, S. M., Oldfield, M. L. G., Lock, G. D., and Rawlinson, A. J., 2002, "A Converging Slot-Hole Film-Cooling Geometry—Part 2: Transonic Guide Vane Heat Transfer and Loss," ASME Paper No. 2001-GT-127, ASME J. Turbomach., **124**, pp. 461–471.
[2] Denton, J. D., 1993, "Loss Mechanisms in Turbomachines," ASME J. Turbomach., **115**, pp. 621–656.
[3] Eckert, E. R. G., and Drake, R. M., 1972, *Analysis of Heat and Mass Transfer*, McGraw Hill, New York, NY, pp. 453–466.
[4] Farmer, J. P., Seager, D. J., and Liburdy, J. A. 1997 "The Effect of Shaping Inclined Slots on Film Cooling Effectiveness and Heat Transfer Coefficient," ASME Paper No. 97-GT-399.
[5] Ligrani, P., Ciriello, S., and Bishop, D. T., 1992 "Heat Transfer, Adiabatic Effectiveness and Injectant Distributions Downstream of a Single Row and Two Staggered Rows of Compound Angle Film-Cooling Holes," ASME J. Turbomach., **114**, pp. 687–700.
[6] Sen, B., Schmidt, D. L., and Bogard, D. G., 1996, "Film Cooling with Compound Angle Holes: Heat Transfer," ASME J. Turbomach., **118**, pp. 800–806.
[7] Schmidt, D. L., Sen, B., and Bogard, D. G., 1994, "Film Cooling with Compound Angle Holes: Adiabatic Effectiveness," ASME Paper No. 94-GT-312.
[8] Gritsch, M., Schulz, A., and Wittig, S., 1998, "Heat Transfer Coefficient Measurements of Film-Cooling Holes with Expanded Exits," ASME Paper No. 98-GT-28.
[9] Gritsch, M., Schulz, A., and Wittig, S., 1997, "Adiabatic Wall Effectiveness Measurements of Film-Cooling Holes with Expanded Exits," ASME J. Turbomach., **120**, pp. 560–567.
[10] Thole, K., Gritsch, M., Schulz, A., and Wittig, S., 1998, "Flowfield Measurements for Film-Cooling Holes with Expanded Exits," ASME J. Turbomach., **120**, pp. 327–336.
[11] Day, C. R. B., Oldfield, M. L. G., and Lock, G. D., 2000, "Aerodynamic Performance of an Annular Cascade of Film Cooled Nozzle Guide Vanes Under Engine Representative Conditions," Exp. Fluids, **29**, pp. 117–129.
[12] Schlichting, H., 1979, *Boundary-Layer Theory*, McGraw-Hill Book Company, Seventh Edition, New York, NY.
[13] Sargison, J. E., Guo, S. M., Oldfield, M. L. G., Lock, G. D., and Rawlinson, A. J., 2000, "The Variation of Heat Transfer Coefficient, Adiabatic Effectiveness and Aerodynamic Loss with Film Cooling Hole Shape," *Proc Turbine 2000, International Symposium on Heat Transfer in Gas Turbine Systems*, Turkey.
[14] Jones, T. V., 1991, "Definition of Heat Transfer Coefficient in the Turbine Situation," IMechE Paper No. C423/046, IMechE Turbomachinery Conference.
[15] Jones, T. V., 1999, "Theory for the use of Foreign Gas in Simulating Film Cooling," Int. J. Heat Fluid Flow, **20**, pp. 349–354.
[16] Kays, W. M., and Crawford, M. E., 1993, *Convective Heat and Mass Transfer*, McGraw-Hill, New York, NY.
[17] Mee, D. J., Ireland, P. T., and Bather, S., 1999, "Measurement of the temperature field downstream of simulated leading-edge film-cooling holes," Exp. Fluids, **27**, pp. 273–283.

A Converging Slot-Hole Film-Cooling Geometry—Part 2: Transonic Nozzle Guide Vane Heat Transfer and Loss

J. E. Sargison
Mem. ASME,
School of Engineering,
University of Tasmania,
Hobart, Tasmania 7001, Australia
e-mail: jane.sargison@utas.edu.au

S. M. Guo

M. L. G. Oldfield
Mem. ASME

Department of Engineering Science,
University of Oxford,
Oxford OX1 3PJ, UK

G. D. Lock
Department of Mechanical Engineering,
University of Bath,
Bath BA2 7AY, UK

A. J. Rawlinson
Rolls Royce plc,
Derby DE24 8BJ, UK

This paper presents the first experimental measurements on an engine representative nozzle guide vane, of a new film-cooling hole geometry, a converging slot-hole or console. The patented console geometry is designed to improve the heat transfer and aerodynamic performance of turbine vane and rotor blade cooling systems. These experiments follow the successful validation of the console design in low-speed flat-plate tests described in Part 1 of this paper. Stereolithography was used to manufacture a resin model of a transonic, engine representative nozzle guide vane in which seven rows of previously tested fan-shaped film-cooling holes were replaced by four rows of consoles. This vane was mounted in the annular vane ring of the Oxford cold heat transfer tunnel for testing at engine Reynolds numbers, Mach numbers and coolant to mainstream momentum flux ratios using a heavy gas to simulate the correct coolant to mainstream density ratio. Heat transfer data were measured using wide-band thermochromic liquid crystals and a modified analysis technique. Both surface heat transfer coefficient and the adiabatic cooling effectiveness were derived from computer-video records of hue changes during the transient tunnel run. The cooling performance, quantified by the heat flux at engine temperature levels, of the console vane compares favourably with that of the previously tested vane with fan-shaped holes. The new console film-cooling hole geometry offers advantages to the engine designer due to a superior aerodynamic efficiency over the fan-shaped hole geometry. These efficiency measurements are demonstrated by results from midspan traverses of a four-hole pyramid probe downstream of the nozzle guide vane.
[DOI: 10.1115/1.1459736]

Introduction

This paper presents heat transfer and efficiency measurements on an engine representative nozzle guide vane in compressible flow using a new console cooling geometry. It follows a companion Part 1 paper [1], which describes the console film-cooling geometry and presents low-speed flat-plate measurements using the console.

Film cooling fulfils an important role in the control of temperature levels and gradients of gas turbine components in environments where the gas temperature is usually above the component melting point and thermal stresses induced by temperature gradients can significantly reduce component life. Research into understanding and optimizing film cooling is fueled by the prospect of increased specific work capacity from the turbine for higher turbine entry temperature. It is also important that the application of film cooling to a hot engine part such as a nozzle guide vane (NGV), however thermally effective, does not significantly reduce the aerodynamic efficiency of the engine part. Denton [2] suggests that, despite an estimated increase in turbine entry temperature of 100 K per 1% coolant mass flow, a reduction of approximately 1% in turbine efficiency per 1% coolant flow can have a large effect on the overall cycle efficiency. This reduction is a viscous effect due to irreversible mixing of the coolant and mainstream flows.

A considerable amount of research has been conducted at low speed over a flat plate, to compare the effect of different arrangements of discrete holes, flared holes, and slots, and a discussion of this work is presented in Part 1 of this paper.

A significantly smaller amount of data relates to film-cooling measurements on three-dimensional surfaces in annular or linear cascades at engine representative flow conditions. The geometry of the surface has been shown by Ito et al. [3], Schwarz and Goldstein, [4] and Ko et al. [5] to affect the position of the jets downstream of the film-cooling holes, and hence the effectiveness and heat transfer coefficient even at low mainstream flow speeds. Ligrani and Camci [6], present a correction to measurements made on a flat plate to allow for the effects of variable property flow. The effects of both NGV geometry and compressible flow conditions on film cooling has been investigated by Arts and Bourguignon [7], Camci and Arts [8], and Drost et al. [9], in linear cascades.

Console

A new film-cooling hole shape is presented in this pair of papers, which provides lateral spreading of the coolant, with heat transfer coefficient and adiabatic effectiveness similar to the slot geometry, and significantly lower aerodynamic loss than the fan-shaped hole geometry. The converging slot-hole, or console film-cooling hole geometry (patent applied for) has been described in Part 1 of this paper, which presented measurements of the performance of the hole in a flat plate in a low-speed wind tunnel. As shown in Fig. 1, the hole is nominally cylindrical at inlet, and the cross-sectional shape changes through the hole to form a slot at outlet. Individual holes in a row of consoles are positioned such that adjacent holes meet just below the surface in order to form a continuous slot at outlet. The cross-sectional area of the console reduces from inlet to outlet and the resultant acceleration reduces losses in the hole, particularly compared with diffusing, fan-shaped holes.

Contributed by the International Gas Turbine Institute and presented at the International Gas Turbine and Aeroengine Congress and Exhibition, New Orleans, Louisiana, June 4–7, 2001. Manuscript received by the IGTI, October 23, 2000. Paper No. 2001-GT-127. Review Chair: R. A. Natole.

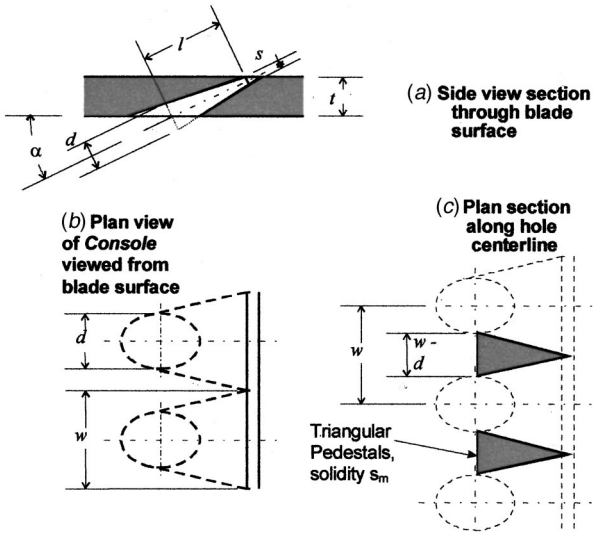

Fig. 1 Basic console configuration

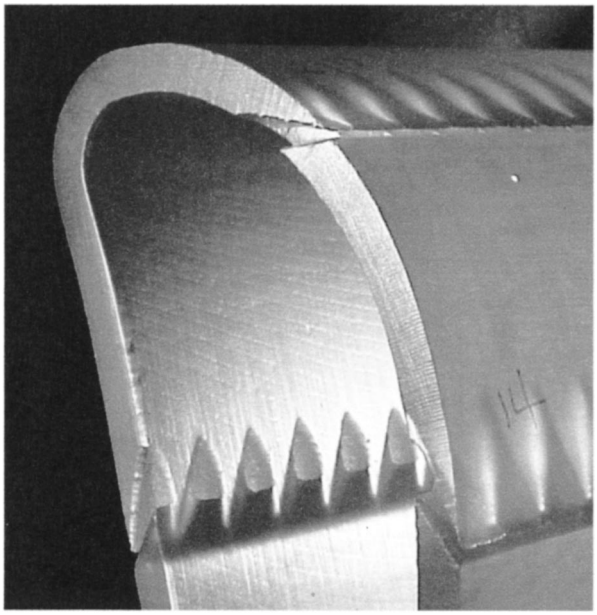

Fig. 3 Photograph of prototype NGV section, manufactured by stereolithography, showing three rows of console cooling holes

The advantage of joining the hole exits is that the ejected coolant film is continuous in the spanwise direction (in contrast to cylindrical holes), and the film therefore benefits from the Coanda effect [10] and will not lift off from the blade surface at typical blowing rates. Evidence of this effect was recorded in the low-speed experiments documented in Part 1 of this paper [1]. The triangular pedestals of material between the holes (Fig. 1), maintain at least 25% of the cross-sectional area through the plane of the holes, compared with 52% for a typical fan-shaped hole film-cooling design. This maintains a structural integrity that cannot be achieved by a traditional straight or shaped slot. Further investigation is required to show that the required mechanical strength of the blade is maintained to design requirements. The console is generated completely by straight lines as shown in Fig. 2. This allows the console to be machined using available drilling techniques (mechanical or laser). Typical rows of consoles in a blade are shown in Fig. 3. The orientation of the holes in Fig. 2 is similar to that of the holes on the bottom LHS of Fig. 3.

The purpose of this second part of the experimental study of the console is to measure its thermal and aerodynamic performance on an NGV in an annular cascade at engine representative flow conditions (correct Mach and Reynolds numbers).

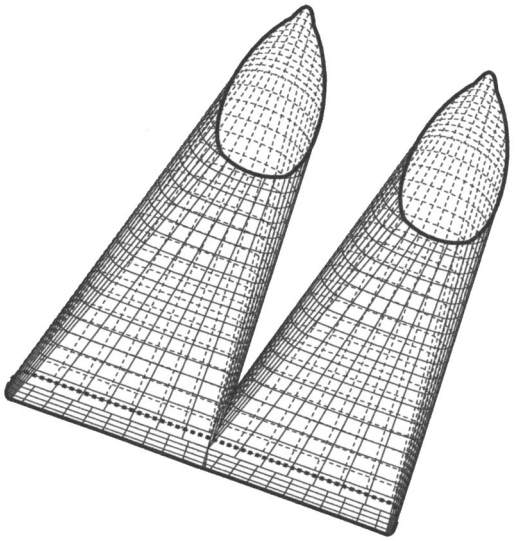

Fig. 2 Uni Graphics surface definition of two console film-cooling holes

Experimental Facility. The experimental results presented in this paper were measured in the Oxford University cold heat transfer tunnel (CHTT), which is a blowdown facility with a main reservoir at ambient temperature. The test section of the tunnel is an annular cascade of 36 NGVs at 1.4 times larger than the engine scale and is described in detail by Martinez-Botas et al. [11]. The test duration is typically 3–5 s, and it is possible to independently vary Reynolds and Mach numbers between experiments. The inlet turbulence intensity is 13% with an integral length scale of 21 mm. This is representative of the exit levels of turbulence in the engine [12]. The experiments presented in this paper were all conducted at engine design conditions and the main parameters are presented in Table 1.

As illustrated in Fig. 4, coolant is fed to the 36 NGVs through calibrated metering orifices. There are three cassettes of five vanes, which can be removed from the tunnel, and the vanes in these cassettes can be interchanged to perform different experiments. Two of these cassettes were used for the current set of experiments, namely the heat transfer and aerodynamic cassettes. The test NGVs used in the cassettes usually have the full cooling configuration typical of engine NGVs consisting of approximately 350 holes arranged in 14 rows or seven rows of holes and four

Table 1 Comparison of tunnel and engine conditions

MEASUREMENT OF THERMAL PERFORMANCE

Parameter	Engine	Tunnel
Inlet Total Pressure	32 bar	2 bar
Coolant/Main Stream Pressure Ratio	1.02	1.02
Coolant/ Main Stream Density Ratio	≈1.8	1.77
Turbine Inlet Temperature	1750-1800 K	290 K
• Exit Reynolds Number	2.02×10^6	2.02×10^6
Exit Mach Number	0.96	0.96
Mass Flow Rate	120 kg/s	38 kg/s

• Based on axial chord and downstream flow conditions

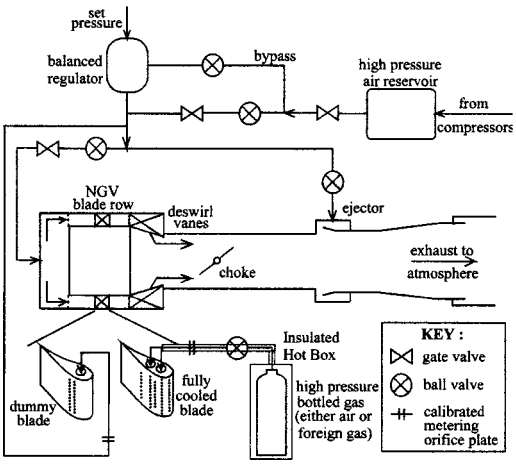

Fig. 4 Schematic diagram of the CHTT

rows of consoles. The NGV with rows of consoles is referred to as the console NGV, and the NGV with rows of fan-shaped holes is referred to as the fanned NGV. The console NGV in position in the CHTT during a test is shown in Figs. 12 and 13 and a schematic diagram of the fanned NGV is shown in Fig. 5. The remainder of the NGVs have a simplified, or ''dummy,'' cooling geometry consisting of approximately 80 holes arranged in four rows which maintain the periodicity of flow around the annulus without the complexity of the full geometry.

In order to maintain as nearly as possible the same mass flow rate of coolant per unit width, for the fanned and console NGVs, the throat area per unit width of each hole geometry was designed to be matched. The console NGV, complete with all the film-cooling holes and consoles such as shown in Fig. 3, was manufactured from resin using stereolithography (Springer [13]), because it was not possible to machine the consoles from acrylic as was used for the fanned NGV. A row of consoles of equal area to a single row of fan-shaped holes could not be produced with the required accuracy using stereolithography and the was concern that they could not be machined in the engine. Because of this, the consoles in rows C1/2, C3/4 and C12/13 were designed such that each row of consoles replaced two rows of fan-shaped film-cooling holes to ensure that the slot height at exit was large enough for manufacture and to try to reduce the number of rows of film-cooling holes. On the suction surface, a larger area console C14 replaced a single fanned row F14. Unfortunately, due to manufacturing tolerances and the differences between the discharge coefficient, C_D, for the fan-shaped holes and consoles, which could not be measured exactly until a blade was made and measured in the CHTT, the comparison between the fanned NGV and console NGV is indicative, but not exact. The mass flow rates from different film-cooling hole rows were measured and the heat transfer and loss results presented are discussed with regard to the measured mass flow rates.

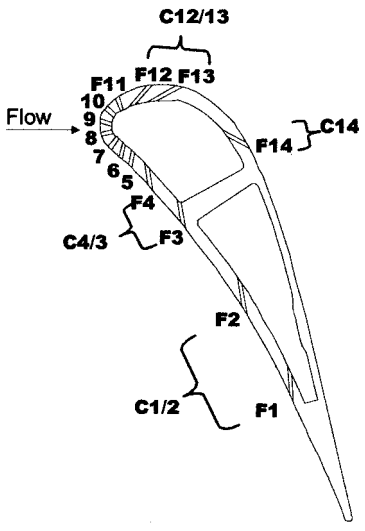

Fig. 5 Fanned NGV film-cooling hole configuration showing replacement of fan-shaped cooling hole rows with console rows

To model the engine situation where the coolant is at a lower temperature, and hence more dense than the mainstream air, a heavy, foreign gas was used to simulate the density ratio as demonstrated by Teekaram et al. [14]. A mixture of SF_6 (30.2% by weight) and Ar (69.8% by weight) was used. The ratio of specific heats of the mixture is the same as air ($\gamma = 1.4$), but the density is 1.77 times that of air. With the density ratio correct, the momentum flux ratio and mass flux ratio are matched to engine conditions, provided that the total pressure ratio of coolant to mainstream is correct. The test NGVs in any experiment are fed from three gas bottles containing foreign gas and the remaining dummy NGVs are fed with air from the main reservoir.

The heat transfer cassette, used to perform the heat transfer experiments presented, contains one stereolithography resin NGV with the full console coolant configuration, flanked by two Perspex nozzle guide vanes with full fanned coolant configuration and two guard vanes with the simplified coolant geometry. These NGVs can be preheated before the experiment by isolating the four passages of the annulus with shutters operated by pneumatic pistons. The shutters are rapidly retracted once the tunnel has reached a steady operating condition. The operation of the heat transfer cassette is described more fully by Guo et al. [15].

Experimental Technique. Thermochromic liquid crystals (TLC) were used on the test NGV to measure heat transfer. The application of TLCs to heat transfer measurement has been previously documented by Ireland et al. [16] and the response time of TLC has been measured by Ireland and Jones [17] to be of the order of 3 ms. In this application, wide-band TLC, which display a color play over a temperature range of 20°C, were sprayed onto the NGV surface over a thin coating of black paint, which enhanced the contrast of the liquid crystal display.

The experimental technique used for the measurement of heat transfer in the CHTT has been described in detail by Sargison et al. [18]. Three miniature CCD cameras positioned in the tunnel recorded the liquid crystal color play and the cameras were arranged to minimize the aerodynamic disturbance in the tunnel, particularly near the test NGV. The images were recorded at 25 frames/s directly to a PC using a frame grabber card. Lighting was supplied inside the tunnel by two 50-W miniature dichroic halogen lamps.

The recorded raw images were stored using the YUV (luminance and 2 chrominance) model (Gonzalez and Woods [19]) and the color history at a single pixel was converted to hue using

$$\text{Hue} = \tan^{-1}\left(\frac{b}{a}\right) \tag{1}$$

where a and b are the magnitudes of the chrominance components, U and V, respectively.

An in-situ calibration of the liquid crystals was required in order to ensure that the effects of lighting and viewing angles were correctly compensated for in the experiment. The NGV was heated to a temperature above the liquid crystal color play range and allowed to cool in still air. The temperature at a number of points on the surface was recorded using thin film thermocouples attached to the NGV surface and hence a calibration curve of temperature versus hue, such as is shown in Fig. 6, could be constructed for each pixel in view.

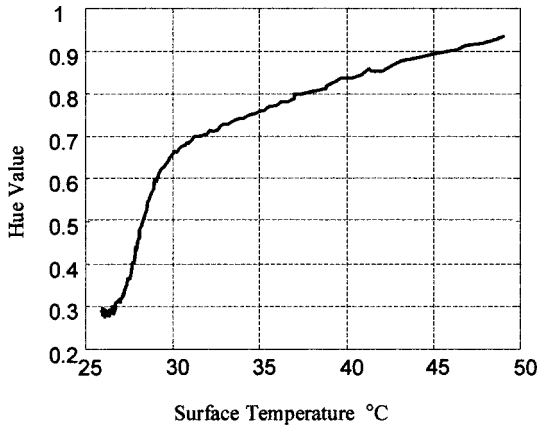

Fig. 6 Surface temperature versus hue for a pixel

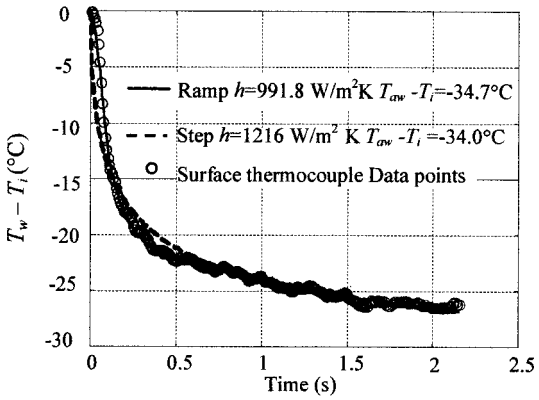

Fig. 8 Thermocouple temperature trace with ramp and step curve fits applied

For each experiment, both the coolant supply and vane passage were heated to the same initial temperature, above the TLC color play temperature range. Note that, unlike the engine case, the mainstream is colder than the coolant. The coolant supply was kept at the same temperature as the vane initial temperature in order to prevent heat transfer between the coolant and the vane during the experiment. Typical NGV wall, cavity and mainstream temperature histories are presented in Fig. 7. When the tunnel is fired the mainstream total temperature has two initial peaks associated with compression heating of the gas upstream of the test section. The shutters shielding the hot test vane are opened once the tunnel has reached steady operating conditions and during the run time the surface temperature is seen to drop rapidly, while the mainstream and coolant temperatures vary by less than 1°C.

During the first 0.25 s of the experiment, the color response cannot be measured because the shutters are opening and the camera iris takes a short time to adjust to the resultant change in lighting. Hence, part of the surface temperature history is not recorded. A typical surface temperature history measured using TLC is presented in Fig. 11.

Analytical Technique. The heat transfer coefficient, h, is defined as the constant of proportionality between the local heat flux q and the difference between the wall temperature T_w and the unknown convection driving temperature of the gas or adiabatic wall temperature, T_{aw} at that point (Jones [20,21])

$$q = h(T_w - T_{aw}) \tag{2}$$

The adiabatic wall temperature is between the coolant temperature T_{oc}, and the mainstream temperature T_{0m} and depends on these temperatures and the level of mixing of the flow. The dependence on temperature is removed by defining an adiabatic effectiveness (Jones [20,21])

$$\eta = \frac{T_{aw} - T_r}{T_{0c} - T_{0m}} \tag{3}$$

The mainstream recovery temperature in defined using the recovery factor, $r = \mathrm{Pr}^{1/3}$, suggested by Kays and Crawford [22]

$$T_r = T_{0m}\left(\frac{1 + r\dfrac{\gamma-1}{2}M^2}{1 + \dfrac{\gamma-1}{2}M^2}\right) \tag{4}$$

The heat transfer coefficient and adiabatic effectiveness can be obtained from the surface temperature history by comparing an analytical solution to the measured transient response of surface temperature to a change in fluid temperature. For uniform, semi-infinite, flat-plate boundary conditions, the instantaneous heat flux can be expressed as an analytical function of the transient surface temperature. The first method used was a comparison with the solution presented by Schultz and Jones [23] for the production of a thermal transient by a step change in fluid temperature

$$\frac{T_w - T_i}{T_{aw} - T_i} = 1 - e^{\beta^2}\,\mathrm{erfc}(\beta) \quad \text{where} \quad \beta = \frac{h\sqrt{t}}{\sqrt{\rho c k}} \tag{5}$$

Here $\sqrt{\rho c k}$ is the thermal product of substrate density, specific heat and thermal conductivity, erfc is the complementary error function, and t is the time.

Using the calibration, the wide-band TLC data can be converted to a wall surface temperature history $T_w(t)$ with known initial surface temperature T_i. Hence, using regression analysis the two unknowns h and T_{aw} in Eq. (5) are solved. If the coolant mainstream and recovery temperatures are known, Eq. (3) then yields the effectiveness.

It was found that the step model was not an accurate model of the facility as it yielded h results significantly higher than those measured using thin film gages [24]. The difference between the results was due to the lack of data critical to the curve fit at the beginning of the temperature trace, due to the shutters obscuring the camera view as they opened and the limited active range of the wide band liquid crystals.

As described in [18], comparison of the full wall temperature history recorded at surface thermocouples with a step change curve fit demonstrated that the step change solution required modification to incorporate a ramp solution in order for the surface temperature to be accurately modeled (Fig. 8).

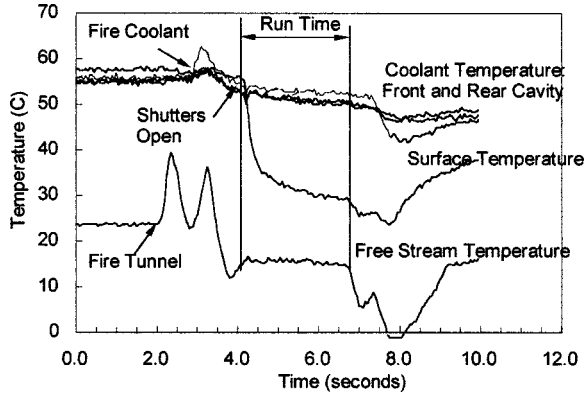

Fig. 7 CHTT experimental temperature histories

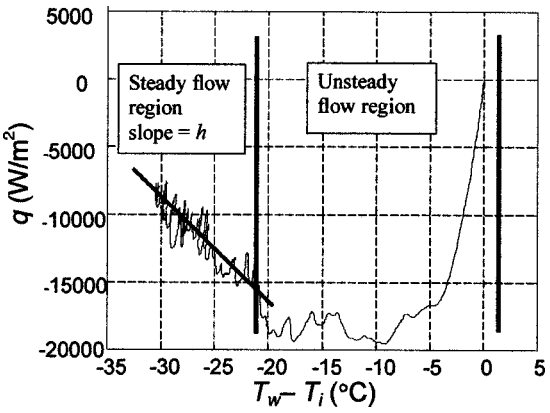

Fig. 9 Heat flux trace obtained from surface thermocouple

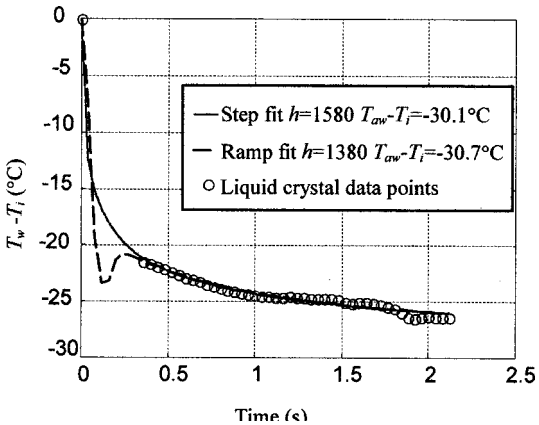

Fig. 11 Comparison of data fits

Having identified that a modified solution was required, it was necessary to determine the shape of the adiabatic wall temperature distribution to be used for the modified curve-fitting routine. The thermocouple temperature trace was transformed to a surface heat flux trace using the impulse response method (MLGO to be published) based on the governing equations for heat transfer from a semi-infinite surface (Doorly and Oldfield [25], Ainsworth et al. [26]). The impulse response method uses deconvolution to derive filter impulse responses of the same length as the data being processed. Figure 9 shows a typical heat flux distribution obtained from thermocouple data using this technique. This figure indicates that the NGV surface does not experience a true step-change in fluid temperature, due to the starting thermal transient. From the plot of heat flux with surface temperature, h is the slope of the steady region, and T_{aw} is the intercept at zero heat flux. In this way the steady state values of h and T_{aw} at the thermocouple location could be obtained and these could be used in combination with the heat flux q, to determine the variation in adiabatic wall temperature in the initial unsteady part of the experiment.

The governing equations for heat transfer are linear in adiabatic wall temperature, but not in heat transfer coefficient, so as a first attempt to improve the analytical model of the transient process it was assumed that h was constant, and the adiabatic wall temperature varied during the experiment.

The adiabatic wall temperature in the nonsteady segment of the experiment may be determined using Eq. (2) where the heat flux and surface temperature are known and h is assumed constant. This assumption is reasonable since the latter is primarily determined by the fluid mechanics rather than the thermal boundary conditions. The adiabatic wall temperature (subtracted from the initial temperature) obtained by this method is shown in Fig. 10.

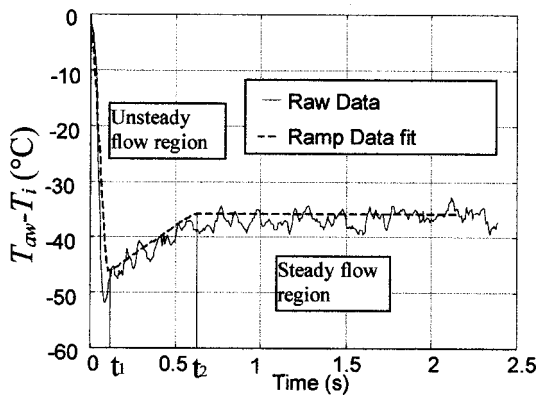

Fig. 10 Adiabatic wall temperature distribution

This temperature history is well modeled as two ramps of time constant t_1 and t_2, an initial overshoot of magnitude $\lambda(T_{aw} - T_i)$, and a horizontal segment.

Ireland and Jones [27] have solved the one-dimensional conduction equation with a semi-infinite boundary condition for a ramp change in adiabatic wall temperature

$$T_w(t) = ma\left[\frac{t}{a} + \frac{1}{a^3} - \frac{2\sqrt{t}}{a^2\sqrt{\pi}} - \frac{e^{a^2 t}\,\mathrm{erfc}(a\sqrt{t})}{a^3}\right] \tag{6}$$

where $a = h/\sqrt{\rho c k}$ and m is the slope of the ramp, T_{aw} versus time.

The assumed adiabatic wall temperature distribution is

$$T_{aw} - T_i = m_1 t + m_2(t-t_1)u(t-t_1) + m_3(t-t_2)u(t-t_2) \tag{7}$$

where $u(t)$ is the unit step function, t_1 and t_2 are the ramp time constants and m_1, m_2, and m_3 are the slope of the three sections of the temperature distribution. If $m_3 = -(m_1 + m_2)$, then the third segment is horizontal as required in this case.

The theoretical wall temperature response to the change in adiabatic wall temperature was produced by summing the wall temperature due to each ramp displaced by the time constant of the ramp, t_1 or t_2

$$T_w(t) = \sum T_{wn}(t-t_n)u(t-t_n) \tag{8}$$

If the time constants t_n are known (from local thermocouple data), then regression can again be applied to the surface temperature history in order to solve for the unknowns (T_{aw}, h and the initial overshoot λ).

The two curve fits to the TLC data points are compared in Fig. 11, with the ramp change providing a lower value of heat transfer coefficient and a better fit to the data points, particularly in the early region of the curve. The ramp fit is also a more accurate fit to thermocouple data as demonstrated in Fig. 8. The value of heat transfer coefficient is closer to the level measured by Lai [28] using thin film gages and there is little difference in T_{aw} between the two analysis techniques.

Experimental Results. The total mass flow rates from the console and fanned NGVs with full film cooling were equal within the measurement uncertainty, although the distribution between the cooling hole rows was different as summarized in Table 2. The coolant from each film-cooling row was measured at static conditions rather than in the CHTT, by matching the correct ratio of coolant total pressure to static pressure for each row as values of C_D with external flow (Rowbury et al. [29]) were not available for the console blade.

The h and η results for fanned and cylindrical hole NGVs presented in the comparative plots were taken from [28]. The differ-

Table 2 Coolant distribution by row

Hole Row (Figure 5)	Percentage of total coolant flow	
	Console	Fanned
1/2	10.8	14
3/4	7.1	7.6
5-11	53.9	47.5
12/13	13.4	20.6
14	14.8	10.2
Total Suction Surface	28.2	30.8
Total Pressure Surface	17.9	21.6
Total Leading Edge	53.9	47.5

ences in the coolant flows reflect the different techniques used to manufacture the blades. The fanned blade was machined from either acrylic or aluminum, with drilled holes. The console blade was manufactured using stereolithography from resin and the holes were created at the same time. The slight difference in area and C_D gave mass flows different from the design values.

Figures 12 and 13 are examples of the raw digital images recorded during the experiments. The cooling film from the console rows on the pressure surface (Fig. 12) has good uniformity and the dark TLC color near the slot exit represents high adiabatic effectiveness. The coolant film on the suction surface, from row 14 (Fig. 13) is not as uniform as the pressure surface, and the peaks of temperature, which equate to high effectiveness, are located behind the point where two adjacent holes in the row of consoles join. This effect was also seen in the low speed testing of the console (Part 1), and is possibly due to the interaction of vortices between two consoles.

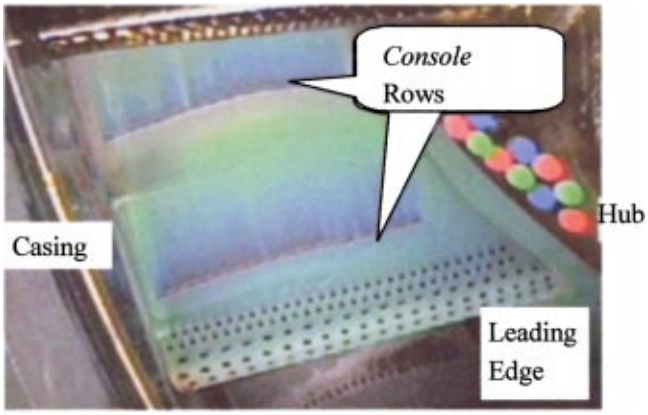

Fig. 12 Console NGV pressure surface with two rows of console film-cooling holes

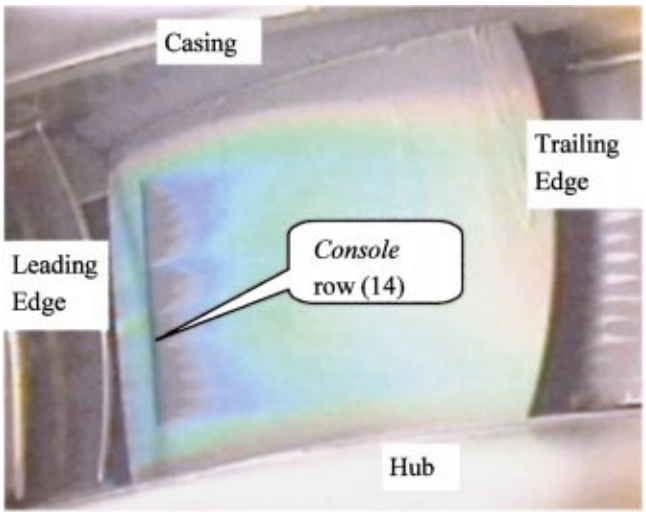

Fig. 13 Console NGV suction surface

The experimental results presented in the following figures are corrected to engine conditions following the technique presented by Jones [21] and used by Guo et al. [15]. The use of foreign gas in the experiments allows the correct density ratio to be produced in the experiment; however, the correction is required to correctly model the molecular properties of the high-temperature mainstream and coolant air in the engine.

The ratio of Nusselt number for the experimental and engine cases that are at the same Reynolds number, coolant to freestream density and velocity ratios is [21]

$$\frac{\mathrm{Nu}_e}{\mathrm{Nu}_x}=\left(\frac{Cp_m}{Cp_w}\right)_x \frac{1+\left[\mathrm{Pr}_m\frac{Cp_w}{Cp_m}\frac{k_m}{k_w}\right]_x f_2}{1+\left[\mathrm{Pr}_m\frac{k_m}{k_w}\right]_e f_2} \tag{9}$$

This equation and the method of deriving the function f_2 is further discussed in [21], and this equation has been converted to a ratio of heat transfer coefficients for the CHTT conditions by Guo et al. [24]

$$\frac{h_e}{h_x}=\frac{x_x}{x_e}\frac{k_e}{k_x}\left(\frac{Cp_m}{Cp_w}\right)_x \frac{1+0.924\left(\frac{Cp_w}{Cp_m}\frac{k_m}{k_w}\right)_x}{1+0.924\left(\frac{k_m}{k_w}\right)_e} \tag{10}$$

Here h_e, and h_x the heat transfer coefficients, k_e and k_x the gas conductivities, Cp_e and Cp_x the gas specific heats at engine and CHTT conditions, respectively. The subscript w refers to the wall value, at which the gas is a mixture of coolant and mainstream. The conductivity and specific heat are calculated with specific accuracy by the relative mole fraction of concentration evaluated at the wall temperature

$$k=k_m(1-\psi_{\mathrm{mole}})+k_c\psi_{\mathrm{mole}} \tag{11}$$

where the concentration by mass is defined

$$\psi_{\mathrm{mass}}=\frac{\eta Cp_m}{(1-\eta)Cp_c+\eta Cp_m}$$

and the mole fraction of coolant concentration is defined

$$\psi_{\mathrm{mole}}=\frac{\psi_{\mathrm{mass}}}{\psi_{\mathrm{mass}}+(1-\psi_{\mathrm{mass}})\frac{M_c}{M_m}}.$$

The correction for adiabatic effectiveness is based on the assumption that the concentration of coolant in the mainstream flow is identical for the experimental and engine conditions. The engine-level effectiveness can be written [21,24]

$$\eta_e=\frac{\eta_x}{\eta_x+(1-\eta_x)\left(\frac{Cp_c}{Cp_m}\right)_x\left(\frac{Cp_m}{Cp_c}\right)_e} \tag{12}$$

where the gas specific heats are evaluated at local recovery temperatures. The effect of this correction is shown in Fig. 14. These corrections were applied to the following results.

The net heat flux reduction parameter defined by Sen et al. [30] has been used to quantify the combined effect of heat transfer coefficient and adiabatic effectiveness by comparing the heat flux with and without film cooling. However, in the case reported here,

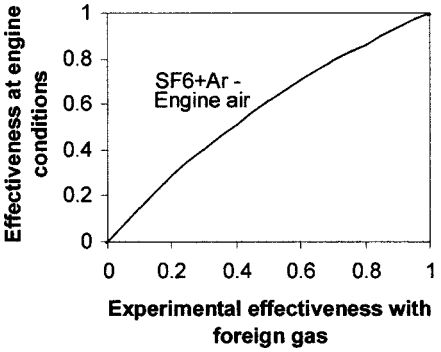

Fig. 14 Film-cooling effectiveness for air at engine conditions versus foreign gas at ambient conditions [21]

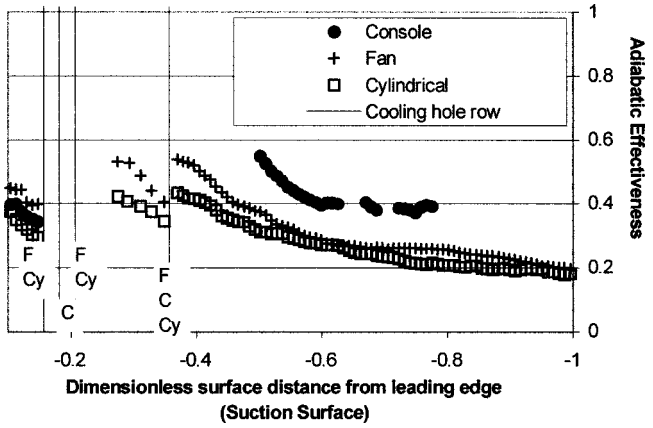

Fig. 15 Adiabatic effectiveness at engine conditions, suction surface

the presence of film cooling around the leading edge of the vane creates an earlier transition than that which would occur, on a vane with no film cooling. Thus, the comparison above is no longer useful due to the differences in the boundary layer state in each case.

Consequently, in the current work, the different film-cooling geometries are compared by use of the predicted total heat flux under engine conditions for each case

$$q = h(T_w - T_{aw}) = h(T_w - T_r)(1 - \eta\theta) \tag{13}$$

where the nondimensional temperature $\theta = (T_{0c} - T_{0m})/(T_w - T_r)$.

For typical engine conditions of $T_{0c} = 880$ K, $T_w = 1200$ K, and $T_{0m} = 1900$ K, the value of the dimensionless temperature, θ, used was $\theta = 1.46$ in low Mach number regions and higher in high Mach number regions where $T_r < T_{0m}$.

The console results presented were analyzed using the technique presented in this paper. In some areas, the curve-fitting technique did not converge, and the data collected in these areas was not considered reliable, and consequently was not included. Ideally, these experiments should be repeated using the thin film gage method developed by Guo et al. [24], to obtain an alternative set of results to complement these existing measurements. The region on the suction surface between dimensionless distances of -0.16 and -0.28 is not viewed by any of the cameras, so no data at all is available in this region. The fanned and cylindrical data are taken from experiments presented by Lai [28], who used double-sided thin film gages to measure the heat transfer coefficient.

Suction Surface Results. The adiabatic effectiveness results for the suction surface in Fig. 15 show that the console exhibits higher effectiveness particularly near to the film-cooling hole row. The vertical dashed lines in these figures and those following mark the position of the cylindrical, fan-shaped and console film-cooling rows (Cy, F, and C, respectively). The fanned film-cooling effectiveness is higher than that for cylindrical holes only near the film-cooling hole row. The heat transfer results in Fig. 16 show that the console varies from a level similar to the cylindrical result to midway between the fanned and cylindrical results. The heat transfer coefficient for the fanned NGV is lower than both the console and cylindrical results for the entire region shown.

The combined effect of adiabatic effectiveness and heat transfer coefficient on the suction surface is shown in Fig. 17 as predicted total heat flux from the surface under engine conditions. The cylindrical holes show a significantly higher level of predicted heat flux than both the console and fanned holes for the entire region. The console data show a significant improvement in predicted heat flux in the region from the film-cooling hole to a distance of -0.8. Downstream of -0.8, the amount of temperature data is limited because the surface temperature falls rapidly below the TLC color play range. In this region the analysis technique is less reliable, and consequently the data in this region has not been included.

Hence, on the suction surface the console performs better than both the fanned and cylindrical rows for the majority of the surface. Note that a total of 28.2 and 30.8% of the coolant mass flow

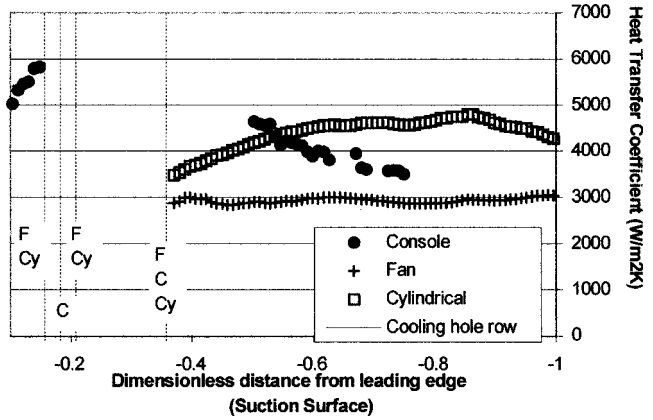

Fig. 16 Heat transfer coefficient at engine conditions, suction surface

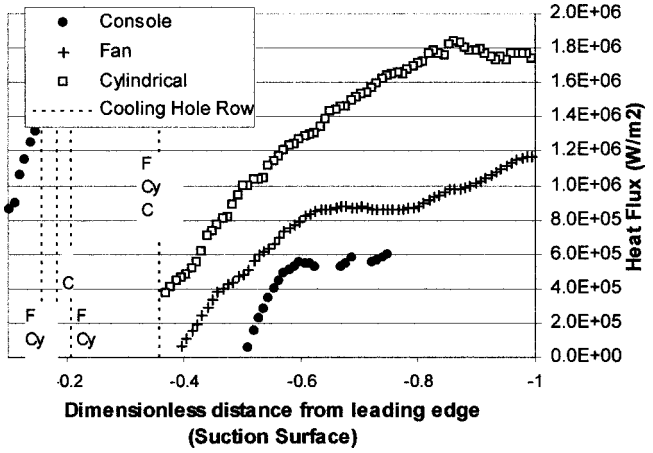

Fig. 17 Predicted heat flux at engine conditions, suction surface

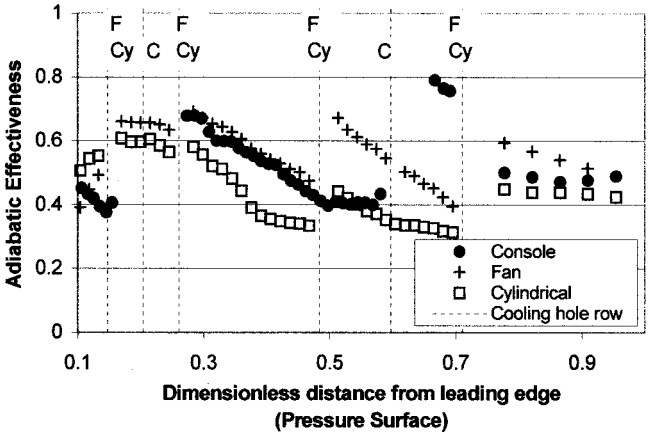

Fig. 18 Adiabatic effectiveness at engine conditions, pressure surface

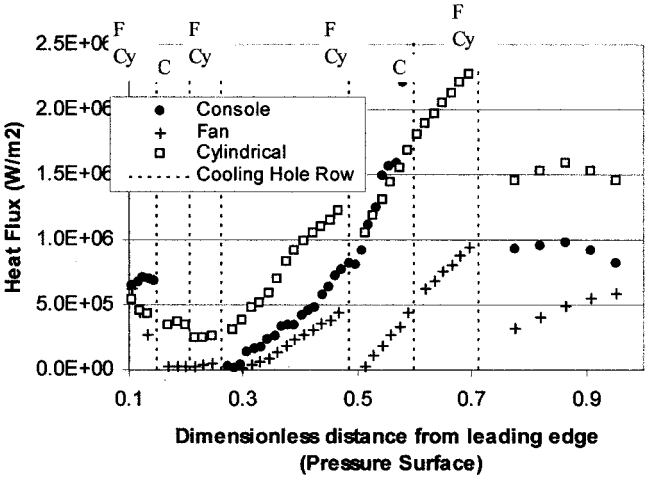

Fig. 20 Predicted heat flux at engine conditions, pressure surface

was supplied to the suction surface through rows C12/13/14 and F12/13/14 for the console and fan-shaped geometries, respectively; see Table 2.

Pressure Surface Results. Figure 18 shows the pressure surface adiabatic effectiveness and illustrates that the film-cooling effectiveness downstream of a console row is almost equal to the level from the fanned row. Regions where the console data falls below the fanned NGV effectiveness are downstream of a new fanned row where there has not been a new console row due to the design decision to replace two rows of fans with a single console. The amount of coolant supplied at each console is 60 and 70% of the amount of coolant supplied from each set of two fanned rows replaced by consoles, so the total amount of coolant supplied to the surface is reduced for the console NGV. The effectiveness results indicate that with an appropriate design, the film-cooling effectiveness distribution on the surface could be made equivalent to the fanned NGV result.

The heat transfer coefficient results in Fig. 19 mirror the flat-plate experimental results [1] in showing that the console has higher heat transfer coefficient than the fanned NGV. The total predicted heat flux result in Fig. 20 again shows a similar level to the fanned NGV downstream of the first console, which becomes significantly higher than the fanned result after the next fanned row. These results should be considered in light of the reduction in coolant flow rate in this area, and the different locations of console rows. The results for the pressure surface certainly indicate that if correctly positioned, the console should achieve the same performance as fanned rows with equal or lower coolant flow rates.

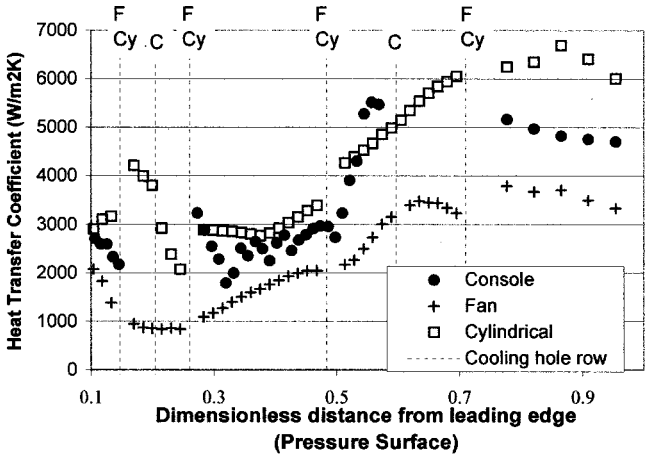

Fig. 19 Heat transfer coefficient at engine conditions, pressure surface

The 95% confidence intervals for the heat transfer coefficient, h, was estimated using a perturbation analysis of the analytical curve fitting routine to be 13% and the error in adiabatic effectiveness was estimated to be 5%. This was as a result of the following sources of error: substrate properties, 1%, surface temperature 0.6%, surface initial temperature, 2%, time, 2%, time constants 4 and 6%. The effects of experimental noise and loss of initial data points were also added to the estimate.

The thermal performance of the console has been shown to be similar to the performance of the fan-shaped film-cooling configuration, and the aerodynamic performance described in the forthcoming will demonstrate the advantages of the console.

Measurement of Aerodynamic Performance

Experimental Apparatus and Technique. The CHTT was used for the measurement of aerodynamic loss, with most parameters as previously described for the heat transfer experiments, except that the aerodynamic cassette was used rather than the heat transfer cassette. The aerodynamic measurements were all conducted at ambient temperature, using foreign gas as coolant to simulate the engine density ratio.

The aerodynamic cassette consists of five NGVs, the first of which is the test vane (stereolithography resin console NGV or aluminum fanned NGV), beside an aluminum NGV with a full-fanned cooling configuration and the remaining aluminum NGVs have simplified cooling geometry (dummy blades). The aerodynamic cassette is fitted with a traverse mechanism, to which the four-hole probe previously calibrated and described by Main [31], Main et al. [32], and also used by Day et al. [33] was attached.

Probe pressures were measured using Kulite XT-190 semiconductor pressure transducers and the frequency response of the probe is estimated to be 300 Hz. The four-hole probe was traversed at approximately 1 m/s circumferentially at midspan across two vane passages downstream of the cascade. The raw probe data was transformed as described by Main [32] and Day et al. [33,34] to yield values of total pressure, Mach number, pitch and swirl angle. A correction was applied to remove the effect of the probe velocity on the measurements. This correction is fully described in [32]. The data was then used to calculate loss using the method of Dzung [35].

Analytical Technique. The aerodynamic efficiency, ε of a NGV can be defined in words as

Table 3 Fully mixed out results

	Fanned	*Console*	*Console* 1-13	*Console* Solid	Fanned Solid
P_2 (bar)	1.12	1.10	1.10	1.14	1.17
P_{o2} (bar)	2.02	2.02	2.02	1.99	1.98
Swirl (°)	74.6	73.1	73.6	74.4	74.6
Mach No	0.96	0.98	0.97		
% m_c	6.0	6.1	5.9		
P_{o1} (bar)	2.07	2.07	2.07		

$$\varepsilon = \frac{\{\text{Actual Kinetic Energy}\}_{\text{mixingplane}}}{\{\text{Theoretical Kinetic Energy}\}_{\text{available}}} \tag{14}$$

where the actual kinetic energy at the mixing plane is measured using the four-hole probe.

The loss coefficient has been defined in different ways in the literature. Denton [2] defines loss coefficient as

$$\zeta = \frac{1-\varepsilon}{\varepsilon} \tag{15}$$

which corresponds to {loss in KE}/{Actual KE}.

The definition of loss coefficient used in the current work follows Day et al. [33]

$$\zeta = 1-\varepsilon \tag{16}$$

which corresponds to {loss in KE}/{theoretical KE}.

Because the flow is not completely mixed at the exit plane, the measured kinetic energy varies and is a function of the measurement location. For this reason, it is usual to relate the nonuniform flow measured at the measurement plane to a uniform, mixed out plane using the equations of continuity of mass, momentum and energy. The procedures described in Day et al. [33,34] were used to calculate the efficiency from the downstream traverse data.

Experimental Results. The midspan parameters measured using the four-hole probe traverse presented in the following figures indicate that console film cooling on an NGV creates significant aerodynamic differences compared to the fan-shaped film-cooling geometry. The mixed out or average values of the parameters in these figures are presented in Table 3.

Figure 21 shows the total pressure downstream of the NGV normalized against the total pressure upstream of the cascade. The console NGV shows a wake that is shifted to the left by 1.5 deg and has a higher minimum pressure compared with the fanned NGV. In order to investigate whether this change was due to the fluid mechanics of console film cooling or to differences in the manufacture of the NGV, the final row of consoles on the suction surface was closed (console 1-13). The effect of blocking the final suction surface row of consoles is to move the wake by 0.5 deg to the right (back towards the fanned result), indicating that there is a definite change in wake position caused by console film-cooling flows.

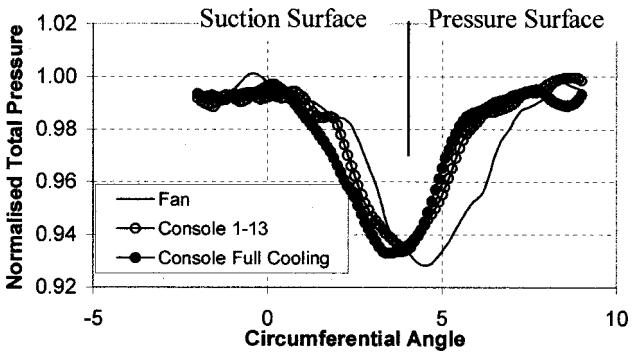

Fig. 21 Normalized total pressure

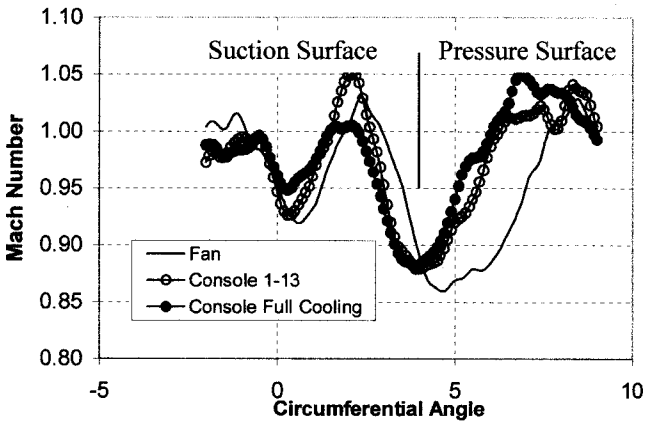

Fig. 22 Mach number

The Mach number distribution (Fig. 22) is changed for the console NGV compared with the fanned NGV, by a shift in the circumferential angle.

The swirl angle (Fig. 23) shows the most significant change in level between the fanned and the console NGVs. The mixed out value of swirl angle for the cooling configurations were 74.6 deg for the fanned, and 73.1 and 73.6 deg for the console NGV with and without row 14, respectively. The difference of 0.5 deg caused by adding the final console row indicates that the console film must have an effect on the swirl angle.

The pitch angle (Fig. 24) is less significantly changed by console film cooling. The largest difference between the fanned NGV and the console NGV results is a pitch angle close to zero near the circumferential angle of 5, compared with the fan NGV pitch angle near -1.

In order to check that the measured changes in wake location and swirl angle were not due to manufacturing differences between the fanned and console NGVs a further experiment was conducted, with all film-cooling holes covered on both NGVs by a Kapton film bonded with 3M high-bond glue. The mixed out values for these solid type experiments are given in the final two columns of Table 3. The differences in swirl angle averaged over three experiments was 0.2 deg. This indicates that although there may be a small shape difference in the two NGVs, the difference is not significant enough to cause the measured 1.5 deg difference in swirl angle with film cooling, and this effect must be caused by the fluid mechanics of console film cooling.

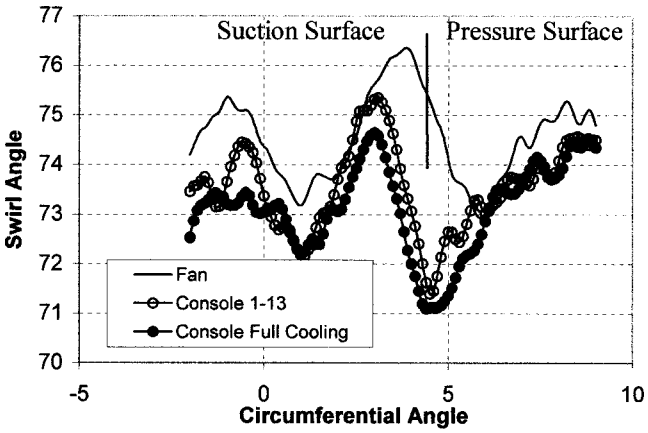

Fig. 23 Swirl angle

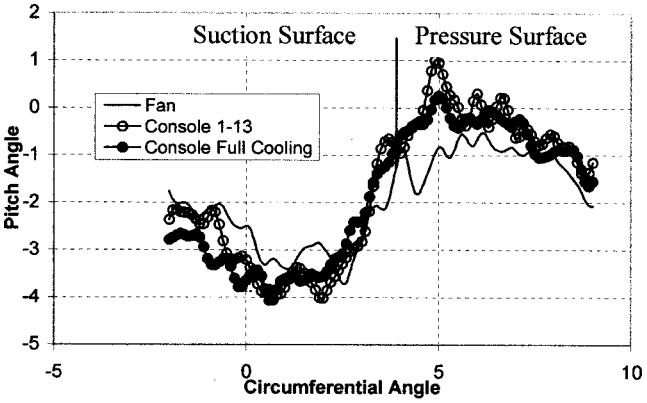

Fig. 24 Pitch angle

Figure 25 shows the final calculated values of aerodynamic loss for the console and fanned film-cooling configurations. The results are normalized against the value of aerodynamic loss for no film cooling of 4.26% [33].

The increase in loss due to film cooling for the console NGV with full cooling is only 20% of that for the full-fanned cooling. For the console NGV with rows 1–13 blowing, the loss is reduced compared with the loss for a NGV with no film cooling. It would seem that the film cooling has altered the point of transition and state of the boundary layer over the vane.

Loss data is also shown for the case where rows 1–2 and 7–14 are blocked with tape, and film cooling only emerges from the leading edge region (rows 3–6). Here the loss is significantly reduced, compared with the case of no film cooling, again due to the influence of film cooling in the boundary layer over the vane, as discussed by Day et al. [33]. This data also illustrates that the aerodynamic loss is mainly generated where the coolant emerges into regions of high Mach number (0.95 at row 14) as expected. Note that Fig. 25 shows that console row C14 has much less loss penalty than the equivalent fan-shaped row F14 in spite of having 45% more mass flow (Table 2).

The 95% confidence level of the absolute uncertainty in the final values of normalized loss presented in Fig. 25 was previously calculated by Day et al. [34] to be ± 0.06. Note that this figure represents the uncertainty in points of loss, not as a fraction of the normalized loss. This means that the difference between the two console results is within the range of the uncertainty, but the difference between the console and the fan results is clearly outside of the range of uncertainty.

The main reason for the superior performance of the console would appear to be that the flow through the film-cooling hole is accelerating. It has been widely established (e.g., Schlichting [10]) that for accelerated flows, the boundary layer generally remains laminar or turbulent boundary layers relaminarize, while even a small amount of diffusion generally induces transition to turbulent flow. The losses due to turbulent flow are significantly higher than laminar flow. Further detailed measurements of the flow in the hole would be required to demonstrate this.

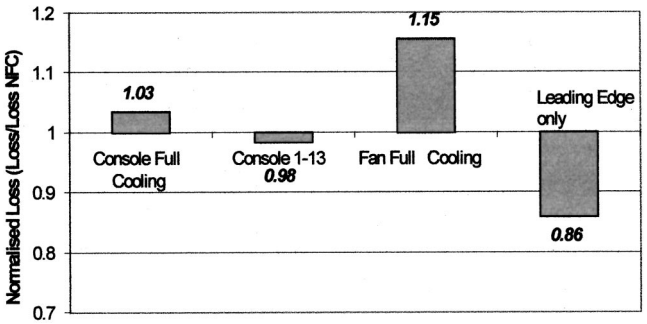

Fig. 25 Comparison of aerodynamic loss for four cooling configurations, normalized by loss without film cooling

Thus the NGV tests confirm the low-speed flat plate results [1] in demonstrating that the console film-cooling holes are significantly more aerodynamically efficient than the fan-shaped holes for a similar cooling performance. They are particularly suitable for use in high Mach number regions.

Conclusions

A new film-cooling hole shape, the converging slot-hole, or console has been presented in this two-part paper. The performance of the console film-cooling hole at engine representative conditions in a model of an engine NGV has been tested and presented. The results have been compared with previously tested fan-shaped film-cooling geometries.

In order to correctly measure the heat transfer coefficient in the transient wide band liquid crystal experiment, the previously published step response technique was modified to more accurately model the ramp change response of the tunnel.

The heat transfer measurements reveal that the console significantly reduces the heat flux to the suction surface of the NGV at engine conditions, when compared to the fan-shaped geometry. The console accomplishes this despite using less coolant than the fan-shaped rows on the suction surface. Measurements on the pressure surface illustrate similar levels of heat flux between the console and fan-shaped geometry downstream of the first console, but further downstream the heat flux to the console NGV is shown to be higher. This result should be interpreted with the knowledge that the mass flow of coolant supplied to each console was 60 and 70% of the amount of coolant supplied to each set of two fan-shaped rows replaced by the consoles. The results for the pressure surface certainly indicate that if correctly positioned by the engine designer (in light of these measurements) the console should achieve the same thermal performance as the fan-shaped holes with equal or lower coolant flow rates. Note that both the console and fan-shaped geometries demonstrated a superior thermal performance when compared with the cylindrical cooling geometry.

The most significant advantage of the console was demonstrated in the aerodynamic experiments. As described in the foregoing, the console demonstrates similar cooling performance to the fan-shaped holes; however, the increase in aerodynamic loss due to film cooling for the full console configuration was only 20% of the increase for the full-fan film cooling. When the final suction surface row of console is covered, the aerodynamic loss is reduced compared with the loss due to a NGV with no film cooling.

Thus, the console film-cooling hole geometry offers an improved cooling performance to the engine designer.

Acknowledgments

This work is supported by Rolls-Royce plc, DERA, DTI CARAD and MOD ARP26c.

Nomenclature

c, Cp = specific heat capacity (constant pressure)
C_D = discharge coefficient
k = thermal conductivity
h = heat transfer coefficient: $h = q/(T_w - T_{aw})$
I = momentum flux ratio $= \rho_c \nu_c^2 / \rho_m \nu_m^2$
KE = kinetic energy
m = slope
M = molecular weight
P = pressure
Pr = Prandtl no., $\mathrm{Pr} = \mu c/k$
q = heat transfer rate
t = time
T = temperature

ν = flow velocity
α = pitch angle (tip to hub angle)
β = swirl angle (vane to vane angle)
ε = aerodynamic efficiency
η = film-cooling effectiveness: $\eta=(T_{aw}-T_r)/(T_{0c}-T_{0m})$
λ = overshoot factor
ρ = density
θ = dimensionless temperature $\theta=(T_{0c}-T_{0m})/(T_w-T_r)$
$\psi_{\text{mass}}, \psi_{\text{mole}}$ = mass fraction and mole fraction
ζ = aerodynamic loss coefficient $\zeta=1-\varepsilon$

Subscripts

2 = mixed out value
$2A$ = measured value
aw = adiabatic wall
c = coolant
e = engine conditions
i = initial condition
m = gas, mainstream
nfc = without film cooling
o = total or stagnation conditions
r = recovery
w = wall, surface
x = experimental conditions

Abbreviations

NGV = nozzle guide vane
CHTT = cold heat transfer tunnel
console = converging slot hole
TLC = thermochromic liquid crystals

References

[1] Sargison, J. E., Guo, S. M., Oldfield, M. L. G., Lock, G. D., and Rawlinson, A. J., 2002, "A Converging Slot-Hole Film-Cooling Geometry—Part 1: Low Speed Flat-Plate Heat Transfer and Loss," ASME Paper No. 2001-GT-0126, ASME J. Turbomach., **124**, pp. 453–460.

[2] Denton, J. D., 1993, "Loss Mechanisms in Turbomachines," ASME J. Turbomach., **115**, pp. 621–656.

[3] Ito, S., Goldstein, R. J., Eckert, E. R. G., 1978, "Film Cooling of a Gas Turbine Blade," ASME J. Eng. Power, **100**, pp. 476–481.

[4] Schwarz, S. G., and Goldstein, R. J., 1989, "The Two-Dimensional Behavior of Film Cooling Jets on Concave Surfaces," ASME J. Turbomach., **111**, pp. 124–130.

[5] Ko, S. Y., Yao, Y. Q., Xia, B., and Tsou, F. K., 1986, "Discrete-Hole Film Cooling Characteristics over Concave and Convex Surfaces," *Proc. 8th International Heat Transfer Conference*, **3**, Hemisphere Publishing Corp., New York, NY, pp. 1297–1301.

[6] Ligrani, P. M., and Camci, C., 1985, "Adiabatic Film Cooling Effectiveness from Heat Transfer Measurements in Compressible, Variable-Property Flow," ASME J. Heat Transfer, **107**, pp. 313–320.

[7] Arts, T., and Bourguignon, A. E., 1990, "Behavior of a Coolant Film with Two Rows of Holes Along the Pressure Side of a High-Pressure Nozzle Guide Vane," ASME J. Turbomach., **112**, pp. 512–521.

[8] Camci, C., and Arts, T., 1985, "Short Duration Measurements and Numerical Simulation of Heat Transfer Along the Suction Side of a Film Cooled Gas Turbine Blade," ASME J. Eng. Gas Turbines Power, **107**, pp. 991–997.

[9] Drost, U., Bolcs, A., Hoffs, A., 1997, "Utilization of the Transient Liquid Crystal Technique for Film Cooling Effectiveness and Heat Transfer Investigations on a Flat Plate and a Turbine Airfoil," ASME Paper No. 97-GT-28.

[10] Schlichting, H., and Gersten, K., 2000, *Boundary Layer Theory*, Springer, Berlin, Germany.

[11] Martinez-Botas, R. F., Main, A. J., Lock, G. D., and Oldfield, M. L. G., 1993, "A Cold Heat Transfer Tunnel for Gas Turbine Research on an Annular Cascade," ASME Paper No. 93-GT-248.

[12] Moss, R. W. and Oldfield, M. L. G., 1991, "Measurements of Hot Combustor Turbulence Spectra," ASME Paper No. 91-GT-351.

[13] Springer, A., 1998, "Evaluating Aerodynamic Characteristics of Wind-Tunnel Models Produced by Rapid Prototyping Methods," J. Spacecr. Rockets, **35**, No. 6.

[14] Teekaram, A. J. H., Forth, C. J. P., and Jones, T. V., 1989, "The Use of Foreign Gas to Simulate the Effects of Density Ratios in Film Cooling," ASME J. Turbomach., **111**, pp. 57–62.

[15] Guo, S. M., Lai, C. C., Jeong, J. H., Jones, T. V., and Oldfield, M. L. G., 1997, "Use of Liquid Crystal Techniques to Measure Film Cooling Heat Transfer and Effectiveness," *90th Symp. Propulsion and Energetics Panel, AGARD*.

[16] Ireland, P. T., Wang, Z. W. and Jones T. V., 1993, "Liquid Crystal Heat Transfer Measurements," von Karman Institute for Fluid Dynamics 1992–1993 Lecture Series.

[17] Ireland, P. T., and Jones, T. V., 1987, "The Response Time of a Surface Thermometer Employing Encapsulated Thermochromic Liquid Crystals," J. Phys. E, **20**, pp. 1195–1199.

[18] Sargison, J. E., Guo, S. M., Oldfield, M. L. G., Lock G. D. and Rawlinson, A. J., 2000, "Use of Liquid Crystal Techniques for a Gas Turbine Film Cooling Study in a Transonic Tunnel," *Proc. 9th Int. Symp. Flow Visualisation*, Heriot-Watt University, Edinburgh, Scotland.

[19] Gonzalez, R. C., and Woods, R. E., 1993, *Digital Image Processing*, Addison-Wesley.

[20] Jones, T. V., 1991, "Definition of Heat Transfer Coefficient in the Turbine Situation," IMechE Paper No. C423/046, IMechE Turbomachinery Conf.

[21] Jones, T. V., 1999, "Theory for the Use of Foreign Gas in Simulating Film Cooling," Int. J. Heat Fluid Flow, **20**, pp. 349–354.

[22] Kays, W. M., and Crawford, M. E., 1993, *Convective Heat and Mass Transfer*, McGraw-Hill, New York, NY.

[23] Schultz, D. L. and Jones, T. V., 1973, "Heat Transfer Measurements in Short-Duration Hypersonic Facilities," *AGARD AG-165*.

[24] Guo, S. M., Lai, C. C., Jones, T. V., Oldfield, M. L. G., Lock, G. D., and Rawlinson, A. J., 1998, "The Application of Thin-Film Technology to Measure Turbine-Vane Heat Transfer and Effectiveness in a Film-Cooled, Engine-Simulated Environment," Int. J. Heat Fluid Flow, **19**, pp. 564–600.

[25] Doorly, J. E., and Oldfield, M. L. G., 1987, "The Theory of Advanced Multilayer Thin Film Heat Transfer Gauges," Int. J. Heat Mass Transf., **30**, No. 6, pp. 1159–1168.

[26] Ainsworth, R. W., Allen, J. L., Davies, M. R. D., Doorly, J. E., Forth, C. J. P., Hilditch, M. A., Oldfield, M. L. G., and Sheard, A. G., 1989, "Developments in Instrumentation and Processing for Transient Heat Transfer Measurements in a Full Stage Model Turbine," ASME J. Turbomach., **111**, pp. 20–27.

[27] Ireland, P. T., and Jones, T. V., 2000, "Liquid Crystal Measurement of Heat Transfer and Shear Stress," Meas. Sci. Technol., **11**, pp. 969–986.

[28] Lai, C. C., 1999, "Fully Film Cooled Nozzle Guide Vane Heat Transfer Measurement and Prediction," D. Phil. thesis, University of Oxford, Oxford, UK.

[29] Rowbury, D. A., Oldfield, M. L. G., and Lock, G. D., 1997, "Engine-Representative Discharge Coefficients Measured in an Annular Nozzle Guide Vane Cascade," ASME Paper No. 97-GT-99.

[30] Sen, B., Schmidt, D. L., and Bogard D. G., 1994, "*Film Cooling with Compound Angle Holes: Heat Transfer*," ASME Paper No. 94-GT-311.

[31] Main A. J., 1994, "Annular Turbine Cascade Aerodynamics," D. Phil. thesis, University of Oxford, Oxford, UK.

[32] Main, A. J., Day, C. R. B., Lock, G. D., and Oldfield, M. L. G., 1996, "Calibration of a Four-Hole Pyramid Probe and Area Traverse Measurements in a Short-Duration Transonic Turbine Cascade Tunnel," Exp. Fluids, **21**, pp. 302–311.

[33] Day, C. R. B., Oldfield, M. L. G., Lock, G. D., 1999, "The Influence of Film Cooling on the Efficiency of an Annular Nozzle Guide Vane Cascade," ASME Paper No. 97-GT-521, ASME J. Turbomach., **121**, pp. 145–151.

[34] Day, C. R. B., Oldfield, M. L. G., and Lock, G. D., 2000, "Aerodynamic Performance of an Annular Cascade of Film Cooled Nozzle Guide Vanes Under Engine Representative Conditions," Exp. Fluids, **292**, pp. 117–129.

[35] Dzung, L. S., 1971, "Konsistente Mittelwerte in der Theorie der Turbomaschinen fur Kompressible Medien," BBC-Mitt., **58**, pp. 485–492.

Perspectives in Modeling Film Cooling of Turbine Blades by Transcending Conventional Two-Equation Turbulence Models

A. Azzi
Faculty of Mechanical Engineering,
University of Oran, USTO,
Oran 31000, Algeria

D. Lakehal[1]
e-mail: lakehal@iet.mavt.ethz.ch
Institute of Energy Technology,
Swiss Federal Institute of Technology Zurich,
ETH-Zentrum/CLT,
CH-8092, Zurich, Switzerland

The paper presents recent trends in modeling jets in crossflow with relevance to film cooling of turbine blades. The aim is to compare two classes of turbulence models with respect to their predictive performance in reproducing near-wall flow physics and heat transfer. The study focuses on anisotropic eddy-viscosity/diffusivity models and explicit algebraic stress models, up to cubic fragments of strain and vorticity tensors. The first class of models are direct numerical simulation (DNS) based two-layer approaches transcending the conventional $k-\varepsilon$ model by means of a nonisotropic representation of the turbulent transport coefficients; this is employed in connection with a near-wall one-equation model resolving the semi-viscous sublayer. The aspects of this new strategy are based on known channel-flow and boundary layer DNS statistics. The other class of models are quadratic and cubic explicit algebraic stress formulations rigorously derived from second-moment closures. The stress-strain relations are solved in the context of a two-layer strategy resolving the near-wall region by means of a nonlinear one-equation model; the outer core flow is treated by use of the two-equation model. The models are tested for the film cooling of a flat plate by a row of streamwise injected jets. Comparison of the calculated and measured wall-temperature distributions shows that only the anisotropic eddy-viscosity/diffusivity model can correctly predict the spanwise spreading of the temperature field and reduce the strength of the secondary vortices. The wall-cooling effectiveness was found to essentially depend on these two particular flow features. The non-linear algebraic stress models were of a mixed quality in film-cooling calculations. [DOI: 10.1115/1.1485294]

Introduction

Film cooling is probably the most efficient blade-cooling mechanism employed in gas-turbine technology. This technique, in which the injected cooling air acts as a buffer between the hot gas and the blade, was found to offer an excellent compromise between the protection of end-walls and aerodynamic efficiency. Since the cooling performance can be influenced by a variety of parameters, i.e., the blade and discharge geometry, injection angle, blowing ratio, freestream turbulence, reliable prediction methods can be of great interest for turbine designers.

Turbulence models employed in film cooling calculations in general do not go beyond the isotropic two-equation type; see Lakehal et al. [1] for a review. However, recent contributions [2] report on calculations with selected Reynolds stress models, but their results revealed that this approach is not systematically better than traditional eddy-viscosity models. Garg and Ameri [3] reported on film-cooling calculations where they compared the Baldwin-Lomax model with different eddy-viscosity models (EVMs). There too, no clear picture emerged from the calculations indicating which of the employed models is superior. Hoda and Acharya [4] conducted a similar study where various closures for turbulent stresses were applied for the prediction of coolant jet in crossflow. The models employed ranged from high and low-Re number $k-\varepsilon$ and $k-\omega$ models to nonlinear eddy viscosity variants. Their contribution led to the conclusion that this type of closure needs further improvements. The main conclusion to be drawn from past experience, including the work of Hoda and Acharya [4], can be formulated as follows: eddy-viscosity models with wall functions are not adequate for film-cooling calculations, and they are especially unsuited for predicting near-wall heat transfer; in particular the lateral spreading of the temperature field is systematically underpredicted. Employed under low-Re number conditions, eddy-viscosity models were found to provide better flow resolution than under high-Re number conditions, but most of them fail to correctly predict the wake of the jet and the associated mixing. Also, a number of researchers point out that the near-wall boundary conditions specified for ω are more accurate than those for ε, which may constitute an advantage for the $k-\omega$ model when used for the prediction of near-wall heat transfer in general.

Turbulence in film-cooling flows—more generally in jets in crossflow—is considerably anisotropic, in particular in the region surrounding the jet exit and very close to the wall, underneath the secondary vortices. This is the reason why anisotropic eddy diffusivity models have been attractive to a number of researchers, including Lakehal et al. [5], Theodoridis et al. [6], and Lakehal et al. [1]. In this alternative route the basic concepts of the $k-\varepsilon$ model are maintained while introducing an anisotropic eddy-viscosity/diffusivity correction for secondary turbulent stresses. Although the method was seen to lead to an improvement, a further extension was found to be necessary in order to apply the model to near-wall regions. In their first attempt to resolve the near-wall region of flow over a symmetrical blade by low-Re $k-\varepsilon$ models, Theodoridis et al. [6] and Lakehal et al. [1] were limited by the need for high resolution near the walls. For this reason they adopted the dynamic, zonal, two-layer model (TLK) of Rodi [7], and their results indeed met with some success [5]. The extension of the anisotropic eddy-viscosity model to low-Re

[1]Formerly at the Institute for Hydromechanics, University of Karlsruhe, Germany.

Contributed by the International Gas Turbine Institute and presented at the International Mechanical Engineering Congress & Exposition, New York, NY, November 11–16, 2001, of THE AMERICAN SOCIETY OF MECHANICAL ENGINEERS. Manuscript received by the IGTI, September 2001; revised manuscript received April 15, 2002. Associate Editor: R. S. Bunker.

flow regions was based on direct numerical simulation (DNS) data of channel and boundary layer flows [1]. This practice was successfully applied to real blade prototypes by Lakehal et al. [1] and Theodoridis et al. [6]; the latter contribution revealed the importance of promoting the turbulent cross fluxes in regions where the rate of turbulence anisotropy is significant, i.e., over the pressure side of the blades.

The present paper presents the latest developments in the approach reported by Lakehal et al. [1]. Briefly, unlike in the earlier proposal of Bergeles et al. [8] in which the attempt to promote the lateral eddy diffusivity was based on the experimental pipe-flow data of Quarmby and Quirk [9] and restricted to the outer core flow, the present model infers information on the rate of turbulence anisotropy from DNS data and thereby covers the entire viscosity-affected layer. Moreover, unlike in [1], the proposed one-equation model adopts its length and velocity scales from known DNS data, too. Finally, the original anisotropy distribution of Bergeles [8] is replaced by an average value of 4.25 in the outercore-flow regions. In a second step, the paper introduces a new zonal modelling strategy combining the explicit algebraic stress models (EASMs) in the outer core flow and the DNS-based one-equation model resolving the near-wall region, also employed in a nonlinear form. The test case studied here represents film cooling of a flat plate by a row of streamwise injected jets which was studied experimentally by Sinha et al. [10,11] and previously by Pietrzyk et al. [12]. Because of its relative simplicity—although the physics of the flow is as complex as in real turbine prototypes—this example has since been widely adopted as a benchmark for code validation [13].

Turbulence Modelling

The Reynolds-stress tensor and the turbulent heat flux are approximated within the context of the $k-\epsilon$ turbulence model, considering both its linear and nonlinear forms. The model is coupled with a one-equation model resolving the near-wall viscosity-affected regions. In the linear context, the near-wall model was employed with the conventional eddy viscosity/diffusivity approach as well as with a nonisotropic variant. In both cases, the length and velocity scales were inferred from available DNS data. For the sake of consistency, in the EASM context the same one-equation model was employed with an isotropic transport coefficient but with use of a nonlinear form. Note that as in most of the available DNS-based near-wall turbulence models, the present strategy has been developed for attached flows with no guarantee on its validity for separated flows. But in the absence of direct simulation data of jets in crossflow, the idea remains the sole reliable alternative. Flow field data for this class of flow do indeed exist [14,15], but give insufficient information about the viscous sublayer where most of the transport mechanisms take place. The best example is the investigation of Kaszeta and Simon [15] who measured the turbulent shear stresses in film-cooling flows with streamwise injection in order to estimate the eddy diffusivities of momentum in both the lateral and wall-normal directions. Although the study brought in a valuable insight into this particular aspect, the authors were not capable of providing a clear picture on the rate of turbulence anisotropy which can be a support for computational modelling. They arrived though at the conclusion that the anisotropy of turbulent transport is too complex to be represented with a simple model such as the one of Bergeles.

The Two-Layer DNS-Based $k-\varepsilon$ Turbulence Model. The two-layer approach represents an intermediate modeling strategy between wall functions and pure low-Re number models. It consists in resolving the viscosity-affected regions close to walls with a one-equation model, while the outer core flow is treated with the standard $k-\varepsilon$ model. In the outer core flow, the usual eddy-viscosity hypothesis is used

$$\overline{u_1' u_j'} = 2/3\delta_{ij}k - 2\Gamma_j S_{ij}; \quad \overline{u_j'\theta} = -\frac{\Gamma_j}{\mathrm{Pr}}\frac{\partial \overline{T}}{\partial x_j} \tag{1}$$

where δ_{ij} is the Kronecker delta, $k \equiv \overline{u_i' u_i'}/2$ is the turbulent kinetic energy, and S_{ij} is the rate of strain tensor. For high-Re flows the turbulent transport coefficient Γ_j is conventionally made isotropic and proportional to the square of a velocity scale ($\mathcal{V}^2 \sim k$) and a time scale ($\mathcal{T} \sim k/\varepsilon$), characterizing the local state of turbulence

$$\Gamma_j \equiv \nu_t = C_\mu k^2/\varepsilon \tag{2}$$

In this expression ν_t is known as the isotropic eddy viscosity, ε represents the rate of dissipation of k, and C_μ stands for a model constant. The distributions of k and ε are determined from the conventional model transport equations, and standard values can be assigned to the model constants. In this flow region the turbulent Prandtl number Pr_t is usually fixed. In the one-equation model, the eddy viscosity is made proportional to a velocity scale $\mathcal{V}$ determined by solving the k-equation, and a length scale ℓ_μ prescribed algebraically. The dissipation rate ε is related to the same velocity scale $\mathcal{V}$ and a dissipation length scale ℓ_ε, also prescribed algebraically. Such models have the advantage of requiring considerably fewer grid points in the viscous sublayer than any pure low-Re scheme (about 10–15 rather than 25–30), and are, therefore, more suitable for complex situations involving more than one wall. Also, because of the fixed length-scale distribution near the wall, these models have been found to give better predictions for adverse pressure gradient boundary layers than pure $k-\varepsilon$ models.

The present two-layer model is in essence a re-formulation of the so-called ($\overline{v'^2}$) velocity-scale-based model (TLV) of Rodi et al. [16], in the sense that $k^{1/2}$ is now re-incorporated as a velocity scale to conform to the TLK model,[2] instead of $(\overline{v'^2})^{1/2}$, whereas ℓ_μ and ℓ_ε are re-scaled on the basis of the same DNS data of Kim et al. [18]

$$\Gamma_j \equiv \sqrt{(\overline{v'^2})}\,\ell_\mu' = C_\mu \sqrt{k}\,\ell_\mu, \quad \ell_\mu = C_l y_n f_\mu \tag{3}$$

$$\varepsilon = k^{3/2}/\ell_\varepsilon, \quad \ell_\varepsilon = \frac{C_l y_n}{2 + C_\varepsilon/(C_l R_y f_\mu)} \tag{4}$$

To conform with the logarithmic law of the wall, the constant C_l is set equal to $\kappa/C_\mu^{3/4}$, where $\kappa = 0.4$ and $C_\mu = 0.082$, and $C_\varepsilon = 17.29$. The near-wall damping function f_μ is determined by the following DNS-based relation:[3]

$$f_\mu = \frac{1}{32}\sqrt{0.116 \times R_y^2 + R_y}; \quad R_y = \sqrt{k}\,y_n/\nu \tag{5}$$

A close inspection of Eq. (4) reveals that the DNS-based distribution of ℓ_ε is in effect different from the one originally proposed in TLK [17]; in which ℓ_ε rises more steeply as the wall is approached. To determine ν_t and ε the same transport equation for k as in the standard model needs to be solved. The outer ($k-\varepsilon$) and the near-wall model can then be matched at a location where viscous effects become negligible i.e., $f_\mu \approx 0.9$.

Prior to further applications, the model was employed first for calculating the fully turbulent channel flow in two dimensions at $\mathrm{Re}_\tau = 211$. Note that this flow (as simulated by means of DNS [19]) is homogeneous in the third direction and the only nonzero shear stress is the $\overline{u'v'}$ component. The computational method is outlined in the corresponding section. The DNS database of this

[2] This model (TLK) employs the one-equation model of Norris and Reynolds [17], where indeed $\mathcal{V} \sim \sqrt{k}$.

[3] The damping function f_μ is used here as the only criteria for switching between the two-equation model resolving the outer core flow and the one-equation model resolving the viscosity-affected layer, i.e., whenever $f_\mu \approx 0.9$. This is known as the dynamic, zonal, two-layer strategy, which contrasts with other implementations in which the grid is explicitly decomposed into near-wall and outer portions.

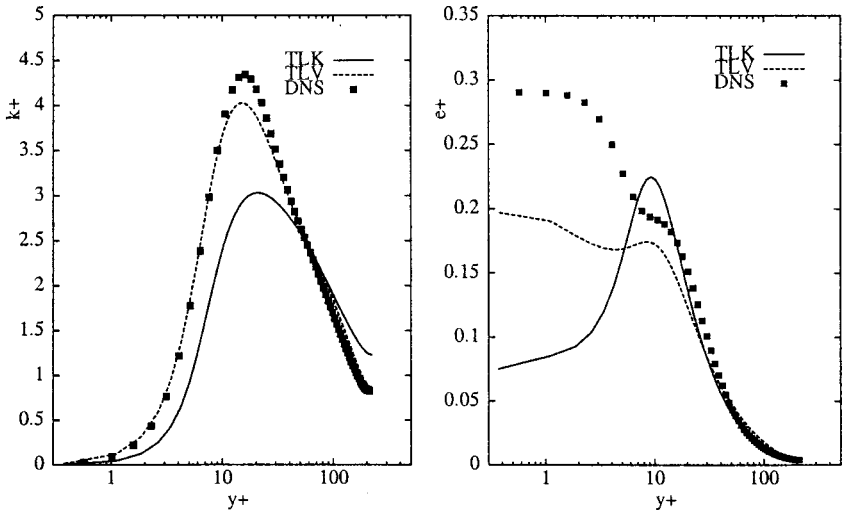

Fig. 1 Normalized profiles in developed channel flow at Re_τ=211; (left) turbulent kinetic energy k^+; (right) dissipation rate ε^+

flow was provided by Gilbert and Kleiser [19]. Figure 1 compares the normalized (by u_τ and ν) profiles of turbulent kinetic energy k^+ and dissipation rate ε^+ with the DNS data. The comparison has shown that up to $y^+=200$ the shear stress predictions with the TLK and TLV two-layer models are almost identical and agree fairly well with the DNS data (results not included here). However, the prediction of k^+ with the TLV model compares very well with the DNS data, while the TLK underpredicts the peak level. This is a consequence of an overpredicted value of ε^+ in the region where k^+ reaches its peak value. As has been the experience with other low-Re schemes, the TLK model fails in predicting the maximum of ε^+, too.

The DNS-Based Anisotropic One-Equation Model. Previous jets in crossflow calculations have shown consistently that with use of EVMs the jets do not spread apart sufficiently because, turbulent transport in the lateral direction is not correctly accounted for. In reality, the eddy-viscosity/diffusivity for transport in the lateral direction should be larger than for transport normal to the wall. In order to account for the anisotropy of the turbulent exchange process in these flows, Bergeles et al. [8] proposed multiplying the eddy viscosity appearing in the cross Reynolds stresses and in the heat fluxes by a factor varying from $\gamma=4.5$ at the log layer to 1.0 at the outer edge of the boundary layer. The near-wall value of $\gamma=4.5$ was inferred from the experimental data of Quarmby and Quirk [9]. This correction was later employed by many others, although its implementation was limited to the momentum equations. Lakehal et al. [1] have shown that further calibration was necessary for extending the approach to near-wall flow regions. Since the normal fluctuations $\overline{v'^2}$ approach zero near the wall much faster than the lateral fluctuations $\overline{w'^2}$, the ratio $\overline{w'^2}/\overline{v'^2}$ reaches much larger values in the viscous sublayer than the value of 4.5 adopted in the original model at the edge of the sublayer. This is exactly the situation the present model is intended to account for when a model resolving the viscosity effected near-wall region is employed.

A systematic derivation of the turbulent transport terms can be made on the basis of simplified individual Reynolds stress and turbulent heat flux equations. Launder et al. [20] showed that by assuming homogeneous turbulent flows near equilibrium and unaffected by external forces, the transport equations for the Reynolds stress tensor may reduce to the following algebraic relation:

$$\overline{u_i' u_j'} = 2/3 k \delta_{ij} - C_s \frac{k}{\varepsilon}\left(P_{ij} - \frac{1}{3}\delta_{ij} P_{ii} \right) \tag{6}$$

where C_s is a model constant taken equal to 0.27, and

$$P_{ij} \equiv -\overline{u_i' u_k'}\frac{\partial u_j}{\partial x_k} - \overline{u_j' u_k'}\frac{\partial \overline{u_i}}{\partial x_k} \tag{7}$$

denotes the production of turbulent stresses. Note that Eq. (6) is the simplified approximation for the second interaction contribution in the pressure-strain term appearing in the Reynolds stress transport equation. It tends to isotropize the production tensor P_{ij}, i.e., the so-called IP model. This degenerate form of approximation was actually found to alone account for main-strain effects in the pressure-strain correlations [21]. Assuming now homogeneity of the flow in the streamwise direction and neglecting $\overline{v'w'}$ compared to $\overline{u'v'}$ and $\overline{u'w'}$ the remaining[4] shear stresses are

$$\overline{u'v'} = -\Gamma_2 \frac{\partial \overline{u}}{\partial y}; \quad \overline{u'w'} = -\Gamma_3 \frac{\partial \overline{u}}{\partial z} \tag{8}$$

where Γ_2 and Γ_3 denote the anisotropic eddy viscosities acting in the normal and lateral directions, respectively

$$\Gamma_2 = C_s \frac{k\overline{v'^2}}{\varepsilon}; \quad \Gamma_3 = C_s \frac{k\overline{w'^2}}{\varepsilon} \tag{9}$$

Recasting the foregoing relations into the following forms:

$$\Gamma_2 = C_s \frac{\overline{v'^2}}{k}\frac{k^2}{\varepsilon}; \quad \Gamma_3 = C_s \frac{\overline{v'^2}}{k}\gamma\frac{k^2}{\varepsilon} \tag{10}$$

reveals that $\Gamma_3/\Gamma_2 \neq 1$, a result systematically violated in conventional EVMs, where $\gamma = \overline{w'^2}/\overline{v'^2}$ is always equal to unity.

In very much the same way the turbulent heat flux $\overline{u_i'\theta}$ can be approximated by the generalized gradient diffusion hypothesis (GGDH)

[4]It is vital to note that this is not the case of the channel flow [19] used previously for validating the TLV approach. Indeed, in that particular flow the shear-stress component $\overline{u'w'}$ is actually zero because the velocity gradient in the cross direction $\partial\overline{u}/\partial z$ is zero. The only interest in using these channel-flow DNS data is to infer a distribution for $\overline{w'^2}$ and $\overline{v'^2}$ which will serve developing appropriate anisotropic distributions for the transport coefficient Γ_j.

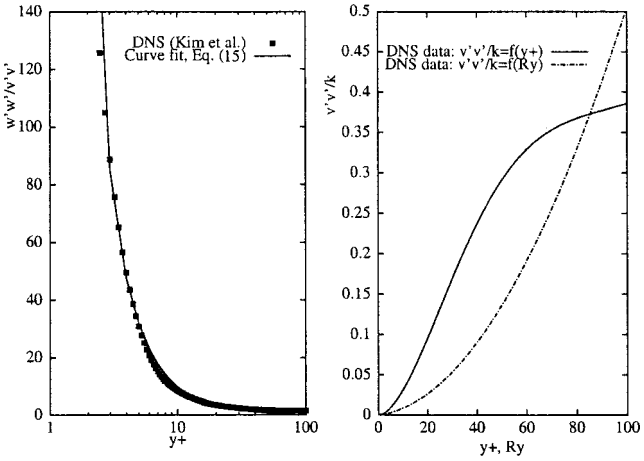

Fig. 2 Analytical correlation versus DNS data for near-wall turbulence anisotropy; (left) $\overline{w'^2}/\overline{v'^2}$, (right) $\overline{v'^2}/k=f(R_y,y^+)$

$$\overline{u_i'\theta}=-C_\theta\frac{k}{\varepsilon}\overline{u_i'u_j'}\frac{\partial\overline{T}}{\partial x_j} \tag{11}$$

which, after having adopted the same simplifications for the flow, yields

$$\overline{v'\theta}=-C_\theta\frac{\overline{v'^2}}{k}\frac{k^2}{\varepsilon}\frac{\partial\overline{T}}{\partial y};\quad \overline{w'\theta}=-C_\theta\frac{\overline{v'^2}}{k}\gamma\frac{k^2}{\varepsilon}\frac{\partial\overline{T}}{\partial z} \tag{12}$$

Here again, the thermal diffusivity coefficients $\Gamma_j^\theta=C_\theta k\overline{u_j'^2}/\varepsilon$ acting in the normal and lateral directions are not equal, i.e., $\Gamma_3^\theta/\Gamma_2^\theta=\gamma$. While Bergeles et al. [8] simplified their model by replacing $\overline{v'^2}$ by $k/3$, yielding the conventional isotropic expressions $\Gamma_2=C_\mu k^2/\varepsilon$ and $\Gamma_2^\theta=\Gamma_2/Pr_t$, the present model bases the variation of $\overline{v'^2}/k$ across the near-wall region on the channel-flow DNS data of Kim, as reported in [16], and that of $\overline{w'^2}/k$, as proposed by Lakehal et al. [1]

$$\overline{v'^2}/k=4.65\times10^{-5}R_y^2+4.00\times10^{-4}R_y \tag{13}$$

$$\overline{w'^2}/k=\overline{v'^2}/k\times\gamma \tag{14}$$

The near-wall behavior of γ, the rate of anisotropy, was derived with the help of the same DNS data, too; viz.

$$\gamma=\mathrm{Max}\left[\frac{10^3(y^+)^{0.42}}{2.682(y^+)^2-5.463},\ 4.25\right] \tag{15}$$

The DNS data for the parameter γ are plotted versus the nondimensional wall distance y^+ in Fig. 2 (left) and compared to the best fit given by Eq. (15). This approximation, which perfectly reflects the strong increase in turbulence anisotropy as the wall is approached is valid in the range $1.5<y^+<43$ only ($\gamma\approx1$ at $y^+<43$). The lower bound of 4.25 appearing in the foregoing expression represents an average value for γ which replaces the original distribution of Bergeles, up to the edge of the boundary layer. This value is derived by examining the experimental data of Ardey [14] and Kaszeta and Simon [15]; the latter authors have found the distribution of Bergeles not in accordance with their data. Admittedly, there is no proof that this relation is valid for separated flows as well. Without really expecting to obtain a general relationship for γ, there is at least one consistent way of using Eq. (15): it consists of alleviating its dependence on the dimensionless wall distance y^+, which can be replaced by the near-wall Reynolds number R_y. The relation between y^+ and R_y follows also from the DNS data of Kim (see Fig. 2 (right)), from which the following approximate correlation is derived:[5]

$$y^+=0.00442\ \ R_y^2+0.294\ \ R_y+0.545 \tag{16}$$

Relation (15) shows that very near the wall the rate of turbulence anisotropy grows drastically so that γ reaches very high values; it reaches the value of 8.5 at the edge of the viscous sublayer, at $y^+=11.6$, whereas the isotropic state of turbulence ($\gamma=1$) is recovered in the log-layer, at $y^+=43$.

Two possibilities are now offered to model the various turbulent transport terms using Eqs. (13) and (14): either one resorts to a pure low-Re model or to a two-layer approach. In the first case, Eq. (13) may be recast into the form of

$$\overline{v'^2}/k=C_\mu f_\mu/C_s \tag{17}$$

and thus the relations given by Eq. (10) reduce to

$$\Gamma_2=C_\mu f_\mu\frac{k^2}{\varepsilon};\quad \Gamma_3=C_\mu f_\mu\gamma\frac{k^2}{\varepsilon} \tag{18}$$

For this, two additional transport equations for k and ε need to be solved. In the one-equation model used in two-layer approach described previously, the eddy viscosity coefficient Γ_j, which was originally based on $(\overline{v'^2})^{1/2}$ as a velocity scale (derived from Eq. (13)), incorporates the parameter γ as follows:

$$\Gamma_2\equiv\sqrt{(\overline{v'^2})}\ell'_\mu=C_\mu\sqrt{k}\ell_\mu;\quad \Gamma_3\equiv\sqrt{(\overline{w'^2})}\ell'_\mu=C_\mu\sqrt{k}\gamma\ell_\mu \tag{19}$$

To complete the model an additional transport equation for k needs to be solved; it takes the following form:

$$\frac{\partial}{\partial x_j}(\rho\overline{u_j}k)=\rho(\mathcal{P}-\varepsilon)+\frac{\partial}{\partial x_j}\left(\Gamma_j^k\frac{\partial k}{\partial x_j}\right)+\mu\nabla^2k \tag{20}$$

where in addition to the turbulent diffusion coefficients $\Gamma_j^k=\Gamma_j/\sigma_k$, the production of turbulent kinetic energy $\mathcal{P}=-u_i'u_j'\overline{u}_{i,j}$ now includes the effect of γ.

To summarize, the two-layer TLVA model consists of the following steps: In the one-equation model resolving flow regions where $f_\mu<0.9$, (i) the turbulent fluxes are determined from Eq. (1), with the transport coefficients Γ_j determined by Eq. (19) and γ by Eq. (15); (ii) the transport equation for k, Eq. (20), is solved in parallel; (iii) the rate of dissipation ε appearing as a sink term in Eq. (20) is determined by the DNS-based prescription (Eq. (4)). In the outercore flow portions where $f_\mu>0.9$, (i) the turbulent fluxes are also determined from Eq. (1), but the transport coefficients Γ_j are now given by Eq. (18) with γ asymptotes towards the average value of 4.25, according to Eq. (15); (ii) the transport equations for k and ε are solved in parallel. The main difference with what has been proposed in [1] is that the distribution for γ away from the viscosity-affected layer as proposed initially by Bergeles is abandoned in favor of an average value of 4.25.

Stress-Strain Relations. Reynolds stress transport equation models are conceptually the most reliable approaches for treating complex strain fields. However, judging from what is known about their complexity and (sometimes) difficulties in handling very simple shear flows (as far as near-wall turbulence is concerned), it is probable that with these models the prediction of film cooling and jets in crossflow in general will not show substantial improvements [2]. A much simpler alternative is now gaining in popularity, consisting of approximating each of the Reynolds stress components rather than solving their transport equation. The original algebraic representation of the Reynolds stress in terms of a series of combinations

[5]Although the best fit to the DNS data was found to be a 5th-order polynomial function, minor differences in the final results were observed using Eq. (16).

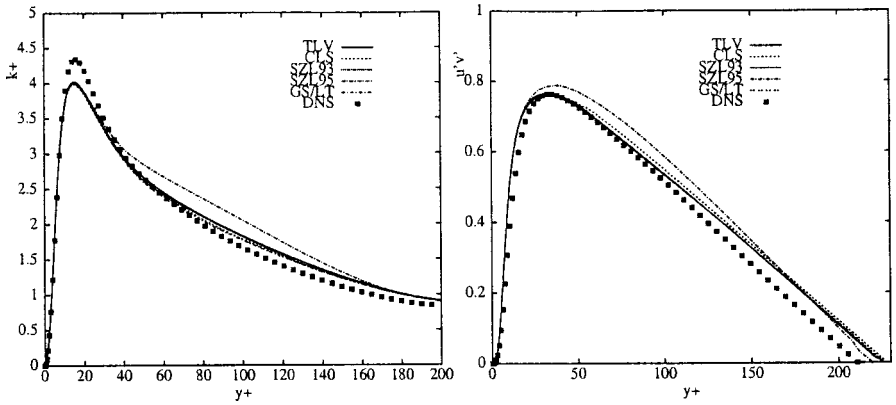

Fig. 3 Normalized profiles in developed channel flow at Re_τ=211; (left) turbulent kinetic energy k^+; (right) shear stress $\overline{u'v'}^+$

between stress and strain, referred to as algebraic stress models (ASMs), was followed by a variety of methods with various levels of sophistication. With this, the models are expected to reproduce secondary flows with better accuracy. Although these relationships may be obtained by invoking various strategies, their common starting point is the assumption of homogeneous turbulent flows in the limit of equilibrium, leading to a similar explicit expression for $\overline{u_i' u_j'}$ which, in non-rotating frames takes the following form:

$$\overline{u_i' u_j'} = \frac{2}{3}\delta_{ij}k - 2\tilde{\nu}_t\left[S_{ij} + \sum_n C^n T_{ij}^n\right]; \quad \tilde{\nu}_t = \tilde{C}_\mu k^2/\varepsilon \quad (21)$$

where the T_{ij}^n are the products of the strain and vorticity tensors, S_{ij} and Ω_{ij}. The available models differ in the way the coefficients C^n and $\tilde{C}_\mu$ are determined, and in the number of strain and vorticity-stress products, i.e., quadratic, cubic, etc. Four model variants have been selected in the present work: three of them are quadratic and one is cubic with respect to S_{ij} and Ω_{ij}; namely, the quadratic models of Shih et al. [22] (SZL93), Shih et al. [23] (SZL95), and Gatski and Speziale [24] (GS), and the cubic variant of Craft et al. [25] (CLS). While the details of each of these models can be found in the corresponding references, here we focus on the GS model, in which

$$T_{ij}^1 = \frac{k}{\varepsilon}(S_{ik}\Omega_{kj} + S_{jk}\Omega_{kj}); \quad T_{ij}^2 = -\frac{k}{\varepsilon}\left(S_{ik}S_{kj} - \frac{1}{3}S_{kl}S_{kl}\delta_{ij}\right)$$

and

$$\tilde{C}_\mu \equiv \frac{C_\mu}{1 - \gamma_1^2 S^2 + \gamma_2^2 \Omega^2}$$

The coefficients γ_1, γ_2, C^1 and C^2, derived from the well-documented SSG pressure-strain model (c.f. [24]), are all proportional to P_k/ε, the ratio of production to dissipation of turbulent kinetic energy. The implications of this dependence are discussed below. The model is strongly dependent on the assumption of weak-to-mild equilibrium of turbulence, greatly reducing its usefulness in practical situations. This constraint is generally incorporated by treating the production-to-dissipation ratio through the equilibrium solution for homogeneous turbulence, i.e., $P_k/\varepsilon \approx 1.89$. However, the necessity to account for the changes in this ratio is now fully accepted because the equilibrium value systematically drives the model into inconsistency when used away from equilibrium. In a recent effort to make the GS model applicable to a broad range of practical flows, Lakehal and Thiele [26] emphasized two important aspects: (i) the development of a generalized relation for P_k/ε, and (ii) the formulation of a better regularization procedure for $\tilde{C}_\mu$. Their proposed to model P_k/ε, by

$$P_k/\varepsilon = \frac{S^2}{4.8 + 1.3\mathrm{Max}(S,\Omega)} \quad (22)$$

which can be seen to meet the requirement of the equilibrium state ($P_k/\varepsilon \approx 1$) for the logarithmic region in channel flow where, by reference to various experimental data, $S = 3.1$. But, more importantly, making use of Eq. (22) results in a distribution of $\tilde{C}_\mu$ that significantly departs from that obtained by the GS model. As an example of marked deficiency, the GS model will fail to predict an impinging flow because $\tilde{C}_\mu$ would then increase incorrectly with S^2, leading to excessive levels of eddy viscosity (Eq. (21)). Furthermore, since S^2 in highly strained flows is actually greater than unity, the regularization procedure of Gatski and Speziale [24], based on a first-order Padé approximation for S^2, was abandoned by Lakehal and Thiele [26] in favor of a more elaborate formulation invoking fourth-order approximation: $S^4 \approx S^4/(1+S^4)$, or, $S^2 \approx S^2/(1+S^4)$. This results in the following expression:

$$\tilde{C}_\mu = \frac{C_\mu(1+S^4)}{1 + S^4(1+\gamma_2^2\Omega^2) - \gamma_1^2 S^2 + \gamma_2^2 \Omega^2} \quad (23)$$

This systematic regularization represents a better alternative to the first-order one proposed originally for flows departing mildly from equilibrium, at least for the range $S^2 < 1$. This correction is hereinafter referred to as GS/LT.

To extend this EASM and all other employed variants to low-Re conditions, the two-layer approach discussed previously is then resorted to. The Reynolds stress is in all cases determined by Eq. (21) rather than by Eq. (1). More precisely, within the outer-core flow the turbulent transport coefficient is $\tilde{\nu}_t$, and ε is determined by solving its own transport equation. The viscosity-affected layer is resolved by the TLV model, but the nonlinear stress-strain products forming the Reynolds stress are now retained. As a result, the models are expected to reproduce the strong anisotropic behavior of the near-wall turbulence without having to resolve the viscous sublayer in great detail, i.e., by use of a pure low-Re scheme. The plane channel flow (in $2D$) is again considered as a validation exercise for the two-layer methodology combining the EASMs with the TLV near-wall one-equation model used in a nonlinear form. It is perhaps important to recall that since this flow [19] is homogeneous in the spanwise direction, the shear-stress component $\overline{u'w'}$ is actually zero because the velocity gradient in that direction $\partial\overline{u}/\partial z$ is zero. This means that the TLVA approach (which would act on this particular shear-stress component $\overline{u'w'}$ only) will behave exactly as the TLV approach.

Figure 3 shows predictions of normalized turbulent kinetic en-

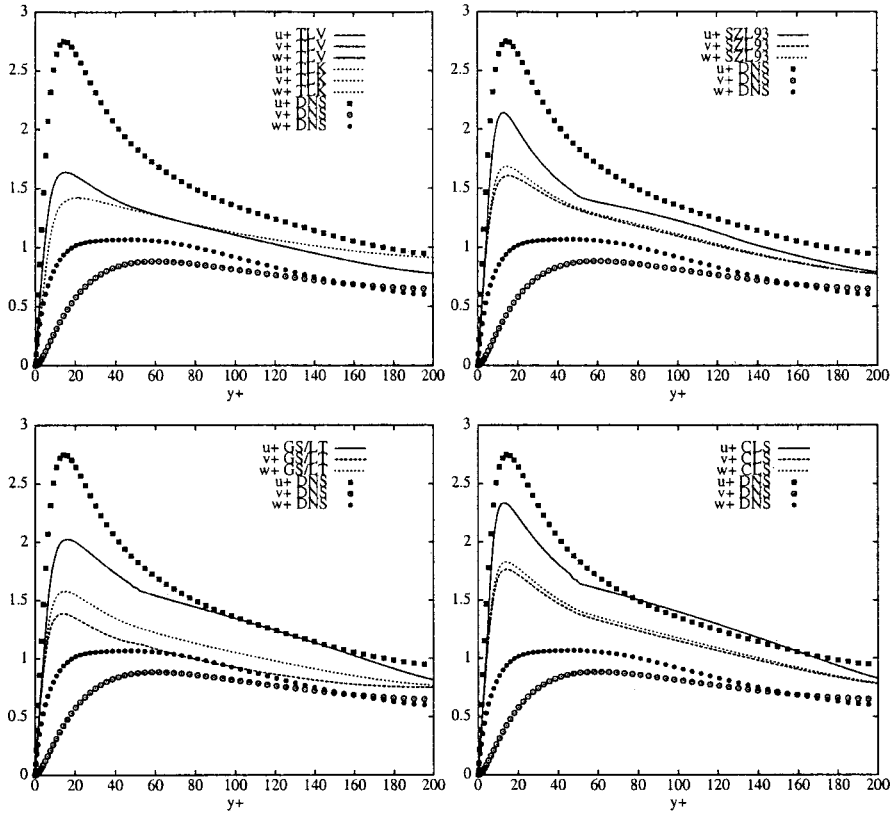

Fig. 4 Normalized rms-velocity profiles in developed channel flow at Re_τ=211; Results obtained with various turbulence models

ergy k^+ and shear stress $\overline{u'v'}^+$ with the DNS data of Gilbert and Kleiser [19]. Apart from the quadratic SZL95 model of Shih et al. [23], both the TLV and the other EASMs deliver results in accordance with the data. The shear stress, which can be seen in Fig. 3 (right) to be generally well predicted, is the only parameter affecting the mean flow. This is supported by Fig. 4, displaying the normal stress components which clearly shows that only with EASMs models can these components be separated, though not as much as in the DNS data. Looking at Fig. 4 confirms the superiority of the TLV model over the TLK (top left panel), but also reveals that for this type of flow the EASMs do not deliver a unique solution. It should be noted that the best results are obtained with the GS/LT quadratic model; the other two EASMs, do not separate the normal and spanwise rms components sufficiently, in particular within the outer core flow region. As mentioned previously, although this behavior is not crucial for a simple shear flow, its implications could be appreciable in the presence of mainstream-induced secondary vortices. More importantly, this validation phase has shown that coupling a nonlinear two-equation model with a nonlinear one-equation model resolving the viscosity-affected layer can be a viable and robust alternative to a pure low-Re scheme.[6]

The Computational Procedure

The governing equations are solved by the use of a three-dimensional finite-volume method that allows the use of arbitrary nonorthogonal grids, employing a cell-centered grid arrangement. A detailed description of the method is reported in Majumdar et al. [27], and the multi-block technique which was introduced afterwards, in Lakehal et al. [5]. The momentum-interpolation technique is used to prevent pressure-field oscillations tending to appear in the cell-centered grid arrangement. The pressure-velocity coupling is achieved by using the well-known SIMPLEC algorithm. The present computations were performed employing the QUICK scheme for all variables applied in a scalar form by means of a deferred-correction procedure and bounded by the Van-Leer harmonic function as limiter. The diffusive fluxes are, however, approximated using second-order central differences. The resulting system of difference equations was solved using the strongly implicit procedure (SIP) algorithm. Convergence was in all cases determined based on a drop in normalized mass and momentum residuals by four orders of magnitude at least. A global mass and energy balance algorithm was employed after each iteration, consisting of a systematic readjustment of the mass fluxes at the outflow.

The Grid and Boundary Conditions

This test case was experimentally investigated by Pietrzyk et al. [12] and Sinha et al. [10,11]. The jets were inclined at an angle of 35 deg with a lateral spacing of $3D$. The injection hole diameter was 12.7 mm and the discharge pipe length-to-diameter ratio L/D was 1.75 in the experiment of Sinha and 3.5 in that of Pietrzyk. The present investigation addresses the only case of $L/D=1.75$. The domain extends $19D$ upstream of the leading edge and $30D$ downstream of the injection location. The topology of the grid is shown in Fig. 5. The approaching boundary layer was fully developed. The simulations performed in the experiment dealt with two density ratios ρ_h/ρ_∞ (=1.2 and 2.0) and various mass flux ratios ranging from $M=0.25$ to 1.0. In the present work calculations were carried out for $\rho_h/\rho_\infty=2$ and $M=0.5$ and 1.0. In the streamwise direction the calculation domain extends from the inflow plane located at $X/D=-8$ to $X/D=25$ and from the channel bottom to $Y/D=6$ in the vertical direction. The downstream exit of the hole is located at $x=0$. In the spanwise direction the domain extends from a plane through the middle of the holes (z

[6]Craft et al. [25] reported on calculations of this flow using their CLS under low-Re conditions; their results were identical to the present ones.

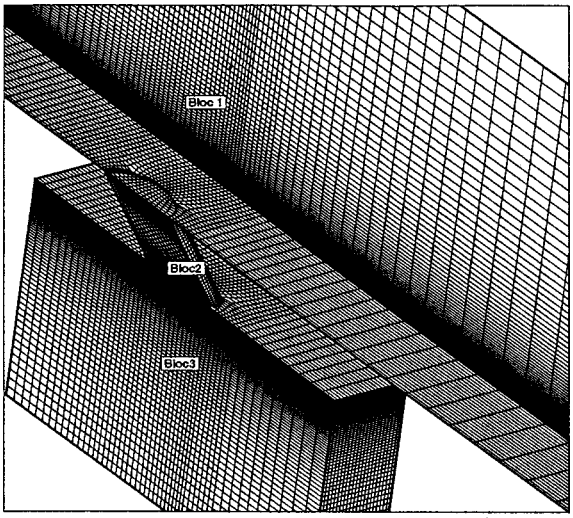

Fig. 5 Details of the computational grid near the injection hole

$=0$) to a plane at $Z/D=1.5$ in the middle between two injection holes, and symmetry conditions are imposed on these planes. A multiblock grid is used to cover the three blocks. The grid adopted for calculations was obtained after a series of tests; it consists of $180\times76\times24$ points in the x, y and z directions respectively. The jet and the plenum are meshed with grids composed of $16\times40\times9$ and $53\times75\times23$ nodes, respectively. The wall neighboring-cells were located so as to always maintain the values of y^+ smaller than 2.0. The number of grid points placed in the viscous sublayer and the buffer layer was typically 15 to 20, but less within the discharge pipe.

The no-slip boundary conditions and $k=0$ were used on the plate surface, and on the plenum internal walls since there the flow has a very low momentum (and thereby very small y^+ at the wall), which invalidates the use of wall functions. Because the upper surface of the domain was set relatively far from the flat plate, symmetry conditions were employed there. A 1/7th-law turbulent boundary layer velocity profile was imposed at $X/D=-8$ in order to match the boundary layer thickness of $0.7D$ at the injection location. The mainstream velocity was set to $U_\infty=20$ m/s, conforming to the experiment, and uniform distributions were specified for k and ε corresponding to a free-stream turbulence intensity of $T_u^\infty=0.5\%$, and a dimensionless eddy viscosity of $\mu_t/\mu=50$. Since the experiment does not provide exact information on the flow at the inlet of the discharge pipe, uniform distributions of k and ε were specified, based on a turbulence intensity of 2% and $\mu_t/\mu=30$. Adiabatic wall conditions were employed when solving the enthalpy equation and zero gradient conditions were used at the outflow boundary. The exact inlet profiles of the temperature and corresponding densities were employed, i.e., $T_\infty=302$ K, $T_h=T_{pln}=153$ K.

Results and Discussion

Pietrzyk et al. [12], who provided detailed measurements of the flow, found that the turbulence is highly anisotropic in the region above the injection hole. They also found that the strength of the vortices scales with the mass flux ratio, and with increasing distance downstream the injection location. The size of the vortices increased and their angular velocity decreased. In their study, the significant levels of $\overline{u'w'}$ were found to be associated with the blowing rate M, too. As far as the density of the jet is concerned, the authors observed the dense jet to penetrate deeper into the mainstream as compared to the unity-density jet. The boundary layer thickness in the near hole region was also found to be 25% greater for the dense jet than the unity-density jet. More details about the effects of increasing jet density on the flow structure are provided by Sinha et al. [11].

Mean Flow Field. Effects of weak compressibility in this example were accounted for by use of the equation of state. It is also important to note that given the poor performance of the SZL95 model, the results were not included for comparison. Contours of wall film-cooling effectiveness η on the channel surface predicted by the TLV model are compared in Fig. 6 with results delivered by the anisotropic TLVA model and the GS/LT and SZL93 EASMs (CLS calculations are not included here); these were coupled with the TLV employed in nonlinear form. For both blowing rates, $M=0.5$ and $M=1$, calculations with the TLVA model, illustrated on top of each panel of Fig. 6, seem to considerably enhance the lateral spreading of the scalar field compared to the TLV model, although smaller values of η are obtained at the centerline of the surface. This indicates that the model shortens the reverse-flow region, or, in other words, it anticipates the reattachment of the jet after separating. Since the corresponding experimental data are not available, this conclusion remains only tentative. Combining now GS/LT and TLV improves only slightly the prediction of the lateral spreading in comparison to the standard model alone, but the values of η at the centerline are now comparable.

The model variant of Shih et al. [22] (SZL93) has little or no advantage at all; the results are even suspected to be incorrect in the centerline region. From this first analysis it clearly appears that increasing the lateral turbulent transport by means of an anisotropic eddy viscosity has a very strong effect on the results, much more so than any of the EASMs. Judging from the wall temperature contours, increasing the blowing rate M lifts the sec-

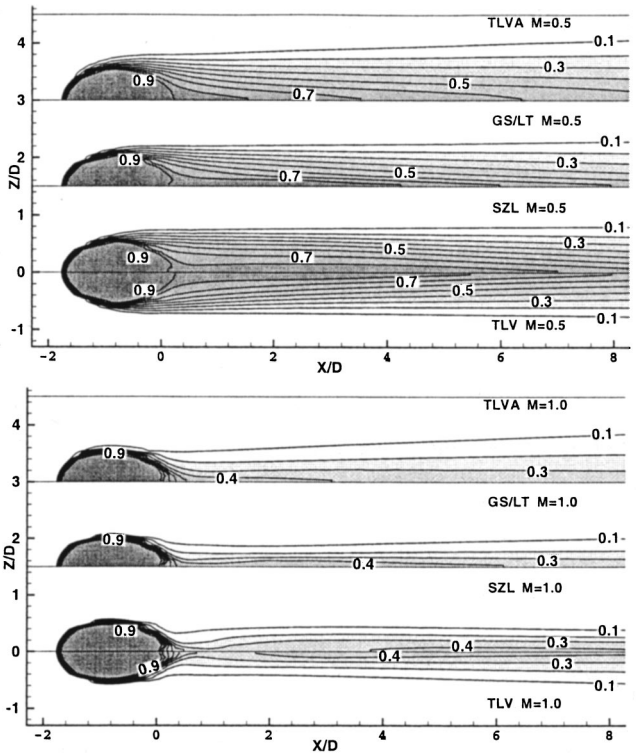

Fig. 6 Contours of wall film-cooling effectiveness for (upper) $M=0.5$ and (lower) $M=1.0$. Calculations with various turbulence models.

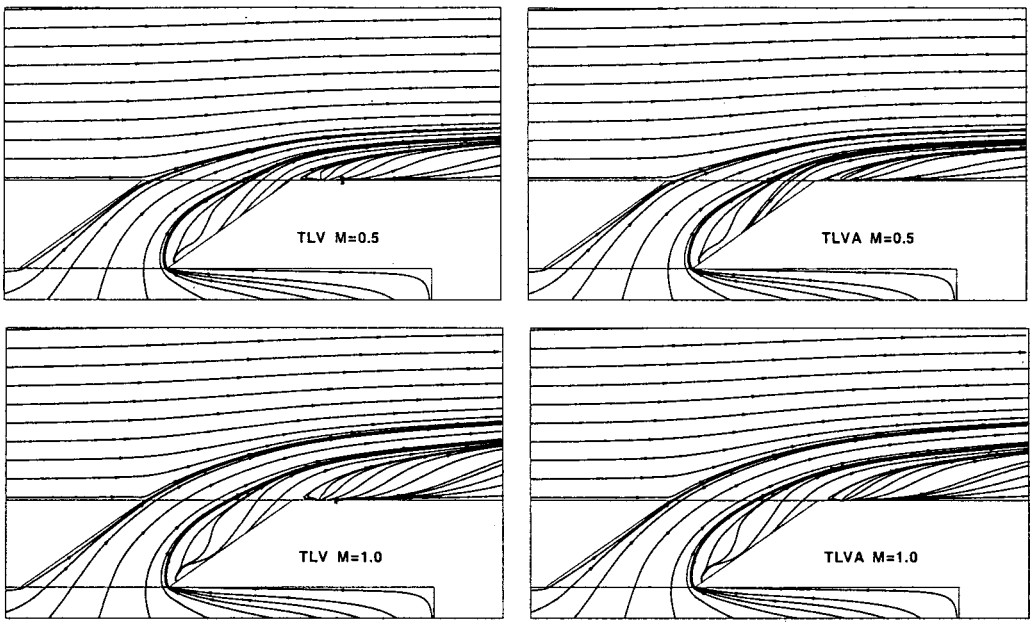

Fig. 7 Streamlines at the midplane ($Z/D=0$) for $M=0.5$ and 1.0. Calculations with the TLV and TLVA models.

ondary vortices further up from the wall. In other words, increasing the mass flux ratio leads to a deeper penetration of the jet into the core flow.

In connection with these results, qualitative illustrations of the flow behavior predicted with the isotropic and anisotropic models TLV and TLVA for both blowing rates of $M=0.5$ and 1.0 are shown in Fig. 7. This displays the flow streamlines in the immediate vicinity of the injection hole generated by following the paths of tracers injected into the oncoming flow and the discharge flow. The figure clearly shows the penetration of the jet into the core flow. It also displays the way the jet is bent towards the surface by the mainstream after injection. The extreme complexity of the flow, especially in the direct interaction region, is well illustrated, and the longitudinal vortices can clearly be seen to partially develop already inside the pipe. The fluid-particle trajectories also show the shearing of the jet by the main stream on the right side, looking in the downstream direction. Also, the figure indicates that the jet initially detaches from the wall and then reattaches downstream. For both blowing rates the TLVA model predicts the jet separation over the plate surface well, although it slightly shortens the recirculation compared to the TLV calculations. The implications of this behavior were already discussed in connection with wall temperature contours.

The secondary-flow velocity vectors and the corresponding temperature contours for $M=0.5$ are plotted in Fig. 8 at a position immediately behind the injection, $X/D=4$. Each panel represents half of the computational domain, since symmetry conditions were applied at the midplane. Results obtained with the TLV model are always shown on the left side of each panel. The system of a pair of counter-rotating longitudinal vortices (kidney vortices), typical to jets in crossflow, can be seen to establish itself in all calculations. The two vortices cause the typical, symmetrical kidney shape of the temperature contours. Near the wall the velocity is directed towards the middle of the jet ($z=0$). Note, too, that near the wall the velocity gradients $d\overline{w}/dy$ (i.e., the vorticity) are very strong, and the outer flow is directed away from the surface. The SZL model considerably compresses the secondary vortex, and the values of η in the center of the vortex seem to be much higher than those of the TLV model. This conforms to the earlier results of wall temperature iso-contours obtained with this model. The GS/LT model behaves almost like TLV. However, in

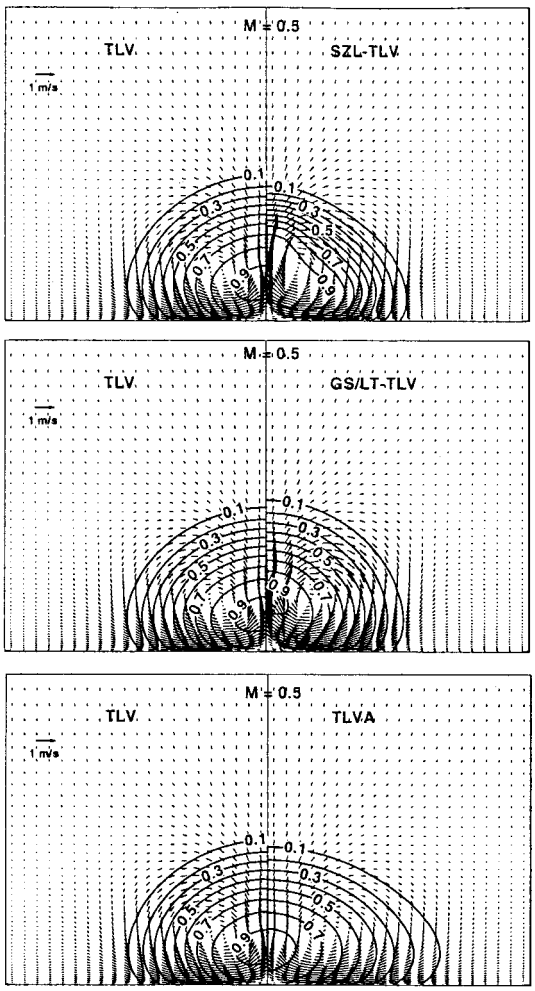

Fig. 8 Formation of the secondary vortices at cross-flow location $X/D=4$. Calculations with various turbulence models for $M=0.5$.

Fig. 8 (bottom), where the anisotropic eddy viscosity correction is applied, the strength of the longitudinal vortex reduces appreciably, and so does the film-cooling effectiveness η. But more importantly, the approach seems to enhance the near-wall lateral spreading of the jet compared to the TLV model alone; the secondary vortex now tends to flatten further against the surface. This result reflects best the effects induced by enhancing the lateral stresses, and moreover, it is in line with the previous discussion in connection with the surface film cooling effectiveness. In similar circumstances, Theodoridis et al. [6], who focused on the flow structure in close proximity to the injection, found that promoting the stresses in the lateral direction produces results that compare best with the data.

Turbulence Field. The turbulence structure around and downstream of the hole region is discussed in Figs. 9 and 10 in terms of contours of turbulence intensities, defined as T_u $(=\sqrt{2k/3}/U_\infty)$, and shear stress $\overline{u'v'}$ (normalized by U_∞) in the symmetry plane X-Y, respectively. Experimental results of Pietrzyk et al. [12] are included for comparison, even if their experiment does not correspond exactly to that of Sinha et al. [11], i.e., L/D was one order of magnitude larger in Pietrzyk's experiment, and the measured turbulence intensities were defined as $(u'^2_{\mathrm{rms}}+v'^2_{\mathrm{rms}})^{1/2}/U_\infty$, ignoring the third turbulence fluctuating component. In [11], however, the turbulence intensity is defined using the three rms components, which corresponds to T_u $(=\sqrt{2k/3}/U_\infty)$. To support this simplification, Pietrzyk et al. [12] argued that u'_{rms} and v'_{rms} alone are likely to represent the essential effects of turbulence in this case.

In general, the predicted contours show the development of strong shear layers in the region surrounding the hole, in conformity with the data. These shear layers were identified in the experiments as the most important source of turbulence due to the interaction of mainstream and injected coolant, and the accompanying flow separation at the hole entrance. The T_u contours plotted in the vertical plane along the centerline show that over the top of the jet the turbulence models employed deliver the same turbulence level (~0.5%), in accord with the experiment (lowest panel). Note also that turbulence intensity levels ranging from 5–9% seem to be already generated upstream of the injection location. The turbulence intensity level (~9.0–10.0%) at the exit location is also well predicted by the models. However, downstream of the hole (at $X/D>3$) the models seems to underpredict turbulence intensity magnitudes, 13% compared to 16%. This is more likely due to the way turbulence intensities were defined in [12], yielding systematically higher levels compared to both our predictions and Sinha's measurements. But, this may not be the only reason; the length-to-diameter of the jet in the present investigation conforms to Sinha's study, in that it is actually smaller than in the experiment of Pietrzyk. In other words, the difference may be due to the fact that turbulence develops with increasing length-to-diameter of the pipe. It is perhaps important to add that earlier data of Pietrzyk—reported in [11]—show a maximum turbulence intensity of 12% rather than 16%. This confusion between original Pietrzyk's data (cited in [11]), Sinha's [11] data, and later Pietrzyk's [12] data does not facilitate the comparison. Nevertheless, what is perhaps worth noting in this comparison is the behavior of the TLV and TLVA models, which provide the best comparison with experiment as far as the thin shear layer neighboring the wall is concerned, immediately downstream of the hole location, where $T_u=5\%$.

The near-hole contours of turbulent shear stresses $\overline{u'v'}$ are compared in Fig. 10. The first indication of the predictive performance of the models is that all of them deliver the same rate of shear stress at the hole exit $(-\overline{u'v'}/U_\infty^2\approx 0.001)$, a level comparable to the measured one. This is somewhat intriguing since the previous figure comparing turbulence intensities reveals a difference between calculations and measurements which has been attributed to the length-to-diameter of the pipe. This means that the shear stresses are not sensitive to changes in this parameter, at least when in the presence of the plenum. Again, the SZL-TLV predictions (second panel) fail totally in predicting the shear stress levels in the entire region surrounding the injection and downstream. Also, downstream of the hole the other EASM model (GS/LT) underestimates the shear-stress levels by about 50%, 0.003% compared to 0.006%. Another interesting observation is that the shear stress level in this location is very well predicted by both TLV and its anisotropic variant TLVA, even if the region over which this maximum level occurs is much larger than in the experiment, extending almost from $X/D=1.0$.

From a physical standpoint, and conforming with the experi-

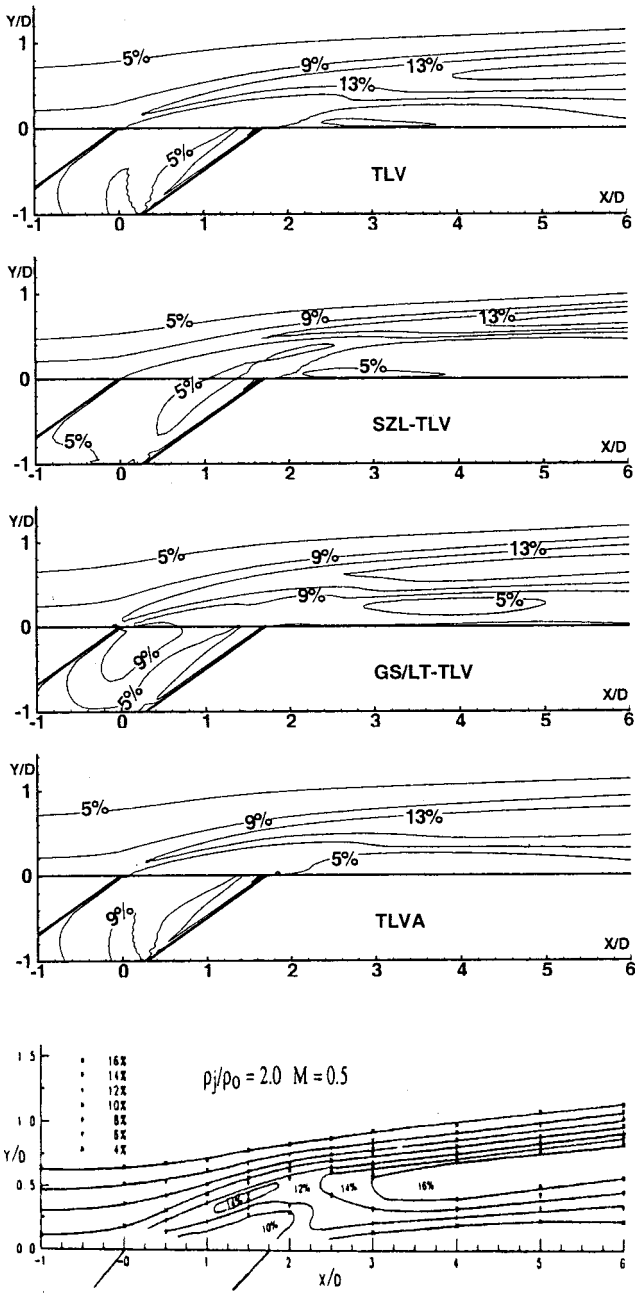

Fig. 9 Near-injection turbulence intensity T_u contours (normalized by U_∞) in the vertical plane ($Z/D=0$). Calculations with various turbulence models and $M=0.5$. Experimental data (lowest panel) of Pietrzyk et al. [12].

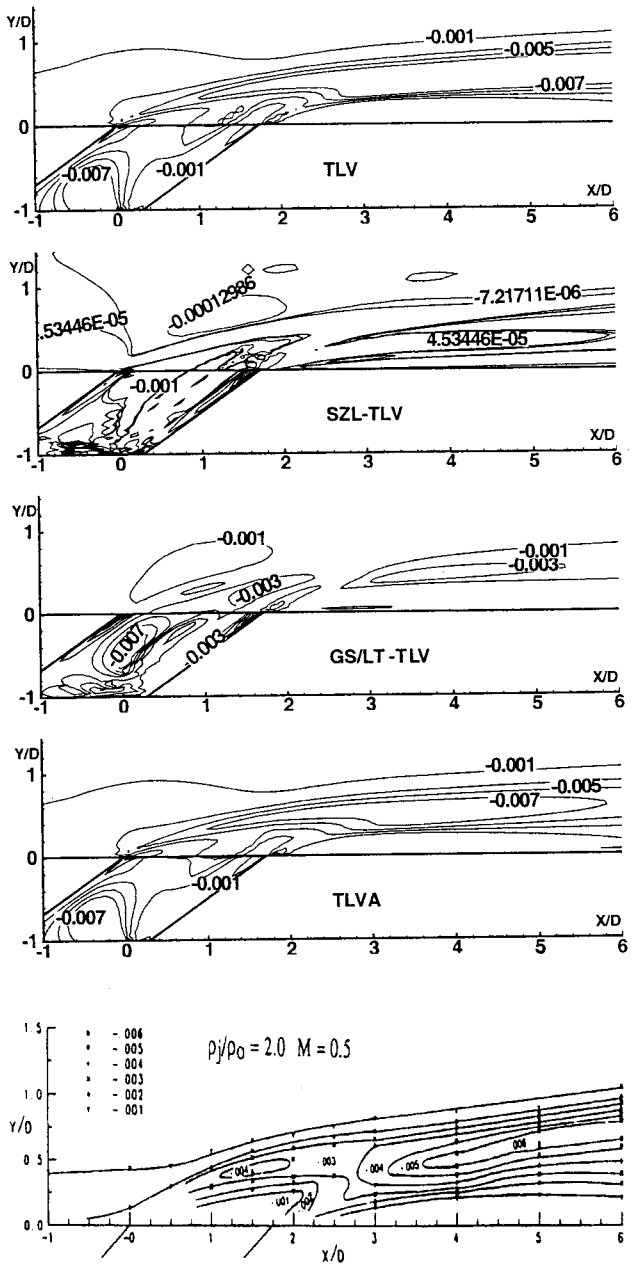

Fig. 10 Near-injection $\overline{u'v'}$ shear-stress contours (normalized by U_∞^2) in the vertical plane ($Z/D=0$). Calculations with various turbulence models and $M=0.5$. Experimental data (lowest panel) of Pietrzyk et al. [12].

ments, the shear layer around the jet is generated locally and dependent on the boundary layer thickness, in contrast to the turbulence intensity which has clearly been seen to persist from the upstream region up to the hole. Higher magnitudes of shear stress and turbulence intensity were found to persist far downstream of the hole, up to $X/D \approx 20$ (results not included here). This was also observed by Pietrzyk [12] and later by Sinha et al. [11].

Mean Thermal Field. In Fig. 11 (upper panels), the film-cooling effectiveness η_- at the centerline of the channel is displayed as a function of downstream distance. Results of various turbulence models are compared with the data of Sinha et al. [10]. Using the standard TLV model without correction, η is predicted too high at the centerline. However, close to the injection the agreement is good, which in itself is a major improvement compared to previous calculations with wall functions reported by Leylek and Zerkle [13] and many others. In fact, in all previous calculations the recirculation zone occurring right behind the injection has not been correctly captured, because the viscous sublayer was not resolved. For $M=0.5$ the nonlinear model SZL, fails completely, whereas results of the quadratic variant GS/LT are much better that with the TLV model, even though η_- around the axis is predicted too high. When the TLVA variant is employed, the prediction becomes closer to the measurements in the region near injection and further downstream of the hole. This is in line with the surface contours of η shown previously, where this strategy has led to a faster change in the peak temperature. The best agreement with measurements is achieved via the anisotropic approach. Looking now at the neighboring figure for $M=1.0$ reveals that the film-cooling effectiveness is still overpredicted by the SZL model, but is underpredicted by the GS/LT variant compared to the left panel. The result of the standard TLV variant is now surprisingly better than for $M=0.5$. The TLVA performance is still the best at the center of the channel.

The distributions of the laterally averaged film-cooling effectiveness $\langle\eta\rangle$ are compared with the data in Fig. 11 (lower panels) for $M=0.5$ and $M=1.0$. For the lowest blowing rate, the level of $\langle\eta\rangle$ is seen to be severely underpredicted by both the TLV and the GS/LT models, while for $M=1.0$ the tendency is clearly in favor for the TLVA model. Note that in all cases the TLVA model correctly predicts the peak temperature right after the discharge hole. Note, too, that, in general, when the film-cooling effectiveness is severely overpredicted on the axis and $\langle\eta\rangle$ is underpredicted, this corresponds to a lateral spreading that is predicted as being too weak. Indeed, when studying this class of flow, the comparison is often restricted to the laterally averaged $\langle\eta\rangle$, and the result may, in fact, be misleading and must therefore be seen as the consequence of a compensation effect of η being predicted too high near the axis, but not spreading sufficiently in the lateral direction.

The jet spreading over the wall is analyzed by examining the spanwise distributions of η on the channel surface plotted in Fig. 12 at $X/D=1$, 3, 6, and 10. The comparison is made for $M=0.5$. Detachment and reattachment of the jet over the wall is suggested by looking at the evolution of the width of high η values as a function of the distance from the hole. High η values at the centerline of the jet (at $Z/D=0$) rapidly decrease with X/D, implying that the jet detaches from the wall immediately after exiting the hole and then reattaches downstream. The behavior of the turbulence models employed may be judged in this respect already. While at $X/D=1$ all models predict the peak temperature reasonably well at the centerline, significant deviations from the measurements are clearly visible at the next locations, where the best performance is due to the anisotropic TLVA model. From this it appears that the other models exaggerate the lift-off of the detached jet from the surface. This result is consistent with the secondary vortices shown in Fig. 8 and with the distributions of centerline effectiveness η_- shown in Fig. 12 (upper left). There indeed, apart from TLVA calculations, the rest exhibit an overpredicted level of centerline effectiveness along the axis of the jet.

More specifically, for each model, Fig. 12 reveals that with the TLV model calculations show significant deviations from the measurements already in the range $Z/D=0.5-0.7$. Calculations with the SZL model clearly show the temperature level to be grossly exaggerated in the center of the vortex, in conformity with what has already been said in the context of Fig. 8. The performance of the GS/LT model can now be seen to be comparable to the TLV model, as was to be expected. But more importantly, the jet spreading is seen to be grossly underpredicted by the isotropic TLV model and the algebraic stress variants, in contrast to the predictions of the TLVA model, which clearly tend to considerably promote the lateral spreading of the scalar field, bringing its level very close to the data. Figure 13 compares the spanwise distribu-

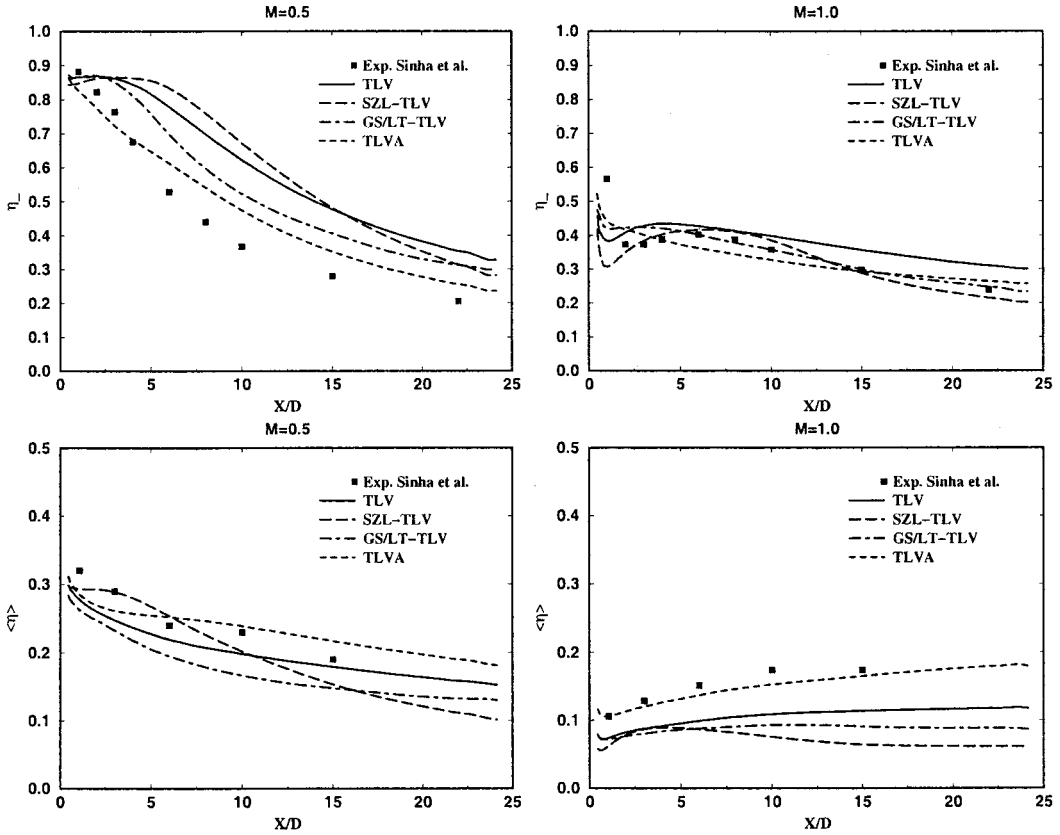

Fig. 11 Comparison of η at the centerline (upper two panels) and the laterally averaged film-cooling effectiveness $\langle\eta\rangle$ (lower panels)

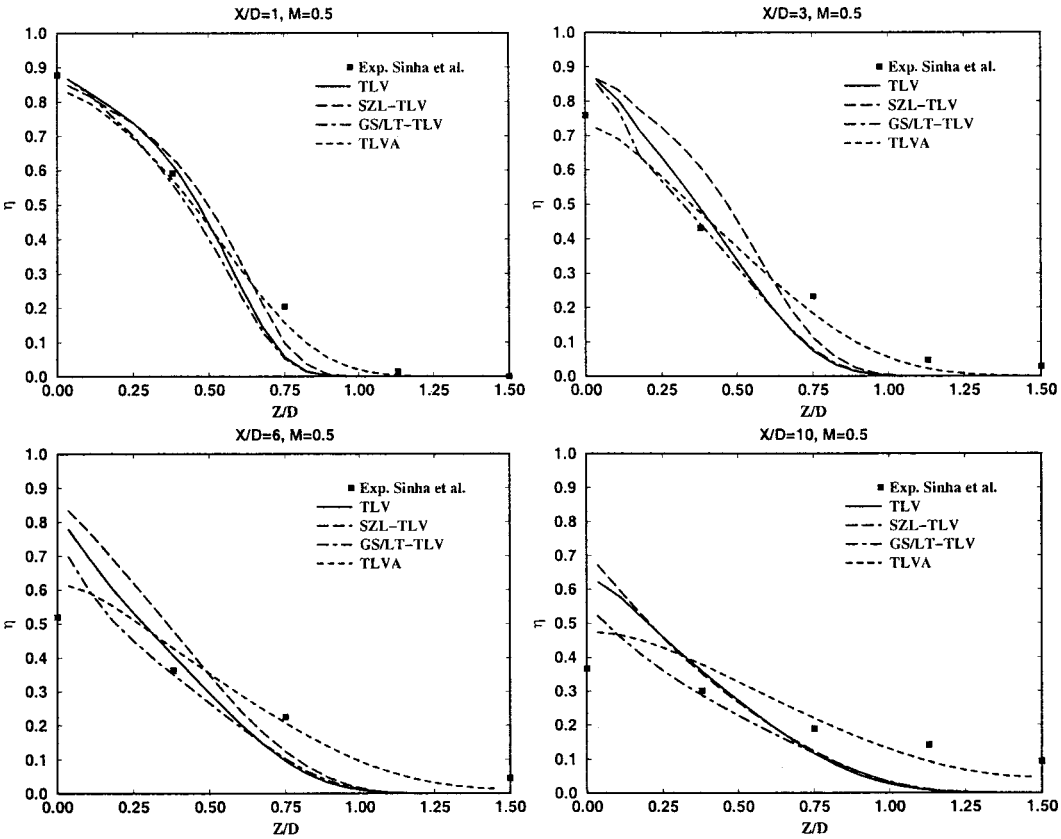

Fig. 12 Distributions of the spanwise film-cooling effectiveness for $M=0.5$ at four cross-flow locations

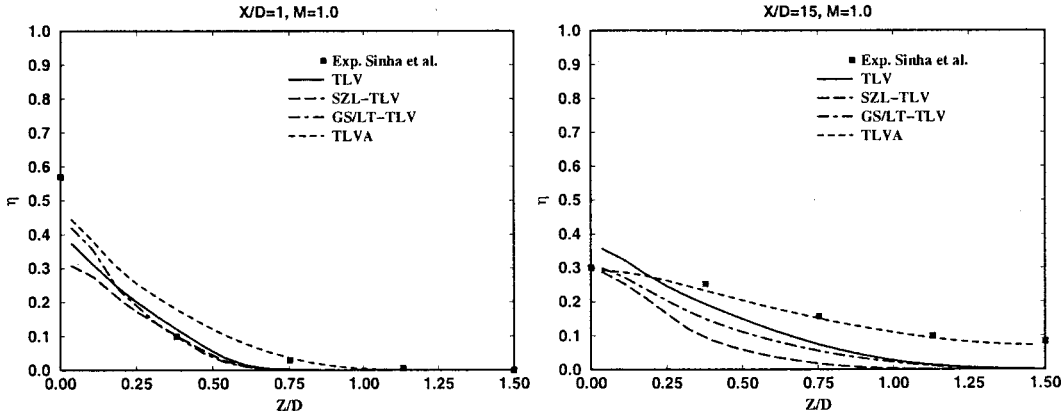

Fig. 13 Distributions of the spanwise film-cooling effectiveness for $M=1.0$ at two cross-flow locations

tions of η on the channel surface for $M=1.0$ at the crossflow locations for which experimental data are available, $X/D=1$ and 15. The superiority of the TLVA approach is once again illustrated, in particular at the second location where $X/D=15$. At the upstream location, however, the model seems to overpredict η around $Z/D=0.3-0.4$ as compared to the other models. In summary, in this section the anisotropic TLVA approach has been shown to remedy two major deficiencies known to afflict both the isotropic and (surprisingly) the nonlinear algebraic stress models: it improves the prediction of detachment and reattachment of the jet and considerably enhances the lateral spreading of the jet. Finally, the foregoing discussion also reveals that the performance of the employed EASMs does not provide a clear picture.

Conclusions

Streamwise injection of film coolant over a flat plate has been simulated for density ratio of two and mass flux ratios of 0.5 and 1.0. The calculations were extended to the injection pipe and to the plenum. A flexible, three-dimensional, finite-volume method using multi-block curvilinear grids was employed, and high-order discretization schemes were used to reduce numerical errors. Various versions of the $k-\varepsilon$ turbulence model were employed to simulate the turbulent exchange processes. These include an isotropic two-layer version resolving the viscous sublayer with a DNS-based one-equation model, a second model variant accounting for the anisotropy of turbulent exchange, also based on the same DNS data, and various quadratic and cubic explicit algebraic stress models combined with the DNS-based near-wall one-equation model.

The flow field and its dependence on the blowing rate appear to be reasonably well predicted, and most of the pertinent physical mechanisms associated with jets in crossflow were also well predicted, including the injection-induced secondary-flow vortices. Calculations of the film cooling of the channel show that the thermal field is more difficult to predict and is very sensitive to numerical details. The basic evolution is however simulated correctly, and so is the influence of the blowing rate. The isotropic two-layer $k-\varepsilon$ model was found to underpredict the lateral spreading of the temperature field, together with an exaggerated size of the kidney vortices. Consequently, the laterally averaged film-cooling effectiveness is generally too low.

The nonlinear algebraic models, which were of a mixed quality, underpredict the lateral spreading of the jet as much as the isotropic TLV model. Furthermore, except for the quadratic GS/LT variant, the other nonlinear models were found to exaggerate the size of the jet and its lifting-off from the wall, leading to a counter effect in terms of wall cooling effectiveness. This was clearly seen in the distributions of local lateral film-cooling effectiveness on the plate surface, where the deviations between calculations and measurements become more evident with increasing distance from the hole. The EASM version of Gatski and Speziale has indeed met with some success compared to the linear isotropic model, but the best results are obtained in connection with the DNS-based anisotropy TLVA model. This model variant has been shown to better predict the secondary vortices associated with the jet, while considerably enhancing the lateral spreading of the scalar field. It was also found that with this approach, turbulence characteristics including intensity and shear stresses are well predicted in the region surrounding the injection location; the latter quantity has shown insensitive to changes in the length-to-diameter of the discharge hole. However, it is important to caution from extending this approach to other more complex flows since the empirical relations for turbulence anisotropy on which the method is based were inferred from DNS data of a channel (attached) flow. Finally, since the model directly depends on the wall distance, it has to be employed with grids with near-wall resolutions of at least $y^+\approx 1.5$.

Acknowledgments

This work was achieved when the first author was in short stay at the Institute of Energy Technology of ETH Zurich, kindly invited by Prof. G. Yadigaroglu.

Nomenclature

D = diameter of discharge pipe
k = turbulent kinetic energy
M = blowing rate or mass flux ratio $=(\rho_h U_h)/(\rho_\infty U_\infty)$
Pr_t = turbulent Prandtl no.
S_{ij} = strain tensor $=(\overline{u}_{i,j}+\overline{u}_{j,i})/2$
S = irreducible invariant of $S_{ij}=k/\varepsilon\sqrt{S_{ij}S_{ij}}$
R_y = near-wall or turbulent Reynolds no. $=y_n\sqrt{k}/\nu$
T_u^∞ = free-stream turbulence level
T_u = local turbulence intensity $=\sqrt{2k/3}/U_\infty$
$\overline{u}_i$ = Cartesian velocity components
U_h = inlet flow velocity in discharge pipe
U_∞ = inlet mainstream velocity
y_n = normal wall distance
y^+ = dimensionless wall distance $=y_n u_T/\nu$
δ = boundary layer thickness
ϵ = dissipation rate of turbulent kinetic energy
f_μ = damping function defined by Eq. (5)
η = film cooling effectiveness $=(T_w-T_\infty)/(T_h-T_\infty)$
$\langle\eta\rangle$ = laterally averaged film-cooling effectiveness
Γ_j/Γ_j^ϕ = turbulent transport coefficients
$\ell_\mu/\ell_\varepsilon$ = length scales in one-equation model
μ = molecular viscosity
$\mu_t/\tilde{\mu}_t$ = turbulent viscosity
Ω_{ij} = vorticity tensor $=(\overline{u}_{i,j}-\overline{u}_{j,i})/2$

Ω = irreducible invariant of $\Omega_{ij} = k/\varepsilon \sqrt{\Omega_{ij}\Omega_{ij}}$
ϕ = general dependent variable
ρ = density
σ's = Prandtl nos.
θ = fluctuating temperature
τ_w = wall friction
u_τ = friction velocity $= \sqrt{\tau_w/\rho}$

Subscripts

∞ = freestream
c = centerline
h = jet
pln = plenum
w = wall

References

[1] Lakehal, D., Theodoridis, G., and Rodi, W., 2001, ''Three Dimensional Flow and Heat Transfer Calculations of Film Cooling at the Leading Edge of a Symmetrical Turbine Blade Mode,'' Int. J. Heat Fluid Flow, **22**, pp. 113–122.

[2] Ferguson, D. J., Walters, K. D., and Leylek, J. H., 1998, ''Performance of Turbulence Models and Near-Wall Treatments in Discrete Jet Film Cooling Simulations,'' ASME paper No 98-GT-438.

[3] Garg, V. K., and Ameri, A. A., 1997, ''Comparison of Two-Equation Turbulence Models for Prediction of Heat Transfer on Film-Cooled Turbine Blades,'' Numer. Heat Transfer, Part A, **31**, pp. 347–371.

[4] Hoda, A., and Acharya, S., 2000, ''Predictions of a Film Cooling Jet in Crossflow with Different Turbulence Models,'' ASME J. Turbomach., **122**, pp. 558–569.

[5] Lakehal, D., Theodoridis, G., and Rodi, W., 1998, ''Computation of Film Cooling of a Flat Plate by Lateral Injection from a Row of Holes,'' Int. J. Heat Fluid Flow, **19**, pp. 418–430.

[6] Theodoridis, G., Lakehal, D., and Rodi, W., 2001, ''3D Calculations of the Flow Field Around a Turbine Blade with Film Cooling Injection Near the Leading Edge,'' Flow, Turbul. Combust., **66**, pp. 57–83.

[7] Rodi, W., 1991, ''Experience with Two-Layer Models Combining the k–ε Model with a One-Equation Model Near the Wall,'' AIAA J., Paper No. 91-0216.

[8] Bergeles, G., Gosman, A. D., and Launder, B. E., 1978, ''The Turbulent Jet in a Cross Stream at Low Injection Rates: a Three-Dimensional Numerical Treatment,'' Numer. Heat Transfer, **1**, pp. 217–242.

[9] Quarmby, A., and Quirk, R., 1974, ''Axisymmetric and Non-Axisymmetric Turbulent Diffusion in a Plain Circular Tube at High Schmidt Number,'' Int. J. Heat Mass Transf., **17**, p. 143.

[10] Sinha, A. K., Bogard, D. G., and Crawford, M. E., 1991, ''Film-Cooling Effectiveness Downstream of a Single Row of Holes with Variable Density Ratio,'' ASME J. Turbomach., **113**, pp. 442–449.

[11] Sinha, A. K., Bogard, D. G., and Crawford, M. E., 1991, ''Gas Turbine Film Cooling: Flowfield due to a Second Row of Holes,'' ASME J. Turbomach., **113**, pp. 450–456.

[12] Pietrzyk, J. R., Bogard, D. G., and Crawford, M. E., 1990, ''Effect of Density Ratio on the Hydrodynamics of Film Cooling,'' ASME J. Turbomach., **113**, pp. 442–449.

[13] Leylek, J. H., and Zirkle, R. D., 1994, ''Discrete-Jet Film Cooling: A Comparison of Computational Results with Experiments,'' ASME J. Turbomach., **116**, pp. 358–368.

[14] Ardey, S. 1998, ''3D-Messung des Stroemungsfeldes um die filmgekuehlte Vorderkante einer Referenzschaufel,'' Abschlussbericht zum TURBOTHERM II-Verbundvorhaben 2.1.8.4 der Arbeitsgemeinschaft Hochtemperatur Gasturbine, Report LRT-Inst. 12-98/02, Universität der Bundeswehr Münich, Germany.

[15] Kaszeta, R. W., and Simon, T. W., 2000, ''Measurement of Eddy Diffusivity of Momentum in Film Cooling Flows with Streamwise Injection,'' ASME J. Turbomach., **122**, pp. 178–183.

[16] Rodi, W., Mansour, N. N., and Michelassi, V., 1993, ''One-Equation Near-Wall Turbulence Modeling with the Aid of Direct Simulation Data,'' ASME J. Fluids Eng., **115**, pp. 196–205.

[17] Norris, L. H., and Reynolds, W. C. 1975, ''Turbulent Channel Flow with a Moving Wavy Boundary,'' Report No. FM-10, Stanford University, Department of Mechanical Engineering.

[18] Kim, J., Moin, P., and Moser, R., 1987, ''Turbulence Statistics in Fully Developed Channel Flow at Low Reynolds Number,'' J. Fluid Mech., **177**, pp. 133–166.

[19] Gilbert, N., and Kleiser, L. 1991, ''Turbulence Model Testing with the Aid of Direct Numerical Simulation Results,'' Proc., 8th Symposium on Turbulent Shear Flows, Paper No 26-1, Munich, Germany, September 9–11.

[20] Launder, B. E., Reece, G., and Rodi, W., 1975, ''Progress in the Development of a Reynolds Stress Turbulence Closure,'' J. Fluid Mech., **68**, pp. 537–566.

[21] Launder, B. E., 1988, ''On the Computation of Convective Heat Transfer in Complex Turbulent Flows,'' ASME J. Heat Transfer, **110**, pp. 1035–1306.

[22] Shih, T. H., Zhu, J., Lumley, J. L., 1993, ''A Realizable Reynolds Stress Algebraic Equation Model,'' Technical Report, NASA TM-105993.

[23] Shih, T. H., Zhu, J., and Lumley, J. L., 1995, ''A New Reynolds Stress Algebraic Equation Model,'' Comput. Methods Appl. Mech. Eng., **125**, pp. 287–302.

[24] Gatski, T. B., and Speziale, C. G., 1993, ''On Explicit Algebraic Stress Models for Complex Turbulent Flows,'' J. Fluid Mech., **254**, pp. 59–78.

[25] Craft, T. J., Launder, B. E., and Suga, K., 1996, ''Development and Application of a Cubic Eddy-viscosity Model of Turbulence,'' Int. J. Heat Fluid Flow, **17**, pp. 108–118.

[26] Lakehal, D., and Thiele, F., 2001, ''Sensitivity of Turbulent Shedding Flows Past Cylinders to Non-Linear Stress-Strain Relations and Reynolds Stress Models,'' Comput. Fluids, **30**, pp. 1–35.

[27] Majumdar, S., Rodi, W., and Zhu, J., 1992, ''Three-Dimensional Finite-Volume Method for Incompressible Flows With Complex Boundaries,'' ASME J. Fluids Eng., **114**, pp. 496–503.

Near-Wall Modeling of Turbulent Convective Heat Transport in Film Cooling of Turbine Blades With the Aid of Direct Numerical Simulation Data

Djamel Lakehal[1]
Institute of Energy Technology,
Swiss Federal Institute of Technology Zurich,
ETH-Zentrum/CLT,
CH-8092 Zurich, Switzerland
e-mail: lakehal@iet.mavt.ethz.ch

The paper presents novel developments in the DNS-based, turbulence modeling strategy of Lakehal et al. developed for calculating jets in crossflow. The particular features of the model include: 1) dynamic coupling of the high-Re $k-\varepsilon$ with a one-equation model resolving the near-wall viscosity-affected layer; 2) inclusion of the anisotropy of turbulent transport coefficients for all transport equations; 3) near-wall variation of the turbulent Prandtl number as a function of the local Reynolds number. Most of the important aspects of the proposed model are based on known DNS statistics of channel and boundary layer flows. The model is validated against experiments for the case of film cooling of a flat plate, where coolant air is injected from a row of streamwise inclined jets. Excellent results were obtained for this configuration as compared to earlier numerical investigations reported in the open literature. The model is then extended to calculate film cooling of a symmetrical turbine blade by a row of laterally injected jets for various blowing rates. Comparison of the calculated and measured wall-temperature distributions show that only with this anisotropy eddy-viscosity/diffusivity model can the spanwise spreading of the temperature field be well predicted and the strength of the secondary vortices reduced. Furthermore, results of additional calculations show that combining the anisotropy eddy viscosity model with the DNS-based relation for turbulent Prandtl number promotes the eddy diffusivity of heat vis-à-vis that of momentum further, leading to an enhanced spanwise spreading of the jet. The performance of this new approach improves with increasing blowing rate. [DOI: 10.1115/1.1482408]

Introduction

Enhancing the thermal performance of gas turbines by an increase of their inlet temperature may cause irreparable damage to the blades. Despite the noticeable progress made in blade metallurgy, a reasonable lifetime of turbine blades can be ensured only by an efficient surface cooling mechanism such as film cooling. This technique indeed offers an excellent compromise between the protection of endwalls and aerodynamic efficiency, since in contrast to convective blade cooling, it minimizes the thermal loads on other components of the turbine. This technique may, however, constitute a source of overall power output loss since the cooling air has to be extracted from the compressors. Thus, optimum film cooling utilizing a minimum amount of cooling air is a major economical requirement.

Film cooling at the leading edge gives rise to very complex flow and heat transfer processes. Its efficiency can be influenced by the following parameters: the blade and discharge geometry (blade curvature, the shape of the injection hole, etc.), the injection angle (perpendicular, streamwise inclined, spanwise inclined), the blowing rate M, also known as the mass-flux ratio, the density and temperature ratio, the freestream turbulence, and the compressibility effects. The flow in the vicinity of the discharge holes is particularly complex due to the interaction of the coolant jet with the flow around the blade. The individual jets are bent over by the mainstream, leading to the formation of longitudinal vortices and a reverse-flow region below the jet. The flow becomes even more complicated when the injection is lateral, which is often the case in practice, since then the cooling film better covers the area to be cooled. The formation and location of the longitudinal vortices depend strongly on inclination and blowing rate. More precisely, the strength and elevation of these vortices depend on the penetration of the injected coolant into the cross flow. In the case of streamwise injection two counter-rotating vortices form, while in the lateral injection configuration there is only one large-scale vortex. The vortices entrain ambient hot gas and move it to the vicinity of the wall and hence influence adversely the cooling effectiveness. This phenomenon is more pronounced at higher blowing rates for which the jets penetrate more deeply into the oncoming flow and the vortices are lifted further from the surface. The foregoing description is in fact an idealization of the flow as if it were perfectly stable and steady, and that is exactly what turbulence models of all types are supposed to predict. The reality of jets in cross flow is more complex than that [1,2]: the flow features a broad band of vortical, large-scale structures, dominated by the well-known kidney vortex, but also includes other unsteady structures such as the horse-shoe vortex, the wake vortices, and the shear layer vortices; these can in fact be reproduced only by means of nontime-averaged-based concepts such as direct and large eddy simulation [1], (DNS) and (LES).

The mass-flux ratio can strongly influence the penetration of the jet momentum into the crossflow around the blade's leading edge. An extended penetration of the jet into the mainstream occurs at high mass-flux ratios only (say for $M>0.5$); it deflects towards the blade surface otherwise. Increasing the mass-flux ratio, the deflection of the injected jet by the oncoming flow becomes more pronounced, and the reverse flow region extends further downstream of the hole. Furthermore, the jet penetrates further into the

[1]Formerly at the Institute for Hydromechanics, University of Karlsruhe, Germany.

Contributed by the International Gas Turbine Institute for publication in the JOURNAL OF TURBOMACHINERY. Manuscript received by the IGTI, April 24, 2001; revised manuscript received April 2, 2002. Associate Editor: R. S. Bunker.

mainstream resulting in a degradation of the cooling in the region near the hole [3]. The way the penetration of the jet into the cross flow occurs was also found to depend on s/D, the jet spacing-to-diameter ratio [4]: jet penetration increases with increasing s/D. The experimental studies of Haven and Kurosaka [2] brought in valuable information about the structure of jets in cross flow in general, and about the effects of injection hole geometry (round holes versus square or rectangular holes) on the cooling efficiency in particular. Mehendale and Han [5] studied the influence of high mainstream turbulence on leading edge film effectiveness and heat transfer coefficient with a blunt body having a semicylindrical leading edge. Their results indicate that film-cooling effectiveness decreases with increasing blowing ratio. They have also shown that high mainstream turbulence ($T_u > 9.5\%$) affects the leading edge film-cooling effectiveness for low blowing ratios only ($M = 0.4$). Detailed information on the behavior of flow and temperature fields around inclined jets for real turbine blades were made available only recently [3,6]. Beeck [7] studied the aerodynamic effect of slot injection near the leading edge of a high pressure turbine blade, the so-called AGTB cascade model. Beeck's work revealed that significant pressure losses may be introduced by the injection system. Expanding on earlier investigations of Beeck [7], Ardey [6] conducted experiments on the three-dimensional variant of the AGTB cascade and provided a detailed data base of velocity and turbulence quantities. This data base has revealed, in particular, the significant anisotropy of turbulence near the wall caused by the strong interaction between the jet and the cross flow; a phenomenon that has recently been confirmed by Findlay et al. [8] for jet injection over a flat plate. Unfortunately, very little information is given on the rate of turbulence anisotropy very near the wall that could be further exploited in developing prediction models.

Review of Some Previous Numerical Investigations

Three-dimensional calculations of film cooling of real turbine blade models are less abundant than calculations of jets in crossflow over flat plates, e.g., [9–12]. There exists even fewer calculations of surface heat transfer of fully film-cooled rotating turbine blades [13]. Various other investigations exploring the effect of several parameters on the flow and temperature fields over different blade prototypes revealed the importance of extending the calculations into the cooling channel, at least for low blowing rates. Turbulence models that have so far been employed in film cooling calculations do not go beyond the two-equation type. An exception is the work of Ferguson et al. [14], who compared the predictive performance of various two-equation turbulence models to the sophisticated Reynolds stress model (RSM). Surprisingly, their RSM calculations were not better than those with eddy viscosity models. Garg and Ameri [15] reported on calculations for the C3X vane and the VKI rotor where they used the Baldwin-Lomax model and various two-equation turbulence models. No clear picture emerged from the calculations indicating which of the employed models is superior. The same Baldwin-Lomax model was also employed by Bohn et al. [16] in their computations of the film cooling of the two-dimensional AGTB cascade [8]. For this particular configuration, which has been widely adopted as a benchmark for code validation, Irmisch [17] and Theodoridis and Rodi [18] used the standard $k-\varepsilon$ model with wall functions while Vogel [19] adopted a low-Reynolds variant. In reference [20], the authors report on the simulation of the flow around the three-dimensional version of the AGTB test-case [6]. Owing to the difficulties in calculating these flows using a full three-dimensional RSM under low-Re conditions, Lakehal et al. [11], Theodoridis et al. [20], and Lakehal et al. [21] opted for another strategy. This consists in retaining the basic architecture of the $k-\varepsilon$ model, while an anisotropic eddy-viscosity/diffusivity correction for secondary stresses is introduced. The extension of the model to low-Re number conditions was in all cases achieved via a dynamic, zonal, two-layer approach [22]. This practice was first applied to jet injection over a flat plate in [11], then to real blade models in [20] and [21]. It was recently compared by Azzi and Lakehal [12] to algebraic stress models employed in connection with a DNS-based two-layer model resolving the viscous sublayer and was found to perform better for the case of streamwise injection over a flat plate, at least for medium blowing rates $M = 0.5$ and 1.0.

Scope of the Paper

The flow in turbine-blade passages is highly three-dimensional and is characterized by a multitude of complex phenomena. In addition, these flows are turbulent to an appreciable extent with a significant inhomogeneity in length and time scales. Coolant jetting increases further the complexity of the flow field, in particular the rate of turbulence anisotropy around the injection location grows appreciably [23,6]. Previous calculations have shown that isotropic turbulence models are not adequate for this class of flow since the lateral spreading of the heat flux is systematically underpredicted. This led many authors to resort to the Bergeles et al. [24] model promoting the turbulent cross fluxes, and their results indeed met with some success. Theodoridis et al. [20], who analyzed the flow in the vicinity of the leading edge of the AGTB turbine blade, concluded that promoting the turbulent fluxes is particularly necessary over the pressure side of the blade, where there is evidence from measurements [6] that the rate of anisotropy is appreciable. Lakehal et al. [21] have then tried to infer information from Ardey's [6] experimental data in view of generalizing Bergeles' correction, but they have faced the same difficulties as Kaszeta and Simon [23] did, in that the turbulent transport has been found too complex than any statistical approach would predict. However, it appeared necessary to further extend the existing model [24] for application very near the wall, and this has been successfully accomplished by use of channel-flow DNS data [21,12], i.e. the so-called TLVA model.

The present contribution introduces a novel development in the modeling practice briefly evoked in the foregoing. The new development in question is in fact an attempt to stimulate the debate on the relationship between eddy diffusivities of momentum and heat across the sublayer. It is proposed to complement the TLVA approach by an additional model in which the variation of the turbulent Prandtl number across the viscosity-affected layer is approximated by a DNS-based empirical relation. This particular attempt constitutes more of an appeal to stimulate reflection on this issue rather than a proposal for a universal model to be applied to all sorts of applications. Further investigations in this direction are obviously needed. It is understandable that these and previous DNS-based models calibrated for attached flows are not systematically valid for separated flows, but in the absence of direct simulation data of jets in crossflow—and before being capable of exploiting them in the statistical sense—the idea remains for the present time the sole reliable alternative. The first test case studied here represents film cooling of a flat plate by a row of streamwise injected jets studied experimentally by Sinha et al. [25]. The test case has widely been adopted as a benchmark for code validation [9,10,12]. The main case study investigated in this paper represents film cooling of a three-dimensional symmetrical blade studied experimentally by Haslinger and Hennecke [3]. The difference between this and the former case is that the plenum was not considered.

Governing Equations and Turbulence Modeling

The conservative form of the averaged transport equations governing steady-state, three-dimensional, incompressible turbulent flows featuring heat convection can be written as

$$\frac{\partial}{\partial x_k}(\rho \overline{u_k}) = 0 \tag{1}$$

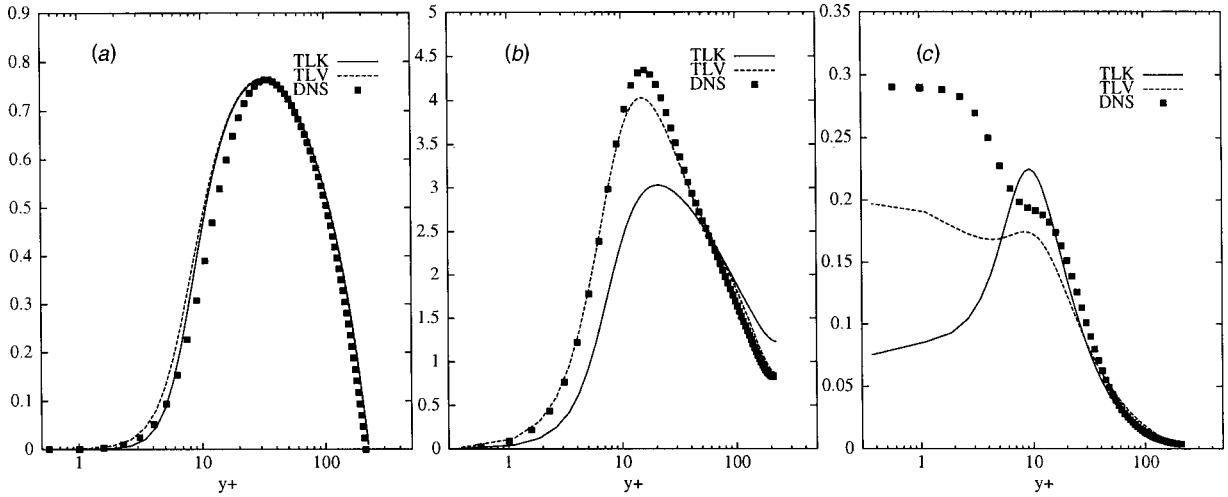

Fig. 1 Normalized profiles in developed channel flow at $Re_\tau=211$ [29]: (*a*) shear stress $\overline{u'v'}^+$; (*b*) turbulent kinetic energy k^+; (*b*) dissipation rate ε^+

$$\frac{\partial}{\partial x_j}(\rho\overline{u_i u_j}) = -\frac{\partial \overline{p}}{\partial x_i} + \frac{\partial}{\partial x_j}\left(\mu\frac{\partial \overline{u_i}}{\partial x_j} - \rho\overline{u_i' u_j'}\right) \tag{2}$$

$$\frac{\partial}{\partial x_j}(\rho\overline{u_j T}) = \frac{\partial}{\partial x_j}\left(\frac{\mu}{\mathrm{Pr}}\frac{\partial \overline{T}}{\partial x_j} - \rho\overline{u_j'\theta}\right) \tag{3}$$

where ρ represents the density, μ the molecular viscosity, $\overline{p}$ the pressure, $\overline{u_j}=(\overline{u},\overline{v},\overline{w})$ the velocity vector, $\overline{T}$ the temperature, Pr the molecular Prandtl number, $\overline{u_i'u_j'}$ the Reynolds-stress tensor, and $\overline{u_j'\theta}$ the turbulent heat flux. Note also that in order to account for *weak* compressibility effects, the fluid density can be computed as a function of both the system pressure and absolute temperature with the aid of the equation of state.

The next subsections will briefly introduce the channel flow DNS-based isotropic TLV model, its anisotropic version, under the TLVA variant [12], then the novel modification relating the near-wall eddy diffusivities of momentum and heat.

The Two-Layer $k-\varepsilon$ Turbulence Model (TLV). The two-layer approach employed here represents an intermediate modeling strategy between the wall-function and the low-Re model approaches. The method consists in resolving the viscosity-affected regions close to walls with a one-equation model, while the outer core flow is resolved with the standard $k-\varepsilon$ model. Such models require considerably fewer grid points in the viscous sublayer than any pure low-Re scheme (about 10–15 rather than 25–30), and hence are more suitable for complex situations involving more than one wall. Also, because of the fixed length-scale distribution near the wall, these models have been found to give better predictions for adverse pressure gradient boundary layers than pure $k-\varepsilon$ models. In the one-equation model, the eddy viscosity is made proportional to a velocity scale and a length scale ℓ_μ. The distribution of ℓ_μ is prescribed algebraically, while the velocity scale is determined by solving the *k*-equation. The dissipation rate ε appearing as the sink term in the *k*-equation is related to *k* and a dissipation length scale ℓ_ε, which is also prescribed algebraically. The two-layer versions available in the literature differ in the way ℓ_μ and ℓ_ε are prescribed. In terms of implementation, the two-layer approach can easily be used in general-purpose CFD codes and does not necessarily require special considerations such as freezing grid portions. As in other low-Re number models, it requires a versatile algorithm for the determination of local distance to the wall.

In the outercore flow, the usual eddy-viscosity hypothesis is applied employing a linear relation of the Reynolds-stress tensor and the corresponding heat flux to the velocity and temperature gradients

$$\rho\overline{u_i'u_j'} = \frac{2}{3}\delta_{ij}\rho k - 2\Gamma_j S_{ij}; \quad \rho\overline{u_j'\theta} = -\frac{\Gamma_j}{\mathrm{Pr}_t}\frac{\partial \overline{T}}{\partial x_j} \tag{4}$$

where δ_{ij} is the Kronecker delta and S_{ij} the rate of strain tensor. The distribution of the transport coefficient Γ_j is made isotropic using the conventional relationship, i.e., $\Gamma_j\equiv\mu_t=C_\mu\rho k^2/\varepsilon$. The distributions of k and ε are determined from the conventional model transport equations, and standard values are assigned to the constants, namely $C_\mu=0.09$; $C_{\varepsilon 1}=1.44$; $C_{\varepsilon 2}=1.92$; $\sigma_k=1.0$ and $\sigma_\varepsilon=1.3$. It is customary in this type of flow to set the turbulent Prandtl number Pr_t to the value 0.9.

In previous two-layer models the near-wall one-equation models always employed $k^{1/2}$ as a velocity scale[2] rather than the friction velocity u_τ. The so-called $(\overline{v'^2})^{1/2}$ velocity-scale-based model (TLV) was proposed by Rodi et al. [28], motivated by the fact that the normal fluctuations are a more relevant velocity scale for the turbulent momentum transfer near the wall than $k^{1/2}$, i.e., $\Gamma_j\equiv\mu_t\equiv(\overline{v'^2})^{1/2}\ell_\mu$ and $\varepsilon\equiv(\overline{v'^2})^{1/2}k/\ell_\varepsilon$. Prior to further applications, the model was employed for calculating the fully turbulent channel flow at the shear-based Reynolds number Re_τ $(=u_\tau y_n/\nu)$ equal to 211. The computational method is outlined in the corresponding section. The DNS database of this flow was provided by Gilbert and Kleiser [29]. Figure 1 compares the normalized (by u_τ and μ) profiles of shear stress $\overline{u'v'}^+$, turbulent kinetic energy k^+, and dissipation rate ε^+ with the DNS data. The figure shows that up to $y^+=200$ the shear stress predictions with both the TLK and the present one (also referred to as TLV) are almost identical and agree fairly well with the DNS data. However, as can be seen from Fig. 1(*b*), the profile of k^+ predicted by the TLV model compares very well with the data, while the TLK calculations underpredict the peak level. This is a consequence of an overpredicted value of ε^+ in the region where k^+ reaches its peak value (c.f. Fig. 1(*c*)). The most evident deviations between the TLK and TLV predictions are displayed in Fig. 1(*c*). It seems that the TLK model totally fails in predicting the maximum of ε^+,

[2]This is the reason why this type of model is commonly referred to as TLK. Rodi's [22] TLK variant (compared to TLV in Fig. 1) employs the one-equation model of Norris and Reynolds [27] to resolve the near-wall region.

as has been the experience with most other low-Re schemes. This is the direct consequence of ℓ_ε^{dns} being smaller than ℓ_ε^{nr} (due to Norris and Reynolds [27]) as the wall is approached.

The DNS-Based Anisotropic Extension (TLVA). As alluded to previously, with simple eddy viscosity models the turbulent transport in the cross direction is not accounted for sufficiently, whereas in reality it should be larger than that normal to the wall, as has been supported by various measurements, e.g. [30,6,23]. To account for the anisotropy of the turbulent exchange processes in these flows, Bergeles et al. [24] proposed multiplying the eddy viscosity appearing in the cross Reynolds stresses and heat fluxes by a factor varying linearly from $f=4.5$ at the log layer to 1.0 at the outer edge of the boundary layer. The near-wall value of $f=4.5$ was inferred from the experimental pipe-flow data of Quarmby and Quirk [30]. More recently, Lakehal et al. [21] have shown that this correction has to be extended to the viscous sublayer, since the normal fluctuations $\overline{v'^2}$ approach zero near the wall much faster than the lateral ones $\overline{w'^2}$. By investigating various sets of boundary layer and channel flow DNS data, they concluded that the ratio $f=\overline{w'^2}/\overline{v'^2}$ reaches much larger values in the viscous sublayer than the value of 4.5 adopted in the original model. This idea was first incorporated within the TLK model in [21] then within the TLV variant in [12] where is was referred to as TLVA. Briefly, in the TLVA the transport coefficient Γ_j appearing in Eqs. (4) is rewritten under the following form:

$$\Gamma_1=\Gamma_2=(\overline{v'^2})^{1/2}\ell_\mu; \quad \Gamma_3=(\overline{w'^2})^{1/2}\ell_\mu \tag{5}$$

where the variations of the length scale $\ell_\mu(=0.33y_n)$ and the velocity scales $\overline{v_i'^2}$ across the viscous region are based on boundary layer and channel-flow DNS data of Kim [31]

$$\overline{v'^2}/k=10^{-5}(4.65R_y^2+40.0R_y); \quad R_y=y_n\sqrt{k}/\nu \tag{6}$$

$$\overline{w'^2}/k=\overline{v'^2}/k\times f \tag{7}$$

with

$$\gamma=\mathrm{Max}\left[\frac{10^3(y^+)^{0.42}}{2.682(y^+)^2-5.463},\ 4.25\right] \tag{8}$$

being the turbulence anisotropy factor. The model is valid in the near-wall region where $1.5<y^+<50$ only. However, beyond the location where $y^+\approx 50$ (or $R_y=80$)—where the two layers are matched dynamically without fixing grids—and up to the edge of the boundary layer, the anisotropy factor f takes the average value of 4.25, instead of the original distribution by Bergles et al. [24]. The details of the model are provided in [21] and [12]. However, the expression for the rate of dissipation was kept isotropic, as in the original TLV model, by re-incorporating $k^{1/2}$ as a velocity scale rather the normal fluctuating velocities,[3] i.e., $\varepsilon=k^{3/2}/\ell_\varepsilon^{DNS}$. The dissipation length scale ℓ_ε^{DNS} was also calibrated with the same DNS data [12]. To complete the model an additional transport equation for k needs to be solved; it takes the commonly used form

$$\frac{\partial}{\partial x_j}(\rho\overline{u_j}k)=\rho(\mathcal{P}-\varepsilon)+\frac{\partial}{\partial x_j}\left(\Gamma_j^k\frac{\partial k}{\partial x_j}\right)+\mu\nabla^2 k \tag{9}$$

but with the transport coefficient $\Gamma_j^k=\Gamma_j/\sigma_k$ and the production term $\mathcal{P}=-\overline{u_i'u_j'}\overline{u}_{i,j}$ having the effect of f included, too. To summarize, the one-equation TLVA model consists of the following steps: (i) the flow and temperature field is solved with the turbulent fluxes being determined from Eq. (4); (ii) the transport equation for k, Eq. (9), is solved in parallel; (iii) the transport coefficients Γ_j are determined by use of Eq. (5); (iv) the rate of dissipation ε in Eq. (9) is determined by the DNS-based prescription [21,12].

The DNS-Based Model for the Turbulent Prandtl Number. The turbulent Prandtl number Pr_t is defined as the ratio of eddy diffusivity of momentum to eddy diffusivity of heat. Considering the two-dimensional boundary layer over a flat plate with constant properties, negligible body force and negligible viscous dissipation, the definition of the turbulent Prandtl number is

$$\mathrm{Pr}_t=\frac{-\overline{u'v'}(\partial\overline{T}/\partial y)}{-\overline{v'\theta}(\partial\overline{u}/\partial y)} \tag{10}$$

The Reynolds analogy which implies that Pr_t converges to a constant value, e.g. $\mathrm{Pr}_t\sim 0.7-0.9$ for $\mathrm{Pr}=0.73$, has been widely adopted as a *consensual* solution for turbulent heat convection problems. However, a multitude of experimental investigations dealing with the dependence and behavior of Pr_t have confirmed that a perfect analogy between eddy diffusivities of momentum and heat exists only within the log-layer (say for $30<y^+<300$). Within the viscosity-affected layer, however, most of these studies have revealed that Pr_t shows a marked increase to values well above unity. Guided by these indications, Kays and Crawford [32] and many others have developed analytical relationships for Pr_t with various degrees of sophistication. But serious doubts have been prevailing about the way in which this parameter varies across the viscous sublayer, i.e., the turbulent eddies while moving in a direction transverse to the mainstream might lose heat and momentum at different rates.

Recent DNS data for similar wall-air-flows, with slight or moderate wall heating, have recently provided new insight into this issue. They indicate that for air flows Pr_t varies somewhat differently in the viscosity-affected layer than has been assumed hitherto. In particular, some of these studies reveal that Pr_t can be smaller than unity within the viscosity-affected layer, being about 0.2 very near the wall, whereas it stabilizes in the outer range where $y^+<100$. Among these numerical experiments the one due to Lu and Hetsroni [33] simulated an open channel flow at $\mathrm{Re}_\infty=3000$ with passive heat transfer, while that of Madavan and Rai [34] simulated transition and turbulence in a spatially evolving boundary layer on a heated plate for $200{,}000<\mathrm{Re}_x<725{,}000$. Lu and Hetsroni's data are shown in Fig. 2; they clearly indicate that Pr_t increases from 0.2 very near the wall and reaches unity only at the edge of the viscous sublayer. A very similar behavior is perceptible from Madavan and Rai's data, which also show values of Pr_t decreasing sharply as the wall is approached.[4] Yet their data reveal that Pr_t does not follow a monotonous trend in the range $0.2<y/\delta<1.0$. It is clear that although a lack of universality[5] is noticeable in the DNS data shown in Fig. 2, there is a common trend to the effect that as the wall is approached the eddy diffusivity of heat increases more rapidly than that of momentum, implying a *high eddy conductivity* [32]. It appears to be important that this behavior be accounted for in a model resolving the viscous sublayer. Furthermore, this is particularly true for film-cooling calculations, since the spreading of the hot film on the blade wall is synonymous to a heated surface, causing a strong temperature gradient in the direction transverse to the mean flow. The following empirical relation for the near-wall behavior of Pr_t was therefore derived in this study from the channel flow DNS data of Lu and Hetsroni in particular:

$$\mathrm{Pr}_t=A_1(y^+)^4+A_2(y^+)^3-A_3(y^+)^2+A_4(y^+)+A_5 \tag{11}$$

where the coefficients A's are given in Table 1. Proper usage of Eq. (11) consists in alleviating its dependence on the dimension-

[3]Azzi and Lakehal [12] re-formulated the TLV model by re-incorporating $k^{1/2}$ in both the transport coefficient Γ_j and the dissipation rate ε. They could have in fact called it a variant of the TLK model (as suggested by one of the reviewers).

[4]These data were originally scaled with y/δ; they have been re-scaled here with y/y^+ on the basis of the information available in the original paper.

[5]This has already been observed in other situations, e.g., the DNS-based near-wall damping of μ_t or of $\overline{v'^2}/k$ depends somewhat on the Reynolds number.

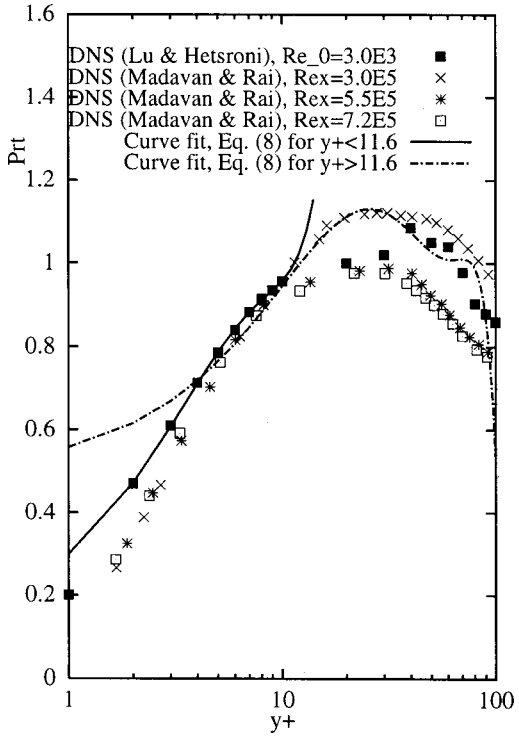

Fig. 2 Correlation for near-wall turbulent Prandtl number $Pr_t = g(y^+)$ fitted against DNS data of Lu and Hetsroni [33] and Madavan and Rai [34]

less wall distance y^+, which can be replaced by the near-wall Reynolds number R_y. An approximate relation between y^+ and R_y based on the data of Kim has already been derived [12]

$$y^+ = 0.00442R_y^2 + 0.294R_y + 0.545 \tag{12}$$

Making Eq. (11) dependent on the local Reynolds number R_y rather on y^+ avoids having to deal with singularities in separated flow regions, where y^+ can go to zero. Note, too, that at the matching location, where $y^+ = 11.6$, the turbulent Prandtl number reaches the value of 0.99. Also, relation (11) is valid up to $y^+ = 94$ only, a location where $Pr_t = 0.76$; this latter value is then used everywhere in the outercore flow. Note also that since the sharp drop in Pr_t cannot be expected in separated flows, the foregoing empirical relationship may occasionally produce countereffects. When employed in connection with the isotropic TLV model, the foregoing approach using Eq. (11) will be referred to as TLV-Pr, whereas its combination with the the anisotropic variant TLVA will be called TLVA-Pr.

The Computational Method

The governing equations are solved using a three-dimensional finite-volume method for arbitrary nonorthogonal grids, employing a cell-centered grid arrangement. A description of the basic method and its recent developments are reported in [11]. The momentum-interpolation technique is used to prevent pressure-field oscillations tending to appear in the cell-centered grid arrangement. The pressure-velocity coupling is achieved by using the well-known SIMPLEC algorithm. The present computations were performed employing the QUICK scheme for all variables applied in a scalar form by means of a deferred-correction procedure and bounded by the Van-Leer Harmonic function as limiter. The diffusive fluxes are approximated using second-order central differences. The resulting system of difference equations was solved using the strongly implicit procedure (SIP) algorithm. Convergence was in all cases determined based on a drop in normalized mass and momentum residuals by four orders of magnitude at least. A global mass and energy balance algorithm was employed after each iteration, consisting of a systematic readjustment of the mass fluxes at the outflow.

Table 1 Coefficients in Eq. (11)

Wall region	A_1	A_2	A_3	A_4	A_5
if $y^+ \leq 11.6$	0.0	$8.8 \cdot 10^{-4}$	0.0239	0.238	0.0836
if $y^+ > 11.6$	$-1.43 \cdot 10^{-7}$	$3.02 \cdot 10^{-5}$	0.00223	0.0645	0.5

Grids and Boundary Conditions

The Flat Plate. This test case was experimentally investigated by Sinha et al. [25]. The jets were inclined at an angle of 35 deg with a lateral spacing of $3D$. The injection hole diameter was 12.7 mm and the discharge pipe length-to-diameter ratio was 1.75. The domain extends $19D$ upstream of the leading edge and $30D$ downstream of the injection location. The topology of the grid is shown in Fig. 3(*a*). The approaching boundary layer was fully turbulent. The simulations performed in the experiment dealt with two density ratios ρ_h/ρ_∞ (=1.2 and 2.0) and various mass-flux ratios ranging from $M = 0.25$ to 1.0. In the present work calculations were carried out for $\rho_h/\rho_\infty = 2$ and $M = 0.5$ only. Results of the simulation with the higher mass-flux ratio can be found in a companion paper by Azzi and Lakehal [12]. In the streamwise direction the calculation domain extends from the inflow plane located at $x/D = -8$ to $x/D = 25$ and from the channel bottom to $y/D = 6$ in the vertical direction. The downstream exit of the hole is located at $x = 0$. In the spanwise direction the domain extends from a plane through the middle of the holes ($z = 0$) to a plane at $z/D = 1.5$ in the middle between two injection holes, and symmetry conditions are imposed on these planes. A multiblock grid is used to cover the three blocks. The grid adopted for calculations was obtained after a series of tests; it consists of $180 \times 76 \times 24$ points in the *x*, *y*, and *z* directions, respectively. The jet and the plenum are meshed with grids composed of $16 \times 40 \times 9$ and $53 \times 75 \times 23$ nodes, respectively. The wall neighboring-cells were located so as to always maintain the values of y^+ smaller than 2.0. The number of grid points placed in the viscous sublayer and the buffer layer was typically 15 to 20, but less within the discharge pipe.

The no-slip boundary conditions and $k = 0$ were used on the plate surface, and on the plenum internal walls since there the flow has a very low momentum (and thereby very small y^+ at the wall), which invalidates the use of wall functions. Because the upper surface of the domain was set relatively far from the flat plate, symmetry conditions were employed there. In accord with the experiment, a 1/7th power-law turbulent boundary layer velocity profile was imposed at $x/D = -8$ in order to match the boundary layer thickness of $0.7D$ at the injection location. The mainstream velocity was set to $U_\infty = 20$ m/s, conforming to the experiment, and uniform distributions were specified for k and ε corresponding to a free-stream turbulence intensity of $T_u = 0.5$ percent, and a dimensionless eddy viscosity of $\mu_t/\mu = 50$. Since the experiment does not provide exact information on the flow at the inlet of the discharge pipe, uniform distributions of k and ε were specified, based on a turbulence intensity of $T_u = 2$ percent and $\mu_t/\mu = 30$. Adiabatic wall conditions were employed when solving the enthalpy equation and zero gradient conditions were used at the outflow boundary. The exact inlet profiles of the temperature and corresponding densities were employed, i.e., $T_\infty = 302$ K, $T_h = T_{pln} = 153$ K.

The AGTB Symmetrical Blade. This AGTB blade prototype as known in the literature was studied experimentally by Haslinger and Hennecke [3]. The blade model is symmetrical with a length of 515 mm and a maximum width of 72 mm. The leading

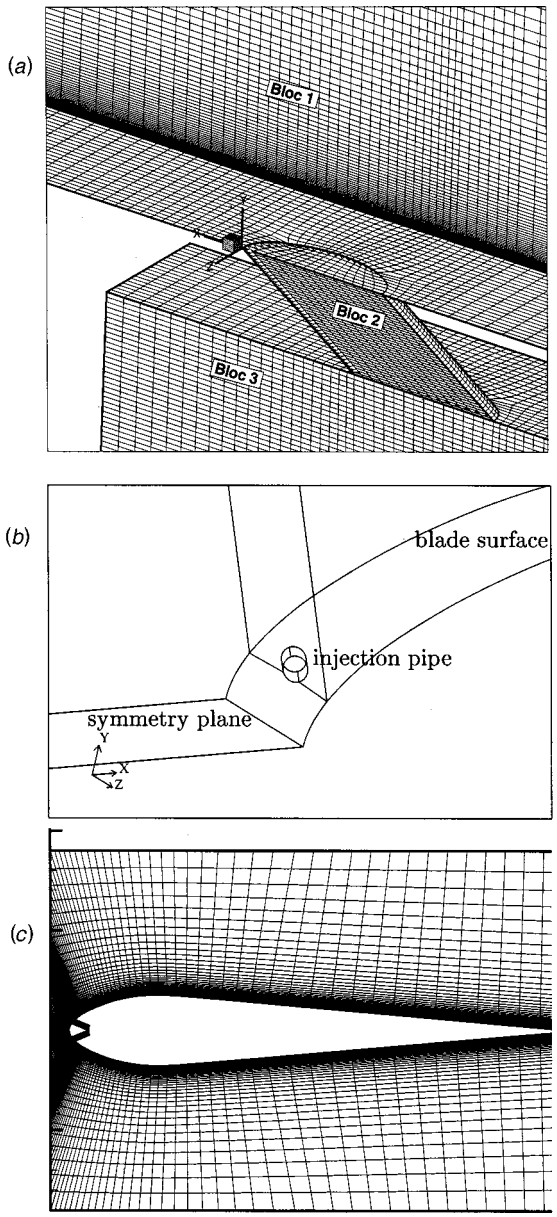

Fig. 3 (*a*) Grid and topology of the first test case; (*b*) the computational domain; and (*c*) the grid in the midplane of the symmetrical blade prototype

edge of the model contains on each side one row of holes ($D=4$ mm) with a lateral spacing of $5D$. Two configurations with different inclinations of the injection channels were investigated in the experiment: one with a streamwise inclination ($\gamma=0$ deg) and one with a lateral inclination of $\gamma=45$ deg between the axis of the pipe and the symmetry axis of the blade, when projected over the horizontal plane x-z, as shown in Fig. 3(*b*). The projection over the vertical plane x-y shows the pipe and the symmetry axis to form an angle of 22 deg. The approach-flow velocities were in the range $U_\infty=15-30$ m/s so that the flow can be considered incompressible. The free-stream turbulence level was below 0.5%, which is understandably much lower than in the practice. Seven mass-flux ratios ($M=0.3-1.5$) were investigated in the experiment. In the present work, calculations were carried out for the case of lateral inclination ($\gamma=45$ deg), an approach velocity of 30 m/s and various mass-flux ratios, i.e., $M=0.3-0.9$. Details on the employed grid as shown in Fig. 3(*c*), including the sensitivity tests for this case can be found in [26] and [21]. It is perhaps useful to note though that the grid stretching ratio was limited to 1.1, and the size of the grid was fixed so as to conform to y^+ ranging in the interval 0.3–3.

On the blade surface and the pipe and plenum internal walls, the employed boundary conditions were the no-slip conditions and $k=0$. On the lower wind-tunnel wall, the viscous-sublayer was bridged and wall functions were used. A uniform streamwise velocity profile was applied ($U_\infty=30$ m/s) at the inflow boundary; the Reynolds number based on D and U_∞ was Re=7950. Uniform distributions were also specified for k and ε corresponding to $T_u=0.5$ percent and $\mu_t/\mu=30$ corresponding to a length scale of about $0.5D$. Note that as in many other experiments, no information about the inlet length scales are available in this one either. Sensitivity tests have shown little effect of varying the oncoming length scale, at least in the interval $20<\mu_t/\mu<50$. Similarly, a uniform velocity profile was set at the inlet of the discharge pipe. Here also, uniform distributions of k and ε were specified, based on a turbulence intensity of $T_u=3\%$ and a length scale of $k^{3/2}/\varepsilon=0.3D$. It is important to note that the pipe was long enough ($6D$) for the flow to fully develop. In both case studies adiabatic wall conditions were employed when solving the enthalpy equation; zero gradient conditions were used at the outflow boundary, and T_∞ was specified to a small value whereas the normalized value of T_h was set equal to 0.01.

Results and Discussion

Streamwise Injection over the Flat Plate. For this test case, calculations were carried out only for $\rho_h/\rho_\infty=2$ and $M=0.5$. Weak compressibility effects were accounted for through use of the equation of state. Contours of film-cooling effectiveness η on the plate surface predicted with the TLV model are compared in Fig. 4 with the results obtained with the anisotropic variant TLVA (upper panel), and the near-wall model for turbulent Prandtl number TLVA-Pr (lower panel), respectively. Calculations with the TLVA model seem to considerably enhance the lateral spreading of the scalar field, albeit smaller values of η are obtained in the centerline of the plate. This indicates that compared to the other models TLVA shortens the reverse-flow region, as will be demonstrated later. The combination TLVA-Pr affects the overall predictions, in that the lateral spreading is further increased and the values of η in the centerline of the plate are now higher. The other model combination TLV-Pr has led to minor improvements only; the results (not shown here) were virtually comparable to those obtained from TLV calculations displayed in Fig. 4. From this analysis it clearly appears that allowing the eddy diffusivity of heat to evolve faster than that of momentum as the wall is approached may have a considerable impact on the results when employed in connection with a model accounting for near-wall turbulence anisotropy.

Contours of local film-cooling effectiveness η_L predicted with the standard two-layer model TLV and the anisotropic version TLVA in the midplane of the hole are displayed in Fig. 5. They suggest that the jet is bent over strongly right after injection, and only a small zone with low or reverse-flow velocities is formed due to the weak acceleration of the fluid. This reverse-flow region has an extent of about one hole diameter or a little more downstream of the injection hole, depending on the model employed. Calculations with the TLVA model suggest indeed that this zone is shorter than with the TLV model, confirming the previous observation in connection with Fig. 4, but more importantly, the decay of the peak temperature becomes somewhat too fast in the downstream region. This result is a consequence of enhancing the turbulent stresses in the lateral direction, as was noticed in [11] and [20]. This behavior can be further explained in the context of Fig. 6, in which the secondary-flow velocity vectors and the corresponding η-contours are plotted at two different locations; right after injection, $x/D=3$, and far downstream of the hole, $x/D=15$. Each panel represents one-half of the computational domain, since symmetry conditions were applied at the midplane. Results obtained with the standard TLV model are shown on the

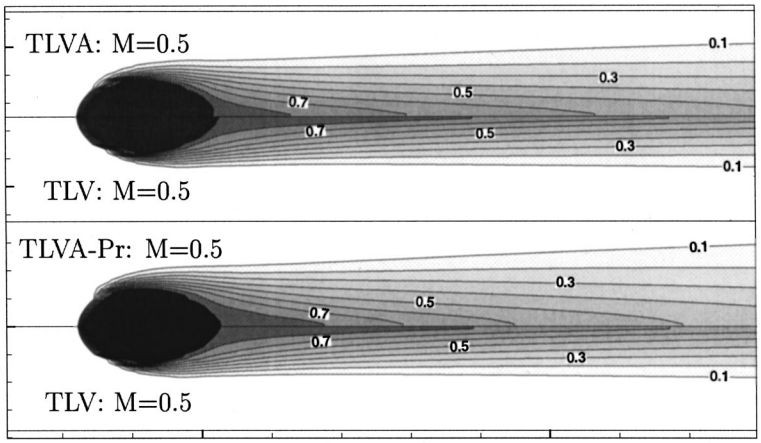

Fig. 4 Contours of wall film-cooling effectiveness η on the channel surface for $M = 0.5$: calculations with various model variants (TLV, TLVA, and TLVA-Pr)

left side of each figure, those with the TLVA variant on the right side of Figs. 6(*a*) and (*b*), and those resulting from the combination TLVA-Pr on the right side of Figs. 6(*c*) and (*d*). The system of a pair of counter-rotating longitudinal vortices (kidney vortices), typical for jets in crossflow, can be seen to establish itself in all calculations. The two vortices cause the typical, symmetrical kidney shape of the temperature contours. Near the wall the velocity is directed towards the middle of the jet ($z=0$). Note, too, that near the wall, immediately after injection ($x/D=3$), the velocity gradients $d\overline{w}/dy$ (i.e., the vorticity) are very strong, and the outer flow is directed away from the blade surface. Far downstream of the hole, however, the velocity gradients loose in strength and the outer flow is now directed towards the plate, reflecting the decay of the longitudinal vortex flow. In Fig. 6(*a*) where the TLVA correction is applied, the strength of the longitudinal vortex is reduced due to the enhanced stresses in the lateral direction, and so is the local film-cooling effectiveness η_L. This trend becomes more pronounced in the far downstream region (see Fig. 6(*b*)), where the peak temperature decays significantly. This confirms the previous result in connection with the wall and local midplane film-cooling effectiveness shown in Figs. 4 and 5 (η and η_L). Further, the TLVA variant seems to considerably enhance the near-wall lateral spreading of the jet, but it also leads to a reduction of the strength of the secondary vortices as compared to the prediction of the TLV model alone; the secondary vortex now tends to flatten further against the surface. In similar circumstances, Theodoridis et al. [20] found that the enhanced stresses in the lateral direction return results that compare reasonably well with the data. Switching on the TLVA-Pr model combining Eq. (11) together with the anisotropic correction TLVA reveals a pronounced spanwise spreading of the jet as the wall is approached (Fig. 6(*c*)). Judging from contours of η_L it seems that the thermal field in the outer flow region is also affected by introducing the correction for turbulent Prandtl number since there Pr_t is smaller than the usual value of 0.9, according to Eq. (11). It is perhaps important to note

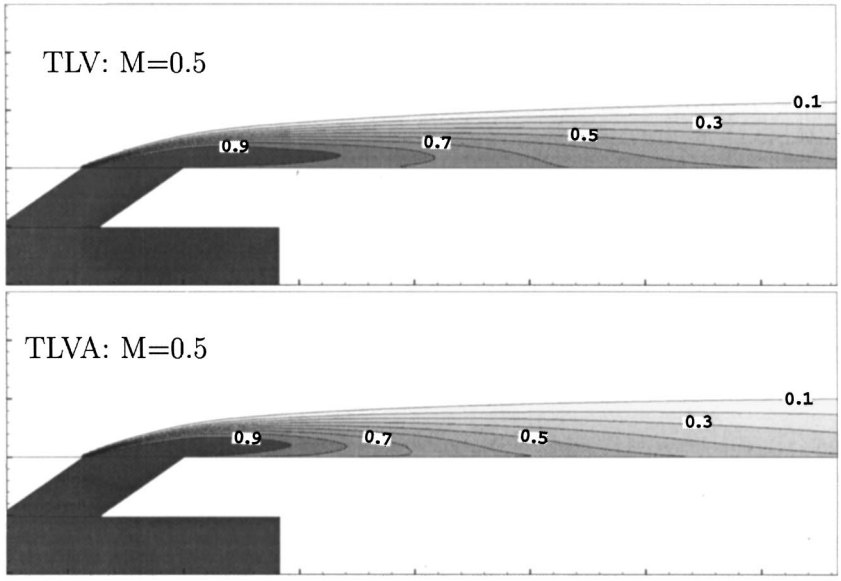

Fig. 5 Contours of local film-cooling effectiveness η_L on the symmetry plane for $M=0.5$: calculations with the TLV model and its anisotropic extension TLVA

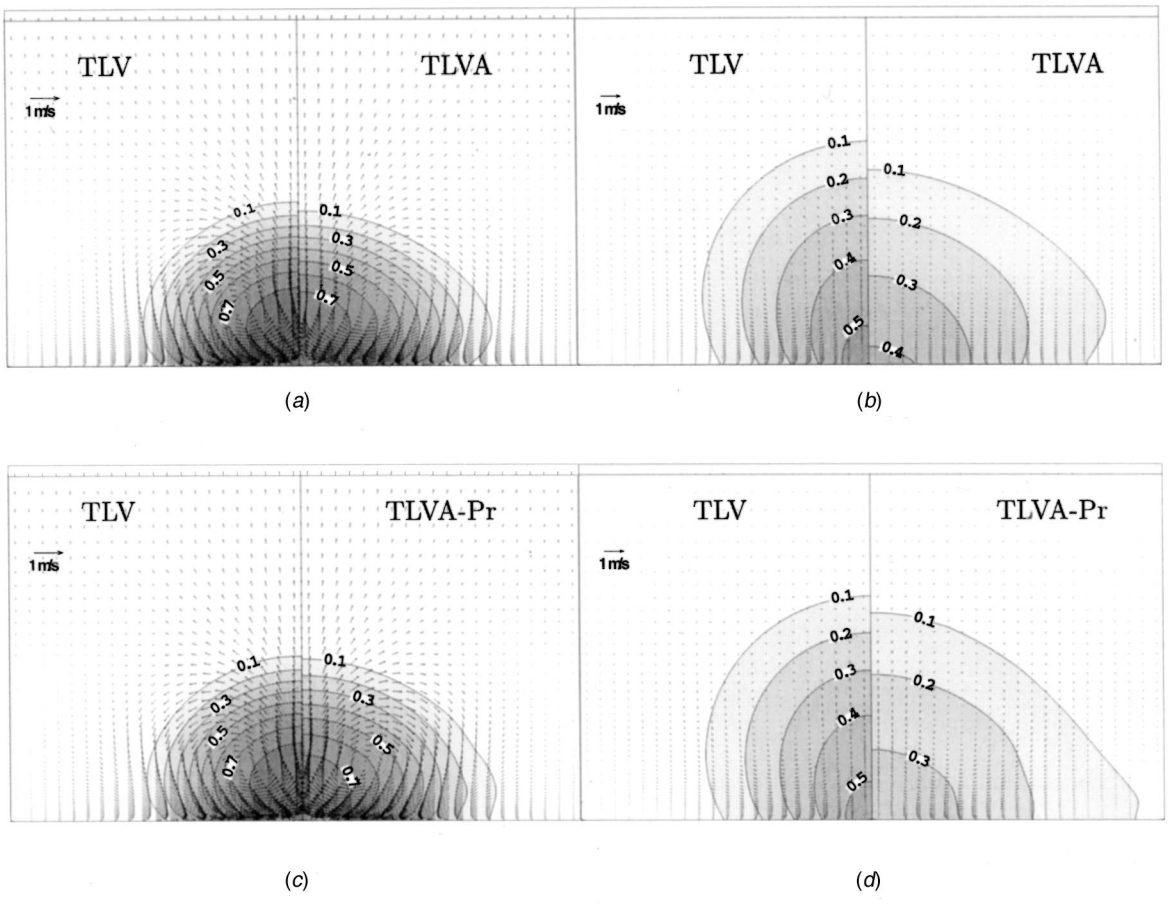

Fig. 6 Formation of the secondary vortices at different locations x/D's for $M=0.5$: calculations with various model variants (TLV, TLVA and TLVA-Pr)—(*a*) $x/D=3$, (*b*) $x/D=15$, (*c*) $x/D=3$, (*d*) $x/D=15$

that the enhanced cross spreading is more perceptible for the smallest contour-values of η_L (≈ 0.1). This indeed gives the impression that the TLVA-Pr approach exaggerates the rate of turbulent transport in that direction.

In Fig. 7, the film-cooling effectiveness η_c in the centerline of the channel (left) and the laterally averaged film-cooling effectiveness, $\langle\eta\rangle$, (right), are displayed as functions of downstream distance; results as obtained with different versions of turbulence models are compared to the measurements of Sinha et al. [25]. Using the standard TLV model without correction, η_c in the centerline is predicted too high. However, close to the injection the agreement is much better, which in itself is a major improvement as compared to previous calculations with wall functions reported by Leylek and Zerkle [9] and many others. In fact, in all other

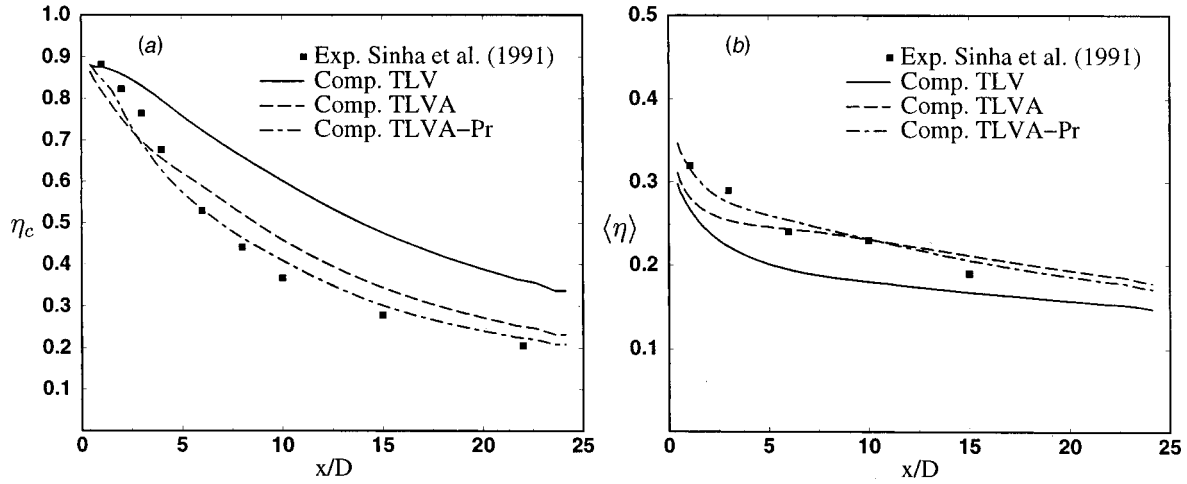

Fig. 7 Comparison of η_c, the centerline film-cooling effectiveness (*a*), and $\langle\eta\rangle$, the laterally averaged film-cooling effectiveness (*b*) for $M=0.5$: calculations with various model variants (TLV, TLVA and TLVA-Pr)

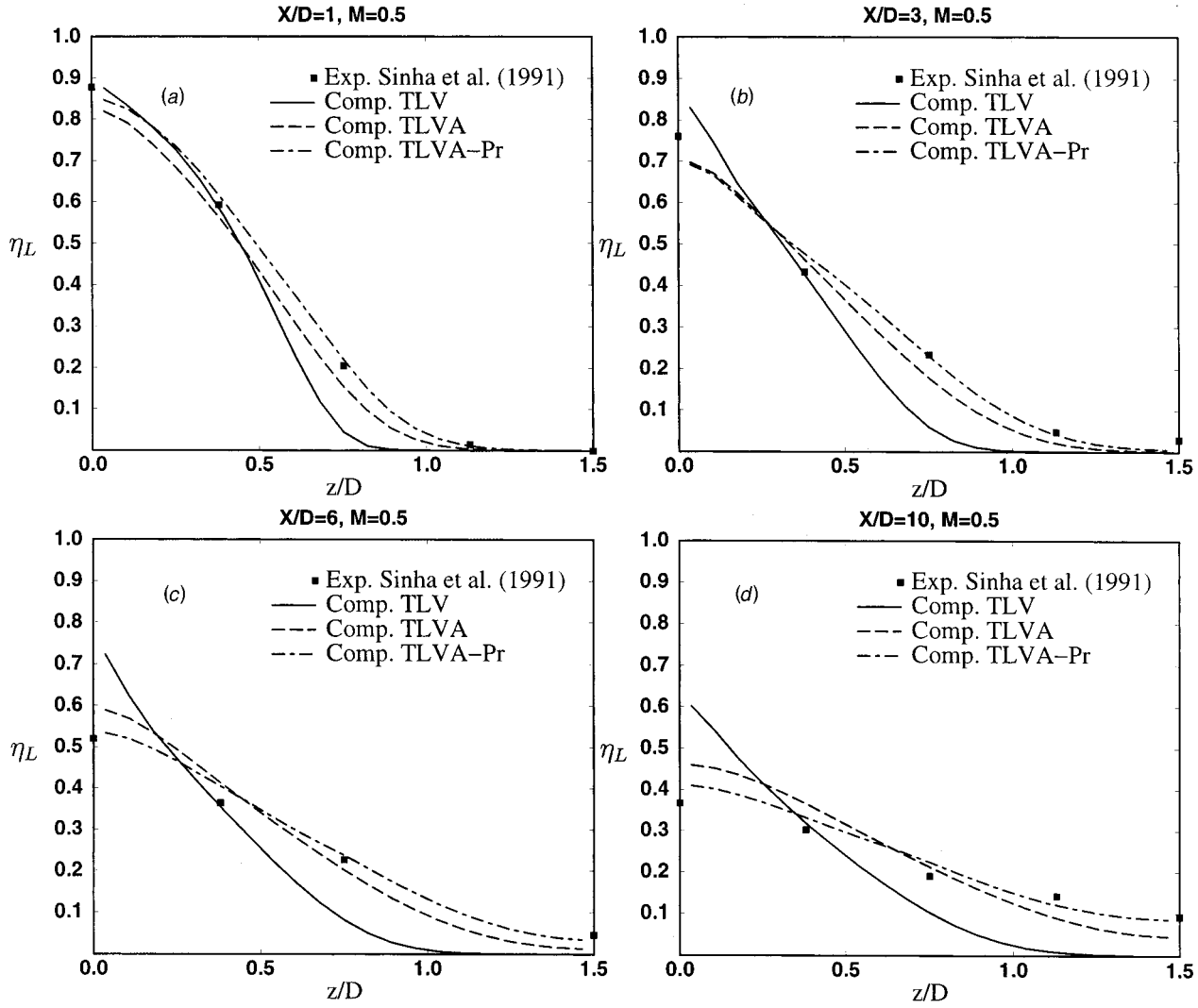

Fig. 8 Comparison of the spanwise distributions of local film-cooling effectiveness η_L for $M=0.5$: calculations with various model variants

calculations of this test case, including the aforementioned ones, the flow separation accompanying the injection was not reproduced because the viscous sublayer was not resolved. When the anisotropic correction TLVA is employed, the η_c-level moves closer to measurements near injection and further downstream of the hole. This is in line with the surface contours of η plotted in Fig. 4, where the TLVA model has led the peak temperature to evolve somewhat faster. As was to be expected, the best agreement with measurements is achieved via the combination TLVA-Pr. Looking now at the neighboring figure confirms the earlier result: the laterally averaged film-cooling effectiveness $\langle\eta\rangle$ is best predicted by a combination of the anisotropy correction for μ_t with the model for Pr_t. Another major performance of this model combination is the correct prediction of the peak temperature (either via η_c or $\langle\eta\rangle$) right after the discharge hole; this clearly indicates that the prediction of the reverse-flow region heavily relies on the way the turbulent Prandtl number varies across the sublayer. This is somewhat intriguing, since the DNS-based relation (Eq. (11)) was developed for attached flows only. The grossly overpredicted η_c-level on the axis by the TLV model, together with the underpredicted $\langle\eta\rangle$ field clearly indicates that the model fails to predict the spreading in the lateral direction. This leads to the following remark: frequently, when studying this class of flow comparison with experiment is restricted to the distribution of the laterally averaged cooling effectiveness $\langle\eta\rangle$; the results may then be misleading and must therefore be seen as the consequence of a compensation effect of η being predicted too high near the axis, but not spreading sufficiently in the lateral direction.

The spanwise distributions of η on the blade surface are plotted in Fig. 8 at $x/D=1$, 3, 6, and 10. TLV calculations show significant deviations from the measurements already in the range $z/D=0.5-0.7$. Close to the discharge hole ($z/D=0$), the peak temperature is also severely overpredicted, except at the first plane $x/D=1$. The correction applied to the turbulent cross heat-flux tends to considerably increase the lateral spreading of the scalar field, bringing it closer to the data. But once again the combination TLVA-Pr results in the best prediction for η_L, both near the axis and towards the outer plane $z/D=1.5$. Note that for this blowing rate and for higher ones, calculations with wall functions have already shown significant deviations from the measurements [9]. As was to be expected, applying Eq. (11) together with the isotropic TLV model resulted only in minor changes in the heat transport as compared to the significant improvements obtained by use of TLVA-Pr. The explanation derives from promoting (twice) the lateral heat flux via the thermal diffusivity coefficient Γ_3^θ by the conjugate effects of the anisotropy factor γ and Eq. (11).

Lateral Injection Over the Turbine Blade Model. Lateral injection takes place at an angle of $\gamma=45$ deg to the x-axis. Figure 9 displays the velocity vectors in the midplane through the hole

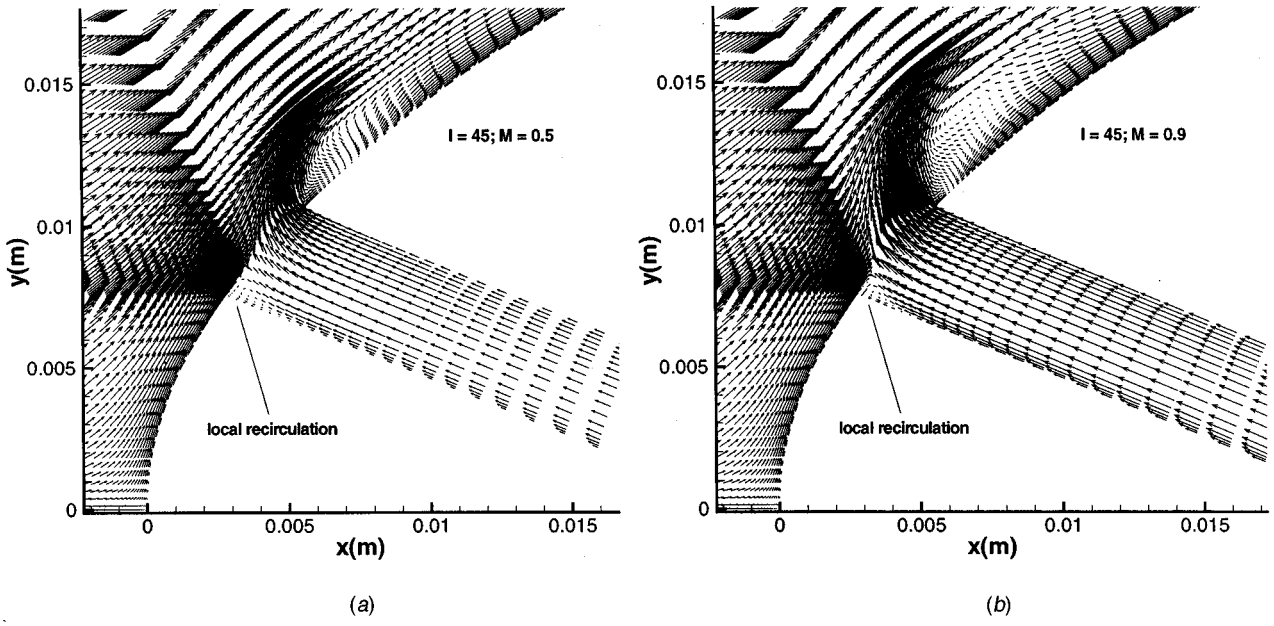

Fig. 9 Velocity vectors in mid-plane through injection hole for $M=0.5$ and 0.9: calculations with the TLV model

for the blowing rates $M=0.5$ and 0.9 as calculated with the two-layer model with extended anisotropic modification TLVA. At the medium blowing rate of $M=0.5$, the jet bends over quickly and there is only a small reverse-flow region adjacent to the wall extending to about $0.7D$ downstream of the injection hole. At the higher blowing rate of $M=0.9$ the picture is quite different and also differs from the flow established in the streamwise injection case reported in [21]. Now the reverse flow underneath the bent-over jet develops further away from the wall; reverse flow near the wall occurs only down to about $0.2D$ from the trailing edge of the hole. Beyond this point the near-wall flow has wall-jet behavior (comprised of mainstream gas), which then develops into a boundary layer further downstream. For both blowing rates, the high near-wall resolution leads to the development of a local recirculation region inside the discharge channel near the leading edge of the injection hole. In reality, the flow inside the discharge pipe is subjected to a turning effect starting from the plenum, which is known to cause the jetting effect at the delivery; the flow separation following the injection is, however, not systematically induced by the this turning effect. In the present study the plenum was not included (Haslinger and Hennecke did not provide any information on the flow in the discharge pipe nor a detailed description of the geometry of the plenum-pipe injection system), and this may have led to a misrepresentation of the exact jetting conditions. But since the pipe was long enough, the flow could have recovered the developed flow conditions before ejection.

For blowing rates $M=0.5$ and 0.7, Fig. 10 compares contours of the adiabatic film-cooling effectiveness η calculated with the standard TLV model, its anisotropic version TLVA, and the combinations TLV-Pr and TLVA-Pr to the measurements. This comparison is aimed at separating the effect introduced by the anisotropic correction (via γ) from that induced by Eq. (11). In this and the following figures on film-cooling effectiveness, the curvilinear abscissa s is the length measured along the blade surface from the stagnation point. In this case of lateral injection, the contours are no longer symmetrical with respect to the $z=0$-axis, but are shifted in the direction of injection. The trajectory of the jet, running along the peaks of each contour, is first inclined with respect to the $z=0$ axis, but further downstream it runs approximately parallel to this axis. This behavior is in general well reproduced by the calculations. Lakehal et al. [21] report that when employing the k-ϵ model with wall functions for this configuration and for the one with streamwise injection, the spreading of the temperature and the decay of the effectiveness in the core region were predicted significantly too small. They have also shown that using the two-layer model variant of Rodi [22] leads systematically to some improvement vis-à-vis the results obtained with wall functions, but not sufficiently to match the data.

For the lowest blowing rate of $M=0.3$ the TLV model (results not included here) was found to fail to capture the lateral extension of the scalar and to overpredict the peak values along the jet axis. With the extended anisotropic correction TLVA the calculation yielded realistic lateral spreading, but a somewhat too rapid decay of η so that $\langle\eta\rangle$ was again a little low, as can be seen from Fig. 11. This confirms possible misleading conclusions for $\langle\eta\rangle$ as remarked previously: the fast decay of η in the jet axis can be compensated by the enhanced lateral spreading. Results for medium blowing rate $M=0.5$ displayed in Fig. 10(a) show the TLV calculations to severely underpredict the spreading in the spanwise direction and to overpredict the peak values along the jet axis, worse than for blowing rate of $M=0.3$. Calculations with the TLVA model not only remedy the lack of spanwise spreading, but also predict reasonably well the decay of η far downstream of the injection location ($s>60$ mm). However, the decay of heat transfer is still somewhat overpredicted in the centerline between the hole and location $s=60$ mm. The rate of lateral spreading is only slightly affected by use of the TLV-Pr model, which also misrepresents the decay of heat in the centerline as was the case with the standard TLV variant. Combining now the TLVA approach with Eq. (11) (TLVA-Pr) yields the best agreement with the data, including the peak levels along the jet axis. The case with the higher blowing rate of $M=0.7$ is displayed in the neighboring panel. Both the lateral spreading of the temperature field and the decay of η in the core region are much better predicted with TLVA than with TLV shown on the upper panel. TLV-Pr performance is again similar to TLV, but for this blowing rate a slight improvement in the spreading can be perceptible at the lateral boundary. In fact, the implications of Eq. (11) on the results become more evident with increasing blowing rate, be it employed within the isotropic or the anisotropic eddy-viscosity model. The reason for this is that with increasing mass-flow rate the jet penetrates deeper into the core flow, in which case hot streams are pumped towards the wall enhancing near-wall temperature gradients. In this circumstance the transport of heat by turbulent motion further enhances in the

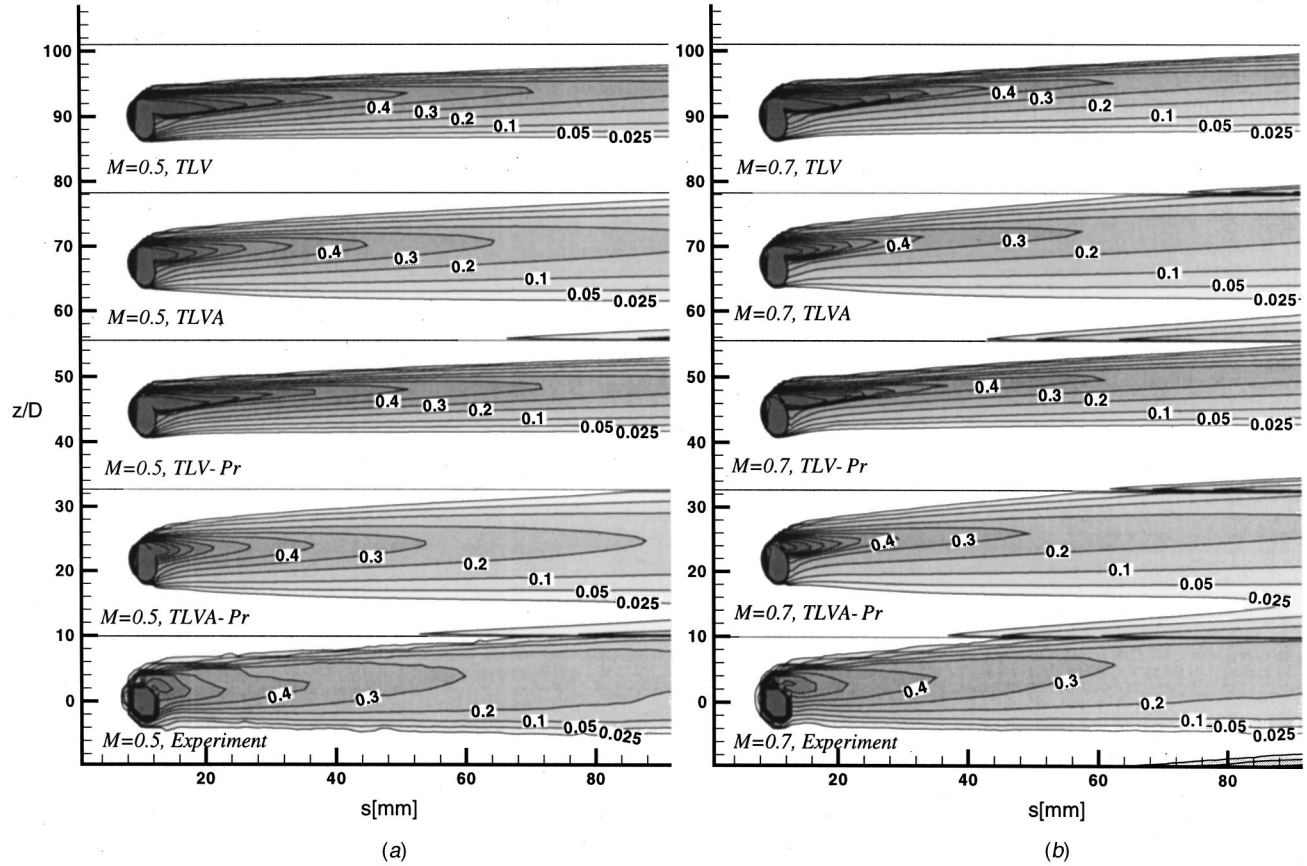

Fig. 10 Contours of film-cooling effectiveness for $M=0.5$ and 0.7: calculations with various model variants

crossflow direction via the flux $\overline{w'\theta} = -\Gamma_3^\theta \partial T/\partial z$. Calculations with TLVA-Pr yield significant spreading (judging in particular from η-contours around the lateral boundaries) in the cross direction at the expense of a shorter heat decay along the jet axis. This can be interpreted as a compensation effect between the streamwise and lateral turbulent heat transport.

Finally, Fig. 11 compares predicted distributions of the laterally averaged film-cooling effectiveness $\langle\eta\rangle$ to the measurements for blowing rates of $M=0.3$, 0.5, 0.7 and 0.9. Results of TLV-Pr combination are not included for comparison. In Fig. 11(*a*) results obtained for the lowest blowing rate of $M=0.3$ are compared against experiments. Calculations with both the TLV model alone and its anisotropic variant TLVA deliver virtually the same results, except in the region behind the injection where the anisotropic correction seems to play a countereffect. In all cases $\langle\eta\rangle$ is predicted too low, especially in the intermediate region where $s/D<35$. A semblance of agreement between calculations and measurements starts to emerge only at that location and above. The performance of the TLVA model for this low blowing rate is now confirmed: the enhanced lateral spreading is hidden by the fact η decays prematurely near the axis. Introducing now the near-wall model for Pr_t together with TLVA leads to only a slight improvement in the downstream region, but near the discharge hole the performance of the model is rather excellent, judging from the peak temperature which is correctly predicted. For the blowing rate of $M=0.5$, Fig. 11(*b*) shows that when resorting to TLVA, $\langle\eta\rangle$ is calculated much too small near the discharge hole as compared to the standard model, but the tendency is inverted in the intermediate and downstream regions where the level of $\langle\eta\rangle$ is now approaching the measured one. With the combination TLVA-Pr the correct shape of the distribution is predicted and altogether the results are the most realistic ones, except that the level is still underpredicted. Note, again, that the model predicts the correct peak temperature right behind the injection which has so far been out of reach of other sophisticated turbulence models. The third and fourth panels 11(*c*) and (*d*) show predictions for higher blowing rates $M=0.7$, 0.9. It can be seen that with the standard TLV model, the agreement with the measurements improves with decreasing M: $\langle\eta\rangle$ is significantly underpredicted in the intermediate region behind the injection hole, but reaches levels close to the measurements further downstream, as was explained above in connection with the contours. Using the TLVA variant leads to significant improvements in the intermediate region, but there the level remains somewhat underpredicted as compared to the data. Calculations with the TLVA-Pr model yield fairly good accord with the measurements over the whole range, including the peak level of $\langle\eta\rangle$ in the reverse-flow region.

The final conclusion to be drawn from the foregoing discussion is that in the isotropic two-layer model, agreement with measurements deteriorates with increasing M; with the anisotropic version the predictions are better for the higher blowing rates ($M>0.5$), and the same is true of the combination TLVA-Pr. Indeed, judging from the secondary velocities shown in Fig. 6 (for the first test case), the jet-induced secondary vortices lift off the blade surface further with increasing M, pushing the ambient gas underneath them, which in turn deteriorates the film-cooling effectiveness. Applying the anisotropic eddy-viscosity model tends to reduce the strength of these symmetrical vortices by flattening them towards the surface which improves the prediction of $\langle\eta\rangle$; but the utility of this measure is positive only in the attached-flow regions. An objective conclusion regarding the performance of the DNS-based model for the turbulent Prandtl number is that either the heat

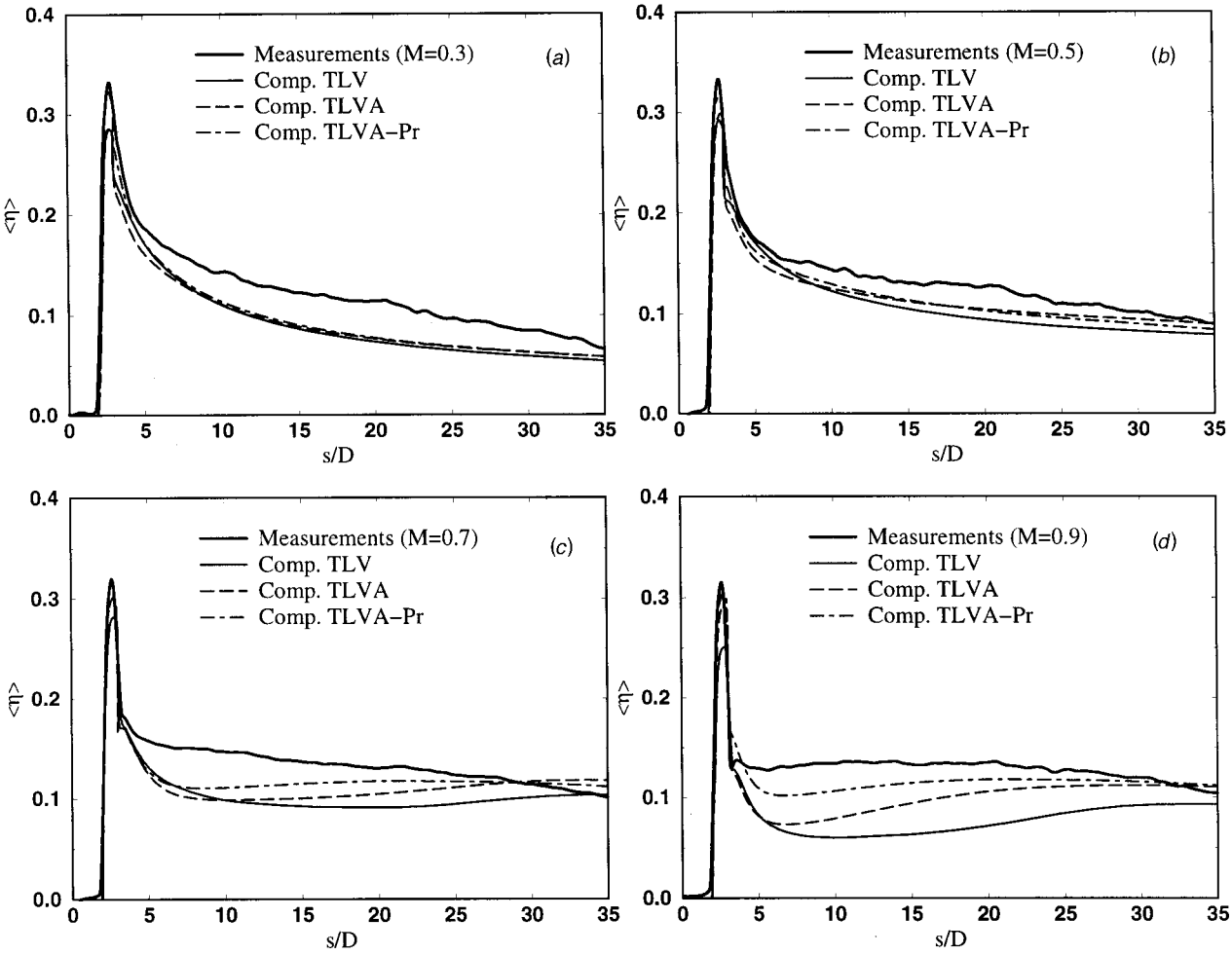

Fig. 11 Laterally averaged film-cooling effectiveness for various *M*'s: calculations with various model variants

diffusivity is really faster than that of momentum as the wall is approached, in which case the obtained results are justifiable, or the measure is *heuristic* and constitutes nothing but a compensation effect. Judging from the results obtained for the flat plate in particular, the author believes that there is a bit of truth in Eq. (11), but there is an obvious need to clarify this issue. Further DNS data need to be provided.

Conclusions

The aim of the work presented in this paper is to contribute to the development of a robust and accurate predictive strategy for calculating the flow and heat transfer in film-cooling situations on turbine blades. Emphasis was primarily placed on the development of a physical model capable of dealing with the strong anisotropy of turbulence across the boundary layer. Furthermore, owing to prevailing doubts about the way the eddy diffusivities of heat and momentum evolve within the sublayer, use was made of DNS data in order to derive information for the development of a model for the turbulent Prandtl number. In summary, the models used to simulate the turbulent momentum and heat exchange processes included a two-layer version resolving the viscous sublayer with a DNS-based one-equation model known as TLV, a second model variant accounting for the anisotropy of turbulent exchange, also based on the same DNS data, referred to as TLVA, and a final model inferring the near-wall evolution of the turbulent Prandtl number from other DNS data. This latter approach was employed together with TLV and TLVA. The incorporation of the model into a general-purpose CFD code is possible but would require some efforts. For instance, in some commercial packages such as CFX-Tascflow, the two-layer approach (e.g., the TLK variant of Rodi) is now offered as an alternative modeling route to pure low-Re number models.

Film cooling was calculated for a flat plate with streamwise cooling-air injection and a symmetrical turbine blade with lateral injection; in the latter configuration, coolant air was injected from one row of holes placed on each side of the leading edge. For injection over the flat plate, calculations were extended to the injection pipe and the plenum. For the blade prototype, the flow and temperature fields were simulated around the blade and inside the injection channels. A flexible three-dimensional finite-volume method on multiblock curvilinear grids was employed, and high-order discretization schemes were used to reduce numerical errors. This class of flow is quite complex, and accurate predictions of the flow and heat transfer are difficult to achieve, particularly in the near field of the injected jet, i.e., the growth and separation of the boundary layer developing on the surface and the jet-induced vortices. An extremely high level of accuracy is thereby required, otherwise models of higher complexity may be of little advantage, as was recently revealed by Azzi and Lakehal [12], who tested various explicit algebraic stress models.

The flow field and its dependence on the blowing rate and injection angle were overall reasonably well predicted; finer details were already well resolved by the isotropic two-layer model. With this model, most of the pertinent physical mechanisms associated with jets in crossflow were also well predicted, including the

injection-induced secondary-flow vortices. A quantitative validation of the flow structure was not possible due to the absence of measurements. However, for other situations like film cooling of a similar nonsymmetrical blade [20] and of a flat plate [11] reasonable agreement with measurements was obtained for the flow field. Calculations of film cooling of the symmetrical blade show that the thermal field is more difficult to predict. The basic evolution is, however, simulated correctly and so is the influence of the blowing rate. The two-layer k-ε model was found to severely underpredict the lateral spreading of the temperature field, together with an exaggerated size of the kidney vortices. As a consequence, the laterally averaged film-cooling effectiveness is generally too low. The discrepancies with the measurements on the blade surface become more evident with increasing blowing rate. The DNS-based anisotropy model promoting the turbulent cross stresses brings overall significant improvements, but the best results are obtained when this approach is employed in connection with the DNS-based near-wall model for turbulent Prandtl number. Since both of the empirical relations for momentum/heat transport and turbulent Prandtl number depend on the wall distance, the near-wall grid clustering has to be appreciably refined so as to capture scales up to $y^+ \approx 1.5$. This is the reason why results of film cooling of the flat plate appear to be generally better than those of the real turbine blade.

Acknowledgments

This work is in part a continuation of an earlier project (TURBOTHERM) started while the author was affiliated with the University of Karlsruhe (Institute for Hydromechanics). The calculations were carried out on the Cray SV1-B/16-8 computer of the ETH Zurich. The author is grateful to Dr. A. Azzi for having made his channel flow data available, and to Dr. Haslinger (University of Darmstadt, Germany) for the experimental data.

Nomenclature

D = diameter of discharge pipe
k = turbulent kinetic energy
L = length scale of turbulence
M = mass-flux ratio $=(\rho_h U_h)/(\rho_\infty U_\infty)$
Pr_t = turbulent Prandtl no.
R_y = near-wall or turbulent Reynolds no. $=y_n\sqrt{k}/\nu$
S_{ij} = strain tensor $=(\overline{u}_{i,j}+\overline{u}_{j,i})/2$
T = temperature
T_u = freestream turbulence level
$\overline{u}_i$ = averaged velocity components
u_i' = fluctuating velocity components
u_τ = friction velocity $=\sqrt{\tau_w/\rho}$
x,y,z = Cartesian coordinates
y_n = normal wall distance
y^+ = dimensionless wall distance $=\rho y\sqrt{\tau_w/\rho}/\mu_l$
δ = boundary layer thickness
ε = dissipation rate of turbulent kinetic energy
η = wall film-cooling effectiveness $=(T_w-T_\infty)/(T_h-T_\infty)$
η_L = local film-cooling effectiveness $=(T-T_\infty)/(T_h-T_\infty)$
η_c = film-cooling effectiveness in centerline of cooled surface
$\langle\eta\rangle$ = laterally averaged wall film-cooling effectiveness
γ = compound angle pipe axis/blade symmetry axis
Γ_j/Γ_j^ϕ = turbulent transport coefficients
κ = von Karman constant
$\ell_\mu/\ell_\varepsilon$ = length scales in one-equation model
μ = molecular viscosity
μ_t = turbulent viscosity
ρ = density
σ's = Prandtl nos.
θ = fluctuating temperature
τ_w = wall friction
ϕ = general dependent variable

Subscripts

∞ = freestream
c = centerline
h = jet
pln = plenum
w = wall

References

[1] Acharya, S., Tyagi, M., and Hoda, A., 2001, "Flow and Heat Transfer Predictions for Film Cooling," Ann. N.Y. Acad. Sci., **934**, pp. 110–125.
[2] Haven, B. A., and Kurosaka, M., 1997, "Kidney and Anti-Kidney Vortices in Crossflow Jets," J. Fluid Mech., **352**, pp. 27–64.
[3] Haslinger, W., and Hennecke, D. K., 1997, "High Resolved Distribution of Adiabatic Film Cooling Effectiveness for Turbine Leading Edge Film Cooling," ISABE Paper No. 97-7113.
[4] Ligrani, P. M., Wigle, J. M., and Jackson, S. W., 1994, "Film-Cooling from Holes with Compound Angle Orientations: Part 2—Results Downstream a Single Row of Holes with 6d Spanwise Spacing," ASME J. Heat Transfer, **116**, pp. 353–362.
[5] Mehendale, A. B., and Han, J. C., 1992, "Influence of Mainstream Turbulence on Leading Edge Film Cooling Heat Transfer." ASME J. Turbomach., **114**, pp. 707–715.
[6] Ardey, S., 1998, "3D-Messung des Stroemungsfeldes um die filmgekuehlte Vorderkante einer Referenzschaufe," Abschlussbericht zum TURBOTHERM II-Verbundvorhaben 2.1.8.4 der Arbeitsgemeinschaft Hochtemperatur Gasturbine, Report LRT-Inst. 12-98/02, Universität der Bundeswehr Münich, Germany.
[7] Beeck, A, 1992, "Stroemungsfelduntersuchungen zum aerodynamischen Verhalten eines hochbelasteten Turbinengitters mit Kuehlluftausblasung an der Vorderkante," Ph.D thesis, Universität der Bundeswehr Munich, Institut fuer Strahlantriebe, Germany.
[8] Findlay, M. J., Salcudean, M., and Gartshore, I. S., 1999, "Jets in a Crossflow—Effects of Geometry and Blowing Ratio," ASME J. Fluids Eng., **121**, pp. 373–378.
[9] Leylek, J. H., and Zirkle, R. D., 1994, "Discrete-Jet Film Cooling: A Comparison of Computational Results with Experiments," ASME J. Turbomach., **116**, pp. 358–368.
[10] Walters, K. D., and Leylek, J. H., 1997, "A Detailed Analysis of Film-Cooling Physics, Part 1: Streamwise Injection with Cylindrical Holes," ASME Paper No. 97-GT-269.
[11] Lakehal, D., Theodoridis, G., and Rodi, W., 1998, "Computation of Film Cooling of a Flat Plate by Lateral Injection from a Row of Holes," Int. J. Heat Fluid Flow, **19**, pp. 418–430.
[12] Azzi, A., and Lakehal, D., 2002, "Perspectives in Modeling Film Cooling of Turbine Blades by Transcending Conventional Two-Equation Turbulence Models," ASME J. Turbomach., **124**, July, pp. 472–484.
[13] Garg, V. K., and Abhari, R. S., 1997, "Comparison of Predicted and Experimental Nusselt Number for a Film Cooled Rotating Blade," Int. J. Heat Fluid Flow, **18**, pp. 452–460.
[14] Ferguson, D. J., Walters, K. D., and Leylek, J. H, 1998, "Performance of Turbulence Models and Near-Wall Treatments in Discrete Jet Film Cooling Simulations," ASME Paper No. 98-GT-438.
[15] Garg, V. K., and Ameri, A. A., 1997, "Comparison of Two-Equation Turbulence Models for Prediction of Heat Transfer on Film-Cooled Turbine Blades," Numer. Heat Transfer, Part A, **31**, pp. 347–371.
[16] Bohn, D. E., Becker, V., Kusterer, K., Ardey, S., and Fottner, L., 1997, "The Influence of Slot Injection and Shower-Head Injection on the 3D Flow Field of a Film-Cooled Turbine Blade under Consideration of Side-Wall Effects," AIAA Pap., No. 97/7162.
[17] Irmisch, S, 1995, "Simulation of Film-Cooling Aerodynamics with a 2-D Navier-Stokes Solver using Unstructured Grids," ASME Paper No. 95-GT-024.
[18] Theodoridis, G., and Rodi, W., 1999, "Calculation of the Flow Around a High-Pressure Turbine Blade with Cooling-Jet Injection from Slots at the Leading Edge," Flow, Turbul. Combust. **62**, pp. 89–110.
[19] Vogel, D. T., 1993, "Numerische Untersuchung des Mischungsverhaltens von Filmkühlstrahlen in Turbinenströmungen," Ph.D thesis, Ruhr-Universität Bochum, Germany.
[20] Theodoridis, G., Lakehal, D., and Rodi, W., 2001, "3D Calculations of the Flow Field Around a Turbine Blade with Film Cooling Injection Near the Leading Edge," Flow, Turbul. Combust., **66**, pp. 57–83.
[21] Lakehal, D., Theodoridis, G., and Rodi, W., 2001, "Three Dimensional Flow and Heat Transfer Calculations of Film Cooling at the Leading Edge of a Symmetrical Turbine Blade Model," Int. J. Heat Fluid Flow, **22**, pp. 113–122.
[22] Rodi, W., 1991, "Experience with Two-Layer Models Combining the k-ε Model with a One-Equation Model Near the Wall," AIAA Pap. No. 91-0216.
[23] Kaszeta, R. W., and Simon, T. W., 2000, "Measurement of Eddy Diffusivity of Momentum in Film Cooling Flows with Streamwise Injection," ASME J. Turbomach., **122**, pp. 178–183.
[24] Bergeles, G., Gosman, A. D., and Launder, B. E., 1978, "The Turbulent Jet in a Cross Stream at Low Injection Rates: a Three-Dimensional Numerical Treatment," Numer. Heat Transfer, **1**, pp. 217–242.
[25] Sinha, A. K., Bogard, D. G., and Crawford, M. E., 1991, "Film-Cooling Ef-

fectiveness Downstream of a Single Row of Holes with Variable Density Ratio,'' ASME J. Turbomach., **113**, pp. 442–449.
[26] Rodi, W., Theodoridis G., and Lakehal, D., 1997, ''Entwicklung eines geeigneten Turbulenz- und Waermeuebergangsmodells fuer ein 3D Berechnungsverfahren der Filmkuehlung an der Schaufelvorderkante,'' Abschlussbericht Institut fuer Hydromechanik, University of Karlsruhe.
[27] Norris, L. H., and Reynolds, W. C., 1975, ''Turbulent Channel Flow with a Moving Wavy Boundary,'' Report No. FM-10, Stanford University, Department of Mechanical Engineering.
[28] Rodi, W., Mansour, N. N., and Michelassi, V., 1993, ''One-Equation Near-Wall Turbulence Modeling with the Aid of Direct Simulation Data,'' ASME J. Fluids Eng., **115**, pp. 196–205.
[29] Gilbert, N., and Kleiser, L., 1991, ''Turbulence Model Testing with the Aid of Direct Numerical Simulation Results,'' Proc., 8th Symposium on Turbulent Shear Flows, Paper No. 26-1, Munich, Germany, September 9–11.
[30] Quarmby, A., and Quirk, R., 1974, ''Axisymmetric and Non-Axisymmetric Turbulent Diffusion in a Plain Circular Tube at High Schmidt Number,'' Int. J. Heat Mass Transf., **17**, p. 143.
[31] Kim, J., Moin, P., and Moser, R., 1987, ''Turbulence Statistics in Fully Developed Channel Flow at Low Reynolds Number,'' J. Fluid Mech., **177**, pp. 133–166.
[32] Kays, W. M., and Crawford, M. E., 1993, *Convective Heat and Mass Transfer*, Third Edition, McGraw-Hill, New York, NY.
[33] Lu, D. M., and Hetsroni, G., 1995, ''Direct Numerical-Simulation of a Turbulent Open-Channel Flow with Passive Heat-Transfer,'' Int. J. Heat Mass Transf., **38**, pp. 3241–3258.
[34] Madavan, N. K, and Rai, M. M., 1995, ''Direct Numerical-Simulation of Boundary Layer Transition on a Heated Flat Plate with Elevated Freestream Turbulence,'' AIAA Pap. No. 95-0771.

Flow Characteristics in Two-Leg Internal Coolant Passages of Gas Turbine Airfoils With Film-Cooling Hole Ejection

D. Chanteloup
e-mail: denis.chanteloup@epfl.ch

A. Bölcs
Mem. ASME

Ecole Polytechnique Fédérale
de Lausanne (EPFL),
Laboratoire de Thermique appliquée
et de Turbomachines (LTT),
1015 Lausanne, Switzerland

A study of flow in two stationary models of two-pass internal coolant passages is presented, which focuses on the flow characteristics in the 180-deg bend region, and downstream of the bend, where the flow is redeveloping. A stereoscopic digital PIV system measured all three velocity components simultaneously to obtain mean velocity, and turbulence quantities of the flow field. The coolant passage model consisted of two square passages, each having a 20 hydraulic diameter length, separated by a rounded-tip web of 0.2 passage widths, and connected by a sharp 180-deg bend with a rectangular outer wall. Ribs were mounted on the bottom and top walls of both legs, with a staggered arrangement, and at 45 deg to the flow. The rib height and spacing were 0.1 and 1.0 passage heights, respectively. The measurements were obtained for a flow condition, with a Reynolds number of 50,000. The geometries are similar in both sections except for one, which is equipped with extraction holes to simulate holes for film cooling. Two series of holes are placed solely in the bottom wall, four holes are located in the bend, and 12 in the downstream leg. The global extraction through the holes was set to 50% of the inlet massflow. This paper presents new measurements of the flow in the straight legs, as well as in the bend of the passage equipped with holes, detailed comparison of the flow upstream, inside and downstream of the bend region between both configurations, and the effects of extraction inside the cooling channels. [DOI: 10.1115/1.1480412]

Introduction

For the design of cooled gas turbine blades, a detailed knowledge of the physical phenomena in the passage is necessary. Although CFD simulations can provide a better understanding of these phenomena, the numerical heat transfer predictions are not yet sufficiently accurate for design purposes. To improve the performance of the CFD codes, a validation of the predictions is necessary and detailed measurements of the flow structure in the passages are required for comparison (see Rowbury et al. [1]).

Several studies described flow characteristics in idealized geometries of internal cooling channels. Rau et al. [2] showed the 3-D flow, and the impinging secondary flow effects on the heat transfer distribution in a straight channel with 90-deg inclined ribs. They showed that the secondary flow pattern strongly determines the hot spots and cold spots in the channel. Schabacker [3] determined the rib presence and rib angle effects on the streamwise flow in 2-pass internal cooling channels. He also described the strong impact of the ribs on the secondary flow field. Chanteloup and Bölcs [4] studied the flow characteristics in a similar channel, with different rib locations. This geometry is the baseline case of the present study. Bons and Kerrebrock [5] gave flow results in a straight smooth rotating channel, measured with PIV. They showed the effect of both Coriolis acceleration and buoyancy, on the smooth channel flow characteristics.

Heat transfer data in internal coolant channels with film cooling extraction is also of great importance to the design of a cooling system. Byerley et al. [6] measured local heat transfer coefficients around the entrance to a normal hole. They reported considerable heat transfer coefficient variations (six times the plain duct local value) around the entrance. Shen et al. [7] noted that in presence of normal ribs, the heat transfer in the vicinity of the holes was increased by about 25%. Although detailed heat transfer measurements in coolant channels with film-cooling holes are available in the literature, the flow in such ducts has not been described to the authors knowledge.

In the present study, the particle image velocimetry (PIV) method was employed for the investigation of the flow field in models of a stationary two-pass coolant passage. The out-of-plane motion of the tracers (perpendicular to the light sheet plane) produces a systematic measurement error depending on the distance from the optical axis, e.g., Lourenco [8]. This measurement error can be avoided by using a stereoscopic PIV setup (Prasad and Adrian [9], Westerweel and Nieuwstadt [10]). A stereoscopic digital PIV system, based on the angular displacement method, was used for the present investigation (Schabacker and Bölcs [11]). This PIV system is capable of simultaneously measuring all three velocity components. Subsequently, an ensemble average of the velocity data in identical spatial windows is calculated to determine the mean and fluctuating velocity field.

This paper presents initial results from the Brite-Euram project for Internal Cooling of Turbine Blades (ICTB) measured with a PIV system. The objective of Chanteloup and Bölcs [4] was to present results in a base configuration and to determine the influence of the rib placement in the near bend regions on the flow fields upstream, inside, and downstream of the bend, and to provide new measurements of developed flow between ribs. The specific objectives of the present paper are to determine the influence of a flow extraction through simulated film-cooling holes in the vicinity of the cooling channel 180-deg turn. It must be noted that the rotational effects (see Johnson et al. [12]), as well as the thermal boundary effects (see Han et al. [13], Zhang et al. [14]), are not considered in the present study. Although these effects are potential major effects for actual turbine design, the present study concentrates on giving valuable information and insight for CFD validation.

Contributed by the International Gas Turbine Institute for publication in the JOURNAL OF TURBOMACHINERY. Manuscript received by the IGTI, June 2001; revised manuscript received March 6, 2002. Associate Editor: R. S. Bunker.

Experimental Setup

Test Facility. A sketch of the test section is shown in Fig. 1. Air was the working medium and was supplied by a continuously running compressor. The air enters the settling chamber with an inner diameter of 600 mm via a 150-mm tube and a conical entrance section with an angle of 30 deg. The settling chamber is equipped with a combination of perforated plates, honeycombs and meshes to reduce unsteadiness and swirl in the flow. A bell mouth entry leads the air from the settling chamber to the test channel.

Both studied configurations have the same inner geometry characteristics. The baseline configuration test section is a two-pass, cooling passage model of a gas turbine blade. The flow path in the downstream and upstream passages has a cross section of 100 mm$\times$100 mm with a corresponding hydraulic diameter, $D_H = 100$ mm, and a length of $20D_H$. The outer walls of the test section are made of 5-mm-thick extruded Plexiglas to obtain good optical properties for the PIV experiment. In the straight-corner bend, the clearance between the tip of the divider plate and the outer wall is equal to 1 D_H. The thickness of the divider plate or web between the two passages is $0.2D_H$. The tip of the divider plate is cylindrically shaped with a $0.1D_H$ radius. Square ribs with an angle of 45 deg to the passage centerline, rib heights of 0.1 hydraulic diameters ($e/D_H = 0.1$), and rib spacing of 10 rib heights ($P/e = 10$) are mounted in a staggered arrangement on the top and bottom wall of the passage. The ribs in the bend region and the dimensions of the bend are shown in Fig. 1. Eighteen ribs are mounted on the top and bottom walls in both the upstream and downstream passages of the model (18*4). The second configuration also called the *hole* configuration, has two series of holes for film-cooling simulation. The total mass flow through 16 holes is 50% of the mass flow in the test model. The high extraction massflow was chosen to investigate the influence of holes on the flow. It has been chosen to place 16 holes solely in the bottom wall, with a hole pitch to hole diameter ratio of 6. The first series of holes is placed in the bend region, $0.2D_H$ from the end wall to simulate tip blade film cooling. Four $0.073D_H$-diameter holes (7.3 mm) are equally displaced between the leading and the trailing outer walls (Fig. 2). Twelve $0.082D_H$-diameter holes (8.2 mm) are located downstream of the bend, the rib pitch to hole pitch ratio is set to 2, in order to have two holes per rib-pitch. This series is situated on the bottom wall downstream leg centerline ($Z = -0.6$). Note that the extraction massflow and the hole to rib placement were not chosen to quantify or optimize a specific geometry, but to characterize the effect of holes on the flow.

A modular concept was chosen for the test section that allows an easy exchange of the components. The total model test section including the test section entrance is turned 90 deg around the *x*-axis to obtain additional measurement planes without changing the flow conditions in the passage. This allows an easy optical access to the positions of interest for the PIV measurements.

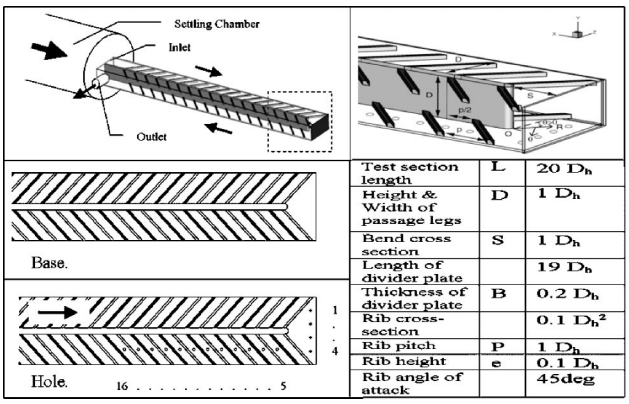

Fig. 1 The internal coolant passage test facility and turn region details

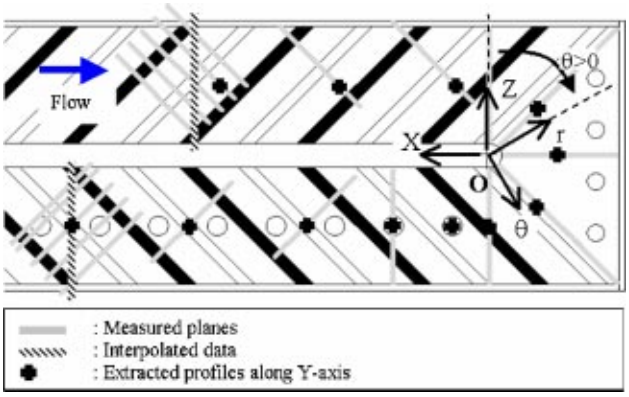

Fig. 2 Measurement sections. The symbols represent the measurement lines (*Y* direction) that will be analyzed in the next sections (Figs. 5 and 6).

Flow Conditions, Measurement Program, and Coordinate Systems. The measurements were obtained at a flow Reynolds number of 50,000 (corresponding to a bulk velocity: $Ub = 7.58$ m/s), at the entrance of the test section. The Reynolds number is based on the 0.1 m hydraulic diameter with an air temperature of 20 C. Upstream of the test rig, the mass flow is measured by means of a 5864S Brooks flow meter with a 1% accuracy. The turbulence level is approximately 3% at the model inlet. An experimental study was conducted to assess the effect a varying test section orientation on the flow. The small variations between the flow conditions are within the measurement uncertainty and can therefore be neglected for the experiments. Tests were made to show that the exact distribution of the inlet velocity profile has not a sensitive influence on the velocity distribution 16 rib modules downstream.

Extraction through the holes is adjusted by increasing the inner configuration pressure level. A butterfly valve, placed far downstream of the test section exit, adjusts the backpressure. A second 5864S Brooks flow meter, measures the exit massflow downstream of the butterfly valve, which is adjusted to obtain 50% Q_{in} extraction. Extractions through each hole have been characterized by hole velocity measurements. The velocity was measured at the outlet of the holes, with a 9-mm-dia turbine flow meter probe placed 2 mm from the hole (*Y* direction). The measured velocity is consequently an average of the free jet velocity profile. A precise positioning device allowed to place the probe at each hole outlet. The total massflow extracted, based on the hole velocity measurements, was found to be 48.5% of Q_{in}, yielding a 3% error in the single hole massflow measurements.

Static pressure measurements in the configurations have been performed with a DRUCK LPM 5480 differential pressure transmitter, with a 6 N/m^2 accuracy.

Detailed measurements of the flow structure in the passage have been obtained in the bend, upstream ($3D_H$) and downstream ($4D_H$) of the 180-deg bend. The definition of the coordinate systems in the test facility is shown in Fig. 2. A Cartesian coordinate system is used for the straight passages and a cylindrical coordinate system is used for the bend region. The origin for both coordinate systems is set on the bottom wall at the center of the rounded end of the divider plate. In the Cartesian (X, Y, Z) system, X is defined as positive in the streamwise direction of the flow downstream of the bend exit, Y is defined positive vertically upwards in the horizontal test section orientation, and Z is defined as shown. In the cylindrical (θ, r, Y) coordinate system, the radial component r is defined as positive in the direction towards the outer wall, the streamwise component θ is defined as positive

following the flow along the circular path centered on the circular bend tip, and Y is defined as for the Cartesian system.

PIV System. Di-Ethyl-Exyl-Sebacate (DEHS) from TOPAS is used as light scattering droplets for the PIV experiments. This light-scattering liquid appeared nontoxic, compared to olive oil or paraffin oil used in the past. A DLR- made Aerosol Generator using Laskin Nozzles generates 1–3-μm-dia DEHS droplets. The droplets are injected upstream of the settling chamber to guarantee a homogeneous seeding density in the test section. The particles produce good light scattering in the 90 deg direction according to the Mie law.

A 1.5-mm-thick light sheet that illuminates the particles is created by a Quantel Twins B Nd-Yag double oscillator pulsed laser. The laser provides light pulses having a maximum energy of 320 mJ at a wavelength of 532 nm. The time delay between a pair of pulses can be adjusted from 1 μs to 1 s with pulse duration of 5 ns. A plano-concave lens (-30 mm focal length) combined with two plano-cylindrical lenses (76.2 and 300 mm focal length) transform the beam into the vertical light sheet.

The imaging system consists of two independent Kodak ES1.0 cameras, each having its own PC. A Nikon Nikkor 55-mm lens is mounted on each camera. The ES1.0 has a CCD interline transfer sensor with a pixel array of 1008(H) by 1018(V) pixels. Each pixel measures nine microns square with a 60% fill factor using a micro lens. The camera outputs 8 bit digital images with 256 gray levels. For a typical recording situation, the cameras are placed with an oblique angle of 4.3 deg at a distance of 0.7 m from the light sheet plane. The pulse separation time is about 40 μs. The complete system, including laser, light sheet optics and camera, is mounted on a traversing system that allows an easy traverse to the position of interest.

The laser components (flash lamp and Q-switch) and the cameras are triggered by 10 Hz TTL signals that are dispatched to all the elements with specific delays. As the different delays between both flash lamps on the one hand, and between each flash lamp and its Pockel cell on the other hand, are all different, they are generated by a programmable sequencer, the SEQUENCER Mod.919.4, made by the DLR Goettingen. The sequencer allows the generation of complex pulse patterns on multiple channels. The pulse width, the pulse interval, the number of pulses and the output channel number are freely programmable and their resolution is of 50 ns.

The frame grabber is an Imaging Technology PCI frame grabber with 2 MB memory onboard. The PCs are equipped with 384 MB RAM and 14 GB hard disk space. During the PIV measurement series, 10 images are written in real time into the PC's RAM memory. Subsequently, the acquisition is stopped and the images are saved on the hard disk. The automation of the process allows storing a maximum of 5000 frames per measurement plane.

Data Reduction. The 3-D PIV measurements are obtained from the combination of two 2-dimensional vector fields; each of them measured from two different observation locations (the right and left cameras). The recordings from the right and left cameras are interrogated independently with the PIV software package VISIFLOW from AEA Technology. The cross-correlation analysis method is used with an interrogation window size of 64 by 64 pixel^2 and 50% overlap between the interrogation windows. The frames provided by the cameras have a 992pixel by 992pixel resolution, which yield a 30 by 30 velocity-vector field per measurement plane. The raw data contains a small number of spurious vectors ($<0.1\%$). The vector field is filtered with a predefined velocity magnitude threshold. Vectors that do not fall within the thresholds are removed and the remaining gaps are filled in with a weighted average of the surrounding vectors.

From the processed vector fields, the instantaneous three-dimensional velocity field can be reconstructed. Matlab homemade reconstruction software was developed at the EPFL-LTT. With angular PIV systems, where both cameras observe the light sheet from the same side, the corresponding interrogation positions in the right and left images do not match in general. Therefore, a calibration of the camera system is performed which also corrects for the distortion of the images in the lenses and the plexiglas walls of the passage.

In addition to the mean-velocity field, the normal and shear stress quantities of the flow are required to evaluate numerical codes. In order to obtain PIV measurements in these forms, the statistical distribution of the velocity components is determined in identical spatial windows from a series of instantaneous PIV measurements. From these statistical distributions, the ensemble average and the statistical central moments are calculated to determine the desired mean-velocity field and Reynolds stresses.

Uncertainty Analysis. Schabacker and Bölcs [11], Schabacker et al. [15], Schabacker [3] demonstrated the applicability of the presented stereoscopic PIV technique in details. Following are comments on small variations from those measurements (see also Raffel et al. [16]). For the present case, the mean number of particles per interrogation window (32 by 32 pixel^2) was set to 30. The average in-plane displacement of the particles is approximately 6 pixel, which is less than $0.25D_I$ in each direction, D_I being the characteristic dimension of the interrogation window. The optimal light sheet position for PIV measurement has the beam waist in the middle of the measurement section. This provides a constant light sheet thickness in the measurement section. In the present investigation, the light sheet energy is so intense in the beam waist that the model Plexiglas walls are burned by the light sheet. The beam waist is placed outside of the section, which leads to a 10% variation of the light sheet thickness (mean thickness $\approx$1.2 mm) inside the section. An experimental study showed that the results are not significantly affected by the variation.

The estimation of the uncertainty of stereoscopic PIV velocity measurements requires the consideration of several aspects. Systematic errors occur due to the uncertainty in the determination of the geometrical parameter such as camera alignment or light sheet location in the test section and the fabrication tolerances of the camera devices and lenses. Nonsystematic errors are mainly due to the uncertainty in the determination of the average particle displacement in the interrogation region. The errors depend on the size of the interrogation region, the time separation between the laser pulses, the magnification of the recording, the out-of-plane velocity component, the turbulence of the flow, the length scale of the flow, etc. The choice of the recording and interrogation parameters is therefore of significant importance for accurate and reliable velocity measurements. Using the method of Bendat and Piersol [17], the mean value of the measured velocities is calculated by taking the instantaneous velocity measurements of the sample, summing the values, and dividing by the number of samples ($N=1250$ per measurement plane in the present study). Note that the number of samples was chosen according to a statistical analysis described in Schabacker and Bölcs [18] and Schabacker [3]

$$\bar{x}=\frac{1}{N}\sum_{i=1}^{N} x_i \tag{1}$$

In the equations x is the *sample mean*. The number of observations N used to compute the estimates is called the *sample size*. Using the method of Bendat and Piersol [17]. The uncertainty for the mean velocity values of the present measurements is of order of 1 percent with a confidence level of 95%. Further details of the uncertainty method are given in Schabacker [3].

Results and Discussion

The objectives of the present paper are to determine the influence of a film-cooling flow extraction on the flow fields upstream, inside and downstream of the bend region, and to provide new measurements of flow between ribs for CFD validation. The fol-

lowing are data and discussion on these topics. Note that all the velocity components are normalized by the inlet bulk velocity: $U_b = 7.58$ m/s.

Extraction Characteristics. The flow field in the tested channels is incompressible, and therefore pressure-driven, yielding the pressure boundary conditions to play a major role in the flow characteristics. The pressure level (the static pressure compared to the atmospheric pressure at the channel inlet, $1D_H$ upstream of the 1st rib module) was set to 913 and 2456 N/m^2 in the baseline, and the *hole* configurations, respectively. The static pressure drop between the inlet and the outlet ($1D_H$ downstream of the last rib module) is 398 N/m^2 in the baseline configuration, and 252 N/m^2 in the *hole* configuration. The plenum chamber for the discharge of the hole flow is the laboratory room, and thus its pressure is the atmospheric pressure. Note that the higher pressure level in the *hole* case is due to the outlet butterfly valve adjusting the extraction massflow. Tests showed Chanteloup and Bölcs [4] that in the baseline case the pressure level did not influence the static pressure distribution along the passage.

Massflow measurements have been performed for each hole, quantifying the ejection distribution along the *hole* channel. Figure 3 gives details of the massflow distribution, as well as the bulk massflow present in the channel with regard to the hole number. Both quantities are normalized by the inlet massflow, 0.089 kg/s. Note that upstream of the 1st hole, the bulk massflow ratio is 1, and 0.5 downstream of the 17th hole.

The ejection through each hole of the bend is approximately constant, 2.3% of Q_{in}. This leads to a 9.2% loss of the inlet massflow in the bend. As the flow recovers the rib-induced developed flow downstream of the bend, the ejection through the holes becomes constant. From the 2nd to the 6th rib module, 6.5% of Q_{in} is ejected per rib module. However, the ejection through every second hole of each rib module is greater than through the first hole. The massflow difference between two consecutive holes reaches 10 to 2% in the 2nd and 6th downstream rib modules, respectively. This can be attributed to the recirculating zone downstream of each rib, where the static pressure is less than after the flow reattachment in front of the bottom ribs (in location of every 2nd hole). Note that the influence of the bend can be noticed in the 1st rib module downstream of the bend, increasing the massflow through the 1st hole.

Flow in the Upstream Leg. A comparison of velocity components in the developed flow region of a similar coolant passage was presented by Bonhoff et al. [19]. Their measurements showed that the flow with a 45-deg rib arrangement differs from the flow in a similar passage with a 90-deg rib arrangement (Schabacker et al. [20]). With 90-deg ribs, a developed flow condition in terms of mean velocity and turbulent kinetic energy was achieved after three rib modules. The flow in the passage with 45-deg rib arrangement required a longer development length. At least eight rib modules were needed to achieve a developed flow condition for the mean velocity components, and 12 rib modules were required for the turbulent kinetic energy of the flow. In the present configuration, 18 rib-modules are placed in the upstream leg, to produce a developed flow field before the 180-deg bend. The analysis of the developed flow in this upstream leg was presented in Fig. 3 of reference [4] for the baseline configuration and is not presented in this paper for the *hole* case. However, the major results can be summarized as follows: The flow in the baseline configuration was shown to be developed in the upstream 16th rib module, and the periodicity associated with this developed state extended up to the bend inlet. In the *hole* configuration, the flow in the 16th rib module has already undergone the bend influence, the streamwise velocity variations reaching 15% at the bend inlet location. The influence of the extraction in the configuration extends well upstream of the extraction region.

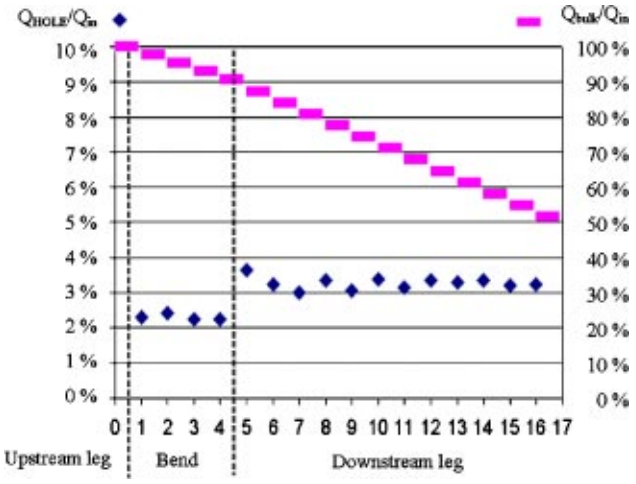

Fig. 3 Hole velocity profile and remaining bulk massflow along the hole configuration centerline

Flow in the Bend Region. The flow in the upstream leg developed region of 180 deg cooling channels has already been described by Schabacker et al. [20] and Chanteloup and Bölcs [4]. It is strongly influenced by the ribs on both opposite walls, yielding two counter-rotating vortices, both occupying half of the cross section. Figure 4 gives a comparison of both the baseline and the *hole* configurations described previously. Mean streamwise velocity contours and secondary flow vectors obtained at $\theta = 0$, 45, 90, 135, and 180 deg in the bend are presented. These average velocity results were obtained from 1250 full-field data sets. For this set of results, the orientation of the view is always into the oncoming flow, with the web at the left-hand side of the figure.

The major difference occurs when comparing the secondary flow motion. The upper vortex ($Y > 0.5$) occupies 70% of the cross section in the case of extraction. The counter-rotating vortex induced by the bottom ribs only occupies the $Y < 0.3$ area. The streamwise component is also influenced by this asymmetry, showing a high velocity zone in the upper part.

The flow in the bend region is more complex than in the ribbed region. The flow in the bend starts with the secondary structure from the ribs at $\theta = 0$ deg. At $\theta = 0$ deg, the streamwise velocity distribution and the secondary flow patterns in the center region show the effects of the bend (Fig. 4). The streamwise flow near the inner web has begun to accelerate, indicating that this flow has entered the bend region. The secondary flow pattern is symmetrically distributed with respect to the mid plane ($Y = 0.5$) for the baseline configuration, whereas in the *hole* configuration, the secondary flow near the outer wall is mainly directed towards the bottom wall. The main impact is the inclusion of a high streamwise velocity core in the channel center region. Note that near the web of both configurations, all the secondary flow vectors are toward the web in both cases.

At $\theta = 45$ deg, the streamwise velocity increases to more than 2 near the inner web, and has a small region of negative velocities in the lower outside corner region. The high streamwise velocity near the inner web is compatible with the conservation of angular momentum in the bend region. The secondary flows are very different from the baseline case, to the *hole* case. In the latter, instead of the four vortices present in the baseline case, only two counter-rotating vortices occur. They have the same rotating direction as the two baseline case upper vortices, but are approximately twice their size. Note that near the web, the secondary flow vectors are directed away from the web in both configurations.

At $\theta = 90$ deg, the streamwise velocities of the flow have decreased near the web. The size of the region near the web where the secondary flow is directed away from the web has increased. The upper baseline case secondary cell seen at 45 deg continues,

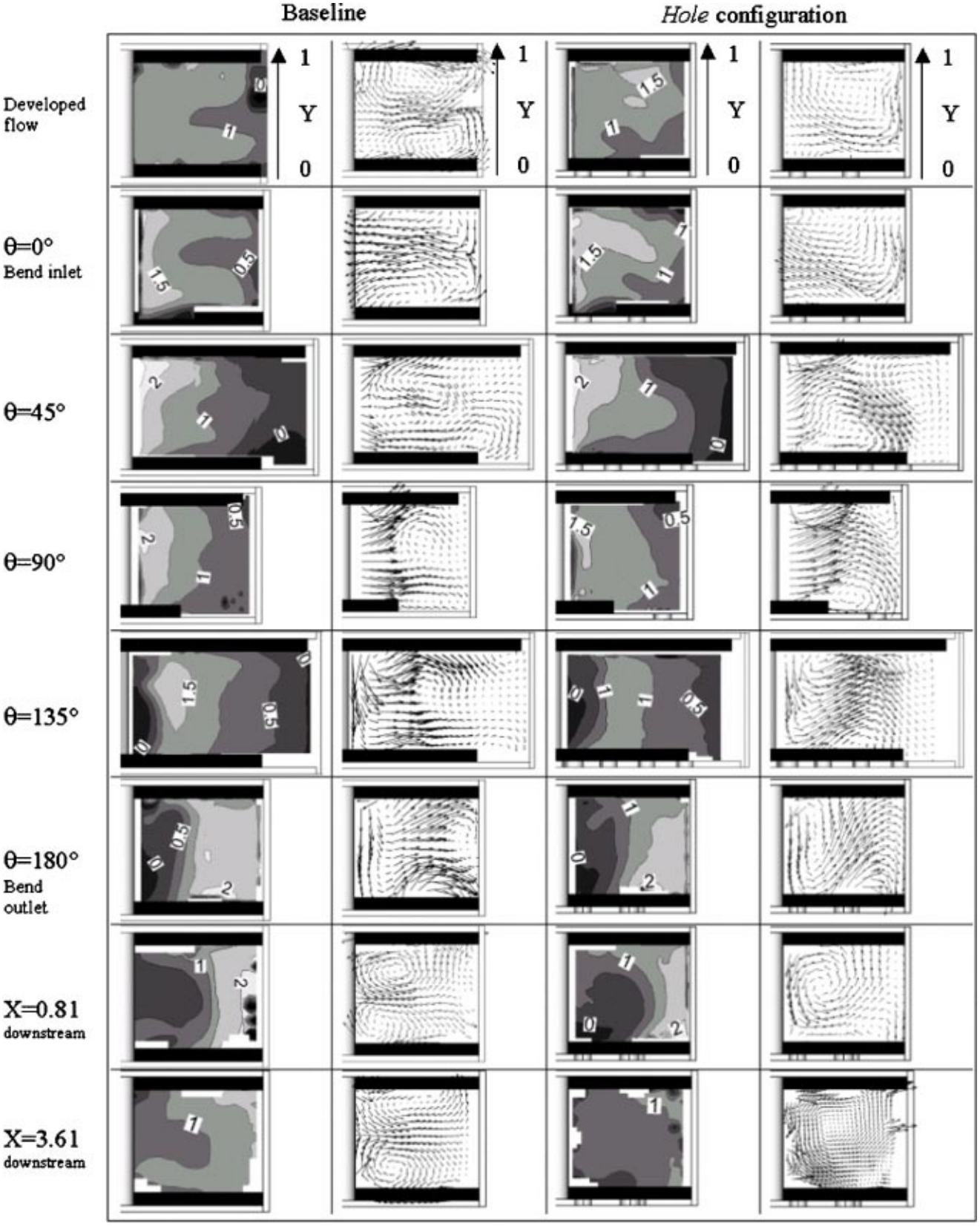

Fig. 4 Mean streamwise velocity contours and secondary flow vectors obtained at $\theta = 0$, 45, 90, 135, and 180 deg in the bend. The contour lines values, U_θ, are plotted on the figures (U_θ / U_b).

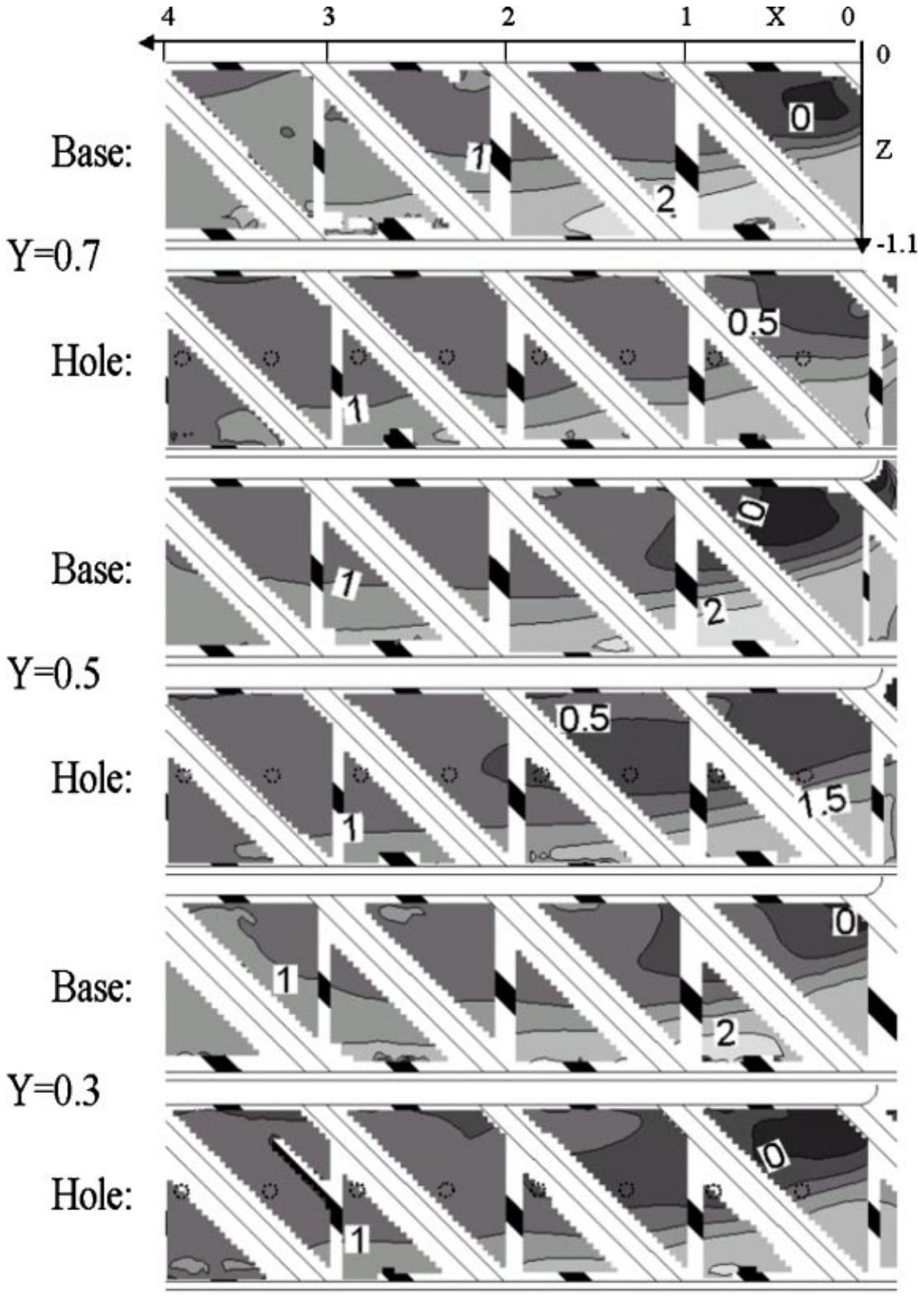

Fig. 5 Streamwise velocity contours immediately downstream of the bend, $0.0<X<4.0$ at three distances from the bottom wall (U/U_b)

but the lower cell has disappeared. The two *hole* case secondary cells are still present, but their locations have been strongly modified by the bend-induced flow.

At $\theta=135$ deg, the flow has separated from the web and the streamwise velocities are negative. The streamwise velocity contours are similar for both configurations. The streamwise velocity contours has a negative value near the outer wall, indicating a small recirculation cell. The *hole* case values are a bit smaller due to the massflow extracted through the first two holes in the bend. The average position of the baseline vortex cell has moved toward the web, and the secondary flow is generally away from the web. The two *hole* case vortices continue to develop.

At $\theta=180$ deg, a small region of recirculation occurs near the web and the lower wall. The rib-induced secondary flow motion is redeveloping. The streamwise profiles are similar in both cases. The effect of the flow extraction is, however, increasing in the *hole* case, yielding smaller streamwise magnitudes. Note that the highest streamwise velocities have moved from near the web to the outer half of the passage, and are 1.5 to 2.0 times the bulk velocity. The secondary flow is very different in the *hole* configuration. The flow goes from the top to the bottom wall along the web, crosses the channel up to the top outer wall, and goes down to the bottom wall along the outer wall. This phenomenon is similar to the upper half of the baseline secondary flow motion.

Downstream of the bend, the secondary flows are redeveloping, having a similar shape to the secondary flow in the upstream leg. The streamwise flow has not recovered from the bend effect. $0.81D_H$ downstream of the bend, the recirculating cell has disappeared in the baseline configuration, but is still present in the *hole* case. Further downstream ($3.6D_H$), the flow has almost recovered from the bend domination, the streamwise and secondary profiles are similar to the inlet profiles, except for the symmetry around the web, due to the rib symmetrical placement each side of the web. The *hole* configuration streamwise velocity magnitude, has also decreased because of the massflow extracted upstream.

Flow in the Downstream Leg. Downstream of the bend is another region with relatively large variations in heat transfer. Figure 5 presents streamwise velocity contours of the downstream turn region, and gives further details of the flow characteristics in the streamwise direction. Corresponding secondary flow measurements are presented in Fig. 4. The center part of the channel is plotted ($0.3<Y<0.7$).

The streamwise velocity component recovers from the bend effect quite similarly in the baseline and the *hole* configurations. The flow becomes more uniform in the spanwise direction as X increases, the rib-induced effects becoming predominant. $4D_H$ downstream of the bend, the streamwise velocity magnitude is 30% lower in the *hole* than in the baseline configuration, this is due to the massflow lost in the upstream holes ($\sim$25% of Q_{in} lost). As described in Chanteloup and Bölcs [4] the bend-induced flow leads to a high non-homogeneity at the downstream leg inlet ($\theta=180$ deg). The high-speed region ($U_\theta/U_b>1$) occupies the outer half part of the duct ($Z<-0.6$) and extends up to $X>2$. Near the web, a recirculating zone appears for $0.3<Y<0.7$ in the baseline configuration, whereas in the *hole* case, it does not appear for $Y=0.7$ and is only present at the very web tip for $Y=0.5$. This confirms the trend observed in Fig. 4, that the entire flow field is displaced toward the bottom wall.

Except for the magnitude differences due to the extraction, both streamwise velocity profiles recover from the bend in the same

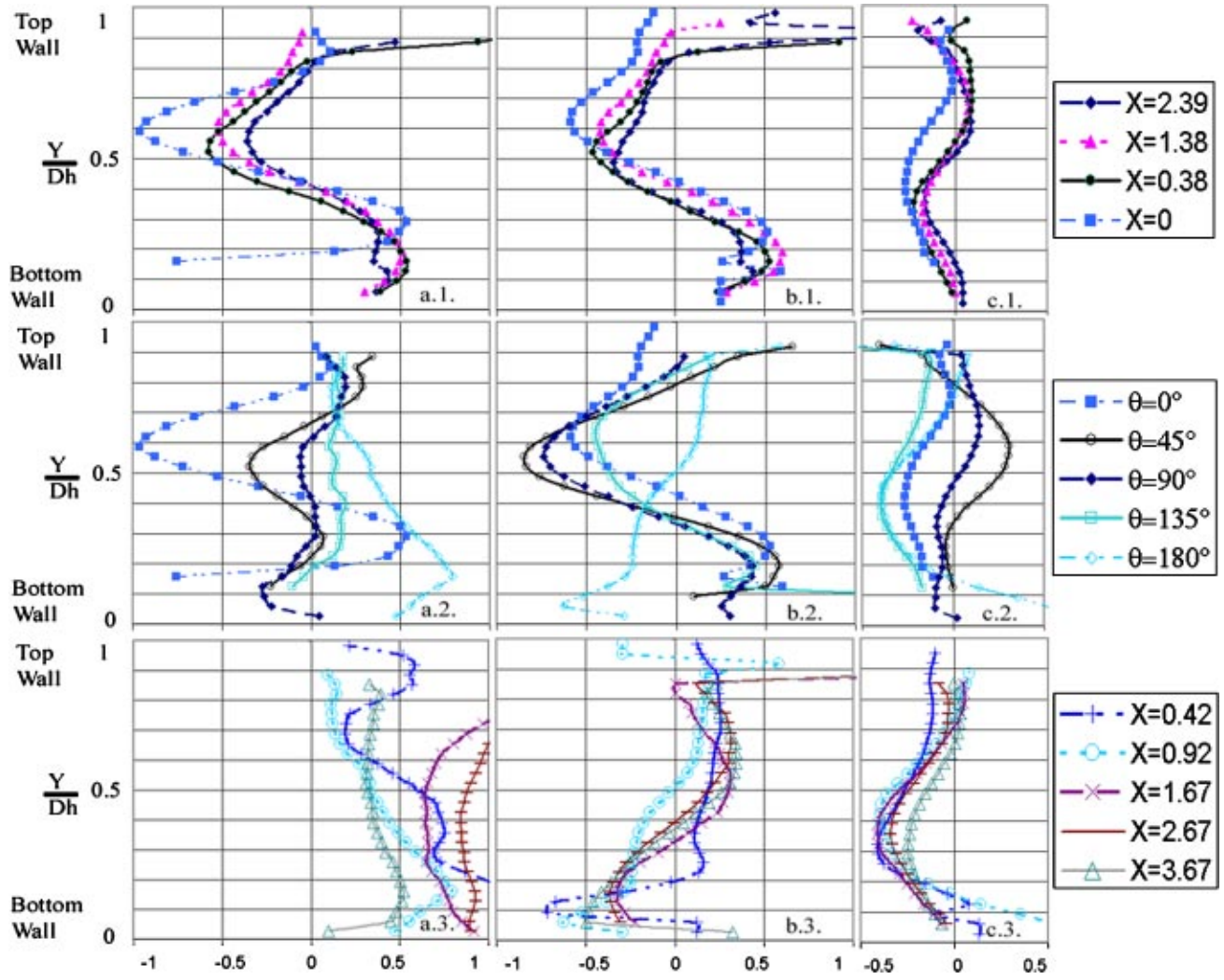

Fig. 6 Centerline velocity profiles differences (baseline-hole), normalized by U_b. {a: Streamwise velocity: U; b: radial velocity (from the web toward the outer walls, i.e. 1:along Z-axis: W; 2: along r-axis: U_r; 3:along Z-axis:-W); c: vertical velocity along Y-axis: V;} (e.g., Fig. 2 for exact locations in the rib modules).

manner, and the streamwise velocity shape in the center part of the duct is not very sensitive to the extraction. The extraction influence is mainly noticeable in the secondary flow profiles.

Extraction Influence. Figure 6 completes the results shown in the previous paragraphs. Velocity profiles differences between the baseline case and the *hole* case, are plotted along the configuration centerline ($Z=0.6$ upstream, $r=0.6$ in the bend, $Z=-0.6$ downstream). They are describing the velocity evolution from the bottom to the top wall, i.e., along the *Y*-axis. Profile positions are described in Fig. 2, they are located beyond the top rib of each rib module in the downstream leg, and between the top and the bottom rib in the upstream leg. The positive values indicate parts where the baseline configuration velocity components are greater than in the *hole* configuration and vice versa.

Upstream of the bend, the extraction has a high influence. At $X=2.4$ in the upstream leg, the differences between both configurations are up to $1U_b$, yielding 70, 100, 100% differences for the velocity along *X*, *Z*, *Y*-axis, respectively. For velocity component values, the reader is referred to Chanteloup and Bölcs [4].

As *X* is diminishing, the flow characteristics are changing. Considering the streamwise velocity, the differences maximums along the centerline increase as the distance to the bend decreases. The evolution of the secondary flow velocity components is less sensitive, as they are much more rib dominated. At the bend inlet, however, the differences are noticeable for every component, showing that the influence of the extraction increases as the flow reaches the zone where the holes are located.

Differences evolve continuously as the flow follows the bend. At $\theta=45$ deg, the profiles are similar to the upstream profiles, especially the secondary flow, which is at $r=0.6$, still governed by the rib induced profile. As θ increases, the bend effect tends to dominate the streamwise profiles, leading to constant positive 15% difference at $\theta=135$ deg. It can be noticed that this difference is mainly due to the amount of flow extracted through the first holes (6.5% of Q_{in}).

The profiles of Fig. 6 downstream of the bend, confirm the results plotted in Fig. 4, the flow field is recovering from the bend effect. The secondary flow field rapidly becomes rib dominated. The streamwise velocity differences are positive, indicating that the bulk velocity diminishes as the massflow extracted, increases. It can be noticed that in profiles aligned with a hole ($X=0.42$, $X=0.92$), all the velocity components are highly influenced by the extraction, up to 20% over the bottom wall.

These results completed by Chanteloup and Bölcs [4] provide a set of measurements that can be used to evaluate CFD codes in the developed flow region of a ribbed channel. These flows in the ''developed periodic'' upstream leg, in the bend region, and in the downstream leg, reflect effects that will probably be obtained in most coolant channels, with and without extraction. As the flow is highly turbulent and pressure-driven, the data provide a good test for codes to predict flow with various turbulence models, wall approximations and meshing strategies.

Conclusions

Three-dimensional velocity measurements were obtained in a two-legged blade coolant passage model with ribs orientated 45 deg to the passage. The model length, the rib locations and the geometry of the web between the coolant passage legs, was representative of gas turbine cooling designs. A comparison is presented between two similar configurations; one is a baseline, while the second one is provided with bleeding holes, simulating the holes for external film cooling of blades.

Adding bleeding holes, and having a high ratio between the channel inlet mass flow and the extracted mass flow, strongly influence the flow in the two-legged cooling channel. It modifies the flow field in the entire test section, in the region where the extraction occurs, but also far upstream in the first leg of the channel. The influence on the streamwise velocity profiles is sensitive, but the greatest influence occurs on the secondary flow motions. The secondary flow moves from its symmetrical shape, in the baseline case, to a strongly asymmetrical shape in the *hole* case, as some part of mass flow is ejected from the channel. The streamwise symmetrical profile is unbalanced toward the wall with extraction, and the symmetry plane ($Y=0.5$) is displaced downward by about 20% of D_H. The secondary flow has to adapt to the streamwise conditions, and as a consequence is highly modified. All along the channel, the lower parts of the baseline secondary flow motion have almost disappeared, and the upper parts have been scaled by a factor 1.5 in the *Y* direction. This asymmetry will probably strongly modify the heat transfer coefficient distribution on the ribbed surfaces.

Measurements along the centerline of the channel show details in the three velocity profiles, which can be used to evaluate numerical simulation methods and meshing strategies, turbulence or wall treatment models. The measurements showed the tendency of the streamwise and cross-stream velocity differences to be similar for various streamwise locations along the duct. The unsteady character of the flow may require time dependent numerical techniques to accurately simulate the flow. The area near the web, and probably upstream of the bend is likely to have large variations in heat transfer, due to the high variations in streamwise velocity, and may produce hot and cold spots, and possibly increased stresses with these thermal gradients.

Acknowledgments

This study was funded by the Swiss Office of Science in cooperation with the BriteEuram Internal Cooling of Turbine Blades project (contract number: BRPR-CT97-0600, project number: BE97-4022).

Nomenclature

- X = Cartesian coordinate in axial duct direction (normalized by D_H)
- Y = Cartesian coordinate in cross duct direction (normalized by D_H)
- Z = Cartesian coordinate in horizontal duct direction (normalized by D_H)
- θ = cylindrical coordinate in streamwise direction
- r = cylindrical coordinate in radial direction
- U = mean velocity component in *x* direction
- V = mean velocity component in *y* direction
- W = mean velocity component in *z* direction
- U_θ = mean velocity component in streamwise direction in bend
- U_r = mean velocity component in radial direction in bend
- U_b = bulk mean velocity
- L = test section length
- D = height and width of passage legs, $D=100$ mm
- D_H = hydraulic diameter $D_h=D$
- B = thickness of divider plate
- P = rib pitch
- e = rib height
- S = section length in bend at 90-deg section

References

[1] Rowbury, D., Parneix, S., Chanteloup, D., and Lees, A., 2001, *Research into the influence of Rotation on the Internal Cooling Turbine Blades*, Proc. AVT Symposium, Heat Transfer and Cooling in Propulsion and Power Systems, Loen, Norway.

[2] Rau, G., Cakan, M., Moeller, D., and Arts, T., 1998, ''The Effect of Periodic Ribs on the Local Aerodynamic and Heat Transfer Performance of a Straight Cooling Channel,'' ASME J. Turbomach., **120**, pp. 368–375.

[3] Schabacker, J., 1998, ''*PIV Investigation of the Flow Characteristics in an Internal Coolant Passages of Gas Turbine Airfoils With Two Ducts Connected by a Sharp 180 deg Bend*,'' *Ph.D. thesis* (Ecole Polytechnique fedérale de Lausanne), Vol. no. 1816.

[4] Chanteloup, D., and Bölcs, A. 2001, ''*PIV Investigation of the Flow Characteristics in 2-Leg Internal Coolant Passages of Gas Turbine Airfoils*,'' Proc. Euroturbo, 4th European Conference on Turbomachinery Fluid Dynamics and Thermodynamics. Firenze, Italy.

[5] Bons, J. P., and Kerrebrock, J. L., 1999, ''Complementary velocity and heat transfer measurements in a rotating cooling passage with smooth walls,'' ASME J. Turbomach., **121**, pp. 651–662.
[6] Byerley, A. R., Jones, T. V., and Ireland, P. T., 1992, ''*Internal Cooling Passage Heat Transfer Near the Entrance to a Film Cooling Hole: Experimental and Computational Results*,'' 92-GT-241, Proc. Int Gas Turbine & Aeroengine Congress & Exhibition. Cologne, Germany.
[7] Shen, J. R., Wang, Z., Ireland, P. T., and Jones, T. V., 1996, ''Heat Transfer Enhancement Within a Turbine Blade Cooling Passage Using Ribs and Combinations of Ribs With Film Cooling Holes,'' ASME J. Turbomach., **118**, July, pp. 428–434.
[8] Lourenco, L. M., 1988, ''*Some Comments on Particle Image Displacement Velocimetry*,'' *Lecture Series* (Von Karman Institute for Fluid Dynamics), Vol. 06.
[9] Prasad, A. K., and Adrian, R. J., 1993, ''*Stereoscopic Particle Image Velocimetry Applied to Liquid Flows*,'' Experiments in Fluids, **15**, pp. 49–60.
[10] Westerweel, J., and Nieuwstadt, F. T., 1991, ''*Performance Tests on 3-Dimensional Velocity Measurements with a Two-Camera Digital Particle-Image-Velocimeter*,'' *Laser Anemometry*, ASME, Vol. 1, pp. 349–355.
[11] Schabacker, J., and Bölcs, A., 1996, ''*Investigation of Turbulent Flow by means of the PIV Method*,'' Proc. 13th Symposium on Measuring Techniques for Transonic and Supersonic Flows in Cascades and Turbomachines. Zurich, Switzerland.
[12] Johnson, B. V., Wagner, J. H., Steuber, G. D., and Yeh, F. C., 1994, ''Heat Transfer in Rotating Serpentine Passages With Trips Skewed to the Flow,'' ASME J. Turbomach., **116**, pp. 113–123.
[13] Han, J. C., Zhang, P., and Lee, C. P., 1992, ''Influence of Surface Heat Flux Ratio on Heat Transfer Augmentation in Square Channels With Parallel, Crossed, and V-Shaped Angled Ribs,'' ASME J. Turbomach., **114**, pp. 872–880.
[14] Zhang, Y. M., Han, J. C., Parsons, J. A., and Lee, C. P., 1995, ''Surface Heating Effect on Local Heat Transfer in a Rotating Two-Pass Square Channel With 60 deg Rib Turbulators,'' ASME J. Turbomach., **117**, pp. 272–278.
[15] Schabacker, J., Bölcs, A., and Johnson, B. V., 1998, ''*PIV Investigation of the Flow Characteristics in an Internal Coolant Passage With Two Ducts Connected by a Sharp 180 deg Bend*,'' 98-GT-544, Proc. International Gas Turbine & Aeroengine Congress & Exhibition. Stockholm, Sweden.
[16] Raffel, M., Willert, C. E., and Kompenhans, J., 1997, *Particle Image Velocimetry. A Practical Guide* (Springer), ISBN 3-540-63683-8.
[17] Bendat, J. S., and Piersol, A. G., 1986, ''*Random Data*,'' *Random Data*, (John Wiley & Sons, Inc.), New York, NY.
[18] Schabacker, J., and Bölcs, A., 1998, ''*Investigation of Internal Flows by Means of the Stereoscopic PIV Method*,'' Proc., 9th Int. Symp. on Applications of Laser Techniques to Fluid Mechanics, Lisbon, Portugal.
[19] Bonhoff, B., Schabacker, J., Parneix, S., Leusch, J., Johnson, B. V., and Bölcs, A., 1998, ''*Experimental and Numerical Study of Developed Flow and Heat Transfer in Coolant Channels with 45 and 90 deg Ribs*,'' 99-GT-123, Proc. Turbulent Heat Transfer II. Manchester, UK.
[20] Schabacker, J., Bölcs, A., and Johnson, B. V., 1999, ''*PIV Investigation of the Flow Characteristics in an Internal Coolant Passage With 45 deg Rib Arrangement*,'' 99-GT-120, Proc. Int. Gas Turbine & Aeroengine Congress & Exhibition. Indianapolis, IN.

Flow Field Simulations of a Gas Turbine Combustor

M. D. Barringer
O. T. Richard
J. P. Walter
S. M. Stitzel
K. A. Thole

Mechanical Engineering Department,
Virginia Polytechnic Institute and
State University,
Blacksburg, VA 24061

The flow field exiting the combustor in a gas turbine engine is quite complex considering the presence of large dilution jets and complicated cooling schemes for the combustor liner. For the most part, however, there has been a disconnect between the combustor and turbine when simulating the flow field that enters the nozzle guide vanes. To determine the effects of a representative combustor flow field on the nozzle guide vane, a large-scale wind tunnel section has been developed to simulate the flow conditions of a prototypical combustor. This paper presents experimental results of a combustor simulation with no downstream turbine section as a baseline for comparison to the case with a turbine vane. Results indicate that the dilution jets generate turbulence levels of 15–18% at the exit of the combustor with a length scale that closely matches that of the dilution hole diameter. The total pressure exiting the combustor in the near-wall region neither resembles a turbulent boundary layer nor is it completely uniform putting both of these commonly made assumptions into question. [DOI: 10.1115/1.1475742]

Introduction

A major factor in decreasing the cost of gas turbine engines, whether they be for military or for commercial uses, is to reduce the maintenance costs. The turbine, particularly the first stage, is subject to very harsh conditions resulting from high-temperature and high-turbulence flows exiting the combustor. Operational experience indicates that some turbine airfoils suffer serious damage while adjacent airfoils remain in good operating condition. This observation suggests that there are significant nonuniformities in the exit combustor flows that have detrimental effects on the airfoils.

To evaluate the effects of these nonuniformities and to further our understanding in how to best integrate the combustor and turbine, a new experimental facility was developed to simulate prototypical combustor exit conditions as the entrance conditions to a first stage, linear, turbine vane cascade. Although this study has not simulated the reacting flow, thereby not including such affects as the heat release due to combustion, it is important to recognize that we should begin by determining whether we can computationally simulate the nonreacting flow field. The heat release, for example, will depend upon the mixing characteristics of the dilution jets. If the dilution jets can not be accurately simulated under the nonreacting conditions, it would be difficult to simulate the reacting flow field. For the design of the facility reported in this paper, nonuniformities in both the span (radial) and pitch (circumferential) directions exiting the combustor have been simulated through the use of combustor liner panels, insuring representative near-platform flows, and dilution jets, insuring representative mainstream flows with high levels of turbulence.

In general, the following objectives for the facility described in this paper are: i) to simulate the flow conditions for a prototypical combustor that is nonreacting, ii) to quantify the exit conditions (inlet conditions for the turbine) for this prototypical combustor, and iii) to quantify the flow field in the downstream vane passage as a result of the nonuniform combustor exit conditions. Specifically, this paper presents the effects that the dilution jets have on the flow and thermal fields exiting the combustor with no downstream turbine vane present. This paper describes those experimentally measured flow and thermal fields after describing the development of the combustor simulator facility.

Contributed by the International Gas Turbine Institute and presented at the International Gas Turbine and Aeroengine Congress and Exhibition, New Orleans, Louisiana, June 4–7, 2001. Manuscript received by the IGTI, November 2000; revised manuscript received March 2001. Paper No. 2001-GT-170. Review Chair: R. A. Natole.

Relevant Past Studies

A majority of the past experimental and computational simulations of a gas turbine have assumed either a simple two-dimensional turbulent boundary layer and a uniform mean field or a constant total pressure entering the first stage turbine vane. As a result of a simple two-dimensional turbulent boundary layer assumption, the resulting secondary flow pattern in the vane passage comprises a horseshoe vortex, which splits into two legs; a suction side leg and a pressure side leg that further develops into the passage vortex. This secondary flow pattern was first suggested by Langston [1] and more recently confirmed by measurements of Kang and Thole [2]. As a result of a constant total pressure assumption, no changes in the streamline pattern would occur as theoretically shown by Munk and Prim [3] and computationally shown to be true by Shang and Epstein [4] and Hermanson and Thole [5]. A uniform total pressure field results in no radial pressure gradient, which is needed to drive the passage vortex. Both assumptions, a two-dimensional turbulent boundary layer or a constant total pressure, are questionable for the nozzle guide vane particularly in the hub and tip regions. These are questionable if one considers that as much as 50% or more of the flow entering the main gas path is fluid that has passed through combustor liners in the form of either film coolant or dilution fluid.

While the experimental studies by Butler et al. [6] and Shang et al. [7] have considered nonuniform inlet temperature profiles, the only study to have measured a realistic total pressure variation was that by Stabe et al. [8]. Stabe et al. [8] simulated a liner flow through the use of a combustor exit radial temperature simulator (CERTS). The CERTS used circumferential slots with no dilution holes. This study clearly indicated changes did occur in the total pressure when using the CERTS as compared to not using the CERTS. Details are not available, however, for comparing the effects that the two different total pressure profiles had on the secondary flow field development in the stator vane section.

Burd and Simon [9] simulated a range of injection flows from a two-dimensional slot upstream of a nozzle guide vane. Although this is an important study, the geometry used does not have all of the elements necessary to represent that of a combustor liner for an aeroengine. In their work, they reported to have made a single-point total pressure measurement at the inlet to their vane cascade. They indicated in their paper that the inlet total pressure field was considered to be uniform for the full range of injection to mainstream mass flow ratios. The thermal field results reported by Burd et al. [10], however, indicated that for a mass flow ratio greater than 3.2%, the injectant (coolant) migrated up the pressure

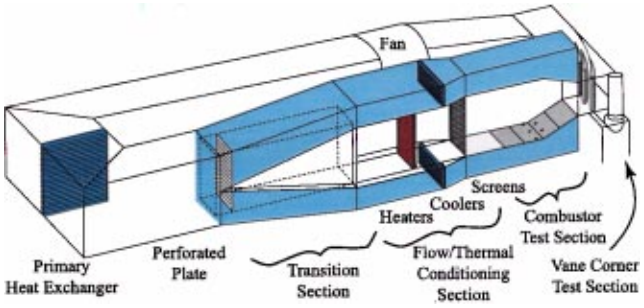

Fig. 1 Illustration of the low speed wind tunnel facility with the combustor simulator section

surface of the vane. This is consistent with having a higher total pressure in the near-wall region. A higher total pressure in the near platform region results in a vortex of opposite rotation as the passage vortex first illustrated by Langston [1]. The results of Burd et al. [10] indicated a vortex that would drive flow up the pressure side of the vane away from the endwall, whereas Langston's passage vortex has the orientation to drive flow down the pressure side of the vane toward the endwall. Recall Langston [1] considered a two-dimensional turbulent boundary layer where the total pressure decreases due to a decrease in velocity as one moves from the midspan to the endwall region. This reversal of the passage vortex was shown to occur computationally by Hermanson and Thole [5] when a higher total pressure occurs in the endwall region.

This summary of relevant literature demonstrates the importance of knowing what the inlet flow conditions are to the first stage vane in the turbine. What is lacking, however, are the needed measurements of the total pressure field and turbulence levels that can be used as boundary conditions for turbine vane simulations. The next logical step in accurately assessing the capabilities of computing turbine flow fields and heat transfer is to evaluate whether the computational codes can accurately simulate these nonuniform inlet flows to the turbine.

Description of Experimental Simulations

Complete measurements of the near wall flows exiting an actual combustor are nearly impossible to achieve in an operating engine. For this purpose, a scaled-up combustor simulator facility was carefully designed to simulate the geometry and flow conditions of an early design of a prototypical aeroengine combustor with these values being provided by industry (Soechting and Cheung [11]). The purpose of making this facility large scale was to allow for good spatial measurement resolution. In general, the wind tunnel simulation included combustor liner panels with many rows of discrete, axially oriented film-cooling holes and two streamwise rows of large dilution holes. At the end of the liner panels, there is a slot in which more coolant is injected into the primary passage. More discussion will follow in this section on the details of the liner panels and exit slot.

The wind tunnel facility itself has been described in numerous previous studies (Kang et al. [12], Kang and Thole [2], and Radomsky and Thole [13,14]) as a closed-loop tunnel with a scaled-up (9X), two passage (one sector), linear cascade. The flow is driven for both the past reported studies as well as the study described in this paper by a single 50-hp axial fan. Downstream of the fan is a large primary heat exchanger core. Somewhat downstream of the heat exchanger core is the linear cascade, which is placed in a corner of the tunnel.

The modifications made to this facility include replacing a 7.3-m long section, located just upstream of the cascade corner test section as illustrated in Fig. 1. The replacement section includes a transition section that splits the flow into a primary flow passage and two symmetric secondary flow passages located on

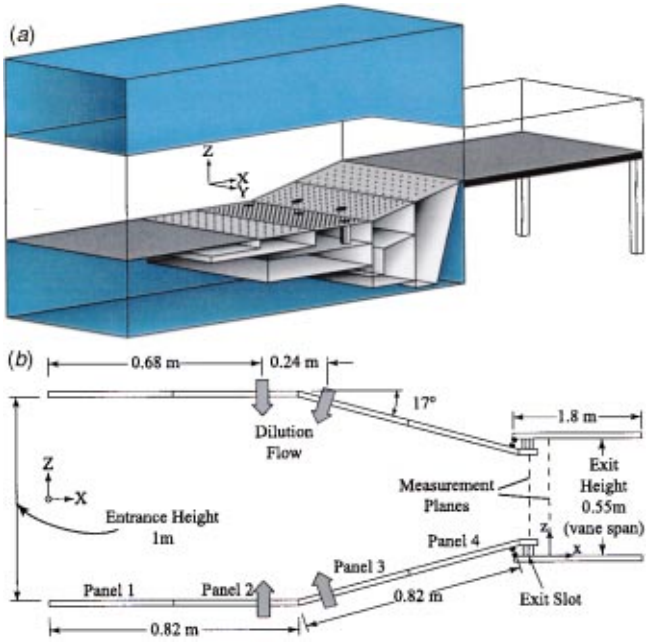

Fig. 2 Illustration of the supply channels for each of the combustor liner and dilution flows (*a*), and geometric details of the primary flow path (*b*).

the top and bottom of the primary flow passage. Within the transition section in the primary flow passage, the flow immediately passes through a perforated plate. The sole purpose of the perforated plate is to provide the necessary pressure drop to control the flow splits between the primary and secondary passages. At a distance 3.5 m downstream of the perforated plate, the flow passes through a thermal and flow conditioning section containing a bank of heaters followed by a series of screens and flow straighteners. The heater section comprises three individually controlled banks of electrically powered, finned bars supplying a maximum total heat addition of 55 kW. This total heat addition is enough to raise the primary passage flow to a temperature 20°C above the secondary flow coolant temperature. A controller unit maintains a set point temperature to within 1°C. Downstream of the flow straighteners, the heated primary flow enters the combustor simulator. In the combustor simulator, secondary coolant flow is injected into the primary flow passage through liner panels and dilution holes. In addition, the flow is accelerated prior to entering the turbine section.

The flow in the secondary passages, also shown in Fig. 1, is first directed through heat exchangers. In addition to heat being rejected from the primary heat exchanger, the heat exchangers in the secondary passages provide additional heat rejection for the coolant flow. The flow in the secondary passages is then directed into a large supply chamber as shown in Fig. 2(*a*). This supply chamber provides the flow necessary for the combustor liner cooling and dilution holes. The exit slot is used for the purpose of providing additional cooling to the platform. In the combustor simulator there are a series of four streamwise panels on both the top and the bottom that contain the film-cooling and dilution holes. To insure the correct coolant flow splits among the liner panels and dilution rows, separate supply chambers for each component were placed within the large supply. These separate chambers are also indicated in Fig. 2(*a*). The coolant flow for the exit slot at the end of the combustor panels was maintained by providing the required pressure in the large supply chamber. Fig. 2(*b*) gives the overall dimensions of the combustor simulator.

Velocity and temperature field measurements were made at the inlet to the combustor section using a hot-wire and thermocouple to verify the flow uniformity. The maximum deviation in the mean

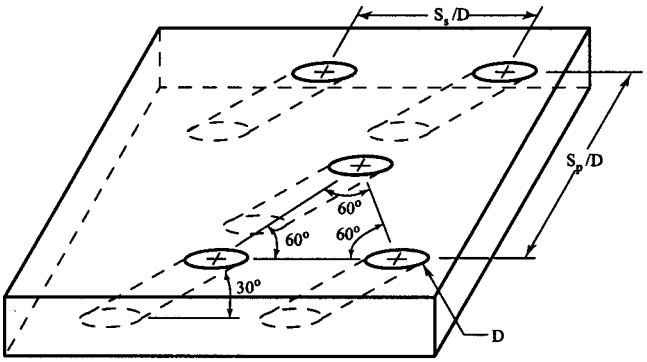

Liner Geometry Feature	S_p/D	S_s/D
Panel 1	10.1	5.8
Panel 2	6.1	3.5
Panel 3	6.1	3.5
Panel 4	10.1	5.8
Dilution Row 1	60 (5.4 D_1)	90.2 (8.1 D_1)
Dilution Row 2	60 (3.8 D_2)	120.8 (7.6 D_2)

Fig. 3 Film-cooling hole pattern for each liner panel

velocity was 1.9%, while the maximum deviation in the temperature was 5.7% (based on the driving temperature potential between the mainstream and coolant). The turbulence level at the entrance to the combustor section, which was a result of the upstream perforated plate, was 3%.

The exit dimensions of the primary channel for the combustor simulator were matched to the inlet dimensions of the pre-existing large-scale turbine vane cascade section [13,14]. This existing cascade represents one sector of an engine with the correctly scaled span-to-chord and pitch-to-chord ratios. The combustor simulator's inlet cross section and overall length were designed based on aeroengine data. The combustor's inlet cross-sectional area was such that the width was chosen to be slightly larger than one sector (to allow for sidewall flow removal) and the height was 1.8 vane spans. The height of the simulator was chosen such that the aeroengine's acceleration parameter (K) through the combustor was matched through the simulator. These acceleration parameters were calculated based on the inlet flow and the added mass flow through the liners and dilution holes matching the simulator to the engine.

Design of Liner Panels and Dilution Holes. Other than performing the measurements in an actual operating engine, it is not feasible to provide a measurement environment with all of a turbine engine's conditions being matched. In designing this combustor simulator, the parameters that were chosen to match an early design of a prototypical combustor included the following: i) the acceleration parameter (K, as defined in the Nomenclature) through the combustor; ii) the scaled combustor exit velocity to insure the correct inlet Reynolds number for the turbine section; iii) the coolant-to-mainstream momentum flux ratios of the liner cooling holes and the dilution holes; iv) the percentage coolant mass flux addition to the primary flow by the liner cooling holes, exit slot, and dilution holes; v) the film-cooling staggered hole pattern shown in Fig. 3; and vi) geometric scaling for the film-cooling hole diameter and the exit slot geometry (9X). Note that the parameters for the prototypical engine combustor were for actual running (hot) operating conditions. The air loading parameter (ALP defined in the Nomenclature, Lefebvre [15]) for the engine simulated was 0.66×10^{-4} and for the wind tunnel design was 0.4×10^{-4}. The loading parameter η_θ (see Nomenclature) given by Walsh and Fletcher [16] for both the engine and wind tunnel simulation was 1.8.

The liners for the combustor simulator were a streamwise series of four different panels that started 2.7 vane chords (1.6 m) upstream of the turbine test section. The first two panel lengths were 41 cm while the third and fourth panels were 38 cm and 46 cm. The panels extended the full width of the test section. The first two panels were horizontal to maintain a constant cross-sectional area while the following two panels were inclined at 17 deg to match the correct flow acceleration. The panels were constructed of 1.27 cm thick urethane foam with a low thermal conductivity ($k=0.037$ W/mK) to allow for adiabatic surface temperature measurements. The dense matrix of film-cooling and dilution holes for each of the panels were cut into the urethane foam using a water jet.

Table 1 Operating conditions and geometry

	Engine			No Dilution			With Dilution		
	$\%\dot{m}_{ex}$	M	I	$\%\dot{m}_{ex}$	M	I	$\%\dot{m}_{ex}$	M	I
Panel 1	3	6.6	13	4	3.1	9.3	3	3.7	14
Panel 2	7	4.6	7	9	2.8	7.8	7	2.8	8
Panel 3	7	2.4	3	9	2.6	6.9	7	2	4
Panel 4	3	1.9	1.5	4	1.8	3.3	3	1.2	1.5
Dilution Row 1	17.5	18	100	—	—	—	17.5	10	100
Dilution Row 2	17.5	7	20	—	—	—	17.5	4.5	20
Exit Slot	1.4	—	—	2.1	—	—	1.4	—	—

The aforementioned parameters, listed in Table 1, are believed to provide a flow field representative to that entering into the turbine. Since the Mach number is generally quite low ($Ma<0.1$) in the combustor, this parameter is not relevant. Another parameter not being matched is the coolant-to-mainstream density ratios, which are typically quite high (between two and three). Although the density ratios are not matched, the jet-to-mainstream momentum flux ratios and percentage of mass flow addition by both the film-cooling and dilution holes are being matched. The momentum flux ratio is the parameter that most affects mixing characteristics of jets in cross-flow. The film cooling hole patterns, shown in Fig. 3, were configured in equilateral triangles and spaced evenly across the panel surface. The diameter of the cooling holes was 0.76 cm giving an $L/D=3.3$.

The dilution hole diameters were also designed to insure the percent mass addition of the dilution fluid and coolant-to-mainstream momentum flux ratios were matched to that of the engine. This first row of dilution holes has three holes evenly spaced with the center hole being aligned with the center of the simulator (and also, when present, the vane stagnation) and located at 42% of the combustor length (0.68 m) downstream of the start of the panels. The dilution holes in the first row have a diameter that is 8.5 cm. The second row of dilution holes was located on the third panel at 56% of combustor length (0.9 m) downstream of the start of the panels. The second row of dilution holes contained two holes having a diameter 12.1 cm. The two dilution holes were staggered with the first row of holes (and also, when present, at the midpitch of the two passages in the vane cascade). As illustrated in Fig. 2(a), the supply chamber for the dilution flow was required to be some distance from the hole exits giving an L/D ratio of 1.5 for both rows. For both rows of dilution holes, the top and bottom dilution holes were aligned with one another in the span and streamwise directions. Many combustors are designed with a swirler followed by dilution holes producing an opposite sense of rotation as the swirl thereby reducing the overall exiting swirl. Since a swirler was not included in this study, the dilution holes were aligned with one another with the aim of having only a small exit swirl.

In addition to liner cooling holes and dilution holes, secondary coolant flow was added to the primary passage through a slot at the exit of the combustor section, which is shown in Fig. 4. The purpose of the feed holes is to control the coolant mass flow from the slot and to provide impingement cooling on the backside of the liner. The pin fins provide a conduction path from the liner to reduce the liner metal temperature. The percent mass flow

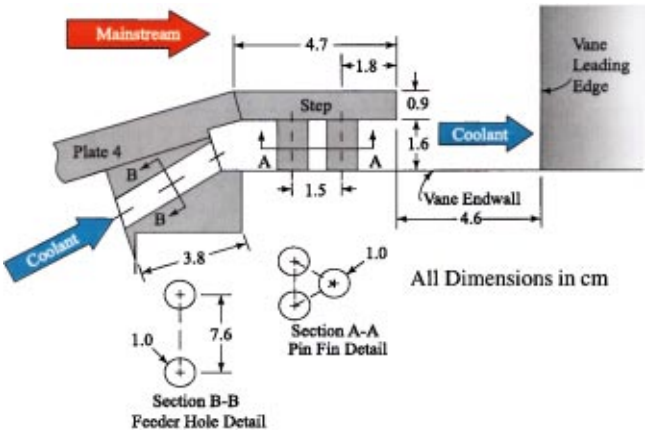

Fig. 4 Schematic illustrating the combustor liner exit slot

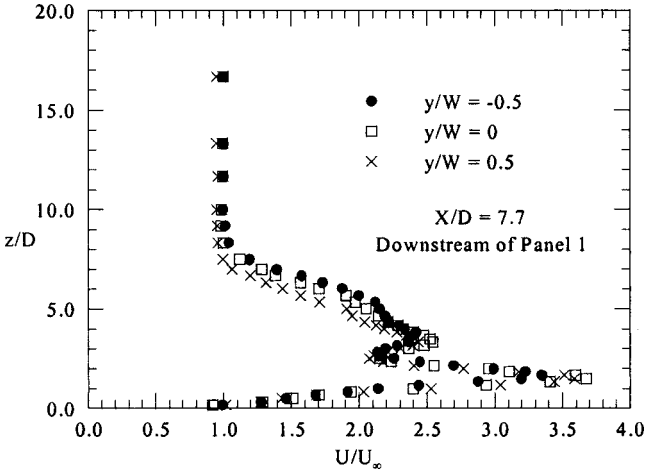

Fig. 6 Measured velocity profiles downstream of the first panel at three different spanwise positions

addition relative to the exit mass flow from this slot as well as all the panels was matched to that of the engine and is reported in Table 1.

Flow Control for the Liner Cooling, Dilution Holes, and Exit Slot. As indicated in Table 1, 44% of the flow from the fan is directed through the primary passage of the combustor simulator while 56% of the flow is directed through the secondary coolant passages to provide the flow for the liner coolant, dilution holes, and exit slot. The correct flows for each of the panels is set using previously determined discharge coefficients, the total pressure in each of the liner supply chambers ($P_{o,c}$), and the exit static pressure (p_∞). A number of experiments were conducted to evaluate the discharge coefficients for the liner cooling panels since it was suspected that an array of cooling holes would not necessarily have the same discharge coefficient as a single hole nor as a single row of holes. Measurements for the discharge coefficients were made using a laminar flow element (the true flow rate) the total pressure in the plenum, and the static pressure at the start of the film-cooling test plate.

To verify our capability in measuring discharge coefficients, comparisons were made to results presented in the literature by Burd and Simon [17]. Figure 5 shows these comparisons as well as the effect of the number of rows of film-cooling holes. Increasing the number of rows tends to slightly increase the discharge coefficient. This may be expected given the fact that as the number of rows of holes increases, the film layer increases causing a reduction in the resistance to the flow resulting in higher discharge coefficients.

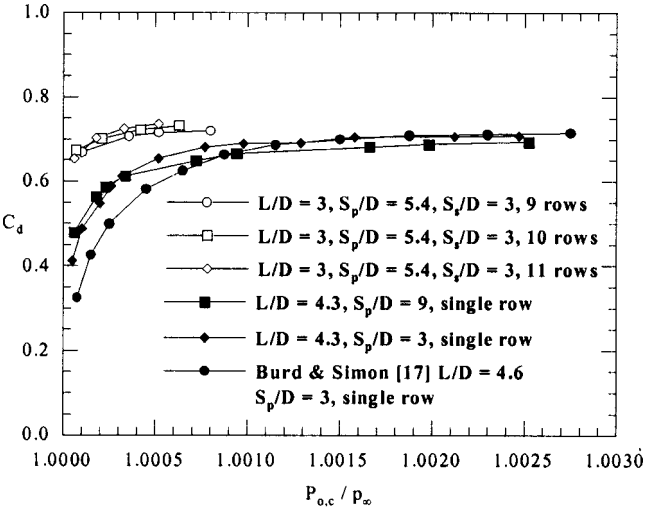

Fig. 5 Measured discharge coefficients of the film-cooling hole arrays

As mentioned earlier and indicated in Fig. 2(*a*), the flow to each of the liner panels comes from individually shutter-controlled supply chambers. Uniformity of the flow exiting the film-cooling holes for each panel was checked by taking a velocity profile with a hot-wire at the end of each panel liner. Figure 6 shows a representative sample of velocity profiles taken at three different spanwise locations downstream of the last row of film-cooling holes on the first panel. The data indicates uniformity among the holes and a double peak in the velocity profile resulting from the jet fluid from the upstream rows being pushed above the jet fluid exiting the last row of cooling holes.

The mass flow through the dilution holes were set by taking a velocity profile across the exit of the holes. There was a relatively large amount of flow exiting the dilution holes (35% of the total combustor exit flow) making it difficult to have a supply chamber large enough. The velocity profiles exiting the dilution holes were relatively flat, which allowed the flow rate for each dilution hole to be accurately calculated. The coolant flow rate through the slot was set by measuring the pressure drop across the feed holes shown in Fig. 4. Given that the feed holes were spaced significantly far apart (eight hole diameters), these feed holes were assumed to act as single holes having a discharge coefficient of 0.7.

Test Section Description. As discussed throughout this paper, the overall objective of these studies is to evaluate realistic combustor exit conditions on the development of the thermal and flow fields in a downstream turbine vane passage. Prior to making this evaluation for a turbine vane in which the flow experiences a large turning, a reference condition was chosen to be the combustor simulator followed by a straight test section with no vane present. By making adiabatic effectiveness measurements downstream of the combustor along a straight endwall with no turning, it provides a baseline for us to evaluate the maximum combustor liner coolant available for cooling the downstream platform. Because of the secondary flow patterns that develop in a vane passage, it is expected that this baseline would be somewhat higher than that which occurs in a vane passage.

The data presented in this paper is for the reference condition of a straight test section with no vane, as illustrated in Fig. 2(*e*). Note that for these measurements, the wind tunnel was converted to an open loop tunnel. This tunnel configuration had the advantage of allowing a long downstream test plate, but had the disadvantage of not allowing the use of a laser Doppler velocimeter due to the

seeding issue. The width and height of the downstream test section were 1.1 m and 0.55 m, respectively. The side and top walls were constructed from 1.27-cm thick acrylic. The bottom wall, which was the test plate, was a composite of 1.27-cm thick urethane foam ($k=0.037$ W/mK) on top with a 3.8-cm thick polystyrene plate as the next layer and a 1.9-cm plywood plate as the base. The top wall had a number of ports in which a crystal fluoride window could be placed for the infrared camera measurements.

Instrumentation and Uncertainty Estimates. Flow field data presented in this paper include measurements of the total pressure field and mean and turbulent velocities. Total pressure measurements were taken with a small Kiel probe having a head diameter of 1.6 mm. A small probe diameter was needed to insure good measurement resolution for the exit slot, which had a height of 16 mm. Streamwise mean velocity measurements were taken with a single hot-wire probe and a Pitot-static probe. Streamwise turbulence levels and length scales were measured using the single hot-wire probe. All of the pressure transducer and hot-wire voltages were converted to pressures and velocities using Labview software.

The mean thermal field and adiabatic surface temperatures were also measured. The thermal field data was collected using a rake having five type E thermocouples. The wire used to construct these thermocouples was 0.25 mm in diameter. To insure minimal conduction effects on the measured temperatures, the lead wires to the bead were bare thermocouple wires that were 6.35 mm long. The urethane foam test plate downstream of the combustor simulator was instrumented with type E thermocouples mounted flush with the surface. These measurements were compared with the surface temperatures measured using an infrared camera. When using the infrared camera, positioning crosses were placed on the endwall plate to scale and translate the pictures spatially. For each image, five pictures (with each picture being averaged over 16 frames) were needed to insure a good average for the surface temperatures. In some areas the pictures were overlapped resulting in a larger number of averages.

To set the flows in each of the supply chambers for the liners, pressure differences between the total pressure in the chamber and a static pressure at the start of the liner plate were measured. To insure the pressure taps were truly sensing the total and static pressures correctly, independent total and static pressures were compared to those made using a pitot-static probe. The differential pressure measurements for each of the supply chambers were read from calibrated transducers with a maximum range of 12.7 mm H_2O. As mentioned previously, the dilution flowrates were set by measuring the velocities at the exit of the dilution holes with a pitot-static probe. The pressure difference across the slot was measured using a transducer having a range of 127 mm H_2O.

The partial derivative and sequential perturbation methods, described by Moffat [18], were used to estimate the uncertainties of the measured values. Precision uncertainties were calculated based on a 95% confidence interval. For the streamwise velocities measured using the hot-wire, 100,000 samples were taken giving an uncertainty, including the bias and precision, of 1.8% for the mean velocity at a turbulence level of 14%. The precision uncertainty for the streamwise rms velocities was 2.6% at that same turbulence level. The integral length scales were calculated using eight samples of 80,000 data points taken at a sampling rate of 20,000 kHz giving a precision uncertainty of 15%. Each total pressure measurement used 60,000 data points to compute the mean values. The estimate of bias and precision uncertainties for the mean pressures, which were presented in non-dimensional form was 7.6% for a $\Delta P=-0.51$, which occurred in the near-wall region of interest. At lower ΔP values, the uncertainties were much higher such that for a $\Delta P=-0.14$, the uncertainty is 27%. The bias and precision uncertainties on the adiabatic effectiveness values, using the five-averaged pictures, was ± 0.038 giving an uncertainty of 6.5% at $\eta=0.59$. The thermal field contour uncertainties, including both bias and precision, at a level of $\theta=0.52$ was 8.2%.

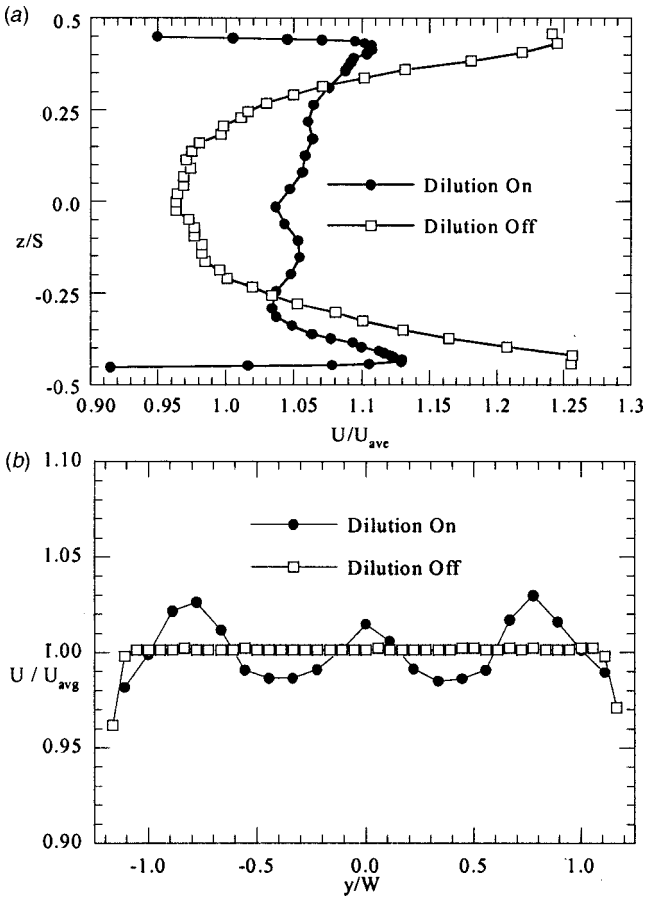

Fig. 7 Mean velocity profiles measured at the exit of the simulator in the span (*a*) and pitch (*b*) with, and without the dilution jets

Experimental Results

As previously mentioned, the data that will be presented in this paper is for the case with no turbine vane present downstream of the combustor simulator. The focus of the results in this paper is on the effects of the dilution jets with regards to the exiting downstream flow and thermal fields. The flow conditions for the two cases are given in Table 1. Note that the two flow conditions, i.e., dilution and no dilution, were achieved by maintaining nearly the same combustor exit velocity thereby requiring a higher inlet velocity for the combustor simulator in the no dilution case. Total pressure, mean and turbulent velocities, and the thermal field were measured in a plane normal to the flow direction either on top of the step or downstream of the slot with both locations being illustrated in Fig. 2(*b*). The downstream location corresponds to the stagnation location of the first vane (if it were present). The measurement plane on top of the step was located five cooling hole diameters upstream of the slot exit ($x/D=-5$, where x is measured from the slot exit), which is 14 cooling hole diameters downstream of the last row of cooling holes on the last panel. Adiabatic effectiveness measurements were made on the plate downstream of the slot.

Flow Field Results. For the conditions without the vane being present, the flow is expected to be symmetric about the midspan and about the midpitch of the test section. The midspan symmetry was verified experimentally and is shown in Fig. 7(*a*)

for the dilution and no dilution cases, while the midpitch symmetry is shown in Fig. 7(*b*). These profiles were taken at a streamwise distance of $x/D=-5$. The spanwise velocity profile (Fig. 7(*a*)) was taken at the midpitch location of the test section, which is aligned with the center of the dilution hole in the first row of dilution holes (and when present the stagnation location of the turbine vane). The pitchwise velocity profile was taken at the midspan of the test section. Note that $z/S=0.5$ corresponds to the endwall location and since this data was taken on top of the slot, the values measured at the wall correspond to a location that is slightly above zero at $z/S=0.455$.

Figure 7 shows very different velocity characteristics for the dilution on and off cases at this location. For the spanwise (radial) profile (Fig. 7(*a*)), the effect of the dilution jets was to flatten out the profile across the span relative to the no dilution case. It is clear that in both cases, there is still a higher speed fluid in the near wall resulting from the coolant injection. The pitchwise (circumferential) profiles (Fig. 7(*b*)), indicate a variation in the velocities for the dilution hole case. The lower velocities in Fig. 7(*b*) correspond to the locations of the second row of dilution holes. Although the second row of dilution jets has a lower momentum flux ratio than the first row of jets, the second row is directed somewhat upstream because of the angle of the third panel. This represents a flow blockage in the mainstream resulting in lower velocities.

Turbulence profiles, based on the measured streamwise rms levels and local mean velocities, are given in Figs. 8(*a*) and (*b*) for the same locations as given in Fig. 7. Since the geometry being used in this study is representative of a combustor, the exiting turbulence levels should be indicative of those found entering the turbine of an engine. Evidence in the literature suggests that the same turbulence levels exist whether combustion is present or not (Zimmerman [19] and Moss [20]). The effect of the dilution jets at this location is to elevate the turbulence level range to be between 15–18%. For the spanwise turbulence profile (Fig. 8(*a*)), the turbulence from the upstream film cooling holes in the near wall region affects the span as high as 25% for the no dilution case with the turbulence levels being higher in the near wall region. The effect of the dilution jets is such that the turbulence in the mainstream is higher than in the near wall region and with the decrease starting at 20% of the span. The pitchwise profiles in Fig. 8(*b*) show two peaks that correspond to the two dilution hole locations in the second row.

Also shown in Fig. 8(*b*) are the measured integral length scales across the pitch at the mid-span of the test rig. These integral length scales were normalized using the diameter of the dilution hole in the first row. As seen on Fig. 8(*b*), the length scale is on the order of the diameter of the dilution hole. It has long been a question among the turbine community as to what is the correct turbulent length scale to simulate. These results, along with the results previously reported by Moss [20], indicate that the integral length scale is a strong function of the dilution hole size. Also shown in Fig. 8(*b*) is an increase in the integral length scale at $y/W=0.25$, which corresponds to the second row of dilution holes. Note that the dilution hole diameter for the second row is 42% larger while the length scale in this region increased by 20%. These length scales can be compared to those simulated in the previous work by Radomsky and Thole [13,14]. While the length scales for the previous work were 10% of the turbine vane pitch, the length scales measured in the current study would be somewhat larger at 14% of the turbine vane pitch.

Figure 8(*c*) shows the energy spectra of the turbulence at the combustor exit for a location with the largest length scale and smallest length scale. While the spectra shows a typical $-5/3$ region and does agree with the von Karman spectra, the inertial subrange extends less than two decades. This is in contrast to the data previously reported by Radomsky and Thole [13] for a turbulence level of 19.5% achieved using their active turbulence generator grid. Results using the active grid showed an inertial subrange that extended slightly more than two decades. These results indicate that at this location the viscous dissipation occurs at lower wave numbers as compared with the active grid results.

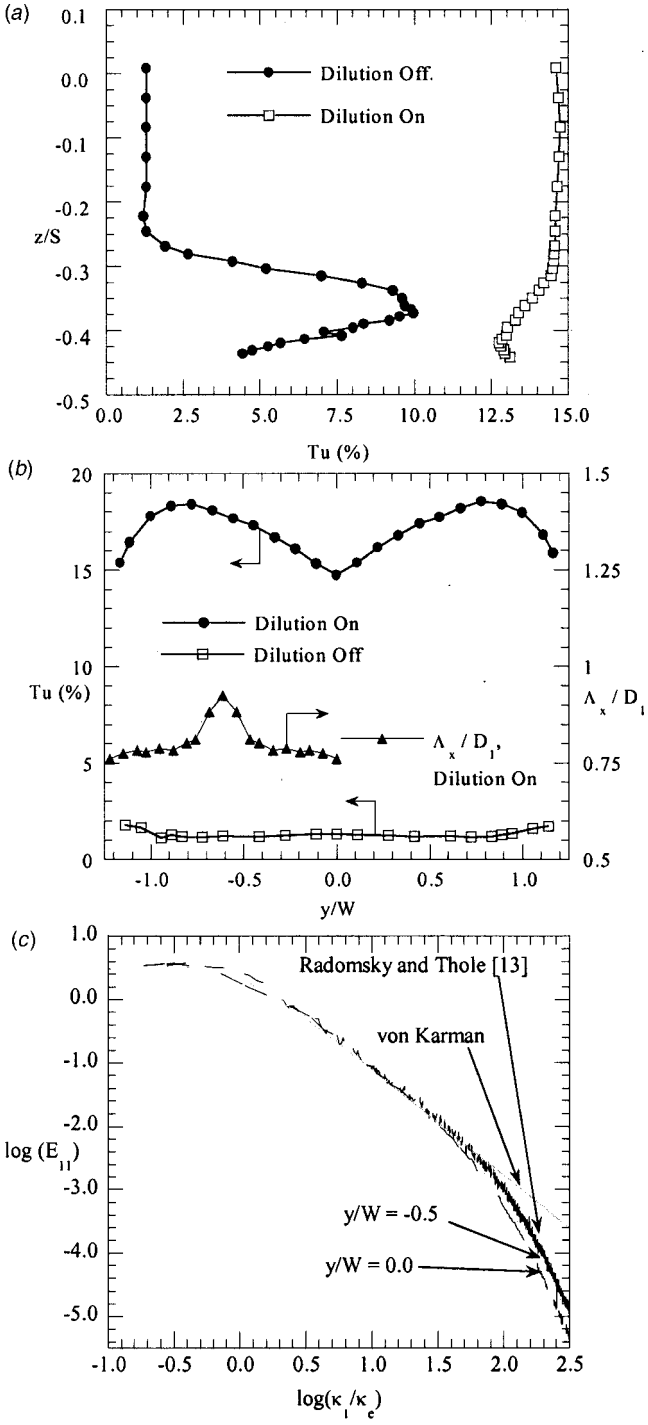

Fig. 8 Turbulence profiles measured at the exit of the combustor simulator in the span (*a*) and pitch (*b*), and streamwise velocity energy spectra (*c*)

Figure 9 shows contours of the normalized streamwise velocity and the local turbulence level for the dilution case. The measured contours given in Fig. 9 were in a plane that was one-quarter of a turbine sector in the pitch (y/W) direction and one-half of a turbine vane span in the Z/S direction. Note that this portion of the exit plane can be mirrored due to symmetry conditions. These measurements were made at a streamwise position relative to the

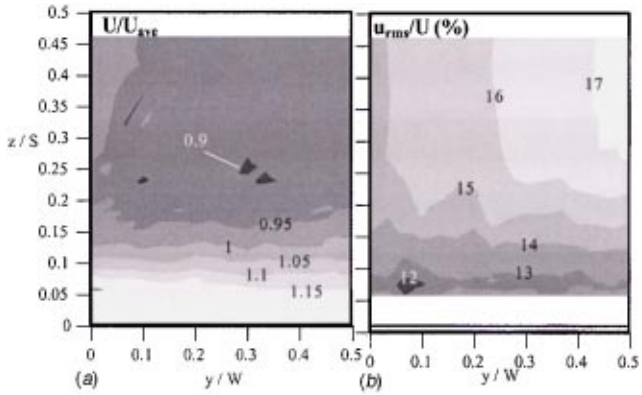

Fig. 9 Contours of normalized streamwise velocity (*a*) and turbulence levels upstream of the slot exit (*b*) for the dilution flow case

end of the slot at $x/D=-5$. Figure 9(*a*) still shows slight remnants of the dilution jets, but with a larger variation in the near wall region as a result of the film cooling injection. The turbulence level contours show a variation from the 14.5–18% with the peak aligned with the center of the dilution jet in the second row. Since the highest turbulence level is associated with the dilution hole, the highest turbulence level would be expected to be at the vane stagnation if the vane were clocked with a dilution hole. This is important to recognize in terms of the high heat transfer augmentation that would occur at the vane leading edge. In general, the lowest turbulence levels are in the near wall region.

As can be seen in Fig. 9 there is a large variation of the velocity and turbulence across the pitch (y/W). For this region, total pressures at the slot exit were measured at a position near the top of the slot. These total pressure variations are presented in Fig. 10 along with a schematic illustrating the feed holes and pin fin locations. The variation in total pressure is quite large and is somewhat periodic corresponding to the feed hole locations. CFD results (which are not presented in this paper) have indicated that the flow exiting the slot is dependent on how the feed holes are aligned with the pin fins and how the secondary flows from the dilution jets interact with the exit slot flow.

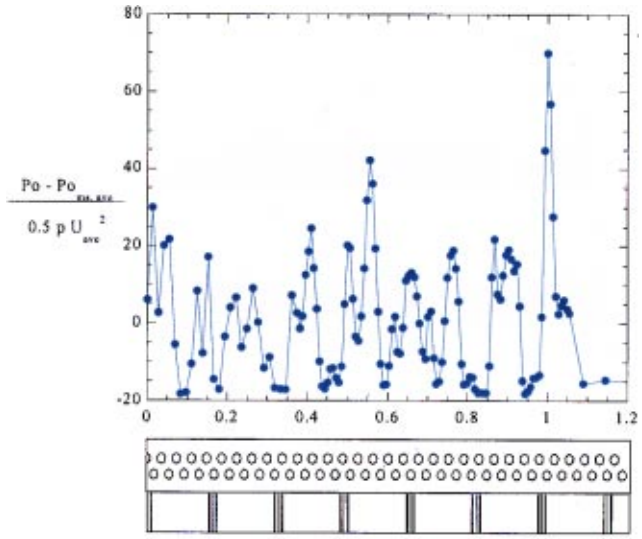

Fig. 10 The nonuniform total pressure profile across the pin-finned exit slot. Below the plot is an indication of where the pin fins and slot feeder holes are located.

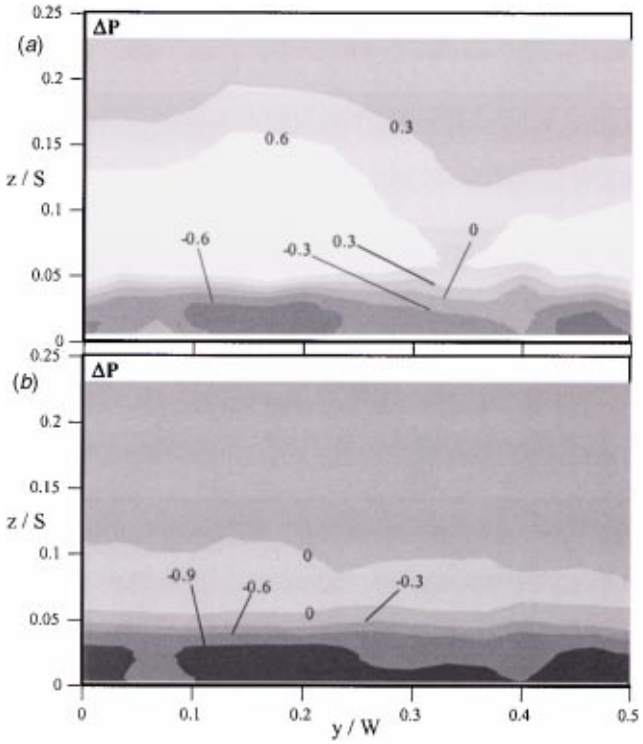

Fig. 11 Nondimensional total pressure profiles of the exit slot for the no dilution (*a*) and dilution cases (*b*)

Contours of the normalized total pressure for the no dilution and dilution cases are shown in Fig. 11. The location for these measurements corresponds to 2.9 step heights downstream of the slot. The differences between the no dilution and dilution cases are quite drastic. While in both cases the total pressure in the near wall region is the lowest pressure, the pressure variation above the slot location is much larger for the no dilution case than for the dilution case. These differences are caused by the effects of the dilution mixing and by the fact that there is a slightly higher momentum flux ratio for the jets exiting the last panel for the no dilution case. There is only a slightly higher total pressure region above the slot for the dilution flow case. The dilution flow enters the combustor with a relatively high total pressure, which in turn raises the total pressure in the primary flow path. As a result, the total pressure variation in the span direction (z/S) is reduced.

Figure 12 presents a pitchwise-averaged, nondimensional total pressure for the dilution and no dilution cases as compared with a total pressure profile if assuming a two-dimensional, turbulent boundary layer. The turbulent boundary layer profile is for a boundary layer having a thickness that is 9% of the span having an $\mathrm{Re}_\theta=3400$. Figure 12 indicates a larger variation for the no dilution case as compared with the dilution case. Neither of these profiles, however, are similar to what occurs for a turbulent boundary layer approaching the vane. Figure 12 indicates that there is an increase in the total pressure followed by a decrease as the wall is approached. It is expected that the resulting secondary flow pattern developing in the turbine would not be the same as that with a turbulent boundary layer.

Thermal Field Results. As mentioned previously in this paper, a heater in the primary flow path and heat exchangers in the secondary flow paths allow for thermal field simulations. For these experiments, the primary flow was heated to levels that were nominally 16°C above the coolant temperatures. The measured thermal fields for the no dilution and dilution cases are given in Fig. 13 for the downstream slot location. Note that the freestream temperature used in the thermal field normalization (θ) and for the

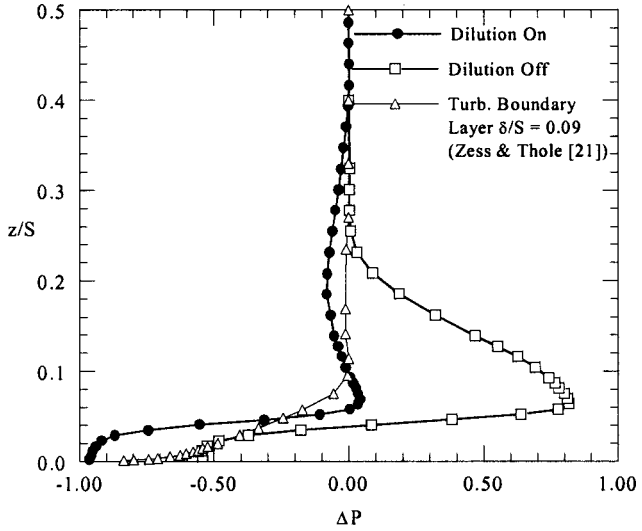

Fig. 12 Spatially averaged nondimensional total pressure profiles downstream of the combustor liner slot for the no dilution and dilution cases compared to a turbulent boundary layer [21]

adiabatic effectiveness levels (η) was based on the mass averaged temperature for the dilution flow case. Since much of the flow at the combustor exit is from either the cooling liner or from the dilution holes, the overall freestream temperature was reduced. To account for this reduced temperature, the mass averaged temperature was calculated and used with the coolant temperature as the driving temperature potential. For the no dilution flow, the freestream temperature used is the temperature of the flow just downstream of the heaters. For the case with no dilution, Fig. 13(*a*) shows that there is very good coverage of the downstream endwall plate. The spanwise extent of the $\theta = 0.7$ level was as high

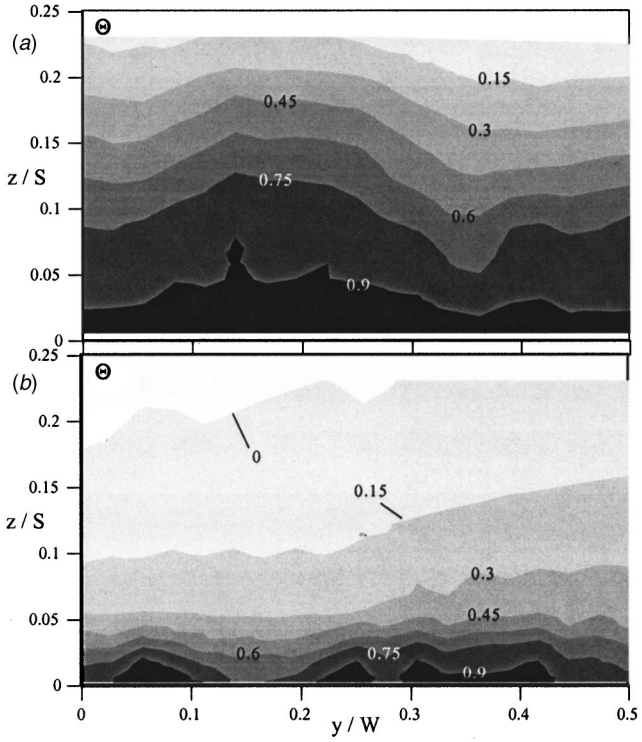

Fig. 13 Nondimensional thermal field contours after the exit slot for no dilution (*a*) and dilution (*b*)

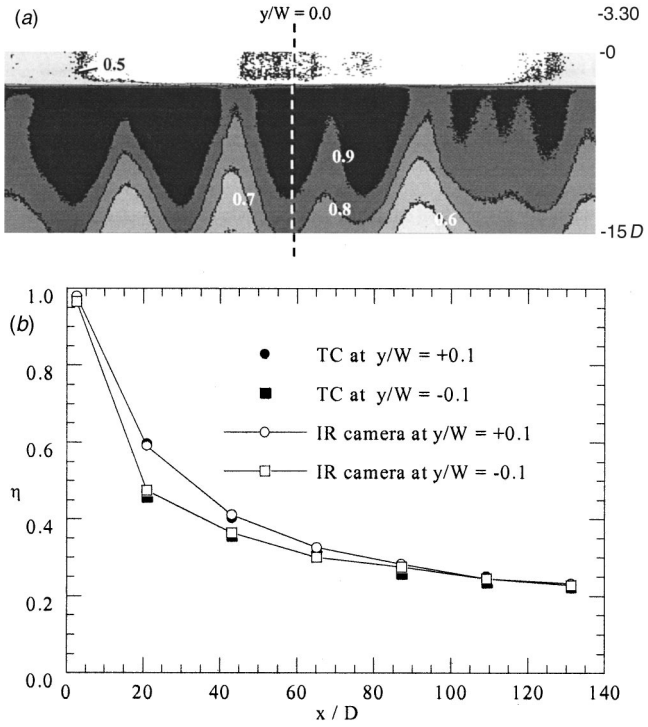

Fig. 14 Adiabatic effectiveness contours (*a*) and downstream levels (*b*) on the endwall for the case with dilution jets

as $z/S = 0.1$ for the no dilution case. In comparison, the case with dilution indicates much less coolant along the endwall as shown in Fig. 13(*b*). The thermal field for the dilution case also shows the slightly cooler temperatures apparent in the main flow as a result of the second row dilution jets.

Adiabatic effectiveness contours close to the slot exit are given in Fig. 14(*a*)(*b*) for the dilution flow case. Note that the first 3.3*D* streamwise distance are contour levels that were measured on top of the pin fin liner plate. The high adiabatic effectiveness levels (~0.5) are from the remnants of the upstream film-cooling holes on the pane. Downstream of the slot, it is quite apparent as to the non-uniformity of the slot exit flow based on the local adiabatic effectiveness levels. The levels just downstream of the slot are quite high even at the location where the leading edge of the vane would be placed ($x = L$).

Figure 14(*a*)(*b*) shows the downstream adiabatic effectiveness levels measured using an IR camera as compared with thermocouples (TC) that are embedded in the surface of the urethane foam endwall plate. There is good agreement between the IR camera and thermocouple measurements at the two different pitchwise positions. Note that both of these pitchwise positions are slightly off the centerline of the endwall test plate and do indicate some variation in the pitch. This is to be expected based on Fig. 14(*a*). At 100*D* downstream, the two different pitchwise measurements indicate the same level suggesting a more uniform coverage. To give a perspective on these distances, a streamwise distance of 130*D* (the last measurement location) corresponds to 1.8 true chord lengths downstream of the turbine vane. At 130*D* downstream, the adiabatic effectiveness levels are still 0.2 indicating that there is a potential for using the combustor liner fluid to cool the downstream turbine platform if there were no secondary flows present in the vane passage.

Conclusions

This paper describes the development of a scaled-up test rig that simulates the aft end of a gas turbine engine combustor. Flow and thermal field measurements were made at the exit of the simu-

lator to determine prototypical conditions for the downstream turbine. These tests were conducted with no turbine vane present to provide a baseline for comparison. With no downstream turbine vane present, the measured adiabatic effectiveness levels on the downstream endwall represent the best that could be achieved along the vane passage endwall if no secondary flows are present.

The results of these measurements put in question the accuracy in assuming either a constant total pressure field or a turbulent boundary layer approaching the turbine vane-endwall juncture. The total pressure field measurements clearly showed a profile much different than would be present for either of the two previously stated assumptions. While the effect of the dilution jets was to reduce the variations in the total pressure and velocity field, there was still some variation in the near-wall region. The measured turbulence indicates that levels entering the turbine for this type of configuration are between 15–18%. The results in this paper also indicate that the length scale of the turbulence scales closely with the turbulence producing mechanism, namely the dilution hole diameter. This latter result is important because generally the dilution hole diameter is known for a particular turbine engine design thus providing information for more accurate heat transfer predictions.

The thermal field contours indicated that the dilution jets increased the mixing of the coolant exiting the slot and the upstream film cooling holes, thereby reducing the coolant available for cooling the downstream platform. Although there was a reduction, the adiabatic effectiveness levels along the downstream platform were still quite high at what would be one chord downstream of the slot exit if the vane were present.

Acknowledgments

The authors gratefully acknowledge United Technologies—Pratt & Whitney for their support of this work. Guidance was received throughout this project from A. Cheung, A. Kohli, M. Ondus, F. Soechting, J. Wagner, and G. Zess.

Nomenclature

ALP = air loading parameter, $\mathrm{ALP}=P_o^{1.75}A_{\mathrm{ref}}D_{\mathrm{ref}}^{0.75}e^{T/300}/\dot{m}$
C = true chord of stator vane
C_d = discharge coefficient, $C_d=\dot{m}/A_{\mathrm{hole}}\sqrt{2\rho(P_{o,c}-p_\infty)}$
D = film cooling hole diameter
D_1, D_2 = dilution hole diameters for first and second rows
$E(\kappa)$ = energy spectra of streamwise fluctuations
E_{11} = defined as $E_{11}=2\pi E(\kappa)/u_{\mathrm{rms}}^2\Lambda_x$
f = frequency
H = test section height
I = momentum flux ratio, $I=\rho_c U_c^2/\rho_\infty U_\infty^2$
K = acceleration parameter defined as $K=(\nu dU_\infty/dx)/U_\infty^2$
k = thermal conductivity
L = film cooling hole length
$\dot{m}$ = mass flow rate
M = mass flux ratio, $M=\rho_c U_c/\rho_\infty U_\infty$
P = vane pitch
P_o, p = total and static pressures
R = gas constant
Re = Reynolds no. defined as $\mathrm{Re}=CU_\infty/\nu$
s = surface distance along vane measured from flow stagnation
S = span of stator vane
S_s, S_p = streamwise, pitchwise film cooling hole spacing
T = temperature
T_{inf} = mass averaged freestream temperature
Tu = turbulence level defined as u_{rms}/U
u_{rms} = root mean square of velocity fluctuations
U = local, mean streamwise velocity component
W = turbine sector width
X,Y,Z = global coordinates defined in Fig. 2(*a*)
x,y,z = local coordinates
η = adiabatic effectiveness, $\eta=(T_{\mathrm{inf}}-T_{\mathrm{aw}})/(T_{\mathrm{inf}}-T_c)$
η_θ = loading parameter, $\dot{m}/(\mathrm{Vol}\ P_o^{1.8}10^{0.00145(T-400)})$
κ = wave number, $\kappa=2\pi f/U$
ΔP = nondimensional pressure, $\Delta P=(P_o-\overline{P_{o,\mathrm{ms}}})/(0.5\rho U_{\mathrm{ave}}^2)$
Λ_x = integral length scale
ρ = density
ν = kinematic viscosity
θ = nondimensional temperature, $\theta=(T_{\mathrm{inf}}-T)/(T_{\mathrm{inf}}-T_c)$

Subscripts

1,2 = dilution row 1 and 2
ave = spatial average
aw = adiabatic wall
in = inlet location of combustor simulator
ms = midspan
ref = combustor reference dimensions
rms = root mean square
ex = exit location of combustor simulator
inf, ∞ = freestream conditions
c = coolant conditions

References

[1] Langston, L. S., 1980, "Crossflows in a Turbine Cascade Passage," ASME J. Eng. Power, **102**, p. 866.
[2] Kang, M., and Thole, K. A., 2000, "Flowfield Measurements in the Endwall Region of a Stator Vane," ASME J. Turbomach., **122**, pp. 458–466.
[3] Munk, M., and Prim, R. C., 1947, "On the Multiplicity of Steady Gas Flows Having the Same Streamline Pattern," Proc. National Academy of Sciences, **33**.
[4] Shang, T., and Epstein, A. H., 1997, "Analysis of Hot Streak Effects on Turbine Rotor Heat Load," ASME J. Turbomach., **119**, pp. 544–553.
[5] Hermanson, K., and Thole, K. A., 2000, "Effect of Inlet Profiles on Endwall Secondary Flows," J. Propul. Power, **16**, pp. 286–296.
[6] Butler, T. L., Sharma, O. P., Joslyn, H. D., and Dring, R. P., 1989, "Redistribution of an Inlet Temperature Distortion in an Axial Flow Turbine Stage," J. Propul. Power, **5**, pp. 64–71.
[7] Shang, T., Guenette, G. R., Epstein, A. H., and Saxer, A. P., 1995, "The Influence of Inlet Temperature Distortion on Rotor Heat Transfer in a Transonic Turbine," AIAA Paper No. 95- 36318.
[8] Stabe, R. G., Whitney, W. J., and Moffitt, T. P., 1984, "Performance of a High-Work Low Aspect Ratio Turbine Tested with a Realistic Inlet Radial Temperature Profile," NASA Technical Memorandum 83655, AIAA Paper No. 84-1161.
[9] Burd, S., and Simon, T., 2000, "Effects of Slot Bleed Injection Over a Contoured Endwall on Nozzle Guide Vane Cooling Performance: Part I—Flow Field Measurements," ASME Paper No. 2000-GT-199.
[10] Burd, S., Satterness, C., and Simon, T., 2000 "Effects of Slot Bleed Injection Over a Contoured Endwall on Nozzle Guide Vane Cooling Performance: Part II—Thermal Measurements," ASME Paper No. 2000-GT-200.
[11] Soechting, F. O., and Cheung, A., 1999, private communication at Pratt & Whitney.
[12] Kang, M., Kohli, A., and Thole, K. A., 1999, "Heat Transfer and Flowfield Measurements in the Leading Edge Region of a Stator Vane Endwall," ASME J. Turbomach., **121**, pp. 558–568.
[13] Radomsky, R., and Thole, K. A., 2000, "Highly Turbulent Flowfield Measurements Around a Stator Vane," ASME J. Turbomach., **122**, pp. 255–262.
[14] Radomsky, R., and Thole, K. A., 2000, "High Freestream Turbulence Effects in the Endwall Leading Edge Region," ASME J. Turbomach. (2000-GT-202), **122**, pp. 699–708.
[15] Lefebvre, A. H., 1998, *Gas Turbine Combustors*, Taylor and Francis, New York, NY.
[16] Walsh, P. P., and Fletcher, Pl, 1998, *Gas Turbine Performance*, Blackwell Science LTD, NJ.
[17] Burd, S., and Simon, T., 1999, "Measurements of Discharge Coefficients in Film Cooling," ASME J. Turbomach., **121**, pp. 243–248.
[18] Moffat, R. J., 1988, "Describing the Uncertainties in Experimental Results," Electronics, **1**, pp. 3–17.
[19] Zimmerman, D. R., 1979, "Laser Anemometer Measurements at the Exit of a T63-C20 Combustor," National Aeronautics and Space Administration, NASA Lewis Research Center, Contract NAS 3-21267.
[20] Moss, R. W., 1992, "The Effects of Turbulence Length Scale on Heat Transfer," University of Oxford, Department of Engineering Science, Report No. OUEL 1924, Ph.D. dissertation.
[21] Zess, G. A., and Thole, K. A., 2002, "Computational Design and Experimental Evaluation of a Leading Edge Fillet on a Gas Turbine Vane," ASME J. Turbomach. (2001-GT-404), **124**, pp. 167–175.